Reconciling fundamental climate variables for determining the Antarctic Mass Balance

Hansen, Nicolaj

Publication date:
2022

Document Version
Publisher's PDF, also known as Version of record

Citation (APA):
Hansen, N. (2022). *Reconciling fundamental climate variables for determining the Antarctic Mass Balance*. Technical University of Denmark.

DTU Space
Department of Geodesy and Earth Observation

Reconciling fundamental climate variables for determining the Antarctic Mass Balance

Nicolaj Hansen PhD Thesis

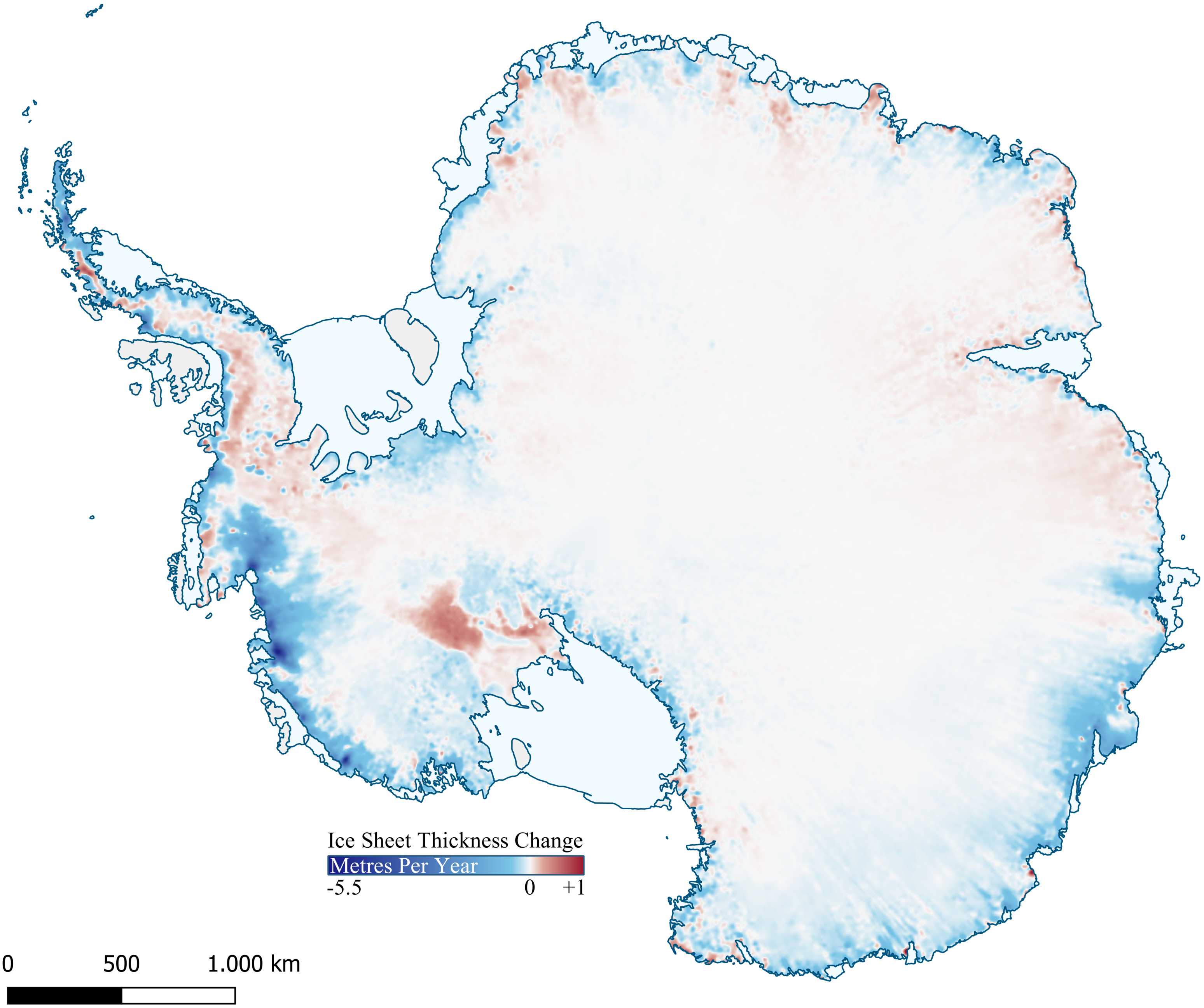

Reconciling fundamental climate variables for determining the Antarctic Mass Balance

PhD Thesis
August, 2022

By
Nicolaj Hansen

Supervision:
Dr. Sebastian Bjerregaard Simonsen, DTU Space
Dr. Ruth Mottram, DMI (Co-supervisor)
Prof. Rene Forsberg, DTU Space (Co-supervisor)

Published by: DTU, Department of Geodesy and Earth Observation, Elektrovej, Building 327, 2800 Kgs. Lyngby Denmark
www.space.dtu.dk

Preface

This thesis was made at the National Space Institute at the Technical University of Denmark (DTU Space) in close collaboration with the Danish Meteorological Institute (DMI), as a part of the completion of the degree of Doctor in Philosophy. The PhD project took place between September 2019 and August 2022 under the supervision of Senior Researcher Sebastian Bjerregaard Simonsen, DTU Space, Senior Climate Scientist Ruth Mottram, DMI, and Professor Rene Forsberg, DTU Space.

Dansk Resume

Afstemning af fundamentale klimavariabler til bestemmelse af den antarktiske massebalance

Den antarktiske iskappe er den største iskappe på Jorden. Den har, hvis isen smelter fuldstændigt, potentialet til at hæve det globale middelhavniveau med 58 meter. Nye studier har vist, at selvom iskappen endnu ikke er den største bidragsyder til nutidens havniveaustigninger, har den antarktiske iskappe øget sit massetab i perioden mellem 1993 og 2018. Derfor er det vigtigt at overvåge og forstå hvordan iskappen på Antarktis udvikler sig.

Denne Ph.D. afhandling fokuserer på at kvantificere klimavariable for at estimere overflademassebalancen og den totale massebalance over Antarktis. Overflademassebalancen er summen af akkumulation (nedbør som både sne og regn) og ablationen (sublimering, fordampning og afstrømning). Overflademassebalancen kan beregnes ud fra numeriske modeller, som i denne afhandling, hvor der bruges en regional klimamodel til at modellere atmosfæren. Ydermere bruges en model der repræsenterer overgangen fra sne til is for at få en realistisk repræsentation af firnen på den antarktiske iskappe. Vi undersøger desuden usikkerheden på den modellerede overflademassebalance fra forskellige regionale klimamodeller. Man anvender typisk tre geodætiske metoder til at estimere massebalancen fra telemåling: altimetri, massebudget og gravimetrisk målinger. To af disse, altimetri og massebudget, kræver kendskab til firnen på iskappen. Når massebudgetmetoden bruges til at estimere massebalancen skal man kende overflademassebalancen og massetabet fra isbjerge der kælver og smeltevand. Overflademassebalancen er her beregnet til at være 1968.0$\pm$279.3 gigaton per år over den del af Antarktis der ligger på grundfjeldet. Overflademassebalancen over den samlede antarktiske iskappe findes til 2574.4 gigaton per år i perioden 1979 til 2021.

I altimetrimetoden anvendes satellitdata fra ICESat-2 til at måle overfladens højdeændringer. For at isolere overfladens højdeændringen, som skyldens isdynamiske signaler, skal der korrigeres for firnens komprimeringshastighed. Denne beregnes med firnmodellen samt en model for den lodrette bevægelse af grundfjeldet under isen. Når vi har korrigeret for signaler, det ikke skyldes isens dynamik, kan vi konvertere volumenændringen til en masseændring såfremt den korrekte konverteringdensitet er kendt. Denne afhandling præsenterer desuden igangværende arbejde med parametrisering af densiteten, som skal anvendes til at opnå en realistisk konvertering fra volumen- til masseændring af Antarktis' iskappe i perioden 2018 til 2021. Endelig præsenteres udvalgte resultater for Grønlands Indlandsis med det formål at vise hvordan metoderne fra dette studie kan anvendes for begge iskapper.

Summary

The Antarctic ice sheet is the largest ice sheet on Earth, it has the potential to raise the global mean sea level by 58 metres if it melts completely. Even though it is not the largest contributor to present-day sea level rise, recent studies have shown that the Antarctic ice sheet has increased its mass loss between 1993 and 2018. It is therefore important to monitor and understand how the ice sheet evolves to understand present and future rates of sea level rise.

This Ph.D. thesis focuses on reconciling climate variables to estimate the surface mass balance and the total mass balance of Antarctica. The surface mass balance is the sum of the accumulation (snowfall and rainfall), and the ablation (sublimation, evaporation, and runoff). Total mass balance includes both SMB and the discharge across the grounding line. In this thesis, a regional atmospheric climate model is used to model the atmosphere and the output used to compute the surface mass balance. To get a realistic representation of the subsurface snow and ice layers, a firn model has also been developed for the Antarctic ice sheet. This thesis investigates the uncertainties in modelled mass balance from different regional climate models and different methods. There are three geodetic methods to derive the mass balance from remote sensing; altimetry, mass budget, and gravimetric measurements. Two of these, altimetry and mass budget, require knowledge of the firn pack over the ice sheet. When using the mass budget method to estimate the mass balance the surface mass balance and the discharge values are need. The surface mass balance is here found to be 1968.0 ± 279.3 Gt year^{-1} over the grounded part of Antarctica and over the total Antarctic ice sheet it is 2574.4 Gt year^{-1} from the period 1979 to 2021.

Applying the altimetry method, the satellite ICESat-2 has been used to measure the surface elevation change. To isolate the surface elevation change, that is due the ice dynamics, we have to correct for the firn compaction rate, for which we use the firn model, and correct for the vertical bedrock movement. When we have corrected for the non-ice dynamic signals we can convert the volume change to mass change if the correct conversion density is known. This thesis therefore also presents new work for determining the appropriate density parametrization to be able to make a realistic conversion from volume change to mass balance change of the Antarctica ice sheet between 2018 and 2021. Finally, this thesis also shows some results for the Greenland ice sheet to show the applicability of the methods of this thesis for both ice sheets.

Publication list

Paper I: Mottram, R., **Hansen, N**., Kittel, C., van Wessem, J. M., Agosta, C., Amory, C., Boberg, F., van de Berg, W. J., Fettweis, X., Gossart, A., van Lipzig, N. P. M., van Meijgaard, E., Orr, A., Phillips, T., Webster, S., Simonsen, S. B., and Souverijns, N.: What is the surface mass balance of Antarctica? An intercomparison of regional climate model estimates, The Cryosphere, 15, 3751–3784, https://doi.org/10.5194/tc-15-3751-2021, 2021.

Paper II: Hansen, N., Langen, P. L., Boberg, F., Forsberg, R., Simonsen, S. B., Thejll, P., Vandecrux, B., and Mottram, R.: Downscaled surface mass balance in Antarctica: impacts of subsurface processes and large-scale atmospheric circulation, The Cryosphere, 15, 4315–4333, https://doi.org/10.5194/tc-15-4315-2021, 2021.

Paper III: Hansen, N., Simonsen, S. B., Boberg, F., Kittel, C., Orr, A., Souverijns, N., van Wessem, J. M., and Mottram, R.:Brief communication: Impact of common ice mask in surface mass balance estimates over the Antarctic ice sheet, The Cryosphere, 16, 711–718, https://doi.org/10.5194/tc-16-711-2022, 2022.

MC Paper I: Verjans, V., Leeson, A. A., McMillan, M., Stevens, C. M., van Wessem, J. M., van de Berg, W. J., van den Broeke, M. R., Kittel, C., Amory, C., Fettweis, X., **Hansen, N.**, Boberg, F., and Mottram, R.,Uncertainty in East Antarctic Firn Thickness Constrained Using a Model Ensemble Approach, Geophysical Research Letters, 48, 7, https://doi.org/10.1029/2020GL092060, 2021.

MC Paper II: Boberg, F., Mottram, R., **Hansen, N.**, Yang, S., and Langen, P. L., Uncertainties in projected surface mass balance over the polar ice sheets from dynamically downscaled EC-Earth models, The Cryosphere, 16, 1, 17–33, 10.5194/tc-16-17-2022,2022.

MC Paper III: Orr, A., Deb, P., Clem, K., Gilbert, E., Boberg, F., Bromwich, D., Colwell, S., **Hansen, N.**, Lazzara, M., Mottram, R., Niwano, M., Phillips, T., Pishniak, D.,d Reijmer, C., van de Berg, W.J., Webster, S., and Zou, X., Summer air temperature extremes over Antarctic ice shelves and potential “hotspots” of surface melting, Journal of Climate, 2022, accepted.

Draft I: Hansen, N., Orr, A., Zou, X., Mottram, R., Gilbert, E., Boberg, F., Simonsen, S. B., Phillips, T., Webster, S., and Bracegirdle, T., Benefits of using a sophisticated standalone snow scheme to simulate a surface melt event over the Ross Ice Shelf, West Antarctica in the HIRHAM5 and MetUM regional atmospheric models, in preparation to Atmospheric Science Letters.

Draft II: Bunde, C., Mottram, R., Boberg, F., **Hansen, N.**, Hvidberg, C., Gierisch, A., and Guo, C., High Resolution Simulations of Eemian Climate in Greenland, in preparation.

Acknowledgements

I would like to express my sincere gratitude to my supervisors Sebastian Bjerregaard Simonsen, Ruth Mottram, and Rene Forsberg, for their help and guidance both at the office and during the periods of working from home.

I would also like to thank all the colleagues at DTU Space and DMI for all the inspiring conversations around the coffee machine and the lunch table.

Furthermore, I would like to thank all the people that made it possible for me to go to the British Antarctic Survey during my external stay. Especially, Andrew Orr who supervised me at BAS and Danny Buss who housed me during my stay in Cambridge.

I would like also to thank my family and friends for all their support during this journey. Finally, to all my peers, thank you for showing me the way in life. I finally got a grip when I learned to let go.

Dearest Thomas,
No words can honour your struggles,
No wishes will bring you back,
Sometimes we lose our way and stop dreaming,
But you gave me the strength to do what I believe in,
Take the thesis, as my eternal gift to you, my cousin.
I hope you found your peace,
It could have been any of us.

Acronyms

AIS Antarctic Ice Sheet.
AP Antarctic Peninsula.
ATLAS Advance Topographic Laser Altimeter System.

D Discharge.

EAIS East Antarctic Ice Sheet.
ELA Equilibrium Line Altitude.
ER Elastic Rebound.
ESM Earth System Model.

GCM General Circulation Model.
GHG Green House Gas.
GIA Glacial Isostatic Adjustment.
GRACE Gravity Recovery and Climate Experiment.
GRACE-FO Gravity Recovery and Climate Experiment Follow On.
GrIS Greenlandic Ice Sheet.

ICESat-2 Ice, Cloud and land Elevation Satellite 2.

MB Mass Balance.

RCM Regional Climate Model.
RCP Representative Concentration Pathways.
RMSE Root-Mean-Square Error.

SAM Southern Annular Mode.
SEC Surface Elevation Change.
SLE Sea Level Equivalent.
SLR Sea Level Rise.
SMB Surface Mass Balance.
SMRT Snow Microwave Radiative Transfer.
SSP Shared Socioeconomic Pathways.

WAIS West Antarctic Ice Sheet.
we Water Equivalent.

Contents

1 Introduction

This thesis will reconcile different climate processes that are important for the Antarctic mass balance, through the use of climate models and remote sensing. Furthermore, this thesis quantifies the spread and uncertainties in the present numerical models of the Antarctic climate and how this is projected into the future. Some Greenlandic results in a few of the papers are also presented, to show that not all methods are specific for Antarctica.

1.1 Motivation

The global sea level has risen on average 3 mm per year since the early 1990's (Horwath et al., 2022; Nerem et al., 2018), with an acceleration of 0.12 ± 0.07 mm year^{-2} between 1993 and 2017 (Ablain et al., 2019). Climate projections estimate that the sea level will continue to rise (Slater et al., 2020). As described in the sixth assessment report of the intergovernmental panel on climate change (Fox-Kemper et al., 2021), it is estimated that the global sea level will rise between 0.28 m for the low Green House Gas (GHG) scenario (Shared Socioeconomic Pathways (SSP)1-1.9) and up to 1.01 metres for the high GHG (SSP5-8.5) scenario by year 2100. Furthermore, it cannot statistically be ruled out that sea level will rise by up to 5 metres by year 2150 under the high GHG (SSP5-8.5) scenario (Fox-Kemper et al., 2021; Lee et al., 2021). Studies from (Slater et al., 2020; Slater & Shepherd, 2018) suggests that currently mass loss from Greenland and Antarctica is following the high GHG scenarios. Kulp and Strauss, 2019 estimates that 230 million people lives within a metre of present-day sea level, so if the projections hold Sea Level Rise (SLR) will have unprecedented consequences for coastal societies, with an estimated impact on a billion people at the end of this century (Hauer et al., 2020), with a cost of trillions of dollars to mitigate (Jevrejeva et al., 2018).

The sea level can rise from thermal expansion, glaciers and ice sheets mass loss and changes in land water storage (Fox-Kemper et al., 2021). In the period from 1993-2018, 8.6% of the SLR came from Antarctic ice mass loss and from 2006-2018 it rose to 10.2% (Fox-Kemper et al., 2021). Even though Antarctica is not yet the main contributor to SLR, it is still very important because the Antarctic Ice Sheet (AIS) is the largest body of fresh water on Earth; it contains enough water to raise global sea level by $\approx$ 58 m (Fretwell et al., 2013; Morlighem et al., 2020). As tabulated in Tab. 1.1 this contribution can be split into the different regions of the continent (see Fig. 1.1 for region).

Region	SLE [m]
Antarctic ice sheet	57.9-58.3
Antarctic Peninsula (AP)	0.2-0.27
West Antarctic Ice Sheet (WAIS)	4.3-5.3
East Antarctic Ice Sheet (EAIS)	52.2-53.3

Table 1.1: Shows the ice volume in Sea Level Equivalent (SLE) for different regions in Antarctica (Fretwell et al., 2013; Morlighem et al., 2020).

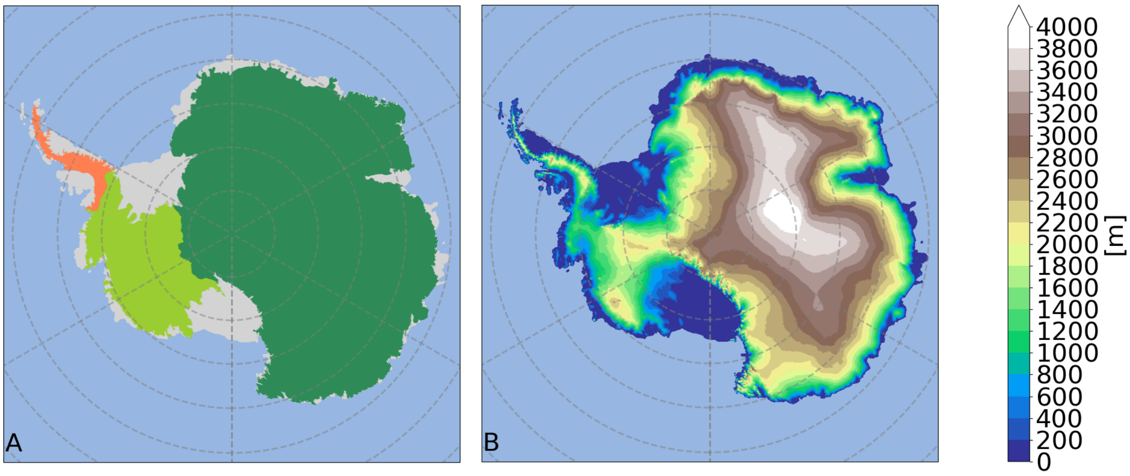

Figure 1.1: Panel A shows the different regions of Antarctica, from left to right, the grounded Antarctic Peninsula (AP) (orange), the grounded West Antarctic Ice Sheet (WAIS) (light green), and the grounded East Antarctic Ice Sheet (EAIS) (dark green), defined by Zwally et al., 2012. The gray coloured areas are the ice shelves defined by Gerrish et al., 2021. Panel B shows the topography from the reference elevation model of Antarctica data set (Howat et al., 2019). The colour bar only applies to panel B.

It should also be stressed that the mass loss from ice sheets does not give a globally uniform SLR. Mass loss leads directly to changes in the gravitational field, a mass loss in Antarctica results in the Northern Hemisphere becoming relatively heavier and thus having a relatively larger gravitational attraction to the ocean water compared to the Southern Hemisphere. Hence, a mass loss from the AIS will give the largest effect on SLR in the Northern Hemisphere and vice versa for the Greenlandic Ice Sheet (GrIS) mass loss (Forsberg et al., 2017). Figure 1.2 shows the SLR fingerprint from the Antarctic contribution between 2002 and 2016.

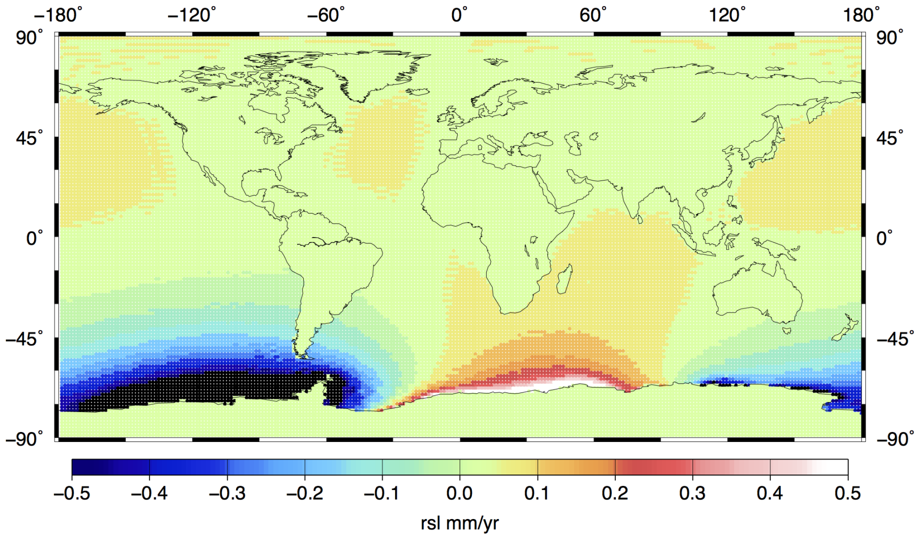

Figure 1.2: SLR distribution from the Antarctic contribution gives an integrated positive signal in the Northern Hemisphere and an integrated negative signal in the Southern Hemisphere. The data is derived from GRACE between 2002 and 2016 and is in mm per year, data can be found in Horwath et al., 2022. Figure courtesy of V. Barletta (DTU Space).

1.1.1 Objectives of the project

The objective of this project is to investigate the current state of the AIS with a focus on the Surface Mass Balance (SMB) and Surface Elevation Change (SEC) by doing the following:

- Assess present-day SMB estimations from Regional Climate Models (RCMs), and their internal variability over Antarctica (**Paper I, III**).
- Tailor and develop a firn model for the AIS (**Paper II**).
- Evaluate important processes in the surface climate in Antarctica (**Draft I, MC Paper I, II, III**).
- Apply SEC from satellites to determine the Mass Balance (MB) of ice sheets (**Work in progress**).

The project is described in this thesis and its structure is as follows; Chap. 1 introduces the thesis, furthermore, it goes into more details about MB estimations and modelling, which were in some cases left out of the papers. Chapter 2 is a summary of the papers that this thesis has contributed to. Chapter 3 is a work in progress chapter on using altimetric observations to compute the SEC and the challenges with converting it to mass changes. Chapter 4 discusses and combines the papers and outline ideas for future work, and finally Chap. 5 concludes the thesis. All papers that are summarized in Chap. 2 can be found in the appendix.

1.2 Estimating the mass balance

The MB describes whether an ice sheet is losing or gaining mass. The MB is expressed in Eq. (1.1), where SMB is the surface mass balance and D is discharge. The SMB (Eq. (1.2)) is the sum of the accumulation (snowfall (Sf) and rainfall (Rf)) and ablation (sublimation (S), evaporation (E), and runoff (RO)). Normally an ice sheet can be divided into an accumulation zone and an ablation zone, where they meet is called the equilibrium line. Below this line, the yearly mean SMB is negative and above the yearly mean SMB is positive. However, in the current climate, most of the grounded AIS have a positive yearly mean SMB. The positive contributions to the MB are snowfall, and rainfall, the negative contributors are sublimation, runoff and discharge. Figure 1.3 illustrates the different variables. Discharge is here defined as ice that has crossed for grounding line, and thereby no longer contributes to SLR.

$$MB = \frac{\delta M}{\delta t} = SMB - D \tag{1.1}$$

$$SMB = Sf + Rf - S - E - RO \tag{1.2}$$

There are three geodetic methods to derive the MB from remote sensing; altimetry, mass budget, and gravimetric measurement (Van den Broeke et al., 2011), only the latter does not include model outputs from (regional) climate models.

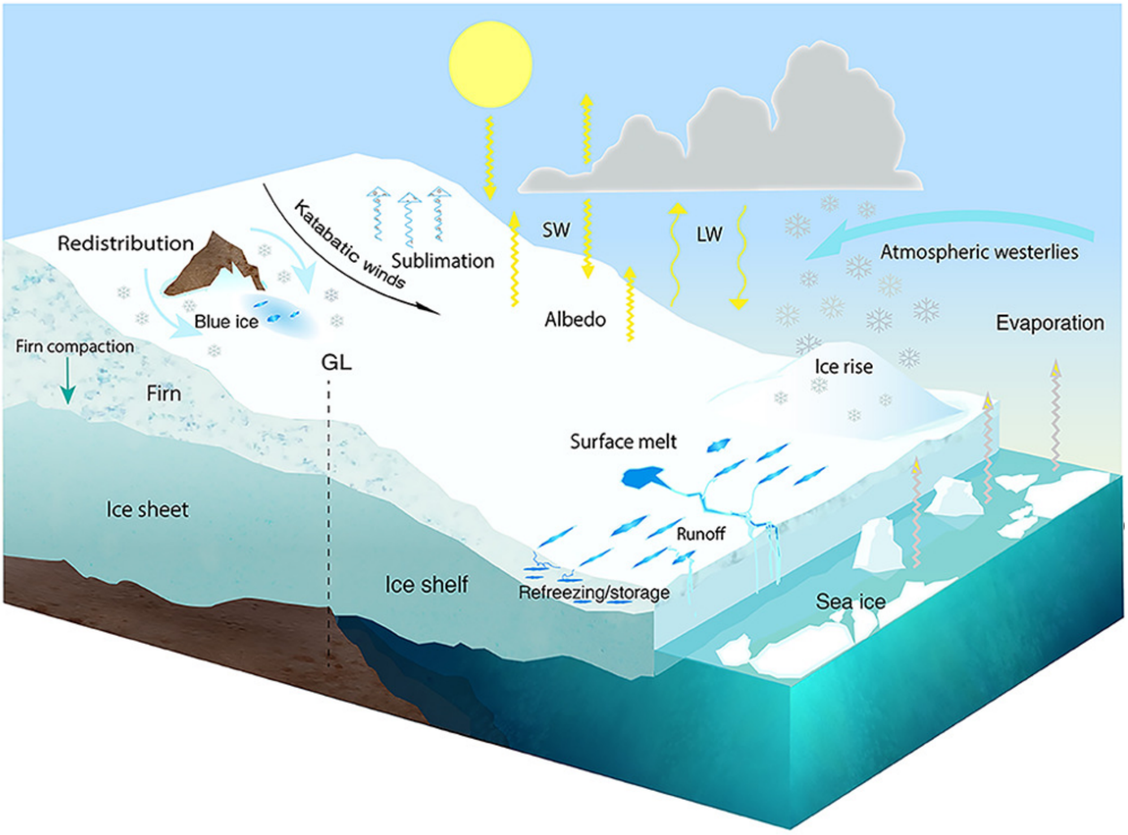

Figure 1.3: Illustrates important surface and subsurface processes that are essential to take into account when calculating the SMB and MB over the Antarctic ice sheet, taken from Lenaerts et al., 2019.

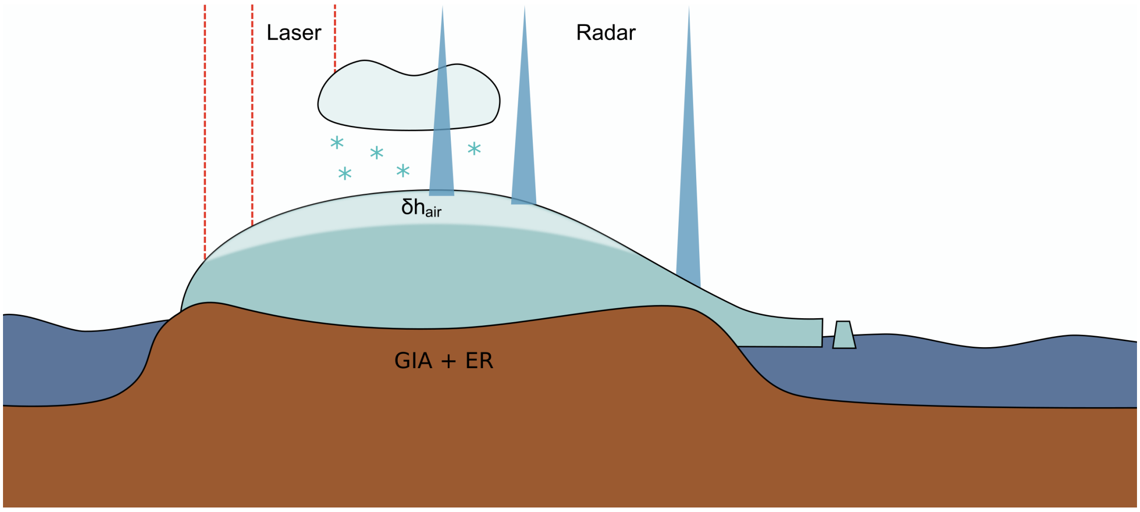

Figure 1.4: Illustrates the concept of laser and radar altimetry for determining mass balance, it also shows the Glacial Isostatic Adjustment (GIA) signal, the Elastic Rebound (ER) signal, and the firn compaction δh_{air}, illustrated by Trine S. Dahl-Jensen.

1.2.1 Altimetry

Using satellite altimetry provides the SEC between different satellite orbits, from where volume changes can be computed. Several satellites have gathered altimetric data for the polar regions, e.g. ICESat, ICESat-2, Cryosat-2. Altimetry is not able to differentiate between the individual surface elevation signals, such as ice dynamic, firn densification and vertical bedrock movement, the latter is a combination of the Glacial Isostatic Adjustment (GIA) and the present-day Elastic Rebound (ER). Since it is only the ice dynamics component that can change the MB, the firn densification and the vertical bedrock movement needs to be corrected for. The GIA and ER are usually modelled. Typically, these vertical bedrock corrections are small (mm to cm per year) compared to firn densification and ice dynamics (Whitehouse, 2018). The firn can change thickness through densification, which can give both negative and positive signals to the SEC. The magnitude of this signal can range from millimetres in cold low precipitation regions to tens of centimetres in the warm high precipitation regions (Kuipers Munneke et al., 2015; **MC Paper I**). It is therefore important to have a representative subsurface model that is forced with a proper atmospheric RCM, to compute the firn densification signal. Satellite altimetry has been used to determine the MB estimates and time series in both Greenland and Antarctica (Khan et al., 2022; Shepherd et al., 2018; Shepherd et al., 2020; Simonsen et al., 2021; Sørensen et al., 2011). The altimetry method has also been used to determine the Greenlandic MB and the Antarctic SEC in this study. See Chap. 3 for details on how the firn densification is calculated in this study and how the SEC is derived using the Ice, Cloud and land Elevation Satellite 2 (ICESat-2). The advantage of this method is that the newer altimetry satellites e.g. ICESat, ICESat-2, and Cryosat-2 have a high spatial resolution (<250 m) meaning that the narrow outlet glaciers can be resolved (Drinkwater et al., 2004; Schutz et al., 2005; Smith et al., 2019a), however, since ICESat and ICESat-2 both use laser altimetry they are unable to measure when it is cloudy. The disadvantage is that numerical models are needed to derive the firn compaction and the vertical bedrock movement, both of which have large variabilities and uncertainties (Martín-Español et al., 2016; **MC Paper I**). An illustration of this method is shown in Fig. 1.4, it shows the altimetric beam from the satellite, the firn layer on top of the ice sheet, it is within this layer that the compaction of firn happens, and the bedrock from where the GIA and ER signals originates from.

1.2.2 Mass budget

This method takes the mass input (SMB) and subtracts the mass output (D). The main advantage of this method is that the required variables are independent of each other. The disadvantages to this method are the spread in SMB results. For example, **Paper I** found, in a RCM intercomparison study, a SMB spread of 580 Gt per year over the grounded AIS. Also, the coarse time resolution of the discharge, ranging from decadal means to yearly values causes uncertainties for this method (Gardner et al., 2018; Rignot et al., 2019; Van den Broeke et al., 2011). Using a high resolution RCM in combination with a surface scheme is key to minimize the errors and uncertainties on SMB estimates. This method has been used over both ice sheets (Enderlin et al., 2014; Gardner et al., 2018; Rignot et al., 2019; Shepherd et al., 2018; Shepherd et al., 2020; Van den Broeke et al., 2011). This study models the Antarctic SMB from 1979-2021 using different numerical models than previous studies, leading to a more robust SMB ensemble, see section 1.3 for more details on numerical modelling.

1.2.3 Gravity

Gravity Recovery and Climate Experiment (GRACE) satellite and its successor Gravity Recovery and Climate Experiment Follow On (GRACE-FO) have been in orbit since 2002, with a gap between 2017 to the beginning of 2019. GRACE/GRACE-FO measures the gravity field, it is thus possible to derive the mass change for every repeat track. The GIA still needs to be accounted for, because it is the solid Earth phenomenon responsible for the mantle flow i.e. moving mass under the ice sheet, which is a part of the gravimetric signal (Barletta et al., 2013). Otherwise it is an independent method, no firn nor climate models are needed, which is the main advantage of this method. This method is thus very good to validate the altimetry and mass budget method against. A disadvantage of using the gravity method is the coarse horizontal resolution (hundreds of km) (Velicogna & Wahr, 2013) meaning ice dynamics on glacier scale are smeared out. This method has been applied for MB estimations for both ice sheets (Barletta et al., 2013; Forsberg et al., 2017; Ramillien et al., 2006; Shepherd et al., 2018; Shepherd et al., 2020).

1.3 Numerical Modelling

Climate models are tools to help better understand the complex processes, and test hypotheses in the climate systems. They use numerical equations, to approximate physical processes, that simulates the transfer and movement of energy and mass and its interactions with land, atmosphere, ocean and other parts of the climate system (McGuffie & Henderson-Sellers, 2014). There are multiple different models for the climate system, depending on the question at hand and the computational infrastructure available. General Circulation Models (GCM) represents the atmosphere, land, ocean, and ice sheet processes globally, these need the GHG concentrations, solar radiation, and aerosols as inputs (Lenaerts et al., 2019). Earth System Models (ESM) simulates the processes of the atmosphere, land, ocean, and ice sheet, like GCMs. However, ESMs also incorporate biogeochemistry and are thus able to compute the different GHG cycles in the model (Kawamiya et al., 2020; Lenaerts et al., 2019). Because both ESMs and GCMs are global models, they are usually simulated in coarse resolution, which does not resolve details on a local scale, for that RCMs can be used. A RCM is an atmospheric model with a limited spatial domain to allow for higher spatial-temporal resolution. With the increased resolution, the topography and local processes are better resolved and adds value to the RCM simulations (Feser et al., 2011; Rummukainen, 2010, 2016). More complex physical processes can also be added in RCMs, optimizing them to specific regions. The RCMs; MAR (Agosta et al., 2019), RACMO2 (Van Wessem et al., 2018), MetUM (Orr et al., 2015), COSMO-CLM^2 (Souverijns et al., 2019), and HIRHAM5 (Langen et al., 2015) all have versions updated to better resolve the climate over polar regions. Because RCMs are limited to a specific domain they need boundary conditions. For historical simulations and projections, these boundary conditions are given by ESMs or GCMs, whereas, for present-day climate simulations, reanalysis data is used for boundary conditions. Reanalysis takes observations and combine them with modern weather forecast models to create a detailed state of the atmosphere. Observation data comes from satellites, weather stations, ships etc.. There are several reanalysis data sets of the atmosphere, two of the most widely used reanalysis data sets for polar RCMs are ERA-interim that runs from 1979 to August 2018 (Dee et al., 2011) and its successor ERA-5 that covers the period 1950 to present (Hersbach et al., 2020).

RCMs generally lacks detailed snow schemes, and offline subsurface models are thus needed, for studying the snow and firn processes. There are several firn models with different complexities (Herron and Langway, 1980; Langen et al., 2017; Simonsen et al., 2013; Vandecrux et al., 2018; **Paper II**), common for these firn models is that they are offline models, meaning that there is no feedback to the atmosphere. Some RCMs are coupled with a multi layer subsurface model (Langen et al., 2015; van Dalum et al., 2022) this is however computationally expensive during high resolution simulations. An illustration of the different models mentioned above and their set-ups is shown in Fig. 1.5, to the left we see a GCM/ESM where the entire globe is covered in 3 dimensional grid cells, the schematic diagram in the lower left corner shows the different physical processes. The top right corner shows a zoom-in on the a the high resolution region, representing a RCM. Finally, in the bottom right corner, there is a sketch of the subsurface processes in the firn pack.

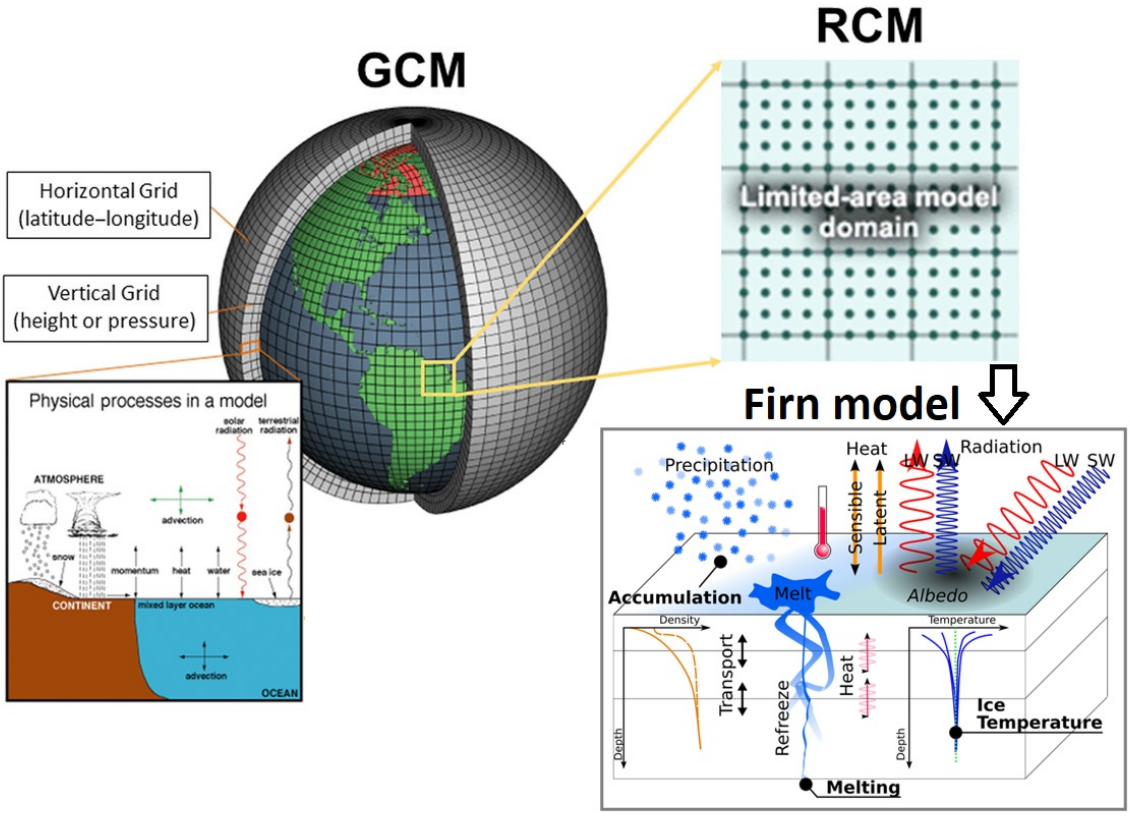

Figure 1.5: Illustrates a GCM that covers the entire globe in 3 dimensional grid cells, the little box in the lower left corner shows some of the physical processes in the ocean and atmosphere, the top right corner represents a RCM, in the lower right corner is schematic of a firn model and its physical processes, modified from Ambrizzi et al., 2018.

The studies covered in this thesis use the RCM HIRHAM5, and a firn model to gain knowledge about the subsurface.

HIRHAM5: is a hydrostatic model, meaning that it uses the hydrostatic approximation, i.e. that the horizontal scale is large compared to the vertical scale and the atmosphere is in horizontal equilibrium. This assumption holds for synoptic scale (>10 km) modelling. HIRHAM5 has 31 atmospheric layers (Christensen et al., 2007) and uses the physics scheme of the GCM ECHAM5 (Roeckner et al., 2003) and the numerical weather forecast model HIRLAM7 (Eerola, 2006).

For all experiments in this study, HIRHAM5 is forced at the lateral boundaries at 6-hourly intervals with temperatures, relative humidity, pressure, and wind vectors at all pressure levels, along with daily values for sea surface temperature and sea ice concentration at the lower boundary. The model uses ERA-interim and ERA-5 reanalysis for the present-day simulations, and ESMs or GCMs for historical simulations and projections. For the Antarctic simulations the resolution is 0.11°(≈12.5 km) and the Greenlandic simulations the resolution is 0.05 °(≈5.5 km), all with a dynamical time step of 90 seconds. The specific model set-ups are described in the papers.

Offline firn model: The firn model was built using the ECHAM5 physics (Roeckner et al., 2003), but has been heavily updated to include more vertical layers with a higher vertical resolution, a sophisticated albedo scheme, complex snow and ice schemes that computes the firn densification, snow state-dependent hydraulic conductivity, grain growth of the snow/firn, formation of superimposed ice and calculates the liquid water budget to control the water saturation retention, refreezing and runoff (Langen et al., 2017). There are two versions of the firn model, which have been compared as a part of this study. The main difference between these two versions is the layering scheme, where one uses an Eulerian framework where the layer thickness has a fixed predefined mass, expressed in metres of Water Equivalent (we), so when there is added mass at the surface an equal amount is moved down to the layer below (Langen et al., 2017). The other version of the firn model uses a Lagrangian framework for the evolution of layers, where the layers are allowed to spilt or merge, based on some criteria, when mass is added or removed at the surface (Vandecrux et al., 2018). Both versions have previously been used and validated over the GrIS (Langen et al., 2017; Vandecrux et al., 2018), but it is in this thesis that they have been set up and run for the AIS (**Paper II**). The firn model runs on a high performance computer, setting up the Antarctic domain required files describing the topography, ice mask, and gradients of the slopes, all in the wanted resolution.

All climate models needs to be spun-up to be in a representative state. A fully spun-up firn pack means that the entire firn column has been renewed by accumulation at least once (Medley et al., 2020), the spin-up is usually performed by repeating a period over and over, here it is important that the period is not too short because it needs to be representative of the full simulation period. It can however be very computationally expensive and time-consuming to spin the full Antarctic firn pack up, due to low accumulation rates in East Antarctica. In this study we have experimented with different spin-up times to see the added value of a longer spin-up period. We have spun-up the firn pack by repeating the period 1980 to 1989 multiple times, this is a valid period to use, as there were no appreciable shifts in the Antarctic climate (Medley et al., 2020).

2 Summary of papers

This chapter contains summaries of all the papers that this thesis contributed to, where the papers in section 2.1 have contributed the most to the design of this thesis. Section 2.1 and **Draft I** in section 2.3 summarizes the papers where I am the lead author or have had a significant role in conceptualizing the framework for the study, carrying out the experiments, analysing and interpret the results, as well as writing the manuscript. The papers summarized in section 2.2 and **Draft II** in section 2.3 are the papers where I had minor contributions consisting of data preparation in form of running the firn model or post-processing HIRHAM5 data to the wanted formats, writing smaller sections and producing results to some of the manuscripts and revising all manuscripts. All papers are can be found in the Appendix.

2.1 Main papers

2.1.1 Paper I: What is the surface mass balance of Antarctica? An intercomparison of regional climate model estimates

*Mottram, R., **Hansen, N.**, Kittel, C., van Wessem, J. M., Agosta, C., Amory, C., Boberg, F., van de Berg, W. J., Fettweis, X., Gossart, A., van Lipzig, N. P. M., van Meijgaard, E., Orr, A., Phillips, T., Webster, S., Simonsen, S. B., and Souverijns, N.: What is the surface mass balance of Antarctica? An intercomparison of regional climate model estimates, The Cryosphere, 15, 3751–3784, https://doi.org/10.5194/tc-15-3751-2021, 2021.*

Multiple individual RCM groups have simulated the Antarctic SMB, which have let to a wide spread of SMB estimates. The aim of this paper was thus to evaluate different RCMs based on their model performance and create a SMB estimate from a model ensemble.

In the study we used five different RCMs: COSMO-CLM^2, HIRHAM5 (in two resolutions, 0.11°and 0.44°), MAR3.10, MetUM, and RACMO2.3p2, to simulate the near surface climate. All the models were forced by the same reanalysis data ERA-interim, in the period of 1987 to 2015. MAR3.10 and RACMO2.3p2 used optimized subsurface schemes for Antarctica, whereas COSMO-CLM^2, HIRHAM5, and MetUM only used very simple subsurface schemes, thus their SMB were calculated from atmospheric outputs. We evaluated the model performances by comparing them to firn temperatures, stake measurements of SMB, and surface pressure, near surface wind speed, and temperatures from automatic weather stations. When computing the continental wide SMB for each model, we integrated over the ice covered area. However, the size of the ice sheet mask differed between the RCMs, we thus created a common ice mask to integrate over, and thereby removed the area bias.

When compared with in-situ measurements, we found that no one model performed better than the others on a continental wide scale. When comparing the modelled SMB spatially good agreement was found between models over large areas of the Antarctic continent, however, there were some local variabilities in the coastal area of West Antarctica and along the Transantarctic Mountains. When the SMB were integrated over the common ice mask we saw a large spread that ranged from 1961 $\pm$ 70 (COSMO-CLM^2)

to 2519 ± 188 Gt year^{-1} (HIRHAM5 low resolution) with an ensemble mean of 2329 ± 94 Gt year^{-1}.

The RACMO2.3p2 was the RCM that simulated a yearly mean SMB closest to the ensemble mean, namely, 70 Gt above the ensemble mean with the low-resolution HIRHAM5 model 190 Gt over the ensemble mean and the COSMO-CLM^2 model 368 Gt below. All the RCM estimates, except COSMO-CLM^2, were within the uncertainty range of the ensemble mean. By investigating each term of the SMB, it was clear that the precipitation term had the largest impact on the model spread.

2.1.2 Paper II: Downscaled surface mass balance in Antarctica: impacts of subsurface processes and large-scale atmospheric circulation

***Hansen, N.**, Langen, P. L., Boberg, F., Forsberg, R., Simonsen, S. B., Thejll, P., Vandecrux, B., and Mottram, R.: Downscaled surface mass balance in Antarctica: impacts of subsurface processes and large-scale atmospheric circulation, The Cryosphere, 15, 4315–4333, https://doi.org/10.5194/tc-15-4315-2021, 2021.*

In **Paper I** the SMB results from HIRHAM5 were only calculated from atmospheric outputs. This means that physics of the subsurface and how meltwater interacts with the firn pack were not taken into account. Therefore, we introduced a complex offline firn model in this paper. The firn model was forced with HIRHAM5 output data from the reanalysis period 1980 to 2017.

We set up, used, and validated two different versions for the firn model, where the main difference between the versions was how they managed the layers within the model. One version used an Eulerian approach where each layer had a predefined thickness, and this layer thickness stayed constant throughout the simulation. The other version used a Lagrangian approach to manage the layer thickness, where the model could split and merge layers based on a number of criteria. This meant that the thickness of the layers was not constant over time. The Eulerian version had 32 layers and the Lagrangian version had 64 layers. To validate the performance of the two versions, we compared in-situ measurements of firn densities profiles, firn temperatures and stake measurements of SMB. Besides the SMB and validation, we also estimated the MB (Eq. 1.1). We used our SMB results and discharge estimate from two different studies and compared the MB estimate to GRACE MB results. Finally, we investigated the relationship between SMB and the Southern Annular Mode (SAM).

The integrated SMB over the total ice sheet was between 2473.5 ± 114.4 and 2564.8 ± 113.7 Gt year^{-1} and for the grounded ice sheet 1963.3 ± 96.2 to 1995.2 ± 95.7 Gt year^{-1}, showing that the ice shelves are most sensitive to the choice of subsurface scheme. When comparing the modelled SMB to the observations, we found that half of them are within ± 13%, however large areas, especially in the interior part of East Antarctica, lacks observations.

For an estimation of the MB we used two different discharge data sets and the modelled SMB over the grounded WAIS, AP, EAIS, and the AIS. Furthermore, we compared the same regions with gravity derived MB from GRACE. We found good agreement with the estimated MB (from both discharge data sets) and GRACE over the WAIS, whereas there was only agreement between GRACE and our MB from one of the discharge data sets over the EAIS. Over the AP both MB estimates and GRACE widely disagrees, which is partly due to the narrowness of the AP and the coarse resolution of GRACE.

Finally, we investigated the relationship between SMB and the phase of the SAM on basin scale (defined by Zwally). We found a statistically robust relation between the SMB and the SAM in 13 out of the 27 basins. This showed, that the forcing data (ERA-interim) in combination with HIRHAM5 resolved the SAM correctly, which is important since the distribution of precipitation and thus SMB is strongly correlated with the phase of the SAM.

2.1.3 Paper III:Brief communication: Impact of common ice mask in surface mass balance estimates over the Antarctic ice sheet

***Hansen, N.**, Simonsen, S. B., Boberg, F., Kittel, C., Orr, A., Souverijns, N., van Wessem, J. M., and Mottram, R.:Brief communication: Impact of common ice mask in surface mass balance estimates over the Antarctic ice sheet, The Cryosphere, 16, 711–718, https://doi.org/10.5194/tc-16-711-2022, 2022.*

As a consequence of creating the common ice mask in **Paper I**, it was detected that a small change in the area could have a large impact on the integrated SMB. The aim of this paper was to quantify the impact of using different ice masks.

This study adopted the same methods to calculate SMB as in **Paper I** with the same RCMs; COSMO-CLM^2, HIRHAM5 (in two resolutions, 0.11°and 0.44°), MAR3.10, MetUM, and RACMO2.3p2. We then compared the SMB from the different RCMs integrated over both the common ice mask (created for **Paper I**) and the individual native ice masks. These comparisons were done over the grounded ice sheet, the ice sheet including ice shelves, and on basin scale (Zwally basin definitions). We computed the Delta values (Δ = common - native) for the percentage differences in area, $\Delta\text{area}_{\%}$; the percentage difference in SMB, $\Delta\text{SMB}_{\%}$; and the difference in Gt year^{-1} $\Delta\text{SMB}_{\text{Gt year}^{-1}}$.

The integrated SMB values over the total AIS, showed that the common ice mask was between 40.5 and 140.6 Gt year^{-1} smaller than when integrated over the native ice masks, the difference corresponded to up to 6.0% of the ensemble mean from **Paper I**. However, the area for the common mask was only between 1.85% and 2.89% smaller than the native masks, there is thus a non-linear relationship between the magnitude of the SMB and the area. This is due to orographic precipitation which is enforced by the steep topography at the coast, especially over the WAIS and the AP, basins 20, 23, 24, and 25. If integrated over the grounded ice sheet, the common ice mask values were between 20.1 and 102.4 Gt year^{-1} smaller than when integrated over the native mask. This is nearly the same as the Antarctic mass imbalance from IMBIE2 (109$\pm$56 Gt year^{-1}), hence, the mask uncertainty could in practise determine if the Antarctica ice sheet is losing or gaining mass. The six different ice masks could make 63 different ice mask combinations including the common mask, there were no single mask that stood out, they all differed arbitrarily around the coast. It should be noted that the common mask were first introduced after the individual RCM simulations were done and this influenced the land-depended fluxes, such as the magnitude of the precipitation would be erroneous.

We believe that there is a pressing need for a community wide ice mask protocol, so the area bias in model intercomparison can be reduced. We suggest that this protocol consists of some agreed upon up-to-date data for ice extent, grounded ice, ice shelves, rocks, elevation, and ice cover percentage. All of these should be in very high (sub-kilometre) resolution and with this data should follow a tool to create the mask in the wanted model resolution. This way we would minimize the biases created by the area and elevation differences and be able to better understand of the differences in model intercomparisons.

2.2 Minor contributions

2.2.1 MC Paper I: Uncertainty in East Antarctic Firn Thickness Constrained Using a Model Ensemble Approach

Verjans, V., Leeson, A. A., McMillan, M., Stevens, C. M., van Wessem, J. M., van de Berg, W. J., van den Broeke, M. R., Kittel, C., Amory, C., Fettweis, X., ***Hansen, N.****, Boberg, F. and Mottram, R., Uncertainty in East Antarctic Firn Thickness Constrained Using a Model Ensemble Approach, Geophysical Research Letters, 48, 7, https://doi.org/10.1029/2020GL092060, 2021.*

Using altimetry to estimate the MB requires knowledge of how the firn evolves over time. However, the firn evolution has large uncertainties in East Antarctica, thus, the aim of this paper was to study the sensitivity, uncertainties, and thickness change in firn densification models by using different RCMs as forcing over the region of East Antarctica.

The model ensemble consisted of the three RCMs; MAR, RACMO2, and HIRHAM5. These were used to force nine different firn densification models with two different values for the surface density, creating an ensemble of 54 scenarios. All three RCMs were forced with the reanalysis data ERA-interim, and all scenarios were simulated in the period between 1992 to 2017.

Over the study period, there was a stable firn thickness in East Antarctica with strong regional variability. In the interior of East Antarctica there were no significant changes, in contrast, there were several areas near to the coast where there were thickening and thinning of the firn. Due to large snowfall rates in Dronning Maud Land, starting in the late 2000's, the firn thickness did increase in this area. Other areas, such as Totten glacier and Shacklenton ice shelf, experienced a thinning in the firn thickness due to a decrease in the snowfall rates. Overall the absolute uncertainties followed the change in the firn thickness, however, the relative uncertainties were the largest in the interior due to the low accumulation rates, furthermore, the trends in the firn thickness were close to zero. In general, the RCMs contributed the most to the ensemble uncertainty, followed by the firn densification model, and then the surface density. It should be noted that in areas where temperature and snowfall increased the uncertainties from the firn densification model and the surface density also increased.

This study also compared the results with altimetry measurements over the same period. Altimetry measures the surface elevation change which consists of the firn thickness signal, ice dynamical imbalance, and vertical bedrock movement. The latter was neglected in this study due to its small signal. In 9 of the 16 basins (defined by Zwally) in East Antarctica, the altimetry and model ensemble uncertainties overlapped, meaning there were no evidence to support a net ice flow imbalance. However, since this was studied on basin scale it is very likely that there were local areas near the glacier outlets where an ice imbalance occurred, such as Totten glacier.

2.2.2 MC Paper II: Uncertainties in projected surface mass balance over the polar ice sheets from dynamically downscaled EC-Earth models

Boberg, F., Mottram, R., ***Hansen, N.****, Yang, S. and Langen, P. L., Uncertainties in projected surface mass balance over the polar ice sheets from dynamically downscaled EC-Earth models, The Cryosphere, 16, 1, 17–33, 10.5194/tc-16-17-2022,2022.*

This study investigated the new version of the ESM EC-Earth version 3 (v3), and evaluated it against the previous version EC-Earth version 2 (v2) for both Greenland and Antarctica. All experiments were downscaled with the RCM HIRHAM5 and to calculate the SMB the firn model was forced with the HIRHAM5 outputs.

Eight experiments were set up, four historical simulations and four high emission projections. For Greenland these consisted of: v2 and v3 historical data from 1990-2010, and v2 RCP8.5 and v3 SSP5-85 from 2080-2100, all in 0.05° resolution. For Antarctica: v2 and v3 historical from 1970-2000, and v2 Representative Concentration Pathways (RCP)8.5 and v3 SSP5-85 from 2070-2100, all in 0.11° resolution. We compared 2-m temperature, sea ice extent, precipitation, and SMB.

The global 2-m temperature from v2 and v3 historical simulations were compared to the reanalysis data from ERA-interim. v2 had a cold bias over Greenland, which had almost disappeared in v3, however, there was a warm bias in v3 over Antarctica. For the projections, the SSP5-85 simulated a warmer mean 2-m temperature than the RCP8.5 for both ice sheets. It was only at the eastern coast of Greenland and the eastern part of Antarctica, where the SSP scenario was colder than the RCP scenario.

An increase in the precipitation at the end of the century was found in both scenarios over both ice sheets. When we compared the two scenarios the relative differences showed that SSP5-85 was more dry in the eastern part of the domains and wetter in the western part of the domains compared to RCP8.5. Even though there was an increase in precipitation there was a decrease in the SMB over Greenland due to an increased runoff. This was also the case for the Antarctic ice shelves. It was only over the grounded AIS that there was an increase in SMB.

The results showed that for the two versions of the ESM EC-Earth differences arose in the SMB at the end of the century even though the GHG emission pathways are similar. The precipitation and runoff rates at the end of the century, over both ice sheets, were higher in the SSP5-8.5 scenario, likely enhanced by the increased temperatures projected under SSP5-8.5 compared to the RCP8.5 scenario.

An increase in GHG concentration leads to larger changes in temperature, runoff, and precipitation for both Greenland and Antarctica in the projected scenario simulations compared to the historical simulations. Furthermore, a higher equilibrium climate sensitivity in v3 SSP5-8.5 leads to higher temperatures, precipitation rates, and runoff rates compared to the RCP8.5 scenario. There are multiple differences between the two versions like updated physics, different resolutions, revised GHG concentration scenarios etc. making it difficult to directly compared results. Nonetheless, this study demonstrated the large range of uncertainties in SMB estimates.

2.2.3 MC Paper III: Summer air temperature extremes over Antarctic ice shelves and potential "hotspots" of surface melting

Orr, A., Deb, P., Clem, K., Gilbert, E., Boberg, F., Bromwich, D., Colwell, S., ***Hansen, N.****, Lazzara, M., Mottram, R., Niwano, M., Phillips, T., Pishniak, D., Reijmer, C., van de Berg, W.J., Webster, S. and Zou, X., Summer air temperature extremes over Antarctic ice shelves and potential "hotspots" of surface melting, Journal of Climate, 2022, accepted.*

Ice shelves cover 75% of the Antarctic coastline and the ice shelves surface climate is purely understood. This paper studied the extreme summer near-surface temperatures from 1979 to 2019 by computing the melt potential, its frequency, and intensity. Finally, it was investigated how or if the temperatures are correlated with large scale atmospheric and oceanic processes.

Two RCMs, HIRHAM5 and MetUM, both run at 0.11° resolution from 1979 to 2019, forced with the reanalysis data from ERA-interim were used for this study. We used modelled 3-hourly 2-m temperatures from December, January, and February (the Antarctic summer), and 3-hourly measured 2-m temperatures from 20 weather stations on or near the ice shelves.

When comparing MetUM and HIRHAM5 with the stations, both models had a cold bias. Some stations were located on rock so it was possible that the rock was heated up and thus created a warm bias. In general, HIRHAM5 had a larger cold bias, large Root-Mean-Square Error (RMSE), and lower correlation than the MetUM when compared to observations. Although the models had this cold bias both modelled the temperature adequately.

We found that the melt potential (defined as temperatures lower than -2 C°) frequency was highest over Larson and Wilkins ice shelves, both on the AP, and lowest over the Ross and Ronne-Filchner ice shelves, especially close to the grounded ice sheet. We saw the same for the melt potential intensity, which was highest (lowest) over the AP (Ross and Ronne-Filchner ice shelves). The large melt potential over the AP is important to note because this region is vulnerable to hydrofractures induced by surface meltwater.

The time series of melt potential showed both significant positive and negative trends at different locations. These trends were governed by local and large scale circulations. In East Antarctica the trends were mainly negative, likely due to the circulation that was strongly correlated with a negative phase of SAM leading to a decreasing melt potential. Whereas, in West Antarctica, the circulation was correlated with El Niño leading to increased melt potential. Assuming climate models projections are correct, this study suggests that there will be an increase (decrease) in melt potential over West (East) Antarctic ice shelves. West Antarctica and the AP will be more likely to lose their ice shelves in the future.

2.3 In Preparation

2.3.1 Draft I: Benefits of using a sophisticated standalone snow scheme to simulate a surface melt event over the Ross Ice Shelf, West Antarctica in the HIRHAM5 and MetUM regional atmospheric models

***Hansen, N.**, Orr, A., Zou, X., Mottram, R., Gilbert, E., Boberg, F., Simonsen, S. B., Phillips, T., Webster, S., and Bracegirdle, T., Benefits of using a sophisticated standalone snow scheme to simulate a surface melt event over the Ross Ice Shelf, West Antarctica in the HIRHAM5 and MetUM regional atmospheric models, in preparation for Atmospheric Science Letters.*

Melt events have become more frequent over the Antarctic ice shelves and will only become more frequent in the future. It is therefore important to be able to model the surface melt correctly in RCMs. Here we investigated a case study for a melt event over the Ross ice shelf, West Antarctica, in January 2016.

We compared the two RCMs HRIHAM5 and MetUM to satellite observations of melt extent. Furthermore, we used the RCM outputs to force the firn model from **Paper II**. We compared the raw RCMs and the firn model results and found that the raw RCM output underestimated the number of melt days due to the lack of a sophisticated firn scheme. When forced through the firn model, we saw an overestimation of the number of melt days. The next step will be to carry out a statistical analysis to investigate if the firn model results are significantly better than the raw results.

Another finding of this study was the fact that the observed melt extent showed a no-melt area in the East side of the Ross ice shelf. This area stayed a no-melt area throughout January. In the results from the firn model, this no-melt area was most pronounced when forced with HIRHAM5 and almost non-existing in the results forced with MetUM. We argue that this is due to a wrong representation of the wind regime in the RCMs. It is known from previous studies that there exists an air stream along the Transantarctic Mountains called the Ross air stream, and that there are katabatic winds flowing from the interior of the ice sheet down onto the ice shelf. We believe that there was a cold pool in the no-melt area created by katabatic winds from the cold interior of East Antarctica. However, in the models, the air stream along the Transantarctic Mountains was stronger than the katabatic winds, meaning that the warm air from Marie Byrd was transported out over the ice shelf, leading to an ice shelf wide melt event in the models.

Even though this study is still in preparation the results so far clearly shows that RCMs with no or only a simple firn scheme, are insufficient to model melt realistically. Hence, a more sophisticated firn model is needed and in complex terrain care should be taken when analysing the wind results.

2.3.2 Draft II: High Resolution Simulations of Eemian Climate in Greenland

Bunde, C., Mottram, R., Boberg, F., ***Hansen, N.****., Hvidberg, C., Gierisch, A. and Guo, C., High Resolution Simulations of Eemian Climate in Greenland, in preparation.*

This study investigated the climate over the GrIS in the Eemian interglacial period (130 thousand to 115 thousand years ago). This period is interesting because climate reconstructions suggest that the climate in the Arctic became 2-4 degrees warmer during the Eemian period, which makes it similar to some end of century projections for the present-day climate.

To simulate the Eemian climate, we used NorESM as the global model and the RCM HIRHAM5 to downscale the simulations. Finally, we used the firn model to compute the SMB. Three 20 years time slices in the Eemian period were used: 130 thousand years (start), 125 thousand years (mid), and 115 thousand years (end) ago, also a pre-industrial and a present-day simulation have been carried out. The three Eemian simulations and the pre-industrial simulations were all forced at the lateral boundaries with NorESM with different GHG concentrations and orbital parameters to represent the different periods. The present-day simulation has been forced with ERA-Interim. The SMB was computed both directly from HIRHAM5 and though the firn model, to investigate the importance of using a firn model. To validate the simulations, temperatures, and accumulation, derived from ice cores isotopes, have been used.

We found that the SMB was lower in the Eemian and pre-industrial periods compared to the present-day SMB and furthermore, we found that integrated over the GrIS the SMB calculated directly from the HIRHAM5 outputs were higher than the SMB from the firn model. We argued that this was due to the extra subsurface layers in the sophisticated energy scheme of the firn model. We also evaluated the spatial differences in the SMB, melt, runoff, temperature, and refreezing between the pre-industrial simulation and the Eemian simulations. In general, we saw the largest anomalies in South Greenland and along the eastern coast. We found that the start of the Eemian period was close to the pre-industrial period.

When comparing our results to the ice cores, we generally found lower temperatures for the modelled Eemian than from ice record proxies and an overestimation of precipitation in the climate models compared to the results from the ice cores.

The integrated SMB values from the firn model in the start of the Eemian was -334.19 Gt year^{-1}, from the mid Eemian period -178.22 Gt year^{-1}, and increased to -99.43 Gt year^{-1} at the end of the Eemian period, and finally in the pre-industrial period the SMB was -323.77 Gt year^{-1}. The present-day SMB is 351.8 Gt year^{-1} for comparison. The low SMB values were enhanced by the lower precipitation in the NorESM, which is due to the coarse resolution of the NorESM.

Finally, we confirmed previous research that suggests, that although the temperature increase during the Eemian period was similar to current climate projections. The Eemian period is not a complete analogue for projected climate change and caution should be taken when interpreting GrIS and SLR records from the Eemian period and applying them to a warmer future.

3 Work in progress

Following Sørensen et al., 2011, who presented a MB estimate for GrIS derived by the Ice, Cloud and land Elevation Satellite (ICESat) (2003-2008), we here make an extension of the MB estimate using ICESat's sucessor ICESat-2 for the GrIS, furthermore we use ICESat-2 to derive a volume change over the grounded part of Antarctica. In the following the principles of SEC will be described, combined with an evaluation on the conversion from volume change to mass change and what one should take into account when doing this for Greenland versus Antarctica. Finally, some preliminary results will be shown.

3.1 Surface Elevation Change

The distance between the Earth's surface and a satellite is measured by altimetry, as mentioned in section 1.2.1. In general the satellite emits a pulse of electromagnetic radiation towards the Earth's surface, where it is reflected and send back to the satellite. The range (R) from the satellite to the surface can be derived from the two-way travel time (T) and the speed of light (c), as described in Eq. 3.1:

$$R = \frac{1}{2}cT \tag{3.1}$$

The satellite used here is ICESat-2 which were launched in September 2018, and has an orbital path with repeat every 91 days and a polar orbit with an inclination of 92°(Smith et al., 2019a). On board ICESat-2 is the Advance Topographic Laser Altimeter System (ATLAS) instrument, which is a photon-counting green laser (532 nm) altimeter (Neumann et al., 2019). In this study we use the fifth release of the ATL06 along-track height (Smith et al., 2019a; Smith et al., 2019b), which provide averaged photon-heights at a 40-metre posting. To get the elevation change from ICESat-2, we use the repeat track method (Sørensen et al., 2018) and perform a least squares regression on all data in 5000 m along-track segments of the satellite track. The regression parameters are given by:

$$H(x,y,t) = H_0(\bar{x},\bar{y}) + \frac{dH}{dt}(t-\bar{t}) + sx(x-\bar{x}) + sy(y-\bar{y}) + \alpha\cos(\omega t) + \beta\sin(\omega t) + \epsilon(x,y,t) \tag{3.2}$$

where $H(x,y,t)$ is the surface elevation at time t and position x and y, H_0 is the mean elevation, and sx and sy describe the surface topography by its slope, $\alpha\cos(\omega t)+\beta\sin(\omega t)$ is the seasonal signal, and ϵ is the residual between the model and the data, the overbars is the mean measurements in a segment (Sørensen et al., 2018; Sørensen et al., 2015).

In general the change in surface elevation of an ice sheet (SEC or $\frac{dH}{dt}$) can be written as follows:

$$\frac{dH}{dt} = \frac{\dot{b}}{\rho} + w_c + w_{ice} + \frac{\dot{b_m}}{\rho} + w_{br} - u_s\frac{dS}{dx} - u_b\frac{dB}{dx} \tag{3.3}$$

where $\dot{b}$ is the SMB, ρ is the density of ice or snow at the surface, w_c is the firn compaction rate, w_{ice} is the vertical ice velocity, $\dot{b_m}$ is basal mass balance, w_{br} is the vertical bedrock velocity, u_s is the horizontal velocity of ice at the surface S and u_b is the horizontal velocity of ice at the bedrock (Sørensen et al., 2011). Here, the latter two terms are assumed to negligible. Then following Eq. 3.3 the observed SEC from ICESat-2 needs to be corrected for the firn compaction and the vertical bedrock movement to isolate the surface elevation change that is due to ice sheet mass change. To get the firn compaction signal, the firn model, forced at the surface with HIRHAM5, can be used to calculate the firn air content expressed as δh_{air} as shown in Eq. 3.4. δh_{air} calculates how much air there is within the firn column, where i are the layers in the modelled firn pack, z is the bottom layer. ρ_{bulk_i} are the density of the firn model layers including ice lenses (Eq. 3.5), ρ_{ice} is the density of ice and is set to 917 kg m^{-3}, and H is the depth of each layer in metres.

$$\delta h_{air} = \sum_{i=1}^{i=z} \left(1 - \frac{\rho_{bulk_i}}{\rho_{ice}}\right) H_i \tag{3.4}$$

$$\rho_{bulk} = \frac{(p_{firn} + p_{ice})}{\left(\frac{p_{firn}}{\rho_{firn}} + \frac{p_{ice}}{\rho_{ice}}\right)} \tag{3.5}$$

where p_{firn} and p_{ice} are the concentrations of firn and ice in each layer, and ρ_{firn} is the density of the firn. δh_{air} is calculated from monthly means and from that a linear fit is computed. This gives the rate of compaction needed in the altimetry method. Further, the vertical bedrock movement data sets have been provided by Spada and Melini, 2019.

3.1.1 Volume to mass conversion

After correcting for the height changes in Eq. 3.3 for non-mass related contributions, the next step is to convert height change to mass change. In essence this is fairly straight forward, multiply the height change with a density, as seen in Eq. 3.6, where $\tilde{\rho}$ is the appropriate density. However, the question becomes should it be the density for snow or ice, this conversion can introduce great uncertainties (Shepherd et al., 2012). For instance, a positive SEC, here defined as the surface moving upwards, will in areas with negligible changes in ice dynamics be due to snow accumulation making $\tilde{\rho}$ = 300-400 kg m^{-3}. Whereas, a negative SEC, here defined as the surface moving downwards, is often caused by surface melt or ice dynamics, in this case $\tilde{\rho}$ will be 917 kg m^{-3}, as we have corrected for changes in firn compaction.

$$\frac{dM}{dt} = \frac{dH_{\text{corrected}}}{dt}\tilde{\rho} \tag{3.6}$$

The simplest way to make the volume to mass conversion is to use a constant density over the entire ice sheet, like Smith et al., 2020 who used the density of ice for both the AIS and GrIS. Other studies have made a density parameterization based on the location, where the ice sheet have been divided into accumulation and ablation zones using the density of snow ,ρ_s, and ice ,ρ_i, respectively (Thomas et al., 2006; Zwally et al., 2021). Sørensen et al., 2011 made another parameterization arguing, that for Greenland, all the elevation changes in the ablation zone (below the Equilibrium Line Altitude (ELA)) are due to ice dynamics or surface melt. In the accumulation zone (above ELA) all the elevation increases are due to snow accumulation and all elevation decreases in the accumulation zone are assumed to be ice dynamics. Leading to the parameterization of $\tilde{\rho}$ in Eq. 3.7, where ρ_s is the snow density calculated in the firn model, and ρ_i is the density of ice.

$$\tilde{\rho}_{GrIS} = \begin{cases} \rho_s \text{ , if } \frac{dH_{\text{corrected}}}{dt} \geq 0 \text{ and H} \geq \text{ELA} \\ \rho_i \text{ , elsewhere} \end{cases} \tag{3.7}$$

The parameterization in Eq. 3.7 is valid for Greenland. However, the parameterization neglects the possibility of a positive surface elevation caused by a dynamical build up of ice, which is observed in West Antarctica near the Siple coast (Shepherd et al., 2019).

The dynamical build up of ice is due to changes in the bedrock near the Siple Coast leading to a decrease in the ice flow velocity (Anandakrishnan & Alley, 1997; Scheuchl et al., 2012). To identify the extent of this area with dynamical build up we use the ice flow velocities from Rignot et al., 2011b and Mouginot et al., 2012 to compute the divergence, ∇, of the ice flow. The sign of the divergence of the ice flow reveals what is largest, the inflow or the outflow of an area. A positive ice flow divergence means that the inflow is smaller than the outflow and vice versa for a negative ice flow divergence. With this knowledge an additional condition can be added to Eq. 3.7, namely if there is a positive SEC and the divergence is negative the density of ice is used, $\tilde{\rho} = \rho_i$. However, this condition assumes that, in an area with a positive elevation change and a negative divergence, the entire signal is due to ice dynamics, where in reality it would likely be a combination of ice dynamics and snow accumulation. To divide these signals one could use a RCM to estimate the accumulation part. This is however ongoing work and this thesis has not definitively found a realistic density parameterization for the AIS. In the next section will some preliminary results be shown.

3.2 Preliminary Results

Panels A and B in Fig 3.1 show the SEC for GrIS and AIS derived from ICESat-2 between October 2018 and September 2021 after a kriging has been performed, panels C and D show spatial errors from ICESat-2. Figure 3.2 show the firn compaction rates, $\frac{dh_{air}}{dt}$, and Fig. 3.3 show the signals from the vertical bedrock movement. Finally, Fig. 3.4 shows the SEC after correcting for the firn response signal and the vertical bedrock movement signal.

The SEC measured from ICESat-2 shows large negative signals around most of the Greenlandic coastline, in Antarctica the largest negative signals are from the outlet glaciers towards Amundsen sea, Fig. 3.1 A and B. The errors from ICESat-2 are largest in mountainous and steep terrain as seen in Southeast Greenland and the Transantarctic Mountains, the AP and Oates Land in Antarctica, Fig. 3.1 C and D. The firn compaction over the GrIS have large negative signals along the Southeast coast and smaller positive signals in the Central east and Northwest region, Fig. 3.2 A. The firn signals for Antarctica are within $\pm$ 5 cm year^{-1} for most of the AIS, it is only around the edge of the grounded AIS that larger signals are detected. Over the AP, around the Ronne-Filcher ice shelf, and Wilkes Land, and George V Land (East Antarctica) are there larger negative signals. Around Princess Elizabeth Land and Amery ice shelf (East Antarctica) and Marie Byrd Land (West Antarctica) there are positive signal (thickening of the firn), Fig. 3.2 B. The vertical bedrock movement signal for GrIS is between 0 and 20 mm year^{-1}, the strongest signals are seen at Jakobshavn glacier (Central west), Rink, Hayes, and Upernavik (Northwest), and Nioghalvfjerds and Zachariae Isstrøm glacier (Northeast), Fig. 3.3 A. Over the AIS the strongest signal $\approx$ 30 mm year^{-1} is seen in West Antarctica near the Pine Island, Thwaites, and Getz glacier and small negative ($\approx$ -2 mm year^{-1}) signals are seen in East Antarctica, Fig. 3.3 B. Figure 3.4 show the corrected SEC for GrIS, panel A, and the associated error, panel C. Large negative signals over the GrIS are seen around the big glaciers Jakobshavn glacier (Central west), Rink, Hayes, Upernavik and Helprin glacier (Northwest), Petermann glacier (North), Zachariae Isstrøm and Nioghalvfjerds glacier (Northeast) Kangerlussauaq glacier (Central east), and Helheim (Southeast), Fig. 3.4. For the grounded AIS the majority of the interior has small SEC $\pm$ 5 cm year^{-1}. There are large (<0.5 m year^{-1}) positive elevation changes in the area of the Kamb ice stream in West Antarctica. The largest negative elevation changes are detected at the glaciers that have outlets to the Amundsen sea (Thwaites, Pine Island, and Getz glacier) and Totten glacier in East Antarctica, Fig. 3.4 B and D. Using the density parametrization from Eq. 3.7 we get a MB for the GrIS of -263.5±42.6 Gt year^{-1} between October 2018 and September 2021.

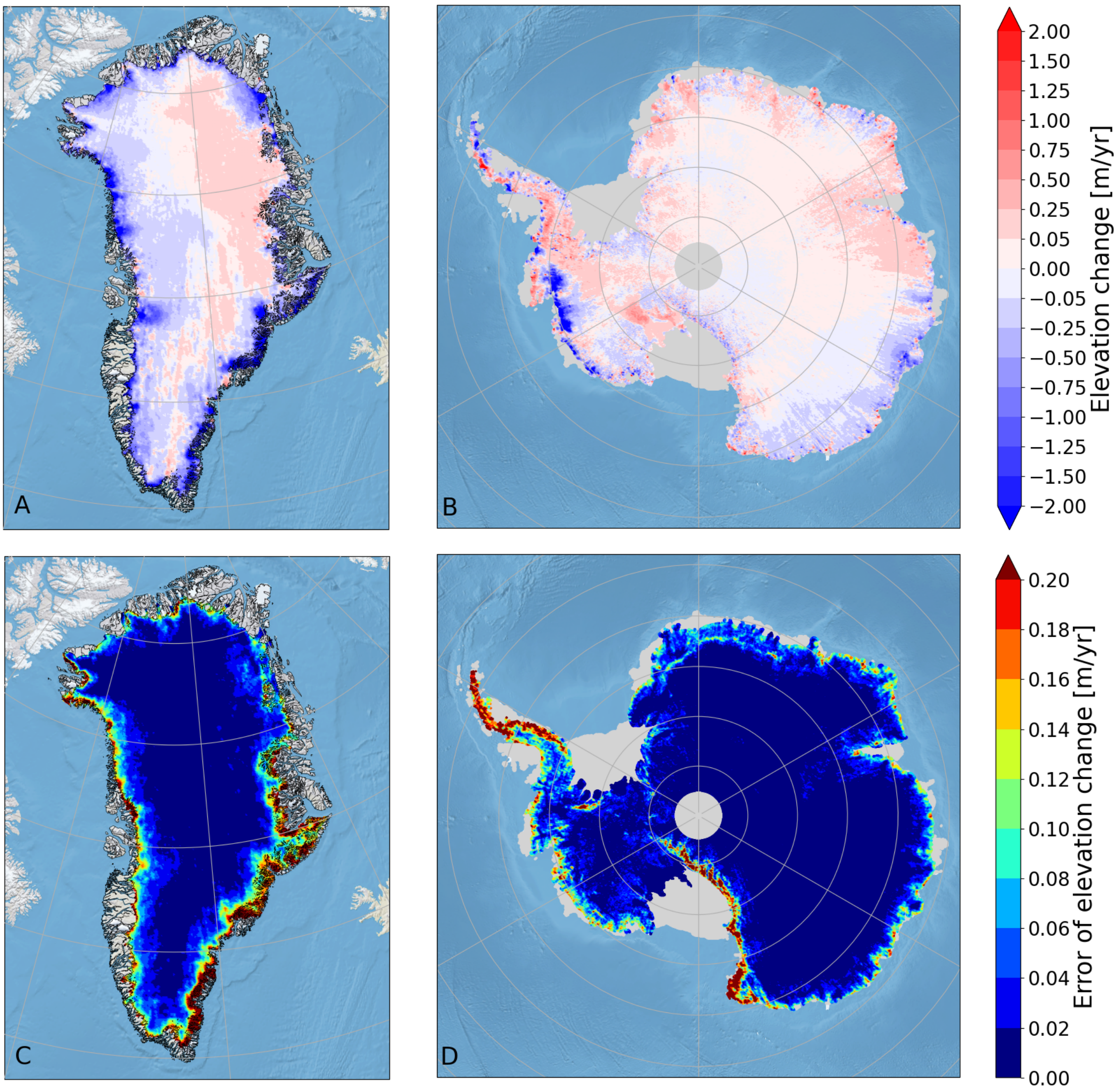

Figure 3.1: Ice sheet elevation change from October 2018 to September 2021 derived from ICESat-2 observations. (A, B) Elevation change, (C, D) the associated error, after kriging. The gray area around Antarctica is the non-grounded ice sheet (Gerrish et al., 2021), and the in the middle is the polar gap. Values are in metre of ice equivalent.

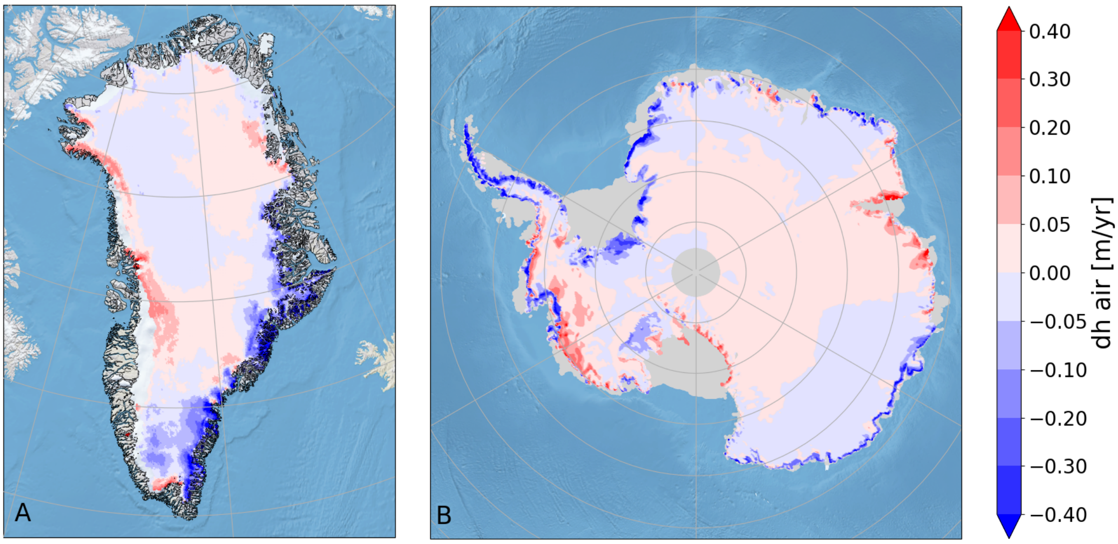

Figure 3.2: Panel A and B shows the firn compaction rate $\frac{dh_{air}}{dt}$. The gray area around Antarctica is the non-grounded ice sheet, and in the middle is the polar gap. Values are in ice equivalent.

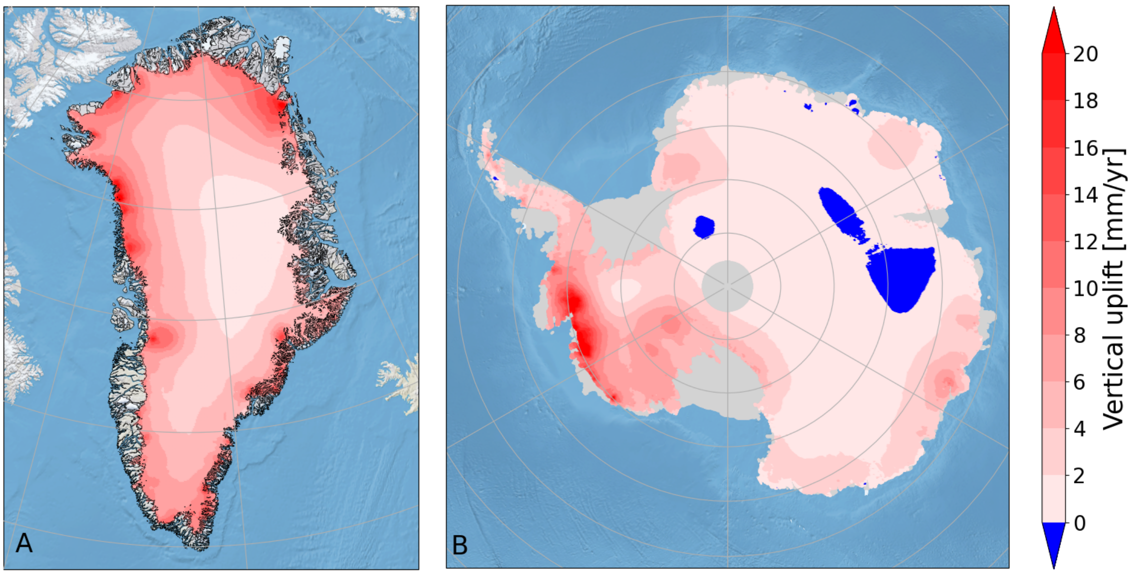

Figure 3.3: Vertical displacement (GIA plus ER), note the unit is mm per year. Data provided by Spada and Melini, 2019. The gray area around Antarctica is the non-grounded ice sheet (Gerrish et al., 2021), and the in the middle is the polar gap.

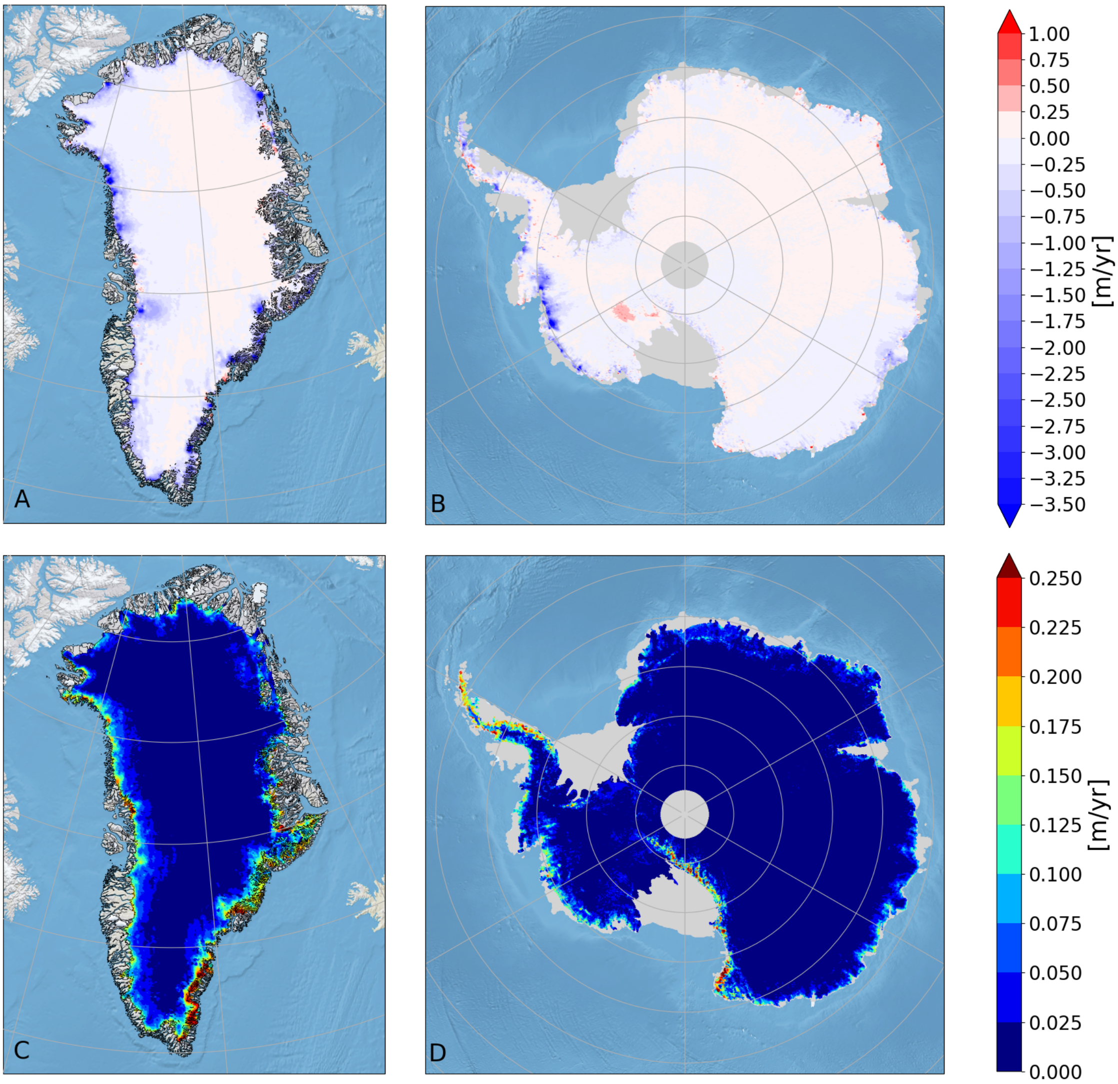

Figure 3.4: Panels A and B show SEC after the correcting for the firn compaction and the vertical bedrock movement, and panel C and D show the error, all panels are expressed in metres of ice equivalent. The gray area around Antarctica is the non-grounded ice sheet (Gerrish et al., 2021), and the in the middle is the polar gap.

4 Discussion

In summary Chap. 2 and 3 presented results for SMB, SEC, and MB of the Antarctic ice sheet and in a few cases also for the GrIS along with various important processes and uncertainties. For Antarctica the yearly SMB over the grounded AIS is 1968.0$\pm$279.3 Gt year^{-1} and over the total AIS is 2574.37 Gt year^{-1} from the period 1979 to 2021, using HIRHAM5 as the driving RCM to force the firn model. The following subsections will elaborate on some of the questions and investigations that came up during this project. A dedicated discussion on the current work on volume to mass conversion can be found in section 3.1.1. The papers have individual discussions specify to their study, the papers can be found in Appendix A.1 to A.8.

4.1 Modelled SMB

Knowing the Antarctic SMB is essential to understand and evaluate the state of the AIS. To compute the ice sheet wide SMB RCMs are used, **Paper I** made a SMB ensemble using different RCMs and found that estimates in the ensemble differed by 580 Gt year^{-1} over the grounded ice sheet, this corresponds to 1.5 mm of global sea level change per year. The reason for this large spread is due to several things, the RCMs are built on different physics, executed at different resolutions which has a large impact on precipitation (Rummukainen, 2016). Furthermore, some RCMs including HIRHAM5, did not have a proper subsurface scheme, leading to different definitions of the SMB equation. For HIRHAM5 the SMB was calculated as precipitation minus sublimation, meaning all the firn physics such as melt, refreezing, percolation and runoff were ignored. These points are what lead to the development of the firn model over the AIS in **Paper II**, which gives a more realistic computation of the SMB in addition to modelling the firn pack. A concern in **Paper I**, when comparing the integrated SMB was that the ice masks within the RCMs differed leading to different areas of the AIS. To avoid any area bias a common ice mask was created. This did however result in a SMB bias studied in **Paper III**, where it was found that a small difference in the area between the common ice mask and the native RCM ice masks could lead to a large difference in the SMB. Even though, it was the ice mask that was the focus of **Paper III**, other physical features such as the model topography and model resolution also adds to the spread in the SMB ensemble in **Paper I**. The aim is not to get all RCMs to agree as they are their own best approximation of the Earth system, the range in the ensemble provides a confidence interval for the reconciled estimate. But if we, in the community, create a community ice mask, as suggested in **Paper III**, we can minimize errors or biases we know are introduced in the post-processing. **Paper III** also found that nearly all the native RCM ice masks were made with data that are decades old. A study from Greene et al., 2022 showed that the area of the Antarctic ice shelves has decreased by 36701 $\pm$ 1465 km^2 from 1997 to 2021, which is equal to 235 $\pm$ 9 grid cells in the firn model at 0.11°resolution. This only confirms the need for an up-to-date community ice mask.

4.1.1 Uncertainties in modelled SMB

For lack of a better method, the uncertainties of the SMB in **Paper I** and **Paper II**, were given as one standard deviation of the modelled SMB time series, which essentially is a measure of the variability in the modelled time series. However, the true uncertainty of the modelled SMB should be determined with the use of observations, Fettweis, 2022 has created a method for doing this. This method was originally created for Greenlandic

SMB, using SMB observations from PROMICE (Machguth et al., 2016), ice cores (Bales et al., 2009; Bales et al., 2001; Ohmura, 1999), and airborne radar transects (Karlsson et al., 2016; Karlsson et al., 2020). Here, the method has been further developed to determine an observation-based SMB uncertainty for the modelled Antarctic SMB, the Antarctic dataset can be found in Wang et al., 2021. In the following section results from both Antarctica and Greenland will be shown. Here we use the RCM HIRHAM5 to force the firn model as described in Sec. 1.3 and in **Paper II**, furthermore the time series are extended through 2021. Overall, the SMB error is estimated from an error function computed from a piecewise linear fit estimated from the 80th percentile best matching RMSE of a model-observation comparison. First, we compare the modelled SMB with the observations. The comparison is only done for the modelled SMB with observations that are located within the grounded ice mask and have a measurement period over at least 6 months in the period of the time series (1980-2021). We then define a range of intervals for the modelled SMB with a spacing of 100 mm we year^{-1}. In each interval we find the mid-point and around each mid-point a local interval is created with an increment of $\pm$ 10 mm we year^{-1}. The objective is to increase this local modelled SMB-interval until at least 100 model-observations pairs are inside the interval bounds. This is repeated around each midway point. Hereafter, we calculate the RMSE of the 80th percentile best matching points in each SMB-interval, and the resulting RMSE points are fitted using a piecewise linear fit. The modelled SMB compared with observations are shown in Fig. 4.1 (A) for Antarctica and (B) for Greenland and the two piecewise error functions are shown in Fig. 4.2 (A) and (B). In the Antarctic data set there are only very few observations with a negative SMB, which is why the piecewise error function is only made for positive values, for SMB values below zero, the error is set to 15%. Because the uncertainty of the SMB is only given over the grounded AIS there are only a few places near the coast we model a negative SMB. The error functions can now be used to estimate the corresponding SMB error of a given value of modelled SMB. The error is subsequently multiplied with the theoretical standard deviation of a uniform distribution between -1 and 1 to add a random error term.

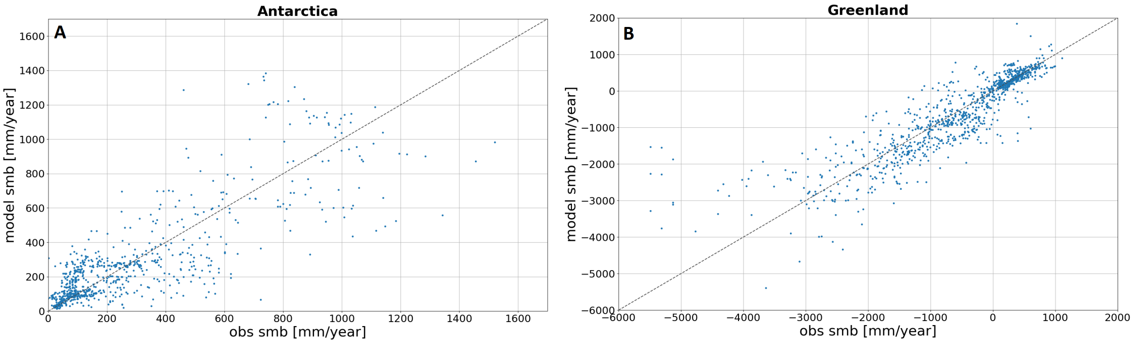

Figure 4.1: The observed SMB, on the x-axes, are compared with the modelled SMB, on the y-axes, of the nearest grid cell for Antarctica (A) and Greenland (B). Note the axes differ.

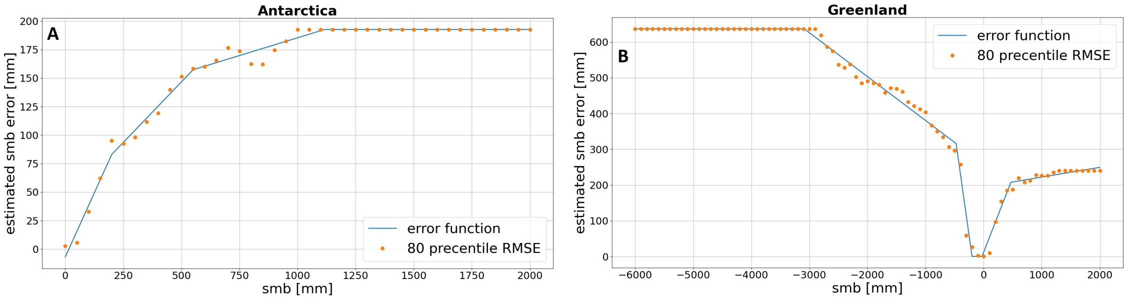

Figure 4.2: The yellow dots are the 80th percentile RMSE and the blue line are piecewise error functions. The x-axes are the magnitudes of modelled SMB and the y-axis are the associated error, for the grounded Antarctica (A) and for Greenland (B). Note the axes differ.

Figure 4.2 shows, for both ice sheets, that when a modelled SMB is small so is the error and vice versa until a limit. For the grounded AIS the error becomes constant around a modelled SMB greater than 1100 mm we year^{-1}. For Greenland the error becomes constant when the modelled SMB is lower than -3000 mm we year^{-1}, as shown in Fig. 4.2. This is caused by a lack of observations, as it is unlikely that too high model values could cause this when compared to other models (Fettweis et al., 2020; **Paper I**).

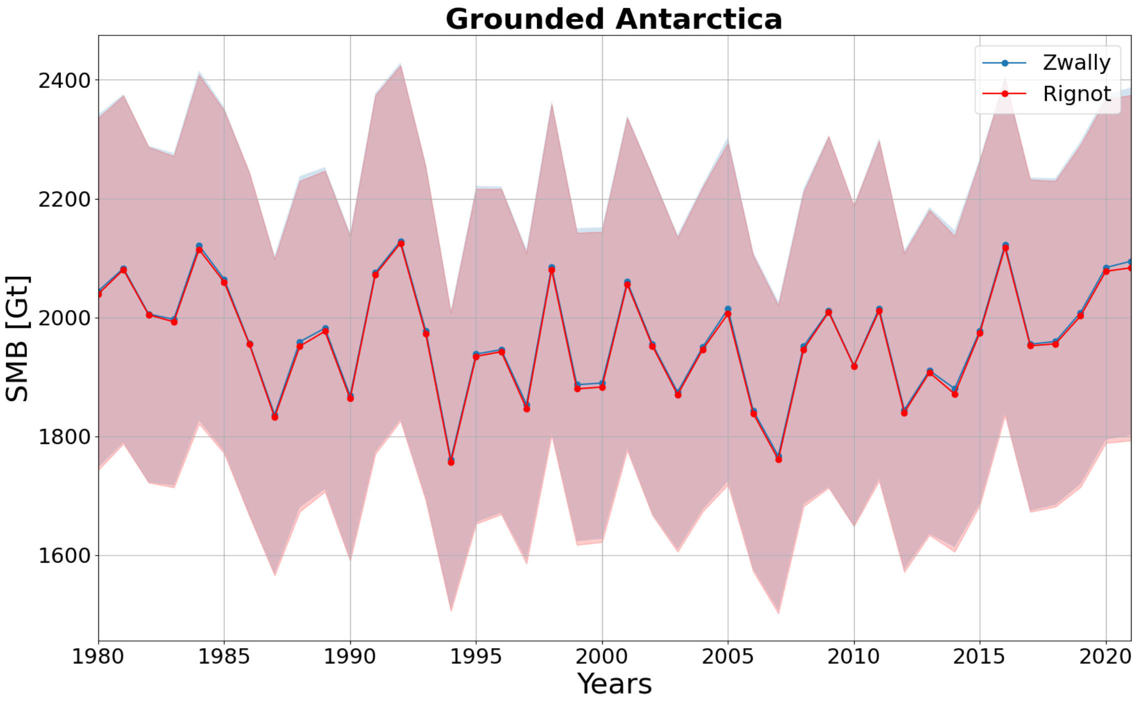

Figure 4.3: The integrated SMB over the grounded AIS in Gt year^{-1} from 1980 to 2021, over the Zwally et al., 2012 defined AIS (blue) and the Rignot et al., 2011a defined AIS (red). The shaded area are the uncertainties.

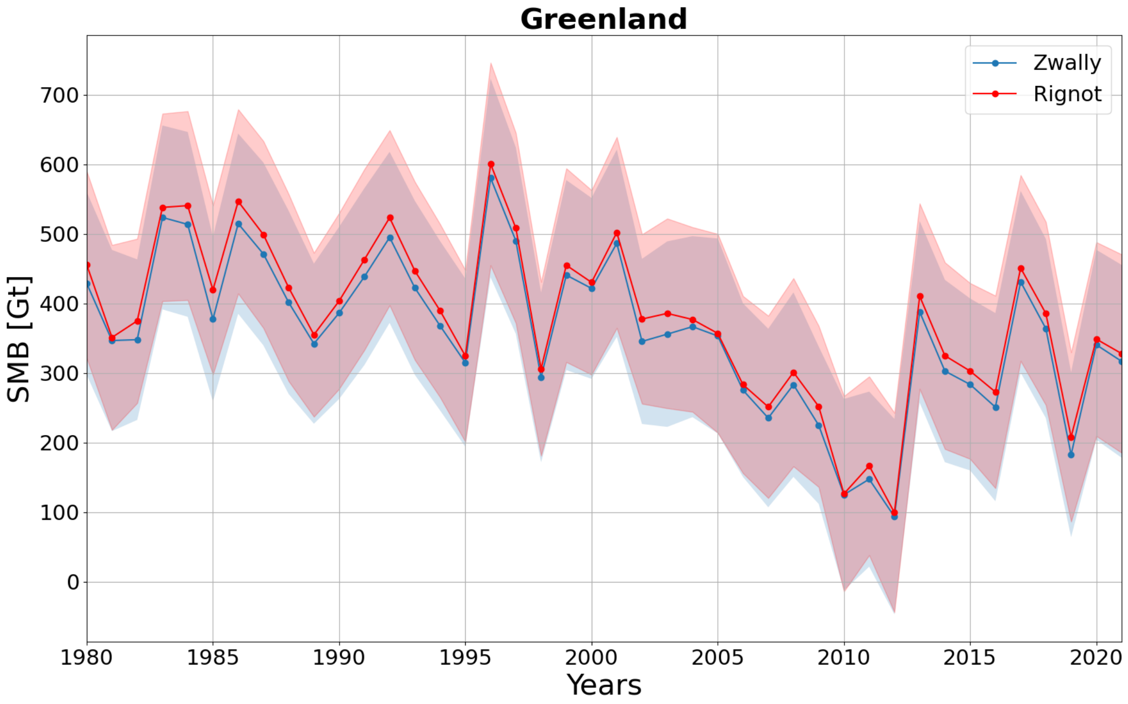

Figure 4.4: The integrated SMB over the GrIS in Gt year^{-1} from 1980 to 2021, over the Zwally et al., 2012 defined GrIS (blue) and the Rignot and Mouginot, 2012 defined GrIS (red). The shaded area are the uncertainties.

Figures 4.3 and 4.4 display time series of the integrated SMB with the calculated uncertainties for the grounded AIS and the GrIS respectively. As shown in **Paper III** ice masks can have a large influence on the results. Therefore, we show results from two different ice masks, for each ice sheet, created by Zwally et al., 2012 and Rignot et al., 2011a. These two ice masks are widely used in intercomparison studies (Shepherd et al., 2018; Shepherd et al., 2020). The mean SMB over the grounded AIS is with the Zwally ice mask 1968.0$\pm$279.3 Gt year^{-1} and with the Rignot ice mask 1963.3$\pm$278.4 Gt year^{-1}, and for the GrIS it is with the Zwally ice mask 358.8$\pm$128.6 Gt year^{-1} and with the Rignot ice mask 377.6$\pm$131.5 year^{-1}, corresponding to an uncertainty of 14.2% for the grounded AIS and $\approx$35% for GrIS. The large difference in uncertainty between the two ice sheets could indicate that HIRHAM5 and the firn model represents the Antarctic SMB better than the Greenlandic SMB. However, there are multiple factors to take into account before making such a conclusion; there are large areas with a negative SMB in Greenland making the SMB range much larger than over the grounded Antarctica (Figs. 4.1 and 4.2), making it much more complex to model the GrIS. Furthermore, the error function becomes constant in Antarctica when the SMB reaches 1100 mm we year^{-1}, whereas in Greenland the error function does not become constant in the positive SMB range. This is due to a lack of observations in the high precipitation areas of Antarctica, which likely leads to an underestimation of the uncertainty on larger SMB values in Antarctica. It requires further analysis to identify the reasons for this uncertainty difference.

The benefit of this method is that the uncertainty estimates are based on real observations. The disadvantage is that this method only searches for model-observation pairs in the range of SMB values, it does not take location into account it purely looks at the uncertainty of the magnitude of the values. If the uncertainty estimates should take location into account, it would require much more data, not to mention seasonal variability especially in Greenland and over the AP.

4.1.2 Melt and Runoff

The runoff over the grounded AIS has for a long time thought to be negligible, as it had been assumed that all meltwater refreezes (Lenaerts et al., 2019; Lenaerts & Van den Broeke, 2012). However, a study by Tuckett et al., 2019 detected surface melt over the grounded AP draining down to the bedrock and causing an increase in dynamical ice loss. So, even though meltwater does not end up as surface runoff, i.e. changing the SMB, it can still impact the MB. The results from this thesis, show that the runoff over the grounded AIS is too large to be neglected (50-80 Gt year $^{-1}$, (**Paper II**)). It is however difficult to validate the results since there are no independent large scale melt volume or runoff observations.

Surface melt over an ice sheet or ice shelves can be detected with remote sensing because the presence of liquid water shows a sharp increase in the microwave brightness temperature (Tedesco, 2009). Several studies have used this method over the AIS (Johnson et al., 2022; Nicolas et al., 2017; Trusel et al., 2013) to determine the melt extent. In **Draft I** we investigate the melt extent in the firn model forced with different RCMs over the Ross Ice shelf as a case study. To some degree we are able to validate the melt extent, although the modelled melt extent is very sensitive to the model resolution (Nicolas et al., 2017; Trusel et al., 2013), especially when it comes to wind induced melt (Carter et al., 2022; Orr et al., 2021; **MC Paper III**). The problems arise in the conversion from melt extent to melt volume. Here, we need to use models, which means that all melt volume estimates are model dependent. The follow-up question is then how much of the meltwater is retained in the firn pack? and how much becomes runoff? Also here we lack large scale observations. Our results of melt and runoff are higher than other RCM results, RACMO2 models a runoff of 3 Gt year^{-1} (Van Wessem et al., 2018) and MAR models a runoff of 1 Gt year^{-1} (without the AP) (Agosta et al., 2019), compared to our values that are greater than 50 Gt year^{-1}. It should be mentioned that the time period, ice masks, and resolution of these models differ, however it is still a significant difference in runoff. But as of now there is no way to make an independent validation.

Many of the most preferred firn models, including the one developed in this thesis, are single column models (Kittel et al., 2021; Van Wessem et al., 2018; **Paper II**), which means that there is no internal horizontal water flow, another limitation when studying the firn pack. As Tuckett et al., 2019 concluded, when surface meltwater drains through channels to the base of the glacier, it can have a clear impact on ice discharge. It would therefore be of great value if horizontal flow features were added to firn models.

Widespread meltwater has already been detected across the AIS in the present-day climate (Kingslake et al., 2017; Zou et al., 2021). Therefore, the firn model becomes even more crucial in order to compute the SMB in a warming climate, as is projected for the end of the century. Here, the simple precipitation minus sublimation approximation, used in **Paper I**, does not hold. Several studies have found that melt and runoff, close to the coast and over the ice shelves will increase in the future (Gilbert & Kittel, 2021; Kittel et al., 2022; Trusel et al., 2015) and this is in agreement with our results from **MC Paper II**. This is yet another confirmation of the importance of the firn model as melt and runoff are not only important parameters for the SMB estimates, melt is already an important factor for the MB in some regions and in the phenomenon of hydrofracturing that occurs over ice shelves (Banwell et al., 2013; Scambos et al., 2009; **MC Paper III**).

4.2 Firn compaction for SEC corrections

The firn compaction response depends on surface mass fluxes and temperatures, it can thus fluctuate on seasonally to multiyear timescales (Kuipers Munneke et al., 2015; Medley et al., 2020; Sørensen et al., 2011; Zwally & Jun, 2002). The main contributor to the surface mass fluxes over the AIS is precipitation, and as seen in **Paper I** there is a large spread in the precipitation both in the integrated amount and the in the spatial distribution. This spread is therefore also seen in the firn compaction in **MC Paper I**, here it is evident that the outputs from RCMs have a large influence on the firn compaction rates. In East Antarctica the RCMs accounts for 72% of the spread in the firn compaction ensemble, the remaining 28% is explained by the choice of firn desification model and surface density. **MC Paper I** only investigates East Antarctica, however, due to the warmer temperatures and larger precipitation fluxes in West Antarctica and over the AP, it is very likely that the RCMs also have the largest impact on the firn compaction in these regions. Projection studies argue that Antarctica over all will get warmer and wetter (Bozkurt et al., 2021; Bracegirdle et al., 2020; **MC Paper II**), so the firn compaction signal will likely only get stronger and more complex in the future. To compute the firn compaction results shown in Fig. 3.2 we have used the RCM HIRHAM5 to force the firn model from **Paper II**. Had another RCM been used to force the firn model then the firn compaction rate would have been different. However, if it had resulted in a significant difference to the final MB result is an open question, which could be investigated in future work. It is worth bearing in mind, especially in Antarctica, that the SEC signal is very small in the interior of the ice sheet, and the firn compaction is not well determined (**MC Paper I**). Meaning that it does not take much to change the sign on the corrected SEC. So if the density parametrization over the AIS, is dependent on the sign of the corrected SEC, like Eq. 3.7 for GrIS, it can be difficult to robustly determine if density should be of snow or ice, which can lead to a larger uncertainty in mass change. Another factor to take into consideration, with regard to the firn compaction, is that the firn model has a larger meltwater volume than other firn models, which will lead to a greater firn densification signal in these high meltwater areas, see Section 4.1.2 for a discussion on melt and runoff.

4.3 Future work

As this thesis evolved some questions got answered, while new questions occurred and new ideas sprang to mind on what to do next. It is clear that in spite of more models simulating SMB there remains a high uncertainty on precipitation in Antarctica, while melt and runoff remain under constrained. These make it challenging to determine the present-day SMB of the AIS. Given the importance of SLR, these outstanding challenges remain to be solved. However, the model and observation framework adopted here can help to tackle these issues in the following manner:

Large scale atmospheric circulation patterns are extremely important in the Antarctic climate (Fogt and Bromwich, 2006; Fogt and Marshall, 2020; **Paper II; MC Paper III**). Being able to resolve these circulations in the RCMs are therefore crucial, to get the most reliable estimates of the present-day and future climate. It could be very interesting to do an intercomparison, like in **Paper I**, on the ability of the different RCMs to resolve the large scale atmospheric circulations in historical simulations and projections using different GCMs. The historical simulations could then be evaluated against reanalysis simulations like in **MC Paper II**. Then a SMB ensemble could be made for the end of the century, using the models that best represent and resolve the large scale atmospheric circulations.

Although melt extent observations already exist, an additional way to possibly get a better understanding would be to take the output from the firn model and use it as input in the Snow Microwave Radiative Transfer (SMRT) model (Picard et al., 2018). The SMRT model can calculate the brightness temperatures of the surface from the ice, snow, and liquid water content computed by the firn model. This can then be compared with the satellite observed brightness temperatures. The idea is that firn model can give 3D outputs so by forcing the SMRT model with liquid water at different depths, it can be investigated if this creates different fingerprints at different frequencies, to make a more advanced algorithm to convert satellite observations of brightness temperatures to melt extents. The disadvantage with this is that we add another model, which has the potential to introduce even more uncertainty.

Ice shelves play an important role in state of the AIS it is therefore important to monitor them, for example with altimetry measurements from ICESat-2. There are however some additional steps to take in the processing of the data, compared to the grounded ice. Some of these steps are tide corrections which can be modelled (Egbert et al., 1994; Padman et al., 2002), and taking into account that the area of ice shelves change over time. Typically, the ice shelves area increases continuously through advection and reduces suddenly due to calving (Smith et al., 2020), the time-scales of the area reductions are dependent on the calving cycle (De Rydt et al., 2019; Fricker et al., 2002; Hogg & Gudmundsson, 2017). Using altimetric measurements over ice shelves have been done by Smith et al., 2020, but it would be very interesting to use the firn model developed in this thesis to get another estimate of the state of the Antarctic ice shelves.

Subtracting the SMB from the MB will give the discharge, which then could be validated with a data set of observed discharge. This would be a way of making a more robust validation of the SMB and the MB. However, this only validates if the absolute value of the MB and the SMB is correct. It would still show a good validation if errors in the MB and the SMB balanced out. Nonetheless, it could be interesting to do.

5 Conclusion

It is of the utmost importance to understand the drivers of change of the AIS because it contains enough fresh water to create serious global disruption via sea level and coastal inundation if it melts. This thesis has investigated and analysed some of the fundamental climate variables for the evolution of the AIS, using state of the art numerical climate models and remote sensing techniques.

Multiple studies have used RCMs to model the Antarctic SMB. In this study an intercomparison has been done with some of the most used RCMs in the Antarctic domain, in the period from 1987 to 2015, using the reanalysis dataset ERA-interim. In this intercomparison temperatures, wind speeds, and SMB values have been compared, a spread of the integrated ice sheet wide SMB of 558 Gt year^{-1} was found, corresponding to 24% of the ensemble mean of 2329$\pm$94 Gt year^{-1} (**Paper I**). The SMB ensemble mean from **Paper I** is lower than other studies, this underestimation is attributed to the choice of ice mask, it was chosen in the intercomparison to satisfy all the RCMs. The choice of ice mask created an underestimation of the integrated SMB of up to 102 Gt year^{-1} over the grounded part of Antarctica, which is close to the ice sheet imbalance of Antarctica (**Paper III**), showing the importance of ice masks in RCMs and how careful one should be in intercomparison studies.

To get the most realistic estimate of SMB it is important to take meltwater percolation and refreezing into account. This was done in **Paper II** by further developing a firn model to represent the Antarctic firn pack. The firn model was able to represent the physics of the firn pack, including but not limited to temperature, density, snow, ice and liquid water content, refreezing and grain growth. The firn model was run with different schemes for handling the model layers in the firn pack, it was found that the choice of layer scheme is important for both surface variables like melt and 3D variables such as density. From the firn model the rate of firn compaction has been computed and used to correct the SEC from ICESat-2, so only the SEC signals from the ice dynamics were left. Altimetric measurement from ICESat-2 have in this thesis been used over both Greenland and the grounded part of Antarctica to measure the SEC. By knowing a realistic density parametrization for Greenland it was possible to convert the volume change to a mass change, the MB for Greenland, in the period from October 2018 to September 2021, was -263.5$\pm$42.6 Gt year^{-1}. The density parametrization for the AIS is still work in progress.

Due to the sheer size of the AIS there are processes, from meltwater percolation to large scale atmospheric circulation, that need to be taken into account when evaluating the state of the present-day ice sheet. Coastal regions all around Antarctica, including the ice shelves, have shown the largest variability in the climate like melt events, warmer temperatures, extreme precipitation events, and stronger firn compaction signals (**Paper I, II; MC Paper I, III; Draft I**). It is also these coastal areas that will experience the largest impact of projected climate change (**MC Paper II**). This thesis has also shown that some of the methods used here are also applicable over the GrIS and in different periods of time (**Draft II; MC Paper II**).

This thesis combined with other studies confirms that even though Antarctica is remote and isolated, the ice sheet still susceptible to changes in the global climate. We live in a golden age of remote sensing and almost unlimited computer resources to execute numerical models. Which, if utilized correctly, could give us an unprecedented understanding of the Antarctic Ice Sheet and its impact on the global climate system.

Bibliography

Ablain, M., Meyssignac, B., Zawadzki, L., Jugier, R., Ribes, A., Spada, G., Benveniste, J., Cazenave, A., & Picot, N. (2019). Uncertainty in satellite estimates of global mean sea-level changes, trend and acceleration. *Earth System Science Data*, *11*(3), 1189–1202. https://doi.org/https://doi.org/10.5194/essd-11-1189-2019

Agosta, C., Amory, C., Kittel, C., Orsi, A., Favier, V., Gallée, H., van den Broeke, M. R., Lenaerts, J., van Wessem, J. M., van de Berg, W. J., et al. (2019). Estimation of the antarctic surface mass balance using the regional climate model mar (1979–2015) and identification of dominant processes. *The Cryosphere*, *13*(1), 281–296. https://doi.org/https://doi.org/10.5194/tc-13-281-2019

Ambrizzi, T., Reboita, M., DA ROCHA, R., & Llopart, M. (2018). The state-ofthe-art and fundamental aspects of regional climate modeling in south america. *Annals of the New York Academy of Sciences, especial edition: Climate Science*, 1–23. https://doi.org/https://doi-org.proxy.findit.cvt.dk/10.1111/nyas.13932

Anandakrishnan, S., & Alley, R. B. (1997). Stagnation of ice stream c, west antarctica by water piracy. *Geophysical Research Letters*, *24*(3), 265–268. https://doi.org/https://doi.org/10.1029/96GL04016

Bales, R. C., Guo, Q., Shen, D., McConnell, J. R., Du, G., Burkhart, J. F., Spikes, V. B., Hanna, E., & Cappelen, J. (2009). Annual accumulation for greenland updated using ice core data developed during 2000–2006 and analysis of daily coastal meteorological data. *Journal of Geophysical Research: Atmospheres*, *114*(D6). https://doi.org/https://doi.org/10.1029/2008JD011208

Bales, R. C., McConnell, J. R., Mosley-Thompson, E., & Csatho, B. (2001). Accumulation over the greenland ice sheet from historical and recent records. *Journal of Geophysical Research: Atmospheres*, *106*(D24), 33813–33825. https://doi.org/https://doi.org/10.1029/2001JD900153

Banwell, A. F., MacAyeal, D. R., & Sergienko, O. V. (2013). Breakup of the larsen b ice shelf triggered by chain reaction drainage of supraglacial lakes. *Geophysical Research Letters*, *40*(22), 5872–5876. https://doi.org/https://doi.org/10.1002/2013GL057694

Barletta, V. R., Sørensen, L. S., & Forsberg, R. (2013). Scatter of mass changes estimates at basin scale for greenland and antarctica. *The Cryosphere*, *7*(5), 1411–1432. https://doi.org/doi:10.5194/tc-7-1411-2013

Boberg, F., Mottram, R., Hansen, N., Yang, S., & Langen, P. L. (2022). Uncertainties in projected surface mass balance over the polar ice sheets from dynamically downscaled ec-earth models. *The Cryosphere*, *16*(1), 17–33. https://doi.org/10.5194/tc-16-17-2022

Bozkurt, D., Bromwich, D. H., Carrasco, J., & Rondanelli, R. (2021). Temperature and precipitation projections for the antarctic peninsula over the next two decades: Contrasting global and regional climate model simulations. *Climate Dynamics*, *56*(11), 3853–3874. https://doi.org/https://doi.org/10.1007/s00382-021-05667-2

Bracegirdle, T. J., Krinner, G., Tonelli, M., Haumann, F. A., Naughten, K. A., Rackow, T., Roach, L. A., & Wainer, I. (2020). Twenty first century changes in antarctic and southern ocean surface climate in cmip6. *Atmospheric Science Letters*, *21*(9), e984. https://doi.org/https://doi.org/10.1002/asl.984

Bunde, C., Mottram, R., Boberg, F., Hansen, N., Hvidberg, C., Gierisch, A., & Guo, C. (2022). High resolution simulations of eemian climate in greenland, in preparation.

Carter, J., Leeson, A., Orr, A., Kittel, C., & van Wessem, J. M. (2022). Variability in antarctic surface climatology across regional climate models and reanalysis datasets. *EGUsphere*, 1–35. https://doi.org/https://doi.org/10.5194/egusphere-2022-86

Christensen, O. B., Drews, M., Christensen, J. H., Dethloff, K., Ketelsen, K., Hebestadt, I., & Rinke, A. (2007). The hirham regional climate model. version 5 (beta).

De Rydt, J., Gudmundsson, G. H., Nagler, T., & Wuite, J. (2019). Calving cycle of the brunt ice shelf, antarctica, driven by changes in ice shelf geometry. *The Cryosphere*, *13*(10), 2771–2787. https://doi.org/https://doi.org/10.5194/tc-13-2771-2019

Dee, D. P., Uppala, S. M., Simmons, A. J., Berrisford, P., Poli, P., Kobayashi, S., Andrae, U., Balmaseda, M., Balsamo, G., Bauer, d. P., et al. (2011). The era-interim reanalysis: Configuration and performance of the data assimilation system. *Quarterly Journal of the royal meteorological society*, *137*(656), 553–597. https://doi.org/https://doi.org/10.1002/qj.828

Drinkwater, M. R., Francis, R., Ratier, G., & Wingham, D. J. (2004). The european space agency's earth explorer mission cryosat: Measuring variability in the cryosphere. *Annals of Glaciology*, *39*, 313–320. https://doi.org/https://doi.org/10.3189/172756404781814663

Eerola, K. (2006). About the performance of hirlam version 7.0. *Hirlam Newsletter*, *51*, 93–102.

Egbert, G. D., Bennett, A. F., & Foreman, M. G. (1994). Topex/poseidon tides estimated using a global inverse model. *Journal of Geophysical Research: Oceans*, *99*(C12), 24821–24852. https://doi.org/https://doi.org/10.1029/94JC01894

Enderlin, E. M., Howat, I. M., Jeong, S., Noh, M.-J., Van Angelen, J. H., & Van Den Broeke, M. R. (2014). An improved mass budget for the greenland ice sheet. *Geophysical Research Letters*, *41*(3), 866–872. https://doi.org/https://doi.org/10.1002/2013GL059010

Feser, F., Rockel, B., von Storch, H., Winterfeldt, J., & Zahn, M. (2011). Regional climate models add value to global model data: A review and selected examples. *Bulletin of the American Meteorological Society*, *92*(9), 1181–1192. https://doi.org/https://doi.org/10.1175/2011BAMS3061.1

Fettweis, X. (2022). Uncertainties on modelled smb. *Personal conversation*.

Fettweis, X., Hofer, S., Krebs-Kanzow, U., Amory, C., Aoki, T., Berends, C. J., Born, A., Box, J. E., Delhasse, A., Fujita, K., et al. (2020). Grsmbmip: Intercomparison of the modelled 1980–2012 surface mass balance over the greenland ice sheet. *The Cryosphere*, *14*(11), 3935–3958. https://doi.org/https://doi.org/10.5194/tc-14-3935-2020

Fogt, R. L., & Bromwich, D. H. (2006). Decadal variability of the enso teleconnection to the high-latitude south pacific governed by coupling with the southern annular mode. *Journal of Climate*, *19*(6), 979–997. https://doi.org/https://doi.org/10.1175/JCLI3671.1

Fogt, R. L., & Marshall, G. J. (2020). The southern annular mode: Variability, trends, and climate impacts across the southern hemisphere. *Wiley Interdisciplinary Reviews: Climate Change*, *11*(4), e652. https://doi.org/https://doi.org/10.1002/wcc.652

Forsberg, R., Sørensen, L., & Simonsen, S. (2017). Greenland and antarctica ice sheet mass changes and effects on global sea level. *Integrative study of the mean sea level and its components* (pp. 91–106). Springer. https://doi.org/https://doi.org/10.1007/s10712-016-9398-7

Fox-Kemper, B., Hewitt, H., C. Xiao, G. A., S.S. Drijfhout, T. E., Golledge, N., M. Hemer, R. K., Krinner, G., Mix, A., Notz, D., Nowicki, S., Nurhati, I., Ruiz, L., Sallée, J.-B., Slangen, A., & Yu, Y. (2021). Ocean, cryosphere and sea level change. in climate change 2021: The physical science basis. contribution of working group i to the sixth assessment report of the intergovernmental panel on climate change, 1211–1362. https://doi.org/10.1017/9781009157896.011

Fretwell, P., Pritchard, H. D., Vaughan, D. G., Bamber, J. L., Barrand, N. E., Bell, R., Bianchi, C., Bingham, R. G., Blankenship, D. D., Casassa, G., Catania, G., Callens, D., Conway, H., Cook, A. J., Corr, H. F. J., Damaske, D., Damm, V., Ferraccioli, F., Forsberg, R., … Zirizzotti, A. (2013). Bedmap2: Improved ice bed, surface and thickness datasets for antarctica. *The Cryosphere*, *7*(1), 375–393. https://doi.org/10.5194/tc-7-375-2013

Fricker, H. A., Young, N. W., Allison, I., & Coleman, R. (2002). Iceberg calving from the amery ice shelf, east antarctica. *Annals of Glaciology*, *34*, 241–246. https://doi.org/doi:10.3189/172756402781817581

Gardner, A. S., Moholdt, G., Scambos, T., Fahnstock, M., Ligtenberg, S., Van Den Broeke, M., & Nilsson, J. (2018). Increased west antarctic and unchanged east antarctic ice discharge over the last 7 years. *The Cryosphere*, *12*(2), 521–547. https://doi.org/https://doi.org/10.5194/tc-12-521-2018

Gerrish, L., Fretwell, P., & Cooper, P. (2021). High resolution vector polygons of the antarctic coastline (7.4)[data set], uk polar data centre, natural environment research council, uk research and innovation. https://doi.org/https://doi.org/10.5285/ee7c6af2-da57-4519-8637-812eec5ff782

Gilbert, E., & Kittel, C. (2021). Surface melt and runoff on antarctic ice shelves at 1.5 c, 2 c, and 4 c of future warming. *Geophysical Research Letters*, *48*(8), e2020GL091733. https://doi.org/https://doi.org/10.1029/2020GL091733

Greene, C., Gardner, A., Schlegel, N., & Fraser, A. (2022). Antarctic calving loss rivals ice-shelf thinning. *Nature*. https://doi.org/https://doi.org/10.1038/s41586-022-05037-w

Hansen, N., Langen, P. L., Boberg, F., Forsberg, R., Simonsen, S. B., Thejll, P., Vandecrux, B., & Mottram, R. (2021). Downscaled surface mass balance in antarctica: Impacts of subsurface processes and large-scale atmospheric circulation. *The Cryosphere*, *15*(9), 4315–4333. https://doi.org/10.5194/tc-15-4315-2021

Hansen, N., Orr, A., Zou, X., Mottram, R., Gilbert, E., Boberg, F., Simonsen, S. B., Phillips, T., Webster, S., & Bracegirdle, T. (2022). Benefits of using a sophisticated standalone snow scheme to simulate a surface melt event over the ross ice shelf, west antarctica in the hirham5 and metum regional atmospheric models. *Atmospheric Science Letters, in preparation*.

Hansen, N., Simonsen, S. B., Boberg, F., Kittel, C., Orr, A., Souverijns, N., van Wessem, J. M., & Mottram, R. (2022). Brief communication: Impact of common ice mask in surface mass balance estimates over the antarctic ice sheet. *The Cryosphere*, *16*(2), 711–718. https://doi.org/10.5194/tc-16-711-2022

Hauer, M. E., Fussell, E., Mueller, V., Burkett, M., Call, M., Abel, K., McLeman, R., & Wrathall, D. (2020). Sea-level rise and human migration. *Nature Reviews Earth & Environment*, *1*(1), 28–39. https://doi.org/https://doi.org/10.1038/s43017-019-0002-9

Herron, M. M., & Langway, C. C. (1980). Firn densification: An empirical model. *Journal of Glaciology*, *25*(93), 373–385. https://doi.org/10.3189/S0022143000015239

Hersbach, H., Bell, B., Berrisford, P., Hirahara, S., Horányi, A., Muñoz-Sabater, J., Nicolas, J., Peubey, C., Radu, R., Schepers, D., et al. (2020). The era5 global reanalysis. *Quarterly Journal of the Royal Meteorological Society*, *146*(730), 1999–2049. https://doi.org/https://doi.org/10.1002/qj.3803

Hogg, A. E., & Gudmundsson, G. H. (2017). Impacts of the larsen-c ice shelf calving event. *Nature Climate Change*, *7*(8), 540–542. https://doi.org/https://doi.org/10.1038/nclimate3359

Horwath, M., Gutknecht, B. D., Cazenave, A., Palanisamy, H. K., Marti, F., Paul, F., Le Bris, R., Hogg, A. E., Otosaka, I., Shepherd, A., et al. (2022). Global sea-level budget and ocean-mass budget, with a focus on advanced data products and uncertainty characterisation. *Earth System Science Data*, *14*(2), 411–447. https://doi.org/10.5194/essd-14-411-2022

Howat, I. M., Porter, C., Smith, B. E., Noh, M.-J., & Morin, P. (2019). The reference elevation model of antarctica. *The Cryosphere*, *13*, 665–674. https://doi.org/10.5194/tc-13-665-2019

Jevrejeva, S., Jackson, L., Grinsted, A., Lincke, D., & Marzeion, B. (2018). Flood damage costs under the sea level rise with warming of 1.5 c and 2 c. *Environmental Research Letters*, *13*(7), 074014. https://doi.org/https://doi.org/10.1088/1748-9326/aacc76

Johnson, A., Hock, R., & Fahnestock, M. (2022). Spatial variability and regional trends of antarctic ice shelf surface melt duration over 1979–2020 derived from passive microwave data. *Journal of Glaciology*, *68*(269), 533–546. https://doi.org/https://doi.org/10.1017/jog.2021.112

Karlsson, N. B., Eisen, O., Dahl-Jensen, D., Freitag, J., Kipfstuhl, S., Lewis, C., Nielsen, L. T., Paden, J. D., Winter, A., & Wilhelms, F. (2016). Accumulation rates during 1311–2011 ce in north-central greenland derived from air-borne radar data. *Frontiers in Earth Science*, *4*, 97. https://doi.org/https://doi.org/10.3389/feart.2016.00097

Karlsson, N. B., Razik, S., Hörhold, M., Winter, A., Steinhage, D., Binder, T., & Eisen, O. (2020). Surface accumulation in northern central greenland during the last 300 years. *Annals of Glaciology*, *61*(81), 214–224. https://doi.org/doi:10.1017/aog.2020.30

Kawamiya, M., Hajima, T., Tachiiri, K., Watanabe, S., & Yokohata, T. (2020). Two decades of earth system modeling with an emphasis on model for interdisciplinary research on climate (miroc). *Progress in Earth and Planetary Science*, *7*(1), 1–13. https://doi.org/https://doi.org/10.1186/s40645-020-00369-5

Khan, S. A., Bamber, J. L., Rignot, E., Helm, V., Aschwanden, A., Holland, D. M., van den Broeke, M., King, M., Noël, B., Truffer, M., et al. (2022). Greenland mass trends from airborne and satellite altimetry during 2011–2020. *Journal of Geophysical Research: Earth Surface*, *127*(4), e2021JF006505. https://doi.org/https://doi.org/10.1029/2021JF006505

Kingslake, J., Ely, J. C., Das, I., & Bell, R. E. (2017). Widespread movement of meltwater onto and across antarctic ice shelves. *Nature*, *544*(7650), 349–352. https://doi.org/https://doi.org/10.1038/nature22049

Kittel, C., Amory, C., Agosta, C., Jourdain, N. C., Hofer, S., Delhasse, A., Doutreloup, S., Huot, P.-V., Lang, C., Fichefet, T., et al. (2021). Diverging future surface mass balance between the antarctic ice shelves and grounded ice sheet. *The Cryosphere*, *15*(3), 1215–1236. https://doi.org/https://doi.org/10.5194/tc-15-1215-2021

Kittel, C., Amory, C., Hofer, S., Agosta, C., Jourdain, N. C., Gilbert, E., Le Toumelin, L., Vignon, É., Gallée, H., & Fettweis, X. (2022). Clouds drive differences in future surface melt over the antarctic ice shelves. *The Cryosphere*, *16*(7), 2655–2669. https://doi.org/https://doi.org/10.5194/tc-16-2655-2022

Kuipers Munneke, P., Ligtenberg, S., Noël, B., Howat, I., Box, J., Mosley-Thompson, E., McConnell, J., Steffen, K., Harper, J., Das, S., et al. (2015). Elevation change of the greenland ice sheet due to surface mass balance and firn processes, 1960–2014. *The Cryosphere*, *9*(6), 2009–2025. https://doi.org/doi.org/10.5194/tc-9-2009-2015

Kulp, S. A., & Strauss, B. H. (2019). New elevation data triple estimates of global vulnerability to sea-level rise and coastal flooding. *Nature communications*, *10*(1), 1–12. https://doi.org/https://doi.org/10.1038/s41467-019-12808-z

Langen, P., Fausto, R. S., Vandecrux, B., Mottram, R. H., & Box, J. E. (2017). Liquid water flow and retention on the greenland ice sheet in the regional climate model hirham5: Local and large-scale impacts. *Frontiers in Earth Science*, *4*, 110. https://doi.org/https://doi.org/10.3389/feart.2016.00110

Langen, P., Mottram, R., Christensen, J., Boberg, F., Rodehacke, C., Stendel, M., Van As, D., Ahlstrøm, A., Mortensen, J., Rysgaard, S., et al. (2015). Quantifying energy and mass fluxes controlling godthåbsfjord freshwater input in a 5-km simulation (1991–2012). *Journal of Climate*, *28*(9), 3694–3713. https://doi.org/https://doi.org/10.1175/JCLI-D-14-00271.1

Lee, J.-Y., Marotzke, J., Bala, G., Cao, L., Corti, S., Dunne, J., Engelbrecht, F., Fischer, E., Fyfe, J., Jones, C., Maycock, A., Mutemi, J., Ndiaye, O., Panickal, S., & Zhou, T. (2021). Future global climate: Scenario-based projections and near term information. in climate change 2021: The physical science basis. contribution of working group i to the sixth assessment report of the intergovernmental panel on climate change, 553–672. https://doi.org/10.1017/9781009157896.006

Lenaerts, J., Medley, B., van den Broeke, M. R., & Wouters, B. (2019). Observing and modeling ice sheet surface mass balance. *Reviews of Geophysics*, *57*(2), 376–420. https://doi.org/https://doi.org/10.1029/2018RG000622

Lenaerts, J., & Van den Broeke, M. (2012). Modeling drifting snow in antarctica with a regional climate model: 2. results. *Journal of Geophysical Research: Atmospheres*, *117*(D5). https://doi.org/https://doi.org/10.1029/2010JD015419

Machguth, H., Thomsen, H. H., Weidick, A., Ahlstrøm, A. P., Abermann, J., Andersen, M. L., Andersen, S. B., Bjørk, A. A., Box, J. E., Braithwaite, R. J., et al. (2016). Greenland surface mass-balance observations from the ice-sheet ablation area and local glaciers. *Journal of Glaciology*, *62*(235), 861–887. https://doi.org/https://doi.org/10.1017/jog.2016.75

Martín-Español, A., King, M. A., Zammit-Mangion, A., Andrews, S. B., Moore, P., & Bamber, J. L. (2016). An assessment of forward and inverse gia solutions for antarctica. *Journal of Geophysical Research: Solid Earth*, *121*(9), 6947–6965. https://doi.org/https://doi.org/10.1002/2016JB013154

McGuffie, K., & Henderson-Sellers, A. (2014). *The climate modelling primer*. John Wiley & Sons.

Medley, B., Neumann, T. A., Zwally, H. J., & Smith, B. E. (2020). Forty-year simulations of firn processes over the greenland and antarctic ice sheets. *The Cryosphere Discussions*, 1–35. https://doi.org/https://doi.org/10.5194/tc-2020-266

Morlighem, M., Rignot, E., Binder, T., Blankenship, D., Drews, R., Eagles, G., Eisen, O., Ferraccioli, F., Forsberg, R., Fretwell, P., et al. (2020). Deep glacial troughs and stabilizing ridges unveiled beneath the margins of the antarctic ice sheet. *Nature Geoscience*, *13*(2), 132–137. https://doi.org/10.1038/s41561-019-0510-8

Mottram, R., Hansen, N., Kittel, C., van Wessem, J. M., Agosta, C., Amory, C., Boberg, F., van de Berg, W. J., Fettweis, X., Gossart, A., van Lipzig, N. P. M., van Meijgaard, E., Orr, A., Phillips, T., Webster, S., Simonsen, S. B., & Souverijns, N. (2021). What is the surface mass balance of antarctica? an intercomparison of regional climate model estimates. *The Cryosphere*, *15*(8), 3751–3784. https://doi.org/10.5194/tc-15-3751-2021

Mouginot, J., Scheuchl, B., & Rignot, E. (2012). Mapping of ice motion in antarctica using synthetic-aperture radar data. *Remote Sensing*, *4*(9), 2753–2767.

Nerem, R. S., Beckley, B. D., Fasullo, J. T., Hamlington, B. D., Masters, D., & Mitchum, G. T. (2018). Climate-change–driven accelerated sea-level rise detected in the altimeter era. *Proceedings of the national academy of sciences*, *115*(9), 2022–2025. https://doi.org/10.1073/pnas.1717312115

Neumann, T. A., Martino, A. J., Markus, T., Bae, S., Bock, M. R., Brenner, A. C., Brunt, K. M., Cavanaugh, J., Fernandes, S. T., Hancock, D. W., et al. (2019). The ice, cloud, and land elevation satellite–2 mission: A global geolocated photon product derived from the advanced topographic laser altimeter system. *Remote Sensing of Environment*, *233*, 111325. https://doi.org/https://doi.org/10.1016/j.rse.2019.111325

Nicolas, J. P., Vogelmann, A. M., Scott, R. C., Wilson, A. B., Cadeddu, M. P., Bromwich, D. H., Verlinde, J., Lubin, D., Russell, L. M., Jenkinson, C., et al. (2017). January 2016 extensive summer melt in west antarctica favoured by strong el niño. *Nature communications*, *8*(1), 1–10. https://doi.org/https://doi.org/10.1038/ncomms15799

Ohmura, A. (1999). Precipitation, accumulation and mass balance of the greenland ice sheet. *Zeitschrift fur Gletscherkunde und Glazialgeologie*, *35*, 1–20.

Orr, A., Deb, P., Clem, K., Gilbert, E., Boberg, F., Bromwich, D., Colwell, S., Hansen, N., Lazzara, M., Mottram, R., Niwano, M., Phillips, T., Pishniak, D., Reijmer, C., van de Berg, W., Webster, S., & Zou, X. (2022). Summer air temperature extremes over antarctic ice shelves and potential “hotspots” of surface melting. *Journal of Climate, accepted*.

Orr, A., Hosking, J., Hoffmann, L., Keeble, J., Dean, S., Roscoe, H., Abraham, N., Vosper, S., & Braesicke, P. (2015). Inclusion of mountain-wave-induced cooling for the formation of pscs over the antarctic peninsula in a chemistry–climate model. *Atmospheric chemistry and physics*, *15*(2), 1071–1086. https://doi.org/https://doi.org/10.5194/acp-15-1071-2015

Orr, A., Kirchgaessner, A., King, J., Phillips, T., Gilbert, E., Elvidge, A., Weeks, M., Gadian, A., Kuipers Munneke, P., van den Broeke, M., et al. (2021). Comparison of kilometre and sub-kilometre scale simulations of a foehn wind event over the larsen c ice shelf, antarctic peninsula using the met office unified model (metum). *Quarterly Journal of the Royal Meteorological Society*, *147*(739), 3472–3492. https://doi.org/https://doi.org/10.1002/qj.4138

Padman, L., Fricker, H. A., Coleman, R., Howard, S., & Erofeeva, L. (2002). A new tide model for the antarctic ice shelves and seas. *Annals of Glaciology*, *34*, 247–254. https://doi.org/https://doi.org/10.3189/172756402781817752

Picard, G., Sandells, M., & Löwe, H. (2018). Smrt: An active–passive microwave radiative transfer model for snow with multiple microstructure and scattering formulations (v1. 0). *Geoscientific Model Development*, *11*(7), 2763–2788. https://doi.org/https://doi.org/10.5194/gmd-11-2763-2018

Ramillien, G., Lombard, A., Cazenave, A., Ivins, E., Llubes, M., Remy, F., & Biancale, R. (2006). Interannual variations of the mass balance of the antarctica and greenland ice sheets from grace. *Global and Planetary Change*, *53*(3), 198–208. https://doi.org/https://doi.org/10.1016/j.gloplacha.2006.06.003

Rignot, E., & Mouginot, J. (2012). Ice flow in greenland for the international polar year 2008–2009. *Geophysical Research Letters*, *39*(11). https://doi.org/https://doi.org/10.1029/2012GL051634

Rignot, E., Mouginot, J., & Scheuchl, B. (2011a). Antarctic grounding line mapping from differential satellite radar interferometry. *Geophysical Research Letters*, *38*(10). https://doi.org/https://doi.org/10.1029/2011GL047109

Rignot, E., Mouginot, J., & Scheuchl, B. (2011b). Ice flow of the antarctic ice sheet. *Science*, *333*(6048), 1427–1430. https://doi.org/DOI:10.1126/science.1208336

Rignot, E., Mouginot, J., Scheuchl, B., Van Den Broeke, M., Van Wessem, M. J., & Morlighem, M. (2019). Four decades of antarctic ice sheet mass balance from 1979–2017. *Proceedings of the National Academy of Sciences*, *116*(4), 1095–1103. https://doi.org/https://doi.org/10.1073/pnas.1812883116

Roeckner, E., Bäuml, G., Bonaventura, L., Brokopf, R., Esch, M., Giorgetta, M., Hagemann, S., Kirchner, I., Kornblueh, L., Manzini, E., et al. (2003). The atmospheric general circulation model echam 5. part i: Model description.

Rummukainen, M. (2010). State-of-the-art with regional climate models. *Wiley Interdisciplinary Reviews: Climate Change*, *1*(1), 82–96. https://doi.org/https://doi.org/10.1002/wcc.8

Rummukainen, M. (2016). Added value in regional climate modeling. *Wiley Interdisciplinary Reviews: Climate Change*, *7*(1), 145–159. https://doi.org/https://doi.org/10.1002/wcc.378

Scambos, T., Fricker, H. A., Liu, C.-C., Bohlander, J., Fastook, J., Sargent, A., Massom, R., & Wu, A.-M. (2009). Ice shelf disintegration by plate bending and hydro-fracture: Satellite observations and model results of the 2008 wilkins ice shelf break-ups. *Earth and Planetary Science Letters*, *280*(1-4), 51–60. https://doi.org/https://doi.org/10.1016/j.epsl.2008.12.027

Scheuchl, B., Mouginot, J., & Rignot, E. (2012). Ice velocity changes in the ross and ronne sectors observed using satellite radar data from 1997 and 2009. *The Cryosphere*, *6*(5), 1019–1030. https://doi.org/10.5194/tc-6-1019-2012

Schutz, B. E., Zwally, H. J., Shuman, C. A., Hancock, D., & DiMarzio, J. P. (2005). Overview of the icesat mission. *Geophysical Research Letters*, *32*(21). https://doi.org/https://doi.org/10.1029/2005GL024009

Shepherd, A., Ivins, E., Rignot, E., Smith, B., Van Den Broeke, M., Velicogna, I., Whitehouse, P., Briggs, K., Joughin, I., Krinner, G., Nowicki, S., Payne, T., Scambos, T., Schlegel, N., Geruo, A., Agosta, C., Ahlstrøm, A., Babonis, G., Barletta, V., … Wouters, B. (2018). Mass balance of the antarctic ice sheet from 1992 to 2017. *Nature*, *558*, 219–222. https://doi.org/https://doi.org/10.1038/s41586-018-0179-y

Shepherd, A., Gilbert, L., Muir, A. S., Konrad, H., McMillan, M., Slater, T., Briggs, K. H., Sundal, A. V., Hogg, A. E., & Engdahl, M. E. (2019). Trends in antarctic ice sheet elevation and mass. *Geophysical Research Letters*, *46*(14), 8174–8183. https://doi.org/https://doi.org/10.1029/2019GL082182

Shepherd, A., Ivins, E., Rignot, E., Smith, B., Van Den Broeke, M., Velicogna, I., Whitehouse, P., Briggs, K., Joughin, I., Krinner, G., et al. (2020). Mass balance of the greenland ice sheet from 1992 to 2018. *Nature*, *579*(7798), 233–239. https://doi.org/https://doi.org/10.1038/s41586-019-1855-2

Shepherd, A., Ivins, E. R., Barletta, V. R., Bentley, M. J., Bettadpur, S., Briggs, K. H., Bromwich, D. H., Forsberg, R., Galin, N., Horwath, M., et al. (2012). A reconciled estimate of ice-sheet mass balance. *Science*, *338*(6111), 1183–1189. https://doi.org/shepherd2012reconciled

Simonsen, S. B., Barletta, V. R., Colgan, W. T., & Sørensen, L. S. (2021). Greenland ice sheet mass balance (1992–2020) from calibrated radar altimetry. *Geophysical Research Letters*, *48*(3), e2020GL091216. https://doi.org/https://doi.org/10.1029/2020GL091216

Simonsen, S. B., Stenseng, L., Ađalgeirsdóttir, G., Fausto, R. S., Hvidberg, C. S., & Lucas-Picher, P. (2013). Assessing a multilayered dynamic firn-compaction model for greenland with asiras radar measurements. *Journal of Glaciology*, *59*(215), 545–558. https://doi.org/doi:10.3189/2013JoG12J158

Slater, T., Hogg, A. E., & Mottram, R. (2020). Ice-sheet losses track high-end sea-level rise projections. *Nature Climate Change*, *10*(10), 879–881. https://doi.org/https://doi-org.proxy.findit.cvt.dk/10.1038/s41558-020-0893-y

Slater, T., & Shepherd, A. (2018). Antarctic ice losses tracking high. *Nature Climate Change*, *8*(12), 1025–1026. https://doi.org/https://doi.org/10.1038/s41558-018-0284-9

Smith, B., Fricker, H. A., Gardner, A. S., Medley, B., Nilsson, J., Paolo, F. S., Holschuh, N., Adusumilli, S., Brunt, K., Csatho, B., et al. (2020). Pervasive ice sheet mass loss reflects competing ocean and atmosphere processes. *Science*, *368*(6496), 1239–1242. https://doi.org/DOI:10.1126/science.aaz5845

Smith, B., Fricker, H. A., Holschuh, N., Gardner, A. S., Adusumilli, S., Brunt, K. M., Csatho, B., Harbeck, K., Huth, A., Neumann, T., Nilsson, J., & Siegfried, M. R. (2019a). Land ice height-retrieval algorithm for nasa's icesat-2 photon-counting laser altimeter. *Remote Sensing of Environment*, *233*, 111352. https://doi.org/https://doi.org/10.1016/j.rse.2019.111352

Smith, B., Hancock, D., Harbeck, K., Roberts, L., Neumann, T., Brunt, K., Fricker, H., Gardner, A., Siegfried, M., Adusumilli, S., Csathó, B., Holschuh, N., Nilsson, J., & Paolo, F. (2019b). Ice, cloud, and land elevation satellite-2 (icesat-2) project algorithm theoretical basis document (atbd) for land ice along-track height product (atl06). *National Aeronautics and Space Administration, Goddard Space Flight Center*.

Sørensen, L. S., Simonsen, S. B., Nielsen, K., Lucas-Picher, P., Spada, G., Adalgeirsdottir, G., Forsberg, R., & Hvidberg, C. S. (2011). Mass balance of the greenland ice sheet (2003–2008) from icesat data–the impact of interpolation, sampling and firn density. *The Cryosphere*, *5*(1), 173–186. https://doi.org/10.5194/tc-5-173-2011

Sørensen, L. S., Simonsen, S. B., Forsberg, R., Khvorostovsky, K., Meister, R., & Engdahl, M. E. (2018). 25 years of elevation changes of the greenland ice sheet from ers, envisat, and cryosat-2 radar altimetry. *Earth and Planetary Science Letters*, *495*, 234–241. https://doi.org/https://doi.org/10.1016/j.epsl.2018.05.015

Sørensen, L. S., Simonsen, S. B., Meister, R., Forsberg, R., Levinsen, J. F., & Flament, T. (2015). Envisat-derived elevation changes of the greenland ice sheet, and a comparison with icesat results in the accumulation area. *Remote Sensing of Environment*, *160*, 56–62. https://doi.org/https://doi.org/10.1016/j.rse.2014.12.022

Souverijns, N., Gossart, A., Demuzere, M., Lenaerts, J., Medley, B., Gorodetskaya, I., Vanden Broucke, S., & van Lipzig, N. (2019). A new regional climate model for polar-cordex: Evaluation of a 30-year hindcast with cosmo-clm2 over antarctica. *Journal of Geophysical Research: Atmospheres*, *124*(3), 1405–1427. https://doi.org/https://doi.org/10.1029/2018JD028862

Spada, G., & Melini, D. (2019). Selen 4 (selen version 4.0): A fortran program for solving the gravitationally and topographically self-consistent sea-level equation in glacial isostatic adjustment modeling. *Geoscientific Model Development*, *12*(12), 5055–5075. https://doi.org/https://doi.org/10.5194/gmd-12-5055-2019

Tedesco, M. (2009). Assessment and development of snowmelt retrieval algorithms over antarctica from k-band spaceborne brightness temperature (1979–2008). *Remote Sensing of Environment*, *113*(5), 979–997. https://doi.org/https://doi.org/10.1016/j.rse.2009.01.009

Thomas, R., Frederick, E., Krabill, W., Manizade, S., & Martin, C. (2006). Progressive increase in ice loss from greenland. *Geophysical Research Letters*, *33*(10). https://doi.org/https://doi.org/10.1029/2006GL026075

Trusel, L. D., Frey, K. E., Das, S. B., Karnauskas, K. B., Kuipers Munneke, P., Van Meijgaard, E., & Van Den Broeke, M. R. (2015). Divergent trajectories of antarctic surface melt under two twenty-first-century climate scenarios. *Nature Geoscience*, *8*(12), 927–932. https://doi.org/https://doi.org/10.1038/ngeo2563

Trusel, L. D., Frey, K. E., Das, S. B., Munneke, P. K., & Van Den Broeke, M. R. (2013). Satellite-based estimates of antarctic surface meltwater fluxes. *Geophysical Research Letters*, *40*(23), 6148–6153. https://doi.org/https://doi.org/10.1002/2013GL058138

Tuckett, P. A., Ely, J. C., Sole, A. J., Livingstone, S. J., Davison, B. J., Melchior van Wessem, J., & Howard, J. (2019). Rapid accelerations of antarctic peninsula outlet glaciers driven by surface melt. *Nature Communications*, *10*(1), 1–8. https://doi.org/https://doi.org/10.1038/s41467-019-12039-2

Van den Broeke, M. R., Bamber, J., Lenaerts, J., & Rignot, E. (2011). Ice sheets and sea level: Thinking outside the box. *Surveys in geophysics*, *32*(4), 495–505. https://doi.org/https://doi.org/10.1007/s10712-011-9137-z

Van Wessem, J. M., Van De Berg, W. J., Noël, B. P., Van Meijgaard, E., Amory, C., Birnbaum, G., Jakobs, C. L., Krüger, K., Lenaerts, J., Lhermitte, S., et al. (2018). Modelling the climate and surface mass balance of polar ice sheets using racmo2–part 2: Antarctica (1979–2016). *The Cryosphere*, *12*(4), 1479–1498. https://doi.org/https://doi.org/10.5194/tc-12-1479-2018

van Dalum, C. T., van de Berg, W. J., & van den Broeke, M. R. (2022). Sensitivity of antarctic surface climate to a new spectral snow albedo and radiative transfer scheme in racmo2. 3p3. *The Cryosphere*, *16*(3), 1071–1089. https://doi.org/https://doi.org/10.5194/tc-16-1071-2022

Vandecrux, B., Fausto, R., Langen, P., Van As, D., MacFerrin, M., Colgan, W., Ingeman-Nielsen, T., Steffen, K., Jensen, N., Møller, M., et al. (2018). Drivers of firn density on the greenland ice sheet revealed by weather station observations and modeling. *Journal of Geophysical Research: Earth Surface*, *123*(10), 2563–2576. https://doi.org/https://doi.org/10.1029/2017JF004597

Velicogna, I., & Wahr, J. (2013). Time-variable gravity observations of ice sheet mass balance: Precision and limitations of the grace satellite data. *Geophysical Research Letters*, *40*(12), 3055–3063. https://doi.org/https://doi.org/10.1002/grl.50527

Verjans, V., Leeson, A. A., McMillan, M., Stevens, C. M., van Wessem, J. M., van de Berg, W. J., van den Broeke, M. R., Kittel, C., Amory, C., Fettweis, X., Hansen, N., Boberg, F., & Mottram, R. (2021). Uncertainty in east antarctic firn thickness constrained using a model ensemble approach. *Geophysical Research Letters*, *48*(7), e2020GL092060. https://doi.org/https://doi.org/10.1029/2020GL092060

Wang, Y., Ding, M., Reijmer, C. H., Smeets, P. C., Hou, S., & Xiao, C. (2021). The antsmb dataset: A comprehensive compilation of surface mass balance field observations over the antarctic ice sheet. *Earth System Science Data*, *13*(6), 3057–3074. https://doi.org/https://doi.org/10.5194/essd-13-3057-2021

Whitehouse, P. L. (2018). Glacial isostatic adjustment modelling: Historical perspectives, recent advances, and future directions. *Earth surface dynamics*, *6*(2), 401–429. https://doi.org/doi.org/10.5194/esurf-6-401-2018

Zou, X., Bromwich, D. H., Montenegro, A., Wang, S.-H., & Bai, L. (2021). Major surface melting over the ross ice shelf part i: Foehn effect. *Quarterly Journal of the Royal Meteorological Society*, *147*(738), 2874–2894. https://doi.org/https://doi.org/10.1002/qj.4104

Zwally, H. J., Giovinetto, M. B., Beckley, M. A., & Saba, J. L. (2012). Antarctic and greenland drainage systems, gsfc cryospheric sciences laboratory.

Zwally, H. J., & Jun, L. (2002). Seasonal and interannual variations of firn densification and ice-sheet surface elevation at the greenland summit. *Journal of Glaciology*, *48*(161), 199–207. https://doi.org/https://doi.org/10.3189/172756502781831403

Zwally, H. J., Robbins, J. W., Luthcke, S. B., Loomis, B. D., & Rémy, F. (2021). Mass balance of the antarctic ice sheet 1992–2016: Reconciling results from grace gravimetry with icesat, ers1/2 and envisat altimetry. *Journal of Glaciology*, *67*(263), 533–559. https://doi.org/doi:10.3189/2015JoG15J071

A Apendix

A.1 Paper I

The Cryosphere, 15, 3751–3784, 2021
https://doi.org/10.5194/tc-15-3751-2021

The Cryosphere
Open Access

What is the surface mass balance of Antarctica? An intercomparison of regional climate model estimates

Ruth Mottram[1], **Nicolaj Hansen**[1,2], **Christoph Kittel**[3], **J. Melchior van Wessem**[4], **Cécile Agosta**[5], **Charles Amory**[3], **Fredrik Boberg**[1], **Willem Jan van de Berg**[4], **Xavier Fettweis**[3], **Alexandra Gossart**[6], **Nicole P. M. van Lipzig**[6], **Erik van Meijgaard**[7], **Andrew Orr**[8], **Tony Phillips**[8], **Stuart Webster**[9], **Sebastian B. Simonsen**[2], and **Niels Souverijns**[6,10]

[1]Research and Development Department, Danish Meteorological Institute, Lyngbyvej 100, Copenhagen, 2100, Denmark
[2]Geodesy and Earth Observation, DTU-Space, Technical University of Denmark, Lyngby, Denmark
[3]Laboratory of Climatology, Department of Geography, SPHERES, University of Liège, Liège, Belgium
[4]Institute for Marine and Atmospheric Research Utrecht, Utrecht University, Utrecht, the Netherlands
[5]Laboratoire des Sciences du Climat et de l'Environnement, LSCE-IPSL, CEA-CNRS-UVSQ,
Université Paris-Saclay, Gif-sur-Yvette, France
[6]Department of Earth and Environmental Sciences, KU Leuven, Belgium
[7]Royal Netherlands Meteorological Institute, De Bilt, the Netherlands
[8]British Antarctic Survey, High Cross, Madingley Road, Cambridge, UK
[9]UK Met Office, FitzRoy Road, Exeter, Devon, EX1 3PB, UK
[10]Unit Remote Sensing and Earth Observation Processes, Flemish Institute for Technological Research (VITO), Mol, Belgium

Correspondence: Ruth Mottram (rum@dmi.dk)

Received: 31 December 2019 – Discussion started: 28 January 2020
Revised: 27 January 2021 – Accepted: 29 January 2021 – Published: 17 August 2021

Abstract. We compare the performance of five different regional climate models (RCMs) (COSMO-CLM^2, HIRHAM5, MAR3.10, MetUM, and RACMO2.3p2), forced by ERA-Interim reanalysis, in simulating the near-surface climate and surface mass balance (SMB) of Antarctica. All models simulate Antarctic climate well when compared with daily observed temperature and pressure, with nudged models matching daily observations slightly better than free-running models. The ensemble mean annual SMB over the Antarctic ice sheet (AIS) including ice shelves is $2329 \pm 94\,\mathrm{Gt\,yr^{-1}}$ over the common 1987–2015 period covered by all models. There is large interannual variability, consistent between models due to variability in the driving ERA-Interim reanalysis. Mean annual SMB is sensitive to the chosen period; over our 30-year climatological mean period (1980 to 2010), the ensemble mean is $2483\,\mathrm{Gt\,yr^{-1}}$. However, individual model estimates vary from 1961 ± 70 to $2519 \pm 118\,\mathrm{Gt\,yr^{-1}}$. The largest spatial differences between model SMB estimates are in West Antarctica, the Antarctic Peninsula, and around the Transantarctic Mountains. We find no significant trend in Antarctic SMB over either period. Antarctic ice sheet (AIS) mass loss is currently equivalent to around $0.5\,\mathrm{mm\,yr^{-1}}$ of global mean sea level rise (Shepherd et al., 2020), but our results indicate some uncertainty in the SMB contribution based on RCMs. We compare modelled SMB with a large dataset of observations, which, though biased by undersampling, indicates that many of the biases in SMB are common between models. A drifting-snow scheme improves modelled SMB on ice sheet surface slopes with an elevation between 1000 and 2000 m, where strong katabatic winds form. Different ice masks have a substantial impact on the integrated total SMB and along with model resolution are factored into our analysis. Targeting undersampled regions with high precipitation for observational campaigns will be key to improving future estimates of SMB in Antarctica.

Published by Copernicus Publications on behalf of the European Geosciences Union.

1 Introduction

The Antarctic ice sheet (AIS) is the largest body of freshwater on the planet and an important contributor to global sea level rise. It is also a significant part of the climate system, contributing freshwater to the ocean and with high relief that influences atmospheric circulation. Studies by Rignot et al. (2011, 2019) and Shepherd et al. (2018) showed the AIS to have had a net loss since at least 2002. Current estimates suggest that around 10 % of observed sea level rise since 1993 is from Antarctica; however that rate of contribution is also increasing (Oppenheimer et al., 2019). Most ice loss in Antarctica occurs as a result of submarine melting, that is melt at the water–ice interface underneath ice shelves, or by the calving of icebergs from ice shelves. Recent ice dynamics studies (DeConto and Pollard, 2016; Edwards et al., 2019; Sutter et al., 2016; Shepherd et al., 2018) have shown that there is potential for rapid ice sheet loss owing to ice sheet dynamics that are currently poorly understood, especially in West Antarctica. Ice sheet models of the AIS have thus largely concentrated on parameterizing sub-shelf and calving processes. However, surface mass balance (SMB), also known as climate mass balance (Cogley et al., 2010), is also of crucial importance in controlling the stability and evolution of the vast ice sheet. Changes in precipitation and increases in surface melt and run-off will change the mass balance and therefore both ice dynamics and the sea level rise contribution from Antarctica in the future. Moreover there has been disagreement between studies focused on the SMB contribution to the total mass budget of Antarctica and therefore the contribution to sea level rise (Scambos and Shuman, 2016; Zwally et al., 2015) that makes it essential to understand potential biases and uncertainties.

SMB is the difference between accumulation and ablation at the surface of a glacier. In Antarctica, accumulation is derived primarily from solid precipitation, but on local or regional scales wind-driven processes can have a significant effect on accumulation rates. Surface ablation in Antarctica is primarily a result of erosion and sublimation due to the high winds and generally dry atmosphere (Scambos et al., 2012; Das et al., 2013; Agosta et al., 2019), although increasing melt rates are documented in some areas (Stokes et al., 2019). In the future, a "Greenlandification" of the ice sheet climate is projected due to anthropologically induced climate change (Trusel et al., 2018). This will lead to more melt with more refreezing in the snowpack as well as increasing run-off.

It is important to distinguish between the continental grounded ice sheet and ice shelves when considering values for SMB integrated over a wider area, whether regional or continent-wide. Snowfall and melt on ice shelves is not directly relevant to sea level rise contributions as they are already floating, but precipitation and ablation on grounded parts of the ice sheet is. As the models used in this study by and large do not distinguish between grounded and floating ice in their ice masks, in this paper when we refer to SMB over an area, we include ice shelves unless specifically noted.

Currently, run-off is a relatively minor contribution (Lenaerts et al., 2019) to mass loss in Antarctica. Increasing snowfall, associated with higher saturated vapour pressure, is expected to dominate future changes in SMB, compensating for the projected increase in surface run-off (Krinner et al., 2008; Lenaerts et al., 2016), but the balance between these processes is still a matter of debate. This makes it even more important to evaluate the effectiveness of modelled precipitation and sublimation across the continent to be able to estimate SMB at present. Accurate SMB estimates are required to both drive ice sheet dynamical models and to accurately partition sea level rise contributions determined from observations. SMB from regional climate models (RCMs) is also used to correct altimetry measurements by accounting for firn compaction processes for remote sensing applications.

The most common way to observe SMB is by geodetic mass balance stakes (Lenaerts et al., 2019), but this is challenging due to the size and environmental conditions in Antarctica, and the most practical alternative is to use output from (high-resolution) RCMs to make continent-wide estimates. There are now an increasing number of RCMs downscaling Antarctic climate simulations available via the CORDEX (CoOrdinated Regional climate Downscaling EXperiments) database. CORDEX is a project of the World Climate Research Programme that aims to produce representative ensembles of regional climate models for different regions of the world. The purpose is to better understand regional climate change, assess regional impacts, and improve adaptation to future climate conditions (http://climate-cryosphere.org/activities/polar-cordex/antarctic, last access: 5 May 2021).

In the polar regions, CORDEX simulations can also be used to assess the mass budget of the large polar ice sheets but have not yet been evaluated together for Antarctica. Souverijns et al. (2019) made a 30-year hindcast with COSMO-CLM^2, and Agosta et al. (2019) estimated the SMB using MAR, while various versions of RACMO2 have been used to estimate the SMB of the AIS (Van Wessem et al., 2014; van Wessem et al., 2018). Both MetUM and HIRHAM5 have been run for the Antarctic domain, but evaluation of the SMB results has not yet been published in peer review literature (Hansen, 2019). Here, we use the framework of the Polar CORDEX project to assess climate model performance in Antarctica for the period 1979–2018 derived from an ensemble of six simulations from five different RCMs. The RCMs cover a range of resolutions, physical and dynamical schemes in the atmosphere, and types of surface and snow and ice schemes. This allows us to determine the relative importance of individual model components needed to accurately model the climate by comparing the modelled SMB against the sparse observational datasets available in Antarctica. We also investigate some of the uncertainties within the individual models and between the ensemble members.

In this paper, we seek to quantify present-day Antarctic SMB and understand the sources of variation as a baseline to assess mass budget changes and better understand sea level rise observations and projections both directly in terms of the amount of meltwater added to oceans and indirectly as surface forcing for ice sheet dynamical models (Robel et al., 2019; Nowicki et al., 2016).

2 Methods

We compare six climate simulations made with five different RCMs (COSMO-CLM^2, HIRHAM5, MAR, MetUM, RACMO) in the newest available version of the given RCM. However, to provide backwards continuity, we also briefly compare three older versions that have been widely used in earlier studies to examine how results have varied (or not) as RCMs have been developed. We assess the climate of Antarctica in the models and derive estimates for SMB. All models were forced on the lateral boundaries with the ERA-Interim climate reanalysis (Dee et al., 2011), but downscaling used different grids, over slightly different domains, and at different resolutions, with slightly different ice masks used in the different model versions (see Fig. A1). Simulations with MAR forced by different reanalyses (Agosta et al., 2019) found that results were rather similar to ERA-Interim, but to exclude additional variability potentially introduced by using different boundary forcings, we chose to use a single common reanalysis only. The MAR, RACMO, and COSMO-CLM^2 models were nudged within the domain using upper-air relaxation, and MetUM was run as a 12 h reinitialized hindcast. With this technique the model is run in weather forecast mode and restarted with new boundary conditions every 12 h. The two versions (high- and low-resolution) of the HIRHAM5 model were allowed to run freely within the domain and forced only on the boundaries.

We first give a brief overview of each of the participating models, summarized in Table 1. The CORDEX protocol (Christensen et al., 2014) prescribes a simulation domain for Antarctica with a minimum common analysis extent and a resolution of 0.44°. Lucas-Picher et al. (2012), Lenaerts et al. (2012b), Franco et al. (2012), and van Wessem et al. (2018), among others, have found that a higher spatial model resolution gives more physically plausible results, especially with respect to precipitation processes in areas with steep terrain. Hence, several participating groups have chosen to run their RCMs at higher spatial resolution. To quantify both the absolute and relative integrated and basin-scale SMB for the continent, we compare outputs from the different models with each other and the ensemble mean. We also evaluate the models with SMB observations (including ice cores and stakes) and near-surface climate observations (surface pressure, temperature, and wind speed) measured across the continent. Unfortunately, as we are constrained to using existing simulations, the models cover slightly differing periods (see Table 1 for details). We have therefore defined a common 30-year climatological period of 1980 to 2010 for all models to simplify the integrated mass budget comparison, except for COSMO-CLM^2, where the period covers 1987 to 2010. Figures that show time series of data show the full period relevant for each model.

2.1 Models

The model versions we include in this paper all fulfil the requirements of being the most up-to-date model version as well as being forced on the boundaries with ERA-Interim reanalysis. We also include the earlier RACMO v2.1 and MAR v3.6 as part of the initial SMB comparison as these models have been widely used and are still available for scientific use online; for example, results from RACMO2.1P were used in compiling the IPCC AR5 climate atlas. However, they are no longer considered up to date and have been replaced by RACMO2.3p2 and MAR$_{\mathrm{v3.10}}$, respectively; therefore we do not consider them in the detailed results analysis in this paper. The models also have snow schemes of differing complexity, so the comparison of SMB necessarily includes slightly different terms for different models. For example, the RACMO model has been developed to include the wind-blown snow sublimation terms in SMB, and both RACMO and MAR$_{\mathrm{v3.10}}$ include melt and refreezing of meltwater. As these terms cannot easily be removed without retuning the models, we have opted to include these within the SMB calculation for these two models. We also explicitly include a second simple SMB calculation Eq. (1) based only on the precipitation and sublimation for a fairer model intercomparison within the results section. The individual model descriptions give further details of each model's outputs.

2.1.1 COSMO-CLM^2

COSMO-CLM^2 is a non-hydrostatic RCM developed at the German Weather Service together with an extensive scientific community (Rockel et al., 2008). The model is applied over the Antarctic at a spatial resolution of ~ 25 km and 40 vertical levels in the atmosphere. The model is forced every 6 h at the boundaries by ERA-Interim. Additionally, this model is coupled to the Community Land Model (version 4.5; Oleson and Lawrence, 2013), with adjustments in the perennial snow proposed by van Kampenhout et al. (2017) to better represent the SMB of ice sheets (COSMO-CLM^2). Apart from this, several model parameters were adjusted for polar regions, particularly those related to the turbulent-kinetic-energy scheme and the cloud scheme. A full description of the set-up over Antarctica including an evaluation of its performance in simulating the Antarctic climate and SMB is available in Souverijns et al. (2019). In this paper, precipitation minus sublimation is taken as a proxy for the SMB.

2.1.2 HIRHAM5

HIRHAM5 is an RCM developed at the Danish Meteorological Institute and run in this study at both low (0.44° ∼ 50 km) and high (0.11° ∼ 12 km) resolution, with all other model elements being kept identical. The model combines the atmospheric dynamics of the HIRLAM7 numerical weather prediction model (Eerola, 2006) and the physics of the ECHAM5 global climate model (GCM) (Roeckner et al., 2003). There are 31 vertical levels in the atmosphere, and the model is forced at 6 h intervals on the lateral boundaries with temperature, pressure, relative humidity, and the wind vectors. Sea surface temperature (SST) and sea ice concentration (SIC) are forced on the lower boundary at daily intervals. The set-up for Antarctica is similar to that of Lucas-Picher et al. (2012) in Greenland, that is with only a very simple surface physics scheme over glacier ice. A subsurface scheme developed for Greenland by Langen et al. (2017) is currently undergoing optimization for Antarctic SMB processes but was not available for use in these simulations. We used the model outputs of precipitation, evaporation, and sublimation to compute a simple SMB.

2.1.3 MetUM

The UK Met Office Unified Model (MetUM) is a numerical modelling system based on non-hydrostatic dynamics (Walters et al., 2017), which can be run as either a global model or a regional mesoscale model, as presented by e.g. Orr et al. (2015). Here, we run version 11.1 of the mesoscale model over the standard Antarctic CORDEX domain at a spatial resolution of 50 km and 70 vertical levels (reaching up to 80 km). The mesoscale model is nested within a global version of the MetUM with a horizontal resolution of N320 (i.e. 640 × 480 longitude–latitude grid implying a nominal 40 km horizontal mesh), which was initialized by ERA-Interim. For this study we ran a series of consecutive twice-daily 24 h forecasts at 00:00 and 12:00 UTC from the beginning of 1980 to the end of 2018. The first 12 h of each forecast were discarded as spin-up, with the remaining output concatenated together to form a continuous time series. Although the mesoscale model includes a multi-layer snow scheme (Walters et al., 2019), in these simulations we used a simplified single-layer scheme with, for example, no refreezing (Cox et al., 1999). We therefore calculate SMB based on output precipitation and sublimation and evaporation.

2.1.4 MAR$_{\mathrm{v3.10}}$

The “Modèle Atmosphérique Régional” (MAR) (Gallée and Schayes, 1994) is a hydrostatic RCM specifically designed for polar areas (e.g. Fettweis et al., 2017; Kittel et al., 2018; Agosta et al., 2019). The model has 24 vertical atmospheric levels and a horizontal resolution of 35 km. MAR is coupled to the 1-D multi-layer surface scheme SISVAT (Soil Ice Snow Vegetation Atmosphere Transfer; De Ridder and Gallée, 1998), which simulates mass and energy fluxes between the atmosphere and the surface. The snow–ice module, based on the CROCUS model (Brun et al., 1992), represents the evolution of the snowpack for 30 snow layers through subroutines of snow metamorphism, surface albedo, meltwater run-off, percolation, retention, and refreezing. MAR is forced with ERA-Interim every 6 h over 1979–2018 at its atmospheric lateral and upper boundaries (pressure, wind, specific humidity, and temperature at each vertical level) and over the ocean surface (SST and SIC). Furthermore, an upper-air relaxation is used to constrain the MAR general atmospheric circulation (van de Berg and Medley, 2016). Relative to previous studies over the AIS (Kittel et al., 2018; Agosta et al., 2019), the version used in this study (MAR$_{\mathrm{v3.10}}$) only improves the cloud lifetime, the model stability, and its computational efficiency, enhancing a larger independence of MAR to its time steps. Furthermore, the definition of the AIS mask has also been improved by taking into account rock outcrops. An extensive description of the adaptation of MAR to the AIS can be found in Agosta et al. (2019).

2.1.5 RACMO2.3p2

The Regional Atmospheric Climate Model RACMO2.3p2 combines the dynamical processes of the High Resolution Limited Area Model (HIRLAM) (Undén et al., 2002) and the physics package CY33r1 of the European Centre for Medium-range Weather Forecasts (ECMWF) Integrated Forecast System (IFS). RACMO2.3p1 was built by porting the polar-physics components that were part of RACMO2.1P into the standard climate model RACMO2.3 developed at the Royal Netherlands Meteorology Institute (KNMI). RACMO2.3p2 is the follow-up of RACMO2.3p1 and has been applied to the polar ice sheets of Greenland and Antarctica by the Institute for Marine and Atmospheric research Utrecht (IMAU). RACMO2.3p2 includes a multi-layer snow model that calculates melt, percolation, refreezing, and run-off of liquid water (Ettema et al., 2010). RACMO2.3p2 also uses a prognostic scheme for snow grain size used to calculate surface albedo (Kuipers Munneke et al., 2011) and a drifting-snow routine that simulates the interaction of drifting snow with the surface and the lower atmosphere (Lenaerts et al., 2012a). For this study, the model operates at a horizontal resolution of ∼ 27 km, with 40 vertical atmospheric levels. Surface topography is based on Cook et al. (2012a) and Bamber and Gomez-Dans (2009). At the lateral and the upper-atmospheric boundaries the model is forced by ERA-Interim reanalysis data every 6 h and at the ocean boundaries by prescribed ocean temperatures and sea ice cover. The model atmosphere is initialized on 1 January 1979 with the ERA-Interim reanalysis data and the snow and firn layers with data generated by the IMAU Firn Densification Model (IMAU-FDM) (Ligtenberg et al., 2011). The precursor version, RACMO2.3p1, includes an older ice mask and surface topography, no upper-air nudging, a more severe drifting-snow formulation eroding more snow, and changes in the formulations of surface melting and precipitation. Further details can be found in van Wessem et al. (2018), who intercompare versions p1 and p2 more fully.

2.1.6 RACMO2.1P

RACMO2.1P is an earlier version of RACMO2 using the ECMWF-IFS physics package CY23r4 that does not include ice cloud supersaturation and utilizes earlier parameterizations for short-wave radiation and boundary-layer turbulence as described in Van Wessem et al. (2014). This version of RACMO2.1 includes the polar multi-layer snow routines as well as the schemes for drifting snow and albedo as described for RACMO2.3p2 above. In essence, its polar-physics components are identical to those in RACMO2.3p1. Simulations with RACMO2.1P have been performed on a modelling domain matching the CORDEX ANT-44 domain in the interior plus a 16-point extension on each domain side for boundary relaxation of ERA-Interim fields. There is also no nudging within the domain in this version.

2.2 Model set-up and outputs

2.2.1 Surface mass balance calculations in RCMs

Two of the models (RACMO and MAR) have subsurface schemes optimized over snow and ice for Antarctica (see references under the model descriptions). The models include parameterizations to account for retention and refreezing of meltwater and also in the case of RACMO2.3p2 wind-driven processes such as erosion at the surface and sublimation of blowing snow. Thus, the definition of the calculation of the SMB changes depending on the complexity of the model. Three models (HIRHAM5, METUM, COSMO-CLM^2) have only simple surface snow physics over ice surfaces in these experiments. The basic SMB we calculate for them in this study is

$$\text{SMB} = \text{precipitation} - \text{evaporation} - \text{sublimation}. \tag{1}$$

For MAR with optimized subsurface schemes, the SMB is calculated from Eq. (2):

$$\begin{aligned}\text{SMB} = {} & \text{precipitation} - \text{evaporation} - \text{sublimation} \\ & - \text{run-off}.\end{aligned} \tag{2}$$

This differs slightly in RACMO2.3p2 and RACMO2.1P as sublimation and erosion of drifting snow (SU_{ds} and ER_{ds}, respectively) are also included as a mass loss term as in Eq. (3):

$$\begin{aligned}\text{SMB} = {} & \text{precipitation} - \text{evaporation} - \text{sublimation} \\ & - \text{run-off} - \text{SU}_{\text{ds}} - \text{ER}_{\text{ds}}.\end{aligned} \tag{3}$$

Both models account for refreezing and retention and thus use run-off rather than melt. Due to the low temperatures in Antarctica, most meltwater refreezes, and run-off is negligible in the current climate (van Wessem et al., 2018; Agosta et al., 2019), so for the remaining models without the multi-layer subsurface schemes, SMB is calculated without the run-off component.

2.2.2 Nudging and upper-atmosphere relaxation

As von Storch et al. (2000) pointed out, nudging, whether spectral or with simpler techniques, keeps a regional model closer to the driving large-scale fields (GCM or reanalysis) and is thus a valuable technique where a close match to observations or to a driving GCM is required. Within Polar CORDEX, upper-air relaxation and other forms of nudging have been included as a standard where observational campaigns in large domains require close matches between modelled and observed weather. For example, Arctic cyclone systems and the presence of clouds in particular appear to be better resolved in models that include nudging (Akperov et al., 2018, and Sedlar et al., 2011). Similarly, nudging of RCMs run over Antarctica ties their synoptic evolution to these of the driving reanalysis, improving the representation of the interannual variability in SMB to similar levels as in the reanalysis as shown in van de Berg and Medley (2016).

In the experiments presented here, COSMO-CLM^2, $\text{MAR}_{\text{v3.10}}$, and RACMO2.3p2 are nudged by adjusting temperature and wind fields to the global fields with a minimum relaxation timescale of 6 h. The strongest relaxation is applied at the top of the atmosphere, and relaxation decreases gradually for lower levels. Below typically 4 km (ocean) to 6.2 km (4 km land topography) no relaxation is applied. In the case of $\text{MAR}_{\text{v3.10}}$, the relaxation of the temperature is weaker than the relaxation of the wind between the highest cloud level and the lowest nudging level. This prevents inconsistency between the temperature inherited from the reanalyses and the humidity and clouds conditioned by the MAR microphysics scheme. Moisture fields are not adjusted by nudging as this would introduce artificial uphill moisture transport. HIRHAM5 and MetUM are not nudged, but MetUM is run in a 12-hourly reinitialization hindcast that keeps the model evolution close to the driving reanalysis.

2.2.3 Grids and land–sea–ice masks

All models have been run for a domain covering the entire Antarctic continent, but not all of the domains are the same. HIRHAM5 0.44° and MetUM use the standard CORDEX domain and grid. However, COSMO-CLM^2 extends this slightly to cover more ocean around Queen Maud Land, while the HIRHAM5 0.11° simulations and $\text{MAR}_{\text{v3.10}}$ were run over slightly smaller domains than the CORDEX domain to reduce computational time, though only after running experiments to determine that e.g. precipitation was not

Table 1. Summary of differences and similarities between the RCMs. Horizontal resolution is given in degrees and (kilometres), while the number of atmospheric levels refers to the vertical resolution. Nudging refers to the level of forcing within the domain; refer to the individual model descriptions for more details.

Model	Period	Resolution [km] (°)	Nudging	SMB scheme	Topography dataset	Atmospheric levels
COSMO-CLM^2	1987–2016	25 (0.22)	Yes	Yes	GLOBE[a]	40
HIRHAM5	1979–2017	50 (0.44); 12.5 (0.11)	No	No	GTOPO[b]	31
MetUM	1979–2018	50 (0.44)	Reinitialized	No	GLOBE[a]	70
MAR$_{v3.6}$	1979–2018	35	Yes	Yes	Bedmap2[c]	23
MAR$_{v3.10}$	1981–2018	35	Yes	Yes	Bedmap2[c]	24
RACMO2.1P$_{v1}$	1979–2012	50 (0.44)	No	Yes	RAMPv2[d]	40
RACMO2.3p2	1979–2018	27 (0.25)	Yes	Yes	Cook, Bamber[e]	40

[a] GLOBE Task Team et al. (1999), [b] Earth Resources Observation and Science Center (1997), [c] Fretwell (2013), [d] Liu (2015), [e] Cook et al. (2012b), Bamber (1994)

affected. RACMO2.3p2 and RACMO2.1 are run for a domain slightly larger than CORDEX but are trimmed back to remove the relaxation zone such that final results are presented on the CORDEX domain. As the model resolutions are different, and each model had its own land–sea mask, the area of Antarctica is not the same in all models, which complicates the SMB results when integrated over the continent. To correct for this areal difference, all the data have been bilinearly regridded to the HIRHAM5 0.11° grid, with the unglaciated land of MAR$_{v3.10}$ included and a threshold for the ice mask of 50 %. This was used to generate a common ice mask for the models in order to calculate the integrated SMB over the ice sheet and ice shelves and in the individual basin. In the Appendix, Fig. A1 shows all masks compared to the common mask. Most models had very few grid points different from the common mask, but these are also areas with high precipitation rates, and this therefore would give measurable differences in annual SMB. We do not report these differences here, but it is important to bear in mind the ice masks used when comparing our results with those from other studies.

Modelled SMB is integrated over drainage basins defined as in Shepherd et al. (2020). The horizontal resolution of the models is not altered, and the drainage basin masks are defined by selecting all model grid points that fall within the drainage basin outlines. In addition to the drainage basins, which are by definition grounded ice, outlines of the ice shelves that the basins drain into are also used. This allows us to partition SMB over the floating ice shelves (ISs) and grounded ice only excluding floating ice shelves (GrISs), as well as the ice sheet as a whole including both grounded ice and floating shelves (ToTIS).

2.3 Observations

2.3.1 Automatic weather station (AWS) observations

We use weather observations to assess how well RCMs reproduce the meteorological conditions over the AIS. Although a detailed evaluation of the near-surface model climates of each of the models is not the purpose of this study, this comparison helps to explain model biases in simulating SMB and especially the coherence between the modelled SMB and the near-surface climate. The original dataset is a compilation of surface pressure, near-surface temperature, and wind speed from 307 AWSs over the ice sheet used in the MET-READER database (Turner et al., 2004) but also collected by the BAS (British Antarctic Survey), IMAU (van Wessem et al., 2014), and the Institut des Géosciences de l'Environnement (IGE) and Institut Polaire Français Institut Paul-Emile Victor (IPEV) (Amory, 2020). The original data were available at several sampling time steps (sub-hourly, hourly, 3-hourly) and were averaged to obtain daily values. Only daily averages computed from more than 75 % of the original data are considered to be representative of the entire measurement (UTC) day and are used for comparison. Several stations displayed suspicious measurements (sudden discontinuity in pressure and temperature, temperature values capped to the lower bound of the measurement range during the whole winter season, etc.), and these were removed from the dataset. Stations occasionally exhibited wind speeds of $0\,\mathrm{m\,s^{-1}}$ for day-long periods, probably as a result of sensor riming. For these cases the daily averages were considered to be no data (see Kittel, 2021 in preparation for details on the full list of AWSs and the data selection protocol). Although we use a homogenized and quality-controlled dataset for the comparison, observations may still be biased in ways that are hard to quantify due to e.g. burial of stations by snow, battery failures, tilt due to strong winds, and other instrument failures that remained undetected, reflecting the difficulties involved in collecting data in the harsh and remote Antarctic environment.

As the different models have different ice masks and topographies, we only retain stations on the common mask where the difference in elevation is lower than 500 m for each model. This gives a total of 184 AWSs (see Fig. A2 in the Appendix for locations of AWS used in this study). We compute the modelled surface pressure, near-surface temperature, and wind speed as well as the model elevation using a four-nearest-neighbours inverse-distance-weighted method. Finally, since the measurement height is not known for every station, we use the vertical level closest to the surface (10 or 2 m) of the models for all comparisons with the observations.

2.3.2 Comparison with 10 m snow temperature observations

Deep snow temperatures in Antarctica are indicative of the annual long-term mean surface air temperature. Here, we use 64 observations of 10 m snow temperature, collected from a broad range of climatic regions of Antarctica, representing a spatially complete picture of climatological surface temperature (Van Wessem et al., 2014), to compare with model output.

2.3.3 Observed SMB

Observations of SMB are sparse over the wide Antarctic continent and have been obtained from diverse measurement techniques such as stake measurements, ice cores, and radar stratigraphy. For the purpose of our model evaluation, we use the SAMBA dataset from Favier et al. (2013), which has been updated with observations from Wang et al. (2016), and yearly values of shallow ice cores from Thomas et al. (2017), giving a total dataset of 7136 observations for various time periods and for a wide range of locations scattered across the AIS. We did not use the radar measurements published by Medley et al. (2014) in this study as the spatial variability is very high and difficult to smooth appropriately for all model grids.

To evaluate the models, we selected observations of SMB on the common ice mask and for which the measurement period falls between 1950 and 2018. These conditions reduced the total number of observations used in the comparison to 3671. We used observations between 1950 and 1987 or 2015 and 2018 that are not fully included in the common modelling period of 1987 to 2015 for evaluation only if they covered more than 5 years. These 1849 SMB observations are compared to modelled values averaged over the common modelling period in order to compute a climatological mean, while we averaged modelled SMB values over the exact same period for the observations between 1987 and 2015 (1822 observations).

Since the models have different resolutions and grids, we do not directly compare the modelled SMB values to the observations. As in Kittel et al. (2018) and Agosta et al. (2019), we compute modelled and observed SMB values in two steps. Firstly, the SMB values modelled in the original resolution were interpolated, as for AWS observations, to the observation location using a four-nearest-neighbours inverse-distance-weighted method. Secondly, all the interpolated SMB values contained in the same grid cell from the common ice mask were averaged as well as the observations to finally create 923 comparison pairs. This leads to a fair comparison for each model that takes into account the benefit of using a higher resolution for a specific model and removing the very high spatial variability in the observations that cannot be reproduced by the models.

Like the meteorological data, SMB observations are subject to measurement biases notably due to post-depositional redistribution of snow and the related formation of sastrugi that can considerably complicate the interpretation of measurements at the very local scale (Andersen et al., 2006). SMB observations should therefore be considered to be a best estimate of accumulation rather than an absolute value. As SMB observations are not evenly distributed over the ice sheet, the comparison statistics are artificially influenced by over- and/or undersampled regions.

3 Results

We first focus on how the RCMs characterize the surface climate over the ice sheet before turning to assessing the SMB and take note of the differences in precipitation distribution.

3.1 Temperature, surface pressure, and wind speed from models and observations

Weather observations in Antarctica extend farther back in time, and there is generally better spatial and temporal coverage than for direct SMB measurements. In Fig. 1, we show Taylor diagrams for pressure, temperature, and wind velocities. Taylor diagrams offer an efficient way to assess model skill by comparing the Pearson correlation coefficient, the centred root mean square error (CRMSE), and the standard deviation of the modelled output with the observed values. CRMSE is equivalent to the root mean square error, but systematic biases are removed by subtracting the mean observation and mean modelled values from each value as shown in Eq. (4):

$$\mathrm{CRMSE} = \sqrt{\frac{\sum_{i=0}^{n}(m_i - o_i)^2}{n} - (\overline{m} - \overline{o})^2}, \tag{4}$$

where n is the number of observations; m_i is the modelled value; o_i is the observed value; and $\overline{m}$ and $\overline{o}$ are the average of the modelled and observed values, respectively.

A perfect model should be in the same place as the observations (shown by the black star in Fig. 1, with a correlation of 1, the same standard deviation, and zero CRMSE).

The farther away a model is from the observations, the more poorly it matches the observed weather. Mean biases and the observational mean are also indicated. In this case, modelled values closest to the dashed line have a more correct representation of the standard deviation, and the closer to the black reference star, the closer the model correlates to the observations values. We list the bias below the diagrams.

Figure 1 analysis shows that, depending on the variable, all the models perform reasonably well though with some variation. With respect to surface pressure, the majority of models are similarly skilful, with the exception of HIRHAM5 0.11°, which has the lowest correlation and highest bias, although the model is still close to the pattern of the standard deviation. The other models have quite a high degree of nudging, including upper-atmosphere pressure fields within the domain, so it is not so surprising to see the good performance here as the nudging forces the models to be closer to the observed pressure. Without nudging, the large domain size in Antarctica means that synoptic-scale systems have more degrees of freedom to evolve away from the observed quantities. This is likely to be a particular problem for higher-resolution models, where there are more grid points between the boundary and a given station compared to a lower-resolution model with fewer grid points. Our results show that the high-resolution (0.11°) version of HIRHAM5, which has many more grid cells than the low-resolution (0.44°) version, has a higher divergence due to internal variability. MetUM is not nudged by surface relaxation but is run in daily reinitialization mode, and while this probably also helps to keep surface pressure close to observed, it is also likely that the large number of atmospheric levels in MetUM also improves modelled surface pressures. The near-surface temperatures in Fig. 1 show that, although overall the models perform well (Pearson correlation of 0.85 and higher), on average all the models are too cold, and only $\mathrm{MAR_{v3.10}}$ and RACMO2.3p2 have a bias of less than 1 K (respectively −0.16 and −0.51 K), with MetUM having the highest bias (−3.44 K). As with the surface pressure analysis, the HIRHAM5 high-resolution simulations have a relatively lower correlation coefficient (0.85 compared to above 0.9 for the other simulations), and this may well be again the consequence of the un-nudged simulations. However, biases in cloud cover and long-wave radiation reaching the surface are likely the main explanation for divergence from observations and should be investigated for all RCMs run for Antarctica as shown by van Wessem et al. (2014). In their study, significant improvements in the RACMO2.3p2 model were obtained by adjustments to the cloud microphysics. Furthermore, the lack of detailed subsurface snowpack schemes including processes such as refreezing (and subsequent latent heat release) and densification also likely has an impact on the near-surface and subsurface temperature bias in HIRHAM5 and MetUM (see also Fig. 2).

Figure 1 shows that all of the models perform less well for wind speeds than for temperature or pressure observations. The wind speed plot shows that all models have higher CRMSE, higher standard deviation, and lower correlation values when compared with observations. Even so, the RACMO2.3p2, MetUM, and $\mathrm{MAR_{v3.10}}$ still show a correlation above 0.9 with observations, suggesting that the nudging schemes in these models are effective in helping to reproduce observed wind speeds. There are also likely to be large uncertainties in the observations, especially at unattended stations, where burial by snow, changes in orientation, and sensor breakdown are more likely. However, the effects of different resolution and differences in turbulent schemes between the models may also be important. In particular, the extremely stable boundary layer over most of Antarctica is hard to represent in models, particularly at lower resolutions (Zentek and Heinemann, 2020). The models appear to fall into two groups on the Taylor diagram: $\mathrm{MAR_{v3.10}}$, MetUM, and RACMO2.3p2 on the one hand and the two HIRHAM5 runs and $\mathrm{COSMO\text{-}CLM^2}$ on the other hand. In the case of $\mathrm{COSMO\text{-}CLM^2}$ wind speeds are output at 20 m and then interpolated to 10 m using Monin–Obukhov theory (Souverijns et al., 2019), which may not be sufficient to properly represent near-surface winds and associated interactions. The HIRHAM5 results may again be biased due to the lack of nudging within the domain. However, it is worth pointing out that HIRHAM5 correctly represents the mean spatial variability (both runs are the closest to the dashed line indicating the standard deviation) and, in the case of the high-resolution run, has a very low bias in the mean observed wind speed.

3.2 Comparison with 10 m snow temperature observations

Figure 2 shows the modelled surface temperature of the RCMs as a function of 64 measurements of temperature at 10 m depth as also used by Van Wessem et al. (2014). The majority of the AIS has negligible snowmelt, and in these regions the 10 m snow temperature is representative of the long-term average annual surface temperature. This comparison, therefore, is a robust assessment of the climatological surface signal calculated by the models also because the observations are evenly scattered across the continent and represent most climatic regions. All models capture the wide range of surface temperatures from ≈ 218 to 260 K. HIRHAM5 0.44° consistently underestimates temperature for most locations, a bias that closely resembles RACMO2.1 in Van Wessem et al. (2014) and which the authors concluded was predominantly related to biases in the downwelling long-wave radiation. The other models overestimate temperature in the higher-elevation, colder locations while underestimating temperature at lower elevations in the coastal regions. For the colder regions below ≈ 240 K, these biases are most likely related to discrepancies in cloud cover, likely snowfall, affecting downwelling longwave radiation and surface albedo. Some of the Antarctic models have been tuned to improve the dry and cold biases in the interior that

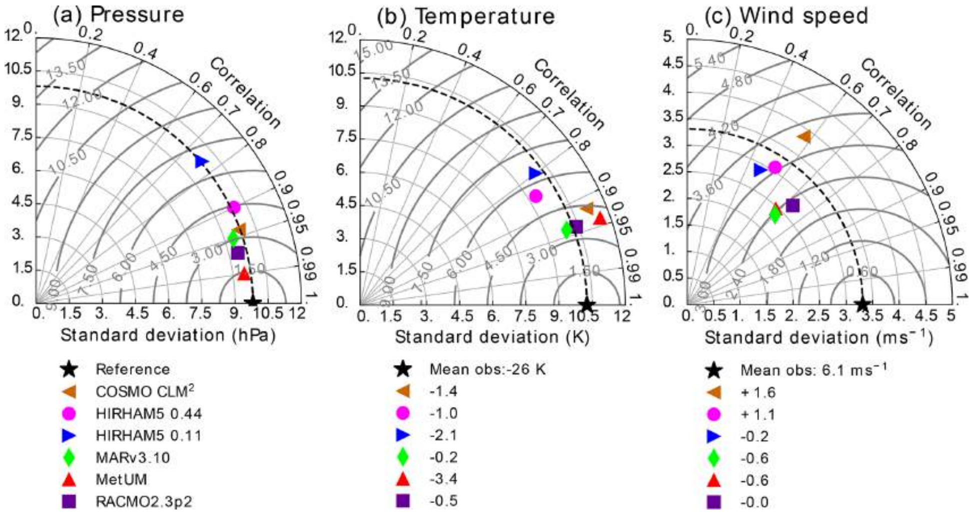

Figure 1. Taylor diagrams showing model performance compared to daily observations of surface pressure **(a)**, near-surface temperature **(b)**, and observed wind speeds **(c)**. The horizontal and vertical axes represent the standard deviation; the dashed line in bold shows the standard deviation of the observations. The Taylor plot also shows the correlation which is measured by the angle with the x axis. Finally, the CRMSE is represented by the curved lines in light grey. The units of standard deviation, CRMSE, mean bias, and mean of the observations are the same (hPa for surface pressure, K for near-surface temperature, and m s^{-1} for wind speed).

were persistent in earlier model versions (see RACMO2.1P; Van Wessem et al., 2014; van Wessem et al., 2018) but now overestimate temperature slightly instead. While subsequent model updates have led to significant improvements in simulated SMB, this has come at the expense of surface temperature due to excessive increases in downwelling radiative fluxes that accompany increases in snowfall.

For the lower-elevation, mostly coastal regions, most models have a cold bias. This bias is likely related to the effects of surface meltwater percolating into the firn and refreezing within, raising deeper snow temperature, implying modelled surface temperature is not a good metric for observed 10 m snow temperatures in the percolation zone. A more accurate comparison would therefore be to directly compare 10 m snow temperatures from the models with the observations. However, not all models calculate snow temperatures, and given the scope of this paper, we only intercompare the surface temperature. Here, Fig. 2 illustrates a consistent intermodel scatter, with mainly the models that do not include a sophisticated snow model outside of this range. This points to a significant potential source of improvements for modelled SMB in the future.

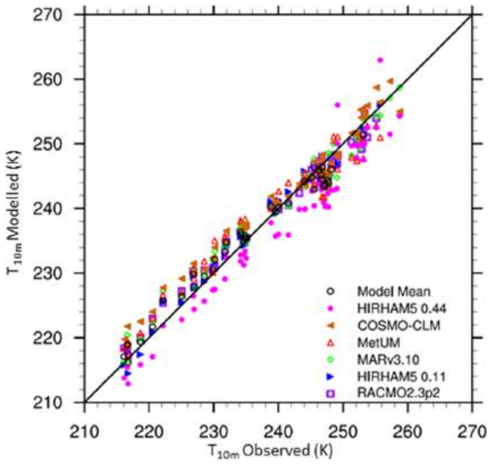

Figure 2. Modelled surface temperature as a function of observed 10 m snow temperature (Van Wessem et al., 2014). Observations not fully located on the model ice mask are excluded.

3.3 Comparison with observed SMB

Evaluating SMB is hindered by poor observations across the cryosphere, particularly in Antarctica, where remoteness and extreme weather conditions add to the challenge of observing SMB. Our analysis uses a large dataset of observations, but there are large areas significantly undersampled (see, for example, Fig. A2). We therefore separate the comparison of modelled and observed SMB into elevation bins in Fig. 3 in order to make the results clearer. Note that Fig. 3 is plotted on logarithmic axes because the distribution of both the observed and simulated SMB is not Gaussian. As linear regression is strongly influenced by the extreme values, which skew r^2 errors in both modelled and observed SMB for the largest values, but is only weakly influenced by the errors in the smallest absolute values, a logarithmic plot better displays how well models reproduce SMB in both high- and low-SMB regions. It is also important to note that for the scatter plots by elevation class, if an observation or one of the models had a negative value, the observation and modelled values were removed from the analysis using logarithmic values for the scatter plots by elevation class (hereafter, rlog is the correlation computed on the logarithm of SMB values) but are retained in the analysis using the original populations. We show detailed statistics for the SMB comparison in Table 2. In order to show the large scatter in the observations and the models clearly, we also plot all modelled SMB values against observed SMB values in Fig. 4. We show individual model comparisons in the Appendix to save space here (Figs. A3, A4, A5, A6, A7, A8).

Apart from COSMO-CLM^2 and HIRHAM5 0.11°, the RCMs show similar root mean square error (RMSE) and r^2 values when compared over the full dataset, but breaking them down by elevation class or locally by regions as in Fig. 4 shows a more complex story. In general, all models, with the possible exception of MAR$_{\text{v3.10}}$, underestimate SMB at the ice shelf observation locations as well as in the low-elevation coastal regions of Antarctica (see also statistics in Table 2a and b and Fig. 3). The highest mean bias, lowest RMSE, and lowest r values in particular are given in the COSMO-CLM^2 and HIRHAM5 0.11° models at the lowest elevations. However, while all the other RCMs underestimate SMB, especially over the Ross Ice Shelf, MAR$_{\text{v3.10}}$ overestimates it, probably related to a poorer representation of the surface climate by the model over this ice shelf. There are indications in Fig. 4 that both HIRHAM simulations overestimate SMB on the Ronne Ice Shelf, but we lack observations to be able to test this properly.

The blowing-snow module included in RACMO2.3p2 may explain the lower bias and RMSE in this model at elevations between sea level and 1200 m and especially 1200 and 2200 m (we show all statistics in detail in Table 2b and c) compared to the other models. A previous comparison shows higher sublimation in RACMO2.3p2 than in MAR$_{\text{v3.10}}$ (Agosta et al., 2019), notably at the elevations where katabatic winds are strong due to the slope of the ice sheet and where the atmosphere is not too cold, enabling large amounts of sublimation from blowing snow particles. COSMO-CLM^2 and HIRHAM5 0.44° have the highest RMSE, while HIRHAM5 0.11, MAR$_{\text{v3.10}}$, and MetUM have similar statistics at this elevation. For the highest elevations (above 2200 m), all the model RMSE scores are relatively low and similar to each other, except HIRHAM5 0.44° (and to a lesser extent MAR$_{\text{v3.10}}$) between 2800 and 3400 m (Table 2e). However, the less extensively optimized models (HIRHAM5 at both resolutions and MetUM) are both too dry over the high plateau of the AIS.

If we look at all the elevation ranges, no model is systematically in the top three for every range, but RACMO2.3p2 has the best comparison with all the observations, closely followed by MetUM, with MAR$_{\text{v3.10}}$ and HIRHAM5 0.44° performing almost equally. It is worth emphasizing though that as Fig. 4 shows, the observations in this elevation class are also very noisy, and the poor relative performance of the models may result as much from unrepresentative and sparse repeat observations as it does from missing or poorly resolved processes in models. Analysis of these results indicates not only areas where models need to be improved but also areas where more observations to test models are desirable, notably between 1200 and 2200, where the mean biases of the models used in this study display large discrepancies (Table 2c). It is also likely that there are compensating errors within each model that hide the true performance. For example, the mean bias between the two different HIRHAM runs has opposite signs in the 1200–2800 m range, likely reflecting the difference in model resolution. Orographic precipitation is very sensitive to slope effects, and the presence of steep topography is very different between the two resolutions, affecting where precipitation falls across the continent. The wide scatter in modelled SMB in the 2200–2800 m elevation range is therefore also likely to reflect in part the resolution of the different models and how well they capture orography and the consequent precipitation. Studies by, for example, Hermann et al. (2018) and Schmidt et al. (2017) show that hydrostatic models like HIRHAM5 and RACMO2.3 typically overestimate precipitation on the upslope and have a dry bias downwind of initial steep topography; this pattern seems to some extent to be repeated in Antarctica in Figs. 3 and 4. Comparing the observations used in this analysis with the RCM ensemble, modelled SMB in Fig. 6 also highlights that the largest differences between models and compared with the ensemble mean are mostly in regions with very few or no observations. These are also regions where precipitation is typically high, making it difficult to assess the ability of models to truly simulate the SMB of Antarctica. Our analysis therefore also helps to identify areas where increased observations will be most useful to help assess and improve model processes.

Mean bias and RMSE for each model by elevation bin is summed up in the Appendix in Figs. A3 to A9. However as Fig. 4 also shows, this is not a straightforward comparison either due to the large areas with only few observations.

3.4 Assessing the surface mass balance of Antarctica

Bearing in mind the results presented in the preceding section evaluating the RCMs, we show here the range of best estimates for Antarctic SMB based on RCMs. Figure 5 shows the modelled specific surface mass balance (SSMB); this is defined as the SMB integrated over the whole basin and divided by the area. We use the 19 drainage basins defined in Shepherd et al. (2020) for the full 9 climate simulations

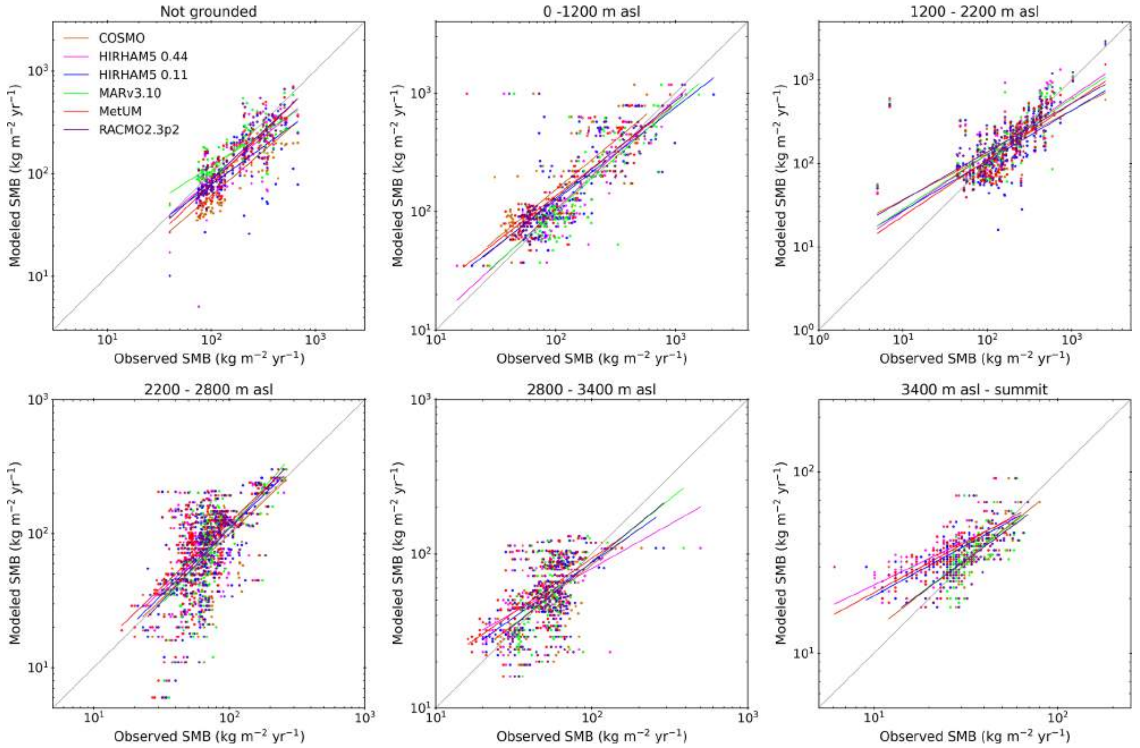

Figure 3. Comparison between modelled SMB and observed SMB in a gridded dataset. Trend lines and points are plotted for each model in a different colour. Note different x and y axes for different elevation bins. The figures are plotted on logarithmic axes because the datasets do not have Gaussian distributions, and this better represents the relative error in both high- and low-SMB regions than linear axes.

as well as the ensemble mean and standard deviation in order to better compare the more recent estimates in this study with older modelled results. Figure 5 also lists the total integrated SMB of the basin in units of gigatonnes (shown by the numbers in a box in each basin). All models simulate a comparable SSMB for the East Antarctic ice sheet (EAIS), with values between 100 and 400 mm yr^{-1}. Due to the moist coastal climates over the ice shelves, SSMB values here reach values as high as 1000 mm yr^{-1}. The main intermodel differences are found over the West Antarctic ice sheet (WAIS) and the Antarctic Peninsula (AP) and are most likely related to differences in horizontal resolution and, therefore, orographic precipitation. The higher-resolution models (RACMO2.3p2, HIRHAM5 0.11°, and MAR$_{\text{v3.10}}$) generate the highest SSMB values over the AP and WAIS basins, up to 2000 mm yr^{-1}. The other models have considerably lower SSMB, especially over the adjacent ice shelves. COSMO-CLM^2 is drier than the ensemble mean and all other models in all basins, with the exception of the Queen Mary Land basin in the EAIS, where HIRHAM5 0.11° is slightly drier, and the interior of the EAIS, where MAR$_{\text{v3.10}}$ is slightly drier. The two areas with the largest ensemble mean deviation are the western-peninsula basin but also the interior of the EAIS bordering the Transantarctic Mountains and including the South Pole. In this region the MAR$_{\text{v3.10}}$ model has the highest SMB (196 Gt), but MetUM has the lowest (77 Gt). Figure 5 also shows some of the striking features in the pattern of SMB present in all the models where the magnitude differs; for example, all models have a steep gradient in the SMB over the Antarctic Peninsula, but this is much more pronounced in HIRHAM5 0.11° than in HIRHAM5 0.44°, demonstrating the importance of resolution in this region. MetUM and COSMO-CLM^2 also show the same pattern but with considerably lower absolute values, particularly on the western side, than the other models. These differences in modelled SMB on the basin scale may have a considerable impact on dynamic ice sheet models used to determine the evolution of the AIS and are consequently important to take into account when selecting SMB to force ice dynamics models. Looking at the total surface mass budget including ice shelves for the period 1980 to 2010 (numbers in the caption and summarized in Table 3) generated by the models, the HIRHAM5 0.44° simulation is the wettest model (2752 Gt yr^{-1}; 2328 Gt excluding ice shelves), while

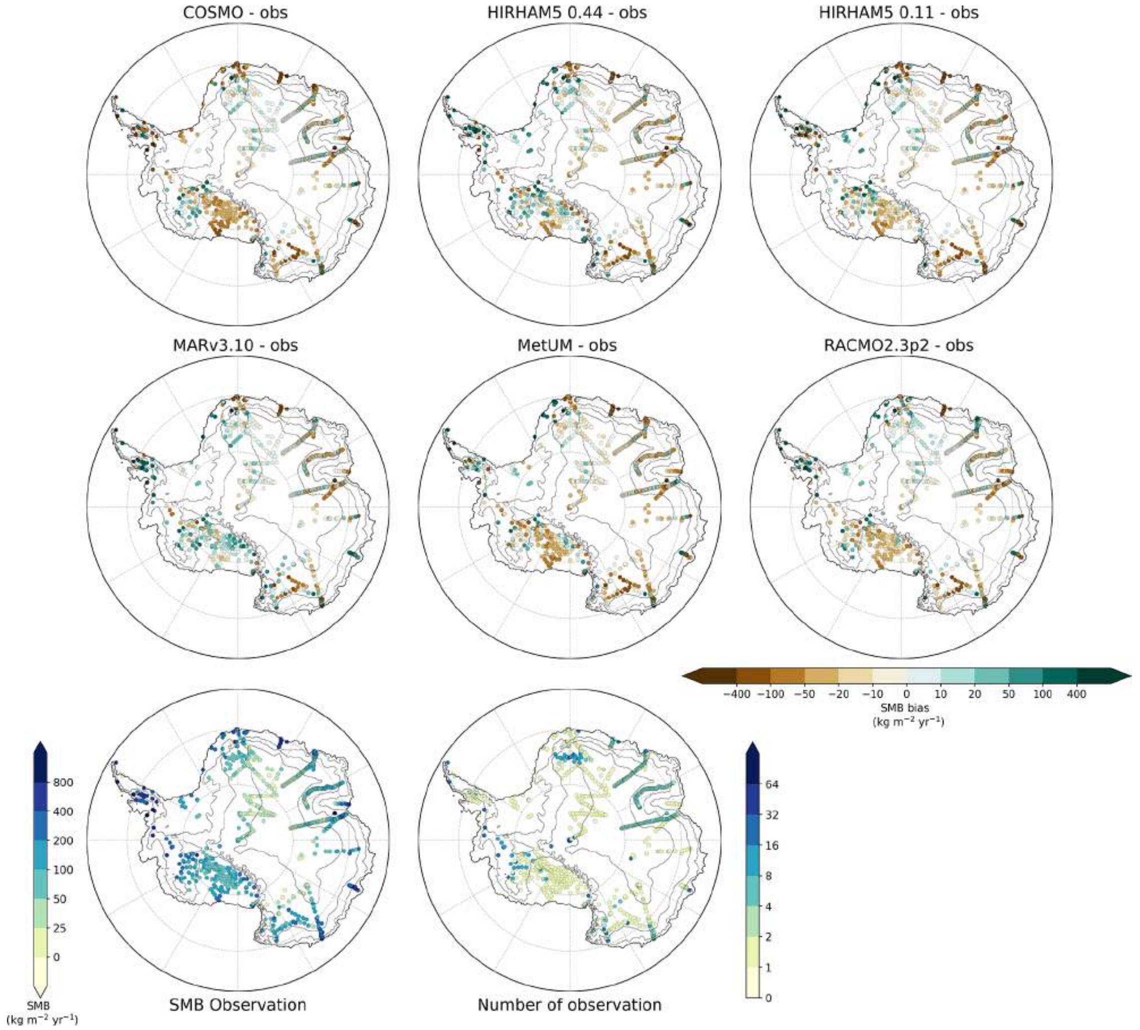

Figure 4. Observed SMB values and the number of observations at each point. The model plots show the difference between observed and modelled SMB for COSMO-CLM^2, HIRHAM5 0.44°, HIRHAM5 0.11°, MAR$_{v3.10}$, MetUM, and RACMO2.3p2.

COSMO-CLM^2 is the driest (2031 Gt yr^{-1}; 1751 Gt excluding ice shelves). The other simulations are all closer to each other and are within an SMB range of $\pm$200 Gt yr^{-1}, while the two dedicated polar models (RACMO2.3p2 and MAR$_{v3.10}$) have only a small difference of 83 Gt yr^{-1} on average, corresponding to around 3 % of the total budget. These two models have been evaluated and optimized for Antarctica the most intensely of all the models (van Wessem et al., 2018; Agosta et al., 2019). We also include MAR3.6 and RACMO2.1 in this figure to give context to earlier studies. The two closest models overall are in fact HIRHAM5 0.11° and MAR$_{v3.10}$, which differ by only 26 Gt overall, with much of the difference accounted for by the SMB of the ice shelves.

As the basin-scale SMB values differ quite substantially between models, in Fig. 6 we plot the mean annual SMB from the ensemble mean and the anomaly to that for each of the different models. The ensemble mean is calculated on a common grid, but the model anomalies are calculated from it on their own grids, which more clearly shows the effects of the different resolutions on the SMB. The figure shows quite substantial agreement between models over large areas of Antarctica but also some considerable local variability. Features such as the Transantarctic Mountains and the

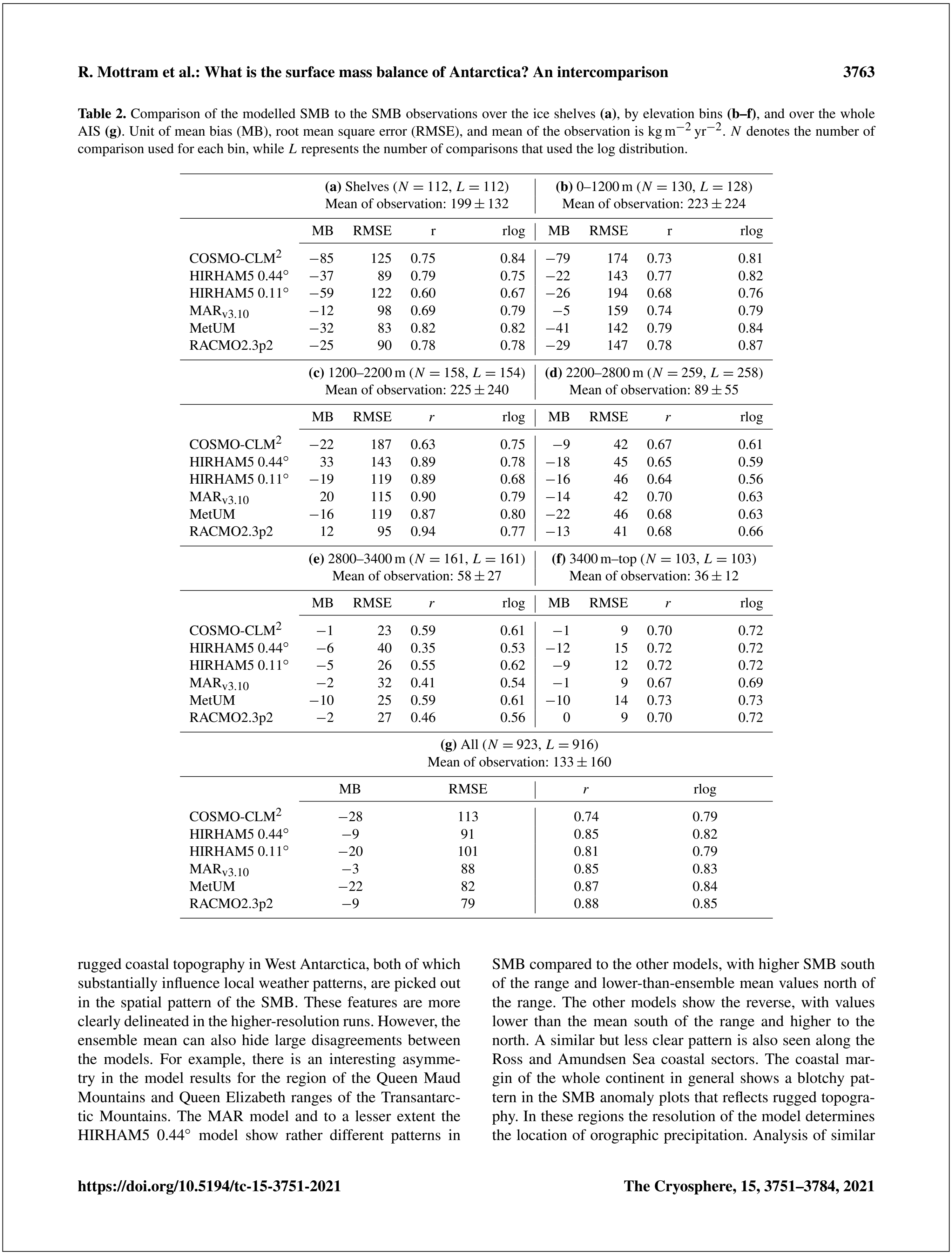

Table 2. Comparison of the modelled SMB to the SMB observations over the ice shelves **(a)**, by elevation bins **(b–f)**, and over the whole AIS **(g)**. Unit of mean bias (MB), root mean square error (RMSE), and mean of the observation is $\mathrm{kg\,m^{-2}\,yr^{-2}}$. N denotes the number of comparison used for each bin, while L represents the number of comparisons that used the log distribution.

	(a) Shelves ($N = 112$, $L = 112$) Mean of observation: 199 ± 132				**(b)** 0–1200 m ($N = 130$, $L = 128$) Mean of observation: 223 ± 224			
	MB	RMSE	r	rlog	MB	RMSE	r	rlog
COSMO-CLM^2	−85	125	0.75	0.84	−79	174	0.73	0.81
HIRHAM5 0.44°	−37	89	0.79	0.75	−22	143	0.77	0.82
HIRHAM5 0.11°	−59	122	0.60	0.67	−26	194	0.68	0.76
MAR$_{\mathrm{v3.10}}$	−12	98	0.69	0.79	−5	159	0.74	0.79
MetUM	−32	83	0.82	0.82	−41	142	0.79	0.84
RACMO2.3p2	−25	90	0.78	0.78	−29	147	0.78	0.87

	(c) 1200–2200 m ($N = 158$, $L = 154$) Mean of observation: 225 ± 240				**(d)** 2200–2800 m ($N = 259$, $L = 258$) Mean of observation: 89 ± 55			
	MB	RMSE	*r*	rlog	MB	RMSE	*r*	rlog
COSMO-CLM^2	−22	187	0.63	0.75	−9	42	0.67	0.61
HIRHAM5 0.44°	33	143	0.89	0.78	−18	45	0.65	0.59
HIRHAM5 0.11°	−19	119	0.89	0.68	−16	46	0.64	0.56
MAR$_{\mathrm{v3.10}}$	20	115	0.90	0.79	−14	42	0.70	0.63
MetUM	−16	119	0.87	0.80	−22	46	0.68	0.63
RACMO2.3p2	12	95	0.94	0.77	−13	41	0.68	0.66

	(e) 2800–3400 m ($N = 161$, $L = 161$) Mean of observation: 58 ± 27				**(f)** 3400 m–top ($N = 103$, $L = 103$) Mean of observation: 36 ± 12			
	MB	RMSE	*r*	rlog	MB	RMSE	*r*	rlog
COSMO-CLM^2	−1	23	0.59	0.61	−1	9	0.70	0.72
HIRHAM5 0.44°	−6	40	0.35	0.53	−12	15	0.72	0.72
HIRHAM5 0.11°	−5	26	0.55	0.62	−9	12	0.72	0.72
MAR$_{\mathrm{v3.10}}$	−2	32	0.41	0.54	−1	9	0.67	0.69
MetUM	−10	25	0.59	0.61	−10	14	0.73	0.73
RACMO2.3p2	−2	27	0.46	0.56	0	9	0.70	0.72

	(g) All ($N = 923$, $L = 916$) Mean of observation: 133 ± 160			
	MB	RMSE	*r*	rlog
COSMO-CLM^2	−28	113	0.74	0.79
HIRHAM5 0.44°	−9	91	0.85	0.82
HIRHAM5 0.11°	−20	101	0.81	0.79
MAR$_{\mathrm{v3.10}}$	−3	88	0.85	0.83
MetUM	−22	82	0.87	0.84
RACMO2.3p2	−9	79	0.88	0.85

rugged coastal topography in West Antarctica, both of which substantially influence local weather patterns, are picked out in the spatial pattern of the SMB. These features are more clearly delineated in the higher-resolution runs. However, the ensemble mean can also hide large disagreements between the models. For example, there is an interesting asymmetry in the model results for the region of the Queen Maud Mountains and Queen Elizabeth ranges of the Transantarctic Mountains. The MAR model and to a lesser extent the HIRHAM5 0.44° model show rather different patterns in SMB compared to the other models, with higher SMB south of the range and lower-than-ensemble mean values north of the range. The other models show the reverse, with values lower than the mean south of the range and higher to the north. A similar but less clear pattern is also seen along the Ross and Amundsen Sea coastal sectors. The coastal margin of the whole continent in general shows a blotchy pattern in the SMB anomaly plots that reflects rugged topography. In these regions the resolution of the model determines the location of orographic precipitation. Analysis of similar

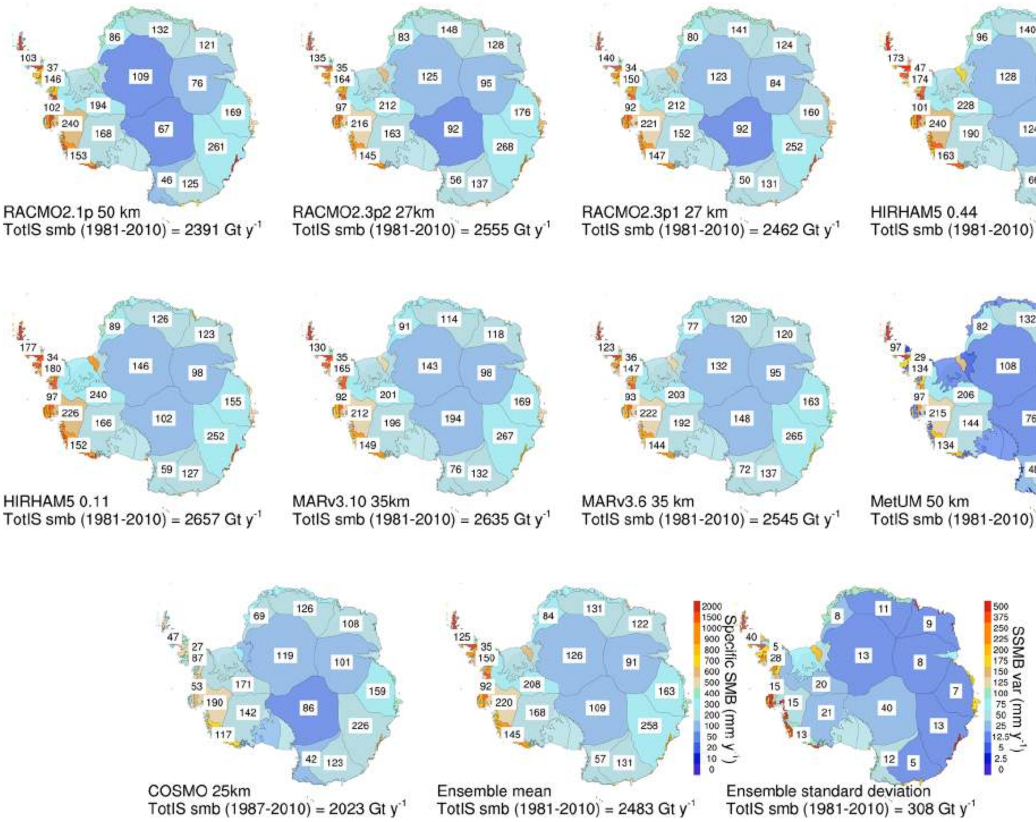

Figure 5. Integrated SMB and specific SMB (SSMB) for the nine models included in this study (RACMO2.1, RACMO2.3p2, RACMO2.3p1, HIRHAM5 50 km, HIRHAM5 12.5 km, $\mathrm{MAR}_{v3.10}$, $\mathrm{MAR}_{v3.6}$, MetUM, and COSMO-CLM^2) as well as the ensemble mean and standard deviation shown. Colours denote the SSMB in millimetres of water equivalent per year for all grounded ice sheet basins as well as the ice shelves these drain into, defined in Shepherd et al. (2019). The numbers included in the basins denote the basin-integrated SMB in Gt yr^{-1} for the grounded ice sheet for the period 1980 to 2010 with the exception of COSMO-CLM^2, where the time series starts in 1987. Finally, the total integrated number for the grounded ice sheet including ice shelves is shown in the figure label.

SMB simulations in Greenland with the HIRHAM, MAR, and RACMO models (Hermann et al., 2018; Schmidt et al., 2017) suggests that in these types of locations HIRHAM and RACMO overestimate precipitation at lower elevations in steep terrain, whereas MAR tends to have a wet bias at a slightly higher elevation, where the other two models are drier. Agosta et al. (2019) related this different pattern of biases in MAR to the advection of precipitation in the model's prognostic precipitation scheme. Understanding these biases is crucial to understanding and interpreting modelled SMB, and comparing Fig. 6 with Fig. 4 it is clear that the locations where there is the highest disagreement between models are also the regions with the poorest systematic observational coverage of SMB, especially in coastal regions and in West Antarctica.

SMB varies not only spatially but also temporally, and average annual SMB values hide large interannual variability of around 4 % in SMB as depicted in Fig. 7. The spread in the range of estimates of SMB is, however, consistent from year to year. The integrated continental SMB calculated over the common mask has a spread of more that 550 Gt between the highest and lowest estimate on average (see also Table 4), but all the models show similar annual- and decadal-scale variability. This implies that the driving model, in this case ERA-Interim, is the most important source of SMB variability but that the individual models are important when considering both the absolute number and the local spatial variability.

We calculate the mean annual SMB and components across the continent including ice shelves, as given in Table 4, over the period 1987 to 2015, for which outputs are available for all the models. Note that this is calculated over

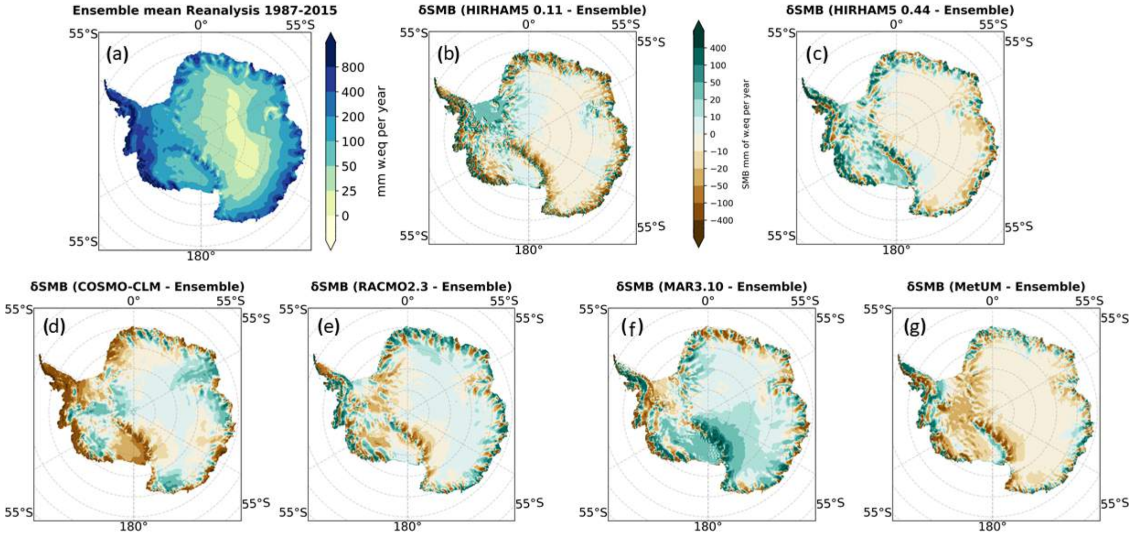

Figure 6. Panel **(a)** shows the SMB ensemble mean for the common period on the common mask. Panels **(b)**–**(g)** show the difference between each model and the ensemble mean.

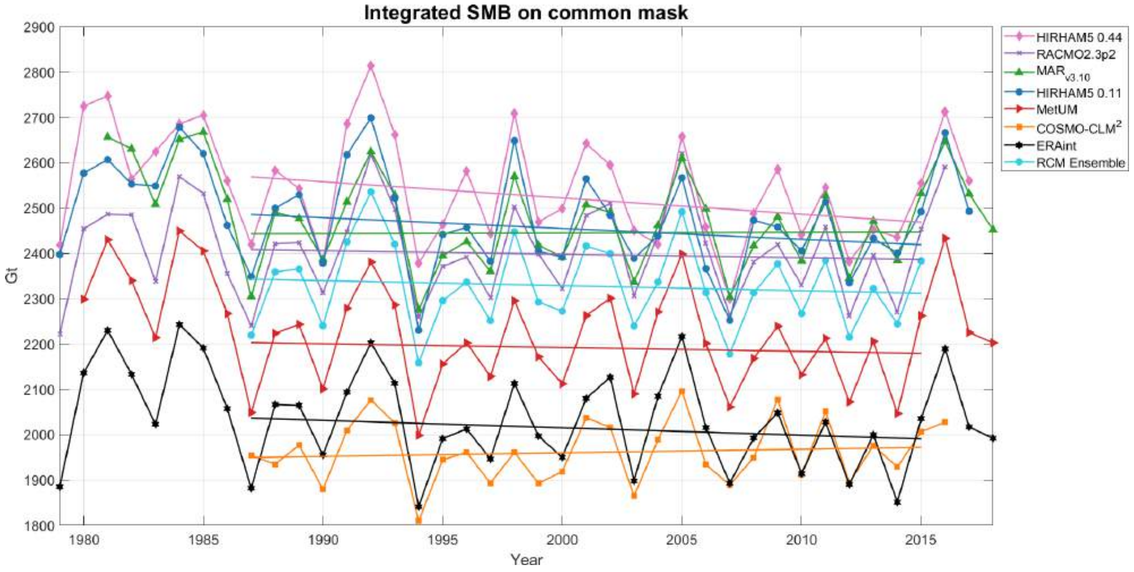

Figure 7. Annually resolved SMB integrated over the common ice mask for the different RCMs in the period 1979–2018. All RCMs are driven by ERA-Interim, and except for MAR$_{v3.10}$ and RACMO2.3p2, SMB is calculated according to Eq. (1). The ensemble is a mean calculated from all six RCMs in the period 1987–2015, where there are data from all the models. All trend lines are calculated for the period 1987–2015.

Table 3. Integrated mean annual SMB for the six models used in this study for the period 1980 to 2010 except for COSMO-CLM^2, where the period was 1987 to 2010. Three older model versions, ensemble mean, and standard deviation as shown in Fig. 5. All calculations done on the original grid of the individual models using a common set of drainage basins and ice mask defined by IMBIE2 (IMBIE2 is the second assessment by the ice mass budget intercomparison exercise, published by Shepherd et al., 2020). The ensemble mean was calculated by transforming all models to the RACMO2.3p2 grid. GrIS denotes grounded ice sheet, IS denotes ice shelf, and ToTIS denotes the full AIS including ice shelves.

Model	GrIS ($\mathrm{Gt\,yr^{-1}}$)	IS ($\mathrm{Gt\,yr^{-1}}$)	ToTIS ($\mathrm{Gt\,yr^{-1}}$)	Area ($10^6\,\mathrm{km^2}$)
RACMO2.1	1929	471	2391	13.85
RACMO2.3p2	2132	430	2555	13.85
RACMO2.3p1	2032	437	2462	13.85
MARv3.10	2227	413	2633	13.92
MARv3.6	2156	395	2545	13.92
HIRHAM5 0.44	2323	437	2752	13.87
HIRHAM5 0.11	2233	434	2657	13.83
MetUM	1883	452	2327	13.82
COSMO-CLM	1743	287	2023	13.84
Ensemble mean	2073	417	2483	13.86
Ensemble Σ	306	77	266	0.085

a common ice mask and a common simulation period and using the simple SMB calculation given in Eq. (1), and results are therefore slightly different to those already published for different models or shown in Fig. 5 or Table 3. The simple SMB is used to compare the models more fairly against each other and with the ERA-Interim-derived SMB in Figs. 7 and 6. In this time series HIRHAM5 0.11° and $\mathrm{MAR_{v3.10}}$ are the closest two models to each other in integrated SMB. RACMO2.3p2 is closest to the ensemble mean, but COSMO-CLM^2 is closest to the driving ERA-Interim modelled values. The trend lines are very sensitive to starting and ending years and in some cases change sign if a longer period is chosen, but as we have only a short common period we have chosen to calculate the trend over the common period. For this chosen period, COSMO-CLM^2 and $\mathrm{MAR_{v3.10}}$ show a slightly increasing trend in SMB, whereas the rest show a slightly declining trend in SMB, although the trend in RACMO2.3 and MetUM is almost flat. The ERA-Interim trend over the period declines slightly more than the MetUM trend, which is otherwise extremely close. The different trends from the models and in particular the sensitivity to different start and end points do not give us confidence to ascribe a statistically significant trend to Antarctic SMB over the whole continent. We note though that all models show a declining trend in the 1990s and early 2000s but with a recent increase in SMB since 2014. The early part of the record appears to have higher variability, but this may be related to changes in data assimilation in the driving reanalysis (Dee et al., 2011).

Figure 8 emphasizes the large variability in SMB on an annual to decadal scale by plotting the variation from the mean for each model and the variation from ERA-Interim for each model. We show that while all the models have more or less the same anomaly when compared to their own mean, the sign of the anomaly compared to the ERA-Interim value can be different. Since the most highly constrained models show the lowest anomaly compared to ERA-Interim, we suggest that most of the variation is related to internal variability (weather) within the domain. Both HIRHAM5 0.11° and 0.44° show the highest values of variability, probably due to the unconstrained nature of the runs, but in different years, different models show higher variability than the others. The lower panel in Fig. 8 demonstrates that MetUM is by far the closest to the driving model, with much less variability than the others (likely due to its frequent reinitialization). HIRHAM5 again shows the highest difference compared to the driving model, but from year to year the model showing maximum difference varies, and there appears to be no systematic pattern as to whether or not modelled SMB is higher or lower than the ERA-Interim reanalysis when quantified on the common mask and over the whole of Antarctica. The implication is that while the driving model controls broad-scale pattern of SMB, the downscaling model adds its own weather variability to the broad-scale pattern. The variability, or weather noise, is unsurprisingly largest in un-nudged models. The effect of this noise on ice sheet dynamics may be small overall, but, as for example, Mikkelsen et al. (2018) show, small stochastic variations in SMB can have a non-negligible impact on ice sheet dynamics.

Since SMB is made up of accumulation and ablation components, and in Antarctica precipitation is the dominant term, Fig. 9 shows the precipitation component only over the common mask for the different models and ERA-Interim. There is a very similar pattern to that in Fig. 7, but compensating effects from sublimation, which is higher in HIRHAM than in MAR, explain the bigger offset between HIRHAM5 0.11° and $\mathrm{MAR_{v3.10}}$. MAR is closer to RACMO2.3 in terms of precipitation, separated by only 10 Gt. The mean values for the SMB components of precipitation, evaporation, and sublimation as well as SMB for the common period 1987–2015 over the common ice mask are also displayed in Table 4. These values confirm that the very much higher precipitation in both HIRHAM5 runs compared to the other models is to some extent compensated for by higher values of sublimation. Precipitation in HIRHAM5 0.44° is 80 Gt higher than that in the 0.11° simulation, which in turn is 68 Gt higher than the next wettest model, $\mathrm{MAR_{v3.10}}$, but precipitation in the RACMO2.3 model is only 10 Gt lower than in MAR. On the other hand, sublimation in HIRHAM5 is higher (192 and 183 Gt in the 0.44 and 0.11° runs, respectively) than in $\mathrm{MAR_{v3.10}}$ (122 Gt), RACMO2.3p2 (158 Gt), and MetUM (175 Gt), but COSMO-CLM and ERA-Interim both have higher values than HIRHAM (262 and 255 Gt, respectively). Although the RACMO2.3p2 model includes sub-

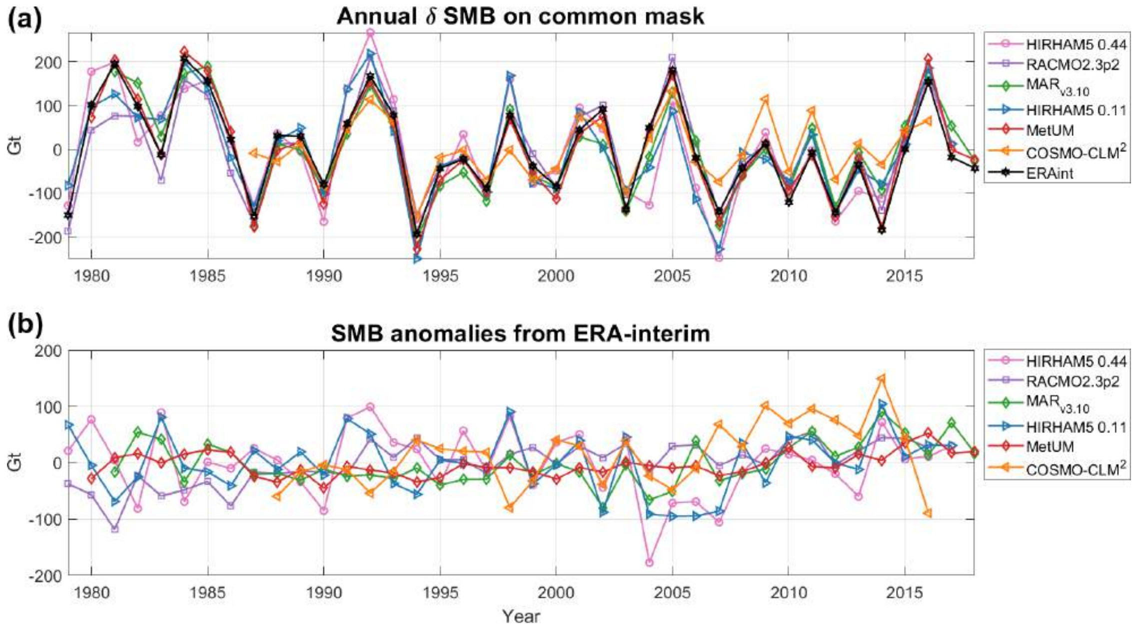

Figure 8. Panel **(a)** shows the annual variability in surface mass balance over the common mask for each of the different RCMs in the period 1979–2018. It is calculated by subtracting the respective model mean from each RCM's SMB time series. Panel **(b)** displays how modelled SMB from each RCM deviates from the ERA-Interim SMB.

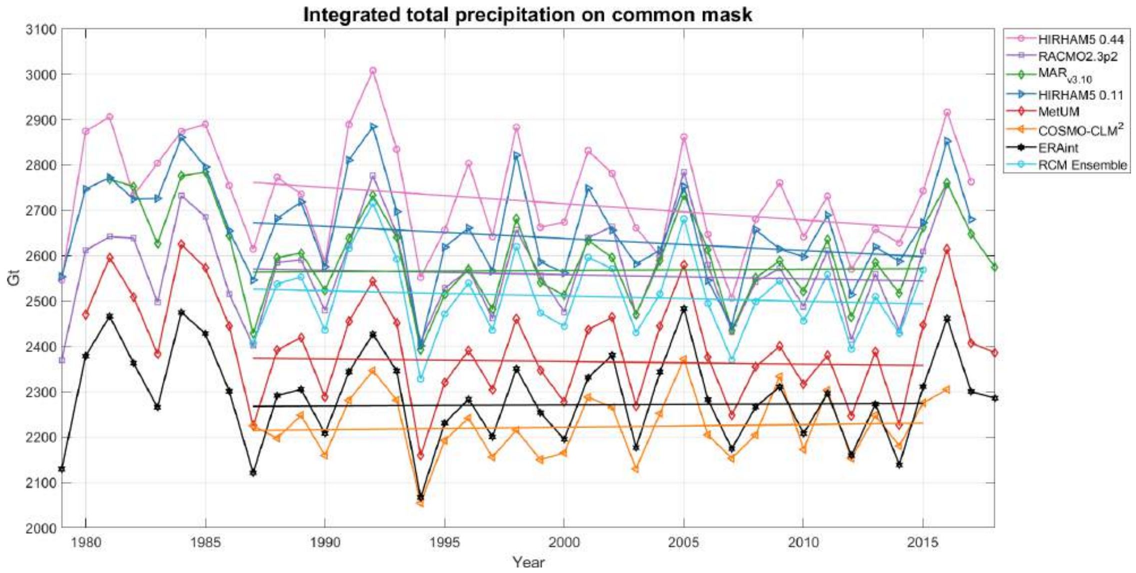

Figure 9. Annually resolved precipitation integrated over the common mask for the different RCMs in the period 1979–2018. All RCMs use ERA-Interim. The ensemble is a mean calculated from all five RCMs in the period 1987–2015, where all models have data.

limation from ventilated snow, the sublimation rates are still lower than all models except $\mathrm{MAR}_{\mathrm{v3.10}}$. MetUM, which performs similarly to RACMO2.3 when compared with SMB observations, has lower precipitation and higher sublimation rates than RACMO2.3, however, suggesting that ventilation of drifting snow alone does not explain the higher sublimation rates. $\mathrm{MAR}_{\mathrm{v3.10}}$ has the lowest sublimation rates of all and COSMO-CLM^2 the highest. Our results suggest that the dry bias in COSMO-CLM^2 is a result in part of the lower precipitation values, which are very close to those of the driving ERA-Interim model but also a consequence of the much higher sublimation values. This dry bias is mostly confined to the coastal regions and peninsula and is identified and discussed in Souverijns et al. (2019). The RACMO2.3 model is closest to the ensemble mean annual precipitation, but as the $\mathrm{MAR}_{\mathrm{v3.10}}$ model mean values are only different to RACMO2.3 by 10 Gt, in some years shown in Fig. 9 it is actually even closer to the ensemble mean than RACMO2.3 is.

4 Discussion

4.1 The surface mass budget of Antarctica

The range of models in this intercomparison study allows us to not only estimate the likely range of SMB over Antarctica but also to identify sources of disagreement and bias within and between models. Accounting for differences in ice mask, the ensemble mean annual SMB integrated over the whole of Antarctica between 1987 and 2018 is $2329 \pm 94\,\mathrm{Gt\,yr^{-1}}$. The RACMO2.3p2 model has a value closest to the ensemble mean, with the high-resolution HIRHAM5 model 190 Gt over this number and the COSMO-CLM^2 model 368 Gt below. The HIRHAM5 0.11° and $\mathrm{MAR}_{\mathrm{v3.10}}$ numbers are almost exactly the same, at 2452 and $2445\,\mathrm{Gt\,yr^{-1}}$, respectively, around 150 Gt above the mean. MetUM and COSMO-CLM^2 are much lower, at about 138 and 368 Gt below the mean, respectively. Given that the models perform fairly similarly when evaluated against SMB observations, we here give all models equal weight, although we suspect that there is a dry bias in COSMO-CLM^2 and a wet bias in HIRHAM5 0.44°. With an identical forcing from ERA-Interim, the present-day estimate of the surface mass budget of Antarctica ranges from 2519 to $1961\,\mathrm{Gt\,yr^{-1}}$, a 558 Gt range that alone is equivalent to around 1.5 mm of global mean sea level rise. Narrowing this range for the purposes of estimating sea level change at present and in the future is an important task, and for this reason we have evaluated the models against observations in Antarctica (see below).

We can compare our results for the total mass budget of Antarctica with those produced by the IMBIE2 study (Shepherd et al., 2020). In Fig. 10 we show the SMB discharge for two different datasets, where the IMBIE2-reconciled (Shepherd et al., 2020) estimate of mean annual discharge is $2103 \pm 56\,\mathrm{Gt\,yr^{-1}}$, and the discharge of $2247 \pm 140\,\mathrm{Gt\,yr^{-1}}$ estimated by Rignot et al. (2019) for the same period is subtracted from SMB calculated from each model. We use the simple SMB calculation in Eq. (1) for the period 1992 to 2017 over the grounded ice sheet only. The Rignot et al. (2019) dataset has a wider uncertainty range than the Shepherd et al. (2020) estimate and a larger discharge that gives a lower total mass budget overall, but in all cases the two overlap within the uncertainty ranges. Note that the RACMO2.3p2 model was used to produce both the IMBIE2 and Rignot et al. (2019) estimates, and it is thus not a truly independent comparison. The earlier MARv3.6 model was also included in the Shepherd et al. (2020) study.

When taking into account the published uncertainties in the observational mass budget estimates of discharge, only the COSMO-CLM^2 and MetUM estimates are completely outside the range defined by the IMBIE study ($109 \pm 56\,\mathrm{Gt\,yr^{-1}}$) for the total mass budget of Antarctica. However, as the statistics in Fig. 1 show, both models perform well compared to the weather station observations, particularly MetUM, and both have higher correlations and lower biases than the two HIRHAM simulations) for pressure and temperature. Comparison with the SMB observations shows that while COSMO-CLM^2 has a large dry bias (of $\sim 40\,\%$) over ice shelves and at lower elevations, at higher elevations the mean bias is close to zero for the COSMO-CLM^2 model and in fact much lower than the other models in the 2800–3400 m elevation range (see Fig. A9). MetUM on the other hand has a middle-of-the-range mean bias at low elevations compared to other models but a much higher ($-25\,\%$ to $-30\,\%$) mean bias as shown in Fig. A9 at the upper elevations. The combination of these results, bearing in mind also the undersampling in the dataset, thus indicates either that some of the components of SMB are poorly captured by the models or that there are compensating errors in the modelled SMB components and/or their spatial variability. Most likely a combination of factors is responsible for the wide variation in integrated SMB estimates. This means that there are large uncertainties in both observations and the biases in models that we discuss in this paper that complicate assessing the contribution to sea level rise from Antarctica from SMB processes.

Unlike previous studies, we detect no obvious strong trend in the modelled SMB in any of the models or in the driving ERA-Interim model. Shorter periods within the time series appear to have quite strong trends. For example, a steady declining trend is apparent through the 1990s and 2000s but appears to reverse after 2014. Our results suggest that strong interannual and decadal variability makes the identification of meaningful trends over periods shorter than multidecadal very difficult. Distinguishing noise from signal will be challenging in the coming decades, and this also emphasizes the importance of long time series of observations. SMB variability is a result of low- and mid-latitude weather variability, but interannual variability is particularly large at the begin-

Table 4. Mean annual SMB and components on common mask for each model averaged over the 1987–2015 period, where all the models overlap. Standard deviations are also shown. SMB is calculated using the simple Eq. (1) to enable a fair comparison.

Model	SMB (Gt yr^{-1})	Precipitation (Gt yr^{-1})	Sublimation (Gt yr^{-1})
HIRHAM5 (0.44°, 0.11°)	2519 ± 118, 2452 ± 107	2711 ± 117, 2635 ± 107	192 ± 12, 183 ± 10
MAR$_{v3.10}$	2445 ± 91	2567 ± 87	122 ± 11
RACMO2.3p2	2399 ± 101	2557 ± 100	158 ± 7
MetUM	2191 ± 101	2366 ± 100	175 ± 9
COSMO-CLM^2	1961 ± 70	2222 ± 72	262 ± 10
ERA-Interim	2016 ± 99	2271 ± 95	255 ± 18
Ensemble mean	2329 ± 94	2498 ± 93	194 ± 9

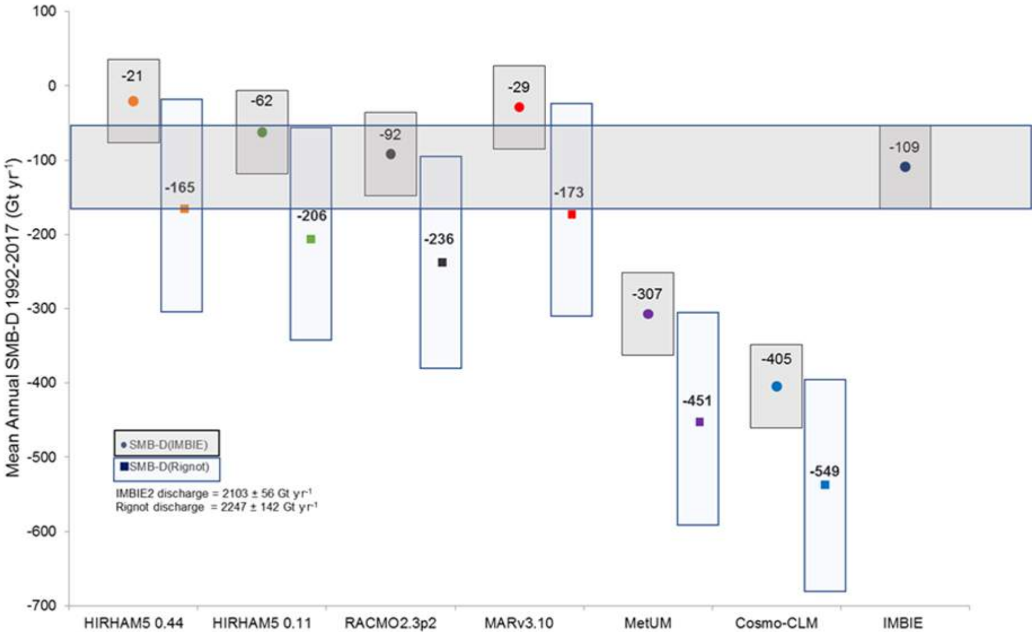

Figure 10. Modelled SMB minus discharge calculated from IMBIE2 results (Shepherd et al., 2020) (filled circles indicate mean; light-grey box indicates IMBIE2 uncertainty range of ±56 Gt yr^{-1}) and Rignot et al. (2019) (mean showed in filled square; uncertainty range of 142 Gt yr^{-1} shown by narrow shaded blue box). The range for the Rignot discharge is taken from Table 1 in Rignot et al. (2019). We assume that the same uncertainty range for the period 2009 to 2017 is applicable over the longer 1992–2017 period. The total mass budget estimated by IMBIE2 is also shown by the horizontal shaded dark-grey box for ease of comparison. Numbers are mean annual SMB-D for the 1992–2017 IMBIE period for each model.

ning of the ERA-Interim period up to 1990, and we hypothesize this is related to improved data assimilation in the Southern Hemisphere in the period between 1979 and 1989 (Dee et al., 2011). The models disagree on both the magnitude and the sign of the overall trend in the 1987–2018 common period of all models. Figure 8 demonstrates that the external forcing model, in this case ERA-Interim, is extremely important in determining both the total SMB and the year-to-year variability in the SMB trend, even though the absolute values are somewhat dependent on the individual RCM. This is not an unexpected result given that these are all limited-area models forced at the boundaries, but it has important implications for estimates of future projections of SMB in Antarctica. Decadal- and multidecadal-scale climate variability expressed in global climate models will have a strong influence on Antarctica mass budget (including the dynamical components via ocean forcing) that may suppress or enhance the anthropogenic forcing in ways that are difficult to predict given the large internal variability in the system. Long climate simulations with large ensembles will be necessary to define the likely range of internal climate variability, and this poses challenges of computing resources when regional downscaling is required to represent the spatial patterns of SMB over the ice sheet at high resolution.

Even between models with similar values for the integrated SMB, there is substantial spatial variability in the pattern of SMB, as shown by the basin-level breakdown in Fig. 5 and the variation from the ensemble mean in Fig. 6. These together show a nuanced picture. Over most of Antarctica, particularly in the east, the variation between models is rather small; the biggest deviations are largely around the coast. These small areas have a disproportionate influence on the continental integrated SMB values due to high accumulation rates. Basins in West Antarctica, and particularly on the Antarctica peninsula, have very large differences, where, for example, HIRHAM5 0.11° shows an average annual SMB of 176 Gt, but COSMO-CLM^2 has the lowest estimate of 46 Gt in the same basin. The MAR model, which shows an integrated SMB value similar to HIRHAM5 over the whole continent, gives 130 Gt in the same basin, closer to the RACMO2.3p2 value of 134 Gt, while MetUM is again lower at 96 Gt. Averaging SMB over the whole continent smooths out a good deal of the spatial variability, which in turn is also important for driving ice dynamics. Equally, as some basins especially in West Antarctica have very high precipitation rates, differences between models in relatively small areas here can make a large contribution to the difference in the integrated numbers over the whole continent.

Similarly, relatively small differences in ice masks that are primarily in coastal regions with high accumulation rates can lead to relatively large differences in SMB estimates (see Fig. A1), as Vernon et al. (2013) have also shown in Greenland. Figure A1 in the Appendix compares the ice masks of all the models. We found that, although the variation looks quite small, the grid points affected include some of the highest precipitation points within the domain, and thus small differences can have large effects. This is one of the main differences between the earlier RACMO2.1, with one of the smallest ice masks, and RACMO2.3 for example. Almost all the other models were larger around the entire coastline. The total SMB integrated over the continent is therefore highly sensitive to the size of the common mask. For example, the SMB for HIRHAM5 0.11° is computed on its native mask and gives an integrated SMB on average 9.95 % higher compared to the common mask result, even though the native mask is only 2.93 % larger than the common mask. These differences suggest that the CORDEX community should agree on a common protocol to calculate the ice mask to reduce uncertainties in Antarctic SMB. The deviation from ensemble mean SMB shown in Fig. 6 suggests that while over the high plateau of East Antarctica there is little deviation in general, much bigger differences occur between model SMB estimates around the Transantarctic Mountains, where the effect of higher resolution becomes obvious in resolving the topography, but model physics also likely play a role. We see a similar effect in the high-relief topography of West Antarctica. Finally, our results show that between 14 % (COSMO-CLM^2) and 19 % (MetUM) of the SMB is accounted for by the ice shelves around Antarctica.

A comparison of the high- and low-resolution HIRHAM5 simulations is interesting here as the models are identical other than resolution. There is a substantial difference in the location of the maximum upslope precipitation as well as the downslope precipitation shadow. We attribute these differences to resolution that allows high-resolution simulations to better represent steep topography. A similar but less marked impact is seen between the earlier RACMO2.1P and newer RACMO2.3p2, though in this case changes in model physics may also be responsible.

4.2 Model evaluation with observations

Evaluating the models against observations is very important for assessing where there are important biases, but evaluation of model performance is significantly hampered by the lack of observations in key regions. Nonetheless, Fig. 1 shows that the models do have skill in simulating surface climate, particularly temperature and pressure. The skill in simulating surface climate does not however translate perfectly to simulating SMB, partly due to the difficulties of modelling and evaluating precipitation. Our analysis shows that, for example, COSMO-CLM^2 better simulated surface climate compared to observations than HIRHAM5, but it has a lower skill in SMB. Variables such as temperature and pressure are more easily measured and are assimilated into the reanalysis used to drive the models. RCMs have also been optimized to give good performance compared to these kinds of observations. However, Antarctic SMB is dominated by the precipitation term that is much harder to measure accurately and also has much higher uncertainty in models.

SMB observations themselves are not always very reliable, and sub-grid-scale surface snow processes, such as the build-up of sastrugi, can give substantially different results over short spatial scales (Andersen et al., 2006). Therefore, it is important to break down the data into different regions and elevation classes to see where models have better or weaker performance. We note the scatter in both models and observations within the different elevation bins and that the two polar-optimized models (MAR and RACMO) perform, broadly speaking, better than the others (see also Figs. A3 to A8 in the Appendix), though the differences are rather small in some of the elevation bins and are not always very significant. It is clear that more work needs to be done to understand exactly how SMB varies spatially over the continent in order to better optimize parameterizations. The use of nudging in models does however seem to make it easier to replicate both observed climate and SMB in RCMs. We discuss further below the use of nudging in regional climate simulations.

4.3 Ice sheet SMB processes

Evaluation against observations helps to identify missing and mischaracterized processes within RCMs. Models that have not undergone specific adjustments for Antarctica represent the SMB in Antarctica more poorly than those that have been adjusted in some regions. However, Table 2 shows that introducing new parameterizations is not unambiguously an improvement as in some elevation bands the unmodified models have lower bias and RMSE, as also shown in the Appendix (Fig. A9). Other biases are also evident in this analysis. The driest model, COSMO-CLM^2, underestimates SMB close to the coast, a region very relevant for total ice sheet mass balance. This is due to an overestimated sublimation amplified by an underestimated snowfall rate close to the coast. High values for the sublimation originate from an underestimated albedo due to ageing of the snow that occurs too fast in the model (Souverijns et al., 2019). The low values for the snowfall rate are likely related to cloud microphysics, namely a too slow conversion of ice to snow or a too slow deposition of water vapour on the solid hydrometeors. Currently, efforts are ongoing to improve the coastal SMB performance in COSMO-CLM^2. The HIRHAM5 climate simulations both appear to have a wet bias, likely again related to the cloud microphysics and precipitation schemes but also probably a result of a diagnostic precipitation scheme commonly used in hydrostatic models. The models typically have a wet bias on the upslope of steep topography and a dry bias on the downslope. The RACMO2.3 model shows a similar, though less pronounced effect that derives also from the IFS physical schemes (Hermann et al., 2018; Schmidt et al., 2017). New prognostic precipitation schemes have been developed for numerical weather prediction models to solve this problem (Forbes et al., 2011), and implementation of a similar prognostic scheme in MAR probably explains the different pattern of SMB in areas with steep topography (Agosta et al., 2019). As RACMO and MAR are the only two models that have a specific subsurface scheme for ice sheets, in this model comparison we have excluded detailed discussion of melt and run-off, and this will likely be the subject of future work. Given the high amount of precipitation over Antarctica, this run-off is still very small in absolute and relative senses, accounting for only 2 Gt of mass loss from the grounded parts of the AIS in RACMO2.3p2 for instance, but as a warming future climate is expected to bring increasing amounts of melt, a more sophisticated treatment that includes refreezing within the snowpack will become increasingly important. More importantly, with respect to the radiative schemes within the models, adding an ice-sheet-specific snowpack to the surface module in MAR and RACMO does improve the surface temperature (and 10 m snow temperature) and therefore the air temperature. This is clear in Fig. 2 and may also be a factor in some of the biases shown in Fig. 1. Improving these surface schemes is therefore important not just for future projections of SMB but also to improve the near-surface climate.

4.4 Model topography and resolution

The inclusion of two simulations with the HIRHAM5 model, varying only the resolution, allows us to assess the impact that higher resolution has on the results, as shown in Fig. 7 and Table 4. The higher-resolution version adds value with higher spatial variability that should better capture local topography and associated weather phenomena. This is especially important in areas of high relief such as in the coastal areas and around the Transantarctic Mountains. These are also the areas where models vary from each other and the ensemble mean the most. While there are very few observations to confirm the better performance on a local scale, the pattern of SMB suggests that the high-relief rugged topography is better captured in HIRHAM5 0.11° than 0.44°. However, the higher-resolution model is not only more computationally expensive; in a simulation where there is no nudging, like here, the larger number of grid points gives increased degrees of freedom for the model to evolve freely and thus introduces more internal variability. While this is not necessarily a problem for climate simulations in the future, the enhanced internal variability is inevitably punished when compared with observations and models that have been internally nudged.

Nudged models (MAR, RACMO, COSMO-CLM^2) show a generally lower variance from the ERA-Interim mean SMB compared to the un-nudged models (HIRHAM5, MetUM), though MetUM, run as a hindcast, shows the closest values to ERA-Interim overall. They also show a closer match to observed climate than the un-nudged model runs. The advantages of nudged runs are thoroughly explored in van de Berg and Medley (2016), who run two versions of RACMO2 for Antarctica, one nudged and one not nudged. They find that RACMO2 nudged gives SMB results that better represent the temporal variability in the observations because the top of the atmosphere is constrained, thus preventing the model from deviating too far from large-scale systems in the mid-latitudes. The nudging as applied in RACMO is not spectral nudging but relaxation of temperature, pressure, and wind fields, and this leads to some systematic mid-tropospheric warming and hence to slightly lower SMB in the interior of Antarctica also. Other studies (Alexandru et al., 2009; Berg et al., 2013) show that spectral nudging can also lead to lower precipitation extremes and reduced vorticity, while Akperov et al. (2018) show better representation of Arctic cyclones in nudged models. The daily reinitialization and close forcing by ERA-Interim also explain why the MetUM modelled SMB is closest to the ERA-Interim values when integrated over the common mask. The MetUM simulation is a hindcast series where the full prognostic model state is replaced daily or twice daily. The series is technically made continuous by construction, but it is in fact likely to be discontinuous in terms of energy, momentum, and moisture budgets, and like all nudged models, they are in general not energy-, moisture-, or momentum-conserving. Berg et al. (2013) argue for caution in applying nudging during climate simulations as, while it compensates for the RCM's deficiencies in mesoscale and large-scale circulation, the assumption is that the driving model represents the large-scale circulation well. In the ERA-Interim reanalysis dataset, this is a minor problem, but for free-running GCMs, large-scale circulation may well be more poorly simulated. As the external forcing controls what is delivered on the boundaries, future projections of Antarctic climate and ice sheet change will be highly controlled by the quality of the forcing on the RCM boundaries. Models nudged internally within the domain will be further constrained in estimates of SMB by the driving models, implying that rigorous assessment of global climate models should be performed before downscaling GCMs for future projections to determine which biases will be introduced (Agosta et al., 2015; Barthel et al., 2020).

5 Conclusions

The Polar CORDEX regional climate simulations for Antarctica are a valuable and freely available dataset for climate researchers. In this paper, we compare the models against each other and against observational datasets. Much more analysis is possible and will be followed up by this group. We hope also to encourage other scientists to make use of the CORDEX dynamically downscaled models. Analysis and model intercomparison are useful techniques to evaluate models and to show directions for model improvements. Our results can be summarized as showing that the RCMs in this analysis produced skilful climate simulations over the Antarctic continent, though with more uncertainty surrounding estimates of SMB due to precipitation uncertainty. There is a high annual and decadal as well as spatial variability in SMB across Antarctica and no clear long-term trend. Model resolution and model dynamics interact in interesting ways in areas with high relief and complex topography that make it important to focus on observational campaigns in these regions. In particular, we argue that given the importance of precipitation for SMB, new observational programmes are needed that focus on accumulation and snow processes, e.g. stakes, firn cores, and radar. Furthermore, focusing on new observations in regions (see, for example, Fig. A2) where there is both a lack of current data and strong disagreement between models will be valuable for understanding climate in Antarctica.

There is closer model agreement on SMB for the interior of the Antarctic ice sheet than there is in the margins and on the Antarctic Peninsula. The largest areas of disagreement between models are primarily in West Antarctica. In this paper we focus mostly on precipitation as well as sublimation and evaporation, but reliable subsurface snow and firn schemes will become increasingly important, particularly when making projections of SMB in the future. Models that have been optimized for the Antarctic climate and which incorporate nudging typically demonstrate more model skill than those which do not.

Appendix A: Additional figures

A1 Model ice masks

All title masks are larger than the common mask: HIRHAM5 0.11° is 2.43 % larger, $\mathrm{MAR}_{\mathrm{v3.10}}$ is 2.89 % larger, RACMO2.3P2 is 1.85 % larger, MetUM is 2.49 % larger, COSMO-CLM^2 is 1.94 % larger, and HIRHAM5 0.44° is 2.49 % larger. Some of the differences are due to inclusion of nunataks and mountain ranges within the continent. The common mask also includes nunataks. The SMB for each model calculated over the common mask (GrIS) with the Rignot et al. (2019) regional basins is given in Table A1 below for the common period of 1981 to 2016 (except COSMO-CLM^2, which starts in 1987).

Table A1. Mean annual SMB for the grounded ice sheet over the total (GAIS), the East Antarctic (EAIS), West Antarctic (WAIS), and Antarctic Peninsula (AP) regions over the common mask for the common 1981–2016 period, where all the models overlap (except COSMO-CLM^2, which is shown for 1987–2015). The ensemble mean is calculated only from models that cover the full period and therefore excludes the COSMO-CLM^2 results but includes the driving ERA-Interim model. SMB here is calculated using the simple Eq. (1) to enable a fair comparison. We used the Rignot et al. (2019) definitions for the different regions of Antarctica.

Model	GAIS ($\mathrm{Gt\,yr^{-1}}$)	EAIS ($\mathrm{Gt\,yr^{-1}}$)	WAIS ($\mathrm{Gt\,yr^{-1}}$)	AP ($\mathrm{Gt\,yr^{-1}}$)
HIRHAM5(0.44°)	2042	1116	699	227
HIRHAM5(0.11°)	1964	1065	658	242
$\mathrm{MAR}_{\mathrm{v3.10}}$	2046	1196	643	206
RACMO2.3p2	1939	1094	632	197
MetUM	1751	996	593	162
COSMO-CLM^2	1668	1023	548	98
ERA-Interim	1623	915	571	137
Ensemble mean	1894	1064	633	195

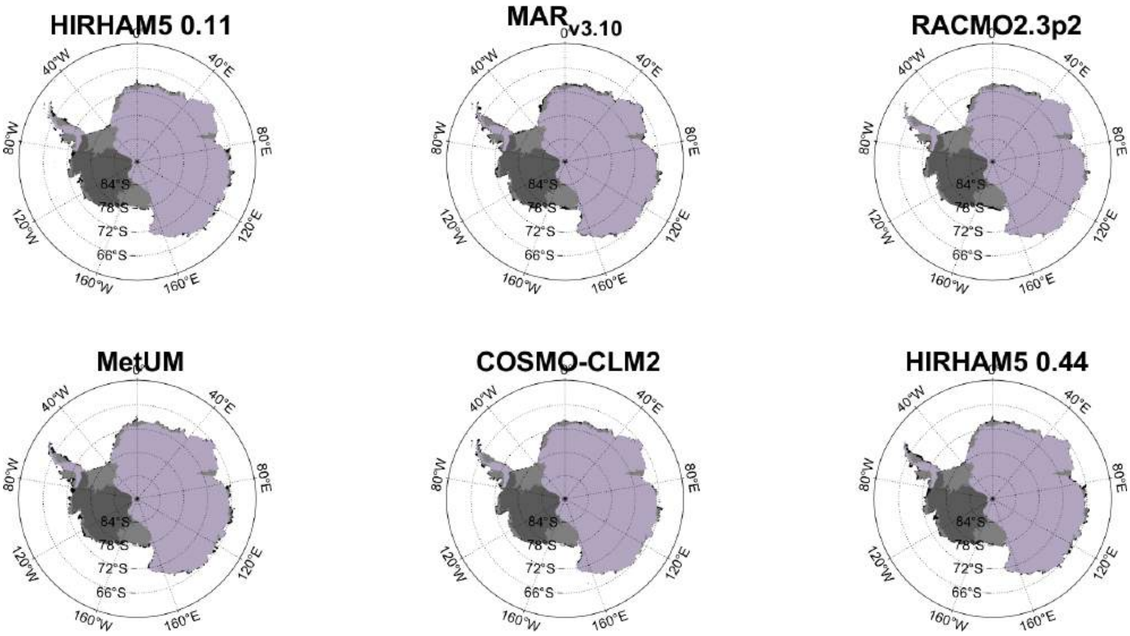

Figure A1. Ice masks used in this study differ for each model, and we therefore define a common mask where all models have ice present in the domain. The sub-figures show where the common mask and the individual model masks are identical; black indicates where individual models have ice that does not occur in the common mask. Most models do not distinguish the physiography between ice shelves and grounded land ice. Overlaid is the regional mask for the grounded ice sheet as calculated by Rignot et al. (2019). Purple shows the grounded ice in the East Antarctic (EAIS) and Antarctic Peninsula (AP) regions; dark grey is the grounded West Antarctic (WAIS) ice sheet. Floating ice shelves within the common mask are shown in light grey.

A2 Comparison with SMB observations

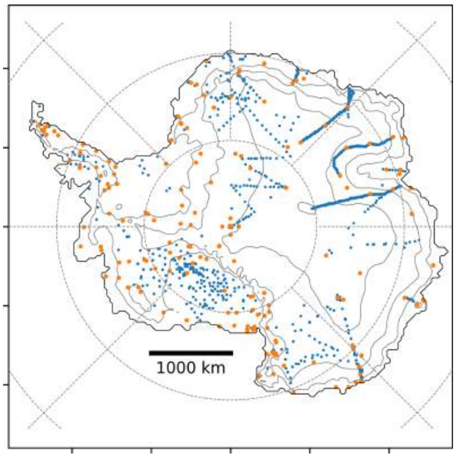

Figure A2. Location of automatic weather stations and SMB observations in Antarctica and used in this study.

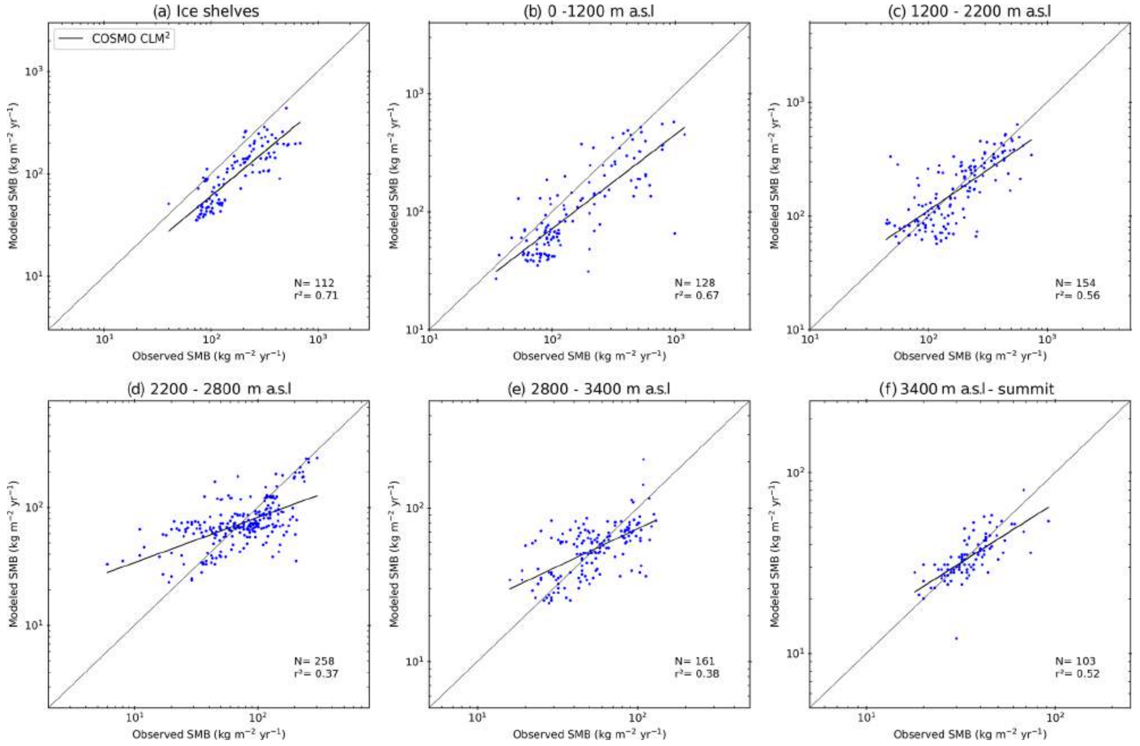

Figure A3. Comparison between COSMO-CLM^2 and observed SMB (units: $\mathrm{kg\,m^{-2}\,yr^{-1}}$) over the ice shelves **(a)** and by elevation classes **(b–f)**. Due to the use of logarithmic axes, only positive values for the observed and modelled SMB from all the RCMs in this study are used (number for each bin N). Finally, the regression coefficient of each regression line is also shown (r^2).

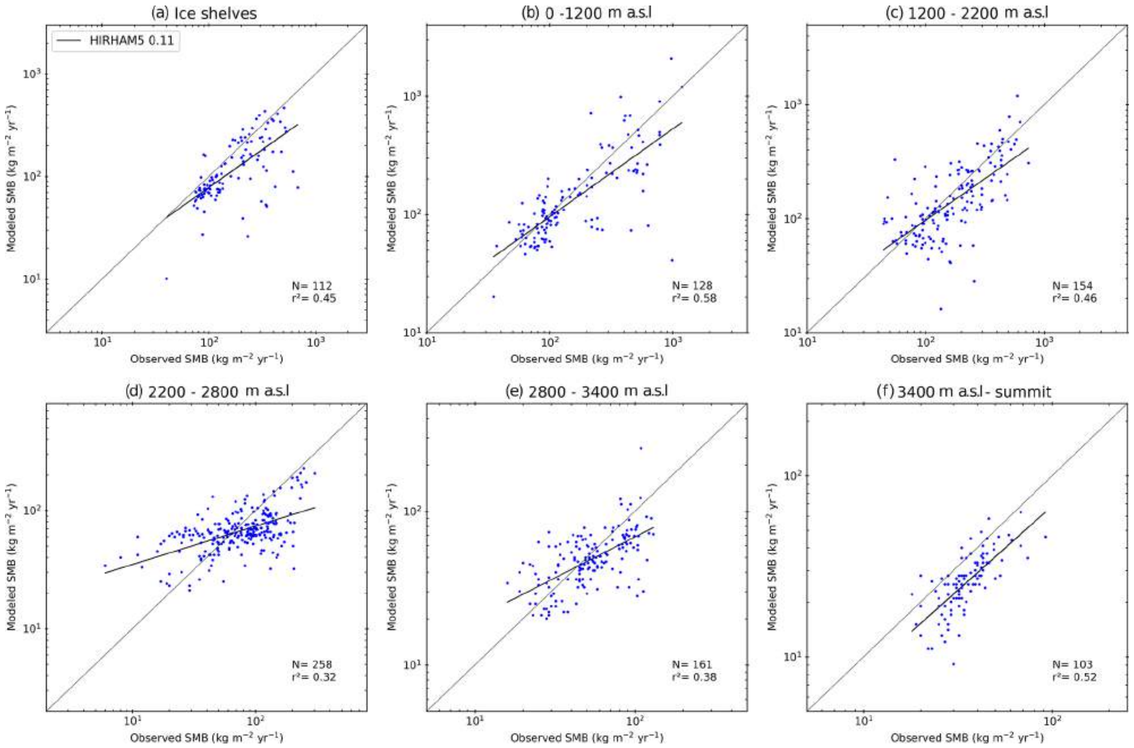

Figure A4. Comparison between HIRHAM5 0.11° and observed SMB (units: $\mathrm{kg\,m^{-2}\,yr^{-1}}$) over the ice shelves **(a)** and by elevation classes **(b–f)**. Due to the use of logarithmic axes, only positive values for the observed and modelled SMB from all the RCMs in this study are used (number for each bin N). Finally, the regression coefficient of each regression line is also shown (r^2).

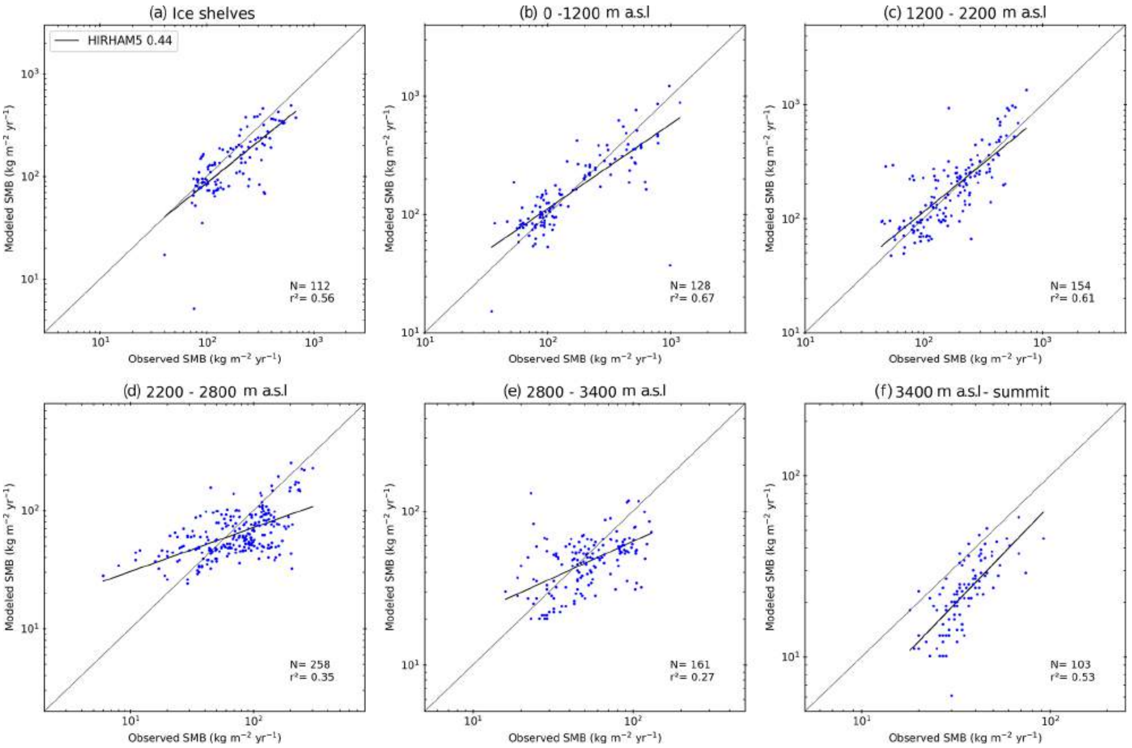

Figure A5. Comparison between HIRHAM5 0.44° and observed SMB (units: kg m^{-2} yr^{-1}) over the ice shelves **(a)** and by elevation classes **(b–f)**. Due to the use of logarithmic axes, only positive values for the observed and modelled SMB from all the RCMs in this study are used (number for each bin N). Finally, the regression coefficient of each regression line is also shown (r^2).

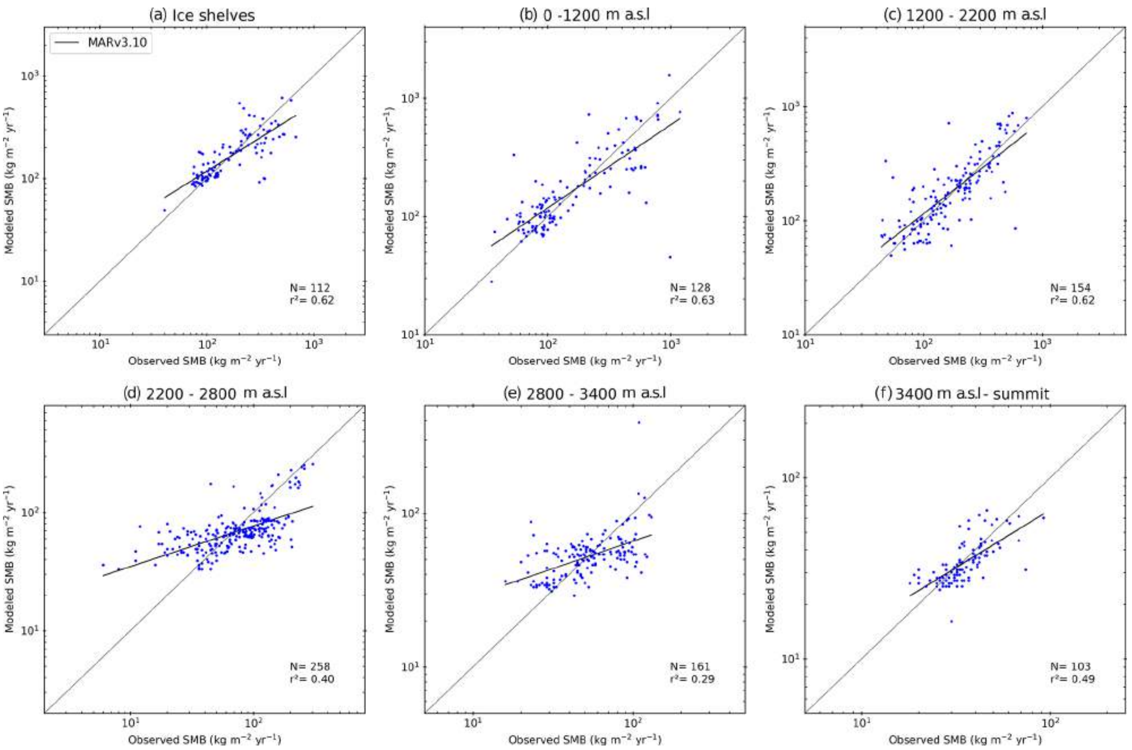

Figure A6. Comparison between $\text{MAR}_{\text{v3.10}}$ and observed SMB (units: $\text{kg m}^{-2}\,\text{yr}^{-1}$) over the ice shelves **(a)** and by elevation classes **(b–f)**. Due to the use of logarithmic axes, only positive values for the observed and modelled SMB from all the RCMs in this study are used (number for each bin N). Finally, the regression coefficient of each regression line is also shown (r^2).

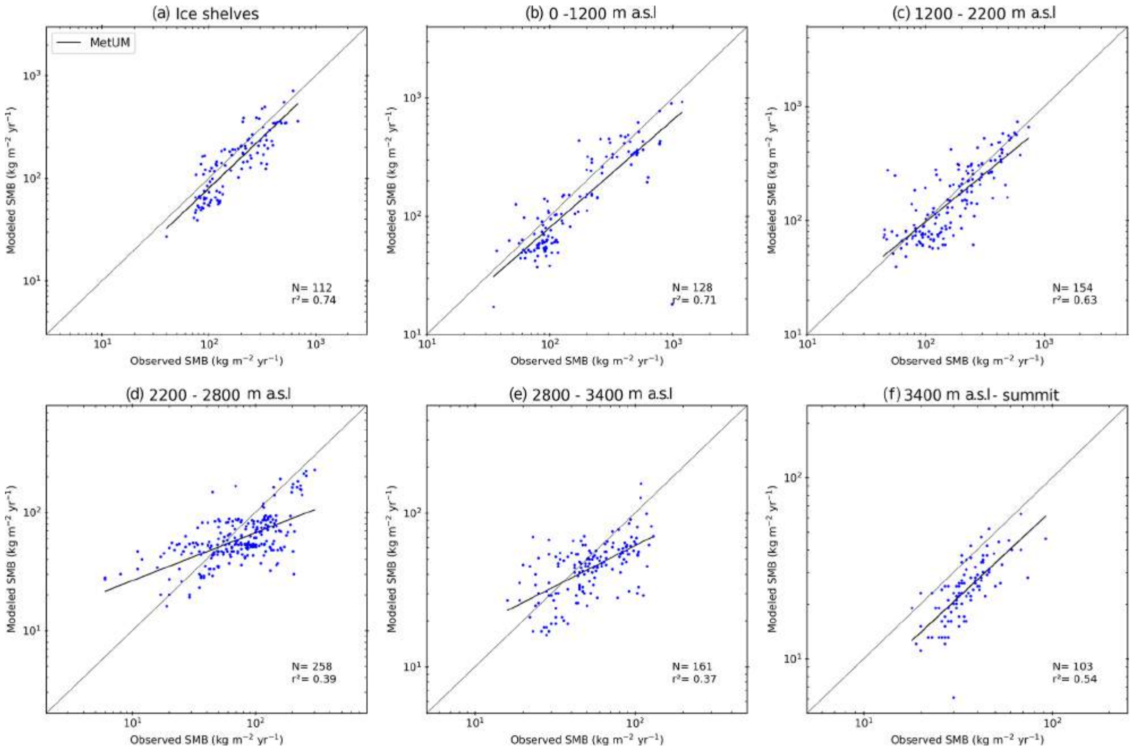

Figure A7. Comparison between MetUM and observed SMB (units: kg m^{-2} yr^{-1}) over the ice shelves **(a)** and by elevation classes **(b–f)**. Due to the use of logarithmic axes, only positive values for the observed and modelled SMB from all the RCMs in this study are used (number for each bin N). Finally, the regression coefficient of each regression line is also shown (r^2).

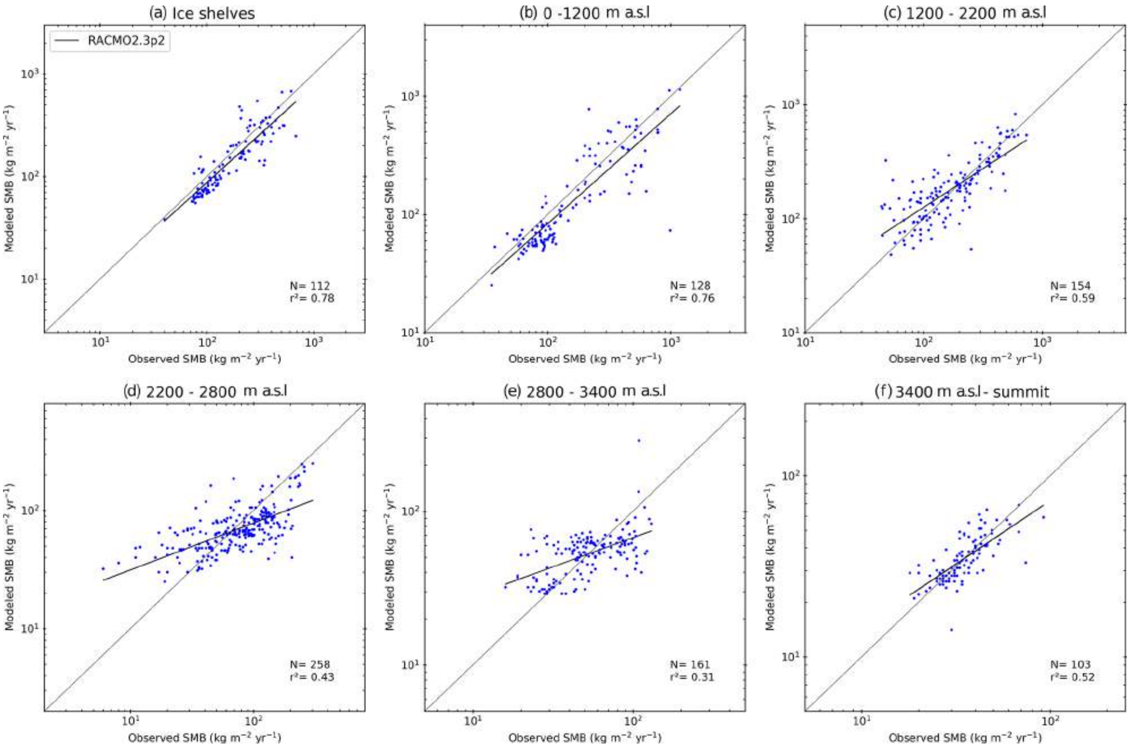

Figure A8. Comparison between RACMO2.3p2 and observed SMB (units: kg m^{-2} yr^{-1}) over the ice shelves **(a)** and by elevation classes **(b–f)**. Due to the use of logarithmic axes, only positive values for the observed and modelled SMB from all the RCMs in this study are used (number for each bin N). Finally, the regression coefficient of each regression line is also shown (r^2).

A3 Mean bias and RMSE

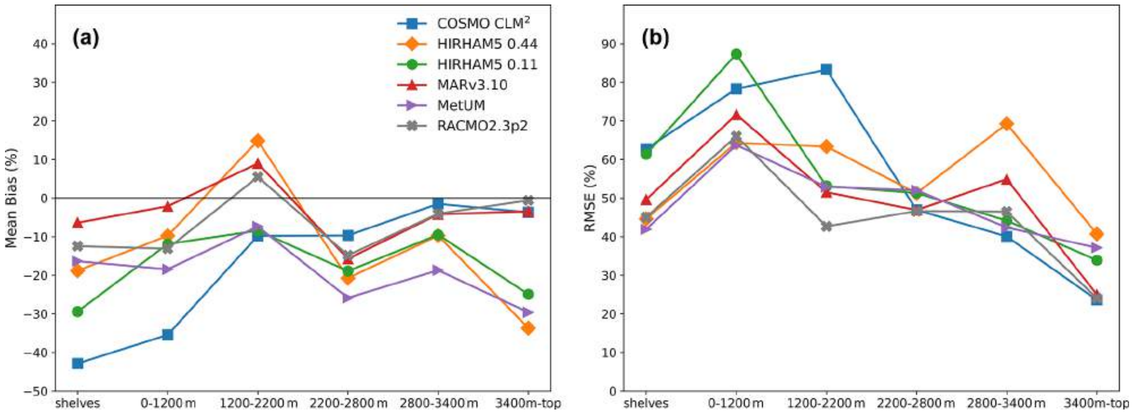

Figure A9. Mean bias and RMSE by elevation bin for each RCM compared to SMB observations as shown in Figs. 3 and 4.

Data availability. Model outputs used in this paper are available to download from the CORDEX archive; see https://www.cordex.org/data-access/how-to-access-the-data/ (CORDEX, 2021) for instructions. In addition The COSMO-CLM^2 monthly output of key variables is open-access and available at https://doi.org/10.5281/zenodo.2539147 (Souverijns, 2019). Output for key variables from the high-resolution HIRHAM5 simulations is available here: http://ensemblesrt3.dmi.dk/data/prudence/temp/RUM/HIRHAM/ANTARCTICA/ERAI/ (Mottram and Boberg, 2021); further data are available on request. MAR3.10 monthly outputs are available here: https://doi.org/10.5281/zenodo.5195636 (Kittel et al., 2020); all other variables are available on request. Modelled SMB for the common period and broken down regionally for all models (see Appendix A1) is open-access and available on Zenodo: https://doi.org/10.5281/zenodo.4590263 (Mottram, 2021).

Author contributions. RM and SBS conceived the study. Analysis of simulations was carried out by CK, JMVW, NH, and RM. Model simulations were carried out by FB, CK, NS, AG, AO, SW, TP, JWVM, and EVM. All authors contributed to the paper.

Competing interests. The authors declare that they have no conflict of interest.

Special issue statement. This article is part of the special issue "The Ice Sheet Model Intercomparison Project for CMIP6 (ISMIP6)". It is not associated with a conference.

Acknowledgements. Acquisition of meteorological data in Adélie Land has been made with the financial and logistical support of the French Polar Institute IPEV (programme CALVA-1013). The authors appreciate the support of the University of Wisconsin-Madison Automatic Weather Station programme for the dataset, data display, and information (NSF grant no. 1924730).

The COSMO-CLM^2 integrations were supported by the Belgian Science Policy Office (BELSPO; grant no. 747 BR/143/A2/AEROCLOUD) and the Research Foundation Flanders (FWO; grant nos. 748 G0C2215N and GOF5318N; EOS ID: 30454083). Computational resources and services were provided by the Flemish Supercomputer Center, funded by the FWO and the Flemish Government, EWI department. Matthias Demuzere, Jan Lenaerts, Irina Gorodetskaya, and Sam Vanden Broucke are gratefully acknowledged for supporting the COSMO-CLM^2 integrations. COSMO-CLM^2 is the community model of the German regional climate research jointly further developed by the CLM community. Computational resources for MAR simulations have been provided by the Consortium des Équipements de Calcul Intensif (CÉCI), funded by the Fonds de la Recherche Scientifique de Belgique (F.R.S. – FNRS) under grant no. 2.5020.11 and the Tier-1 supercomputer (Zenobe) of the Fédération Wallonie Bruxelles infrastructure funded by the Walloon Region under grant agreement no. 1117545. Christoph Kittel's work was supported by the Fonds de la Recherche Scientifique – FNRS under grant no. T.0002.16.

Melchior van Wessen, Willem Jan van de Berg, and Erik van Meijgaard acknowledge the ECMWF for the use of their computing and archive facilities for the RACMO2 simulations.

Ruth Mottram, Nicolaj Hansen, and Sebastian B. Simonsen acknowledge the ESA Climate Change Initiative for the Greenland ice sheet funded via ESA-ESRIN contract no. 4000104815/11/I-NB and the Sea Level Budget Closure CCI project funded via ESA-ESRIN contract no. 4000119910/17/I-NB. HIRHAM5 regional climate model simulations were carried out by Ruth Mottram and Fredrik Boberg as part of the ice2ice project, a European Research Council project under the European Community's Seventh Framework Programme (FP7/ 2007–2013)/ ERC grant agreement 610055. Data analysis was supported by the Danish state through the National Centre for Climate Research (NCKF).

Financial support. This publication was supported by PROTECT. This project has received funding from the European Union's Horizon 2020 research and innovation programme under grant agreement no. 869304 and PROTECT contribution number 19.

Review statement. This paper was edited by Ayako Abe-Ouchi and reviewed by Jan Lenaerts, Masashi Niwano, and one anonymous referee.

References

Agosta, C., Fettweis, X., and Datta, R.: Evaluation of the CMIP5 models in the aim of regional modelling of the Antarctic surface mass balance, The Cryosphere, 9, 2311–2321, https://doi.org/10.5194/tc-9-2311-2015, 2015.

Agosta, C., Amory, C., Kittel, C., Orsi, A., Favier, V., Gallée, H., van den Broeke, M. R., Lenaerts, J. T. M., van Wessem, J. M., van de Berg, W. J., and Fettweis, X.: Estimation of the Antarctic surface mass balance using the regional climate model MAR (1979–2015) and identification of dominant processes, The Cryosphere, 13, 281–296, https://doi.org/10.5194/tc-13-281-2019, 2019.

Akperov, M., Rinke, A., Mokhov, I. I., Matthes, H., Semenov, V. A., Adakudlu, M., Cassano, J., Christensen, J. H., Dembitskaya, M. A., Dethloff, K., Fettweis, X., Glisan, J., Gutjahr, O., Heinemann, G., Koenigk, T., Koldunov, N. V., Laprise, R., Mottram, R., Nikiéma, O., Scinocca, J. F., Sein, D., Sobolowski, S., Winger, K., and Zhang, W.: Cyclone Activity in the Arctic From an Ensemble of Regional Climate Models (Arctic CORDEX), 123, 2537–2554, https://doi.org/10.1002/2017JD027703, 2018.

Alexandru, A., de Elia, R., Laprise, R., Separovic, L., and Biner, S.: Sensitivity Study of Regional Climate Model Simulations to Large-Scale Nudging Parameters, Mon. Weather Rev., 137, 1666–1686, https://doi.org/10.1175/2008MWR2620.1, 2009.

Amory, C.: Drifting-snow statistics from multiple-year autonomous measurements in Adélie Land, East Antarctica, The Cryosphere, 14, 1713–1725, https://doi.org/10.5194/tc-14-1713-2020, 2020.

Andersen, K. K., Ditlevsen, P. D., Rasmussen, S. O., Clausen, H. B., Vinther, B. M., Johnsen, S. J., and Steffensen, J. P.: Retrieving a common accumulation record from Greenland ice cores for the past 1800 years, J. Geophys. Res.-Atmos., 111, D15106, https://doi.org/10.1029/2005JD006765., 2006.

Bamber, J. L.: A digital elevation model of the Antarctic ice sheet derived from ERS-1 altimeter data and comparison with terrestrial measurements, Annals Glaciology, 20, 48–54, 1994.

Bamber, J. L., Gomez-Dans, J. L., and Griggs, J. A.: A new 1 km digital elevation model of the Antarctic derived from combined satellite radar and laser data – Part 1: Data and methods, The Cryosphere, 3, 101–111, https://doi.org/10.5194/tc-3-101-2009, 2009

Barthel, A., Agosta, C., Little, C. M., Hattermann, T., Jourdain, N. C., Goelzer, H., Nowicki, S., Seroussi, H., Straneo, F., and Bracegirdle, T. J.: CMIP5 model selection for ISMIP6 ice sheet model forcing: Greenland and Antarctica, The Cryosphere, 14, 855–879, https://doi.org/10.5194/tc-14-855-2020, 2020.

Berg, P., Döscher, R., and Koenigk, T.: Impacts of using spectral nudging on regional climate model RCA4 simulations of the Arctic, Geosci. Model Dev., 6, 849–859, https://doi.org/10.5194/gmd-6-849-2013, 2013.

Brun, E., David, P., Subul, M., and Brunot, G.: A numerical model to simulate snow-cover stratigraphy for operational avalanche forescating, J. Glaciol., 38, 13–22, 1992.

Christensen, O., Gutowski, W., Nikulin, G., and Legutke, S.: CORDEX Archive design, Danish Meteorological Institute, Copenhagen, Denmark, 2014.

Cogley, J. G., Hock, R., Rasmussen, L. A., Arendt, A. A., Bauder, A., Braithwaite, R. J., Jansson, P., Kaser, G., Möller, M., Nicholson, L., and Zemp, M.: Glossary of Glacier Mass Balance and Related Terms, IHP-VII Technical Documents in Hydrology No. 86, IACS Contribution No. 2, UNESCO-IHP, Paris, France, 114 pp., 2010.

Cook, A. J., Murray, T., Luckman, A., Vaughan, D. G., and Barrand, N. E.: A new 100-m Digital Elevation Model of the Antarctic Peninsula derived from ASTER Global DEM: methods and accuracy assessment, Earth Syst. Sci. Data, 4, 129–142, https://doi.org/10.5194/essd-4-129-2012, 2012a.

Cook, A. J., Murray, T., Luckman, A., Vaughan, D. G., and Barrand, N. E.: Antarctic Peninsula 100 m Digital Elevation Model Derived from ASTER GDEM, Boulder, Colorado, USA, National Snow and Ice Data Center, https://doi.org/10.7265/N58K7711, 2012b.

CORDEX: The World Climate Research Programme Project "Co-Ordinated Regional Downscaling Experiment", available at: https://cordex.org/data-access/how-to-access-the-data/, last access: 1 June 2021.

Cox, P., Betts, R., Bunton, C., Essery, R., Rowntree, P., and Smith, J.: The impact of new land surface physics on the GCM simulation of climate and climate sensitivity, Clim. Dynam., 15, 183–203, 1999.

Das, I., Bell, R. E., Scambos, T. A., Wolovick, M., Creyts, T. T., Studinger, M., Frearson, N., Nicolas, J. P., Lenaerts, J. T., and Van Den Broeke, M. R.: Influence of persistent wind scour on the surface mass balance of Antarctica, Nat. Geosci., 6, 367–371, https://doi.org/10.1038/ngeo1766, 2013

De Ridder, K. and Gallée, H.: Land surface-induce regional climate change in Southern Israel, J. Appl. Meteorol., 37, 1470–1485, 1998.

DeConto, R. and Pollard, D.: Contribution of Antarctica to past and future sea-level rise, Nature, 531, 591–597, https://doi.org/10.1038/nature17145, 2016.

Dee, D. P., Uppala, S. M., Simmons, A. J., Berrisford, P., Poli, P., Kobayashi, S., Andrae, U., Balmaseda, M. A., Balsamo, G., Bauer, P., Bechtold, P., Beljaars, A. C. M., van de Berg, L., Bidlot, J., Bormann, N., Delsol, C., Dragani, R., Fuentes, M., Geer, A. J., Haimberger, L., Healy, S. B., Hersbach, H., Hólm, E. V., Isaksen, L., Kållberg, P., Köhler, M., Matricardi, M., McNally, A. P., Monge-Sanz, B. M., Morcrette, J.-J., Park, B.-K., Peubey, C., de Rosnay, P., Tavolato, C., Thépaut, J.-N., and Vitart, F.: The ERA-Interim reanalysis: configuration and performance of the data assimilation system, Q. J. Roy. Meteor. Soc., 137, 553–597, https://doi.org/10.1002/qj.828, 2011.

Edwards, T. L., Brandon, M. A., Durand, G., Edwards, N. R., Golledge, N. R., Holden, P. B., Nias, I. J., Payne, A. J., Ritz, C., and Wernecke, A.: Revisiting Antarctic ice loss due to marine ice-cliff instability, Nature, 566, 58–64, https://doi.org/10.1038/s41586-019-0901-4, 2019.

Earth Resources Observation and Science Center/U.S. Geological Survey/U.S. Department of the Interior: USGS 30 ARC-second Global Elevation Data, GTOPO30, Research Data Archive at the National Center for Atmospheric Research, Computational and Information Systems Laboratory, https://doi.org/10.5065/A1Z4-EE71, 1997.

Eerola, K.: About the performance of HIRLAM version 7.0, Hirlam Newsletter, 51, 93–102, available at: https://hirlam.org/index.php/hirlam-documentation/doc_view/473-hirlam-newsletter-no-51-article14-eerola-performance-hirlam7-0 (last access: 1 June 2021), 2006.

Ettema, J., van den Broeke, M. R., van Meijgaard, E., and van de Berg, W. J.: Climate of the Greenland ice sheet using a high-resolution climate model – Part 2: Near-surface climate and energy balance, The Cryosphere, 4, 529–544, https://doi.org/10.5194/tc-4-529-2010, 2010.

Favier, V., Agosta, C., Parouty, S., Durand, G., Delaygue, G., Gallée, H., Drouet, A.-S., Trouvilliez, A., and Krinner, G.: An updated and quality controlled surface mass balance dataset for Antarctica, The Cryosphere, 7, 583–597, https://doi.org/10.5194/tc-7-583-2013, 2013.

Fettweis, X., Box, J. E., Agosta, C., Amory, C., Kittel, C., Lang, C., van As, D., Machguth, H., and Gallée, H.: Reconstructions of the 1900–2015 Greenland ice sheet surface mass balance using the regional climate MAR model, The Cryosphere, 11, 1015–1033, https://doi.org/10.5194/tc-11-1015-2017, 2017.

Forbes, R., Tompkins, A., and Ungatch, A.: A new prognostic bulk microphysics scheme for the IFS, Technical Memorandum 649, ECMWF, available at: http://www.ecmwf.int/sites/default/files/elibrary/2011/9441-new-prognostic-bulk-microphysics-scheme-ifs.pdf (last access: 1 June 2021), 2011.

Franco, B., Fettweis, X., Lang, C., and Erpicum, M.: Impact of spatial resolution on the modelling of the Greenland ice sheet surface mass balance between 1990–2010, using the regional climate model MAR, The Cryosphere, 6, 695–711, https://doi.org/10.5194/tc-6-695-2012, 2012.

Fretwell, P., Pritchard, H. D., Vaughan, D. G., Bamber, J. L., Barrand, N. E., Bell, R., Bianchi, C., Bingham, R. G., Blankenship, D. D., Casassa, G., Catania, G., Callens, D., Conway, H., Cook, A. J., Corr, H. F. J., Damaske, D., Damm, V., Ferraccioli, F., Forsberg, R., Fujita, S., Gim, Y., Gogineni, P., Griggs,

J. A., Hindmarsh, R. C. A., Holmlund, P., Holt, J. W., Jacobel, R. W., Jenkins, A., Jokat, W., Jordan, T., King, E. C., Kohler, J., Krabill, W., Riger-Kusk, M., Langley, K. A., Leitchenkov, G., Leuschen, C., Luyendyk, B. P., Matsuoka, K., Mouginot, J., Nitsche, F. O., Nogi, Y., Nost, O. A., Popov, S. V., Rignot, E., Rippin, D. M., Rivera, A., Roberts, J., Ross, N., Siegert, M. J., Smith, A. M., Steinhage, D., Studinger, M., Sun, B., Tinto, B. K., Welch, B. C., Wilson, D., Young, D. A., Xiangbin, C., and Zirizzotti, A.: Bedmap2: improved ice bed, surface and thickness datasets for Antarctica, The Cryosphere, 7, 375–393, https://doi.org/10.5194/tc-7-375-2013, 2013.

Gallée, H. and Schayes, G.: Development of a Three-Dimensional Meso-γ Primitive Equation Model: Katabatic Winds Simulation in the Area of Terra Nova Bay, Antarctica, Mon. Weather Rev., 122, 671–685, https://doi.org/10.1175/1520-0493(1994)122<0671:DOATDM>2.0.CO;2, 1994.

GLOBE Task Team and others (Hastings, D. A., Dunbar, P. K., Elphingstone, G. M., Bootz, M., Murakami, H., Maruyama, H., Masaharu, H., Holland, P., Payne, J., Bryant, N. A., Logan, T. L., Muller, J.-P., Schreier, G., and MacDonald, J. S.), eds.: The Global Land One-kilometer Base Elevation (GLOBE) Digital Elevation Model, Version 1.0, National Oceanic and Atmospheric Administration, National Geophysical Data Center, 325 Broadway, Boulder, Colorado 80305-3328, USA, Digital data base on the World Wide Web, available at: http://www.ngdc.noaa.gov/mgg/topo/globe.html (last access: 1 June 2021) and CD-ROMs, 1999.

Hansen, N.: Modelling the present day and future climate of Antarctica, Master's thesis, The Technical University of Denmark, Anker Engelunds Vej 1 Bygning 101A 2800 Kgs. Lyngby, Denmark, 2019.

Hermann, M., Box, J. E., Fausto, R. S., Colgan, W. T., Langen, P. L., Mottram, R., Wuite, J., Noël, B., van den Broeke, M. R., and van As, D.: Application of PROMICE Q-Transect in Situ Accumulation and Ablation Measurements (2000–2017) to Constrain Mass Balance at the Southern Tip of the Greenland Ice Sheet, J. Geophys. Res.-Earth, 123, 1235–1256, https://doi.org/10.1029/2017JF004408, 2018.

Kittel, C., Amory, C., Agosta, C., Delhasse, A., Doutreloup, S., Huot, P.-V., Wyard, C., Fichefet, T., and Fettweis, X.: Sensitivity of the current Antarctic surface mass balance to sea surface conditions using MAR, The Cryosphere, 12, 3827–3839, https://doi.org/10.5194/tc-12-3827-2018, 2018.

Kittel, C., Amory, C., Agosta, C., and Fettweis, X.: MARv3.10 outputs: What is the Surface Mass Balance of Antarctica? An Intercomparison of Regional Climate Model Estimates [data set], Zenodo, https://doi.org/10.5281/zenodo.5195636, 2020.

Kittel, C.: Present and future sensitivity of the Antarctic surface mass balance to oceanic and atmospheric forcings: insights with the regional climate model MAR, PhD thesis, Université de Liège, Liège, Belgique, available at: https://orbi.uliege.be/handle/2268/258491, last access: 1 June 2021.

Krinner, G., Guicherd, B., Ox, K., Genthon, C., and Magand, O.: Influence of oceanic boundary conditions in simulations of Antarctic climate and surface mass balance change during the coming century, J. Climate, 21, 938–962, 2008.

Kuipers Munneke, P., Van den Broeke, M., Lenaerts, J., Flanner, M., Gardner, A., and Van de Berg, W.: A new albedo parameterization for use in climate models over the Antarctic ice sheet, J. Geophys. Res.-Atmos., 116, D05114, https://doi.org/10.1029/2010JD015113, 2011.

Langen, P. L., Fausto, R. S., Vandecrux, B., Mottram, R. H., and Box, J. E.: Liquid water flow and retention on the Greenland ice sheet in the regional climate model HIRHAM5: Local and large-scale impacts, Front. Earth Sci., 4, 110, https://doi.org/10.3389/feart.2016.00110, 2017.

Lenaerts, J. T., Van den Broeke, M., Déry, S., Van Meijgaard, E., Van de Berg, W., Palm, S. P., and Sanz Rodrigo, J.: Modeling drifting snow in Antarctica with a regional climate model: 1. Methods and model evaluation, J. Geophys. Res.-Atmos., 117, D05108, https://doi.org/10.1029/2011JD016145, 2012a.

Lenaerts, J. T., Van Den Broeke, M. R., Scarchilli, C., and Agosta, C.: Impact of model resolution on simulated wind, drifting snow and surface mass balance in Terre Adélie, East Antarctica, J. Glaciol., 58, 821–829, 2012b.

Lenaerts, J. T., Vizcaino, M., Fyke, J., Van Kampenhout, L., and van den Broeke, M. R.: Present-day and future Antarctic ice sheet climate and surface mass balance in the Community Earth System Model, Clim. Dynam., 47, 1367–1381, 2016.

Lenaerts, J. T., Medley, B., van den Broeke, M. R., and Wouters, B.: Observing and Modeling Ice-Sheet Surface Mass Balance, Rev. Geophys., 376–420, https://doi.org/10.1029/2018RG000622, 2019.

Ligtenberg, S. R. M., Helsen, M. M., and van den Broeke, M. R.: An improved semi-empirical model for the densification of Antarctic firn, The Cryosphere, 5, 809–819, https://doi.org/10.5194/tc-5-809-2011, 2011.

Liu, H., Jezek, K. C., Li, B., and Zhao, Z.: Radarsat Antarctic Mapping Project Digital Elevation Model, Version 2, Boulder, Colorado USA, NASA National Snow and Ice Data Center Distributed Active Archive Center, https://doi.org/10.5067/8JKNEW6BFRVD, 2015.

Lucas-Picher, P., Wulff-Nielsen, M., Christensen, J. H., Aðalgeirsdóttir, G., Mottram, R., and Simonsen, S. B.: Very high resolution regional climate model simulations over Greenland: Identifying added value, J. Geophys. Res.-Atmos., 117, https://doi.org/10.1029/2011JD016267, 2012.

Medley, B., Joughin, I., Smith, B. E., Das, S. B., Steig, E. J., Conway, H., Gogineni, S., Lewis, C., Criscitiello, A. S., McConnell, J. R., van den Broeke, M. R., Lenaerts, J. T. M., Bromwich, D. H., Nicolas, J. P., and Leuschen, C.: Constraining the recent mass balance of Pine Island and Thwaites glaciers, West Antarctica, with airborne observations of snow accumulation, The Cryosphere, 8, 1375–1392, https://doi.org/10.5194/tc-8-1375-2014, 2014.

Mikkelsen, T. B., Grinsted, A., and Ditlevsen, P.: Influence of temperature fluctuations on equilibrium ice sheet volume, The Cryosphere, 12, 39–47, https://doi.org/10.5194/tc-12-39-2018, 2018.

Mottram, R.: Regional Surface Mass Balance of Antarctica (1981–2016) estimated from five high resolution Regional Climate Models (Version 1.0) [Data set], Zenodo, https://doi.org/10.5281/zenodo.4590263, 2021.

Mottram, R. and Boberg, F.: Atmospheric climate model output from the regional climate model HIRHAM5 forced with ERA-Interim for Antarctica, available at: http://ensemblesrt3.dmi.dk/data/prudence/temp/RUM/HIRHAM/ANTARCTICA/ERAI/, last access: 1 June 2021.

Nowicki, S. M. J., Payne, A., Larour, E., Seroussi, H., Goelzer, H., Lipscomb, W., Gregory, J., Abe-Ouchi, A., and Shepherd, A.: Ice Sheet Model Intercomparison Project (ISMIP6) contribution to CMIP6, Geosci. Model Dev., 9, 4521–4545, https://doi.org/10.5194/gmd-9-4521-2016, 2016.

Oleson, K. W. and Lawrence, D. M.: Technical description of version 4.5 of the Community Land Model (CLM), Tech. Rep. July, NCAR, Boulder, Colorado, https://doi.org/10.5065/D6RR1W7M, 2013.

Oppenheimer, M., Glavovic, B. C., Hinkel, J., van de Wal, R., Magnan, A. K., Abd-Elgawad, A., Cai, R., Cifuentes-Jara, M., DeConto, R. M., Ghosh, T., Hay, J., Isla, F., Marzeion, B., Meyssignac, B., and Sebesvari, Z.: Sea Level Rise and Implications for Low-Lying Islands, Coasts and Communities, in: IPCC Special Report on the Ocean and Cryosphere in a Changing Climate, edited by: Pörtner, H.-O., Roberts, D. C., Masson-Delmotte, V., Zhai, P., Tignor, M., Poloczanska, E., Mintenbeck, K., Alegri´a, A., Nicolai, M., Okem, A., Petzold, J., Rama, B., and Weyer, N. M., Cambridge University Press, Cambridge, UK, 126 pp., 2019.

Orr, A., Hosking, J. S., Hoffmann, L., Keeble, J., Dean, S. M., Roscoe, H. K., Abraham, N. L., Vosper, S., and Braesicke, P.: Inclusion of mountain-wave-induced cooling for the formation of PSCs over the Antarctic Peninsula in a chemistry–climate model, Atmos. Chem. Phys., 15, 1071–1086, https://doi.org/10.5194/acp-15-1071-2015, 2015.

Rignot, E., Velicogna, I., van den Broeke, M. R., Monaghan, A., and Lenaerts, J. T.: Acceleration of the contribution of the Greenland and Antarctic ice sheets to sea level rise, Geophys. Res. Lett., 38, https://doi.org/10.1029/2011GL046583, 2011.

Rignot, E., Mouginot, J., Scheuchl, B., Broeke, M. v. d., Wessem, M. J. v., and Morlighem, M.: Four decades of Antarctic Ice Sheet mass balance from 1979–2017, P. Natl. Acad. Sci. USA, 116, 1095–1103, https://doi.org/10.1073/pnas.1812883116, 2019.

Robel, A. A., Seroussi, H., and Roe, G. H.: Marine ice sheet instability amplifies and skews uncertainty in projections of future sea-level rise, P. Natl. Acad. Sci. USA, 116, 14887–14892, 2019.

Rockel, B., Will, A., and Hense, A.: The Regional Climate Model COSMO-CLM (CCLM), Meteorologische Zeitschrift, 17, 347–348, https://doi.org/10.1127/0941-2948/2008/0309, 2008.

Roeckner, E., Bäuml, G., Bonaventura, L., Brokopf, R., Esch, M., Giorgetta, M., Hagemann, S., Kirchner, I., Kornblueh, L., Manzini, E., Rhodin, A., Schlese, U., Schulzweida, U., and Tompkins, A: The atmospheric general circulation model ECHAM 5. PART I: Model description, Max Planck Institute, Hamburg, Germany, 2003.

Scambos, T. and Shuman, C.: Comment on "Mass gains of the Antarctic ice sheet exceed losses" by Zwally, H. J. and others, J. Glaciol., 62, 599–603, https://doi.org/10.1017/jog.2016.59, 2016.

Scambos, T., Frezzotti, M., Haran, T., Bohlander, J., Lenaerts, J., van Den Broeke, M., Jezek, K., Long, D., Urbini, S., Farness, K., Neumann, T., Albert, M., and Winther, J.: Extent of low-accumulation "wind glaze" areas on the East Antarctic plateau: implications for continental ice mass balance, J. Glaciol., 58, 633–647, https://doi.org/10.3189/2012JoG11J232, 2012.

Schmidt, L. S., Aðalgeirsdóttir, G., Guðmundsson, S., Langen, P. L., Pálsson, F., Mottram, R., Gascoin, S., and Björnsson, H.: The importance of accurate glacier albedo for estimates of surface mass balance on Vatnajökull: evaluating the surface energy budget in a regional climate model with automatic weather station observations, The Cryosphere, 11, 1665–1684, https://doi.org/10.5194/tc-11-1665-2017, 2017.

Sedlar, J., Tjernström, M., Mauritsen, T., Shupe, M. D., Brooks, I. M., Persson, P. O. G., Birch, C. E., Leck, C., Sirevaag, A., and Nicolaus, M.: A transitioning Arctic surface energy budget: the impacts of solar zenith angle, surface albedo and cloud radiative forcing, Clim. Dynam., 37, 1643–1660, 2011.

Shepherd, A., Fricker, H. A., and Farrell, S. L.: Trends and connections across the Antarctic cryosphere, Nature, 558, 223–232, https://doi.org/10.1038/s41586-018-0171-6, 2018.

Shepherd, A., Ivins, E., Rignot, E., Smith, B., van den Broeke, M., Velicogna, I., Whitehouse, P., Briggs, K., Joughin, I., Krinner, G., Nowicki, S., Payne, T., Scambos, T., Schlegel, N., A, G., Agosta, C., Ahlstrøm, A., Babonis, G., Barletta, V. R., Bjørk, A. A., Blazquez, A., Bonin, J., Colgan, W., Csatho, B., Cullather, R., Engdahl, M. E., Felikson, D., Fettweis, X., Forsberg, R., Hogg, A. E., Gallee, H., Gardner, A., Gilbert, L., Gourmelen, N., Groh, A., Gunter, B., Hanna, E., Harig, C., Helm, V., Horvath, A., Horwath, M., Khan, S., Kjeldsen, K. K., Konrad, H., Langen, P. L., Lecavalier, B., Loomis, B., Luthcke, S., McMillan, M., Melini, D., Mernild, S., Mohajerani, Y., Moore, P., Mottram, R., Mouginot, J., Moyano, G., Muir, A., Nagler, T., Nield, G., Nilsson, J., Noël, B., Otosaka, I., Pattle, M. E., Peltier, W. R., Pie, N., Rietbroek, R., Rott, H., Sandberg Sørensen, L., Sasgen, I., Save, H., Scheuchl, B., Schrama, E., Schröder, L., Seo, K.-W., Simonsen, S. B., Slater, T., Spada, G., Sutterley, T., Talpe, M., Tarasov, L., van de Berg, W. J., van der Wal, W., van Wessem, M., Vishwakarma, B. D., Wiese, D., Wilton, D., Wagner, T., Wouters, B., Wuite, J., and The IMBIE Team: Mass balance of the Greenland Ice Sheet from 1992 to 2018, Nature, 579, 233–239, https://doi.org/10.1038/s41586-019-1855-2, 2020.

Shepherd, A., Gilbert, L., Muir, A. S., Konrad, H., McMillan, M., Slater, T., Briggs, K. H., Sundal, A. V., Hogg, A. E., and Engdahl, M.: Trends in Antarctic Ice Sheet Elevation and Mass, Geophys. Res. Lett., 46, 8174–8183, https://doi.org/10.1029/2019GL082182, 2019.

Souverijns, N., Gossart, A., Demuzere, M., Lenaerts, J. T. M., Medley, B., Gorodetskaya, I. V., Vanden Broucke, S., and van Lipzig, N. P. M.: A New Regional Climate Model for POLAR-CORDEX: Evaluation of a 30-Year Hindcast with COSMO-CLM2 Over Antarctica, J. Geophys. Res.-Atmos., 124, 1405–1427, https://doi.org/10.1029/2018JD028862, 2019.

Souverijns, N., Gossart, A., Demuzere, M., Lenaerts, J. T. M., Medley, B., Gorodetskaya, I. V., Vanden Broucke, S., and van Lipzig, N. P. M.: Atmospheric climate model output of the COSMO-CLM2 regional climate model hindcast run over Antarctica (1987–2016) (Version COSMO-CLM version 5.0_clm6 – Community Land Model version 4.5), Data set, Zenodo, https://doi.org/10.5281/zenodo.2539147, 2019.

Stokes, C. R., Sanderson, J. E., Miles, B. W., Jamieson, S. S., and Leeson, A. A.: Widespread distribution of supraglacial lakes around the margin of the East Antarctic Ice Sheet, Sci. Rep., 9, 1–14, 2019.

Sutter, J., Gierz, P., Grosfeld, K., Thoma, M., and Lohmann, G.: Ocean temperature thresholds for Last Interglacial West Antarctic Ice Sheet collapse, Geophys. Res. Lett., 43, 2675–2682, 2016.

Thomas, E. R., van Wessem, J. M., Roberts, J., Isaksson, E., Schlosser, E., Fudge, T. J., Vallelonga, P., Medley, B., Lenaerts, J., Bertler, N., van den Broeke, M. R., Dixon, D. A., Frezzotti, M., Stenni, B., Curran, M., and Ekaykin, A. A.: Regional Antarctic snow accumulation over the past 1000 years, Clim. Past, 13, 1491–1513, https://doi.org/10.5194/cp-13-1491-2017, 2017.

Trusel, L. D., Das, S. B., Osman, M. B., Evans, M. J., Smith, B. E., Fettweis, X., McConnell, J. R., Noël, B. P., and van den Broeke, M. R.: Nonlinear rise in Greenland runoff in response to post-industrial Arctic warming, Nature, 564, 104–108, https://doi.org/10.1038/s41586-018-0752-4, 2018.

Turner, J., Colwell, S. R., Marshall, G. J., Lachlan-Cope, T. A., Carleton, A. M., Jones, P. D., Lagun, V., Reid, P. A., and Iagovkina, S.: The SCAR READER project: toward a high-quality database of mean Antarctic meteorological observations, J. Climate, 17, 2890–2898, 2004.

Undén, P., Rontu, L., Järvinen, H., Lynch, P., Calvo, J., Cats, G., Cuxart, J., Eerola, K., Fortelius, C., Garcia-Moya, J.-A., Jones, C., Lenderlink, G., McDonald, A., McGrath, R., Navascués, B., Nielsen, N.-W., Odegaard, V., Rodríguez, E., Rummukainen, M., Rõõm, R., Sattler, K., Sass, B.-H., Savijärvi, H., Schreur, B.-W., Sigg, R., The, H., and Tijm, A.: HIRLAM-5 Scientific Documentation, available at: http://hirlam.org/index.php/hirlam-documentation/doc_download/308-unden-et-al-2002 (last access: 1 June 2021), 2002

van de Berg, W. J. and Medley, B.: Brief Communication: Upper-air relaxation in RACMO2 significantly improves modelled interannual surface mass balance variability in Antarctica, The Cryosphere, 10, 459–463, https://doi.org/10.5194/tc-10-459-2016, 2016.

van Kampenhout, L., Lenaerts, J. T. M., Lipscomb, W. H., Sacks, W. J., Lawrence, D. M., Slater, A. G., and van den Broeke, M. R.: Improving the Representation of Polar Snow and Firn in the Community Earth System Model, J. Adv. Model. Earth Syst., 9, 2583–2600, https://doi.org/10.1002/2017MS000988, 2017.

van Wessem, J. M., Reijmer, C. H., Morlighem, M., Mouginot, J., Rignot, E., Medley, B., Joughin, I., Wouters, B., Depoorter, M. A., Bamber, J. L., Lenaerts, J. T. M., De Van Berg, W. J., Van Den Broeke, M. R., and Van Meijgaard, E.: Improved representation of East Antarctic surface mass balance in a regional atmospheric climate model, J. Glaciol., 60, 761–770, https://doi.org/10.3189/2014JoG14J051, 2014.

van Wessem, J. M., Reijmer, C. H., Lenaerts, J. T. M., van de Berg, W. J., van den Broeke, M. R., and van Meijgaard, E.: Updated cloud physics in a regional atmospheric climate model improves the modelled surface energy balance of Antarctica, The Cryosphere, 8, 125–135, https://doi.org/10.5194/tc-8-125-2014, 2014.

van Wessem, J. M., van de Berg, W. J., Noël, B. P. Y., van Meijgaard, E., Amory, C., Birnbaum, G., Jakobs, C. L., Krüger, K., Lenaerts, J. T. M., Lhermitte, S., Ligtenberg, S. R. M., Medley, B., Reijmer, C. H., van Tricht, K., Trusel, L. D., van Ulft, L. H., Wouters, B., Wuite, J., and van den Broeke, M. R.: Modelling the climate and surface mass balance of polar ice sheets using RACMO2 – Part 2: Antarctica (1979–2016), The Cryosphere, 12, 1479–1498, https://doi.org/10.5194/tc-12-1479-2018, 2018.

Vernon, C. L., Bamber, J. L., Box, J. E., van den Broeke, M. R., Fettweis, X., Hanna, E., and Huybrechts, P.: Surface mass balance model intercomparison for the Greenland ice sheet, The Cryosphere, 7, 599–614, https://doi.org/10.5194/tc-7-599-2013, 2013.

von Storch, H., Langenberg, H., and Feser, F.: A Spectral Nudging Technique for Dynamical Downscaling Purposes, Mon. Weather Rev., 128, 3664–3673, https://doi.org/10.1175/1520-0493(2000)128<3664:ASNTFD>2.0.CO;2, 2000.

Walters, D., Boutle, I., Brooks, M., Melvin, T., Stratton, R., Vosper, S., Wells, H., Williams, K., Wood, N., Allen, T., Bushell, A., Copsey, D., Earnshaw, P., Edwards, J., Gross, M., Hardiman, S., Harris, C., Heming, J., Klingaman, N., Levine, R., Manners, J., Martin, G., Milton, S., Mittermaier, M., Morcrette, C., Riddick, T., Roberts, M., Sanchez, C., Selwood, P., Stirling, A., Smith, C., Suri, D., Tennant, W., Vidale, P. L., Wilkinson, J., Willett, M., Woolnough, S., and Xavier, P.: The Met Office Unified Model Global Atmosphere 6.0/6.1 and JULES Global Land 6.0/6.1 configurations, Geosci. Model Dev., 10, 1487–1520, https://doi.org/10.5194/gmd-10-1487-2017, 2017.

Walters, D., Baran, A. J., Boutle, I., Brooks, M., Earnshaw, P., Edwards, J., Furtado, K., Hill, P., Lock, A., Manners, J., Morcrette, C., Mulcahy, J., Sanchez, C., Smith, C., Stratton, R., Tennant, W., Tomassini, L., Van Weverberg, K., Vosper, S., Willett, M., Browse, J., Bushell, A., Carslaw, K., Dalvi, M., Essery, R., Gedney, N., Hardiman, S., Johnson, B., Johnson, C., Jones, A., Jones, C., Mann, G., Milton, S., Rumbold, H., Sellar, A., Ujiie, M., Whitall, M., Williams, K., and Zerroukat, M.: The Met Office Unified Model Global Atmosphere 7.0/7.1 and JULES Global Land 7.0 configurations, Geosci. Model Dev., 12, 1909–1963, https://doi.org/10.5194/gmd-12-1909-2019, 2019.

Wang, Y., Ding, M., van Wessem, J. M., Schlosser, E., Altnau, S., van den Broeke, M. R., Lenaerts, J. T., Thomas, E. R., Isaksson, E., Wang, J., and Sun, W: A comparison of Antarctic Ice Sheet surface mass balance from atmospheric climate models and in situ observations, J. Climate, 29, 5317–5337, https://doi.org/10.1175/JCLI-D-15-0642.1, 2016.

Zentek, R. and Heinemann, G.: Verification of the regional atmospheric model CCLM v5.0 with conventional data and lidar measurements in Antarctica, Geosci. Model Dev., 13, 1809–1825, https://doi.org/10.5194/gmd-13-1809-2020, 2020.

Zwally, H. J., Li, J., Robbins, J. W., Saba, J. L., Yi, D., and Brenner, A. C.: Mass gains of the Antarctic ice sheet exceed losses, J. Glaciol., 61, 1019–1036, https://doi.org/10.3189/2015JoG15J071, 2015.

A.2 Paper II

The Cryosphere, 15, 4315–4333, 2021
https://doi.org/10.5194/tc-15-4315-2021

The Cryosphere
Open Access

Downscaled surface mass balance in Antarctica: impacts of subsurface processes and large-scale atmospheric circulation

Nicolaj Hansen[1,2], Peter L. Langen[a], Fredrik Boberg[1], Rene Forsberg[2], Sebastian B. Simonsen[2], Peter Thejll[1], Baptiste Vandecrux[3], and Ruth Mottram[1]

[1]DMI, Lyngbyvej 100, Copenhagen, 2100, Denmark
[2]DTU-Space, Kongens Lyngby, Denmark
[3]Geological Survey of Denmark and Greenland, Copenhagen, Denmark
[a]now at: iClimate, Department of Environmental Science, Aarhus University, Roskilde, Denmark

Correspondence: Nicolaj Hansen (nichsen@space.dtu.dk)

Received: 24 February 2021 – Discussion started: 17 March 2021
Revised: 9 August 2021 – Accepted: 16 August 2021 – Published: 8 September 2021

Abstract. Antarctic surface mass balance (SMB) is largely determined by precipitation over the continent and subject to regional climate variability related to the Southern Annular Mode (SAM) and other climatic drivers at the large scale. Locally however, firn and snowpack processes are important in determining SMB and the total mass balance of Antarctica and global sea level. Here, we examine factors that influence Antarctic SMB and attempt to reconcile the outcome with estimates for total mass balance determined from the GRACE satellites. This is done by having the regional climate model HIRHAM5 forcing two versions of an offline subsurface model, to estimate Antarctic ice sheet (AIS) SMB from 1980 to 2017. The Lagrangian subsurface model estimates Antarctic SMB of $2473.5 \pm 114.4\,\mathrm{Gt\,yr^{-1}}$, while the Eulerian subsurface model variant results in slightly higher modelled SMB of $2564.8 \pm 113.7\,\mathrm{Gt\,yr^{-1}}$. The majority of this difference in modelled SMB is due to melt and refreezing over ice shelves and demonstrates the importance of firn modelling in areas with substantial melt. Both the Eulerian and the Lagrangian SMB estimates are within uncertainty ranges of each other and within the range of other SMB studies. However, the Lagrangian version has better statistics when modelling the densities. Further, analysis of the relationship between SMB in individual drainage basins and the SAM is carried out using a bootstrapping approach. This shows a robust relationship between SAM and SMB in half of the basins (13 out of 27). In general, when SAM is positive there is a lower SMB over the plateau and a higher SMB on the westerly side of the Antarctic Peninsula, and vice versa when the SAM is negative. Finally, we compare the modelled SMB to GRACE data by subtracting the solid ice discharge, and we find that there is a good agreement in East Antarctica but large disagreements over the Antarctic Peninsula. There is a large difference between published estimates of discharge that make it challenging to use mass reconciliation in evaluating SMB models on the basin scale.

1 Introduction

The Antarctic Ice Sheet (AIS) has the potential to raise global sea level by 58 m (Fretwell et al., 2013) and it is therefore of utmost importance to understand its role in present sea level change in order to project it into the future. At present the AIS contributes $0.3 \pm 0.16\,\mathrm{mm\,yr^{-1}}$ to sea level rise based on the average ice mass loss of $109 \pm 56\,\mathrm{Gt\,yr^{-1}}$ between 1992 and 2017 (Shepherd et al., 2018). An accelerating mass loss has been observed in West Antarctica and over the Antarctic Peninsula (AP) in the last 4 decades (Forsberg et al., 2017; Rignot et al., 2019). In the light of this acceleration, climatic changes are of particular interest due to their role in inducing ice sheet dynamic instability, by changing the mass influx to the ice sheet. The ice sheet mass balance (MB) can be split into atmospheric and ice dynamic components:

$$\mathrm{MB} = \mathrm{SMB} - D, \tag{1}$$

where D is the solid ice discharge in the form of iceberg calving, and SMB is the surface mass balance composed of pre-

Published by Copernicus Publications on behalf of the European Geosciences Union.

cipitation (P, snowfall and rain), sublimation and evaporation (S) from the surface, runoff (RO) of meltwater, and erosion of blowing snow. However, blowing snow is not taken into consideration in this study, so the SMB is defined here as $\mathrm{SMB} = P - S - \mathrm{RO}$. Of these components, precipitation is by far the largest contributor (Krinner et al., 2007) and consists primarily of snow at higher altitudes. Melt and runoff of surface melt are largely confined to ice shelves and elevations less than 1400 m a.m.s.l. (above mean sea level) (Bell et al., 2018). Sublimation and evaporation are however important across most of the continent due to low humidity and high wind speeds (Palm et al., 2017). If $\mathrm{SMB} < D$, the total mass balance is negative and the ice sheet loses mass and thereby contributes to global sea level rise. Here we focus on the SMB component of the mass balance, to pinpoint the immediate forcing to ice sheet dynamic instability. To estimate the SMB, we use an atmospheric regional climate model (RCM) to force a subsurface model, which outputs the SMB.

Regional climate models are most often used to downscale coarser global models and reanalysis because they add further detail, due to their higher resolution, e.g. in the mountainous areas where the climate can be affected by local orography creating katabatic winds or orographic forced precipitation (Rummukainen, 2010; Feser et al., 2011; Rummukainen, 2016). Furthermore, RCMs also improve the physical representations of specific processes over polar areas (Lenaerts et al., 2019). Mottram et al. (2021) evaluated Antarctic SMB calculated from the outputs from five different RCM simulations driven by ERA-Interim (1987–2017). These five models showed mean annual SMB ranging from 1961 ± 70 to $2519 \pm 118\,\mathrm{Gt\,yr^{-1}}$. In the literature, individual evaluations of different RCMs such as COSMO-CLM^2 (Souverijns et al., 2019), MAR v3.6.4: (Agosta et al., 2019), and RACMO2.3p2 (van Wessem et al., 2018) are found to be in the same SMB range. The overall model spread in SMB models corresponds to approximately 2 mm of sea level change per year. Mottram et al. (2021) also showed that when compared to in situ observation from both automatic weather stations and glaciological stake measurements, the data availability proved insufficient to distinguish between better-performing model estimates. Fettweis et al. (2020) found similar conclusions for Greenland, where the RCMs displayed different strengths and weaknesses when evaluated both spatially and temporally. Mottram et al. (2021) and Verjans et al. (2021) furthermore showed that subsurface processes that drive melt and refreezing are extremely important when estimating the SMB. Hence, we here include firn processes by forcing a newly developed full-subsurface SMB model for Antarctica with the RCM HIRHAM5 (Christensen et al., 2007) over 1979–2017, to assess the effects of firn processes on estimates of ice sheet SMB. This subsurface model accounts for the physical properties of the uppermost part of the AIS, including density and temperature and the SMB.

Acknowledging that it might be challenging to judge the performance of the SMB model against in situ observations (Mottram et al., 2021), we also compare our modelled SMB results with a GRACE gravimetry estimate of the mass balance to determine any systematic biases. Finally, studies have shown that precipitation is not only the largest contributor to Antarctic SMB (Krinner et al., 2007; Agosta et al., 2019), but it also has a spatial heterogeneous distribution varying over time, which affects the SMB (Fyke et al., 2017). Regional-scale events like the heavy snowfall in Dronning Maud Land have an important measurable effect on Antarctic SMB (Lenaerts et al., 2013; Turner et al., 2019). Different representations of these may explain differences between modelled SMB (e.g. Mottram et al., 2021) as well as discrepancies between the GRACE mass balance and $\mathrm{SMB} - D$ solutions. Our study therefore also quantifies how regional climate indices affect SMB on a basin scale.

Regional circulation patterns including ENSO (El Niño–Southern Oscillation), the BAM (Baroclinic Annular Mode), and the Pacific–South American patterns (PSA1 and PSA2) have previously been identified as important determinants on weather and climate variability in Antarctica (Turner, 2004; Irving and Simmonds, 2016; Marshall and Thompson, 2016). However, empirical orthogonal functional analysis of Southern Hemisphere 500 hPa geopotential height (Marshall et al., 2017) demonstrates that the Southern Annular Mode (SAM) is the most important of these regional circulation indices. Further, Kim et al. (2020) found a multi-decadal relationship between the SAM and variations in the SMB; for these reasons we concentrate on its effects in this study. The SAM is an atmospheric phenomenon found across the extratropical Southern Hemisphere that influences the climate over and around Antarctica (Fogt and Marshall, 2020). Marshall et al. (2017) found that the phase of the SAM, which describes pressure anomalies and precipitation in the Southern Hemisphere (Fogt and Bromwich, 2006), strongly affects the precipitation pattern over the AIS. Studies have shown that the phase of SAM can have a great impact on the surface climate in Antarctica, such as the temperature (Thompson and Solomon, 2002; Van Lipzig et al., 2008), sea ice extent (Hall and Visbeck, 2002), pressure (Van Den Broeke and Van Lipzig, 2004), and especially precipitation (Van Den Broeke and Van Lipzig, 2004; Medley and Thomas, 2019). Other studies (Marshall et al., 2017; Dalaiden et al., 2020) have found that a positive SAM reduces precipitation over the Antarctic plateau and increases it over the western AP and in some coastal areas in East Antarctica. Finally Vannitsem et al. (2019) found that the Antarctic SMB is influenced by the SAM in most of the coastal areas of East Antarctica and large parts of West Antarctica. Therefore, we also investigate the spatial distribution of SMB over the grounded AIS (GAIS) in relation to the phase of the SAM.

The aims of this study are thus to estimate present-day Antarctic SMB using our subsurface model forced with the RCM HIRHAM5 and compare and evaluate two subsurface model versions against each other and in situ data. Furthermore, we estimate the MB, using our modelled SMB results combined with discharge values, and compare it with GRACE. Finally, we investigate the relationship between the SAM and the SMB. This is done in the following structure: first, the methods are presented, where the RCM HIRHAM5, the two subsurface models, and their set-up are described. This is followed by the results, where the modelled SMB results are shown, including evaluation against in situ measurements of SMB, firn temperature, and density. Finally, the MB is estimated and evaluated against GRACE data, and we discuss the influence of SAM on SMB, followed by the conclusions.

2 Methods

2.1 HIRHAM5 regional climate model

The HIRHAM5 RCM is a hydrostatic model with 31 atmospheric layers, developed from the physics scheme of the ECHAM5 global climate model (Roeckner et al., 2003) and the numerical weather forecast model HIRLAM7 (Eerola, 2006). HIRHAM5 has been optimized to model ice sheet surface processes that are often neglected or simplified in global circulation models. For a full description we refer to Christensen et al. (2007) and Lucas-Picher et al. (2012). Here HIRHAM5 is forced at the lateral boundaries at 6-hourly intervals with relative humidity, temperature, wind vectors, and pressure from the ERA-Interim reanalysis (Dee et al., 2011). Further, daily values for sea ice concentration and sea surface temperature are also used. HIRHAM5 calculates the full surface energy balance at the surface, based on model physics as described in Lucas-Picher et al. (2012), Langen et al. (2015) and Mottram et al. (2017). HIRHAM5 also calculates the amount of snowfall, rainfall, water vapour deposition and snow sublimation that occurs at the surface. Finally, for the HIRHAM5 Antarctic simulations, we used the Antarctic domain defined in the Coordinated Regional Climate Downscaling Experiment (CORDEX) (Christensen et al., 2014) and downscaled it further to 0.11° (≈ 12.5 km) spatial resolution with a dynamical time step of 90 s.

2.2 Subsurface model

The subsurface model was originally built on ECHAM5 physics (Roeckner et al., 2003) but has been updated to include a sophisticated albedo scheme. Following Langen et al. (2015) the shortwave albedo is computed internally and uses a linear ramping of snow albedo between 0.85 below −5 °C and 0.65 at 0 °C for the upper-level temperature. The albedo of bare ice is constant at 0.4. Furthermore, a transition albedo is calculated for thin snow layers on ice, based on Oerlemans and Knap (1998) with an *e*-folding depth of 3.2 cm for snow. Moreover, the snow and ice scheme is further developed and thereby updates the subsurface snow layers with snowfall, melt, retention of liquid water, refreezing, runoff, sublimation, and rain (Langen et al., 2015, 2017). Thereby, the subsurface model is forced with the snowfall, rainfall, evaporation, sublimation, and surface energy fluxes from HIRHAM5. These include net latent and sensible heat fluxes and downwelling shortwave and longwave radiative fluxes for 6-hourly intervals over the period 1979–2017. To reduce RCM spin-up effects, such as misrepresentation of the physical state of the atmosphere, e.g. temperature, the first year is removed from the results. Furthermore, the model has been tuned to mimic the average behaviour of the ice sheet surface at a 5–12 km scale. It cannot resolve subpixel processes. However, the small-scale features caused by surface melt translate into an increase in water content in the model. The subsurface scheme is updated hourly by interpolating the 6-hourly forcing files to 1-hourly time steps. To ensure a smooth transition between two 6-hourly files, a linear interpolation in time between the two nearest 6-hourly files is used. The horizontal resolution of the subsurface model follows the 0.11° native resolution of HIRHAM5.

As the Antarctic SMB may be sensitive to the subsurface model set-up, here we use two versions of the subsurface model (Langen et al., 2017). Common for both model versions is the albedo scheme, their meltwater percolation, firn compaction, and heat diffusion schemes. Meltwater in excess of the irreducible water content (Coléou and Lesaffre, 1998) is transferred vertically from one layer to the next using a parameterization of Darcy flow developed by Hirashima et al. (2010), with hydraulic conductivity values calculated from Van Genuchten (1980) and Calonne et al. (2012) and coefficients from Hirashima et al. (2010). The impact of ice content on a layer's conductivity is described by the parameterization by Colbeck (1975). When meltwater can infiltrate into a subfreezing layer, it is refrozen and latent heat is released. Firn density is updated at each time step for compaction under each layer's overburden pressure using the parameterization by Vionnet et al. (2012).

The two model versions differ in the management of the layers within the model. The first model version developed by Langen et al. (2017) has 32 subsurface layers with a fixed predefined mass, expressed in metres of water equivalent (m w.e.), given by $D_N = D_1\lambda^{N-1}$, where N is the given layer and $D_1 = 0.065$ m w.e. This fixed model implies an Eulerian framework, meaning that when snowfall occurs at the surface, it is added to the first layer, and an equal mass from that layer is shifted to the underlying layer. The same goes for each layer in the model column. The same procedure is followed when mass is removed from the top layer due to runoff or sublimation. Then each layer takes from their underlying neighbour an amount of snow/firn equivalent to the mass lost at the surface. The temperature and density of the layers are updated as the average between the snow or firn that is received by the layer, and what remains there. In the following we refer to this model version as the Fixed model.

The second model version uses a Lagrangian framework for the layer evolution developed by Vandecrux et al. (2018, 2020a, b). Layers evolve through a splitting and merging dynamic based on a number of weighted criteria. This dynamical model, henceforth referred to as the Dyn model, has 64 subsurface layers, the number of which are fixed during the simulation. When snowfall occurs at the surface, it is first stored in a “fresh snow bucket”. When this snow bucket reaches 0.065 m w.e., its content is added as a new layer at the surface of the subsurface scheme, and two layers need to be merged elsewhere in the model column. The layer merging scheme assesses how likely a layer is to be merged with its underlying neighbour based on seven criteria: the layers’ difference in temperature, density, grain size, water content, ice content, depth, and the thickness of the layers. The first five criteria make it preferable to merge layers with small differences. The sixth criterion makes it preferable to merge deep layers rather than shallow layers. In this case the shallow layer limit is set to 5 m w.e.; this criterion carries twice the weight of the first five. The final criterion says that no layer can be thicker than a maximum thickness, in this case 10 m w.e.; this is set to avoid the deepest layers continuing to grow. A weighted average of the criteria, where the first five are weighted equally, while the depth and thickness criteria are weighted double and triple respectively, is used by the model to determine which layers should be merged. When surface sublimation or runoff occurs, it is taken from the snow bucket and then from the top layer. When a layer decreases in thickness and its mass reaches 0.065 m w.e., then it is merged with the underlying layer, and another layer can be split in two elsewhere in the model column. The splitting routine is based on two criteria: thickness of the layer where thick layers are more likely to split and shallowness where shallow layers are more likely to split. The two criteria are weighted 60/40. However, the minimum thickness of any layer is always 0.065 m w.e. to avoid numerical instability. The bottom of the lowest model layer is assumed to exchange mass and energy with an infinite layer of ice with a temperature, like in the Fixed model (Langen et al., 2015), calculated from climatological mean of the HIRHAM5 2 m temperature.

Another difference between the two model versions is that the dynamic-layer model simultaneously melts the snow and ice content of the top layer while the Fixed-layer model melts the snow content first and then the ice content of the top layer. This update aims at preventing the top layer from becoming only ice and a barrier to meltwater infiltration. Furthermore, the Dyn model’s runoff is routed downstream using Darcy’s law and the local surface slope, whereas the Fixed model follows Zuo and Oerlemans (1996), and excess water in a layer cannot be transferred to the underlying neighbour. Both the Fixed and Dyn versions require a fresh snow density value when adding snowfall at the surface. We here use the Antarctic parameterization from Kaspers et al. (2004), who use local climatological means of skin temperature, 10 m wind speed, and accumulation rates; here the means from HIRHAM5 have been used.

2.3 Experimental set-up

The Fixed model was initialized with a firn column with uniform density of 330 kg m^{-3} and a temperature at the bottom of the firn pack given by the climatological mean of the HIRHAM5 2 m temperature. Spin-up was performed by repeating a decade (1980–1989) multiple times. The state of the subsurface at the end of each decade was used as the initial state for the next iteration. There were no appreciable shifts in the Antarctic climate from 1980–2019 (Medley et al., 2020), so the 1980s can be used as a representative decade for spinning up the subsurface. The Fixed subsurface scheme was spun up over 25 iterations (250 years). Afterwards, the actual experiment ran from 1979–2017. To limit computing time, the dynamical model was initialized with the last spin-up from the Fixed model and extrapolated to the 64 layers of the Dyn model. From then, additional spin-ups (1980–1989) ensured that the dynamical splitting and merging of layers had time to evolve throughout the firn pack. Two spin-up experiments have been carried out for the Dyn model: one that uses 3 decades of additional spin-up (Dyn03), resulting in a total of 280 spin-up years (250 from the fixed model and 30 years in the dynamical model), and one that uses 15 decades of spin-up (Dyn15), resulting in a total of 400 spin-up years.

All three model simulations (summarized in Table 1) provide outputs of monthly and yearly means of all 3D variables (density, grain size, firn temperature, and ice/water/firn content) and daily 2D fields (SMB, runoff, superimposed ice, melt, albedo, ground heat flux, refreezing, diagnosed snow depth (which is an estimate based on the snow concentration in each layer), and net shortwave and net longwave radiation) of the surface variables. Furthermore daily columns for specified coordinates interpolated to the nearest grid cell have been retrieved for comparison of in situ measurements. For the two simulations with dynamical layer thickness, the daily 3D fields are interpolated into a fixed grid, with the same number of layers, so time averages could be calculated.

2.4 Regional drivers and mass balance

The SAM is characterized in Fogt and Bromwich (2006) as the zonal pressure anomalies in the high southern latitudes having opposite sign to those of the midlatitudes. The SAM drives the westerly winds around Antarctica, but the stream oscillates north–south. The SAM can have three phases: positive, neutral, or negative, where positive creates a higher pressure over the midlatitudes and lower pressure over Antarctica and thus moves the westerly winds closer to Antarctica. A negative SAM creates a lower pressure over the midlatitudes and a higher pressure over Antarctica, moving the westerly winds north. When neutral there is no pressure difference anomaly. To investigate how the phase of SAM affects the SMB, monthly SAM data, as calculated by Marshall (2018), have been used. From 1980–2017, 261 months

Table 1. Model overview and main differences.

	Fixed	Dyn03	Dyn15
Thickness	Constant over time and space	Varies over time and space	Varies over time and space
No. of layers	32	64	64
Spin-up [yr]	250	280	400
Melt	First snow and then ice	Snow and ice simultaneously	Snow and ice simultaneously

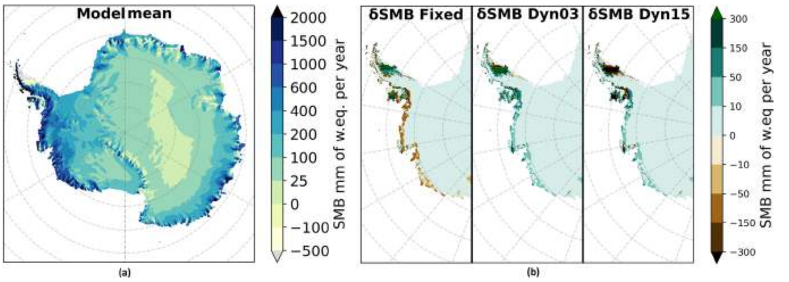

Figure 1. Mean SMB from 1980 to 2017 in mm yr^{-1} of w.e. **(a)** The mean of the model mean; note the nonlinear colour bar. **(b)** West AIS where the δSMB has the largest differences between model versions (model minus ensemble mean).

showed a positive SAM (SAM+), 193 months showed a negative SAM (SAM−), and 2 months were neutral. The SAM data are given as one monthly number, i.e. one number for the entire Antarctic domain. To see whether there is a link between SAM and SMB, the monthly SMB values were divided into two groups: SAM+ and SAM−. Then the mean SMB for all months with SAM+ was subtracted from the mean SMB for the entire period and likewise for SAM−. To examine whether there was a statistically robust difference in the δSMB signals, we performed a bootstrapping analysis, using 1200 random resamplings without replacement of the SAM data, to see whether the δSMB signals could be replicated randomly and if it could be produced randomly whether the signal would not be robust. Statistically robustness has been defined as δSMB values falling outside the 5th–95th percentile range. In order to maintain the seasonal variability in the SMB, the SAM data were shuffled in sets of 12 – in this way the order of the months was maintained and thus the seasonal cycle retained. Then confidence intervals were determined as the 5th and 95th percentiles of the distribution of the resampled δSMB values.

Observing the mass balance can be helpful to assess the spatial patterns of SMB and evaluate the modelled results. Mass balance can be derived from gravimetric measurements from space. Here GRACE/GRACE-FO mass loss time series data were computed for the period 2002–2020, using a mascon approach based on CSR R6 level-2 data, complete to harmonic degree 96 (Forsberg et al., 2017). The lowest-degree terms were substituted with satellite laser ranging data and glacial isostatic adjustment corrections from the model of Whitehouse et al. (2012). From Eq. (1) we know that MB should be equal to SMB minus discharge (SMB − D). So to evaluate our SMB model performance, GRACE and SMB − D have been plotted. The discharge values were derived from two studies: Gardner et al. (2018) and Rignot et al. (2019). Gardner et al. (2018) gave values from 2008 and 2015; here we took the mean value and used D_{Gardner} over the period. Rignot et al. (2019) have derived decadal mean discharge values from 1999–2010 and 2010–2017; for D_{Rignot} the relevant discharge values were used. The SMB value used here is for the grounded AIS only, and since the modelled SMB values are quite similar over the grounded AIS, it is only shown here for the Dyn15 simulation.

3 Results

In the model mean (1980–2017) of the three SMB simulations (Fig. 1a), we see that the majority of the total AIS (ToAIS) has a positive SMB; only a few regions show a negative SMB: Larsen ice shelf, George IV ice shelf, coastal regions of Queen Maud Land, the Transantarctic Mountains, near Amery ice shelf, and some coastal areas in East Antarctica. Near Vostok in East Antarctica, the SMB is less than 25 mm w.e. yr^{-1}. The SMB increases towards the coast due to higher precipitation. The highest SMB is greater than 2000 mm w.e. yr^{-1} and is found on the windward (western) side of the AP, whereas the most negative SMB, −500 mm w.e. yr^{-1}, is found on the leeward (eastern) side of the AP (Fig. 1a). All the model simulations show nearly identical SMB values over the GAIS; however they differ the most near the coast in West Antarctica and the AP as Fig. 1b shows. Here, we see that δSMB (model mi-

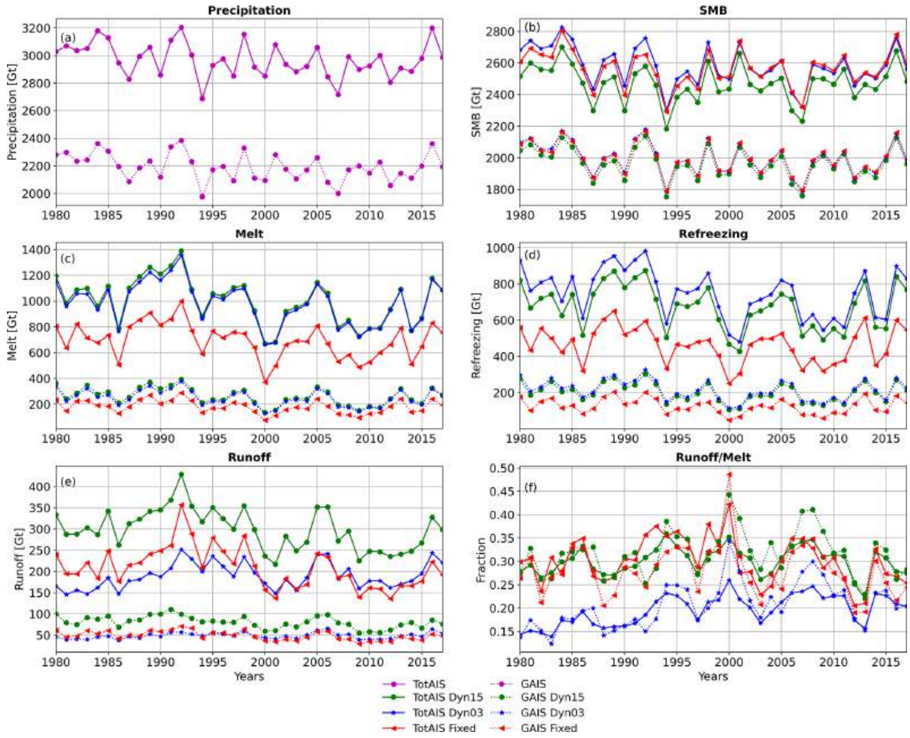

Figure 2. Integrated precipitation **(a)**, SMB **(b)**, melt **(c)**, refreezing **(d)**, and runoff **(e)** all in $\mathrm{Gt\,yr^{-1}}$. Panel **(f)** shows the runoff to melt fraction. For the three model simulations, for the entire AIS with ice shelves (ToAIS), and for the GAIS. Note different values on the *y* axis.

nus mean) shows that the Fixed version has a higher SMB of up to 550 mm w.e. over the Larsen ice shelf relative to the model mean. In Dyn03 the SMB values differ between −350 and 400 mm w.e. from the model mean. This change occurs over a few grid cells. In Dyn15 the SMB differs up to −650 mm w.e. compared to the model mean over the Larsen ice shelf. Since the Fixed version is above the model mean, over the Larsen ice shelf, and Dyn15 is below the model mean, it looks like the rapid change from negative to positive δSMB in Dyn03 over Larsen ice shelf is due to lack of spin-up. Below the AP, off the coast of Ellsworth Land and Marie Byrd Land, the Fixed version models a lower (−75 mm w.e.) SMB than Dyn03 (35 mm w.e.) and Dyn15 (50 mm w.e.) all relative to the model mean. Around Alexander Island in the Bellingshausen Sea, both the Fixed and Dyn15 versions have a lower SMB compared to Dyn03. The differences in spatial distribution show that in areas where melt occurs, the SMB is very sensitive to which subsurface scheme is used.

The model differences are seen in the integrated values for precipitation, SMB, melt, refreezing, and runoff, for both ToAIS and the GAIS (Fig. 2), and summarized in Table 2. As all model simulations are forced using the same precipitation field (Fig. 2a) and since the precipitation is the main driver of the SMB, the variability of the modelled SMB closely follows the precipitation variability. The spread in modelled mean melt, refreezing, and runoff are respectively 1 %, 11 %, and 8 % smaller when including the ice shelves compared to only taking the GAIS, whereas the spread in mean SMB becomes 3 % greater. To better compare the melt, refreezing, and runoff from the different simulations, the fraction of runoff to melt is shown in Fig. 2f. Dyn03 has the smallest runoff fraction whereas Dyn15 and Fixed are quite close to each other. This implies that even though the magnitudes between the simulations are quite different, the refreezing capacity of the Fixed and Dyn15 versions are near equal, and Dyn03 has the smallest refreezing capacity. Note also that the melt is 289 and 309 $\mathrm{Gt\,yr^{-1}}$ higher in Dyn03 and Dyn15 respectively, compared to the Fixed model. Again this is focused largely over the ice shelves, especially over the Larsen and Amery ice shelves where Dyn03 and Dyn15 have more bare ice and thus a lower albedo.

3.1 Evaluation against observations

Koenig and Montgomery (2019) have, in the SumUp dataset, collected accumulation rates over Antarctica. Here we eval-

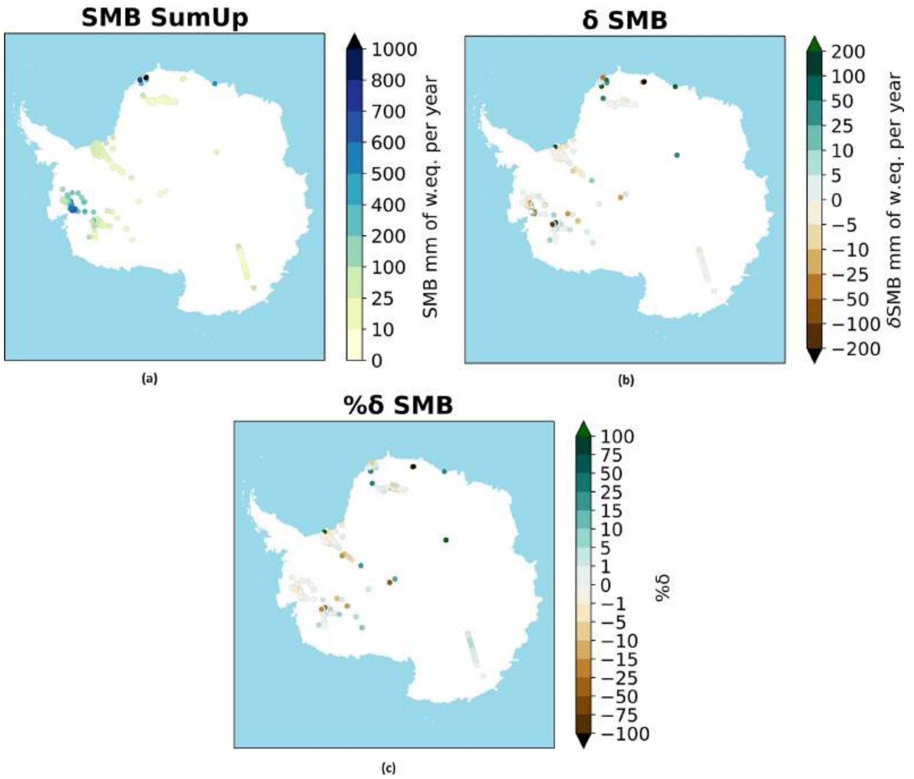

Figure 3. **(a)** The SMB from SumUp. **(b)** The δSMB (SumUp minus model ensemble mean) and **(c)** the change in percent.

Table 2. Yearly mean SMB, melt, refreezing, runoff, precipitation, and runoff fraction (runoff over melt), ± with respective standard deviations, for both the total ice sheet (ToAIS) and the grounded ice sheet (GAIS). Note that all the model simulations are forced with the same precipitation.

Model		SMB [Gt yr^{-1}]	Melt [Gt yr^{-1}]	Refreezing [Gt yr^{-1}]	Runoff [Gt yr^{-1}]	Precipitation [Gt yr^{-1}]	Runoff fraction [%]
Fixed	ToAIS	2564.8 ± 113.7	695.3 ± 132.4	463.7 ± 97.3	208.3 ± 47.5	2970.9 ± 122.1	0.30 ± 0.06
	GAIS	1995.2 ± 95.7	180.0 ± 49.5	125.1 ± 40.3	48.8 ± 10.4	2193.8 ± 98.0	0.28 ± 0.05
Dyn03	ToAIS	2583.4 ± 121.6	984.2 ± 166.1	748.9 ± 132.5	189.6 ± 29.9	–	0.20 ± 0.03
	GAIS	1995.4 ± 99.3	247.7 ± 61.7	215.3 ± 54.1	48.6 ± 7.0		0.21 ± 0.05
Dyn15	ToAIS	2473.5 ± 114.4	1004.5 ± 173.7	674.5 ± 121.7	299.5 ± 47.1	–	0.30 ± 0.03
	GAIS	1963.3 ± 96.2	262.3 ± 65.8	200.8 ± 51.3	80.6 ± 13.7		0.32 ± 0.05

uated the modelled SMB values against the SumUp accumulations assuming that over most of the AIS accumulation is nearly equivalent to SMB. The SumUp dataset has yearly measurements for some locations and mean values for longer periods for other locations. To make it consistent, we computed the yearly mean at each location, shown in Fig. 3a, and compared it with the nearest grid cell in the ensemble mean for the period from 1980 to 2017. If there was more than one measurement in one grid cell, an average was used (Fig. 3b). Lastly, we computed the change between the observations and the ensemble mean in percent (Fig. 3c). In total 2221 measurements have been used, located in 251 different grid cells. The SumUp accumulation dataset has areas with a high concentration of measurements, like Marie Byrd Land, Dronning Maud Land, and Dome Charlie; however, in East Antarctica there are larger areas that are not represented in the SumUp dataset. The accumulation ranges from near 0 to 100 mm w.e. yr^{-1} at the South Pole, Dronning Maud Land, and Dome Charlie and up towards 1000 mm w.e. yr^{-1} in Marie Byrd Land and the coast of Dronning Maud Land. Figure 3b shows the difference between the model ensemble mean and the in situ observations where it is seen that there are some large numerical differences in Marie Byrd Land and near the coast in Dronning Maud Land. Figure 3c displays the difference in percent for the δSMB; it shows that only three of the 251 grid cell comparisons have a difference greater than ±100 %. Furthermore half of the 251 comparison points fit within ±13 %.

Modelled firn densities are evaluated using the SumUp dataset (Koenig and Montgomery, 2019). When disregarding firn cores shallower than 2 m, there were 139 density profiles left (Fig. 4). All the references for the firn profiles can be found in the reference list. These profiles vary in depth, from a few metres to 100 m, but the majority are drilled to 10 m depth. Knowing the coring date, we compare it to the modelled density of the nearest grid cell on the same date. Before the inter-comparison, the modelled and observed density profiles were interpolated to the same vertical resolution (if the model resolution is higher than the core resolution, the model is interpolated to fit the core resolution and vice versa). In the SumUp dataset 96 profiles had the exact date given, and seven SumUp profiles only had year and month given. Here the modelled mean density of the given month was compared. Finally 36 cores had only the year given; in these cases the modelled mean density of January was compared, as we assume they were most likely collected in the middle of the standard Antarctic summer field season. To evaluate the model performance we calculate mean difference (MD) and standard deviation (SD) between the modelled and observed firn densities. A statistical comparison of the mean difference and 1 standard deviation between the firn cores and the modelled densities is given in Table 3 for the three simulations. Summed up over the AIS, all simulations overestimate the densities below 550 kg m^{-3} and underestimate the densities above 550 kg m^{-3}. It is seen that the Fixed version outperforms Dyn03 and Dyn15 for densities below 550 kg m^{-3}. Conversely, Dyn03 and Dyn15 outperform the Fixed version for densities above 550 kg m^{-3}. All three simulations show the best statistics for higher densities. The agreement with the in situ cores also varies spatially (Fig. 5). Generally the spatial density bias is consistent between the models.

Over the Filchner–Ronne ice shelf, in Dronning Maud Land and in Marie Byrd Land the distribution of profiles are quite dense; these areas are marked with boxes (Fig. 5). All simulations overestimate the density of firn over the Filchner–Ronne ice shelf. Of the 36 cores on the Filchner–Ronne ice shelf, only two have underestimated densities in the simulations. The rest of the cores have overestimated densities from 2.5 and up to 200 kg m^{-3}. In general all three simulations have the largest biases in this region. If the cores on the Filchner–Ronne were not included in the statistics, the mean deviation for densities below 550 kg m^{-3} would be between 36–38 kg m^{-3}; for densities above 550 kg m^{-3} the mean deviation would not change much. Mottram et al. (2021) show that the HIRHAM5 model estimates higher precipitation over the Filchner–Ronne ice shelf than other RCMs, and the overestimate in density may therefore relate to overestimated precipitation in this area, which is compliant with our Fig. 3. However, as they also note, the lack of continuous SMB observations makes it difficult to be certain if and by how much precipitation is overestimated in this region. It could also be due to an overestimation for melt and refreezing over the ice shelf.

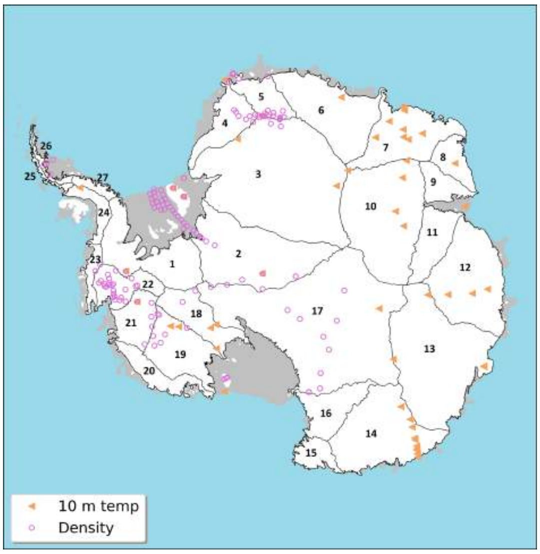

Figure 4. The white colour shows the GAIS, and the grey colours show the locations of ice shelves. The spatial distribution of observations are shown with light brown triangles for borehole temperatures and magenta circles for the location of the density profiles. The grounded basins are derived from Zwally et al. (2012) and outlined by black lines.

Table 3. Mean difference between the modelled and observed firn densities (model – core) and standard deviation of the modelled densities above and below 550 kg m^{-3}. In total 139 cores were used; see Fig. 4 for locations.

	Fixed [kg m^{-3}]	Dyn03 [kg m^{-3}]	Dyn15 [kg m^{-3}]
MD ($\rho < 550\,\mathrm{kg\,m^{-3}}$)	43.4	65.6	65.7
SD ($\rho < 550\,\mathrm{kg\,m^{-3}}$)	24.2	28.1	26.6
MD ($\rho > 550\,\mathrm{kg\,m^{-3}}$)	−19.2	−5.4	−4.1
SD ($\rho > 550\,\mathrm{kg\,m^{-3}}$)	17.5	21.9	19.4

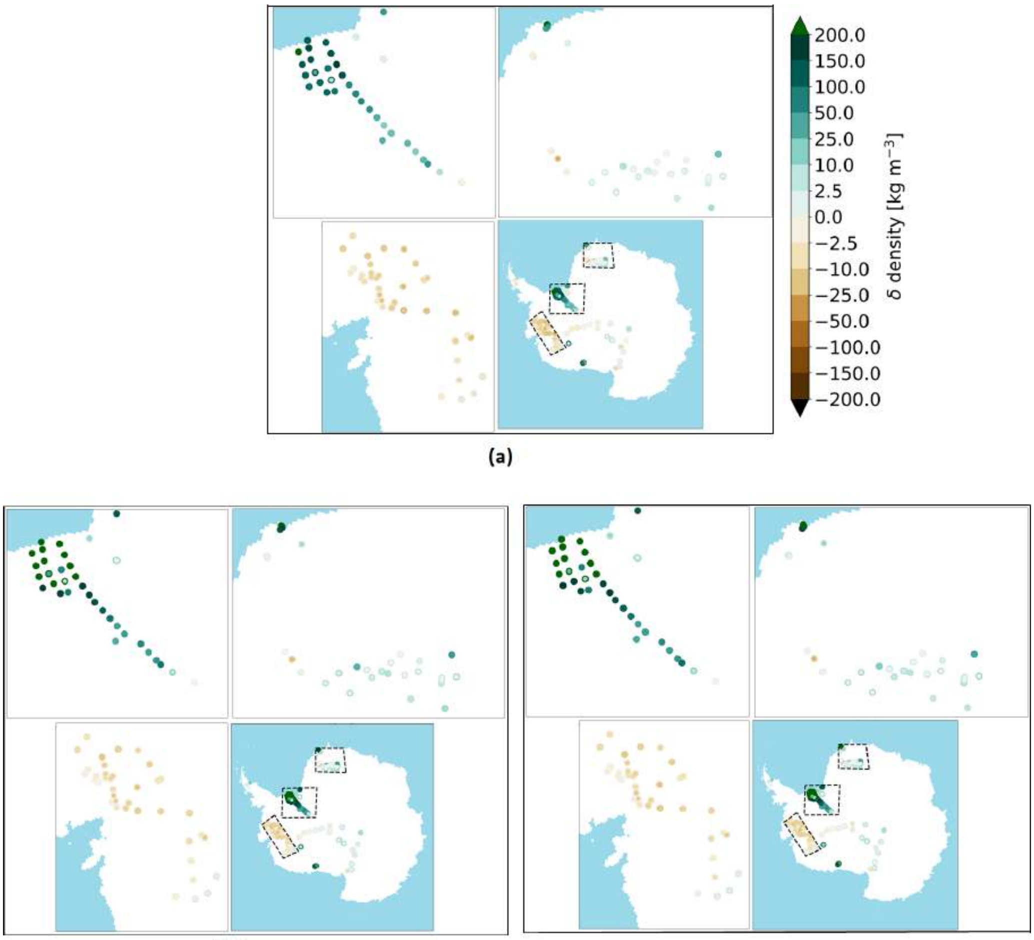

(a)

(b)

(c)

Figure 5. The density bias between simulations and the observations (model minus core). The outer ring represents densities less than 550 kg m^{-3}, and the inner circle represents densities greater than 550 kg m^{-3}. Panel **(a)** is the Fixed model, **(b)** is Dyn03, and **(c)** is Dyn15. Each panel shows the entire AIS with three dashed black boxes. Each box outlines a zoom-in area: from east to west the Dronning Maud Land, Filchner–Ronne ice shelf, and Marie Byrd Land. All panels have the same colour bar.

In Dronning Maud Land there are 30 cores with a very small bias. The majority of the core densities agree within ±25 kg m^{-3}, apart from three cores near the coast that are overestimated by 100 kg m^{-3} in all three simulations.

Marie Byrd Land shows a general pattern of underestimated densities in 37 cores in all simulations. However, Dyn03 and Dyn15 have lower biases compared to the Fixed. In Dyn03 and Dyn15, four cores were underestimated by more than 25 kg m^{-3}, compared to five cores in the Fixed model. Both Dyn03 and Dyn15 have six cores where the mean deviations are between 0 and 2.5 kg m^{-3} for densities less than 550 kg m^{-3}, but they underestimate densities greater than 550 kg m^{-3}, with a mean deviation between 10 and 25 kg m^{-3}.

For the Ross ice shelf cores and near the South Pole, the Fixed simulation overestimates most of the cores, some of them by 50 to 100 kg m^{-3} for densities less than 550 kg m^{-3} and more than 100 kg m^{-3} for densities greater than 550 kg m^{-3}. However, for Dyn03 and Dyn15 we also observe an overestimation of most cores, but only six of them are overestimated by more than 25 kg m^{-3}.

Figure 6 shows 4 of the 139 firn cores: core BER02C90_02 (Wagenbach et al., 1994) (Fig. 6a), core DML03C98_09 (Oerter et al., 2000) (Fig. 6b), core FRI14C90_336 (Graf

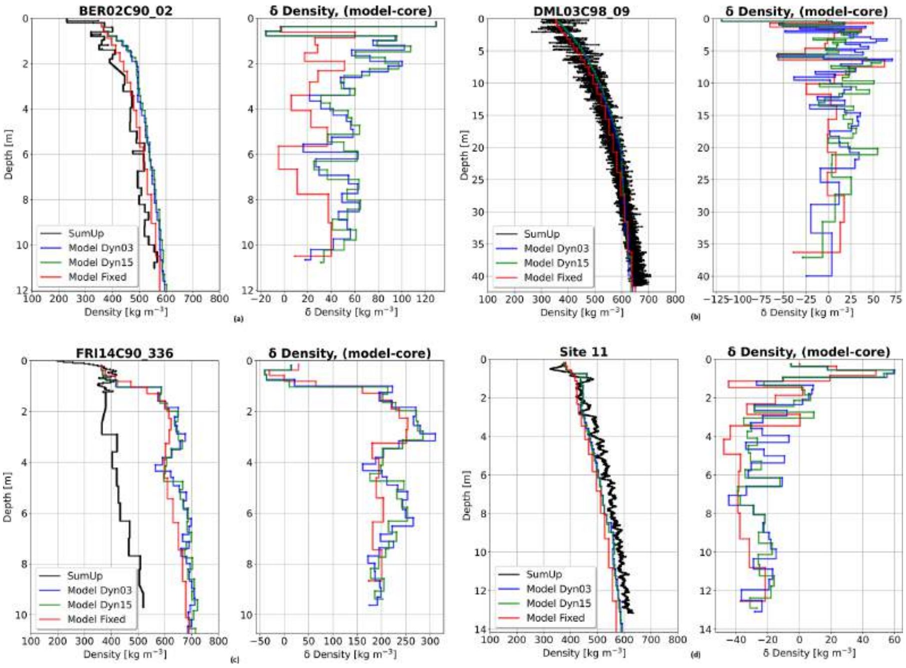

Figure 6. Examples of density profiles. In each of the four subfigures, the left-hand plot shows the firn core in black and the modelled density from Fixed, Dyn03, and Dyn15 in red, blue, and green. The right-hand plot shows the difference. The cores are **(a)** BER02C90_02 taken in 1990 (Wagenbach et al., 1994), **(b)** DML03C98_09 taken in 1998 (Oerter et al., 2000), **(c)** FRI14C90_336 taken in 1990 (Graf and Oerter, 2006), and **(d)** Site 11 taken in 2013 (Morris et al., 2017).

and Oerter, 2006) (Fig. 6c), and core Site 11 (Morris et al., 2017) (Fig. 6d). These four cores are selected because they are located in different regions of the AIS, and, furthermore, they show different examples of under-/overestimations of modelled densities. The Fixed simulation fit quite well (±20 kg m^{-3}) with the core taken on Berkner Island (Fig. 6a), whereas Dyn03 and Dyn15 show a larger bias mainly at the surface and the top 3 m of the firnpack. The core from Dronning Maud Land (Fig. 6b) has a high vertical resolution; the deeper the cores go, the smaller the biases become. Cores FRI14C90_336 and Site 11 are taken on the Ronne ice shelf and in Marie Byrd Land respectively. The model densities in FRI14C90_336 are overestimated below 1 m depth, and the mean bias is 200 kg m^{-3}. At Site 11 all simulations underestimate the density; however below 2 m depth, the underestimation is nearly constant with a mean bias of −20 kg m^{-3}.

The modelled subsurface temperatures are evaluated against observed 10 m firn temperature measurements from 49 boreholes (van den Broeke, 2008) (see Fig. 4 for the locations). Most of the temperatures were taken in the 1980s and 1990s; however only the year or decade is known for when these were taken. Therefore they are compared with the modelled mean 10 m firn temperature from 1980–2000. We evaluated the model performance using the root-mean-square difference (RMSD), mean difference (MD), and coefficient of determination (R^2). Subsurface temperatures are only sparsely available in Antarctica. The measured 10 m firn temperatures are compared with the modelled mean 10 m firn temperature of the nearest grid cell (Fig. 7). The red, blue, and green lines are the regression lines of first order, for Fixed, Dyn03, and Dyn15; they have an R^2 of 0.98, 0.97, and 0.98, respectively. It is assumed that the in situ temperatures are true, so the errors are in the modelled temperatures. For temperatures below −30 °C the three simulations are in agreement, but in warmer firn temperatures > −30 °C, the agreement becomes worse. The mean deviation of the three model simulations is listed Table 4.

4 Discussion

The annual SMB for the three simulations (Table 2) is of the same magnitude as the previous HIRHAM5 SMB estimate of 2659 Gt yr^{-1} for the ToAIS (Mottram et al., 2021). However, we model a lower SMB, with only Fixed and Dyn03 within 1 standard deviation range of Mottram et al. (2021). The lower SMB estimates are due to the inclusion of the runoff compo-

Table 4. Mean deviation, root-mean-square deviation, and coefficient of determination, for the modelled and observed 10 m temperature.

	Fixed	Dyn03	Dyn15
MD [°C]	0.42	0.52	0.46
RMSD [°C]	1.66	1.77	1.71
R^2	0.98	0.97	0.98

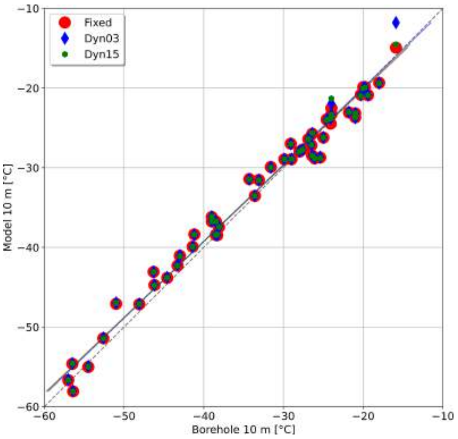

Figure 7. The dots are 10 m temperature from boreholes vs. mean model 10 m temperature. The solid lines are the regression lines of first order, and the grey dashed line shows the diagonal.

nent in the SMB calculation. The initial SMB results from HIRHAM5 in Mottram et al. (2021) were only calculated from precipitation, evaporation, and sublimation. Calculating the SMB by including a subsurface model results in a more realistic SMB, due to the fact that it takes surface and subsurface processes like energy fluxes, meltwater percolation, and refreezing into account.

The spatial distribution of SMB fits reasonably well compared with the SumUp accumulation measurements; however, more measurements, especially in East Antarctica, are needed to be able to do a complete evaluation. Furthermore, the spatial distribution of SMB broadly agrees with other studies (Van de Berg et al., 2005; Krinner et al., 2007; Agosta et al., 2019; Souverijns et al., 2019). However, the total integrated mean SMB in these published studies differs, likely due to a number of different reasons. The ice mask, model resolution and domain, and nudging (if any) are identified as a source of differences in Mottram et al. (2021). However, differences in model parameterizations affecting components such as sublimation and precipitation are also important. For example, the modelled annual mean precipitation in HIRHAM5 is 2971 ± 122 Gt, in COSMO-CLM^2 it is 2469 ± 78 (Souverijns et al., 2019), and in RACMO2.3p2 it is 2396 ± 110 Gt (van Wessem et al., 2018). However, the geographical distribution of precipitation is uneven between these models, with COSMO-CLM^2 being much drier in western Antarctica than other models in the comparison. Even using a common ice mask, Mottram et al. (2021) found that the difference in precipitation is around 500 Gt yr^{-1} between HIRHAM5 (the wettest model) and COSMO-CLM^2 (the driest model in the intercomparison). The high precipitation in regions of high relief in HIRHAM5 is attributed to a wet bias in the precipitation scheme, also identified in southern Greenland and similarly occurring in the RACMO2.3p2 regional climate model (Hermann et al., 2018). In both models this wet bias in steep topography is related to the precipitation and cloud micro-physics schemes (Mottram et al., 2021). Areas with a negative SMB can be due to large melt rates, which is what we see in the model over the Larsen ice shelf with melt values between 1200 and increasing toward the west to 2300 mm w.e. yr^{-1} and SMB values in the range of 300 to 1800 mm w.e. yr^{-1} increasing toward the west. In general all three simulations display a higher melt compared to other RCM studies, e.g. 71 Gt yr^{-1} in RACMO2.3p2 (van Wessem et al., 2018) or 40 Gt yr^{-1} in MARv3.6.4 (Agosta et al., 2019). These two numbers are without the AP, but they are nevertheless very low compared to our melt rates. Trusel et al. (2013) derived satellite-based melt rate estimates from 1999 to 2009, and over that period, the Larsen ice shelf experienced the largest melt of around 400 mm w.e. yr^{-1}. However, these estimates were derived using RACMO2.1, and the satellite detects melt areas on the Larsen ice shelf that were not simulated in RACMO2.1, most likely due to coarse resolution, so 400 mm w.e. yr^{-1} might be on the low end. Nevertheless, Trusel et al. (2013) estimates are still 3 to 6 times lower than our simulation. This suggests that the subsurface model may compute a melt rate that is too high in at least some locations.

Negative SMB values can also be due to high sublimation rates in, e.g., blue ice areas (Hui et al., 2014). For example, Kingslake et al. (2017) found blue ice in Dronning Maud Land and near the Transantarctic Mountains. In these areas our SMB model mean also shows negative SMB between −50 and −400 mm w.e. yr^{-1}. A closer investigation (not shown) reveals that the negative SMB values in these areas are driven by the sublimation and thereby consistent with the creation of blue ice areas.

The differences in SMB between the model simulations (Fig. 1b) are largest near the coast in West AIS and especially on the Larsen ice shelf. This is confirmed in Fig. 2b, where the difference in integrated SMB between the model simulations is greater when the ice shelves are included. We attribute the differences between the Fixed and Dyn models to the following differences in model designs. The increased vertical resolution in the Dyn models, with a higher vertical resolution (the top layers can be 6.5 cm w.e. thick) means that the cold content in the upper layers is depleted faster, and it starts to melt while the layer below is potentially still below freezing. Conversely the top layers in the Fixed model get thicker rather quickly, which means it takes longer to be brought to melting point and start melting. Furthermore, the two versions of the subsurface model have different melting schemes. In both versions one layer can contain snow and ice at the same time, described with a fraction. However, in the Fixed model snow melts first and then, if there is more energy left, the ice melts. Conversely, the Dyn melts snow and ice simultaneously. This simultaneous melting of snow and ice was introduced in the Dyn version to prevent the top layer from being depleted of its snow content and left only with ice (Vandecrux et al., 2018). A top layer composed of ice would then prevent surface melt from infiltrating below the top layer. By melting snow and ice simultaneously, there is always snow in the top layer for meltwater infiltration to happen. This difference of infiltration may cause the snowmelt to refreeze less and more water to run off than the simultaneous melt of snow and ice. To investigate these differences in melt, refreezing, and runoff, the runoff fractions have been plotted in Fig. 2f and listed in Table 2. Here it is seen that even though the difference in melt between Dyn03 and Dyn15 is only around 20 Gt yr^{-1}, the difference between the runoff and melt fractions is larger. The Fixed model melts around 300 Gt yr^{-1} less than the dynamical versions, but the runoff-to-melt ratio is the same for Fixed and Dyn15. This means that Fixed and Dyn15 have the same relative runoff, leading to the same relative refreezing, indicating that this difference does not cause a significant partition of melt between refreezing and runoff.

The difference in SMB between the three simulations confirms how complex it is to estimate the SMB. Just by changing the subsurface scheme, the final result differs by 90 Gt yr^{-1}. By keeping the same subsurface scheme and changing the spin-up length, the final result differs by 110 Gt yr^{-1}. These changes in SMB illustrate the consequences of including dynamic firn processes since the layer density and temperature and other firn properties are better conserved, potentially allowing more retention and refreezing where there is capacity or reducing it where there is not. Although these differences are currently only a few percent of the total SMB, as the climate warms and melt becomes more widespread in Antarctica (e.g. Boberg et al., 2020; Kittel et al., 2021), accounting for these processes will become more important. Moreover, on local and regional scales, the differences are more important when determining mass balance in basins or outlet glacier/ice shelves.

The differences between versions with a different spin-up period suggest that the snowpack is not quite in equilibrium in all locations. Therefore, SMB calculations consequently vary due to the amount of melt calculated during the initialization period. Retention and refreezing of meltwater during spin-up cause different profiles of temperature and density to develop depending on how long the spin-up lasts. These results therefore emphasize the importance of adequate spin-up and assessment of the effects of snowpack spin-up in producing and using SMB in Antarctica.

Vandecrux et al. (2020b) found that the Fixed version smoothes the firn density profiles, when compared to the dynamical version; this is confirmed by our results. One of the criteria for the dynamical version is that it prefers to merge layers deeper than 5 m of water equivalent, meaning that the top 5 m w.e. has a high vertical resolution, which makes it easier to detect changes in density. In areas such as the AP, Ronne–Filchner ice shelf, Ross ice shelf, and coastal areas of Dronning Maud Land where seasonal melt occurs (Zwally and Fiegles, 1994; Wille et al., 2019), meltwater can percolate into the firn and refreeze, creating ice lenses that change the density but that cannot be detected if the subsurface scheme has layers with a fixed mass even if the vertical resolution is increased (Vandecrux et al., 2020b). Not only is there a difference between the models when evaluating density profiles, but this study also shows the importance of spatial evaluation. Here the three simulations follow the same pattern by over-/underestimating the densities in the same areas (Fig. 5). This systematic bias may indicate either further tuning of densification routines is necessary or that there are systematic biases in accumulation, leading to these errors. The subsurface scheme does not currently incorporate wind-blowing snow processes that may prove important in correcting biases in accumulation. On the other hand, although 0.11° is a high-resolution model in Antarctica and thus better captures topographic variability than lower-resolution models, it is still relatively coarse when it comes to capturing steep topography. Errors in orographic precipitation are difficult to measure even in well-instrumented basins and are poorly captured in Antarctica where observations are few and far between. The densification bias becomes especially important when using altimetry data to estimate the total MB, like in Shepherd et al. (2018) and Rignot et al. (2019). Here the firn densification rate is needed to correct the altimetry data (Griggs and Bamber, 2011).

Since the density cores are primarily taken from West Antarctica and Dronning Maud Land, these statistics represent complex areas with high precipitation and melt–refreezing events, whereas density comparisons from less complex areas (low precipitation and no melt–refreezing) such as East Antarctica are sparse. Nonetheless they are still very important. Based on the statistics from these model setups, the Dyn version is preferred when modelling densities above 550 kg m^{-3}.

The simulated 10 m firn temperature depends on the thickness and number of layers above the 10 m point. The thickness of a layer determines how conductive heat fluxes are resolved in the near-surface snow. A thicker layer will have more thermal inertia and will require more energy to be warmed up. A thin layer can respond much more quickly to fluctuations in the surface energy balance. Differences in simulated temperatures between models, as we see in Table 4, can therefore be explained by vertical resolution, which

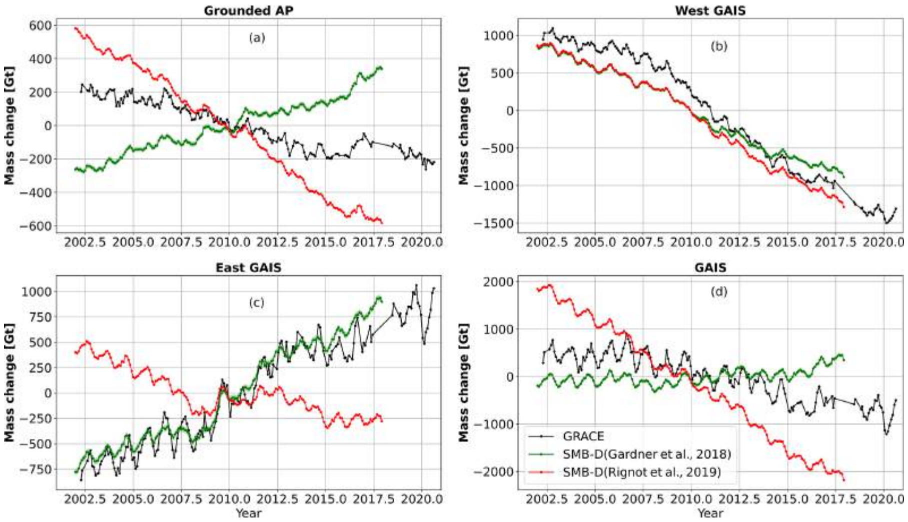

Figure 8. Integrated relative mass change over the grounded Antarctic Peninsula **(a)**, the grounded West AIS **(b)**, grounded East AIS **(c)**, and the GAIS **(d)**. GRACE relative mass change from 2002 to 2020 (black graph). SMB minus discharge (green/red graphs). SMB values are from the Dyn15 simulation, and discharge values are derived by Gardner et al. (2018) (in green) and Rignot et al. (2019) (in red). Note that the *y* axis differs from panel to panel.

affects both their calculation of temperature and how the heat is conducted to a depth of 10 m. Note that the models also use different thermal conductivity parameterizations.

4.1 Satellite gravimetric mass balance

Over the AP there is a large disagreement between $\mathrm{SMB}-D_{\mathrm{Gardner}}$ and $\mathrm{SMB}-D_{\mathrm{Rignot}}$, the mean discharge values differ by 90 Gt yr^{-1}, with D_{Rignot} being the largest. This results in opposite trends of $\mathrm{SMB}-D$. $\mathrm{SMB}-D_{\mathrm{Gardner}}$ shows a mass gain of around 600 Gt, and $\mathrm{SMB}-D_{\mathrm{Rignot}}$ shows approximate mass loss of 1150 Gt over the period, whereas GRACE has a mass loss of around 400 Gt for the period (Fig. 8a). There are times when the variability between GRACE and the two SMB-D graphs follows each other, e.g. local peak around year 2006, 2011, and 2017. Since the discharge is plotted as a constant, this variability originates from the SMB model, most likely precipitation. This means that the D_{Gardner} value is too small, D_{Rignot} values are too large, or the SMB magnitude is too low or high depending on which discharge is used. As the resolution of GRACE is quite coarse, it can add to the uncertainties over the AP, because of narrow topography. Over the grounded West AIS the trend of GRACE, $\mathrm{SMB}-D_{\mathrm{Rignot}}$, and $\mathrm{SMB}-D_{\mathrm{Gardner}}$ agrees. They all see a mass loss, of around 2000, 2150, and 1700 Gt, respectively, for the overlapping period (Fig. 8b). The discharge values from the two studies differ only by 2 Gt yr^{-1} from 2002 to 2010 but by 50 Gt yr^{-1} from 2010 to 2017, with D_{Gardner} being the lowest. GRACE measures a smaller mass loss in the beginning of the period, and then around 2009 the GRACE mass loss increases. Both Gardner et al. (2018) and Rignot et al. (2019) have found an increasing discharge in West Antarctica. However due to the limited temporal resolution from Gardner et al. (2018), the discharge is assumed constant, resulting in an equal offset in $\mathrm{SMB}-D$ from 2002–2009, but then diverging results from 2010. This shows that in areas where there are large changes in the dynamic mass loss, discharge values with a higher temporal resolution are needed.

Over the East GAIS the agreement between GRACE and $\mathrm{SMB}-D_{\mathrm{Gardner}}$ is remarkably good. Between 2009 and 2011 large snowfall events were observed in Dronning Maud Land (Boening et al., 2012; Lenaerts et al., 2013) (basins 5–8 in Fig. 4). These snowfall events led to rapid mass gain, which is seen in both GRACE and $\mathrm{SMB}-D_{\mathrm{Gardner}}$, especially in 2009–2010 (Fig. 8c). This mass gain is less pronounced in $\mathrm{SMB}-D_{\mathrm{Rignot}}$ because it estimates an overall mass loss for the period. In the SMB signal there are yearly variabilities; however, these variabilities are larger in the GRACE data compared to $\mathrm{SMB}-D$. For the entire GAIS GRACE detects a mass loss of 900 Gt, $\mathrm{SMB}-D_{\mathrm{Gardner}}$ shows a mass gain of 500 Gt, and $\mathrm{SMB}-D_{\mathrm{Gardner}}$ shows a mass loss of 4000 Gt, for the overlapping period 2002–2017. The majority of that difference between GRACE and $\mathrm{SMB}-D_{\mathrm{Gardner}}$ can be attributed to the AP. The difference between GRACE and $\mathrm{SMB}-D_{\mathrm{Rignot}}$ arises from the AP and East GAIS.

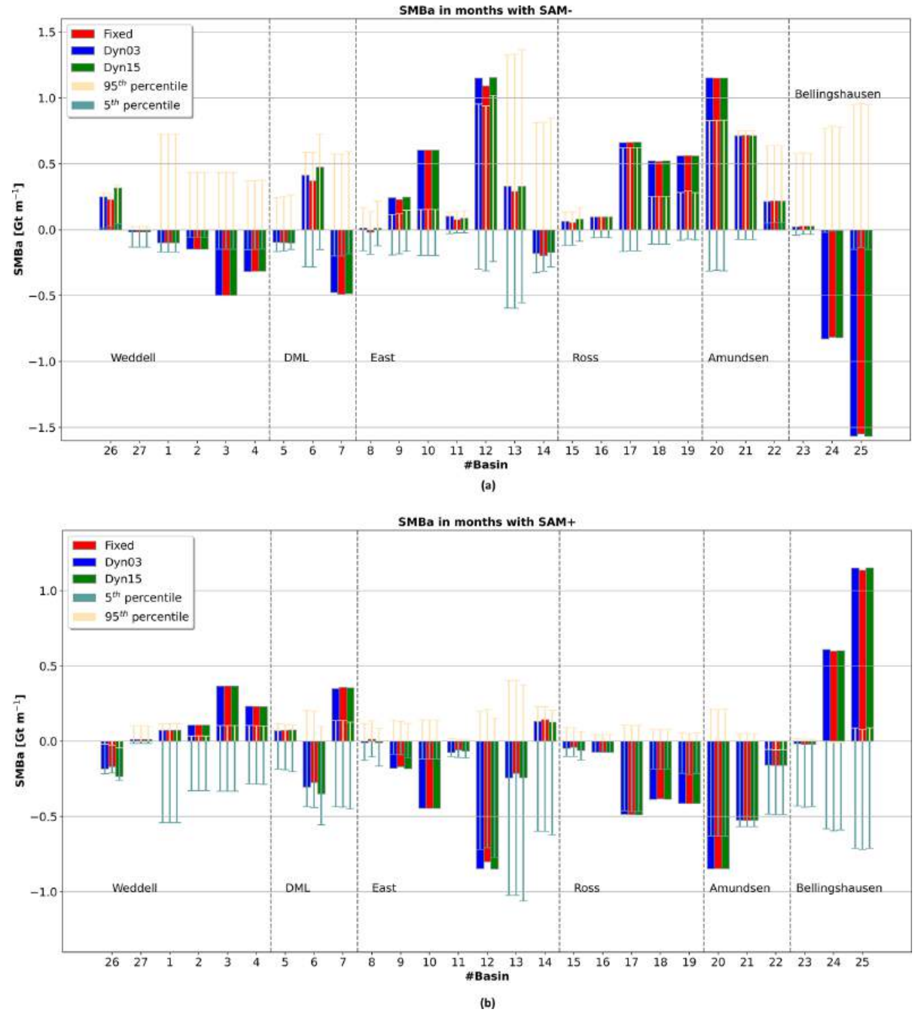

Figure 9. SMBa (monthly values minus mean values) in months for SAM− **(a)** and SAM+ **(b)**, for each basin. The vertical dashed lines split the basins into areas. Starting from the left, we show basins towards the Weddell Sea, Dronning Maud Land, eastern coast, Ross Sea, western coast/Amundsen Sea, and Bellingshausen Sea. The thin bars are the 5th and 95th percentiles, for the bootstrapping analysis with 1200 runs. Locations of the basins can be seen in Fig. 4. In basins where the SMBa values fall outside the percentiles, there is a robust relationship between the SMB and SAM.

4.2 Circulation effects on SMB and the Southern Annular Mode

We observe a robust (outside the 5th–95th percentile range) relationship between SMB and SAM in 13 out of the 27 basins (Fig. 9a and b). For each phase of the SAM, SMB anomalies (SMBa) are defined as the SMB in months with a SAM− or SAM+ monthly mean minus SMB over the full period. The SMBa for SAM−, when the westerlies are further away from the Antarctic continent, shows magnitudes well outside the percentiles for all model simulations. Basins 2 and 3 that have outlets to the Filchner–Ronne ice shelf (EAIS); basin 4 in Dronning Maud Land (EAIS); basin 7 in Enderby Land (EAIS); basins 9, 10, and 12 surrounding the Amery ice shelf (EAIS); basins 17, 18, and 19 with an outlet into Ross ice shelf; basin 20 in Marie Byrd Land (WAIS); and basins 24 and 25 located on the windward side of the AP are particularly affected by SAM−. For SAM+, when the westerlies are closer to the continent the SMBa magnitudes are generally smaller and have an opposite sign; however we see the same pattern in the same basins as for SAM−. A SAM+ phase results in a relatively low pressure over the AIS compared to the midlatitudes, and we see a negative SMBa in 16 of 27 basins, namely 6, 9–13, 15–23, and 26 (Fig. 9b). Marshall et al. (2017) reported a similar signal for precipitation, which confirms our results since precipitation is the main driver of SMB. Basin 26 shows a negative SMBa, and basin 27 has a slightly positive SMBa, which is due to the steep orography on the windward side of the AP creating a shadowing effect on the leeward side of the AP. For SAM− the SMBa signal is opposite, and the mean magnitude of the signal is 26 % larger in all basins (Fig. 9a). During months of SAM+ the average SAM index is 1.45. Figure 9 shows that basins 1–5, 7, 14, 24–25, and 27 have SMB anomalies (SMBa) of the same sign as the SAM: SMB is 0.28 Gt per month higher than average in the case of SAM+ and 0.39 Gt per month lower than average in the case of SAM−. Those basins are mostly located in the east, Ross, and Amundsen Sea sectors. Contrastingly, basins 6, 8–13, 15–23, and 26 have SMB 0.32 Gt per month below average in months of SAM+ and 0.43 Gt per month above average in months of SAM−. These basins are mostly located in the Weddell Sea, Dronning Maud Land, and Bellingshausen sectors. For months with SAM− the average SAM index is −1.36. We can see that for SAM of similar absolute magnitude, SAM− has a stronger impact on SMB over the GAIS.

In both positive and negative SAM events basins 24 and 25 on the windward side of the AP show strong correlation between the SAM index and SMB magnitude also reported by Marshall et al. (2017). So even though the AP is narrow (50 to 300 km across) the SAM plays an important role. Comparing with Vannitsem et al. (2019), we see agreement in large parts of West Antarctica. However, it is difficult to compare in East Antarctica because we use basins, and most of them go far inland, whereas Vannitsem et al. (2019) defined narrow coastal regions and one large plateau region.

From 1980 to 2017 the SAM has become more positive (Fogt and Marshall, 2020), this positive trend in the SAM is attributed to stratospheric ozone depletion (Thompson et al., 2011; Fogt et al., 2017). If this trend continues the basins on the leeward side of the AP will see a smaller mass gain in the future, which could accelerate the collapse of the Larsen ice shelf. This is also seen in basins 9, 10, 11, and 12 surrounding the Amery ice shelf and basin 21 where Thwaites glacier is located. Not all of the above-mentioned basins show δSMB signals that are statistically robust (i.e. the signals are within the 5th or 95th percentiles), but if the trend in the positive SAM continues, it might become an important factor in the future (Fogt and Marshall, 2020).

It is thus important to take the SAM phases into account when investigating the SMB at a regional scale. Furthermore it is extremely important that global circulation models resolve the SAM realistically if future climate projections are to be used with confidence to make projections of sea level rise from Antarctica.

5 Conclusions

We estimate the Antarctic SMB to range from 2583.4 ± 121.6 to $2473.5 \pm 114.4\,\mathrm{Gt\,yr^{-1}}$ over the total area of the ice sheet including shelves and between 1995.4 ± 99.3 and 1963.3 ± 96.2 over the grounded part, for the period from 1980 to 2017. The difference is due to different subsurface models forced with HIRHAM5 outputs. The Dyn03 version has the highest integrated SMB over the ToAIS (GAIS) at 2583.4 ± 121.6 (1995.4 ± 99.3) $\mathrm{Gt\,yr^{-1}}$, and Dyn15 has the lowest 2473.5 ± 114.4 (1963.3 ± 96.2) $\mathrm{Gt\,yr^{-1}}$. The Fixed version is $\approx 19\,\mathrm{Gt\,yr^{-1}}$ lower than Dyn03 over the ToAIS and $0.2\,\mathrm{Gt\,yr^{-1}}$ lower than Dyn03 over the GAIS. The simulations compute nearly equal SMB over the interior. The main differences are seen in the coastal areas of West AIS and the AP. The Dyn15 simulation gives the smallest SMB estimate and is thus closest to other studies (van Wessem et al., 2018; Souverijns et al., 2019; Agosta et al., 2019); however it is still 200–300 $\mathrm{Gt\,yr^{-1}}$ higher. Evaluating the modelled density profiles shows the Lagrangian model set-up has the lowest bias and standard deviation in density differences for densities greater than $550\,\mathrm{kg\,m^{-3}}$; for densities less than $550\,\mathrm{kg\,m^{-3}}$ the Eulerian performance is best. In general all models overestimate the densities on the Filchner–Ronne ice shelf and underestimate the densities in Marie Byrd Land and around the Ross ice shelf. It is therefore clear that there are regional systematic biases. To evaluate our simulated SMB, we compare our simulations with the SumUp accumulation rates. Half of the comparing sites fit with ±13 %; moreover we also compare our simulations to MB estimations (SMB minus discharge) from GRACE. We use discharge from two sources: Gardner et al. (2018) and Rignot et al. (2019). There are large differences between the discharge values over the AP, leading to our simulations overestimating MB when using D_{Gardner} and underestimating MB when using D_{Rignot}. Over the East GAIS the MB is underestimated using D_{Rignot} but fits quite well to the GRACE MB when using D_{Gardner}. These disagreements between the two observational datasets makes it hard to distinguish how well the modelled SMB fits with total mass balance estimates.

Regional precipitation is strongly linked to the phase of the SAM as shown by the bootstrap analysis. By using outputs from HIRHAM5 forced with ERA-Interim to resolve the SAM correctly, robust signals are identified in 13 out of 27 basins. It is clear that the phase of the SAM affects the spatial distribution of SMB. When SAM is negative, there is a lower SMB on the windward side of the Antarctica Peninsula and a higher SMB over the plateau and vice versa when SAM is positive. This makes the SAM an important factor to evaluate in global models when downscaling models for projecting future Antarctic climate.

Code availability. A MATLAB version of the subsurface model code used in these study is available here: https://doi.org/10.5281/zenodo.4542767 (Vandecrux, 2021).

Data availability. A selection of the HIRHAM5 data are available here: http://ensemblesrt3.dmi.dk/data/prudence/temp/RUM/HIRHAM/ANTARCTICA/ (Mottram and Boberg, 2021), and a selection of the subsurface model data are available here: https://doi.org/10.5281/zenodo.5005265 (Hansen et al., 2021).

More data are available by contacting nichsen@space.dtu.dk.

Author contributions. NH, SBS, and RM conceived the study. NH ran the subsurface model simulations with help from PLL, made the plots, and performed the analysis under guidance from RM, SBS, PLL, PT, BV, and RF. HIRHAM5 model simulation was carried out by FB and RM. The Fixed model was developed by PLL, and the dynamical versions were developed by BV and PLL. RF prepared the GRACE data. All authors contributed to writing the paper.

Competing interests. The authors declare that they have no conflict of interest.

Acknowledgements. This publication was supported by PROTECT. Data analysis was supported by the Danish state through the National Centre for Climate Research (NCKF). We also gratefully acknowledge the ESA CCI Ice Sheets project as a forum for the interchange of ideas that led directly to this study.

Financial support. This project has received funding from the European Union's Horizon 2020 research and innovation programme under grant agreement no. 869304, PROTECT contribution number 18. HIRHAM5 regional climate model simulations were carried out by Ruth Mottram and Fredrik Boberg as part of the ice2ice project, a European Research Council project under the European Community's Seventh Framework Programme (FP7/2007-2013)/ERC grant agreement 610055. GRACE data analysis was supported by ESA Climate Change Initiative for the Greenland ice sheet funded via ESA ESRIN contract number 4000104815/11/I-NB and the Sea Level Budget Closure CCI project funded via ESA-ESRIN contract number 4000119910/17/I-NB.

Review statement. This paper was edited by Alexander Robinson and reviewed by Christoph Kittel and one anonymous referee.

References

Agosta, C., Amory, C., Kittel, C., Orsi, A., Favier, V., Gallée, H., van den Broeke, M. R., Lenaerts, J. T. M., van Wessem, J. M., van de Berg, W. J., and Fettweis, X.: Estimation of the Antarctic surface mass balance using the regional climate model MAR (1979–2015) and identification of dominant processes, The Cryosphere, 13, 281–296, https://doi.org/10.5194/tc-13-281-2019, 2019.

Bell, R. E., Banwell, A. F., Trusel, L. D., and Kingslake, J.: Antarctic surface hydrology and impacts on ice-sheet mass balance, Nat. Clim. Change, 8, 1044–1052, 2018.

Boberg, F., Mottram, R., Hansen, N., Yang, S., and Langen, P. L.: Higher mass loss over Greenland and Antarctic ice sheets projected in CMIP6 than CMIP5 by high resolution regional downscaling EC-Earth, The Cryosphere Discuss. [preprint], https://doi.org/10.5194/tc-2020-331, 2020.

Boening, C., Lebsock, M., Landerer, F., and Stephens, G.: Snowfall-driven mass change on the East Antarctic ice sheet, Geophys. Res. Lett., 39, L21501, https://doi.org/10.1029/2012GL053316, 2012.

Calonne, N., Geindreau, C., Flin, F., Morin, S., Lesaffre, B., Rolland du Roscoat, S., and Charrier, P.: 3-D image-based numerical computations of snow permeability: links to specific surface area, density, and microstructural anisotropy, The Cryosphere, 6, 939–951, https://doi.org/10.5194/tc-6-939-2012, 2012.

Christensen, O., Gutowski, W., Nikulin, G., and Legutke, S.: CORDEX Archive design, Danish Climate Centre, Danish Meteorological Institute, Danish Meteorological Institute. Technical Report, available at: https://is-enes-data.github.io/cordex_archive_specifications.pdf (last access: May 2020), 2014.

Christensen, O. B., Drews, M., Christensen, J. H., Dethloff, K., Ketelsen, K., Hebestadt, I., and Rinke, A.: The HIRHAM regional climate model, Version 5 (beta), Danish Climate Centre, Danish Meteorological Institute, Danish Meteorological Institute, Technical Report, 2007.

Colbeck, S.: A theory for water flow through a layered snowpack, Water Resour. Res., 11, 261–266, https://doi.org/10.1029/WR011i002p00261, 1975.

Coléou, C. and Lesaffre, B.: Irreducible water saturation in snow: experimental results in a cold laboratory, Ann. Glaciol., 26, 64–68, 1998.

Dalaiden, Q., Goosse, H., Lenaerts, J. T., Cavitte, M. G., and Henderson, N.: Future Antarctic snow accumulation trend is dominated by atmospheric synoptic-scale events, Commun. Earth Environ., 1, 1–9, 2020.

Dee, D. P., Uppala, S. M., Simmons, A. J., Berrisford, P., Poli, P., Kobayashi, S., Andrae, U., Balmaseda, M. A., Balsamo, G., Bauer, P., Bechtold, P., Beljaars, A. C. M., van de Berg, L., Bidlot, J., Bormann, N., Delsol, C., Dragani, R., Fuentes, M., Geer, A. J., Haimberger, L., Healy, S. B., Hersbach, H., Hólm, E. V., Isaksen, L., Kållberg, P., Köhler, M., Matricardi, M., McNally, A. P., Monge-Sanz, B. M., Morcrette, J.-J., Park, B.-K., Peubey, C., de Rosnay, P., Tavolato, C., Thépaut, J.-N., and Vitart, F.: The ERA-Interim reanalysis: Configuration and performance of the data assimilation system, Q. J. Roy. Meteorol. Soc., 137, 553–597, 2011.

Eerola, K.: About the performance of HIRLAM version 7.0, Hirlam Newslett., 51, 93–102, 2006.

Feser, F., Rockel, B., von Storch, H., Winterfeldt, J., and Zahn, M.: Regional climate models add value to global model data: a review and selected examples, B. Am. Meteorol. Soc., 92, 1181–1192, 2011.

Fettweis, X., Hofer, S., Krebs-Kanzow, U., Amory, C., Aoki, T., Berends, C. J., Born, A., Box, J. E., Delhasse, A., Fujita, K., Gierz, P., Goelzer, H., Hanna, E., Hashimoto, A., Huybrechts, P., Kapsch, M.-L., King, M. D., Kittel, C., Lang, C., Langen, P. L., Lenaerts, J. T. M., Liston, G. E., Lohmann, G., Mernild, S. H., Mikolajewicz, U., Modali, K., Mottram, R. H., Niwano, M., Noël, B., Ryan, J. C., Smith, A., Streffing, J., Tedesco, M., van de Berg, W. J., van den Broeke, M., van de Wal, R. S. W., van Kampenhout, L., Wilton, D., Wouters, B., Ziemen, F., and Zolles, T.: GrSMBMIP: intercomparison of the modelled 1980–2012 surface mass balance over the Greenland Ice Sheet, The Cryosphere, 14, 3935–3958, https://doi.org/10.5194/tc-14-3935-2020, 2020.

Fogt, R. L. and Bromwich, D. H.: Decadal variability of the ENSO teleconnection to the high-latitude South Pacific governed by coupling with the southern annular mode, J. Climate, 19, 979–997, 2006.

Fogt, R. L. and Marshall, G. J.: The Southern Annular Mode: variability, trends, and climate impacts across the Southern Hemisphere, Wiley Interdisciplin. Rev.: Clim. Change, 11, e652, https://doi.org/10.1002/wcc.652, 2020.

Fogt, R. L., Goergens, C. A., Jones, J. M., Schneider, D. P., Nicolas, J. P., Bromwich, D. H., and Dusselier, H. E.: A twentieth century perspective on summer Antarctic pressure change and variability and contributions from tropical SSTs and ozone depletion, Geophys. Res. Lett., 44, 9918–9927, 2017.

Forsberg, R., Sørensen, L., and Simonsen, S.: Greenland and Antarctica ice sheet mass changes and effects on global sea level, in: Integrative Study of the Mean Sea Level and Its Components, Space Sciences Series of ISSI, Springer, 58, 91–106, 2017.

Fretwell, P., Pritchard, H. D., Vaughan, D. G., Bamber, J. L., Barrand, N. E., Bell, R., Bianchi, C., Bingham, R. G., Blankenship, D. D., Casassa, G., Catania, G., Callens, D., Conway, H., Cook, A. J., Corr, H. F. J., Damaske, D., Damm, V., Ferraccioli, F., Forsberg, R., Fujita, S., Gim, Y., Gogineni, P., Griggs, J. A., Hindmarsh, R. C. A., Holmlund, P., Holt, J. W., Jacobel, R. W., Jenkins, A., Jokat, W., Jordan, T., King, E. C., Kohler, J., Krabill, W., Riger-Kusk, M., Langley, K. A., Leitchenkov, G., Leuschen, C., Luyendyk, B. P., Matsuoka, K., Mouginot, J., Nitsche, F. O., Nogi, Y., Nost, O. A., Popov, S. V., Rignot, E., Rippin, D. M., Rivera, A., Roberts, J., Ross, N., Siegert, M. J., Smith, A. M., Steinhage, D., Studinger, M., Sun, B., Tinto, B. K., Welch, B. C., Wilson, D., Young, D. A., Xiangbin, C., and Zirizzotti, A.: Bedmap2: improved ice bed, surface and thickness datasets for Antarctica, The Cryosphere, 7, 375–393, https://doi.org/10.5194/tc-7-375-2013, 2013.

Fyke, J., Lenaerts, J. T. M., and Wang, H.: Basin-scale heterogeneity in Antarctic precipitation and its impact on surface mass variability, The Cryosphere, 11, 2595–2609, https://doi.org/10.5194/tc-11-2595-2017, 2017.

Gardner, A. S., Moholdt, G., Scambos, T., Fahnstock, M., Ligtenberg, S., van den Broeke, M., and Nilsson, J.: Increased West Antarctic and unchanged East Antarctic ice discharge over the last 7 years, The Cryosphere, 12, 521–547, https://doi.org/10.5194/tc-12-521-2018, 2018.

Graf, W. and Oerter, H.: Density, δ^{18}O, deuterium, and tritium of firn core FRI14C90_336, PANGAEA, https://doi.org/10.1594/PANGAEA.548629, 2006.

Griggs, J. and Bamber, J.: Antarctic ice-shelf thickness from satellite radar altimetry, J. Glaciol., 57, 485–498, https://doi.org/10.3189/002214311796905659, 2011.

Hall, A. and Visbeck, M.: Synchronous variability in the Southern Hemisphere atmosphere, sea ice, and ocean resulting from the annular mode, J. Climate, 15, 3043–3057, 2002.

Hansen, N., Langen, P. L., Boberg, F., Forsberg, R., Simonsen, S. B., Thejll, P., Vandercrux, B., and Mottram, R.: Downscaled surface mass balance in Antarctica: impacts of subsurface processes and large-scale atmospheric circulation, Zenodo [data set], https://doi.org/10.5281/zenodo.5005265, 2021.

Hermann, M., Box, J. E., Fausto, R. S., Colgan, W. T., Langen, P. L., Mottram, R., Wuite, J., Noël, B., van den Broeke, M. R., and van As, D.: Application of PROMICE Q-transect in situ accumulation and ablation measurements (2000–2017) to constrain mass balance at the southern tip of the Greenland Ice Sheet, J. Geophys. Res.-Earth, 123, 1235–1256, 2018.

Hirashima, H., Yamaguchi, S., Sato, A., and Lehning, M.: Numerical modeling of liquid water movement through layered snow based on new measurements of the water retention curve, Cold Reg. Sci. Technol., 64, 94–103, 2010.

Hui, F., Ci, T., Cheng, X., Scambo, T. A., Liu, Y., Zhang, Y., Chi, Z., Huang, H., Wang, X., Wang, F., Zhao, C., Jin, Z., and Wang, K.: Mapping blue-ice areas in Antarctica using ETM+ and MODIS data, Ann. Glaciol., 55, 129–137, 2014.

Irving, D. and Simmonds, I.: A new method for identifying the Pacific–South American pattern and its influence on regional climate variability, J. Climate, 29, 6109–6125, 2016.

Kaspers, K. A., van de Wal, R. S. W., van den Broeke, M. R., Schwander, J., van Lipzig, N. P. M., and Brenninkmeijer, C. A. M.: Model calculations of the age of firn air across the Antarctic continent, Atmos. Chem. Phys., 4, 1365–1380, https://doi.org/10.5194/acp-4-1365-2004, 2004.

Kim, B.-H., Seo, K.-W., Eom, J., Chen, J., and Wilson, C. R.: Antarctic ice mass variations from 1979 to 2017 driven by anomalous precipitation accumulation, Scient. Rep., 10, 1–9, 2020.

Kingslake, J., Ely, J. C., Das, I., and Bell, R. E.: Widespread movement of meltwater onto and across Antarctic ice shelves, Nature, 544, 349–352, 2017.

Kittel, C., Amory, C., Agosta, C., Jourdain, N. C., Hofer, S., Delhasse, A., Doutreloup, S., Huot, P.-V., Lang, C., Fichefet, T., and Fettweis, X.: Diverging future surface mass balance between the Antarctic ice shelves and grounded ice sheet, The Cryosphere, 15, 1215–1236, https://doi.org/10.5194/tc-15-1215-2021, 2021.

Koenig, L. and Montgomery, L.: Surface Mass Balance and Snow Depth on Sea Ice Working Group (SUMup) snow density subdataset, Greenland and Antartica, Arctic Data Center [data set], 1950–2018, https://doi.org/10.18739/A26D5PB2S, 2019.

Krinner, G., Magand, O., Simmonds, I., Genthon, C., and Dufresne, J.-L.: Simulated Antarctic precipitation and surface mass balance at the end of the twentieth and twenty-first centuries, Clim. Dynam., 28, 215–230, 2007.

Langen, P. L., Mottram, R. H., Christensen, J. H., Boberg, F., Rodehacke, C. B., Stendel, M., van As, D., Ahlstrøm, A. P., Mortensen, J., Rysgaard, S., Petersen, D., Svendsen, K. H., Aðalgeirsdóttir, G., and Cappelen, J.: Quantifying energy and mass fluxes controlling Godthåbsfjord freshwater input in a 5-km simulation (1991–2012), J. Climate, 28, 3694–3713, 2015.

Langen, P. L., Fausto, R. S., Vandecrux, B., Mottram, R. H., and Box, J. E.: Liquid water flow and retention on the Greenland ice sheet in the regional climate model HIRHAM5: Local and large-scale impacts, Front. Earth Sci., 4, 110, https://doi.org/10.3389/feart.2016.00110, 2017.

Lenaerts, J. T., van Meijgaard, E., van den Broeke, M. R., Ligtenberg, S. R., Horwath, M., and Isaksson, E.: Recent snowfall anomalies in Dronning Maud Land, East Antarctica, in a historical and future climate perspective, Geophys. Res. Lett., 40, 2684–2688, 2013.

Lenaerts, J. T., Medley, B., van den Broeke, M. R., and Wouters, B.: Observing and modeling ice sheet surface mass balance, Rev. Geophys., 57, 376–420, 2019.

Lucas-Picher, P., Wulff-Nielsen, M., Christensen, J. H., Aðalgeirsdóttir, G., Mottram, R., and Simonsen, S. B.: Very high resolution regional climate model simulations over Greenland: Identifying added value, J. Geophys. Res.-Atmos., 117, D02108, https://doi.org/10.1029/2011JD016267, 2012.

Marshall, G.: The Climate Data Guide: Marshall Southern Annular Mode (SAM) Index (Station-based), Last modified 19 Mar 2018, edited by: National Center for Atmospheric Research Staff, available at: https://climatedataguide.ucar.edu/climate-data/marshall-southern-annular-mode-sam-index-station-based (last access: February 2021), 2018.

Marshall, G. J. and Thompson, D. W.: The signatures of large-scale patterns of atmospheric variability in Antarctic surface temperatures, J. Geophys. Res.-Atmos., 121, 3276–3289, 2016.

Marshall, G. J., Thompson, D. W., and van den Broeke, M. R.: The signature of Southern Hemisphere atmospheric circulation patterns in Antarctic precipitation, Geophys. Res. Lett., 44, 11–580, 2017.

Medley, B. and Thomas, E.: Increased snowfall over the Antarctic Ice Sheet mitigated twentieth-century sea-level rise, Nat. Climate Change, 9, 34–39, 2019.

Medley, B., Neumann, T. A., Zwally, H. J., and Smith, B. E.: Forty-year Simulations of Firn Processes over the Greenland and Antarctic Ice Sheets, The Cryosphere Discuss. [preprint], https://doi.org/10.5194/tc-2020-266, in review, 2020.

Morris, E., Mulvaney, R., Arthern, R., Davies, D., Gurney, R. J., Lambert, P., De Rydt, J., Smith, A., Tuckwell, R., and Winstrup, M.: Snow densification and recent accumulation along the iSTAR traverse, Pine Island Glacier, Antarctica, J. Geophys. Res.-Earth, 122, 2284–2301, 2017.

Mottram, R. and Boberg, F.: Atmospheric climate model output from the regional climate model HIRHAM5 forced with ERA- Interim for Antarctica [data set], available at: http://ensemblesrt3.dmi.dk/data/prudence/temp/RUM/HIRHAM/ANTARCTICA/, last access: 1 June 2021.

Mottram, R., Boberg, F., Langen, P., Yang, S., Rodehacke, C., Christensen, J. H., and Madsen, M. S.: Surface mass balance of the Greenland ice sheet in the regional climate model HIRHAM5: Present state and future prospects, Low Temperat. Sci., 75, 105–115, 2017.

Mottram, R., Hansen, N., Kittel, C., van Wessem, J. M., Agosta, C., Amory, C., Boberg, F., van de Berg, W. J., Fettweis, X., Gossart, A., van Lipzig, N. P. M., van Meijgaard, E., Orr, A., Phillips, T., Webster, S., Simonsen, S. B., and Souverijns, N.: What is the surface mass balance of Antarctica? An intercomparison of regional climate model estimates, The Cryosphere, 15, 3751–3784, https://doi.org/10.5194/tc-15-3751-2021, 2021.

Oerlemans, J. and Knap, W.: A 1 year record of global radiation and albedo in the ablation zone of Morteratschgletscher, Switzerland, J. Glaciol., 44, 231–238, 1998.

Oerter, H., Wilhelms, F., Jung-Rothenhäusler, F., Göktas, F., Miller, H., Graf, W., and Sommer, S.: Physical properties of firn core DML03C98_09, PANGAEA, https://doi.org/10.1594/PANGAEA.58410, 2000.

Palm, S. P., Kayetha, V., Yang, Y., and Pauly, R.: Blowing snow sublimation and transport over Antarctica from 11 years of CALIPSO observations, The Cryosphere, 11, 2555–2569, https://doi.org/10.5194/tc-11-2555-2017, 2017.

Rignot, E., Mouginot, J., Scheuchl, B., van den Broeke, M., van Wessem, M. J., and Morlighem, M.: Four decades of Antarctic Ice Sheet mass balance from 1979–2017, P. Natl. Acad. Sci. USA, 116, 1095–1103, 2019.

Roeckner, E., Bäuml, G., Bonaventura, L., Brokopf, R., Esch, M., Giorgetta, M., Hagemann, S., Kirchner, I., Kornblueh, L., Manzini , E., Rhodin, A., Schlese, U., Schulzweida, U., and Tompkins, A.: The atmospheric general circulation model ECHAM 5. PART I: Model description, Max-Planck-Institut für Meteorologie, PuRe Report No. 349, 2003.

Rummukainen, M.: State-of-the-art with regional climate models, Wiley Interdisciplin. Rev.: Clim. Change, 1, 82–96, 2010.

Rummukainen, M.: Added value in regional climate modeling, Wiley Interdisciplin. Rev.: Clim. Change, 7, 145–159, 2016.

Shepherd, A., Ivins, E., Rignot, E., Smith, B., Van Den Broeke, M., Velicogna, I., Whitehouse, P., Briggs, K., Joughin, I., Krinner, G., Nowicki, S., Payne, T., Scambos, T., Schlegel, N., Geruo, A., Agosta, C., Ahlstrøm, A., Babonis, G., Barletta, V., Blazquez, A., Bonin, J., Csatho, B., Cullather, R., Felikson, D., Fettweis, X., Forsberg, R., Gallee, H., Gardner, A., Gilbert, L., Groh, A., Gunter, B., Hanna, E., Harig, C., Helm, V., Horvath, A., Horwath, M., Khan, S., Kjeldsen, K. K., Konrad, H., Langen, P., Lecavalier, B., Loomis, B., Luthcke, S., McMillan, M., Melini, D., Mernild, S., Mohajerani, Y., Moore, P., Mouginot, J., Moyano, G., Muir, A., Nagler, T., Nield, G., Nilsson, J., Noel, B., Otosaka, I., Pattle, M. E., Peltier, W. R., Pie, N., Rietbroek, R., Rott, H., Sandberg-Sørensen, L., Sasgen, I., Save, H., Scheuchl, B., Schrama, E., Schröder, L., Seo, K. W., Simonsen, S., Slater, T., Spada, G., Sutterley, T., Talpe, M., Tarasov, L., Van De Berg, W. J., Van Der Wal, W., Van Wessem, M., Vishwakarma, B. D., Wiese, D., and Wouters, B.: Mass balance of the Antarctic Ice Sheet from 1992 to 2017, Nature, 558, 219–222, 2018.

Souverijns, N., Gossart, A., Demuzere, M., Lenaerts, J., Medley, B., Gorodetskaya, I., Vanden Broucke, S., and van Lipzig, N.: A New Regional Climate Model for POLAR-CORDEX: Evaluation of a 30-Year Hindcast with COSMO-CLM2 Over Antarctica, J. Geophys. Res.-Atmos., 124, 1405–1427, 2019.

Thompson, D. W. and Solomon, S.: Interpretation of recent Southern Hemisphere climate change, Science, 296, 895–899, 2002.

Thompson, D. W., Solomon, S., Kushner, P. J., England, M. H., Grise, K. M., and Karoly, D. J.: Signatures of the Antarctic ozone hole in Southern Hemisphere surface climate change, Nat. Geosci., 4, 741–749, 2011.

Trusel, L. D., Frey, K. E., Das, S. B., Munneke, P. K., and Van Den Broeke, M. R.: Satellite-based estimates of Antarctic surface meltwater fluxes, Geophys. Res. Lett., 40, 6148–6153, 2013.

Turner, J.: The el nino–southern oscillation and antarctica, Int. J. Climatol., 24, 1–31, 2004.

Turner, J., Phillips, T., Thamban, M., Rahaman, W., Marshall, G. J., Wille, J. D., Favier, V., Winton, V. H. L., Thomas, E., Wang, Z., van den Broeke, M., Hosking, J. S., and Lachlan-Cope, T.: The dominant role of extreme precipitation events in Antarctic snowfall variability, Geophys. Res. Lett., 46, 3502–3511, 2019.

Van de Berg, W., Van den Broeke, M., Reijmer, C., and Van Meijgaard, E.: Characteristics of the Antarctic surface mass balance, 1958–2002, using a regional atmospheric climate model, Ann. Glaciol., 41, 97–104, 2005.

van den Broeke, M.: Depth and density of the Antarctic firn layer, Arct. Antarct. Alp. Res., 40, 432–438, 2008.

Van Den Broeke, M. R. and Van Lipzig, N. P.: Changes in Antarctic temperature, wind and precipitation in response to the Antarctic Oscillation, Ann. Glaciol., 39, 119–126, 2004.

Van Genuchten, M. T.: A closed-form equation for predicting the hydraulic conductivity of unsaturated soils, Soil Sci. Soc. Am. J., 44, 892–898, 1980.

Van Lipzig, N. P., Marshall, G. J., Orr, A., and King, J. C.: The relationship between the Southern Hemisphere Annular Mode and Antarctic Peninsula summer temperatures: Analysis of a high-resolution model climatology, J. Climate, 21, 1649–1668, 2008.

van Wessem, J. M., van de Berg, W. J., Noël, B. P. Y., van Meijgaard, E., Amory, C., Birnbaum, G., Jakobs, C. L., Krüger, K., Lenaerts, J. T. M., Lhermitte, S., Ligtenberg, S. R. M., Medley, B., Reijmer, C. H., van Tricht, K., Trusel, L. D., van Ulft, L. H., Wouters, B., Wuite, J., and van den Broeke, M. R.: Modelling the climate and surface mass balance of polar ice sheets using RACMO2 – Part 2: Antarctica (1979–2016), The Cryosphere, 12, 1479–1498, https://doi.org/10.5194/tc-12-1479-2018, 2018.

Vandecrux, B.: BaptisteVandecrux/SEB_Firn_model: GEUS surface energy balance and firn model v0.3, Zenodo [code], https://doi.org/10.5281/zenodo.4542767, 2021.

Vandecrux, B., Fausto, R. S., Langen, P. L., van As, D., MacFerrin, M., Colgan, W. T., Ingeman-Nielsen, T., Steffen, K., Jensen, N. S., Møller, M. T., and Box, J. E.: Drivers of firn density on the Greenland ice sheet revealed by weather station observations and modeling, J. Geophys. Res.-Earth, 123, 2563–2576, 2018.

Vandecrux, B., Fausto, R., Van As, D., Colgan, W., Langen, P., Haubner, K., Ingeman-Nielsen, T., Heilig, A., Stevens, C., Mac-Ferrin, M., Niwano, M., Steffen, K., and Box, J. E.: Firn cold content evolution at nine sites on the Greenland ice sheet between 1998 and 2017, J. Glaciol., 66, 591–602, https://doi.org/10.1017/jog.2020.30, 2020a.

Vandecrux, B., Mottram, R., Langen, P. L., Fausto, R. S., Olesen, M., Stevens, C. M., Verjans, V., Leeson, A., Ligtenberg, S., Kuipers Munneke, P., Marchenko, S., van Pelt, W., Meyer, C. R., Simonsen, S. B., Heilig, A., Samimi, S., Marshall, S., Machguth, H., MacFerrin, M., Niwano, M., Miller, O., Voss, C. I., and Box, J. E.: The firn meltwater Retention Model Intercomparison Project (RetMIP): evaluation of nine firn models at four weather station sites on the Greenland ice sheet, The Cryosphere, 14, 3785–3810, https://doi.org/10.5194/tc-14-3785-2020, 2020b.

Vannitsem, S., Dalaiden, Q., and Goosse, H.: Testing for dynamical dependence: Application to the surface mass balance over Antarctica, Geophys. Res. Lett., 46, 12125–12135, 2019.

Verjans, V., Leeson, A., McMillan, M., Stevens, C., van Wessem, J. M., van de Berg, W. J., van den Broeke, M., Kittel, C., Amory, C., Fettweis, X., Hansen, N., Boberg, F., and Mottram, R.: Uncertainty in East Antarctic firn thickness constrained using a model ensemble approach, Geophys. Res. Lett., 48, e2020GL092060, https://doi.org/10.1029/2020GL092060, 2021.

Vionnet, V., Brun, E., Morin, S., Boone, A., Faroux, S., Le Moigne, P., Martin, E., and Willemet, J.-M.: The detailed snowpack scheme Crocus and its implementation in SURFEX v7.2, Geosci. Model Dev., 5, 773–791, https://doi.org/10.5194/gmd-5-773-2012, 2012.

Wagenbach, D., Graf, W., Minikin, A., Trefzer, U., Kipfstuhl, S., Oerter, H., and Blindow, N.: Density, δ^{18}O, deuterium, and tritium of firn core BER02C90_02, PANGAEA, https://doi.org/10.1594/PANGAEA.548622, 1994.

Whitehouse, P. L., Bentley, M. J., Milne, G. A., King, M. A., and Thomas, I. D.: A new glacial isostatic adjustment model for Antarctica: calibrated and tested using observations of relative sea-level change and present-day uplift rates, Geophys. J. Int., 190, 1464–1482, 2012.

Wille, J. D., Favier, V., Dufour, A., Gorodetskaya, I. V., Turner, J., Agosta, C., and Codron, F.: West Antarctic surface melt triggered by atmospheric rivers, Nat. Geosci., 12, 911–916, 2019.

Zuo, Z. and Oerlemans, J.: Modelling albedo and specific balance of the Greenland ice sheet: calculations for the Søndre Strømfjord transect, J. Glaciol., 42, 305–317, https://doi.org/10.3189/S0022143000004160, 1996.

Zwally, H. J., Giovinetto, M. B., Beckley, M. A., and Saba, J. L.: Antarctic and Greenland drainage systems, GSFC Cryospheric Sciences Laboratory, availble at: http://icesat4.gsfc.nasa.gov/cryo_data/ant_grn_drainage_systems.php (last access: January 2021), 2012.

Zwally, J. H. and Fiegles, S.: Extent and duration of Antarctic surface melting, J. Glaciol., 40, 463–475, https://doi.org/10.3189/S0022143000012338, 1994.

A.3 Paper III

The Cryosphere, 16, 711–718, 2022
https://doi.org/10.5194/tc-16-711-2022

The Cryosphere
Open Access

Brief communication: Impact of common ice mask in surface mass balance estimates over the Antarctic ice sheet

Nicolaj Hansen[1,2], **Sebastian B. Simonsen**[2], **Fredrik Boberg**[1], **Christoph Kittel**[3], **Andrew Orr**[4], **Niels Souverijns**[5,6], **J. Melchior van Wessem**[7], **and Ruth Mottram**[1]

[1]Danish Meteorological Institute, Copenhagen, Denmark
[2]Geodesy and Earth Observation, DTU Space, Technical University of Denmark, Kongens Lyngby, Denmark
[3]Laboratory of Climatology, Department of Geography, SPHERES, University of Liège, Liège, Belgium
[4]British Antarctic Survey, High Cross, Madingley Road, Cambridge, UK
[5]Department of Earth and Environmental Sciences, KU Leuven, Leuven, Belgium
[6]Environmental Modelling Unit, Flemish Institute for Technological Research (VITO), Mol, Belgium
[7]Institute for Marine and Atmospheric research Utrecht, Utrecht University, Utrecht, the Netherlands

Correspondence: Nicolaj Hansen (nichsen@space.dtu.dk)

Received: 1 October 2021 – Discussion started: 27 October 2021
Revised: 28 January 2022 – Accepted: 31 January 2022 – Published: 25 February 2022

Abstract. Regional climate models compute ice sheet surface mass balance (SMB) over a mask that defines the area covered by glacier ice, but ice masks have not been harmonised between models. Intercomparison studies of modelled SMB therefore use a common ice mask. The SMB in areas outside the common ice mask, which are typically coastal and high-precipitation regions, is discarded. Ice mask differences change integrated SMB by between 40.5 and 140.6 Gt yr^{-1} (1.8 % to 6.0 % of ensemble mean SMB), equivalent to the entire Antarctic mass imbalance. We conclude there is a pressing need for a common ice mask protocol.

1 Introduction

Detailed estimates of the surface mass balance (SMB) of the Antarctic ice sheet (AIS) are important for interpreting observed ice and sea-level-rise budgets. SMB is the difference between accumulation and ablation at the surface of the ice sheet, which in Antarctica is positive due to the precipitation term dominating, especially in coastal areas, where high relief is often found due to complex/steep orography leading to orographic precipitation (Lenaerts et al., 2019).

Multiple regional climate models (RCMs) are now used to provide estimates of present-day and projected SMB. A selection of five of these were recently the subject of an intercomparison exercise (Mottram et al., 2021) to explore their commonalities and differences. Modelled present-day SMB for the total AIS (ToAIS, which we define as the ice sheet including ice shelves) in the scientific literature ranges from 2177 ± 80 to 2583 ± 122 Gt yr^{-1} (van Wessem et al., 2018; Souverijns et al., 2019; Agosta et al., 2019; Hansen et al., 2021a). The intercomparison in Mottram et al. (2021) gives an ensemble mean of 2329 ± 94 Gt yr^{-1} for the common period of 1987 to 2015 with a range of 1961 ± 70 to 2519 ± 118 Gt yr^{-1} for individual models. Their results also show that while all models vary on an interannual basis directed by the driving ERA-Interim reanalysis, the spread in mean annual SMB estimates originates predominantly from differences in the dynamical core, physical parameterisations, model set-up and the digital elevation model (DEM). Spatial differences in the pattern of SMB can be attributed locally to resolution and differences in orography, but continental-scale variability in the distribution of precipitation is related predominantly to model physics and dynamical cores (Mottram et al., 2021). While all models were able to reproduce observed temperatures, pressures and wind speeds measured at automatic weather stations across the continent, models with nudging or daily reinitialisation had in general smaller biases but even so differing regional patterns of SMB (see e.g. Fig. 4 in Mottram et al., 2021). Comparisons with the

Published by Copernicus Publications on behalf of the European Geosciences Union.

limited SMB observations available show that different models perform better in different regions and at different altitudes, making it challenging to draw general conclusions on a continental scale. Although there are multiple reasons for the range in estimates of SMB, we focus solely on the ice masks in this study in order to assess differences in SMB introduced in post-processing of model estimates. The Mottram et al. (2021) intercomparison study used a common ice mask to remove continent-wide present-day SMB differences related to variations in native ice mask extent. Ice masks are typically made up of a binary grid that defines ice-covered areas, including ice shelves, and the ocean.

Here, we aim to quantify the importance of the ice mask in explaining the difference in SMB simulated by the five RCMs used in the Mottram et al. (2021) intercomparison study: COSMO-CLM^2 (Souverijns et al., 2019), HIRHAM5 (Hansen et al., 2021a), MARv3.10 (Agosta et al., 2019), MetUM (Orr et al., 2015) and RACMO2.3p2 (van Wessem et al., 2018). We investigate the importance of the different native ice masks by creating a surface categorisation that shows the number of models that are represented in each grid cell. Furthermore, we show the spatial differences on a basin scale induced by the common mask. All the native masks have been regridded onto the same grid at a 0.11° ($\approx$ 12.5 km) resolution.

Usually, SMB estimates over the AIS are confined to the grounded AIS because it is only the mass change over the grounded AIS that results directly in sea-level change (Lenaerts et al., 2019). However, we include the ice shelves in all results due to their buttressing of the main ice sheet and thereby importance for the general ice sheet dynamics (Dupont and Alley, 2005). We also show the integrated ΔSMB for the grounded ice sheet in Table 1. Thinning of the ice shelves has already been observed, which results in less buttressing and increased discharge from the grounded ice into the ocean (Gudmundsson et al., 2019). Further, the largest change in end-of-century-projected AIS surface mass balance is shown to occur over the ice shelves (Kittel et al., 2021); it is therefore an important feature to get right in Antarctic modelling.

2 Methods

The five models were run in the Antarctic domain from 1987 to 2015 at different horizontal spatial resolutions and different land–sea mask data sets: COSMO-CLM^2 at a 0.22° resolution, with an ice mask created with data from the Scientific Committee on Antarctic Research (SCAR) Antarctic Digital Database version 5.0 published in 2006 (Lawrence et al., 2019); HIRHAM5 at two resolutions of 0.11 and 0.44°, with an ice mask derived from data created by the United States Geological Survey (USGS) Earth Resources Observation and Science (EROS) Center and consisting of Advanced Very High Resolution Radiometer (AVHRR) data at a 1 km resolution collected from 1992 to 1993 (Eidenshink and Faudeen, 1994); MetUM at a 0.44° resolution, which has an ice mask created from the International Geosphere-Biosphere Programme (IGBP) data in combination with 1 km AVHRR data from the period of 1992 to 1993 (Loveland et al., 2000); MARv3.10 at a 0.32° resolution, with an ice mask created from Bedmap2, which consists of a combination of different data sources such as satellite images, radar and laser altimetry gathered between 2000 and 2010 (Fretwell et al., 2013); and RACMO2.3p2 at a 0.25° resolution, with an ice mask made from a 1 km DEM that was created from the combination of ERS-1 data from 1994 and ICESat data from 2003 to 2008 (Bamber et al., 2009).

Mottram et al. (2021) regridded all native ice masks and SMB estimates to a common grid of 0.11°. We adopt this approach and refer to Mottram et al. (2021) for details. We then compare the SMB over the common mask and the native ice masks used in each individual original model simulation. The common mask is defined as all points where all the regridded native ice masks have grid cells that are covered with permanent ice. We break the simulated SMB down to the basin scale using Antarctic drainage basins derived from Zwally et al. (2012), including ice shelves (see Fig. 1). Note that the Zwally et al. (2012) basins define an outer edge of the ToAIS; in all cases the native masks are slightly larger than the Zwally et al. (2012) definition. To make the grounded ice sheet values in Table 1, we derived the values of the grounded ice sheet, using the data set for grounded ice from Zwally et al. (2012), since not all the native masks explicitly distinguished grounded from floating ice. This way we insured all the native masks and the common mask were compared equally. In Table 2 we opted to define differences only over the basins defined in Zwally et al. (2012) in order to be consistent with other studies. Both the area and the SMB have been calculated for the common mask and native masks in each of the 27 basins. Three values are given for each model basin: $\Delta\text{area}_{\%}$, the percentage difference in area; $\Delta\text{SMB}_{\%}$, the percentage difference in SMB; and $\Delta\text{SMB}_{\text{Gt yr}^{-1}}$, the difference in SMB in Gt yr^{-1}. All calculations are derived by subtracting the regridded native mask from the common mask ($\Delta = \text{common} - \text{native}$).

3 Results

Comparing the area of the common mask to the area of the native masks, we see that the common mask is between 1.85 % and 2.89 % smaller than the different native masks (Table 1). This results in integrated SMB values that are between 40.5 and 140.6 Gt yr^{-1} smaller when using the common mask compared to the native mask, which is up to 6.04 % of the ensemble mean SMB (Mottram et al., 2021) (Table 1). The two HIRHAM5 simulations are very close to having identical areas; however the SMB is larger in the 0.11° simulation, which is most likely due to the steep coastal orography being better resolved and thus leading to increased orographic precipitation (Webster et al., 2008). In the rightmost column $\Delta\mathrm{SMB}_{\mathrm{Gt\,yr^{-1}}}$ over the grounded AIS is shown; when excluding the ice shelves there are still differences between the common mask and the native masks of between 20.1 and 102.4 Gt yr^{-1} (Table 1). It should be pointed out that a small Δ value is not necessarily more correct than a large Δ value in terms of true area size or SMB magnitude. It solely refers to how close it is to the common mask and the ensemble mean from Mottram et al. (2021).

The different model–mask combinations are shown in Fig. 1. Around the Antarctic Peninsula (basins 24–27) there are large mask disagreements over the Larsen C ice shelf and at the tip of the peninsula and the surrounding islands. Parts of the West AIS, especially glaciers such as Getz (basin 20), Thwaites (basin 21) and Abbot (basin 23), also have large mask disagreements as do, in the East AIS, places like the Fimbul, Amery and West ice shelves (Fig. 1). All around the coastline we see, going from the ice sheet and out towards the ocean, that the number of ice masks outside the common mask decreases. Furthermore, two of the masks, COSMO-CLM^2 and MARv3.10, contain non-iced grid cells in their native masks, simulating some parts of non-ice-covered parts of the Transantarctic Mountains (Fig. 1a). Moreover, it is shown how well the common mask agrees to a newly derived ice mask. We compare the common mask to the Reference Elevation Model of Antarctica (REMA; Howat et al., 2019) mask over the Antarctic Peninsula (AP); here it is clear that the common mask is smaller than REMA in most coastal areas around the AP (Fig. 1b).

In order to investigate the regional and basin-scale variability, Table 2 shows values of $\Delta\mathrm{area}_{\%}$, $\Delta\mathrm{SMB}_{\%}$ and $\Delta\mathrm{SMB}_{\mathrm{Gt\,yr^{-1}}}$ for each of the models and for each basin. $\Delta\mathrm{SMB}_{\mathrm{Gt\,yr^{-1}}}$ for basins 20, 23, 24 and 25 is the most sensitive to changes in the mask definition, up to 42.2 Gt yr^{-1}. Of these four, two basins (20 and 23) are in West Antarctica and two on the windward side of the Antarctic Peninsula (24 and 25). Furthermore, the relative difference between $\Delta\mathrm{area}_{\%}$ and $\Delta\mathrm{SMB}_{\%}$ in the model–basin combinations shows large variability between the models and between the basins (Table 2). Summed over all the basins COSMO-CLM^2 has the smallest relative difference between $\Delta\mathrm{area}_{\%}$ and $\Delta\mathrm{SMB}_{\%}$. COSMO-CLM^2 also has the smallest $\Delta\mathrm{SMB}_{\mathrm{Gt\,yr^{-1}}}$ integrated over the 27 basins, which shows that COSMO-CLM^2 is the least affected by the change in ice mask (Table 1). Examination of Mottram et al. (2021) shows that COSMO-CLM^2 is the driest model in the intercomparison and HIRHAM5 0.44° is the wettest, followed by HIRHAM5 0.11° and RACMO2.3p2. All six model simulations show differences of between 0 and -2 Gt yr^{-1} in $\Delta\mathrm{SMB}_{\mathrm{Gt\,yr^{-1}}}$ in basins 2 and 3, which have outlets to the Weddell Sea; basins 8, 9, 10 and 11 surrounding the Amery ice shelf; basins 16, 17, 18, 19 surrounding the Ross ice shelf; basin 22 with an outlet in the Amundsen Sea; and basin 27 on the lee side of the Antarctic Peninsula. Of these 12 basins, 8 of them are in East Antarctica.

4 Discussion

We find the differences between common and native ice mask areas to be small ($< 3\,\%$), but they alter the SMB by up to 6 % over the ToAIS (140.6 Gt yr^{-1}) when compared to the ensemble mean from Mottram et al. (2021). RACMO2.3p2, MARv3.10 and HIRHAM5 0.11° all have $\Delta\mathrm{SMB}_{\mathrm{Gt\,yr^{-1}}}$ values close to or larger than their given uncertainties for their respective SMB estimate. This means that the effect of using the common mask in estimating SMB is close to or greater than the standard deviation of annual mean SMB estimates derived from the interannual variability in modelled SMB. We consider the standard deviation to be a minimum estimate of uncertainty within each model with actual uncertainties likely to be considerably larger but difficult to estimate accurately (Lenaerts et al., 2019). Over the grounded AIS the common mask alters the SMB by up to 102 Gt yr^{-1}; see Table 1. This difference in SMB is close in magnitude to the grounded AIS mass loss of 109 ± 56 Gt yr^{-1} between 1992 and 2017 determined by the second Ice Sheet Mass Balance Inter-comparison Exercise (IMBIE2; Shepherd et al., 2018) and thereby essentially determines if the AIS is losing or gaining mass. This means that small changes in SMB can lead to a non-negligible change in the total mass budget of the AIS. The model mean of the grounded $\Delta\mathrm{SMB}_{\mathrm{Gt\,yr^{-1}}}$ is 54.2 Gt yr^{-1}, which would make a sizeable change in the mass balance results (Table 1). Basin 25 has few or no ice shelves; thus it has one of the largest impacts for $\Delta\mathrm{SMB}_{\mathrm{Gt\,yr^{-1}}}$ for both the grounded basin (not shown) and when ice shelves are included.

Given the importance of the ice shelves to the dynamics of grounded ice, we argue that they are important to include in SMB models accurately. Furthermore, we speculate that there may be similar considerations when defining the grounded ice sheet for SMB assessments. This clearly shows the RCMs ice mask is key in integrated assessments of the Antarctic mass balance. These differences between area change and SMB change are the result of the area differences being located in the coastal regions, some of which are also high-relief regions, leading to effects on the SMB that are disproportionately high relative to the area.

In each grid cell between one and six native masks can have ice in them; this results in 63 combinations of model coverage, in addition to the common mask (not shown). These different area coverage combinations around the ice sheet are partly driven by differences in ice masks and partly by differences in resolution. However, we cannot identify any systematic or model-specific biases on a regional scale. The native ice masks vary around the coastline arbitrarily, which is partly due to the time when the ice mask was created and what data are used to create the native ice mask. For example,

Table 1. From left to right the columns show the RCM name; $\Delta\text{area}_{\%}$ and $\Delta\text{SMB}_{\text{Gt yr}^{-1}}$ – both between the common mask and the native mask over the ToAIS; $\Delta\text{SMB}_{\%}$ – the difference between $\Delta\text{SMB}_{\text{Gt yr}^{-1}}$ and the SMB ensemble mean from Mottram et al. (2021), which is 2329 Gt yr^{-1}, the yearly SMB for the individual models integrated over the common mask with uncertainties of 1 standard deviation; and finally $\Delta\text{SMB}_{\text{Gt yr}^{-1}}$ over the grounded AIS.

Model	Δarea [%]	ΔSMB [Gt yr^{-1}]	ΔSMB [%]	SMB [Gt yr^{-1}]	Grounded ΔSMB [Gt yr^{-1}]
HIRHAM5 0.11°	−2.43	−140.6	−6.04	2452 ± 107	−102.4
HIRHAM5 0.44°	−2.49	−69.5	−2.99	2518 ± 118	−40.7
MARv3.10	−2.89	−91.9	−3.95	2445 ± 91	−54.1
COSMO-CLM^2	−1.94	−40.5	−1.77	1961 ± 70	−20.1
RACMO2.3p2	−1.85	−119.6	−5.13	2399 ± 101	−74.0
MetUM	−2.49	−57.6	−2.47	2191 ± 101	−33.9

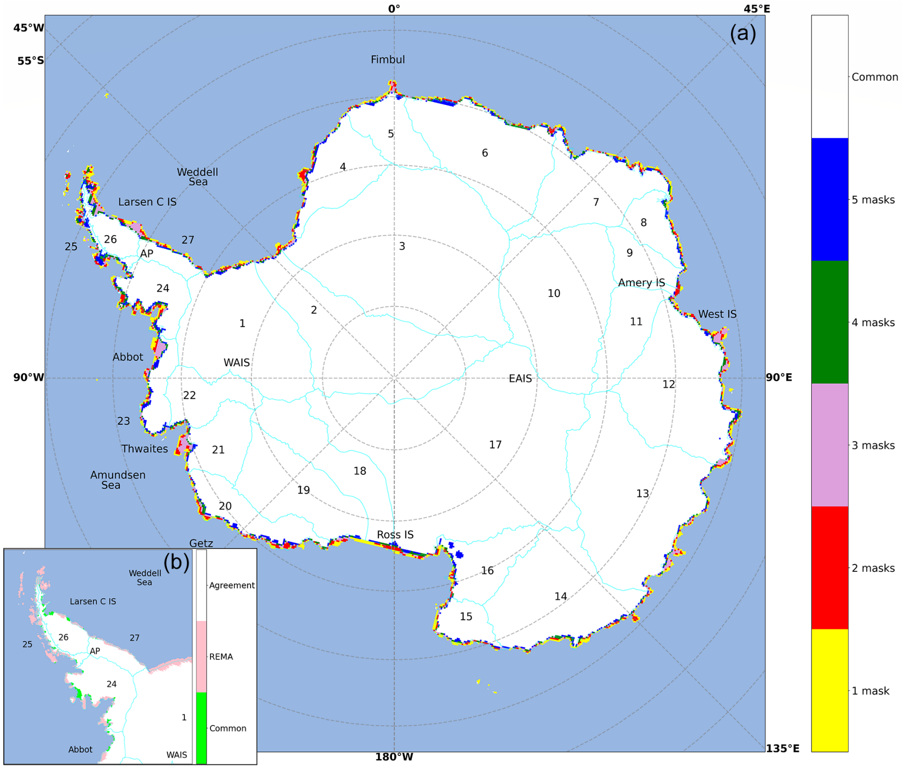

Figure 1. Panel **(a)** shows the ice mask agreement; the white area is the common mask (i.e. where all six masks have ice), and the colours around the coastline represents the number of native masks that have ice outside the common mask. The numbers refer to the 27 drainage basins with ice shelves, outlined in turquoise, and IS is short for ice shelf and AP, WAIS and EAIS are the Antarctic Peninsula, West AIS and East AIS respectively. Panel **(b)** is a section of the AP displaying the REMA mask, the common mask and where they agree.

the HIRHAM5 and MetUM ice masks are created from data collected 3 decades ago, yet there have been multiple calving events since the data collection. The native ice masks from COSMO-CLM^2 and MARv3.10 are created from data collected more recently and in a higher resolution. The higher resolution is also a benefit over the Antarctic Peninsula and in coastal areas where there is complex orography, where a higher resolution can also change the orographic precipitation.

The common mask is introduced during the post-processing stage after running the RCMs with their native masks. This has the disadvantage that model variables where

Table 2. Rows 1 to 27 are basins, and the columns are the RCMs. There are two numbers in each grid cell: the bottom number in magenta is the difference in area between the common mask and native masks ($\Delta\text{area}_{\%}$) in each basin. The upper number in orange shows the difference in SMB between the common mask and native masks ($\Delta\text{SMB}_{\%}$) in each basin. The grid cell colour shows the difference in SMB in Gt yr^{-1} ($\Delta\text{SMB}_{\text{Gt yr}^{-1}}$). All calculations are derived by subtracting the native mask from the common mask ($\Delta = \text{common} - \text{native}$). The differences are shifted left if $\Delta\text{area}_{\%}$ is greater than $\Delta\text{SMB}_{\%}$ and right if $\Delta\text{SMB}_{\%}$ is greater than $\Delta\text{area}_{\%}$. The bottom row is the summed ΔSMB values over 27 basins, for each model.

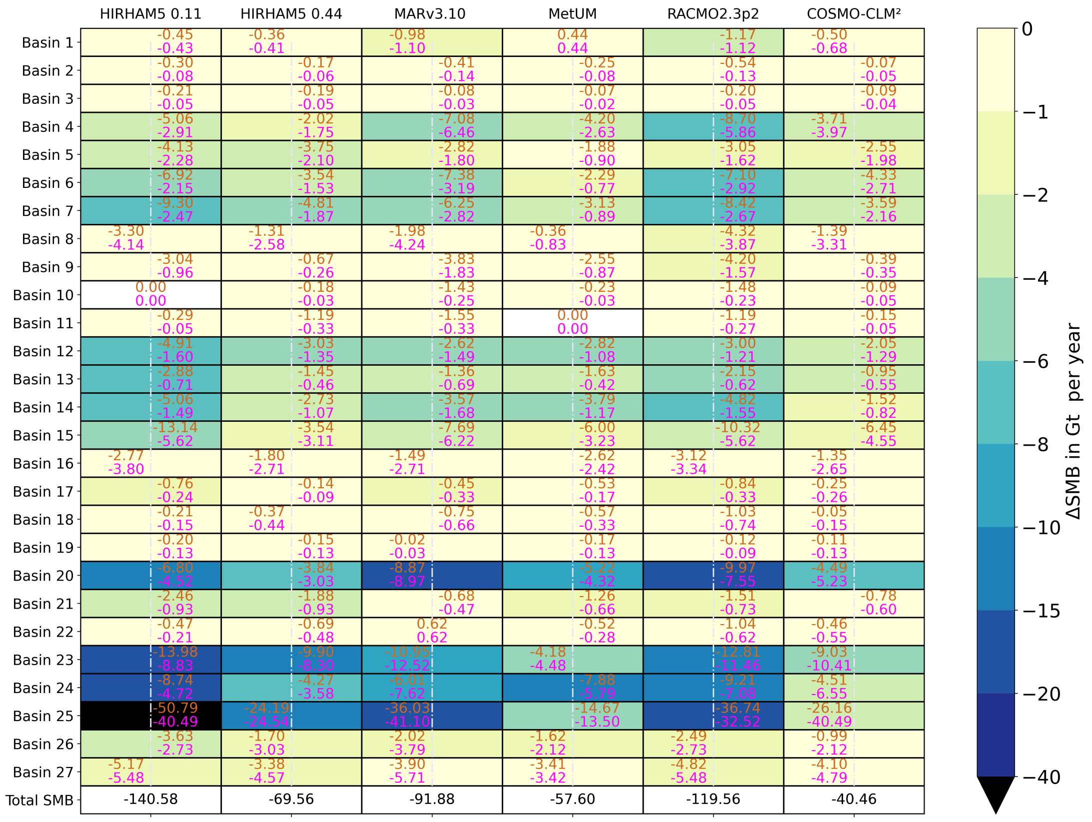

	HIRHAM5 0.11	HIRHAM5 0.44	MARv3.10	MetUM	RACMO2.3p2	COSMO-CLM²
Basin 1	-0.45 -0.43	-0.36 -0.41	-0.98 -1.10	0.44 0.44	-1.17 -1.12	-0.50 -0.68
Basin 2	-0.30 -0.08	-0.17 -0.06	-0.41 -0.14	-0.25 -0.08	-0.54 -0.13	-0.07 -0.05
Basin 3	-0.21 -0.05	-0.19 -0.05	-0.08 -0.03	-0.07 -0.02	-0.20 -0.05	-0.09 -0.04
Basin 4	-5.06 -2.91	-2.02 -1.75	-7.08 -6.46	-4.20 -2.63	-8.70 -5.86	-3.71 -3.97
Basin 5	-4.13 -2.28	-3.75 -2.10	-2.82 -1.80	-1.88 -0.90	-3.05 -1.62	-2.55 -1.98
Basin 6	-6.92 -2.15	-3.54 -1.53	-7.38 -3.19	-2.29 -0.77	-7.10 -2.92	-4.33 -2.71
Basin 7	-9.30 -2.47	-4.81 -1.87	-6.25 -2.82	-3.13 -0.89	-8.42 -2.67	-3.59 -2.16
Basin 8	-3.30 -4.14	-1.31 -2.58	-1.98 -4.24	-0.36 -0.83	-4.32 -3.87	-1.39 -3.31
Basin 9	-3.04 -0.96	-0.67 -0.26	-3.83 -1.83	-2.55 -0.87	-4.20 -1.57	-0.39 -0.35
Basin 10	0.00 0.00	-0.18 -0.03	-1.43 -0.25	-0.23 -0.03	-1.48 -0.23	-0.09 -0.05
Basin 11	-0.29 -0.05	-1.19 -0.33	-1.55 -0.33	0.00 0.00	-1.19 -0.27	-0.15 -0.05
Basin 12	-4.91 -1.60	-3.03 -1.35	-2.62 -1.49	-2.82 -1.08	-3.00 -1.21	-2.05 -1.29
Basin 13	-2.88 -0.71	-1.45 -0.46	-1.36 -0.69	-1.63 -0.42	-2.15 -0.62	-0.95 -0.55
Basin 14	-5.06 -1.49	-2.73 -1.07	-3.57 -1.68	-3.79 -1.17	-4.82 -1.55	-1.52 -0.82
Basin 15	-13.14 -5.62	-3.54 -3.11	-7.69 -6.22	-6.00 -3.23	-10.32 -5.62	-6.45 -4.55
Basin 16	-2.77 -3.80	-1.80 -2.71	-1.49 -2.71	-2.62 -2.42	-3.12 -3.34	-1.35 -2.65
Basin 17	-0.76 -0.24	-0.14 -0.09	-0.45 -0.33	-0.53 -0.17	-0.84 -0.33	-0.25 -0.26
Basin 18	-0.21 -0.15	-0.37 -0.44	-0.75 -0.66	-0.57 -0.33	-1.03 -0.74	-0.05 -0.15
Basin 19	-0.20 -0.13	-0.15 -0.13	-0.02 -0.03	-0.17 -0.13	-0.12 -0.09	-0.11 -0.13
Basin 20	-6.80 -4.52	-3.84 -3.03	-8.87 -8.97	-5.22 -4.32	-9.97 -7.55	-4.49 -5.23
Basin 21	-2.46 -0.93	-1.88 -0.93	-0.68 -0.47	-1.26 -0.66	-1.51 -0.73	-0.78 -0.60
Basin 22	-0.47 -0.21	-0.69 -0.48	0.62 0.62	-0.52 -0.28	-1.04 -0.62	-0.46 -0.55
Basin 23	-13.98 -8.83	-9.90 -8.30	-10.95 -12.52	-4.18 -4.48	-12.81 -11.46	-9.03 -10.41
Basin 24	-8.74 -4.72	-4.27 -3.58	-6.01 -7.62	-7.88 -5.79	-9.21 -7.08	-4.51 -6.55
Basin 25	-50.79 -40.49	-24.19 -24.54	-36.03 -41.10	-14.67 -13.50	-36.74 -32.52	-26.16 -40.49
Basin 26	-3.63 -2.73	-1.70 -3.03	-2.02 -3.79	-1.62 -2.12	-2.49 -2.73	-0.99 -2.12
Basin 27	-5.17 -5.48	-3.38 -4.57	-3.90 -5.71	-3.41 -3.42	-4.82 -5.48	-4.10 -4.79
Total SMB	-140.58	-69.56	-91.88	-57.60	-119.56	-40.46

the fluxes are linked to the orography, such as precipitation, can introduce a bias if the native mask is located differently in the domain compared to the common mask. The same orography bias can be true for winds and thus the sublimation rates as well. High precipitation rates are often strongly linked to the steep orography in coastal areas around Antarctica, especially in West Antarctica and on the windward side of the Antarctic Peninsula (basins 24 and 25), which is also where we see the largest differences in $\Delta\text{SMB}_{\text{Gt yr}^{-1}}$ in Table 2. Comparing the size of the common mask with the REMA mask over the Antarctic Peninsula shows that the common mask is smaller around most of the coastline (Fig. 1b).

The large differences in $\Delta\text{SMB}_{\text{Gt yr}^{-1}}$ and $\Delta\text{area}_{\%}$ found in this study suggest the need for more work to be done on a community basis to define a common mask, ideally before further RCM runs are conducted with the aim of contributing to any model intercomparison study. As the computational demands vary from model to model, we cannot expect the modelling groups to run on the same spatial grid resolution. Therefore, we suggest a three-stage effort be undertaken:

Step 1. Agree on a state-of-the-art DEM of the Antarctic continent, with a sufficiently high spatial resolution to be appropriate for even kilometre and sub-kilometre models (Orr et al., 2021). This could in our minds be REMA (Howat et al., 2019) at a 100 m grid resolution. This 100 m grid would form the basis for a community grid.

Step 2. Agree on a state-of-the-art delineation of surface types, such as bare rock, ice shelves or ice sheet, for the Antarctic continent, again with the highest possible resolution. Here, we see the grid-independent delineation of Antarctic glaciers as provided by the Randolph Glacier Inventory's shapefiles (RGI Consortium, 2017), combined with the shapefiles from the High resolution vector polygons of the Antarctic coastline data set (Gerrish et al., 2021) as a possibility. These two will then be combined to give the ice mask on the 100 m grid.

Step 3. Provide the community with a common tool for projecting the 100 m grid onto the RCM grid. We suggest that this tool will as a minimum give the variables to be used in further model intercomparisons – grid area (we suggest the Antarctic domain as defined in the Coordinated Regional Climate Downscaling Experiment (CORDEX)); surface elevation; surface types so one can distinguish between grounded ice, floating ice (glaciers/tongues) and rocks/mountain ridges; and ice-cover percentage. The ice-cover percentage will then provide the information needed to have the models contributing equally despite being run at different model resolutions, as the topography of the ice sheet is the same for all models. We imagine the tool consists of required data in a high resolution and a script that can create the grid file in the desired resolution, possibly in a netCDF format since most modelling groups are used to working in this format and it will be easy to handle. Ideally the ice mask would evolve over time as the continent changes; however, we feel it is important to first standardise the approach to creating and using ice masks. Thus, we suggest that it is noted in the mask file which data sets are used to create it and when the data sets were last updated.

5 Conclusions

We have quantified the importance of the choice of ice mask for the Antarctic domain by comparing six different ice masks from the RCM – COSMO-CLM^2, HIRHAM5 (in two resolutions), MARv3.10, MetUM and RACMO2.3p2 – with the common mask defined by Mottram et al. (2021). We find differences of between 40.5 and 140.6 Gt yr^{-1} over the ToAIS and differences of between 20.1 and 102.4 yr^{-1} over the grounded AIS (Table 1), comparing the native mask to the common mask integrated over all the basins in Antarctica. Looking at individual basins, we find area differences from 0 % (HIRHAM5 0.11° basin 10 and MetUM basin 11) up to 40.49 % (HIRHAM5 0.11° basin 25) between the common and native masks (Table 2). Furthermore, area changes do not map to SMB change linearly (Table 2). The biggest differences are in basins 20, 23, 24 and 25, showing that areas with high SMB are most sensitive to mask differences (Table 2). As the native masks are created from different data sets, they do not all include the same ice shelves and ice tongues. We speculate that we introduce a shift in value by first defining the common mask after RCM simulations have been performed on their native masks. Most of the model variables in the SMB equation are sensitive to the orography and therefore sensitive to the representation of it when integrating over the common mask. The effort of defining a common mask should ideally be a community effort and should be done before conducting further model intercomparisons and contributing to joint assessments of mass balance such as the IMBIE assessment.

Data availability. The common and native grid estimates of SMB over native and common masks are available at https://doi.org/10.11583/DTU.16438236.v1 (Hansen et al., 2021b).

Author contributions. NH, RM and SBS conceived the study and wrote the initial draft manuscript. Analysis of simulations was carried out by NH and SBS. Model simulation output and ice masks were provided by FB, CK, AO, JMvW and NS. All authors revised and contributed to the final manuscript.

Competing interests. The contact author has declared that neither they nor their co-authors have any competing interests.

Acknowledgements. Ruth Mottram and Fredrik Boberg acknowledge the support of the Danish state through the National Centre for Climate Research (NCKF). The COSMO-CLM^2 team uses computational resources and services provided by the Flemish Supercomputer Center, funded by the FWO and the Flemish Government EWI department.

Financial support. This project has received funding from the European Union's Horizon 2020 research and innovation programme (PROTECT contribution number 29 (grant no. 869304)). The COSMO-CLM^2 integrations were supported by the Belgian Science Policy Office (BELSPO (grant no. 747 BR/143/A2/AEROCLOUD)) and the Research Foundation – Flanders (FWO (grant nos. 748 G0C2215N and GOF5318N; EOS ID 30454083)).

Review statement. This paper was edited by Joseph MacGregor and reviewed by two anonymous referees.

References

Agosta, C., Amory, C., Kittel, C., Orsi, A., Favier, V., Gallée, H., van den Broeke, M. R., Lenaerts, J. T. M., van Wessem, J. M., van de Berg, W. J., and Fettweis, X.: Estimation of the Antarctic surface mass balance using the regional climate model MAR (1979–2015) and identification of dominant processes, The Cryosphere, 13, 281–296, https://doi.org/10.5194/tc-13-281-2019, 2019.

Bamber, J. L., Gomez-Dans, J. L., and Griggs, J. A.: A new 1 km digital elevation model of the Antarctic derived from combined satellite radar and laser data – Part 1: Data and methods, The Cryosphere, 3, 101–111, https://doi.org/10.5194/tc-3-101-2009, 2009.

Dupont, T. and Alley, R.: Assessment of the importance of ice-shelf buttressing to ice-sheet flow, Geophys. Res. Lett., 32, https://doi.org/10.1029/2004GL022024, 2005.

Eidenshink, J. C. and Faudeen, J. L.: The 1 km AVHRR global land data set: first stages in implementation, Int. J. Remote Sens., 15, 3443–3462, https://doi.org/10.1080/01431169408954339, 1994.

Fretwell, P., Pritchard, H. D., Vaughan, D. G., Bamber, J. L., Barrand, N. E., Bell, R., Bianchi, C., Bingham, R. G., Blankenship, D. D., Casassa, G., Catania, G., Callens, D., Conway, H., Cook, A. J., Corr, H. F. J., Damaske, D., Damm, V., Ferraccioli, F., Forsberg, R., Fujita, S., Gim, Y., Gogineni, P., Griggs, J. A., Hindmarsh, R. C. A., Holmlund, P., Holt, J. W., Jacobel, R. W., Jenkins, A., Jokat, W., Jordan, T., King, E. C., Kohler, J., Krabill, W., Riger-Kusk, M., Langley, K. A., Leitchenkov, G., Leuschen, C., Luyendyk, B. P., Matsuoka, K., Mouginot, J., Nitsche, F. O., Nogi, Y., Nost, O. A., Popov, S. V., Rignot, E., Rippin, D. M., Rivera, A., Roberts, J., Ross, N., Siegert, M. J., Smith, A. M., Steinhage, D., Studinger, M., Sun, B., Tinto, B. K., Welch, B. C., Wilson, D., Young, D. A., Xiangbin, C., and Zirizzotti, A.: Bedmap2: improved ice bed, surface and thickness datasets for Antarctica, The Cryosphere, 7, 375–393, https://doi.org/10.5194/tc-7-375-2013, 2013.

Gerrish, L., Fretwell, P., and Cooper, P.: High resolution vector polygons of the Antarctic coastline (7.4) [Data set], UK Polar Data Centre, Natural Environment Research Council, UK Research and Innovation, https://doi.org/10.5285/cdeb448d-10de-4e6e-b56b-6a16f7c59095, 2021.

Gudmundsson, G. H., Paolo, F. S., Adusumilli, S., and Fricker, H. A.: Instantaneous Antarctic ice sheet mass loss driven by thinning ice shelves, Geophys. Res. Lett., 46, 13903–13909, https://doi.org/10.1029/2019GL085027, 2019.

Hansen, N., Langen, P. L., Boberg, F., Forsberg, R., Simonsen, S. B., Thejll, P., Vandecrux, B., and Mottram, R.: Downscaled surface mass balance in Antarctica: impacts of subsurface processes and large-scale atmospheric circulation, The Cryosphere, 15, 4315–4333, https://doi.org/10.5194/tc-15-4315-2021, 2021a.

Hansen, N., Simonsen, S. B., Mottram, R., Orr, A., Boberg, F., Kittel, C., van Wessem, J. M., and Souverijns, N.: Brief communication: Impact of common ice mask in surface mass balance estimates over the Antarctic ice sheet, Technical University of Denmark [data set], https://doi.org/10.11583/DTU.16438236.v1, 2021b.

Howat, I. M., Porter, C., Smith, B. E., Noh, M.-J., and Morin, P.: The Reference Elevation Model of Antarctica, The Cryosphere, 13, 665–674, https://doi.org/10.5194/tc-13-665-2019, 2019.

Kittel, C., Amory, C., Agosta, C., Jourdain, N. C., Hofer, S., Delhasse, A., Doutreloup, S., Huot, P.-V., Lang, C., Fichefet, T., and Fettweis, X.: Diverging future surface mass balance between the Antarctic ice shelves and grounded ice sheet, The Cryosphere, 15, 1215–1236, https://doi.org/10.5194/tc-15-1215-2021, 2021.

Lawrence, D. M., Fisher, R. A., Koven, C. D., Oleson, K. W., Swenson, S. C., Bonan, G., Collier, N., Ghimire, B., van Kampenhout, L., Kennedy, D., Kluzek, E., Lawrence, P. J., Li, F., Li, H., Lombardozzi, D., Riley, W. J., Sacks, W. J., Shi, M., Vertenstein, M., Wieder, W. R., Xu, C., Ali, A. A., Badger, A. M., Bisht, G., van den Broeke, M., Brunke, M. A., Burns, S. P., Buzan, J., Clark, M., Craig, A., Dahlin, K., Drewniak, B., Fisher, J. B., Flanner, M., Fox, A. M., Gentine, P., Hoffman, F., Keppel-Aleks, G., Knox, R., Kumar, S., Lenaerts, J., Leung, L. R., Lipscomb, W. H., Lu, Y., Pandey, A., Pelletier, J. D., Perket, J., Randerson, J. T., Ricciuto, D. M., Sanderson, B. M., Slater, A., Subin, Z. M., Tang, J., Thomas, R. Q., Val Martin, M., and Zeng, X.: The Community Land Model Version 5: Description of New Features, Benchmarking, and Impact of Forcing Uncertainty, J. Adv. Model. Earth Sy., 11, 4245–4287, https://doi.org/10.1029/2018MS001583, 2019.

Lenaerts, J. T. M., Medley, B., van den Broeke, M. R., and Wouters, B.: Observing and Modeling Ice Sheet Surface Mass Balance, Rev. Geophys., 57, 376–420, https://doi.org/10.1029/2018RG000622, 2019.

Loveland, T. R., Reed, B. C., Brown, J. F., Ohlen, D. O., Zhu, Z., Yang, L., and Merchant, J. W.: Development of a global land cover characteristics database and IGBP DISCover from 1 km AVHRR data, Int. J. Remote Sens., 21, 1303–1330, https://doi.org/10.1080/014311600210191, 2000.

Mottram, R., Hansen, N., Kittel, C., van Wessem, J. M., Agosta, C., Amory, C., Boberg, F., van de Berg, W. J., Fettweis, X., Gossart, A., van Lipzig, N. P. M., van Meijgaard, E., Orr, A., Phillips, T., Webster, S., Simonsen, S. B., and Souverijns, N.: What is the surface mass balance of Antarctica? An intercomparison of regional climate model estimates, The Cryosphere, 15, 3751–3784, https://doi.org/10.5194/tc-15-3751-2021, 2021.

Orr, A., Hosking, J. S., Hoffmann, L., Keeble, J., Dean, S. M., Roscoe, H. K., Abraham, N. L., Vosper, S., and Braesicke, P.: Inclusion of mountain-wave-induced cooling for the formation of PSCs over the Antarctic Peninsula in a chemistry–climate model, Atmos. Chem. Phys., 15, 1071–1086, https://doi.org/10.5194/acp-15-1071-2015, 2015.

Orr, A., Kirchgaessner, A., King, J., Phillips, T., Gilbert, E., Elvidge, A., Weeks, M., Gadian, A., Kuipers Munneke, P., van den Broeke, M., Webster, S., and McGrath, D.: Comparison of kilometre and sub-kilometre scale simulations of a foehn wind event over the Larsen C Ice Shelf, Antarctic Peninsula using the Met Office Unified Model (MetUM), Q. J. Roy. Meteor. Soc., 147, 3472–3492, https://doi.org/10.1002/qj.4138, 2021.

RGI Consortium: Randolph Glacier Inventory – A Dataset of Global Glacier Outlines: Version 6.0, Technical Report, Global Land Ice Measurements from Space, https://doi.org/10.7265/N5-RGI-60, 2017.

Shepherd, A., Ivins, E., Rignot, E., Smith, B., Van Den Broeke, M., Velicogna, I., Whitehouse, P., Briggs, K., Joughin, I., Krinner, G., Nowicki, S., Payne, T., Scambos, T., Schlegel, N., Geruo, A., Agosta, C., Ahlstrøm, A., Babonis, G., Barletta, V., Blazquez, A., Bonin, J., Csatho, B., Cullather, R., Felikson, D., Fettweis, X., Forsberg, R., Gallee, H., Gardner, A., Gilbert, L., Groh, A., Gunter, B., Hanna, E., Harig, C., Helm, V., Horvath, A., Horwath, M., Khan, S., Kjeldsen, K. K., Konrad, H., Langen, P., Lecavalier, B., Loomis, B., Luthcke, S., McMillan, M., Melini, D., Mernild, S., Mohajerani, Y., Moore, P., Mouginot, J., Moyano, G., Muir, A., Nagler, T., Nield, G., Nilsson, J., Noel, B., Otosaka, I., Pattle, M. E., Peltier, W. R., Pie, N., Rietbroek, R., Rott, H., Sandberg-Sørensen, L., Sasgen, I., Save, H., Scheuchl, B., Schrama, E., Schröder, L., Seo, K. W., Simonsen, S., Slater, T., Spada, G., Sutterley, T., Talpe, M., Tarasov, L., Van De Berg, W. J., Van Der Wal, W., Van Wessem, M., Vishwakarma, B. D., Wiese, D., and Wouters, B.: Mass balance of the Antarctic Ice Sheet from 1992 to 2017, Nature, 558, 219–222, 2018.

Souverijns, N., Gossart, A., Demuzere, M., Lenaerts, J., Medley, B., Gorodetskaya, I., Vanden Broucke, S., and van Lipzig, N.: A New Regional Climate Model for POLAR-CORDEX: Evaluation of a 30-Year Hindcast with COSMO-CLM2 Over Antarctica, J. Geophys. Res.-Atmos., 124, 1405–1427, 2019.

van Wessem, J. M., van de Berg, W. J., Noël, B. P. Y., van Meijgaard, E., Amory, C., Birnbaum, G., Jakobs, C. L., Krüger, K., Lenaerts, J. T. M., Lhermitte, S., Ligtenberg, S. R. M., Medley, B., Reijmer, C. H., van Tricht, K., Trusel, L. D., van Ulft, L. H., Wouters, B., Wuite, J., and van den Broeke, M. R.: Modelling the climate and surface mass balance of polar ice sheets using RACMO2 – Part 2: Antarctica (1979–2016), The Cryosphere, 12, 1479–1498, https://doi.org/10.5194/tc-12-1479-2018, 2018.

Webster, S., Uddstrom, M., Oliver, H., and Vosper, S.: A high-resolution modelling case study of a severe weather event over New Zealand, Atmos. Sci. Lett., 9, 119–128, https://doi.org/10.1002/asl.172, 2008.

Zwally, H. J., Giovinetto, M. B., Beckley, M. A., and Saba, J. L.: Antarctic and Greenland Drainage Systems, GSFC Cryospheric Sciences Laboratory, 2012.

A.4 MC Paper I

Geophysical Research Letters

RESEARCH LETTER

10.1029/2020GL092060

Uncertainty in East Antarctic Firn Thickness Constrained Using a Model Ensemble Approach

V. Verjans[1], **A. A. Leeson**[1], **M. McMillan**[1], **C. M. Stevens**[2,3,4], **J. M. van Wessem**[5], **W. J. van de Berg**[5], **M. R. van den Broeke**[5], **C. Kittel**[6], **C. Amory**[6,7], **X. Fettweis**[6], **N. Hansen**[8,9], **F. Boberg**[8], and **R. Mottram**[8]

[1]Lancaster Environment Centre, Lancaster University, Lancaster, UK, [2]Department of Earth and Space Sciences, University of Washington, Seattle, WA, USA, [3]Earth System Science Interdisciplinary Center, University of Maryland, College Park, MD, USA, [4]Department NASA Goddard Space Flight Center, Greenbelt, MD, USA, [5]Institute for Marine and Atmospheric Research Utrecht, Utrecht University, Utrecht, The Netherlands, [6]Department of Geography, Laboratory of Climatology, SPHERES Research Unit, University of Liège, Liège, Belgium, [7]University Grenoble Alpes, CNRS, Institut des Géosciences de L'Environnement, Grenoble, France, [8]Danish Meteorological Institute, Copenhagen, Denmark, [9]Department of Geodynamics, DTU Space, Technical University of Denmark, Kongens Lyngby, Denmark

Key Points:

- By developing an ensemble of 54 model scenarios, we constrain firn thickness change uncertainty in East Antarctica over 1992–2017
- In 9 of 16 basins, modeled firn thickness and altimetry trends agree; elsewhere uncertainty is underestimated or ice flow imbalance exists
- Model uncertainty reaches 1 cm yr^{-1} with snowfall, firn compaction and snow density having spatially variable contributions to uncertainty

Supporting Information:

Supporting Information may be found in the online version of this article.

Correspondence to:

V. Verjans,
v.verjans@lancaster.ac.uk

Citation:

Verjans, V., Leeson, A. A., McMillan, M., Stevens, C. M., van Wessem, J. M., van de Berg, W. J., et al. (2021). Uncertainty in East Antarctic firn thickness constrained using a model ensemble approach. *Geophysical Research Letters*, *48*, e2020GL092060. https://doi.org/10.1029/2020GL092060

Received 11 DEC 2020
Accepted 5 MAR 2021

Abstract

Mass balance assessments of the East Antarctic ice sheet (EAIS) are highly sensitive to changes in firn thickness, causing substantial disagreement in estimates of its contribution to sea-level. To better constrain the uncertainty in recent firn thickness changes, we develop an ensemble of 54 model scenarios of firn evolution between 1992 and 2017. Using statistical emulation of firn-densification models, we quantify the impact of firn compaction formulation, differing climatic forcing, and surface snow density on firn thickness evolution. At basin scales, the ensemble uncertainty in firn thickness change ranges between 0.2 and 1.0 cm yr^{-1} (15%–300% relative uncertainty), with the choice of climate forcing having the largest influence on the spread. Our results show the regions of the ice sheet where unexplained discrepancies exist between observed elevation changes and an extensive set of modeled firn thickness changes estimates, marking an important step toward more accurately constraining ice sheet mass balance.

Plain Language Summary

Firn is the transition stage between snow and ice. The total thickness of the firn layer varies in time and space. In East Antarctica, uncertainty about this variability has a large impact on satellite-based estimates of ice sheet mass change. We combine statistical surrogates of firn-densification models with different climate models over the entire East Antarctic ice sheet. Our ensemble of model combinations demonstrates that firn thickness estimates are poorly constrained. Accounting for their respective uncertainties, modeled firn thickness change and satellite measurements of elevation change are consistent over most of East Antarctica. However, we identify several areas of mismatch between model estimates and elevation change observations, which likely indicates that further improvements are required either in models or in measurement techniques. Alternatively, these disagreements can hint at possible imbalances in the flow of ice, below the firn layer. We quantify how much different sources of uncertainty contribute to the total uncertainty in modeled firn thickness change. The amount of snowfall estimated by climate models mostly dominates the uncertainty, but modeled firn compaction rates and uncertainty in surface snow density also have major contributions in certain areas.

1. Introduction

The Antarctic ice sheet (AIS) is the largest ice body on Earth, holding a total potential contribution to sea-level rise of ~57.2 m (Rignot et al., 2019). The AIS is divided into three entities: the Antarctic Peninsula (AP) and the West and East Antarctic ice sheets (WAIS and EAIS, respectively). The EAIS has shown less dynamic instabilities than the WAIS and AP over the past four decades, but it holds ~90% of the total AIS ice mass and is the area with highest uncertainty concerning recent mass trends (Rignot et al., 2019; Shepherd et al., 2018). A layer of firn, the intermediary stage between snow and ice, covers ~99% of the AIS (Winther et al., 2001). The firn layer thickness, defined here as the depth from the surface until the firn-ice transition, varies from 0 to more than 100 m (van den Broeke, 2008). Firn thickness also fluctuates in time due to changes in firn compaction rates and climatic conditions, primarily net snow accumulation. These fluctuations affect ice sheet mass balance assessments derived from satellite-based altimetry. Measured surface elevation changes are converted into mass changes, but the conversion requires precise knowledge of variability in firn thickness and mass. Atmospheric reanalysis products, Regional Climate Models (RCMs) and Firn Densification Models (FDMs) are therefore used to simulate changes of firn properties and, ultimately, to evaluate ice sheet mass changes with precision (Kuipers Munneke et al., 2015; Li & Zwally, 2011; McMillan et al., 2016; Shepherd et al., 2019; Smith et al., 2020).

By simulating mass fluxes (snowfall, sublimation, and melt), RCMs estimate the surface mass balance (SMB) of ice sheets, which partly determines the evolution of the firn layer. These fluxes and modeled surface temperatures also serve as input forcing for FDMs that explicitly simulate firn compaction rates. Such coupling is required to reproduce seasonal and multi-annual fluctuations in compaction rates (Arthern et al., 2010). Uncertainty in SMB estimates across Antarctica are typically assessed by comparing outputs from different RCMs. While SMB is key to firn thickness evolution because it determines the amount of snow removed and added at the surface, it does not capture the effects of fluctuating firn compaction that must be estimated with FDMs. Differences between FDMs can lead to substantial spread in modeled firn thickness and air content (Lundin et al., 2017), especially if scaled up to ice sheet extent.

Compared to the AP and the WAIS, observed elevation changes across the EAIS over the past 25 years have been generally smaller, and largely driven by snowfall and compaction variability (Davis et al., 2005; Shepherd et al., 2018, 2019). Altimetry-derived mass balance assessments of the EAIS are very sensitive to estimates of firn thickness fluctuations because these are of the same order of magnitude as measured elevation changes. This sensitivity complicates the interpretation of altimetry measurements in this area, and it is unclear whether to attribute elevation changes to ice dynamical imbalance or firn thickness change (Scambos & Shuman, 2016; Shepherd et al., 2018; Zwally et al., 2015). These conflicting assessments motivate precise uncertainty analyses of coupled RCM-FDM systems over the EAIS. Previously, such analyses have been computationally limited; running multiple FDMs for many years at the spatial resolution of RCM grids over the EAIS requires many thousands of simulations. The extent to which estimates of firn thickness change vary by combining different FDMs with different RCMs remains an open question.

To overcome computational limitations and thus improve evaluation of uncertainty in the evolution of firn thickness, we build statistical emulators of nine FDMs. An emulator is a fast and statistically driven approximation of a more complex physical model (O'Hagan 2006; Sacks et al., 1989). By combining the FDM emulators with climatic output from three state-of-the-art polar RCMs, we develop an ensemble of 54 scenarios of EAIS firn thickness change. We exploit these scenarios to constrain uncertainty analyses of firn thickness fluctuations on the EAIS and to quantify the contributions of various sources of uncertainty to the spread of modeled results.

2. Methods

2.1. Ensemble Configuration

To generate our ensemble, we first calibrate each of the nine FDM emulators to its corresponding FDM (Table 1) in a representative range of EAIS climate conditions, and then we use it to emulate compaction rates across the entire EAIS. Changes in SMB as well as climatic forcing for the emulators are computed from three RCMs: RACMO2, MAR and HIRHAM (Table 1). Our modeled scenarios of firn thickness change span the 1992–2017 period. This period is chosen to match the long-term altimetry record of Shepherd et al. (2019), hence facilitating intercomparison of observed elevation changes and modeled firn thickness change experiments of this study. We limit our analysis to the EAIS because surface melt there is minor compared to the AP and WAIS, and FDM fidelity remains questionable for simulating wet firn compaction, water percolation and refreezing (Steger et al., 2017; Vandecrux et al., 2020; Verjans et al., 2019).

Table 1
The Nine Firn Densification Models (FDM), Three Regional Climatic Models (RCM) and Two Surface Density Parameterizations (ρ_0) Used in This Study

	References
FDM	
Armap	Arthern et al. (2010); Verjans et al. (2020)
GSFC-FDMv0	Smith et al. (2020)
Cr	Vionnet et al. (2012); van Kampenhout et al. (2017)
HL	Herron and Langway (1980)
HLmap	Herron and Langway (1980); Verjans et al. (2020)
Lig	Ligtenberg et al. (2011)
LZ15	Li and Zwally (2015)
LZmap	Li and Zwally (2011); Verjans et al. (2020)
Morris	Morris and Wingham (2014)
RCM	
RACMO2.3p2 (27 km)	van Wessem et al. (2018)
MARv3.11 (35 km)	Agosta et al. (2019); Kittel et al. (2020)
HIRHAM5 (12.5 km)	Christensen et al. (2007)
ρ_0	
L11	Ligtenberg et al. (2011)
fixed-350	Smith et al. (2020)

Note. The horizontal resolutions of the RCM grids are given in brackets. All RCMs were forced by the ERA-Interim reanalysis at their boundaries (Dee et al., 2011). See supplementary information for details on the FDMs

2.2. Firn Thickness Change Calculations

Observed ice sheet elevation changes, once corrected for glacial isostatic adjustment, are composed of two different signals: one related to ice dynamical imbalance and one to firn thickness change. In this study, we focus on the latter. The change in firn thickness at time step t, $dh_f(t)$, is given by:

$$dh_f(t) = dh_{\mathrm{acc}}(t) - dh_M(t) - dh_c(t) - dh_{\mathrm{ice}}(t) \tag{1}$$

with all components expressed in meters and considered positive, and t set to a daily time step in this study. The subscript M refers to surface firn removal by melting and *acc* refers to net snow accumulation. Both dh_{acc} and dh_M depend on the RCM-computed mass fluxes and on the value assumed for surface snow density, but they are independent of FDM calculations. The component dh_c is the emulated firn compaction term (Section 2.3). The last component, dh_{ice}, quantifies changes in the flux through the lower boundary of the firn column and thus captures changes in the rate of conversion from firn to ice. Changes in dh_{ice} act on much longer timescales than the other components (Kuipers Munneke et al., 2015; Zwally & Li, 2002). As such, dh_{ice} can be set constant and equal to the average rate of conversion from firn to ice over a reference period (we use 1979–2009, following Ligtenberg et al., 2011), dh^r_{ice}. By assuming firn thickness in steady state, thus without trend, over the reference period, dh^r_{ice} balances the reference period averages of the other components:

$$dh^r_{\mathrm{ice}} = dh^r_{\mathrm{acc}} - dh^r_M - dh^r_c \tag{2}$$

Substituting dh^r_{ice} for dh_{ice} in Equation 1 yields Equation 3. This is equivalent to calculating firn thickness change by computing anomalies in each of the *acc*, M and c components with respect to their average value in the reference period (Li & Zwally, 2015).

$$dh_f(t) = dh_{\mathrm{acc}}(t) - dh_M(t) - dh_c(t) - dh^r_{\mathrm{ice}} \tag{3}$$

In this study, we are interested in the cumulative 1992–2017 firn thickness changes. We thus integrate Equation 3 over this time period to compute a total firn thickness change dh_f^{tot}.

2.3. Emulation of Firn Compaction

The nine FDM emulators are first calibrated at 50 sites on the EAIS and over the entire time span (1979–2017) covered by the output of RCMs (Supplementary Information for details). The goal of the emulation is to capture both long- and short-term sensitivity of dh_c to climatic forcing. The long-term (1979–2017) mean and trend in dh_c are estimated by linear regressions on the long-term means and trends of temperature, accumulation and melt. These linear regressions are specific to each FDM and show good performance in capturing the FDM-computed means and trends at the calibration sites ($R^2 > 0.99$ and $R^2 > 0.97$, respectively). Gaussian Process regression complements the linear regression by capturing short-term fluctuations from the long-term trends as a function of detrended values of temperature and accumulation. We evaluate the emulation capabilities in a leave-one-out cross-validation framework; the nine FDM emulators reproduce the FDM output well, both for the total 1979–2017 dh_c ($R^2 > 0.99$, RMSE = 0.49 m, corresponding to 3.5% of the mean total dh_c) and for daily values ($R^2 > 0.99$, RMSE = 0.15×10^{-3} m) (supplementary information for details).

2.4. Uncertainty Contributions

In order to evaluate uncertainty on the time series of cumulative $dh_f(t)$ and on dh_f^{tot}, we construct a model ensemble; the spread arising from a large number of simulations provides an estimate of uncertainty (e.g., Déqué et al., 2007). Our ensemble includes all combinations of the nine FDM emulators and the three RCMs (Table 1). Furthermore, surface snow density, ρ_0, contributes to uncertainty in all components of dh_f (e.g., Agosta et al., 2019; Ligtenberg et al., 2011). As such, we use two different possibilities for the value of ρ_0: the climate-dependent parameterization of Ligtenberg et al. (2011) and the approach of Smith et al. (2020), which takes a constant value of 350 kg m^{-3} (B. Medley, personal communication, 2020) (Table 1). The different combinations of RCM, FDM and ρ_0 provide 54 different firn thickness change scenarios across the EAIS. We refer to the spread in the model ensemble results as the total ensemble uncertainty to distinguish it from the true uncertainty, which may not be captured by the ensemble. We then use the analysis of variance (ANOVA) theory to partition the total ensemble uncertainty among the three factors RCM, FDM, and ρ_0 (Déqué et al., 2007; von Storch & Zwiers, 1999; Yip et al., 2011). This approach allows us to decompose the variance in model results into the contribution of each factor and of each interaction between these factors (Equation 4).

$$\sigma^2 = \eta^2_{RCM} + \eta^2_{FDM} + \eta^2_{\rho_0} + \eta^2_{RCM-FDM} + \eta^2_{RCM-\rho_0} + \eta^2_{FDM-\rho_0} + \eta^2_{RCM-FDM-\rho_0} \tag{4}$$

where σ^2 is the variance in the ensemble results (m^2) and the η^2 terms are the contributions from each factor and interaction between factors to σ^2. Interaction effects stem from a nonlinear behavior of the three uncertainty sources. Contributions are calculated by computing the sum of squares associated with each η^2 term.

$$\begin{cases} \eta_i^2 = \dfrac{1}{N_i} \sum\limits_{i=1}^{N_i} \left(x_{i..} - x_{...} \right)^2 \\ \eta_{i-j}^2 = \dfrac{1}{N_i\, N_j} \sum\limits_{i=1}^{N_i} \sum\limits_{j=1}^{N_j} \left(x_{ij.} - x_{i..} - x_{.j.} + x_{...} \right)^2 \\ \eta_{i-j-k}^2 = \dfrac{1}{N_i\, N_j\, N_k} \sum\limits_{i=1}^{N_i} \sum\limits_{j=1}^{N_j} \sum\limits_{k=1}^{N_k} \left(x_{ijk} - x_{ij.} - x_{i.k} - x_{.jk} + x_{i..} + x_{.j.} + x_{..k} - x_{...} \right)^2 \end{cases} \tag{5}$$

where N denotes the number of possible levels for a factor (3 for RCMs, 9 for FDMs, 2 for ρ_0), x denotes the value of the variable of interest (dh_f^{tot}) and a dot represents the arithmetic mean with respect to the index it is substituted for. Because the sums of squares in Equation 5 are averaged departures from a mean, these terms are biased estimates of the variance (Déqué et al., 2007). An unbiased estimate should be divided by

$N\!-\!1$, but dividing by N results in η^2 terms fulfilling Equation 4. As such, any ratio $\eta^2\ /\ \sigma^2$ is only interpreted as a percentage of contribution to the total ensemble uncertainty. We group together all η^2 terms capturing an interaction effect to quantify the nonlinear behavior of the model experiments with respect to the three factors (η^2_{intr}).

3. Results

3.1. Ensemble Scenarios

The model ensemble shows a stable firn thickness over 1992–2017 for most of (Figure 1) the EAIS, but strong regional changes are evident in several of the 16 basins. The large interior basins (2, 3, 10, 17) show no significant thickness change; the 2σ uncertainty ranges of the ensemble results encompass zero. In contrast, the ensemble shows a significant and pronounced (>0.49 m) firn thickening in Dronning Maud Land (basins 5–8), driven by high snowfall rates since 2009 (Boening et al., 2012; Medley et al., 2018). Conversely, decreases in snowfall rates cause firn thinning (>0.25 m) in the areas of Shackleton ice shelf and Totten glacier (basins 12–13), which coincide with localized zones of high ice flow velocities (Rignot et al., 2019). Low accumulation since 2005 also induced thinning in Victoria Land (basin 14) (Velicogna et al., 2014). In such cases of accumulation anomalies, the firn compaction signal must be accounted for as it partially mitigates the overall change in firn thickness; increased accumulation provides more pore space and thus higher compaction rates, while decreased accumulation has the opposite effect. In other basins, the ensemble suggests thickening (e.g., basins 3–4) or thinning (e.g., basins 9 and 15) but high variability among model scenarios precludes any firm conclusion.

Model uncertainties in basin-averaged rates of firn thickness change range between 0.2 and 1.0 cm yr^{-1}, translating into relative uncertainties between 15% and 300% (Table 2). Despite low absolute uncertainties, the interior basins (2, 3, 10, 16, 17) show the largest relative values because their trends in dh_f are close to zero (<0.4 cm yr^{-1}). Basins with trends exceeding 1 cm yr^{-1} have lower relative uncertainties. Yet, some of these still exhibit relative uncertainties higher than 25% (4, 5, 8, 13, 15). The relative importance of the RCM, FDM, and ρ_0 factors on the model spread varies between basins. An area-weighted averaging demonstrates the general predominance of the RCM factor (72%) followed by the FDM (20%), ρ_0 (4%) and interaction (4%) factors. The high influence of RCM choice is mostly due to the large and direct impact of SMB on firn thickness. In addition, there is an indirect impact of RCM output as forcing for FDMs and for the climate-dependent L11 parameterization of ρ_0.

Cold basins with low snowfall rates (e.g., 2–3, 10–11) are characterized by particularly high contributions of η^2_{RCM} (>90% of σ^2). In such dry conditions, small discrepancies between RCM-modeled snowfall anomalies translate into large relative differences in firn thickness change. FDM contribution to the total ensemble uncertainty increases in basins with higher temperature and accumulation (e.g., 5–7, 12–13), with η^2_{FDM} explaining ~30%–45% of the spread. These climatic settings drastically increase both the sensitivity of FDMs to temperature fluctuations and the absolute compaction rates. Consequently, small relative differences in compaction rates between the FDMs result in large absolute differences in firn thickness change. Moreover, high total snowfall amounts mitigate the impact of small differences between RCM estimates of accumulation, thus reducing η^2_{RCM}. Another aspect that favors high $\eta^2_{FDM}\ /\ \sigma^2$ values is spatial variability of climatic conditions within basins; within basins spanning many climatic zones, there is more likely to be a region in which the FDMs disagree on compaction rates. Contribution of $\eta^2_{\rho_0}$ is highest in basins with large and positive snowfall anomalies (basins 5–8). In such basins, it accounts for up to 28% of the model spread because the thickening caused by the anomaly is sensitive to the snow density parameterization. Basins 16 and 17 illustrate the role of interaction effects. In these basins, MAR simulates substantially higher temperatures and accumulation rates, causing larger disagreements between FDMs forced by MAR than between FDMs forced by RACMO2 or HIRHAM. This nonconstancy of variance across FDMs for different RCMs leads to a significant interaction term η^2_{intr}. Because interaction effects account for a non-negligible part of the model spread in all basins (1%–8% of σ^2), our results demonstrate the importance of combining RCMs, FDMs, and ρ_0 within different model experiments to assess firn thickness change uncertainty.

Table 2

For Each EAIS Basin, Ensemble Mean (dh_f^{tot}) and Standard Deviation (σ_f^{tot}) of Firn Thickness Change

Basin	dh_f^{tot} [cm]	σ_f^{tot} [cm]	trend dh_f [cm yr^{-1}]	σ^{trend} dh_f [cm yr^{-1}]	$\frac{\sigma^{trend}\, dh_f}{\lvert trend\ dh_f \rvert}$ [%]	Altimetry trend [cm yr^{-1}]	η^2_{RCM} / σ^2 [%]	η^2_{FDM} / σ^2 [%]	$\eta^2_{\rho 0}$ / σ^2 [%]	η^2_{intr} / σ^2 [%]
2	−9.1	6.5	−0.3	±0.3	100	0.3 ± 2.3	92.1	6.2	0.2	1.5
3	7.3	8.8	0.5	±0.4	80	0.7 ± 0.1	97.6	1.4	0.0	1.0
4	26.7	21.3	2	±0.8	40	3.3 ± 0.4 *	97.3	1.0	0.4	1.3
5	70.9	12.6	2.2	±0.6	27	4.4 ± 0.6 *	49.4	32.5	15.3	2.8
6	54.1	6.9	2	±0.3	15	1.8 ± 0.3	28.5	42.6	26.1	2.8
7	49.0	6.8	1.9	±0.3	16	1.6 ± 0.3	18.9	46.0	28.2	6.9
8	68.9	16.0	3.6	±1.0	28	4.1 ± 0.4	71.9	11.8	12.6	3.7
9	−13.1	9.1	0.8	±0.7	88	3.0 ± 0.7 *	69.5	23.9	0.3	6.3
10	−10.2	5.5	−0.1	±0.3	300	0.0 ± 0.2	92.5	6.2	0.1	1.3
11	6.3	2.2	0.5	±0.2	40	0.4 ± 0.4	84.9	6.0	5.6	3.5
12	−44.8	12.0	−0.8	±0.4	50	1.8 ± 0.4 *	51.0	40.8	3.9	4.3
13	−25.5	9.0	−1.2	±0.5	42	−0.7 ± 0.4	60.8	32.8	3.4	3.1
14	−17.3	7.9	−2.3	±0.4	17	−1.5 ± 0.2 *	74.6	21.1	1.3	3.1
15	−18.4	9.4	−2.7	±0.9	33	−6.2 ± 1.5 *	72.1	21.6	1.2	5.2
16	2.2	5.0	−0.2	±0.4	200	−0.1 ± 0.3	95.5	1.4	0.0	3.1
17	3.3	2.5	−0.3	±0.2	67	0.3 ± 0.1 *	70.5	21.6	0.1	7.9

Note. Mean (trend dhf) and standard deviation ($\sigma^{\text{trend}} dh_f$) of the linear trends fitted to the ensemble scenarios, and their ratio $\left(\frac{\sigma^{\text{trend}}\, dh_f}{\lvert \text{trend } dh_f \rvert} \right)$. Altimetry trends are from Shepherd et al. (2019). Superscript * denotes non-overlapping uncertainty ranges from altimetry and from the model ensemble. η^2 / σ^2 ratios show contributions of the sources of uncertainty to the ensemble spread

3.2. Comparison With Altimetry

We compare our estimates of basin-wide trends in firn thickness with elevation trends reported by Shepherd et al. (2019) (Table 2, Figure 2). Firn thickness change is only a single component of the ice sheet elevation change signal, which also captures ice dynamical imbalance. Thus, accurate estimations of firn thickness change can be compared to measured elevation changes to identify areas of dynamical imbalance (Hawley et al., 2020; Kuipers Munneke et al., 2015; Li & Zwally, 2011). For 9 of the 16 basins, the model ensemble uncertainty ranges and the altimetry uncertainty ranges overlap. In these cases, our results provide no evidence to support the existence of net ice flow imbalance. However, basin-wide averaging may conceal localized dynamic changes. On Totten glacier (within basin 13) for example, ice dynamical imbalance close to the grounding line makes a substantial contribution to recent mass loss and thus to local elevation decrease (Li et al., 2016). On the other hand, the uncertainty ranges do not overlap for several basins, highlighting the need to better understand the source of the discrepancies in these regions. In such cases, three possibilities, or combinations thereof, should be considered: (1) the model ensemble may fail to represent the true firn thickness change over the 1992–2017 period, (2) the 1σ uncertainty range associated with the altimetry measurements may not adequately capture the true signal or (3) a component of the elevation changes may be related to ice dynamical imbalance.

At this stage, identifying the exact cause of the discrepancy remains speculative. The long response time of ice flow makes any dynamical imbalance challenging to evaluate because long-term trends may still outweigh recent changes (Zwally et al., 2015). Moreover, disagreements persist between simulated SMB and field observations in certain regions (Wang et al., 2016), which can lead to substantial differences in mass balance partitioning (Martin-Español et al., 2017; Mohajerani et al., 2019). Similarly, different sources

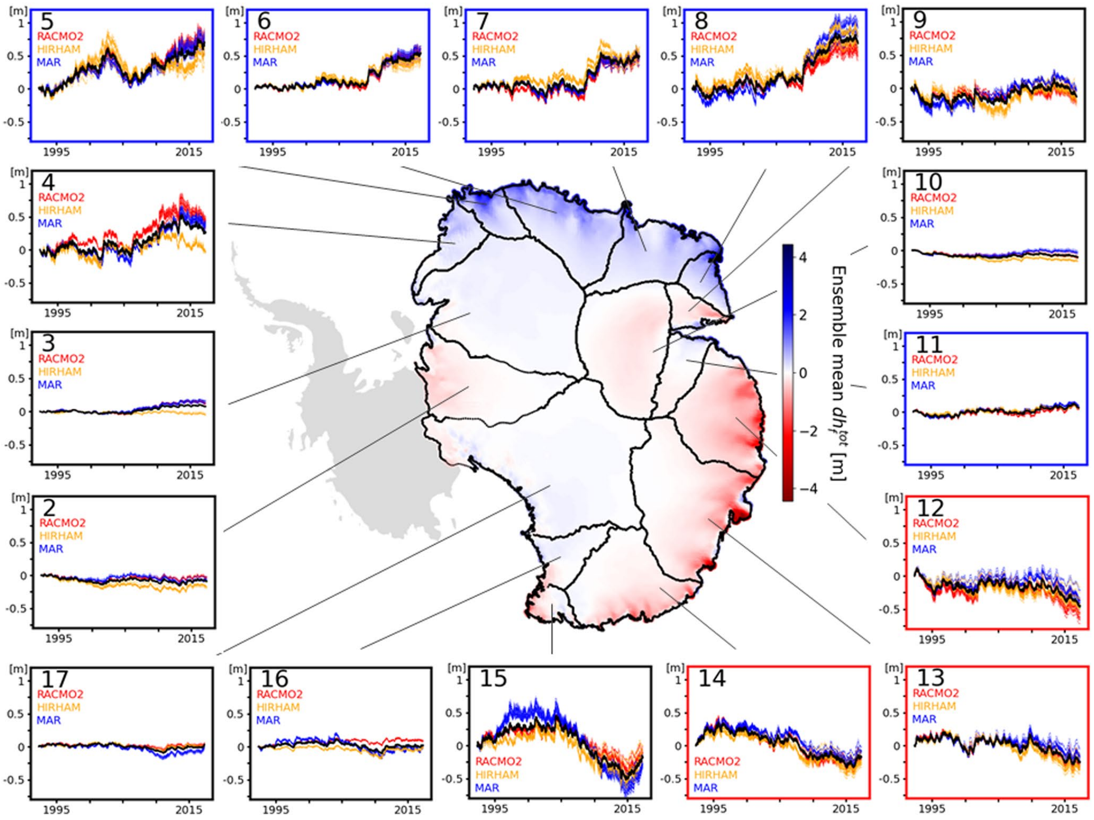

Figure 1. Ensemble mean 1992–2017 firn thickness change (dh_f^{tot}) in each EAIS basin. Simulation results are interpolated by nearest-neighbor to a common 12.5 km grid. The map uses a 3×3 median filter. Each inset shows the basin-averaged modeled time series of all the 54 model scenarios. Red, yellow, and blue curves represent scenarios forced with RACMO2, HIRHAM, and MAR, respectively. Each curve represents a particular RCM-FDM-ρ_0 combination. The thick black curve represents the ensemble mean. Basin numbers are displayed within the insets. Frame colors show whether dh_f^{tot} is significantly positive (blue), negative (red) or not significantly different from zero (black) (at $\pm 2\sigma$). Basin limits follow Zwally et al. (2015).

of altimetry data, inter-satellite bias correction, and other processing steps induce uncertainty in altimetry signals (Shepherd et al., 2019). We use several basins where ensemble- and altimetry-based trends disagree to illustrate these factors. In basins 4 and 5, Medley et al. (2018) demonstrated that global climate models underestimate recent increases in snowfall. A similar underestimation from the RCMs used here would explain the lower ensemble trend compared to the observed elevation trend. In basin 12, significant changes in ice discharge may hint at a dynamic imbalance causing the disagreement (Rignot et al., 2019). However, this area also shows major discrepancies in SMB anomalies from different model estimates (Wang et al., 2016) and from probabilistic inversion techniques (Martin-Español et al., 2017), suggesting that modeling SMB in this region is challenging. Basin 15 is characterized by sparse satellite sampling but also shows a large spread in our model ensemble and is thus poorly constrained. The relatively high model- and altimetry-uncertainties may both be related to the complex topography of this basin. Finally, a robust evaluation of FDM-reliability in all possible EAIS areas and climatic conditions does not exist and models may fail to predict true compaction rates. The objective of comparing ensemble firn thickness trends and altimetry trends is not to draw hasty conclusions about dynamical imbalance, but rather to highlight areas which deserve greater attention because recent measurements and current state-of-the-art model scenarios do not match.

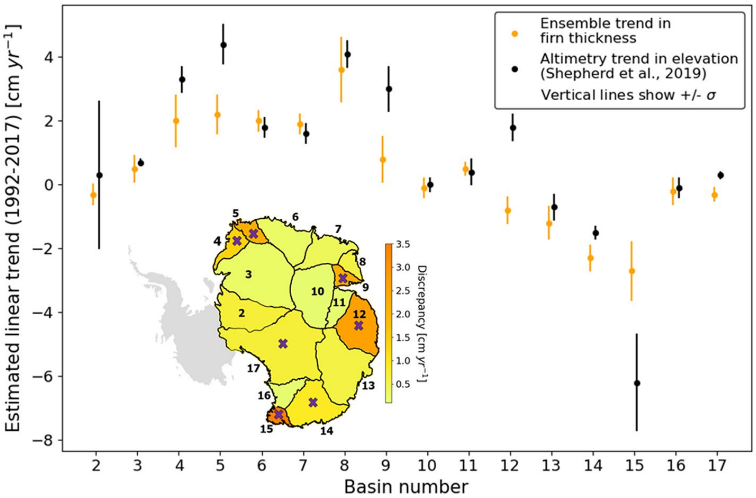

Figure 2. Comparison of 1992–2017 altimetry-based elevation trends and firn thickness trends of the ensemble, with their respective 1σ uncertainty ranges. Map shows the absolute ensemble-altimetry differences, crosses highlight basins with non-overlapping uncertainty ranges.

In critically evaluating our work, it is important to highlight sources of uncertainty that are not accounted for in the ensemble. We use three RCMs forced by ERA-Interim at their boundaries. Different atmospheric reanalyzes could, in theory, be used to force the RCMs or could be directly taken over the EAIS domain itself. Both the L11 and fixed-350 parameterizations of ρ_0 assume a time-invariant surface density because possible seasonal and interannual variabilities are unknown. The ensemble is limited by the deterministic RCM, FDM, and ρ_0 combinations considered here. In the future, the work could be extended to consider stochastic perturbations and parametric uncertainties in climate input, FDMs, and ρ_0, thereby providing a larger range of results. In principle, the process of emulation might lead to localized discrepancies between the emulator and a corresponding FDM, although evaluation (Supplementary Information) shows that this is unlikely when averaged over large spatial areas, as is done here. One critical assumption is the reference climatic period of 1979–2009. Different ice core analyses and model-based studies disagree on the existence of a trend in Antarctic SMB over the last decades and centuries, but several agree on existing regional trends (Frezzotti et al., 2013; Medley & Thomas, 2019; Monaghan et al., 2006; Previdi & Polvani, 2016). The year 1979 coincides with the start of satellite data assimilation into atmospheric products, and thus with the earliest RCM output, motivating this choice of reference period for practical reasons (e.g., Ligtenberg et al., 2011; Rignot et al., 2019). However, we cannot discount that substantially lower/higher past accumulation rates would result in under/over-estimating recent firn thickness change, thus providing a possible cause of disagreement with elevation change measurements. Nevertheless, because all model scenarios use the same reference period, it has a minor impact on both the total ensemble uncertainty and the uncertainty partitioning; using another reference period could shift the estimates of each scenario but would affect differences between the estimates only marginally.

4. Conclusions

Our model ensemble experiment provides a range of modeled scenarios of 1992–2017 firn thickness change on the EAIS that encompass current state-of-the-art modeling capabilities. Using statistical emulation of firn model output, we compute a total of 54 scenarios to assess variability associated with different RCMs, FDMs and surface snow density parameterizations. The ensemble agrees that firn thickness changes in the interior are minor, but there are pronounced thickening and thinning patterns in coastal areas. At basin-level, the uncertainty on the model estimates ranges between 0.2 and 1.0 cm yr^{-1} and is generally dominated by differences between RCMs due to the strong and direct effect of SMB on firn thickness. However, in basins with high snowfall and with large spatial variability of climatic conditions, FDM-related variability increases up to 46% of the total ensemble uncertainty. The surface snow density factor has a large impact on uncertainty in basins with recent increases in snowfall rates, reaching a maximum contribution of 28%. Finally, non-linear interactions between the three sources of uncertainty are substantial across the EAIS. Our results demonstrate that refining SMB estimates in RCMs is the priority for constraining future assessments of firn thickness change. However, as snowfall and temperatures are expected to increase in Antarctica (Lenaerts et al., 2019; Ligtenberg et al., 2013), FDMs and snow density will increasingly contribute to model uncertainty and should not be neglected. By comparing the ensemble scenarios with satellite measurements of elevation changes over the same 1992–2017 period, we find that these estimates are consistent over a majority of basins. Nonetheless, we identify several basins where model estimates do not match altimetry measurements. While ice dynamical imbalance could be the source of the discrepancies in these regions, so too could be inadequacies in the respective uncertainty characterizations. As such, our analysis serves to highlight specific areas where further focus on potential sources of errors in model and altimetry results is needed in order to better constrain mass balance assessments in East Antarctica.

Data Availability Statement

All the modelled annually averaged firn thickness change time series of this study are available at: https://doi.org/10.5281/zenodo.4515142. All the altimetry data shown in Table 2 and Figure 2 are from Table 1 in Shepherd et al. (2019).

Acknowledgments
The authors thank Andrew Shepherd for constructive discussions about our results. AL acknowledges support from EPSRC, *A Data Science for the Natural Environment* (EP/R01860X/1). M. McMillan was supported by the UK Natural Environment Research Council Centre for Polar Observation and Modeling (grant number cpom300001). MvdB acknowledges support from the Netherlands Earth System Science Centre (NESSC). The authors thank editor Mathieu Morlighem, reviewer Eric Keenan and one anonymous reviewer for providing insightful comments and for their handling of the review process.

References

Agosta, C., Amory, C., Kittel, C., Orsi, A., Favier, V., Gallée, H., et al. (2019). Estimation of the Antarctic surface mass balance using the regional climate model MAR (1979-2015) and identification of dominant processes. *The Cryosphere*, *13*(1), 281–296. https://doi.org/10.5194/tc-13-281-2019

Arthern, R. J., Vaughan, D. G., Rankin, A. M., Mulvaney, R., & Thomas, E. R. (2010). In situ measurements of Antarctic snow compaction compared with predictions of models. *Journal of Geophysical Research*, *115*(F3), F03011. https://doi.org/10.1029/2009jf001306

Boening, C., Lebsock, M., Landerer, F., & Stephens, G. (2012). Snowfall-driven mass change on the East Antarctic ice sheet. *Geophysical Research Letters*, *39*(21). https://doi.org/10.1029/2012gl053316

Christensen, O. B., Drews, M., Christensen, J. H., Dethloff, K., Ketelsen, K., Hebestadt, I., & Rinke, A. (2007). *The HIRHAM regional climate model, version 5 (Technical Report No. 06-17)*. Danish Meteorological Institute

Davis, C. H., Li, Y., McConnell, J. R., Frey, M. M., & Hanna, E. (2005). Snowfall-driven growth in East Antarctic ice sheet mitigates recent sea-level rise. *Science*, *308*(5730), 1898–1901. https://doi.org/10.1126/science.1110662

Dee, D. P., Uppala, S. M., Simmons, A. J., Berrisford, P., Poli, P., Kobayashi, S., et al. (2011). The ERA-Interim reanalysis: Configuration and performance of the data assimilation system. *Quarterly Journal of the Royal Meteorological Society*, *137*(656), 553–597. https://doi.org/10.1002/qj.828

Déqué, M., Rowell, D. P., Lüthi, D., Giorgi, F., Christensen, J. H., Rockel, B., et al. (2007). An intercomparison of regional climate simulations for Europe: Assessing uncertainties in model projections. *Climatic Change*, *81*(S1), 53–70. https://doi.org/10.1007/s10584-006-9228-x

Frezzotti, M., Scarchilli, C., Becagli, S., Proposito, M., & Urbini, S. (2013). A synthesis of the Antarctic surface mass balance during the last 800 yr. *The Cryosphere*, *7*(1), 303–319. https://doi.org/10.5194/tc-7-303-2013

Hawley, R. L., Neumann, T. A., Stevens, C. M., Brunt, K. M., & Sutterley, T. C. (2020). Greenland ice sheet elevation change: Direct observation of process and attribution at summit. *Geophysical Research Letters*, *81*, 53–70

Herron, M. M., & Langway, C. C. (1980). Firn densification: An empirical model. *Journal of Glaciology*, *25*(93), 373–385. https://doi.org/10.3189/s0022143000015239

Kittel, C., Amory, C., Agosta, C., Jourdain, N. C., Hofer, S., Delhasse, A., et al. (2020). *Diverging future surface mass balance between the Antarctic ice shelves and grounded ice sheet*. The Cryosphere Discussion. https://doi.org/10.5194/tc-2020-291

Kuipers Munneke, P., Ligtenberg, S. R. M., Noël, B. P. Y., Howat, I. M., Box, J. E., Mosley-Thompson, E., et al. (2015). Elevation change of the Greenland Ice Sheet due to surface mass balance and firn processes, 1960-2014. *The Cryosphere*, *9*(6), 2009–2025. https://doi.org/10.5194/tc-9-2009-2015

Lenaerts, J. T. M., Medley, B., Broeke, M. R., & Wouters, B. (2019). Observing and modeling ice sheet surface mass balance. *Reviews of Geophysics*, *57*(2), 376–420. https://doi.org/10.1029/2018rg000622

Ligtenberg, S. R. M., Helsen, M. M., & van den Broeke, M. R. (2011). An improved semi-empirical model for the densification of Antarctic firn. *The Cryosphere*, *5*(4), 809–819. https://doi.org/10.5194/tc-5-809-2011

Ligtenberg, S. R. M., van de Berg, W. J., van den Broeke, M. R., Rae, J., & van Meijgaard, E. (2013). Future surface mass balance of the Antarctic ice sheet and its influence on sea level change, simulated by a regional atmospheric climate model. *Climate Dynamics*, *41*(3–4), 867–884. https://doi.org/10.1007/s00382-013-1749-1

Li, J., & Zwally, H. J. (2011). Modeling of firn compaction for estimating ice-sheet mass change from observed ice-sheet elevation change. *Annals of Glaciology*, *52*(59), 1–7. https://doi.org/10.3189/172756411799096321

Li, J., & Zwally, H. J. (2015). Response times of ice-sheet surface heights to changes in the rate of Antarctic firn compaction caused by accumulation and temperature variations. *Journal of Glaciology*, *61*(230), 1037–1047. https://doi.org/10.3189/2015jog14j182

Li, X., Rignot, E., Mouginot, J., & Scheuchl, B. (2016). Ice flow dynamics and mass loss of Totten glacier, East Antarctica, from 1989 to 2015. *Geophysical Research Letters*, *43*(12), 6366–6373. https://doi.org/10.1002/2016gl069173

Lundin, J. M. D., Stevens, C. M., Arthern, R., Buizert, C., Orsi, A., Ligtenberg, S. R. M., et al. (2017). Firn Model Intercomparison Experiment (FirnMICE). *Journal of Glaciology*, *63*(239), 401–422. https://doi.org/10.1017/jog.2016.114

Martin-Español, A., Bamber, J. L., & Zammit-Mangion, A. (2017). Constraining the mass balance of East Antarctica. *Geophysical Research Letters*, *44*(9), 4168–4175. https://doi.org/10.1002/2017gl072937

McMillan, M., Leeson, A., Shepherd, A., Briggs, K., Armitage, T. W. K., Hogg, A., et al. (2016). A high-resolution record of Greenland mass balance. *Geophysical Research Letters*, *43*(13), 7002–7010. https://doi.org/10.1002/2016gl069666

Medley, B., McConnell, J. R., Neumann, T. A., Reijmer, C. H., Chellman, N., Sigl, M., & Kipfstuhl, S. (2018). Temperature and snowfall in Western Queen Maud Land increasing faster than climate model projections. *Geophysical Research Letters*, *45*(3), 1472–1480. https://doi.org/10.1002/2017gl075992

Medley, B., & Thomas, E. R. (2019). Increased snowfall over the Antarctic Ice Sheet mitigated twentieth-century sea-level rise. *Nature Climate Change*, *9*, 34–39. https://doi.org/10.1038/s41558-018-0356-x

Mohajerani, Y., Velicogna, I., & Rignot, E. (2019). Evaluation of regional climate models using regionally-optimized GRACE Mascons in the Amery and Getz ice shelves basins, Antarctica. *Geophysical Research Letters*, *46*(23), 13883–13891. https://doi.org/10.1029/2019gl084665

Monaghan, A. J., Bromwich, D. H., Fogt, R. L., Wang, S.-H., Mayewski, P. A., Dixon, D. A., et al. (2006). Insignificant change in Antarctic snowfall since the International Geophysical Year. *Science*, *313*(5788), 827–831. https://doi.org/10.1126/science.1128243

Morris, E. M., & Wingham, D. J. (2014). Densification of polar snow: Measurements, modeling, and implications for altimetry. *Journal of Geophysical Research: Earth Surfaces*, *119*(2), 349–365. https://doi.org/10.1002/2013jf002898

O'Hagan, A. (2006). Bayesian analysis of computer code outputs: A tutorial. *Reliability Engineering & System Safety*, *91*(10–11), 1290–1300. https://doi.org/10.1016/j.ress.2005.11.025

Previdi, M., & Polvani, L. M. (2016). Anthropogenic impact on Antarctic surface mass balance, currently masked by natural variability, to emerge by mid-century. *Environmental Research Letters*, *11*(9), 094001. https://doi.org/10.1088/1748-9326/11/9/094001

Rignot, E., Mouginot, J., Scheuchl, B., van den Broeke, M., van Wessem, M. J., & Morlighem, M. (2019). Four decades of Antarctic Ice Sheet mass balance from 1979-2017. *Proceedings of the National Academy of Sciences of the United States of America*, *116*(4), 1095–1103. https://doi.org/10.1073/pnas.1812883116

Sacks, J., Welch, W. J., Mitchell, T. J., & Wynn, H. P. (1989). Design and analysis of computer experiments. *Statistical Science*, *4*(4), 409–423. https://doi.org/10.1214/ss/1177012413

Scambos, T., & Shuman, C. (2016). Comment on 'Mass gains of the Antarctic ice sheet exceed losses' by H. J. Zwally and others. *Journal of Glaciology*, *62*(233), 599–603. https://doi.org/10.1017/jog.2016.59

Shepherd, A., Gilbert, L., Muir, A. S., Konrad, H., Mcmillan, M., Slater, T., et al. (2019). Trends in Antarctic ice sheet elevation and mass. *Geophysical Research Letters*, *46*(14), 8174–8183. https://doi.org/10.1029/2019gl082182

Shepherd, A., Ivins, E., Rignot, E., Smith, B., van den Broeke, M., Velicogna, I., et al. (2018). Mass balance of the Antarctic Ice Sheet from 1992 to 2017. *Nature*, *558*(7709), 219–222. https://doi.org/10.1038/s41586-018-0179-y

Smith, B., Fricker, H. A., Gardner, A. S., Medley, B., Nilsson, J., Paolo, F. S., et al. (2020). Pervasive ice sheet mass loss reflects competing ocean and atmosphere processes. *Science*, *368*(14), 1239–1242. https://doi.org/10.1126/science.aaz5845

Steger, C. R., Reijmer, C. H., van den Broeke, M. R., Wever, N., Forster, R. R., Koenig, L. S., et al. (2017). Firn meltwater retention on the Greenland Ice Sheet: A model comparison. *Frontiers of Earth Science*, *5*. https://doi.org/10.3389/feart.2017.00003

Vandecrux, B., Mottram, R., Langen, P. L., Fausto, R. S., Olesen, M., Stevens, C. M., et al. (2020). The firn meltwater Retention Model Intercomparison Project (RetMIP): Evaluation of nine firn models at four weather station sites on the Greenland ice sheet. *The Cryosphere*, *14*(11), 3785–3810. https://doi.org/10.5194/tc-14-3785-2020

van den Broeke, M. (2008). Depth and density of the Antarctic firn layer. *Arctic Antarctic and Alpine Research*, *40*(2), 432–438. https://doi.org/10.1657/1523-0430(07-021)[broeke]2.0.co;2

van Kampenhout, L., Lenaerts, J. T. M., Lipscomb, W. H., Sacks, W. J., Lawrence, D. M., Slater, A. G., & van den Broeke, M. R. (2017). Improving the representation of polar snow and firn in the community earth system model. *Journal of Advances in Modeling Earth Systems*, *9*(7), 2583–2600. https://doi.org/10.1002/2017ms000988

van Wessem, J. M., van de Berg, W. J., Noël, B. P. Y., van Meijgaard, E., Birnbaum, G., Jakobs, C. L., et al. (2018). Modeling the climate and surface mass balance of polar ice sheets using RACMO2, part 2: Antarctica (1979–2016). *The Cryosphere*, *12*(4), 1479–1498. https://doi.org/10.5194/tc-12-1479-2018

Velicogna, I., Sutterley, T. C., & van den Broeke, M. R. (2014). Regional acceleration in ice mass loss from Greenland and Antarctica using GRACE time-variable gravity data. *Geophysical Research Letters*, *41*(22), 8130–8137. https://doi.org/10.1002/2014gl061052

Verjans, V., Leeson, A. A., Nemeth, C., Stevens, C. M., Kuipers Munneke, P., Noël, B., & van Wessem, J. M. (2020). Bayesian calibration of firn densification models. *The Cryosphere*, *14*(9), 3017–3032. https://doi.org/10.5194/tc-14-3017-2020

Verjans, V., Leeson, A. A., Stevens, C. M., MacFerrin, M., Noël, B., & van den Broeke, M. R. (2019). Development of physically based liquid water schemes for Greenland firn-densification models. *The Cryosphere*, *13*(7), 1819–1842. https://doi.org/10.5194/tc-13-1819-2019

Vionnet, V., Brun, E., Morin, S., Boone, A., Faroux, S., Le Moigne, P., et al. (2012). The detailed snowpack scheme Crocus and its implementation in SURFEX v7.2. *Geoscientific Model Development*, *5*(3), 773–791. https://doi.org/10.5194/gmd-5-773-2012

von Storch, H., & Zwiers, F. W. (1999). *Statistical analysis in climate research*. Cambridge University Press

Wang, Y., Ding, M., Van Wessem, J. M., Schlosser, E., Altnau, S., van den Broeke, M. R., et al. (2016). A comparison of Antarctic Ice Sheet surface mass balance from atmospheric climate models and in situ observations. *Journal of Climate*, *29*(14), 5317–5337. https://doi.org/10.1175/JCLI-D-15-0642.1

Winther, J.-G., Jespersen, M. N., & Liston, G. E. (2001). Blue-ice areas in Antarctica derived from NOAA AVHRR satellite data. *Journal of Glaciology*, *47*(157), 325–334. https://doi.org/10.3189/172756501781832386

Yip, S., Ferro, C. A. T., Stephenson, D. B., & Hawkins, E. (2011). A simple, coherent framework for partitioning uncertainty in climate predictions. *Journal of Climate*, *24*(17), 4634–4643. https://doi.org/10.1175/2011jcli4085.1

Zwally, H. J., & Li, J. (2002). Seasonal and interannual variations of firn densification and ice-sheet surface elevation at the Greenland Summit. *Journal of Glaciology*, *48*(161), 199–207. https://doi.org/10.3189/172756502781831403

Zwally, H. J., Li, J., Robbins, J. W., Saba, J. L., Yi, D., & Brenner, A. C. (2015). Mass gains of the Antarctic ice sheet exceed losses. *Journal of Glaciology*, *61*(230), 1019–1036. https://doi.org/10.3189/2015jog15j071

References From the Supporting Information

Andiranakis, I., & Challenor, P. G. (2012). The effect of the nugget on Gaussian process emulators of computer models. *Computational Statistics and Data Analysis*, *56*(12), 4215–4228. https://doi.org/10.1016/j.csda.2012.04.020

Liu, H., Ong, Y. S., Shen, X., & Cai, J. (2020). When Gaussian process meets Big Data: A review of scalable GPs. *IEEE Transactions on Neural Networks and Learning Systems*, *31*(11). https://doi.org/10.1109/TNNLS.2019.2957109

Quiñonero-Candela, J., Rasmussen, C. E., & Williams, C. K. I. (2007). *Large scale learning machines* (pp. 203–223). MIT Press.

Rasmussen, C. E., & Williams, C. K. I. (2006). *Gaussian processes for machine learning*. MA:MIT Press.

Rios, G., & Tobar, F. (2018). Learning non-Gaussian time series using the box-cox Gaussian process. In *Proceedings of the international joint conference on neural networks 2018*.

Seeger, M., Williams, C., & Lawrence, N. (2003). Fast Forward Selection to Speed up Sparse Gaussian Process Regression. Artificial Intelligence and Statistics Volume 9. EPFL-CONF-161318.

Stevens, C. M., Verjans, V., Lundin, J. M. D., Kahle, E. C., Horlings, A. N., Horlings, B. I., & Waddington, E. D. (2020). The Community Firn Model (CFM) v1.0. *Geoscientifc Model Development*, *13*(9), 4355–4377. https://doi.org/10.5194/gmd-13-4355-2020

A.5 MC Paper II

The Cryosphere, 16, 17–33, 2022
https://doi.org/10.5194/tc-16-17-2022

The Cryosphere Open Access EGU

Uncertainties in projected surface mass balance over the polar ice sheets from dynamically downscaled EC-Earth models

Fredrik Boberg[1], **Ruth Mottram**[1], **Nicolaj Hansen**[1,2], **Shuting Yang**[1], **and Peter L. Langen**[3]

[1]Danish Meteorological Institute, Copenhagen Ø, 2100, Denmark
[2]National Space Institute, Kongens Lyngby, 2800, Denmark
[3]iClimate, Department of Environmental Science, Aarhus University, Roskilde, 4000, Denmark

Correspondence: Fredrik Boberg (fbo@dmi.dk)

Received: 9 May 2021 – Discussion started: 20 May 2021
Revised: 10 November 2021 – Accepted: 19 November 2021 – Published: 4 January 2022

Abstract. The future rates of ice sheet melt in Greenland and Antarctica are an important factor when making estimates of the likely rate of sea level rise. Global climate models that took part in the fifth Coupled Model Intercomparison Project (CMIP5) have generally been unable to replicate observed rates of ice sheet melt. With the advent of the sixth Coupled Model Intercomparison Project (CMIP6), with a general increase in the equilibrium climate sensitivity, we here compare two versions of the global climate model EC-Earth using the regional climate model HIRHAM5 downscaling of EC-Earth for Greenland and Antarctica. One version (v2) of EC-Earth is taken from CMIP5 for the high-emissions Representative Concentration Pathway 8.5 (RCP8.5) scenario and the other (v3) from CMIP6 for the comparable high-emissions Shared Socioeconomic Pathway 5-8.5 (SSP5-8.5) scenario. For Greenland, we downscale the two versions of EC-Earth for the historical period 1991–2010 and for the scenario period 2081–2100. For Antarctica, the periods are 1971–2000 and 2071–2100, respectively. For the Greenland Ice Sheet, we find that the mean change in temperature is 5.9 °C when downscaling EC-Earth v2 and 6.8 °C when downscaling EC-Earth v3. Corresponding values for Antarctica are 4.1 °C for v2 and 4.8 °C for v3. The mean change in surface mass balance at the end of the century under these high-emissions scenarios is found to be $-290\,\mathrm{Gt\,yr^{-1}}$ (v2) and $-1640\,\mathrm{Gt\,yr^{-1}}$ (v3) for Greenland and $420\,\mathrm{Gt\,yr^{-1}}$ (v2) and $80\,\mathrm{Gt\,yr^{-1}}$ (v3) for Antarctica. These distinct differences in temperature change and particularly surface mass balance change are a result of the higher equilibrium climate sensitivity in EC-Earth v3 (4.3 K) compared with 3.3 K in EC-Earth v2 and the differences in greenhouse gas concentrations between the RCP8.5 and the SSP5-8.5 scenarios.

1 Introduction

The melt of ice sheets and glaciers now accounts for a greater proportion of observed sea level rise than thermal expansion (Chen et al., 2013; IPCC, 2019). With around 150 million people living within 1 m of the current global mean sea level (Anthoff et al., 2006), understanding the likely rate of sea level rise is crucial for planning infrastructure and coastal development. Global climate models (GCMs) that took part in the fifth Coupled Model Intercomparison Project (CMIP5, Taylor et al., 2012) have generally been unable to replicate observed rates of ice sheet melt in Greenland in the present day (Fettweis et al., 2013), and estimates of sea level contributions from both large polar ice sheets are tracking at the upper end of the range of estimates from these models (Slater et al., 2020). Natural climate variability in the Southern Ocean makes estimating Antarctic surface mass balance (SMB) using climate models complicated and can mask trends related to global warming (Mottram et al., 2021). These uncertainties in the current ice sheet response from observations and models give rise to the possibility that the rate of sea level rise over the course of the 21st century may be underestimated in current climate assessments driven by CMIP5 and earlier model intercomparisons (Slater et al., 2020).

While the CMIP5 experiments were driven by the representative concentration pathways (RCPs; van Vuuren et al., 2011), models in the sixth intercomparison project (CMIP6,

Published by Copernicus Publications on behalf of the European Geosciences Union.

Eyring et al., 2016) use a new set of emissions and land use scenarios based on socioeconomic developments, shared socioeconomic pathways (SSPs; Riahi et al., 2017; O'Neill et al., 2016). Here we use only one of the SSPs, called SSP5-8.5, characterized by fossil-fuel-driven development that is the only SSP consistent with emissions high enough to realize an anthropogenic radiative forcing of 8.5 $\mathrm{W\,m^{-2}}$ in 2100. The total forcing of SSP5-8.5 at 2100 therefore matches that of the RCP8.5 used in CMIP5, but the pathway is different as is the composition in terms of different contributions. For instance, in SSP5-8.5, CO_2 emissions and concentrations are somewhat higher than in RCP8.5, but this is compensated for by other constituents such as CH_4 and N_2O. In this study, we compare results forced by two versions of the EC-Earth coupled global model for RCP8.5 with EC-Earth v2 and SSP5-8.5 with EC-Earth v3. These two scenarios were chosen as they are the most similar to each other between the CMIP5 and CMIP6 experiments that have been carried out with both model versions.

Several different participating models in the latest generation of GCMs run for CMIP6 (Eyring et al., 2016) have demonstrated an increase in the equilibrium climate sensitivity (ECS) of the models compared to the previous versions in CMIP5 (Voosen, 2019; Zelinka et al., 2020). ECS is defined as the time-averaged near-surface air warming in response to doubling CO_2 in the atmosphere relative to pre-industrial climate, after the climate system has come into equilibrium. ECS is a commonly used metric to quantify the global warming in response to increases in atmospheric CO_2 including fast feedbacks in the climate system. The higher the ECS, the greater the likelihood of the climate system reaching higher levels of global warming and the smaller the permissible carbon emissions in order to meet a particular climate target. Therefore the ECS is also highly relevant for climate policy.

EC-Earth v3 has a higher ECS of 4.3 K compared to 3.3 K of EC-Earth v2 from CMIP5 due mainly to a more advanced treatment of aerosols (Wyser et al., 2020b). In this paper, we compare downscaled climate simulations from both versions for Greenland and Antarctica, run with the HIRHAM5 regional climate model (RCM) to examine the impact of the higher ECS on estimates of ice sheet surface mass budget for both Greenland and Antarctica over the 21st century. Higher ECS leads to more rapid atmospheric warming for a given forcing and thus enhanced rates of ice sheet melt. However, as precipitation often increases in lockstep with a warmer atmosphere, this enhanced melt may be offset to some degree by enhanced snowfall.

The relative performance of EC-Earth on a regional scale in the polar regions has been investigated in several studies, notably by Barthel et al. (2020) for CMIP5 models and also in a new work in preparation by Cecile Agosta (personal communication, 2021) for EC-Earth v3 in the context of the full CMIP6 ensemble. Barthel et al. (2020) show that EC-Earth v2 has a large bias for Greenland but with a projected RCP8.5 warming close to the CMIP5 ensemble mean. For Antarctica, Barthel et al. (2020) shows that EC-Earth v2 is among the best models in the atmosphere but performs poorly in ocean subsurface and surface conditions. EC-Earth v2 has also been used in a number of studies with a focus on Greenland and the Arctic, showing that it has an Arctic cold bias. In EC-Earth v3, this Arctic cold bias has more or less disappeared, and the current study aims at investigating how this would affect the SMB for Greenland.

The SMB, sometimes also called the climatic mass balance, of ice sheets and glaciers is the balance between precipitation, evaporation, sublimation and runoff of snow and glacier ice (Lenaerts et al., 2019). SMB controls the dynamical evolution of ice sheets by driving ice sheet flow from areas of high accumulation to regions of high ice loss. Surface melt and runoff accounts for around 50 % of the ice lost from Greenland (The IMBIE Team, 2020). When considering the Antarctic Ice Sheet as a whole, dynamical ice loss by calving and the submarine melting of ice shelves are the main mechanisms of ice loss, while SMB processes over the continent, with some exceptions, especially in the Antarctic Peninsula, lead to mass gain. It is important to note that calving and submarine melting of ice shelves do not directly lead to sea level rise as the ice has already left the grounded part of the ice sheet and is floating. However, these ice shelves play an important role in buttressing grounded ice, and their loss could trigger large-scale retreat and acceleration of marine-terminating glaciers. As one mechanism of ice shelf collapse is the accumulation of surface melt leading to hydrofracture as for instance shown in the collapse of Larsen B (Skvarca et al., 2004), it is important to also calculate SMB over ice shelves, particularly given recent work (Kittel et al., 2021) suggesting large uncertainty over ice shelf SMB in future projections.

As suggested by Fettweis et al. (2013), SMB in Greenland, derived by dynamical downscaling of ERA-Interim reanalysis (Dee et al., 2011) with regional climate models, has a larger runoff component compared with CMIP5 models. This has been attributed to, for instance, a cooler-than-observed Arctic in EC-Earth v2 by Mottram et al. (2017) or inadequate representation of Greenland blocking and the North Atlantic Oscillation (NAO) by Hanna et al. (2018). Hofer et al. (2017) and Ruan et al. (2019) also show that cloud properties in climate models are the means by which the NAO modulates ice sheet melt, and inadequacies in their representation may be a further source of uncertainty within projections of ice sheet SMB in both Greenland and Antarctica.

Relatively few RCMs have been run or studied in depth for the SMB of Antarctica, and results used in international ice sheet modelling intercomparisons have by and large focused on using results from MAR and RACMO (e.g. Lenaerts et al., 2016; Agosta et al., 2013, 2019; Kittel et al., 2018; Van Wessem et al., 2015, 2018). Results of a recent intercomparison of regional models all forced by ERA-Interim (Mottram et al., 2021) show a wide spread of estimates of present-day SMB (from 1960 to 2520 $\mathrm{Gt\,yr^{-1}}$) related in large part to different resolutions and precipitation schemes. However, a comparison of future projections from previous studies (Ligtenberg et al., 2013; Hansen, 2019; Agosta et al., 2013; Kittel et al., 2021) suggests that on the scale of decades to centuries a clear upward trend in SMB with large interannual and decadal variability is expected due to enhanced snowfall in a warmer climate.

Both the Greenland and the Antarctic ice sheets are important to understanding when estimating sea level rise due to both their absolute possible contribution to sea level and the different timescales and processes that could drive their disintegration. The Antarctic Ice Sheet stores approximately 90 % of Earth's freshwater, a potential contribution to the mean sea level of 58 m (Fretwell et al., 2013). Thus, the Antarctic Ice Sheet has the potential to be the single largest contributor to future sea level rise. The Greenland Ice Sheet contains around 7 m of mean sea level rise (Aschwanden et al., 2019) and has in the last 2 decades seen increasing mass loss (450–500 Gt yr^{-1}) due to both large meltwater runoff amounts and enhanced calving from outlet glaciers (Mankoff et al., 2019).

Recent projections from both Greenland and Antarctica have started to include coupled climate and dynamical ice sheet models from both intermediate complexity models and fully coupled regional and global models (Robinson et al., 2012; Vizcaino et al., 2013; Levermann et al., 2020; Le clec'h et al., 2019; Madsen et al., 2021). However, most studies still rely on offline ice sheet models forced by higher-resolution regional climate models that downscale from global models. In Antarctica, as most ice loss is dynamically driven, SMB is primarily used to provide accurate forcing for ice sheet models. Ice Sheet Model Intercomparison Project for CMIP6 (ISMIP6) models (Goelzer et al., 2018) suggest a wide spread in projections of sea level rise for Greenland from 70 to 130 mm (Goelzer et al., 2020), including both dynamical and SMB contributions calculated from several different GCMs.

In this study we investigate the differences between two different versions of the GCM EC-Earth, using an identical version of the regional climate model HIRHAM5, for the Greenland and Antarctica ice sheets (see Fig. 1). The two EC-Earth models are EC-Earth v2.3 and EC-Earth v3.3 (hereafter referred to as EC-Earth2 and EC-Earth3) and are run for CMIP5 and CMIP6, respectively. The comparison focuses on temporal changes (end of the century relative to a reference period) in temperature, precipitation and the surface mass balance.

In Sect. 2 we introduce the model domains and the two versions of the GCM EC-Earth as well as the regional climate model HIRHAM5. In Sect. 3 we present, using time slice experiments and for both Greenland and Antarctica, changes in temperature and precipitation using the two versions of EC-Earth, followed by the resulting changes in surface mass balance for both ice sheets. The paper ends with a discussion in Sect. 4 and a conclusion in Sect. 5.

Table 1. List of all eight time slice experiments. The Greenland runs are 20 years long, while the runs for Antarctica are 30 years long, not counting the first spin-up year in each experiment.

Domain	Resolution	EC-Earth forcing	Period
Greenland	0.05°	v2 historical	1990–2010
		v2 RCP8.5	2080–2100
		v3 historical	1990–2010
		v3 SSP5-8.5	2080–2100
Antarctica	0.11°	v2 historical	1970–2000
		v2 RCP8.5	2070–2100
		v3 historical	1970–2000
		v3 SSP5-8.5	2070–2100

2 Methods and materials

Here we compare regionally downscaled climate simulations for Greenland and Antarctica (see Fig. 1 and Table 1) run with two different versions of EC-Earth and an identical version of the HIRHAM5 RCM. The two EC-Earth models, i.e. EC-Earth2 and EC-Earth3, are run for CMIP5 and CMIP6, respectively. For reasons of computational cost we run four time slice experiments with HIRHAM5 driven with EC-Earth forcings for each domain. For Greenland, these cover the period 1990–2010 with historical forcing with both versions of EC-Earth and the period 2080–2100 with CMIP5 RCP8.5 for EC-Earth2 and CMIP6 SSP5-8.5 for EC-Earth3. The historical forcing ends in 2005 for CMIP5, and therefore for the last 5 years of the 1990–2010 period we use RCP4.5 scenario forcing. For Antarctica, the time slice experiments cover the period 1970–2000 with historical forcing and the period 2070–2100 with RCP8.5 and SSP5-8.5. The first year in each time slice experiment is used for spin-up of atmospheric conditions and is not included in the analysis. The difference between time periods for the two regions (1991–2010 vs. 1971–2000 and 2081–2100 vs. 2071–2100) given in Table 1 is a result of the two regions being part of two different studies using the EC-Earth2 downscalings. The subsequent EC-Earth3 downscalings were performed for the same time periods as with the EC-Earth2 downscalings to facilitate a direct comparison between EC-Earth versions.

For the four time slice experiments in Greenland we include an offline spin-up routine on the built-in HIRHAM5 subsurface conditions running for 100 years, recycling the first spin-up year from each of the HIRHAM5 simulations. The HIRHAM5 model output for the full time slice simulations for Greenland is subsequently put into a stand-alone offline subsurface model (Langen et al., 2017). Spin-ups of more than 100 years are performed on each of these offline time slice simulations. For the four time slice experiments for Antarctica, there is no initial offline spin-up routine on the built-in HIRHAM5 subsurface conditions available. Instead, we put the HIRHAM5 output into the stand-alone offline sub-

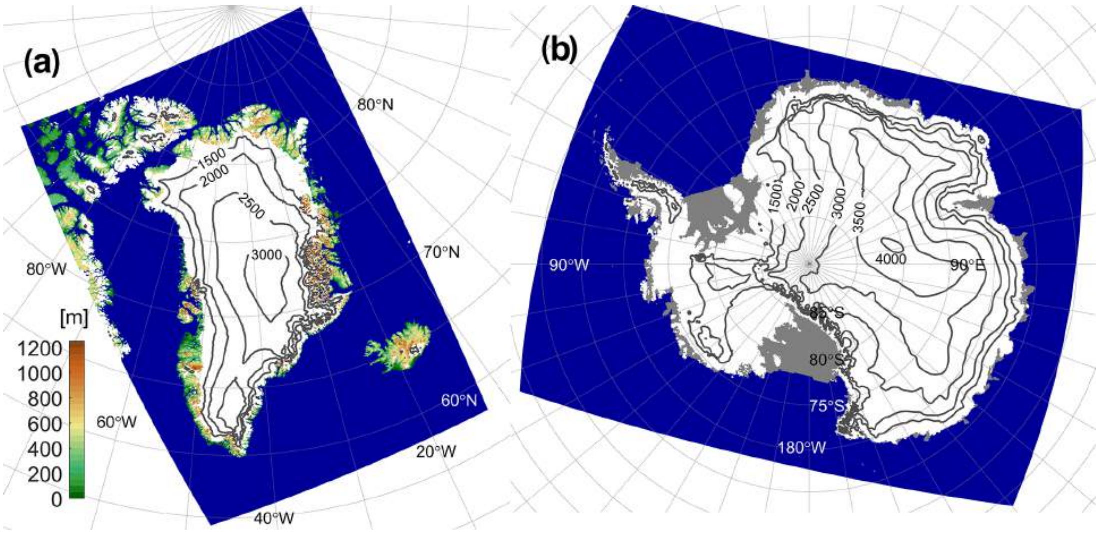

Figure 1. Topography for the two model domains. Sea points are given in blue; non-glacial land grid points are given in green and brown; Antarctic ice shelves are given in grey, while glacial points are given in white with surface elevation contour lines added. The Greenland domain **(a)** has a model resolution of about 5.5 km (0.05°), while the Antarctica domain **(b)** has a model resolution of about 12.5 km (0.11°).

surface model (Hansen et al., 2021) where we perform a 130-year spin-up for the two historical simulations for Antarctica and an additional 50 years of spin-up for the two scenario simulations. The spin-up time for the scenario runs is shorter in the offline subsurface model since we use the historical spin-up condition as a starting point for the scenario spin-up. The outputs from HIRHAM5 (precipitation and evaporation + sublimation) and the subsurface model (runoff) are used to calculate the SMB of the ice sheets over these periods in order to be able to compare the different forcings. The HIRHAM5 downscaling in combination with the offline subsurface model gives a more realistic representation of the surface energy balance over the ice sheet as well as surface snow properties and firn-pack processes that lead to retention and refreezing of meltwater. The current version of HIRHAM5 does not have drifting snow implemented.

EC-Earth is a GCM evolving from the seasonal forecast system of the ECMWF (Hazeleger et al., 2010) and developed by a large European consortium. EC-Earth2 is the model used to contribute to CMIP5 and is based on the ECMWF Integrated Forecasting System (IFS) CY31R1, the NEMO version 2 ocean model and the sea ice model LIM2 (Hazeleger et al., 2012). EC-Earth2 is run on a spectral resolution of T159 (equivalent to ∼ 125 km) and 62 vertical levels up to 5 hPa for the atmosphere and a 1° × 1° tripolar grid with 46 vertical levels for the ocean and sea ice. The new generation of the EC-Earth model is a full Earth system model and has been developed to perform CMIP6 experiments. A detailed description of this model is given by Döscher et al. (2021). However, the CMIP6 historical and SSP5-8.5 experiments used in the downscaling in this study were performed with only the GCM configuration, i.e. EC-Earth3. EC-Earth3 has upgraded all components of EC-Earth2, with the IFS cy36r4 for the atmosphere model and the NEMO version 3.6 for the ocean with the sea ice model LIM3 embedded. EC-Earth3 also runs at a higher resolution than EC-Earth2. The spatial resolution of the atmosphere is about 80 km horizontally (T255) and 91 vertical levels up to 0.01 hPa for the atmosphere. The ocean model uses the same 1° × 1° tripolar grid as EC-Earth2 but with 75 vertical levels. EC-Earth contributed to CMIP5 and CMIP6 historical and scenario experiments with ensembles of 15 and 25 members in total, performed on various platforms by respective consortium members. The differences among these members are only on the initial states which are taken from different snapshots in a 500-year-long control run under the pre-industrial condition (Taylor et al., 2012; Eyring et al., 2016). The simulations used in this study were the members r3i1p1 for CMIP5 and r5i1p1f1 for CMIP6, carried out at the Danish Meteorological Institute. Figure 2a and b show the 1991–2010 mean temperature relative to ERA-Interim for EC-Earth2 and EC-Earth3, respectively. The negative bias over Greenland for EC-Earth2 in Fig. 2a is not present for EC-Earth3 in Fig. 2b. EC-Earth3 has, however, a positive bias over Antarctica. Figure 2c and d show the difference in the change in 2 m temperature and sea surface temperature, respectively, between the EC-Earth3 using SSP5-8.5 and the EC-Earth2 using RCP8.5 at the end of the century relative to the reference period. For 2 m temperature in Fig. 2c we see a positive difference for both Greenland and Antarctica:

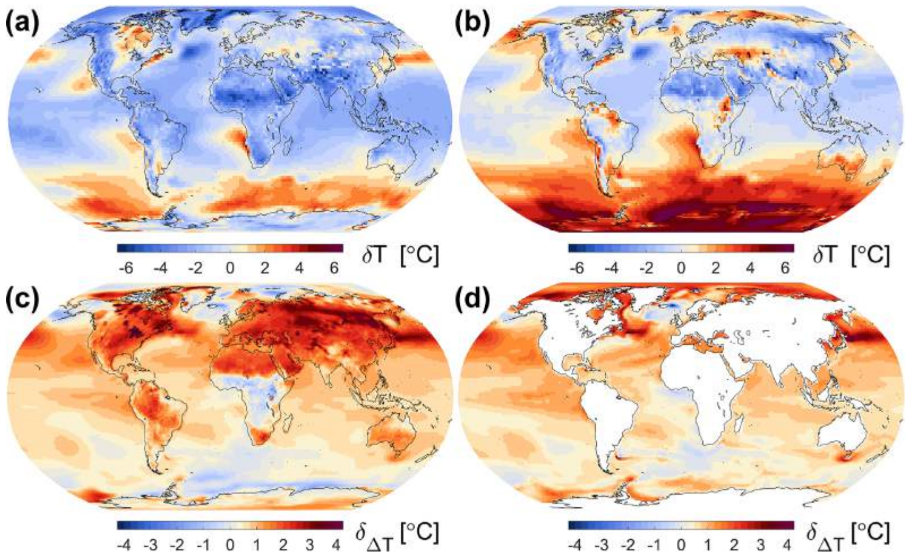

Figure 2. Temperature bias relative to ERA-Interim for 1991 to 2010 for EC-Earth2 **(a)** and EC-Earth3 **(b)**. Difference in the change in 2 m temperature **(c)** and sea surface temperature **(d)** for EC-Earth3 using SSP5-8.5 relative to EC-Earth2 using RCP8.5 for the 2081–2100 period relative to the 1991–2010 historical period.

between 1 and 3 °C along the coastal regions for Greenland and about 1 °C in the central parts of Antarctica. There is also a clear difference in sea surface temperature change between the two versions of EC-Earth in Fig. 2d: between 1 and 3 °C along the coast of Greenland and between 1 and 2 °C along the coast of Antarctica. Besides leading to a thinning and a retreat of the ice sheets (if the increase in melt and subsequent runoff outpace the increase in precipitation), these differences in both atmospheric temperature and sea surface temperature are reflected in differences in end-of-winter sea ice extent shown in Fig. 3.

Figure 4 shows how EC-Earth2 and EC-Earth3 relate to other CMIP5 and CMIP6 models for changes in temperature and relative changes in precipitation over the ice sheets. We have used one realization for each available GCM containing both a historical run and an RCP8.5/SSP5-8.5 scenario run, giving a total of 41 CMIP5 model runs including 2 EC-Earth realizations and 28 CMIP6 model runs including 7 EC-Earth realizations. Furthermore, all models are regridded to a common grid, and due to the coarse horizontal resolution of the GCMs all land grid points for Greenland and Antarctica are treated as ice sheet points. For the Greenland Ice Sheet the EC-Earth2 model (panel a) is located at the upper part of the scatter plot with the largest changes in precipitation and temperature. This is also true for the EC-Earth3 model (panel c) even though EC-Earth3 gives the lowest changes compared with the other EC-Earth members. For the Antarctic Ice Sheet the EC-Earth2 model (panel b) is located in the middle of the distribution for both precipitation and temperature. This holds also for the EC-Earth3 model (panel d). Comparing Fig. 4a and c for Greenland and Fig. 4b and d for Antarctica, we see a shift in the ensemble mean temperature going from CMIP5 to CMIP6 (0.3 °C for Greenland and 0.4 °C for Antarctica) of a similar order to when going from EC-Earth2 to EC-Earth3 (0.5 °C for Greenland and 0.4 °C for Antarctica). We also note that the spread of the EC-Earth members for a specific domain and a specific generation is relatively small compared to the full distribution, indicating that sampling issues associated with the relatively short time slices are of minor concern.

The HIRHAM5 regional climate model (Christensen et al., 2006) is based on the HIRLAM7 weather forecasting model (Undén et al., 2002), where the physical routines have been replaced by those within the ECHAM5 climate model (Roeckner et al., 2003). HIRHAM5 uses 31 atmospheric levels, and for the Greenland domain, the model is run at a resolution of 0.05° (about 5.5 km) with 20-year-long time slices, while the Antarctica simulation is run at a resolution of 0.11° (about 12.5 km) with 30-year-long time slices. The HIRHAM5 model has previously been validated against observations for Greenland (e.g. Boberg et al., 2018; Langen et al., 2017; Lucas-Picher et al., 2012) and Antarctica (Mottram et al., 2021; Hansen, 2019). Boberg et al. (2018) showed that monthly means of observed temperature on the west Greenland Ice Sheet compare well with the EC-Earth2 downscaling using HIRHAM5 for the period 1993–2010 with a mean bias between +1 and −2 °C. Langen et al. (2017) compared 1041 SMB observations from 351 locations in the ablation

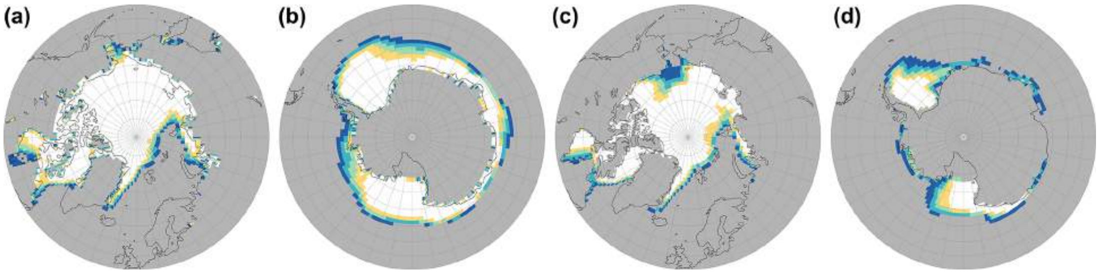

Figure 3. Mean end-of-winter sea ice extent for the 2081–2100 period. Panels **(a)** and **(b)** are for the RCP8.5 scenario using EC-Earth2, and panels **(c)** and **(d)** are for the SSP5-8.5 scenario using EC-Earth3. Panels **(a)** and **(c)** are for the month of March, while panels **(b)** and **(d)** are for the month of September.

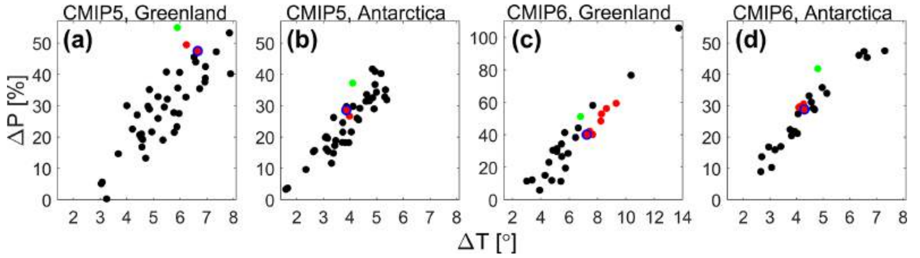

Figure 4. Relative change in precipitation as a function of change in temperature for 41 CMIP5 and 28 CMIP6 models for the Greenland and Antarctic ice sheets. The change is calculated for the same time periods as for our RCM runs (see Table 1). Panels **(a)** and **(b)** are for CMIP5, and panels **(c)** and **(d)** are for CMIP6. Panels **(a)** and **(c)** are for Greenland, while panels **(b)** and **(d)** are for Antarctica. Red symbols refer to EC-Earth members, while all other models are given by black dots. The red-and-blue dots highlight the EC-Earth members used for downscaling in this study. The green dots are corresponding values for the HIRHAM5 simulations presented in this study.

area of the Greenland Ice Sheet with an ERA-Interim-driven HIRHAM5 simulation and found a regression slope of 0.95, a correlation coefficient of 0.75, a RMSE of 0.98 m w.e. and a mean bias of −3 %, indicating only a slightly underestimated net surface mass loss rate. Moreover, comparing the simulation to 68 ice cores in the accumulation area of the Greenland Ice Sheet, they found the simulated mean annual accumulation rate to have a −5 % bias, 25 % RMSE and correlation coefficient of 0.9. Mottram et al. (2021) showed, using station observations, that ERA-Interim-forced HIRHAM5 simulations have a negative bias of −2 °C for Antarctica. Using SMB observations, Mottram et al. (2021) found a model mean bias of $-20\,\mathrm{kg\,m^{-2}\,yr^{-1}}$, a RMSE of $101\,\mathrm{kg\,m^{-2}\,yr^{-1}}$ and a correlation coefficient of 0.81, indicating a small underestimation of the surface mass balance. Mottram et al. (2021) also compared Antarctic Ice Sheet SMB estimates taken from five different RCMs forced with ERA-Interim and found that HIRHAM5 had an SMB value for grounded ice about 10 % above the ensemble mean and an SMB value for the ice shelves about 4 % above the ensemble mean. They concluded that HIRHAM5 SMB values were in the upper range compared with the other models but that the SMB values were almost exactly the same as for the MARv3.10 model, although with a clear difference between the SMB components.

3 Results

The temporal and regional changes for temperature, precipitation and SMB taken from dynamical downscalings of EC-Earth2 and EC-Earth3 are presented in this section. As a reference for these variables we use a HIRHAM5 run driven by ERA-Interim, which in turn has been evaluated by Langen et al. (2017) and Mottram et al. (2021) and compared with other similar climate models for Greenland in Fettweis et al. (2020) and Antarctica in Mottram et al. (2021).

3.1 Modelled temperature

Figure 5a and c show the annual mean change in 2 m temperature for Greenland and Antarctica, respectively, using HIRHAM5 downscaled with EC-Earth3 for 2081–2100 and 2071–2100 for the SSP5-8.5 scenario relative to the 1991–2010 and 1971–2000 historical runs (cf. Table 2). Figure 5b and d show the difference between the changes given in Fig. 5a and c and the equivalent change using EC-Earth2

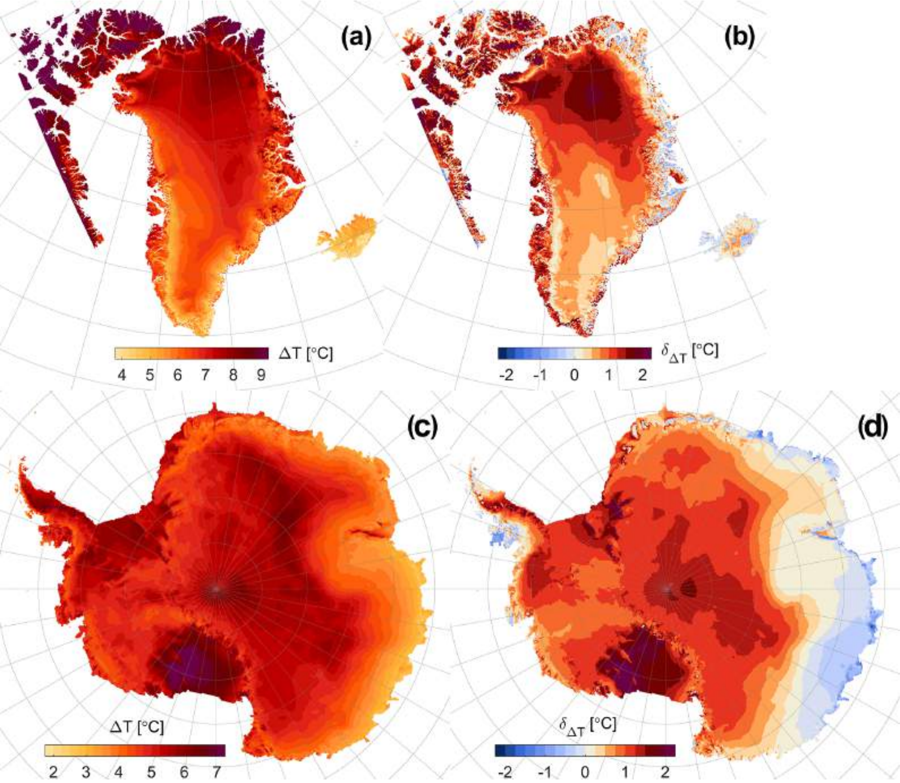

Figure 5. Change in 2 m temperature for Greenland for 2081–2100 relative to 1991–2010 for the EC-Earth v3 SSP5-8.5 scenario **(a)**. Difference in the change in 2 m temperature for EC-Earth3 SSP5-8.5 relative to EC-Earth2 RCP8.5 **(b)**. Change in 2 m temperature for Antarctica for 2071–2100 relative to 1971–2000 for the SSP5-8.5 scenario **(c)**. Difference in the change in 2 m temperature for SSP5-8.5 relative to RCP8.5 **(d)**. Note that the colour bar limits in panels **(a)** and **(c)** differ.

for the same time periods but using the RCP8.5 forcing scenario. Therefore positive values in Fig. 5b and d do not imply that the scenario period in the EC-Earth3 SSP5-8.5 downscaling is warmer than the scenario period in the EC-Earth2 RCP8.5 downscaling – just that the *change* in temperature is larger from the historical period to the SSP5-8.5 runs compared with the change between the historical simulation and the RCP8.5 runs. The mean change in temperature over the ice sheet is 5.9 °C for Greenland using EC-Earth2 and 6.8 °C using EC-Earth3. For Antarctica the values are 4.1 °C using EC-Earth2 and 4.8 °C using EC-Earth3.

The mean temperature values presented here for the EC-Earth2 and EC-Earth3 downscalings are compared with ERA-Interim downscalings using HIRHAM5 for the reference periods in Table 2. We notice that the temperature for the ERA-Interim-driven run is close to the EC-Earth3-driven run for Greenland for the 1991–2010 period. The temperature for the EC-Earth2 downscaling is lower, which can be explained by the negative bias in the forcing data. For Antarctica (see Table 2), the downscaled ERA-Interim mean temperature is very close to the downscaled EC-Earth2 mean value, while the downscaled EC-Earth3 value is higher due to the positive temperature bias for Antarctica in EC-Earth3. Also note that since ERA-Interim data are only available from 1979 to August 2019, the time period used for the ERA-Interim-driven simulation for Antarctica is 8 years shorter than the GCM-driven historical runs.

For Greenland (Fig. 5b), the change in temperature for the EC-Earth3 run using the SSP5-8.5 scenario is shown to be higher for most of the domain compared with the change in temperature for the EC-Earth2 run using the RCP8.5 scenario. The difference is most pronounced for the northern part of the ice sheet as well as for the non-glacial northern, western and southern coastline. Along the eastern coastline, the difference in temperature change between the two downscalings is close to zero. For Antarctica (Fig. 5d), we see similar values to those for the Greenland Ice Sheet except for in the eastern part of Antarctica and on the western side of the

Table 2. Temperature (Temp) in degrees Celsius and SMB components including precipitation (Precip), evaporation + sublimation (Evap + Subl) and surface runoff (Runoff) in Gt yr^{-1} for grounded ice for all eight time slice experiments. The temperature is given as a mean for each period, while the SMB components are given as mean yearly sums for each period. ΔSMB is the temporal change between the scenario period and the reference period. δ(ΔSMB) is the model difference in ΔSMB between EC-Earth3 and EC-Earth2. Also included are values for the two ERA-Interim-driven HIRHAM5 simulations for Greenland and Antarctica. For Antarctica, SMB component numbers in parentheses denote ice shelf values. Note that the time period used for the ERA-Interim-driven simulation for Antarctica is 8 years shorter than the GCM-driven historical runs.

Domain	GCM	Period	Temp	Precip	Evap + Subl	Runoff	SMB	ΔSMB	δ(ΔSMB)
Greenland	ERA-Interim	1991–2010	−19.3	786	52	435	299	n/a	n/a
	EC-Earth2	1991–2010	−23.2	728	26	219	482	−287	−1350
		2081–2100	−17.3	1045	32	817	196		
	EC-Earth3	1991–2010	−20.2	850	24	620	206	−1637	
		2081–2100	−13.5	1125	7	2549	−1431		
Antarctica	ERA-Interim	1979–2000	−36.2	2356 (632)	156 (40)	75 (172)	2124 (420)	n/a	n/a
	EC-Earth2	1971–2000	−35.9	2625 (706)	178 (42)	79 (210)	2345 (454)	417	−337
		2071–2100	−31.8	3395 (881)	235 (45)	321 (706)	2762 (130)		
	EC-Earth3	1971–2000	−32.6	3137 (810)	226 (45)	261 (593)	2650 (172)	80	
		2071–2100	−27.8	4111 (1055)	287 (32)	1094 (1945)	2730 (−922)		

n/a: not applicable.

peninsula. This pattern is probably related to the temperature change difference in the GCMs seen in Fig. 2c along part of the coastal stretches of Antarctica, which in turn could be explained by a change in model bias and/or as a result of aerosol differences between the two GCM versions. As the phase of the southern annular mode (SAM) also controls the spatial variability in precipitation and temperature on annual to decadal scales in Antarctica, the pattern may also reflect different phases of the SAM in the two versions that are, at least in part, a result of internal variability rather than climate forcing (Fogt and Marshall, 2020). The largest differences in temperature change for Antarctica are found on the eastern part of the peninsula, the Filchner Ice Shelf and the Ross Ice Shelf.

3.2 Modelled precipitation

For precipitation, we see a positive relative change for both domains (Fig. 6a and c) using EC-Earth3 and the SSP5-8.5 scenario when downscaling using HIRHAM5 (see Table 2). For Greenland, the largest relative change is found for the northeastern part, while the southeastern part of Greenland has changes close to zero. For Antarctica, the largest changes are found in the interior, while the coastal areas show a more moderate increase. When comparing the difference in relative changes in precipitation (Fig. 6b and d), we see negative values for the eastern part of the domains and positive values for the western parts. These east–west patterns are reminiscent of those in the differences in temperature changes shown in Fig. 5b and d and in turn are similar to spatial patterns shown in ice core records by Medley and Thomas (2019), which they relate to SAM variability. This suggests that understanding internal variability in global models is important for interpreting SMB projections in Antarctica. For Greenland, the largest positive differences in relative precipitation change are found over the ice sheet in the northwest and to some extent also the southwest and northeast. For Antarctica, the region with a positive difference in relative precipitation change is more pronounced, covering most of the central and western parts.

The precipitation values on grounded ice for the reference periods are compared with downscaled ERA-Interim values using HIRHAM5 in Table 2. For Greenland, the ERA-Interim-driven run has a precipitation amount between the two EC-Earth downscalings, with EC-Earth2 having a value 7 % lower and EC-Earth3 having a value 8 % higher than the ERA-Interim downscaled value. For Antarctica, the EC-Earth2 downscaling has a mean precipitation 11 % higher than the ERA-Interim-driven run, while the downscaled EC-Earth3 has a 33 % higher precipitation amount, most likely linked to the positive temperature bias in EC-Earth3 for Antarctica.

3.3 Modelled SMB

Figure 7 shows the change in SMB for Greenland (panels a and b) and Antarctica (panels c and d). Figure 7a and c show downscaled EC-Earth2 for the RCP8.5 scenario, while Fig. 7b and d show downscaled EC-Earth3 for the SSP5-8.5 scenario, all relative to the historical periods (see Table 1). For EC-Earth2 we obtain a change (2081–2100 relative to 1991–2010) in SMB of −290 Gt yr^{-1} for the entire Green-

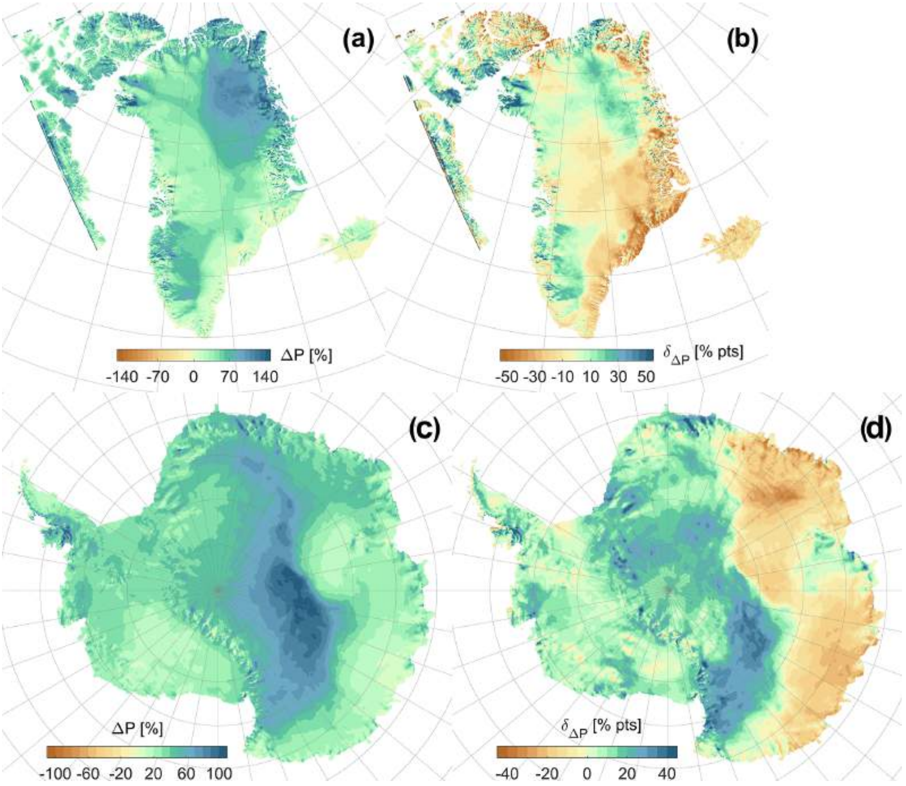

Figure 6. Relative change in total precipitation for Greenland for 2081–2100 relative to 1991–2010 for the EC-Earth3 SSP5-8.5 scenario downscaling **(a)**. Difference in the relative change in total precipitation for Greenland for the EC-Earth3 SSP5-8.5 relative to EC-Earth2 RCP8.5 downscaling **(b)**. Relative change in total precipitation for Antarctica for 2071–2100 relative to 1971–2000 for the EC-Earth3 SSP5-8.5 scenario downscaling **(c)**. Difference in the relative change in total precipitation for Antarctica for the EC-Earth3 SSP5-8.5 relative to EC-Earth2 RCP8.5 downscaling **(d)**. Note the differences in colour bar limits.

land Ice Sheet with areas along the western part displaying changes in the range of -2 to $-1\,\mathrm{m\,yr^{-1}}$. For EC-Earth3 (Fig. 7b) almost the entire Greenland Ice Sheet shows a negative change (2081–2100 relative to 1991–2010) in the SMB with values well below $-2\,\mathrm{m\,yr^{-1}}$ along the margin. Over the 20-year period at the end of the century for which the model is run, the accumulated SMB anomaly is $-1640\,\mathrm{Gt\,yr^{-1}}$. This is equivalent to an additional 4.6 mm of sea level rise per year from the Greenland Ice Sheet at the end of the century, in line with estimates published by Hofer et al. (2020). We also note that the area in the southeast part of the Greenland Ice Sheet with positive contributions for the EC-Earth2 run in Fig. 7a is no longer present for the EC-Earth3 run in Fig. 7b. For Antarctica on grounded ice, we obtain a change (2071–2100 relative to 1971–2000) in SMB of $420\,\mathrm{Gt\,yr^{-1}}$ for the EC-Earth2 simulation (Fig. 7c) and a value of $80\,\mathrm{Gt\,yr^{-1}}$ for the EC-Earth3 simulation (Fig. 7d). Importantly, the location of the negative SMB in the model coincides with the vulnerable west Antarctic outlet glaciers, whose destabilization could lead to rapid retreat and dynamical ice loss, multiplying many times the effects of the enhanced ice sheet loss.

The SMB values for the reference periods (1991–2010 for Greenland and 1971–2000 for Antarctica) are compared with downscaled ERA-Interim values (1991–2010 for Greenland and 1979–2000 for Antarctica) using HIRHAM5 in Table 2. For Greenland, the ERA-Interim-driven run has an SMB value between the two EC-Earth downscalings, with EC-Earth2 having a value $180\,\mathrm{Gt\,yr^{-1}}$ above and EC-Earth3 $90\,\mathrm{Gt\,yr^{-1}}$ below the ERA-Interim downscaled value. For Antarctica, the EC-Earth2 and EC-Earth3 downscalings have a mean SMB $220\,\mathrm{Gt\,yr^{-1}}$ and $530\,\mathrm{Gt\,yr^{-1}}$, respectively, above the ERA-Interim-driven run. The large SMB difference for the EC-Earth3 run for Antarctica is mostly attributable to the difference in precipitation between the ERA-Interim and EC-Earth3 runs, but we also note a very high runoff value of $261\,\mathrm{Gt\,yr^{-1}}$ in the EC-Earth3 run.

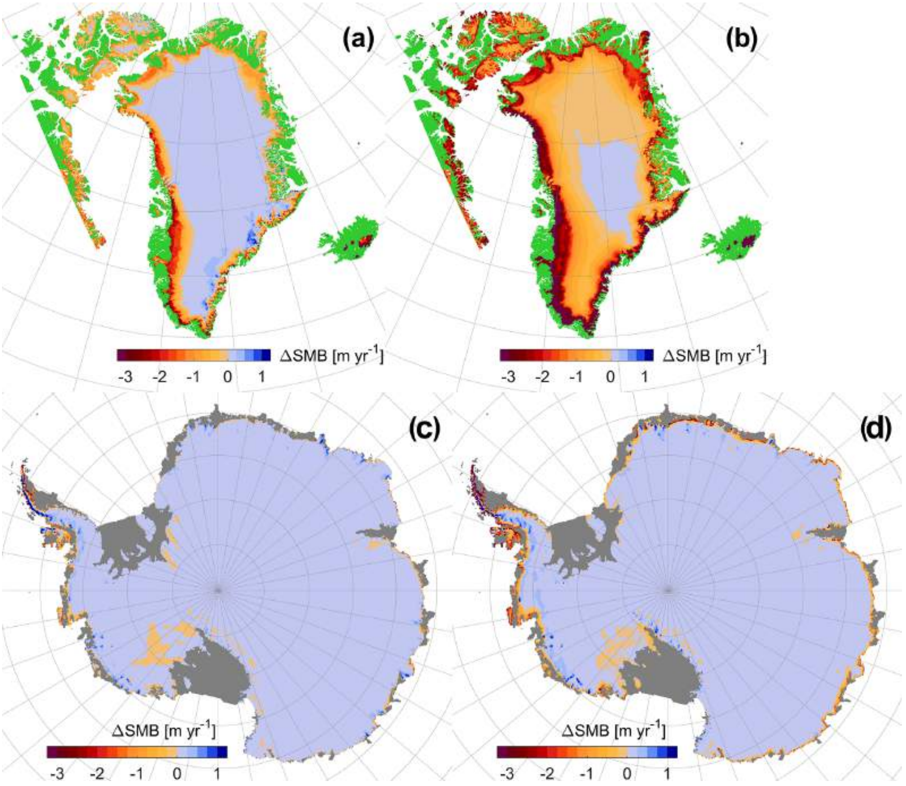

Figure 7. Changes in surface mass balance for Greenland for the period 2081–2100 relative to 1991–2010 for the EC-Earth2-driven run using RCP8.5 **(a)** and the EC-Earth3-driven run using SSP5-8.5 **(b)**. Changes in surface mass balance for Antarctica for the period 2071–2100 relative to 1971–2000 for the EC-Earth2-driven run using RCP8.5 **(c)** and the EC-Earth3-driven run using SSP5-8.5 **(d)**. Units are metres of water equivalent per year. The green colour represents non-glacial land grid points, and the grey colour represents Antarctic ice shelves (cf. Fig. 1).

Also given in Table 2 are the SMB components for the Antarctic ice shelves in parentheses. We see that the two EC-Earth downscalings have comparable numbers for precipitation compared with the ERA-Interim run, which also holds for the EC-Earth2 run for runoff. However, the runoff for the EC-Earth3 run is clearly above the ERA-Interim value owing to the warm bias in EC-Earth3. Gilbert and Kittel (2021) used MAR to downscale four GCMs and found, for the historical period, ice shelf SMB values in the range of 441 to 526 Gt yr^{-1}. Our values using HIRHAM downscaling ERA-Interim and EC-Earth2 are at the lower end of this range, while the EC-Earth3 downscaling has a lower SMB value due to the warm Antarctic bias in EC-Earth3. Kittel et al. (2021) presented end-of-century changes in the runoff component in the range of 32 to 260 Gt yr^{-1} for the grounded ice and 69 to 558 Gt yr^{-1} for the ice shelves. The end-of-century changes in the runoff component for our EC-Earth2 downscalings are 242 and 496 Gt yr^{-1} for grounded ice and ice shelves, respectively, placing it near the upper ends of both ranges. The end-of-century changes in runoff for our EC-Earth3 downscaling for Antarctica are well above these values, with 835 Gt yr^{-1} for grounded ice and 1352 Gt yr^{-1} for the ice shelves. These runoff values are probably a result of the warm bias in EC-Earth3 but partly also inherited from using HIRHAM5, showing high absolute runoff values when downscaling ERA-Interim (see Table 2).

When looking at yearly sums of the two ice sheet components, precipitation minus sublimation and evaporation and runoff, we can further study the differences between EC-Earth3 and EC-Earth2 for our two model domains (cf. Table 2). For Greenland during the historical period 1991–2010 (Fig. 8a), the runoff component for the downscaled EC-Earth3 simulation is about 400 Gt yr^{-1} larger than for EC-Earth2, while the precipitation minus sublimation and evaporation component has a mean difference of about 120 Gt yr^{-1} with relatively large variations for both simulations. For

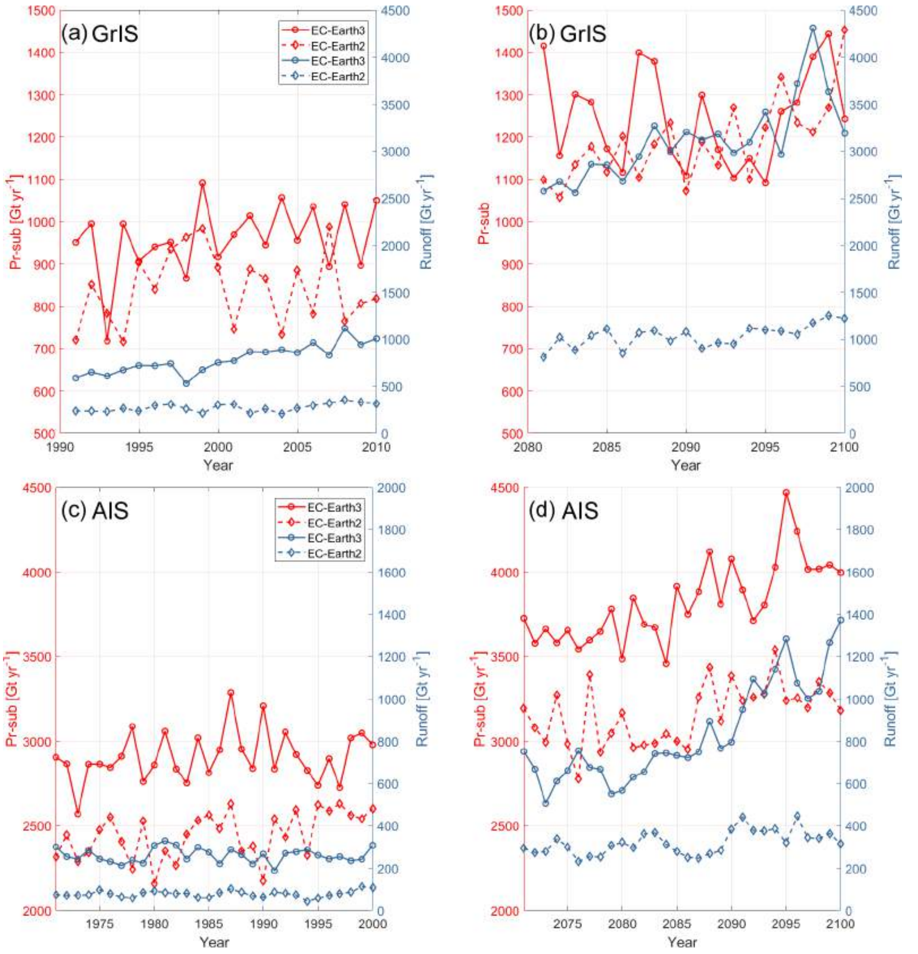

Figure 8. Integrated values of precipitation minus sublimation and evaporation (in red using the left *y* axis) and surface runoff (in blue using the right *y* axis) for the Greenland Ice Sheet (GrIS; **a, b**) and Antarctica Ice Sheet (AIS; **c, d**) using HIRHAM5 downscalings of EC-Earth. EC-Earth2 is marked with diamonds, and EC-Earth3 is marked with circles.

Greenland during the scenario period 2081–2100 (Fig. 8b), the two simulations show a similar difference (now a mean difference of 105 Gt yr^{-1}) with respect to the historical period 1991–2010 for the precipitation minus sublimation and evaporation component, whereas runoff shows a steady increase in the difference between the simulations, reaching in excess of 2300 Gt yr^{-1} at the end of the century. The downscaled end-of-century SMB values for EC-Earth2 and EC-Earth3 (196 and −1431 Gt yr^{-1}, respectively) can be compared with the ensemble mean SMB, using downscaled CMIP5 and CMIP6 GCMs given by Hofer et al. (2020), of about −300 Gt yr^{-1} for CMIP5 and −1000 Gt yr^{-1} for CMIP6.

For Antarctica during the historical period 1971–2000 (Fig. 8c), we see a mean difference of about 460 Gt yr^{-1} for precipitation minus sublimation and evaporation (cf. Table 2) between the two simulations, but for the runoff component, the difference is about 180 Gt yr^{-1} and only small variations are seen, especially for the EC-Earth2 run. For Antarctica during the scenario period 2071–2100 (Fig. 8d), we see that the gap between both precipitation minus sublimation + evaporation and runoff increases with time, reaching a difference of more than 800 Gt yr^{-1} for both by the end of the century. The downscaled end-of-century SMB values for EC-Earth2 and EC-Earth3 (2762 and 2730 Gt yr^{-1}, respectively) are comparable to the likely SMB range, using CMIP5 and CMIP6 ensembles given by Gorte et al. (2020), of 2630 ± 663 Gt yr^{-1} for CMIP5 and 2418 ± 374 Gt yr^{-1} for CMIP6.

As the large differences between model versions in ΔSMB (1350 Gt yr^{-1} for Greenland and 340 Gt yr^{-1} for Antarctica) are mostly dominated by differences in runoff changes rather than precipitation changes (see Table 2), we attribute them to the warmer reference period for both regions in combination with an approximately 1 °C higher end-of-century warming in both Greenland and Antarctica for EC-Earth3 relative to EC-Earth2. Furthermore, by comparing the spatially averaged temperature values with the runoff values in Table 2, we obtain an exponential relationship (not shown) that suggests large increases in runoff for relatively small increases in temperature.

4 Discussion

Our results show that for two different versions of the driving global model, substantial differences arise in ice sheet surface mass balance at the end of the century when driven by similar greenhouse gas emission pathways. The runoff and precipitation rates at the end of the century over both Greenland and Antarctica are higher and are likely enhanced by the higher temperatures projected under SSP5-8.5 than under RCP8.5. The higher temperatures in the EC-Earth3-driven downscalings for the SSP5-8.5 scenario compared with those for the EC-Earth2-driven downscalings for the RCP8.5 scenario are partly caused by a higher equilibrium climate sensitivity (4.3 K compared with 3.3 K in EC-Earth2). The difference between the greenhouse gas emission pathways in SSP5-8.5 and RCP8.5 also play an important role, however. Gidden et al. (2019) found that the radiative forcing in SSP5-8.5 matched that of RCP8.5 closely but that there were clear differences between the individual greenhouse gas components of the forcing as well as the aerosols. Wyser et al. (2020a) compared an EC-Earth run in CMIP6 (called EC-Earth3 Veg) and the CMIP5 EC-Earth run and concluded that 50 % or more of the end-of-century global temperature increase going from CMIP5 to CMIP6 was due to changes in the greenhouse gas concentrations rather than model changes.

In Fig. 4, we compare CMIP5 with CMIP6 ensembles where the EC-Earth members are given as red dots, and the two versions used in this study (v2 and v3) have a blue ring around them. Also included are values for the HIRHAM5 downscalings (green dots) for both EC-Earth2 and EC-Earth3 and for both Greenland and Antarctica. By comparing the green dots with the blue rings we see, for Greenland (Fig. 4a and c), a weakening of the temperature increases (0.8 °C for EC-Earth2 and 0.4 °C for EC-Earth3) after downscaling but at the same time a strengthening of the precipitation increases (8 percentage points for EC-Earth2 and 11 percentage points for EC-Earth3). For Antarctica (Fig. 4b and d), however, we see a strengthening of the temperature increases (0.2 °C for EC-Earth2 and 0.5 °C for EC-Earth3) but again a strengthening of the precipitation increases (9 percentage points for EC-Earth2 and 13 percentage points for EC-Earth3). So downscaling leads in all cases to a larger increase in precipitation than what is given in the GCM. For temperature, the warming effect is uniform for both versions of EC-Earth but reversed between Greenland (weakening) and Antarctica (strengthening).

For this study, only one RCM has been used when comparing the downscaling of two GCMs. Future work will expand this to a multi-model and multi-member ensemble. However, the HIRHAM5 model has been used for downscaling EC-Earth2 and reanalysis data for both Greenland and Antarctica in a number of studies (Langen et al., 2017; Boberg et al., 2018; Hansen, 2019; Mottram et al., 2021), and the model output has been evaluated thoroughly, giving it validity for climate modelling as a single member for polar conditions against which other models can be compared.

Our results for Greenland and Antarctica are in line with previous work using MAR (Hofer et al., 2020; Kittel et al., 2021), showing a general increase in melt and runoff rates for Greenland and Antarctica when driven by selected CMIP6 models compared with CMIP5. Hofer et al. (2020) used MAR to downscale six CMIP5 GCMs and five CMIP6 GCMs for the Greenland Ice Sheet and found an ensemble mean change for the 2081–2100 period of about −700 Gt yr^{-1} (−400 Gt yr^{-1} for the CMIP5 runs and −1100 Gt yr^{-1} for the CMIP6 runs), which is comparable to the values given in Table 2. Kittel et al. (2021) used MAR to downscale two CMIP5 GCMs and two CMIP6 GCMs for the Antarctic Ice Sheet and found that changes in precipitation, runoff and the resulting SMB increase when going from CMIP5 to CMIP6 but with a significant model spread. Table 2 shows similar trends for precipitation and runoff. However, the change in the runoff component for Antarctica (+834 Gt yr^{-1}) is clearly higher than the 32–260 Gt yr^{-1} range given by Kittel et al. (2021), resulting in a negative trend in the SMB change going from EC-Earth2 (+417 Gt yr^{-1}) to EC-Earth3 (+80 Gt yr^{-1}). However, the scientific argument of the paper is that the change in temperature for the end-of-century high-emissions scenario is higher in the EC-Earth3 downscaling compared with the EC-Earth2 downscaling for both Greenland and Antarctica. This difference in temperature change leads to a negative value in the $\delta\Delta$(SMB) (rightmost column in Table 2). The positive temperature bias for Antarctica in EC-Earth3 does indeed give very high runoff rates and precipitation amounts but, as seen in Table 2, does not affect the sign of the $\delta\Delta$(SMB) value.

Bracegirdle et al. (2015) used 37 CMIP5 models and showed that, due to a large intermodel spread in sea ice area, the change in temperature using the RCP8.5 scenario for Antarctica was in the range of 0 to 6 °C while the change in precipitation was in the range of 0 % to almost 40 %. This large model spread for future climate change for Antarctica clearly shows the importance of using large model ensembles for climate projections. Analysis of the CMIP6 ensemble for Antarctic sea ice by Roach et al. (2020) showed some improvement in regional sea ice distribution and historical sea ice extent as well as a slight narrowing of the multi-model ensemble spread in CMIP6 compared to CMIP5. Although the wide spread in projections indicates that a large multimodel ensemble is desirable, comparing two slightly different versions of the same model is helpful to determine which changes may be affected by the difference in the driving models as well as the emission pathways, particularly given the difference in ECS between the two versions. The importance of sea surface temperature and sea ice extent to SMB in Antarctica, especially in coastal regions (Kittel et al., 2018), means that variability in ocean and sea ice representation in model projections has large implications for SMB estimates.

5 Conclusion

Due to a higher ECS in the driving GCM EC-Earth3 within CMIP6 compared with the driving GCM EC-Earth2 within CMIP5 together with changes in greenhouse gas concentrations between the RCP8.5 and the SSP5-8.5 scenarios, we find larger changes in both temperature and precipitation for both Greenland and Antarctica in the end-of-century scenario runs compared with the historical simulations. These differences lead to important changes over the polar ice sheets with a change in SMB of around $-1640\,\mathrm{Gt\,yr^{-1}}$ for Greenland and $+80\,\mathrm{Gt\,yr^{-1}}$ for Antarctica at the end of the century. Comparing these numbers with those obtained from the older EC-Earth2 runs ($-290\,\mathrm{Gt\,yr^{-1}}$ for Greenland and $+420\,\mathrm{Gt\,yr^{-1}}$ for Antarctica) suggests that for very high emission pathways, considerable uncertainty still exists for sea level rise contributions from the polar ice sheets due to climate change – even within a single model family. The difference between these two versions corresponds to a sea level rise difference of $3.7\,\mathrm{mm\,yr^{-1}}$ from Greenland and $1.0\,\mathrm{mm\,yr^{-1}}$ for Antarctica at the end of the century compared with earlier estimates based on EC-Earth2.

We find that it is difficult to directly compare the downscalings of EC-Earth2 and EC-Earth3 since the forcing conditions are not equal due to revised greenhouse gas concentration scenarios. However this allows us to demonstrate the potentially wide uncertainties in SMB estimates. Moreover the role of natural variability and the impact of climate change on regional circulation patterns that affect SMB are clearly areas that need more research in the future. The results presented here using EC-Earth3 within CMIP6 are therefore important to consider when communicating to the adaptation and mitigation communities.

Data availability. HIRHAM5 simulation data and SMB model output for all eight time slice simulations as well as EC-Earth2 and EC-Earth3 data are available upon request to the corresponding author.

Author contributions. FB, RM, NH and PLL designed the experiments, and FB carried them out. FB performed the HIRHAM5 simulations. SY developed the model code for EC-Earth and performed the simulations. FB prepared the manuscript with contributions from all co-authors.

Competing interests. At least one of the (co-)authors is a member of the editorial board of *The Cryosphere*. The peer-review process was guided by an independent editor, and the authors also have no other competing interests to declare.

Acknowledgements. This work is supported by the NordForsk-funded Nordic Centre of Excellence project (award 76654) "Arctic Climate Predictions: Pathways to Resilient, Sustainable Societies" (ARCPATH). This work has also been supported by the Horizon 2020 EUCP European Climate Prediction system under grant agreement no. 776613. The work is also supported by the project "Producing RegIoNal ClImate Projections Leading to European Services" (PRINCIPLES, C3S_34b Lot2), part of the Copernicus Climate Change Service (C3S) provided by the European Union's Copernicus Programme and managed by the European Commission. The authors would also like to acknowledge the support of the Danish state through the National Centre for Climate Research (NCKF).

Financial support. This publication was supported by PROTECT. This project has received funding from the European Union's Horizon 2020 research and innovation programme (grant no. 869304, PROTECT contribution number 26).

Review statement. This paper was edited by Masashi Niwano and reviewed by two anonymous referees.

References

Agosta, C., Favier, V., Krinner, G., Gallée, H., Fettweis, X., and Genthon, C.: High-resolution modelling of the Antarctic surface mass balance, application for the twentieth, twenty first and twenty second centuries, Clim. Dynam., 41, 3247–3260, https://doi.org/10.1007/s00382-013-1903-9, 2013.

Agosta, C., Amory, C., Kittel, C., Orsi, A., Favier, V., Gallée, H., van den Broeke, M. R., Lenaerts, J. T. M., van Wessem, J. M., van de Berg, W. J., and Fettweis, X.: Estimation of the Antarctic surface mass balance using the regional climate model MAR (1979–2015) and identification of dominant processes, The Cryosphere, 13, 281–296, https://doi.org/10.5194/tc-13-281-2019, 2019.

Anthoff, D., Nicholls, R. J., Tol, R. S. J., and Vafeidis, A.: Global and regional exposure to large rises in sea level: A sensitivity analysis, Tyndall Centre Working Paper 96, Tyndall Centre for Climate Change Research, Norwich, UK, 2006.

Aschwanden, A., Fahnestock, M. A., Truffer, M., Brinkerhoff, D. J., Hock, R., Khroulev, C., Mottram, R., and Khan, S. A.: Contribution of the Greenland Ice Sheet to sea level over the next millennium, Sci. Adv., 5, eaav9396, https://doi.org/10.1126/sciadv.aav9396, 2019.

Barthel, A., Agosta, C., Little, C. M., Hattermann, T., Jourdain, N. C., Goelzer, H., Nowicki, S., Seroussi, H., Straneo, F., and Bracegirdle, T. J.: CMIP5 model selection for ISMIP6 ice sheet model forcing: Greenland and Antarctica, The Cryosphere, 14, 855–879, https://doi.org/10.5194/tc-14-855-2020, 2020.

Boberg, F., Langen, P. L., Mottram, R. H., Christensen, J. H., and Olesen, M.: 21st-century climate change around Kangerlussuaq, west Greenland: From the ice sheet to the shores of Davis Strait, Arctic Antarct. Alp. Res., 50, S100006, https://doi.org/10.1080/15230430.2017.1420862, 2018.

Bracegirdle, T. J., Stephenson, D. B., Turner, J., and Phillips, T.: The importance of sea ice area biases in 21st century multimodel projections of Antarctic temperature and precipitation, Geophys. Res. Lett., 42, 10832–10839, https://doi.org/10.1002/2015GL067055, 2015.

Chen, J., Wilson, C., and Tapley, B.: Contribution of ice sheet and mountain glacier melt to recent sea level rise, Nat. Geosci., 6, 549–552, https://doi.org/10.1038/ngeo1829, 2013.

Christensen, O. B., Drews, M., Christensen, J. H., Dethloff, K., Ketelsen, K., Hebestadt, I., and Rinke, A.: The HIRHAM regional climate model, version 5, Danish Meteorological Institute, Tech. Rep. 06-17, 22 pp., 2006.

Dee, D. P., Uppala, S. M., Simmons, A. J., Berrisford, P., Poli, P., Kobayashi, S., Andrae, U., Balmaseda, M. A., Balsamo, G., Bauer, P., Bechtold, P., Beljaars, A. C. M., van de Berg, L., Bidlot, J., Bormann, N., Delsol, C., Dragani, R., Fuentes, M., Geer, A. J., Haimberger, L., Healy, S. B., Hersbach, H., Hólm, E. V., Isaksen, L., Kållberg, P., Köhler, M., Matricardi, M., McNally, A. P., Monge-Sanz, B. M., Morcrette, J.-J., Park, B.-K., Peubey, C., de Rosnay, P., Tavolato, C., Thépaut, J.-N., and Vitart, F.: The ERA-Interim reanalysis: configuration and performance of the data assimilation system, Q. J. Roy. Meteor. Soc., 137, 553–597, https://doi.org/10.1002/qj.828, 2011.

Döscher, R., Acosta, M., Alessandri, A., Anthoni, P., Arneth, A., Arsouze, T., Bergmann, T., Bernadello, R., Bousetta, S., Caron, L.-P., Carver, G., Castrillo, M., Catalano, F., Cvijanovic, I., Davini, P., Dekker, E., Doblas-Reyes, F. J., Docquier, D., Echevarria, P., Fladrich, U., Fuentes-Franco, R., Gröger, M., v. Hardenberg, J., Hieronymus, J., Karami, M. P., Keskinen, J.-P., Koenigk, T., Makkonen, R., Massonnet, F., Ménégoz, M., Miller, P. A., Moreno-Chamarro, E., Nieradzik, L., van Noije, T., Nolan, P., O'Donnell, D., Ollinaho, P., van den Oord, G., Ortega, P., Prims, O. T., Ramos, A., Reerink, T., Rousset, C., Ruprich-Robert, Y., Le Sager, P., Schmith, T., Schrödner, R., Serva, F., Sicardi, V., Sloth Madsen, M., Smith, B., Tian, T., Tourigny, E., Uotila, P., Vancoppenolle, M., Wang, S., Wårlind, D., Willén, U., Wyser, K., Yang, S., Yepes-Arbós, X., and Zhang, Q.: The EC-Earth3 Earth System Model for the Climate Model Intercomparison Project 6, Geosci. Model Dev. Discuss. [preprint], https://doi.org/10.5194/gmd-2020-446, in review, 2021.

Eyring, V., Bony, S., Meehl, G. A., Senior, C. A., Stevens, B., Stouffer, R. J., and Taylor, K. E.: Overview of the Coupled Model Intercomparison Project Phase 6 (CMIP6) experimental design and organization, Geosci. Model Dev., 9, 1937–1958, https://doi.org/10.5194/gmd-9-1937-2016, 2016.

Fettweis, X., Franco, B., Tedesco, M., van Angelen, J. H., Lenaerts, J. T. M., van den Broeke, M. R., and Gallée, H.: Estimating the Greenland ice sheet surface mass balance contribution to future sea level rise using the regional atmospheric climate model MAR, The Cryosphere, 7, 469–489, https://doi.org/10.5194/tc-7-469-2013, 2013.

Fettweis, X., Hofer, S., Krebs-Kanzow, U., Amory, C., Aoki, T., Berends, C. J., Born, A., Box, J. E., Delhasse, A., Fujita, K., Gierz, P., Goelzer, H., Hanna, E., Hashimoto, A., Huybrechts, P., Kapsch, M.-L., King, M. D., Kittel, C., Lang, C., Langen, P. L., Lenaerts, J. T. M., Liston, G. E., Lohmann, G., Mernild, S. H., Mikolajewicz, U., Modali, K., Mottram, R. H., Niwano, M., Noël, B., Ryan, J. C., Smith, A., Streffing, J., Tedesco, M., van de Berg, W. J., van den Broeke, M., van de Wal, R. S. W., van Kampenhout, L., Wilton, D., Wouters, B., Ziemen, F., and Zolles, T.: GrSMBMIP: intercomparison of the modelled 1980–2012 surface mass balance over the Greenland Ice Sheet, The Cryosphere, 14, 3935–3958, https://doi.org/10.5194/tc-14-3935-2020, 2020.

Fogt, R. L. and Marshall, G. J.: The Southern Annular Mode: Variability, trends, and climate impacts across the Southern Hemisphere, WIREs Clim. Change, 11, e652, https://doi.org/10.1002/wcc.652, 2020.

Fretwell, P., Pritchard, H. D., Vaughan, D. G., Bamber, J. L., Barrand, N. E., Bell, R., Bianchi, C., Bingham, R. G., Blankenship, D. D., Casassa, G., Catania, G., Callens, D., Conway, H., Cook, A. J., Corr, H. F. J., Damaske, D., Damm, V., Ferraccioli, F., Forsberg, R., Fujita, S., Gim, Y., Gogineni, P., Griggs, J. A., Hindmarsh, R. C. A., Holmlund, P., Holt, J. W., Jacobel, R. W., Jenkins, A., Jokat, W., Jordan, T., King, E. C., Kohler, J., Krabill, W., Riger-Kusk, M., Langley, K. A., Leitchenkov, G., Leuschen, C., Luyendyk, B. P., Matsuoka, K., Mouginot, J., Nitsche, F. O., Nogi, Y., Nost, O. A., Popov, S. V., Rignot, E., Rippin, D. M., Rivera, A., Roberts, J., Ross, N., Siegert, M. J., Smith, A. M., Steinhage, D., Studinger, M., Sun, B., Tinto, B. K., Welch, B. C., Wilson, D., Young, D. A., Xiangbin, C., and Zirizzotti, A.: Bedmap2: improved ice bed, surface and thickness datasets for Antarctica, The Cryosphere, 7, 375–393, https://doi.org/10.5194/tc-7-375-2013, 2013.

Gidden, M. J., Riahi, K., Smith, S. J., Fujimori, S., Luderer, G., Kriegler, E., van Vuuren, D. P., van den Berg, M., Feng, L., Klein, D., Calvin, K., Doelman, J. C., Frank, S., Fricko, O., Harmsen, M., Hasegawa, T., Havlik, P., Hilaire, J., Hoesly, R., Horing, J., Popp, A., Stehfest, E., and Takahashi, K.: Global emissions pathways under different socioeconomic scenarios for use in CMIP6: a dataset of harmonized emissions trajectories through the end of the century, Geosci. Model Dev., 12, 1443–1475, https://doi.org/10.5194/gmd-12-1443-2019, 2019.

Gilbert, E. and Kittel, C.: Surface melt and runoff on Antarctic ice shelves at 1.5 °C, 2 °C, and 4 °C of future warming, Geophys. Res. Lett., 48, e2020GL091733, https://doi.org/10.1029/2020GL091733, 2021.

Goelzer, H., Nowicki, S., Edwards, T., Beckley, M., Abe-Ouchi, A., Aschwanden, A., Calov, R., Gagliardini, O., Gillet-Chaulet, F., Golledge, N. R., Gregory, J., Greve, R., Humbert, A., Huybrechts, P., Kennedy, J. H., Larour, E., Lipscomb, W. H., Le clec'h, S., Lee, V., Morlighem, M., Pattyn, F., Payne, A. J., Rodehacke, C., Rückamp, M., Saito, F., Schlegel, N., Seroussi, H., Shepherd, A., Sun, S., van de Wal, R., and Ziemen, F. A.: Design and results of the ice sheet model initialisation experiments initMIP-Greenland: an ISMIP6 intercomparison, The Cryosphere, 12, 1433–1460, https://doi.org/10.5194/tc-12-1433-2018, 2018.

Goelzer, H., Nowicki, S., Payne, A., Larour, E., Seroussi, H., Lipscomb, W. H., Gregory, J., Abe-Ouchi, A., Shepherd, A., Simon, E., Agosta, C., Alexander, P., Aschwanden, A., Barthel, A., Calov, R., Chambers, C., Choi, Y., Cuzzone, J., Dumas, C., Edwards, T., Felikson, D., Fettweis, X., Golledge, N. R., Greve, R., Humbert, A., Huybrechts, P., Le clec'h, S., Lee, V., Leguy, G., Little, C., Lowry, D. P., Morlighem, M., Nias, I., Quiquet, A., Rückamp, M., Schlegel, N.-J., Slater, D. A., Smith, R. S., Straneo, F., Tarasov, L., van de Wal, R., and van den Broeke, M.: The future sea-level contribution of the Greenland ice sheet: a multimodel ensemble study of ISMIP6, The Cryosphere, 14, 3071–3096, https://doi.org/10.5194/tc-14-3071-2020, 2020.

Gorte, T., Lenaerts, J. T. M., and Medley, B.: Scoring Antarctic surface mass balance in climate models to refine future projections, The Cryosphere, 14, 4719–4733, https://doi.org/10.5194/tc-14-4719-2020, 2020.

Hanna, E., Fettweis, X., and Hall, R. J.: Brief communication: Recent changes in summer Greenland blocking captured by none of the CMIP5 models, The Cryosphere, 12, 3287–3292, https://doi.org/10.5194/tc-12-3287-2018, 2018.

Hansen, N.: Modelling the present day and future climate of Antarctica, Master's thesis, The Technical University of Denmark, Anker Engelunds Vej 1 Bygning 101A 2800 Kgs. Lyngby, Denmark, 2019.

Hansen, N., Langen, P. L., Boberg, F., Forsberg, R., Simonsen, S. B., Thejll, P., Vandecrux, B., and Mottram, R.: Downscaled surface mass balance in Antarctica: impacts of subsurface processes and large-scale atmospheric circulation, The Cryosphere, 15, 4315–4333, https://doi.org/10.5194/tc-15-4315-2021, 2021.

Hazeleger, W., Severijns, C., Semmler, T., Ştefănescu, S., Yang, S., Wang, X., Wyser, K., Dutra, E., Baldasano, J. M., Bintanja, R., Bougeault, P., Caballero, R., Ekman, A. M. L., Christensen, J. H., van den Hurk, B., Jimenez, P., Jones, C., Kållberg, P., Koenigk, T., McGrath, R., Miranda, P., van Noije, T., Palmer, T., Parodi, J. A., Schmith, T., Selten, F., Storelvmo, T., Sterl, A., Tapamo, H., Vancoppenolle, M., Viterbo, P., and Willén, U.: EC-Earth: a seamless earth-system prediction approach in action, B. Am. Meteorol. Soc., 91, 1357–1364, 2010.

Hazeleger, W., Wang, X. Severijns, C., Ştefănescu, S., Bintanja, R., Sterl, A., Wyser, K., Semmler, T., Yang, S., van den Hurk, B., van Noije, T., van der Linden, E., and van der Wiel, K.: EC-Earth V2. 2: description and validation of a new seamless earth system prediction model, Clim. Dynam., 39, 2611–2629, 2012.

Hofer, S., Tedstone, A. J., Fettweis, X., and Bamber, J. L.: Decreasing cloud cover drives the recent mass loss on the Greenland Ice Sheet, Sci. Adv., 3, e1700584, https://doi.org/10.1126/sciadv.1700584, 2017.

Hofer, S., Lang, C., Amory, C., Kittel, C., Delhasse, A., Tedstone, A., and Fettweis, X.: Greater Greenland Ice Sheet contribution to global sea level rise in CMIP6, Nat. Com., 9, 523–528, 2020.

IPCC: IPCC Special Report on the Ocean and Cryosphere in a Changing Climate, edited by: Pörtner, H.-O., Roberts, D. C., Masson-Delmotte, V., Zhai, P., Tignor, M., Poloczanska, E., Mintenbeck, K., Alegría, A., Nicolai, M., Okem, A., Petzold, J., Rama, B., Weyer, N. M., in press, 2019.

Kittel, C., Amory, C., Agosta, C., Delhasse, A., Doutreloup, S., Huot, P.-V., Wyard, C., Fichefet, T., and Fettweis, X.: Sensitivity of the current Antarctic surface mass balance to sea surface conditions using MAR, The Cryosphere, 12, 3827–3839, https://doi.org/10.5194/tc-12-3827-2018, 2018.

Kittel, C., Amory, C., Agosta, C., Jourdain, N. C., Hofer, S., Delhasse, A., Doutreloup, S., Huot, P.-V., Lang, C., Fichefet, T., and Fettweis, X.: Diverging future surface mass balance between the Antarctic ice shelves and grounded ice sheet, The Cryosphere, 15, 1215–1236, https://doi.org/10.5194/tc-15-1215-2021, 2021.

Langen, P. L., Fausto, R. S., Vandecrux, B., Mottram, R. H., and Box, J. E.: Liquid Water Flow and Retention on the Greenland Ice Sheet in the Regional Climate Model HIRHAM5: Local and Large-Scale Impacts, Front. Earth Sci., 4, 110, https://doi.org/10.3389/feart.2016.00110, 2017.

Le clec'h, S., Charbit, S., Quiquet, A., Fettweis, X., Dumas, C., Kageyama, M., Wyard, C., and Ritz, C.: Assessment of the Greenland ice sheet–atmosphere feedbacks for the next century with a regional atmospheric model coupled to an ice sheet model, The Cryosphere, 13, 373–395, https://doi.org/10.5194/tc-13-373-2019, 2019.

Lenaerts, J. T. M., Vizcaino, M., Fyke, J., van Kampenhout, L., and van den Broeke, M. R.: Present-day and future Antarctic ice sheet climate and surface mass balance in the Community Earth System Model, Clim. Dynam., 47, 1367–1381, https://doi.org/10.1007/s00382-015-2907-4, 2016.

Lenaerts, J. T. M., Medley, B., van den Broeke, M. R., and Wouters, B.: Observing and Modeling Ice Sheet Surface Mass Balance, Rev. Geophys., 57, 376–420, https://doi.org/10.1029/2018RG000622, 2019.

Levermann, A., Winkelmann, R., Albrecht, T., Goelzer, H., Golledge, N. R., Greve, R., Huybrechts, P., Jordan, J., Leguy, G., Martin, D., Morlighem, M., Pattyn, F., Pollard, D., Quiquet, A., Rodehacke, C., Seroussi, H., Sutter, J., Zhang, T., Van Breedam, J., Calov, R., DeConto, R., Dumas, C., Garbe, J., Gudmundsson, G. H., Hoffman, M. J., Humbert, A., Kleiner, T., Lipscomb, W. H., Meinshausen, M., Ng, E., Nowicki, S. M. J., Perego, M., Price, S. F., Saito, F., Schlegel, N.-J., Sun, S., and van de Wal, R. S. W.: Projecting Antarctica's contribution to future sea level rise from basal ice shelf melt using linear response functions of 16 ice sheet models (LARMIP-2), Earth Syst. Dynam., 11, 35–76, https://doi.org/10.5194/esd-11-35-2020, 2020.

Ligtenberg, S., Berg, W. J., Van den Broeke, M., Rae, J., and Meijgaard, E.: Future surface mass balance of the Antarctic ice sheet and its influence on sea level change, simulated by a regional atmospheric climate model, Clim. Dynam., 41, 867–884, https://doi.org/10.1007/s00382-013-1749-1, 2013.

Lucas-Picher, P., Wulff-Nielsen M., Christensen J. H., Aðalgeirsdóttir G., Mottram R., and Simonsen S. B.: Very high resolution regional climate model simulations over Greenland: Identifying added value, J. Geophys. Res., 117, D02108, https://doi.org/10.1029/2011JD016267, 2012.

Madsen, M. S., Yang, S., Adageirsdottir, G., Svendsen, S. H., Rodehacke, C. B., Ringgaard, I. M.: The role of an interactive Greenland Ice Sheet in the coupled ice sheet-climate model EC-Earth-PISM, Clim. Dynam., in review, 2021.

Mankoff, K. D., Colgan, W., Solgaard, A., Karlsson, N. B., Ahlstrøm, A. P., van As, D., Box, J. E., Khan, S. A., Kjeldsen, K. K., Mouginot, J., and Fausto, R. S.: Greenland Ice Sheet solid ice discharge from 1986 through 2017, Earth Syst. Sci. Data, 11, 769–786, https://doi.org/10.5194/essd-11-769-2019, 2019.

Medley, B. and Thomas, E. R.: Increased snowfall over the Antarctic Ice Sheet mitigated twentieth-century sea-level rise, Nat. Clim. Change, 9, 34–39, https://doi.org/10.1038/s41558-018-0356-x, 2019.

Mottram, R., Boberg, F., Langen, P. L., Yang, S., Rodehacke, C., Christensen, J. H., and Madsen, M. S.: Surface mass balance of the Greenland ice sheet in the regional climate model HIRHAM5: Present state and future prospects, Low Temperature Science, 75, 105–115, https://doi.org/10.14943/lowtemsci.75.105, 2017.

Mottram, R., Hansen, N., Kittel, C., van Wessem, J. M., Agosta, C., Amory, C., Boberg, F., van de Berg, W. J., Fettweis, X., Gossart, A., van Lipzig, N. P. M., van Meijgaard, E., Orr, A., Phillips, T., Webster, S., Simonsen, S. B., and Souverijns, N.: What is the surface mass balance of Antarctica? An intercomparison of regional climate model estimates, The Cryosphere, 15, 3751–3784, https://doi.org/10.5194/tc-15-3751-2021, 2021.

O'Neill, B. C., Tebaldi, C., van Vuuren, D. P., Eyring, V., Friedlingstein, P., Hurtt, G., Knutti, R., Kriegler, E., Lamarque, J.-F., Lowe, J., Meehl, G. A., Moss, R., Riahi, K., and Sanderson, B. M.: The Scenario Model Intercomparison Project (ScenarioMIP) for CMIP6, Geosci. Model Dev., 9, 3461–3482, https://doi.org/10.5194/gmd-9-3461-2016, 2016.

Riahi, K., van Vuuren, D. P., Kriegler, E., Edmonds, J., O'Neill, B. C., Fujimori, S., Bauer, N., Calvin, K., Dellink, R., Fricko, O., Lutz, W., Popp, A., Crespo Cuaresma, J., Samir, K. C., Leimbach, M., Jiang, L.,Kram, T., Rao, S., Emmerling, J., Ebi, K., Hasegawa, T., Havlik, P.,Humpenöder, F., Da Silva, L. A., Smith, S., Stehfest, E., Bosetti, V., Eom, J.,Gernaat, D., Masui, T., Rogelj, J., Strefler, J., Drouet, L., Krey, V., Luderer, G., Harmsen, M., Takahashi, K., Baumstark, L., Doelman, J. C., Kainuma, M., Klimont, Z., Marangoni, G., Lotze-Campen, H., Obersteiner, M., Tabeau, A., and Tavoni, M.: The Shared Socioeconomic Pathways and their energy, land use, and greenhouse gas emissions implications: An overview, Global Environ. Change, 42, 153–168, https://doi.org/10.1016/j.gloenvcha.2016.05.009, 2017.

Roach, L. A., Dörr, J., Holmes, C. R., Massonnet, F., Blockley, E. W., Notz, D., Rackow, T., Raphael, M. N., O'Farrell, S. P., Bailey, D. A., and Bitz, C. M.: Antarctic Sea Ice Area in CMIP6, Geophys. Res. Lett., 47, e2019GL086729, https://doi.org/10.1029/2019gl086729, 2020.

Robinson, A., Calov, R., and Ganopolski, A.: Multistability and critical thresholds of the Greenland ice sheet, Nat. Clim. Change, 2, 429–432, https://doi.org/10.1038/nclimate1449, 2012.

Roeckner, E., Bäuml, G., Bonaventura, L., Brokopf, R., Esch, M., Giorgetta, M., Hagemann, S., Kirchner, I., Kornblueh, L., Manzini, E., Rhodin, A., Schlese, U., Schulzweida, U., and Tompkins, A.: The atmospheric general circulation model ECHAM5. Part 1. Model description, Report no. 349, Max-Planck-Institut für Meteorologie (MPI-M), Hamburg, Germany, 2003.

Ruan, R., Chen, X., Zhao, J., Perrie, W., Mottram, R., Zhang, M., Diao, Y., Du, L., and Wu, L.: Decelerated Greenland Ice Sheet melt driven by positive summer North Atlantic Oscillation, J. Geophys. Res.-Atmos., 124, 7633–7646, https://doi.org/10.1029/2019JD030689, 2019.

Slater, D. A., Felikson, D., Straneo, F., Goelzer, H., Little, C. M., Morlighem, M., Fettweis, X., and Nowicki, S.: Twenty-first century ocean forcing of the Greenland ice sheet for modelling of sea level contribution , The Cryosphere, 14, 985–1008, https://doi.org/10.5194/tc-14-985-2020, 2020.

Skvarca, P., De Angelis, H., and Zakrajsek, A.: Climatic conditions, mass balance and dynamics of Larsen B ice shelf, Antarctic Peninsula, prior to collapse, Ann. Glaciol., 39, 557–562, https://doi.org/10.3189/172756404781814573, 2004.

Taylor, K. E., Stouffer, R. J., and Meehl, G. A.: An Overview of CMIP5 and the experiment design, B. Am. Meteorol. Soc., 93, 485–498, https://doi.org/10.1175/BAMS-D-11-00094.1, 2012.

The IMBIE Team: Mass balance of the Greenland Ice Sheet from 1992 to 2018, Nature, 579, 233–239, https://doi.org/10.1038/s41586-019-1855-2, 2020.

Undén, P., Rontu, L., Järvinen, H., Lynch, P., Calvo, J., Cats, G., Cuxart, J., Eerola, K., Fortelius, C., Garcia-Moya, J A., Jones, C., Lenderlink, G., McDonald, A., McGrath, R., Navascues, B., Woetman Nielsen, N., Ødegaard, V., Rodrigues, E., Rummukainen, M., Rõõm, R., Sattler, K., Hansen Sass, B., Savijärvi, H., Wichers Schreur, B., Sigg, R., The, H., and Tijm, A.: HIRLAM-5 Scientific Documentation, Scientific Report, available at: http://www.hirlam.org/index.php/hirlam-documentation/doc_download/270-hirlam-scientific-documentation-december-2002 (last access: 15 December 2021), 2002.

van Vuuren, D. P., Edmonds, J., Kainuma, M., Riahi, K., Thomson, A., Hibbard, K., Hurtt, G. C., Kram, T., Krey, V., Lamarque, J.-F., Masui, T., Meinshausen, M., Nakicenovic, N., Smith, S. J., and Rose, S. K.: The representative concentration pathways: an overview, Clim. Change 109, 5, https://doi.org/10.1007/s10584-011-0148-z, 2011.

van Wessem, J. M., Reijmer, C. H., van de Berg, W. J., van den Broeke, M. R., Cook, A. J., van Ulft, L. H., and van Meijgaard, E.: Temperature and Wind Climate of the Antarctic Peninsula as Simulated by a High-Resolution Regional Atmospheric Climate Model, J. Climate, 28, 7306–7326, https://doi.org/10.1175/JCLI-D-15-0060.1, 2015.

van Wessem, J. M., van de Berg, W. J., Noël, B. P. Y., van Meijgaard, E., Amory, C., Birnbaum, G., Jakobs, C. L., Krüger, K., Lenaerts, J. T. M., Lhermitte, S., Ligtenberg, S. R. M., Medley, B., Reijmer, C. H., van Tricht, K., Trusel, L. D., van Ulft, L. H., Wouters, B., Wuite, J., and van den Broeke, M. R.: Modelling the climate and surface mass balance of polar ice sheets using RACMO2 – Part 2: Antarctica (1979–2016), The Cryosphere, 12, 1479–1498, https://doi.org/10.5194/tc-12-1479-2018, 2018.

Vizcaíno, M., Lipscomb, W. H., Sacks, W. J., van Angelen, J. H., Wouters, B., and van den Broeke, M. R.: Greenland Surface Mass Balance as Simulated by the Community Earth System Model. Part I: Model Evaluation and 1850–2005 Results, J. Climate, 26, 7793–7812, https://doi.org/10.1175/JCLI-D-12-00615.1, 2013.

Voosen, P.: New climate models forecast a warming surge, Science, 364, 222–223, https://doi.org/10.1126/science.364.6437.222, 2019.

Wyser, K., Kjellström, E., Koenigk, T., Martins, H., and Döscher, R.: Warmer climate projections in EC-Earth3-Veg: the role of changes in the greenhouse gas concentrations from CMIP5 to CMIP6, Environ. Res. Lett., 15-5, 054020, 2020a.

Wyser, K., van Noije, T., Yang, S., von Hardenberg, J., O'Donnell, D., and Döscher, R.: On the increased climate sensitivity in the EC-Earth model from CMIP5 to CMIP6, Geosci. Model Dev., 13, 3465–3474, https://doi.org/10.5194/gmd-13-3465-2020, 2020b.

Zelinka, M. D., Myers, T. A., McCoy, D. T., Po-Chedley, S., Caldwell, P. M., Ceppi, P., Klein, S. A., and Taylor, K. E.: Causes of higher climate sensitivity in CMIP6 models, Geophys. Res. Lett., 47, e2019GL085782, https://doi.org/10.1029/2019GL085782, 2020.

A.6 MC Paper III

Summer air temperature extremes over Antarctic ice shelves and potential "hotspots" of surface melting

Andrew Orr[a], Pranab Deb[b], Kyle Clem[c], Ella Gilbert[a], Fredrik Boberg[d], David Bromwich[e], Steve Colwell[a], Nicolaj Hansen[d,f], Matthew Lazzara[g,h], Ruth Mottram[d], Masashi Niwano[i], Tony Phillips[a], Denys Pishniak[j], Carleen Reijmer[k], Willem Jan van de Berg[k], Stuart Webster[l], and Xun Zou[e,m]

[a]*British Antarctic Survey, Cambridge, UK.*

[b]*Indian Institute of Technology, Kharagpur, India.*

[c]*Victoria University of Wellington, Wellington, New Zealand.*

[d]*Danish Meteorological Institute, Copenhagen, Denmark.*

[e]*Byrd Polar and Climate Research Center, Columbus, USA.*

[f]*Geodesy and Earth Observation, DTU-Space, Technical University of Denmark, Lyngby, Denmark.*

[g]*University of Wisconsin-Madison, Madison, USA.*

[h]*Madison Area Technical College, Madison, USA.*

[i]*Meteorological Research Institute, Japan Meteorological Agency, Tsukuba, Japan.*

[j]*National Antarctic Scientific Center, Kyiv, Ukraine.*

[k]*Utrecht University, Utrecht, The Netherlands.*

[l]*Met Office, Exeter, UK.*

[m]*Scripps Institution of Oceanography, La Jolla, USA.*

Corresponding author: Andrew Orr, anmcr@bas.ac.uk

ABSTRACT

Understanding of the spatiotemporal characteristics of temperature extremes exceeding the melt threshold over Antarctic ice shelves is severely limited but important to identify those that are vulnerable to possible melt-induced hydrofracture. We investigate this using an index describing summertime "melt potential" (MP), characterised by two components measuring the frequency (MP-freq) and intensity (MP-int) of daily maximum temperatures exceeding a melt threshold of 271.15 K, based on output from high-resolution hindcasts (1979-2019) using the MetUM and HIRHAM5 atmospheric models. MP-freq is highest for Antarctic Peninsula ice shelves (exceeding 70%), lowest (around 10%) for Ronne-Filchner and Ross ice shelves, and typically between 40 and 60% for other ice shelves. Many ice shelves are characterised by strong spatial gradients in MP-int, which varies from 0 to 5 K. Hotspots of MP are apparent over some ice shelves, which we attribute to local scale processes associated with warm signatures, such as foehn events, katabatic winds, and barrier winds. Ice shelves in East Antarctica and the eastern section of West Antarctica show a decreasing trend in MP-freq. The regional circulation patterns associated with high MP values over West Antarctic and East Antarctic ice shelves are remarkably consistent for their respective region but tied to different large-scale climate forcings. The West Antarctic circulation shows a strong connection with El Niño activity, particularly anomalous central tropical Pacific sea surface temperatures and/or deep convection in the South Pacific Convergence Zone. By contrast, the East Antarctic circulation resembles an extratropical circulation pattern characteristic of the negative Southern Annular Mode.

1. Introduction

The floating ice shelves that fringe around 75% of Antarctica's coastline have undergone unprecedented thinning and shrinking in recent decades (Paolo et al., 2015). The melting responsible for this can be either from below due to increased incursions of relatively warm water (Pritchard et al., 2012) and/or above due to warming air temperatures (Scambos et al., 2000). In relation to the latter, the presence of substantial surface meltwater ponds is widespread over many Antarctic ice shelves during summertime (Kingslake et al., 2017; Stokes et al., 2019; Arthur et al., 2020; Dell et al., 2020; Banwell et al., 2021) in response to intense or prolonged surface melting (Trusel et al., 2013; Nicolas et al., 2017; Kuipers Munneke et al., 2018; Johnson et al., 2021). Ensuing vertical fracturing (hydrofracturing) can occur if the meltwater enters downward and enlarges fractures in the ice (Scambos et al., 2000; MacAyeal et al., 2003; Banwell et al., 2013, 2015, 2019), potentially triggering their catastrophic collapse (Lai et al., 2020; Lhermitte et al., 2020). This has occurred over several ice shelves on the Antarctic Peninsula in recent decades (Rott et al., 1996; Doake et al., 1998; Scambos et al., 2000, 2009; Glasser et al., 2011).

Ice shelves play an essential role in controlling Antarctic ice sheet stability by restraining (buttressing) the flow of inland ice into the ocean (Rott et al., 1996; Rignot et al., 2019). Their thinning and/or collapse therefore causes acceleration of glacier flow into the ocean, resulting in increased rates of ice sheet mass loss and consequent sea level rise (Pritchard et al., 2012; Rignot et al., 2019). Further summertime atmospheric warming in the future will likely result in increased surface melt intensities over many of Antarctica’s ice shelves (Trusel et al., 2015; Chyhareva et al., 2019; Bozkurt et al., 2021; Feron et al., 2021; Gilbert and Kittel, 2021). This is expected to cause more catastrophic ice shelf collapses like those seen on the Antarctic Peninsula, because other ice shelves could be vulnerable to hydrofracture if inundated with meltwater (Lai et al., 2020). Consequently, ice shelf loss in the coming decades could prompt significant dynamic destabilisation/retreat of the Antarctic ice sheet, accelerating ice loss and sea level rise (DeConto et al., 2021).

Important local scale processes that are associated with warm signatures and ice shelf surface melting include foehn winds (Orr et al., 2008, 2021; Elvidge et al., 2016; Zou et al., 2021; Gilbert et al., 2022), katabatic winds (Parish and Bromwich, 1989; Bromwich et al., 1992; Heinemann et al., 2019), and barrier winds (Orr et al., 2004; Coggins et al., 2014). Foehn events especially are known to cause extreme anomalous warming in Antarctica, with temperature spikes of >10 K attributed to them (e.g., Spiers et al., 2010; Bozkurt et al., 2018). Relevant synoptic scale processes include warm air intrusions and atmospheric rivers, which can also result in rapid increases in near-surface temperature of >10 K and sometimes the co-occurrence of instances of foehn (Nicolas and Bromwich, 2011; Nicolas et al., 2017; Bozkurt et al., 2018; Scott et al., 2019; Wille et al., 2019, 2022; Clem et al., 2020, Djoumna and Holland, 2021). Additionally, the many synoptic-scale depressions that travel around Antarctica can result in abrupt warming over coastal locations (Simmonds and Keay, 2000a; Orr et al., 2014).

Air temperature and surface melt are closely related (Trusel et al., 2015), with surface melting occurring when near-surface air temperatures are greater than a temperature threshold of

271.15 K (Nicolas et al., 2017). However, a comprehensive understanding of the spatiotemporal characteristics of summertime temperatures over Antarctica's ice shelves remains elusive because a) in situ meteorological observations are sparse and unevenly distributed and b) atmospheric models typically lack the requisite fine spatial resolution required to properly resolve the smaller ice shelves that extend around 100 km from the grounding line to the calving front (Deb et al., 2018). Moreover, occurrences of temperature extremes and the local and synoptic meteorological influences and remote effects that can cause them are especially poorly quantified (Wei et al., 2019). Temperature extremes may play an important role in ice shelf surface melt by exceeding the melt threshold for short periods even when daily mean temperatures are below this.

Here we address this knowledge deficit by using outputs from two high horizontal resolution (12 km) regional atmospheric model hindcasts (1979-2019) to better understand the spatiotemporal characteristics of temperature extremes that could cause surface melting of Antarctic ice shelves. Analysing output from two models enables model-dependence and consistency to be assessed. The high spatial resolution of the models enables both an improved representation of the local scale processes that impact ice shelf surface melt and coverage of the smaller ice shelves by multiple grid boxes (Deb et al., 2016, 2018). The simulations are from contributions to the coordinated regional downscaling experiment (CORDEX; Gutowski et al., 2016). We also examine how local and remote effects govern these characteristics by examining the influence of large-scale atmospheric circulation and local thermal advection associated with the Southern Annular Mode (SAM) and El Niño – Southern Oscillation (ENSO). These factors have all been shown previously to play a key role in surface climate variability over Antarctica's ice shelves (Deb et al., 2018; Nicolas et al., 2017; Clem et al., 2018; Scott et al., 2019).

2. Models, data, and methods

a. Atmospheric models

The atmospheric models used are the UK Met Office Unified Model (MetUM) and HIRHAM5. See Mottram et al. (2021) for a description of the setup and approach used by both models. The dynamically downscaled models are a) run over the standard Antarctic CORDEX domain shown in Figure 1 at a grid spacing of 0.11° (~12 km) for the period December 1979 through to February 2019 and b) forced by ERA-Interim reanalysis data (Dee et al., 2011). We use instantaneous 3-hourly outputs of near-surface temperature, which for the MetUM is based on 1.5 m air temperature $T_{1.5m}^{MetUM}$, while for HIRHAM5 it is 2 m air temperature $T_{2m}^{HIRHAM5}$. This yields 39 summer melt seasons from 1979 to 2018 – i.e., the summer 1979 represents the December of 1979 and January-February of 1980.

b. Datasets and climate indices

Summer near-surface temperature measurements with a time resolution of 3-hourly or better are collected from 20 weather stations (six staffed and fourteen automatic) situated either on or close to Antarctic ice shelves (Lazzara et al., 2012). See Figure 1 for locations. The temperature sensors are located at a standard height of >1.5 m and are naturally (wind) ventilated. The temperature measurements are post-processed to create 3-hourly datasets, which are subsequently used to compute a timeseries of observed summer daily maximum temperatures for each station. The use of natural ventilated sensors can result in daytime measured temperatures being warm biased (by up to 10 K) on occasions of high incoming solar radiation and low wind speed (Genthon et al., 2011). Additionally, some of the weather stations are located on rock outcrops, which during summer could also result in warm biased daytime temperatures. Table 1 gives further details of the 20 stations.

The location and geographic extent of the Antarctic ice shelves are based on maps assembled from 2007-2009 satellite-based data, which is part of the Making Earth System Data Records for Use in Research Environments (MEaSUREs) program (Mouginot et al., 2017).

We use timeseries of existing summertime climate indices describing ENSO (Huang et al., 2017a) for the period 1979-2018 based on a) station-based Southern Oscillation Index (SOI) and b) sea-surface temperature (SST) anomalies in the Niño 4 region (5°N-5°S, 160°E-150°W) from the National Oceanic and Atmospheric Administration (NOAA) Optimum Interpolation SST analysis (Huang et al., 2021). Timeseries of existing summertime climate indices describing the SAM are also used, based on Marshall (2003).

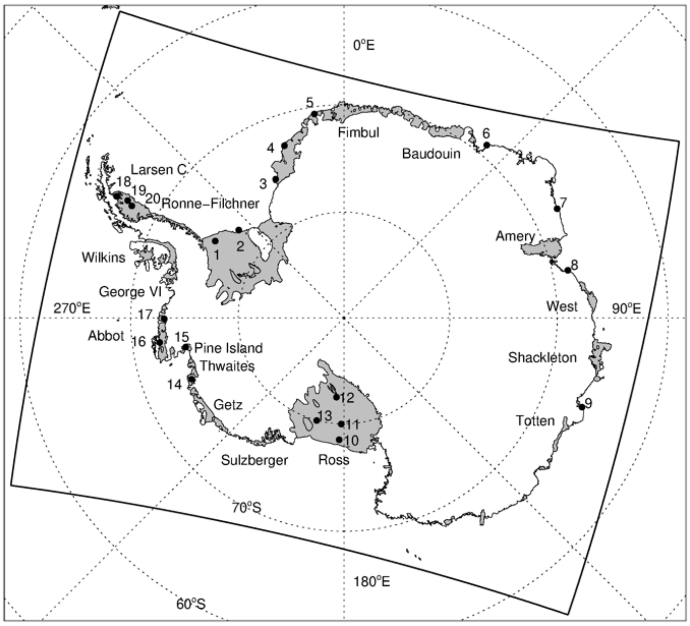

Figure 1: Map showing the location and names of the 16 ice shelves examined, as well as the locations of the 20 weather stations used (labelled 1 to 20). The solid box surrounding Antarctica shows the regional domain used by the MetUM and HIRHAM5 simulations. The ice shelves examined are seven in East Antarctica (Ronne-Filchner, Fimbul, Baudouin, Amery, West, Shackleton, Totten), six in West Antarctica (Ross, Sulzberger, Getz, Thwaites, Pine Island, Abbot), and three on the Antarctic Peninsula (George VI, Wilkins, Larsen C).

Spatial variability in tropical convection is examined using a) monthly-mean outgoing longwave radiation (OLR) at 2.5° × 2.5° horizontal resolution from the NOAA Interpolated OLR dataset (Liebmann and Smith, 1996) and b) monthly-mean SST at 2° × 2° horizontal resolution from the NOAA Extended Reconstructed Sea Surface Temperature V5 dataset (Huang et al., 2017b). Variability in atmospheric circulation is investigated using several monthly-mean fields from the European Centre for Medium-range Weather Forecasts (ECMWF) fifth generation atmospheric reanalysis ERA5 (Hersbach et al., 2020) at 1.5° × 1.5° horizontal resolution, including stream function and horizontal wave flux at 200 hPa (Takaya and Nakamura, 2001), geopotential height and horizontal wind at 500 hPa, 2 m air temperature, 10 m wind components, and mean sea level pressure (MSLP).

No.	Station name	Lat. (°N), Lon. (°E)	No. days	Surface type	Elev. (m)	MetUM Elev. (m)	HIRHAM5 Elev. (m)
1	Limbert	-75.87, -59.15	1570	Ice	58	0	0
2	Filchner	-77.07, -50.11	616	Ice	50	0	0
3	Halley	-75.43, -26.22	3555	Ice	30	1.65	0
4	Drescher	-72.87, -19.07	930	Ice	50	0	0
5	Neumayer	-70.67, -8.25	3131	Ice	50	1	0
6	Syowa	-69.00, 39.57	3368	Rock	21	5.8	0
7	Mawson	-67.6, 62.87	3329	Rock	16	165.3	89.0
8	Davis	-68.57, 77.97	3334	Rock	13	15.1	3.0
9	Casey	-66.27, 110.52	2492	Rock	42	56.3	19.3
10	Vito	-78.50, -177.75	1180	Ice	50	0	0
11	Gill	-79.98, -178.57	2877	Ice	54	0	0
12	Lettau	-82.48, -174.59	2368	Ice	38	0	0
13	Margaret	-79.98, -165.10	992	Ice	67	0	0
14	Bear Peninsula	-74.55, -111.88	685	Rock	342	183.0	168.9
15	Evans Knoll	-74.85, -100.40	700	Rock	178	7.5	51.5
16	Thurston Island	-72.53, -97.56	629	Rock	245	225.0	96.8
17	Lepley Nunatak	-73.11, -90.30	599	Rock	159	68.9	20.1
18	Scar Inlet	-65.93, -61.85	390	Ice	50	4.5	0
19	Larsen Ice Shelf	-67.0, -61.47	1868	Ice	43	1.6	0
20	Larsen C South	-67.57, -62.15	483	Ice	50	0.75	0

Table 1. Details of the 20 weather stations used in the study, showing (from left to right) the number used to label them in Figure 1 (No.), station name (Station name), latitude and longitude [Lat. (°N), Lon. (°E)], the number of days of data availability during the study period (No. days), surface type the station is sitting on (Surface type), surface elevation of the station (Elev.), corresponding elevation of MetUM orography (MetUM Elev.), and corresponding elevation of HIRHAM5 orography (HIRHAM5 Elev.). Six of the stations are staffed (specifically Halley, Neumayer, Syowa, Mawson, Davis, and Casey) and the remaining fourteen are automatic.

c. Methodology

The 3-hourly values of $T_{1.5m}^{MetUM}$ and $T_{2m}^{HIRHAM5}$ are used to compute a timeseries of daily maximum temperatures for 39 summer seasons from 1979 to 2018 for both models. A statistical analysis is made between the model and observed summer daily maximum temperatures for each of the 20 weather station locations, based on mean bias, root-mean-square-error (RMSE), and correlation (Deb et al., 2016). The model-based temperatures at the station locations are computed by bilinear interpolation of the four surrounding grid points. Any adjustment to $T_{1.5m}^{MetUM}$ and $T_{2m}^{HIRHAM5}$ to account for differences between the actual and model height of the orography was assumed to be small and therefore not included. This assumption is justified as a) over the ice shelves the difference between the actual and model height is typically less than 100 m (Table 1) and b) during summer the atmospheric boundary layer over ice shelves is either neutrally or weakly stably stratified, i.e., temperature is only weakly dependent on height (Krinner and Genthon, 1999; Kuipers Munneke et al., 2012).

The MetUM and HIRHAM5 timeseries of summer daily maximum temperatures are used to create a probability distribution function (PDF) at each grid point over an Antarctic ice shelf for each model. We subsequently use these PDFs and the close relationship between air temperature and surface melting (Trusel et al., 2015) to describe an air temperature-based measure of potential melt, which we refer to as the “melt potential” (MP). This is characterised by two components measuring the frequency and intensity of daily maximum temperatures exceeding a temperature/melt threshold value T_0, which we consider to be 271.15 K (-2.0°C). This is the same value chosen by Nicolas et al. (2017), who show that surface melting can occur even when the temperature is below the freezing point due to the absorption of solar radiation by the snowpack. The frequency component (hereafter referred to as MP-freq) is defined as the percentage of the area under the curve of the PDFs greater than T_0. The intensity component (hereafter referred to as MP-int) is defined as the difference between the 95th percentile of the distribution of summer daily maximum temperatures and T_0. Essentially these two numbers describe the right-hand-side tail of the PDFs for daily maximum temperatures exceeding the threshold T_0, i.e., conveying physical information such as the likelihood of being exposed to incidences of high-melt or low-melt.

Climatological MP-freq and MP-int indices (i.e., calculated for all 39 summer seasons) are subsequently computed for 16 individual ice shelves from the daily maximum temperature distribution at each grid point over the ice shelf, with the MEaSUREs dataset used to define the ice shelf areas. Figure 1 shows the locations of the ice shelves selected, consisting of seven in East Antarctica (Ronne-Filchner, Fimbul, Baudouin, Amery, West, Shackleton, Totten), six in West Antarctica (Ross, Sulzberger, Getz, Thwaites, Pine Island, Abbot), and three on the Antarctic Peninsula (George VI, Wilkins, Larsen C). Additionally, climatological MP indices are computed and mapped for all Antarctic ice shelves to determine localised “hotspots”.

The associated timeseries of summer MP indices for the 16 ice shelves examined is subsequently used to investigate long-term trends and interannual variability. Change-points in the trends are detected by applying a sequential Mann-Kendall test to the timeseries (Mann, 1945) after a Butterworth lowpass filter has been applied to remove cycles with periodicity > 20 years, with change-points identified if the timeseries before and after are statistically significant. Finally, the MP-freq timeseries and the various ERA5 fields are used together with correlation and composite analyses to investigate how remote effects and atmospheric circulation patterns can cause high MP values over East and West Antarctic ice shelves (Clem et al., 2018; Deb et al., 2018). Statistical significance of correlations and composite anomalies is calculated using a two-tailed Student’s *t*-test, with a confidence interval of 95%.

3. Results

a. Comparison of modelled and observed daily maximum temperatures

When compared to the measured values, the MetUM summer daily maximum temperatures derived from $T_{1.5m}^{MetUM}$ show a cold bias at most of the 20 weather station locations (Figure 2), which is typically less than -1 K (Table 2). Only Filchner station shows a relatively substantial warm bias of 1.6 K (Figure 2, Table 2). However, larger MetUM cold biases of around -2 K (Figure 2, Table 2) are apparent at four sites situated in East Antarctica (Syowa, Mawson, Davis, and Casey), which is perhaps related to these sites being located on rock outcrops (Table 1) and the observations consequently affected by a possible warm bias (section 2b). Furthermore, MetUM cold biases are particularly evident for temperatures above T_0 at some sites (e.g., Larsen Ice Shelf, Larsen C South, Limbert, Filchner, Halley, Drescher), which is possibly related to daytime measured temperatures being warm biased on occasions of high incoming solar radiation and low wind speed (section 2b). The HIRHAM5 summer daily maximum temperatures derived from $T_{2m}^{HIRHAM5}$ typically have a larger cold bias, larger root-mean-square-error (RMSE), and lower correlation than the MetUM results (Figure 2, Table 2). A much larger cold bias (up to -4 K) in the HIRHAM5 temperatures is especially evident at sites located on Ross (Vito, Gill, Lettau, and Margaret) and Ronne-Filchner (Limbert and Filchner).

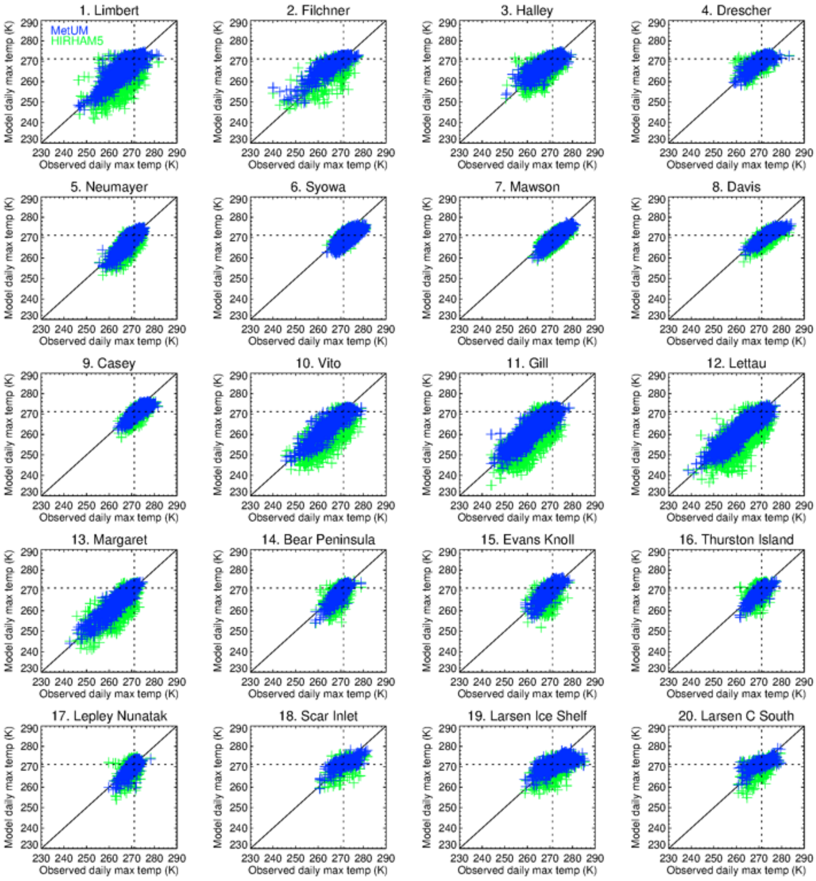

Figure 2: Scatterplots comparing the observed daily maximum temperature and MetUM (blue) and HIRHAM5 (green) model daily maximum temperature at each of the 20 weather stations. The dashed lines show the temperature/melt threshold value $T_0 = 271.15$ K. The headings for each panel show the name of each station and the number used to label them in Figure 1.

No.	Station name	Daily maximum temperature (MetUM, HIRHAM5)		
		RMSE (K)	BIAS (K)	CORR
1	Limbert	2.68, 5.83	-0.29, -3.03	0.87, 0.69
2	Filchner	3.13, 4.38	1.57, -0.75	0.89, 0.72
3	Halley	1.93, 2.97	0.09, -1.06	0.82, 0.66
4	Drescher	1.93, 2.72	-0.54, -0.97	0.79, 0.61
5	Neumayer	1.58, 3.07	-0.05, -1.69	0.87, 0.75
6	Syowa	2.92, 2.51	-2.25, -1.90	0.68, 0.73
7	Mawson	2.95, 3.45	-2.64, -2.95	0.87, 0.77
8	Davis	2.97, 3.87	-2.63, -3.40	0.87, 0.74
9	Casey	2.18, 2.62	-1.75, -1.98	0.83, 0.75
10	Vito	2.53, 6.35	-0.67, -4.43	0.90, 0.73
11	Gill	2.37, 5.62	-0.14, -3.67	0.90, 0.76
12	Lettau	2.40, 6.07	-0.33, -4.19	0.91, 0.76
13	Margaret	2.39, 5.00	0.66, -2.56	0.91, 0.75
14	Bear Peninsula	2.03, 3.58	-0.59, -1.43	0.82, 0.58
15	Evans Knoll	2.02, 3.88	0.39, -1.23	0.83, 0.57
16	Thurston Island	1.82, 3.24	-0.84, -0.82	0.82, 0.51
17	Lepley Nunatak	1.88, 3.29	-0.21, -0.47	0.78, 0.49
18	Scar Inlet	2.56, 3.29	-0.38, -1.20	0.71, 0.62
19	Larsen Ice Shelf	2.92, 3.63	-1.28, -2.12	0.62, 0.57
20	Larsen C South	2.28, 3.12	0.24, -1.00	0.72, 0.62

Table 2: Statistical analysis of the model-based summer daily maximum temperatures at the 20 weather stations used in the study, showing the number used to label each site in Figure 1 (No.), the station name (Station name), root-mean-square-error (RMSE), bias (BIAS), and correlation (CORR). In the final three columns of the table, the MetUM results are given first and the HIRHAM5 results second (i.e., MetUM, HIRHAM5).

The good performance of the MetUM suggests that PDFs of daily maximum temperatures over Antarctic ice shelves derived from its output are broadly representative of actual conditions, which gives us confidence that the MP values derived are physically realistic; much of our ensuing investigation will therefore focus on analysis of the MetUM results. However, the MP values derived from HIRHAM5 output are still an important as they enable the dependency / consistency between models and robustness of the findings to be assessed (Gutowski et al., 2016).

b. Hotspots of "melt potential"

Figure 3 shows that the MetUM and HIRHAM5 climatological PDFs of summer daily maximum temperatures for the 16 ice shelves investigated are broadly similar, i.e., the consistency between models is evidence that the results are robust. The associated values of MP-freq and MP-int for each ice shelf are shown in Table 3 (as well as displayed on Figure 3). The PDFs for 14 of the 16 ice shelves show a peak occurring for temperatures above T_0 (the exception being Ronne-Filchner and Ross). The area of the PDF exceeding T_0 (i.e., MP-freq) is highest for Larsen C and Wilkins on the Antarctic Peninsula (over 70%), lowest for Ronne-Filchner and Ross (around 10%), and typically between 40 and 60% for the other West and East Antarctic ice shelves. The MetUM MP-freq values are typically higher than HIRHAM5 values (except for George VI), although the disagreement is within 10% for most of the ice shelves (but around 30% for Ronne-Filchner, Fimbul, Baudouin, and Amery), which is consistent with HIRHAM5 having a larger cold bias than the MetUM. Some of the highest values of MetUM MP-int are for George VI (4.2 K), Wilkins (3.5 K), and Larsen C (3.2 K) (Table 3), while the lowest are for Ronne-Filchner and Ross (1-2 K). For East Antarctica, the values of MetUM MP-int range from 2.7-3.2 K (excluding Ronne-Filcher), while for West Antarctica the value is around 2.8 K (excluding Ross and Pine Island). The value for Pine Island (3.7 K) is the highest outside of the Antarctic Peninsula and suggests that this ice shelf is vulnerable to extreme surface melt events in addition to the well-known basal melting (Jenkins et al., 2010, 2016). The MetUM MP-int values are either similar or higher than HIRHAM5 values (except for Ross, Wilkins, Larsen C), with any disagreement within 10% or less.

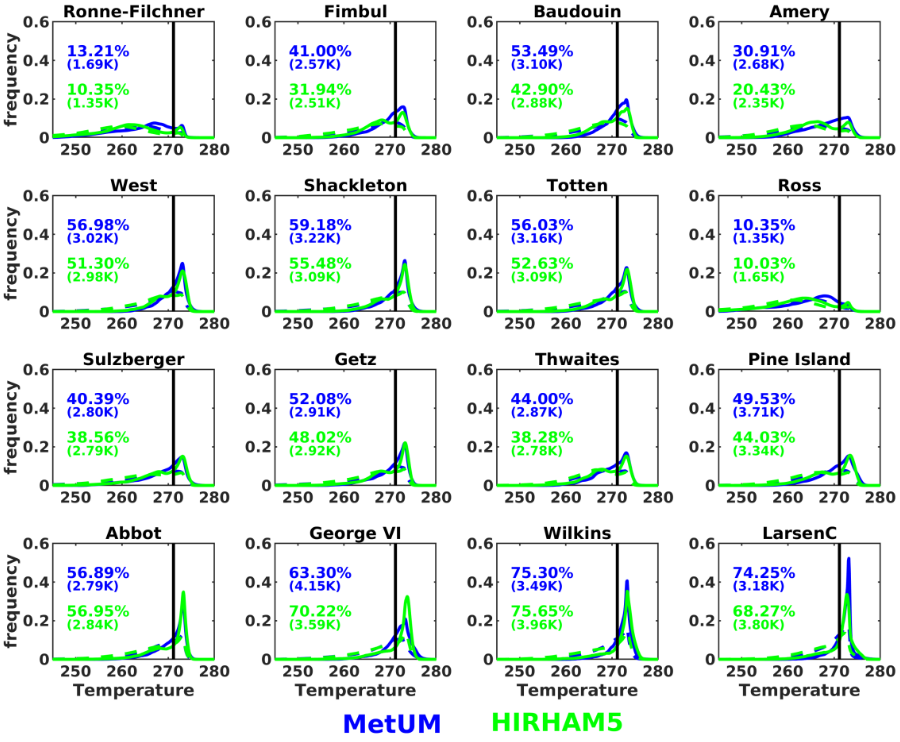

Figure 3: Probability distribution functions (PDFs) of summer daily maximum near-surface temperature for 16 Antarctic ice shelves (solid lines) based on MetUM (blue) and HIRHAM5 (green) output. The numbers show the “melt potential” (MP) values calculated from these distributions, which measure the frequency (MP-freq, %) and intensity (MP-int, K) of daily maximum temperatures exceeding a temperature/melt threshold value $T_0 = 271.15$ K (shown as the vertical solid line). Values of MP-freq and MP-int are shown for both MetUM (blue) and HIRHAM5 (green), with the values of MP-int shown in parenthesis. These numbers are also shown in Table 1. Also shown is the PDFs of summer daily mean temperature (dashed lines). The ice shelves examined are (from top left to bottom right): Ronne-Filchner, Fimbul, Baudouin, Amery, West, Shackleton, Totten, Ross, Sulzberger, Getz, Thwaites, Pine Island, Abbot, George VI, Wilkins, and Larsen C.

Ice shelf	MetUM, HIRHAM5	
	MP-freq (%)	MP-int (K)
Ronne-Filchner	13.2, 10.4	1.7, 1.4
Fimbul	41.0, 31.9	2.7, 2.5
Baudouin	53.5, 42.9	3.1, 2.9
Amery	30.9, 20.4	2.7, 2.4
West	57.0, 51.3	3.0, 3.0
Shackleton	59.2, 55.5	3.2, 3.1
Totten	56.0, 52.6	3.2, 3.1
Ross	10.4, 10.0	1.4, 1.7
Sulzberger	40.4, 38.6	2.8, 2.8
Getz	52.1, 48.0	2.9, 2.9
Thwaites	44.0, 38.3	2.9, 2.8
Pine Island	49.5, 44.0	3.7, 3.3
Abbot	56.9, 57.0	2.8, 2.8
George VI	63.3, 70.2	4.2, 3.6
Wilkins	75.3, 75.7	3.5, 4.0
Larsen C	74.3, 68.3	3.2, 3.8

Table 3: Climatological values of MP-freq (%, second column) and MP-int (K, third column) for the 16 ice shelves examined based on MetUM (shown first) and HIRHAM5 (shown second) output. These values are also shown in Figure 3.

Figure 3 also shows the PDFs of summer daily average temperature (dashed lines), which for many of the ice shelves are primarily determined by climatological factors like latitude and insolation. For many of the ice shelves, this curve shows a peak that occurs at roughly the same temperature as the peak in daily maximum temperature (solid lines). For example, for Larsen C and Wilkins the solid and dashed curves are analogous, albeit noticeably different in size, i.e., a much smaller area for summer daily average temperatures greater than T_0. The high values of MP-freq and MP-int for Larsen C and Wilkins (74.3% and 3.2 K for Larsen C and 75.3% and 3.4

K for Wilkins, based on MetUM) are therefore consistent with these being some of the warmest regions of Antarctica. In the case of Larsen C this is due to its location being relatively far north (so higher insolation during summer) and from the frequent occurrence of warm foehn winds (Orr et al., 2008; Elvidge et al., 2016; Gilbert et al., 2022). For Wilkins its location on the western coast of the Peninsula means it is strongly influenced by the circumpolar westerly flow around Antarctica, which is blocked by the orography of the Peninsula and deflected to the right, resulting in relatively warm maritime northerly winds over Wilkins (Orr et al., 2004). By contrast, the low values of MP-freq and MP-int for Ronne-Filcher and Ross (13.2% and 1.7 K for Ronnie-Filchner and 10.4% and 1.4 K for Ross, based on MetUM) are consistent with these being much further south and therefore some of the coldest regions considered, meaning that summer daily maximum (and average) temperatures are typically below T_0 (Costanza et al., 2016).

To map localised hotspots of MP, Figure 4 shows the spatial pattern of MP-freq and MP-int over all Antarctic ice shelves. The MetUM MP-freq (Figure 4a) shows that the highest values are again found on the Antarctic Peninsula, which approach 100% over the northern section of Larsen C, i.e., each summer day this region experiences daily maximum temperatures above T_0. This is followed by West Antarctica and the region of East Antarctica east of Amery, then the region of East Antarctica to the west of Amery (Dronning Maud Land), and finally Ross and Ronne-Filchner. The Ross, Ronne-Filchner, and Larsen C are sufficiently large to show a distinct latitudinal gradient in MP-freq, which is consistent with the broad-scale latitudinal air temperature gradient. Additionally, regional differences in MP-freq are apparent between ice shelves located at similar latitudes in both West and East Antarctica. In West Antarctica, MP-freq is higher over ice shelves located in eastern sectors compared to western sectors, which is consistent with the climatological influence of the Amundsen Sea Low on temperatures (Hosking et al., 2013; Scott et al., 2019). In the region of East Antarctica to the west of Amery, values are also higher over ice shelves located in eastern sectors, which is consistent with the influence of the climatological zonal wavenumber 3 pattern (Goyal et al., 2021).

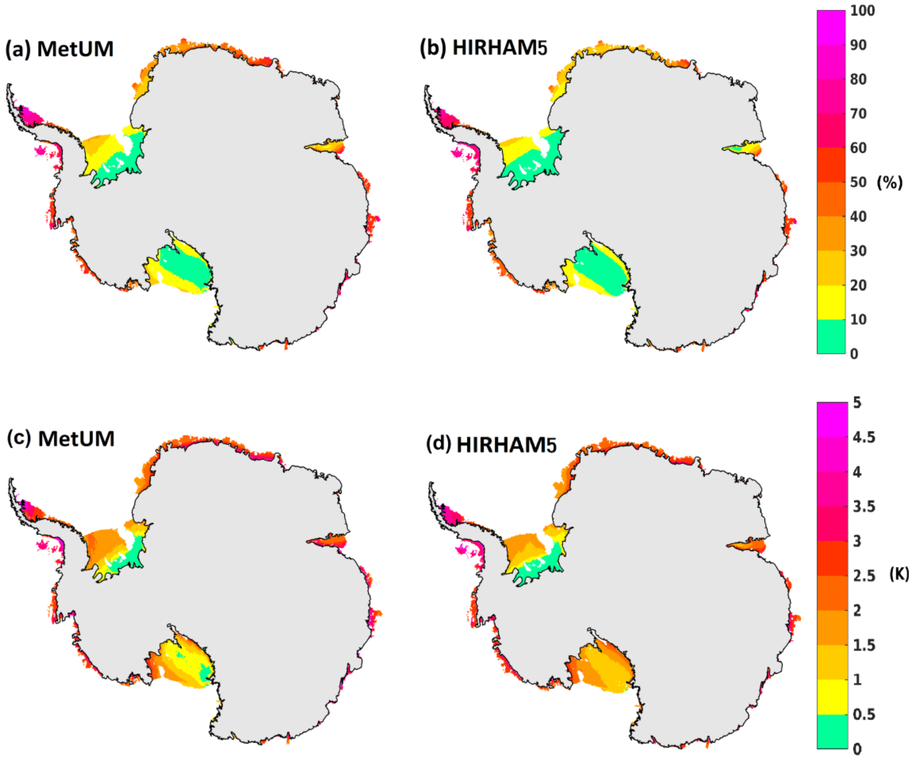

Figure 4: Climatological "melt potential" (MP) for Antarctic ice shelves, which measure the frequency (MP-freq; top) and intensity (MP-int; bottom) of daily maximum near-surface temperatures exceeding a temperature/melt threshold value $T_0 = 271.15$ K based on MetUM (left) and HIRHAM5 (right) output.

Hotspots of MetUM MP-freq are particularly apparent over Amery and Ross. The Amery ice shelf is characterised by increased values over its southern and northern edges (resulting in a minimum over its central section), with the high values over the southern edge likely caused by the pronounced funnelling of katabatic winds that occurs here and the associated warming (Parish and Bromwich, 1991). Katabatic winds can cause warming through increased mixing in the stable boundary layer resulting in relatively warmer air from aloft being mixed to the surface, as well as by adiabatic warming (Parish and Bromwich, 1989; Bromwich et al., 1992; Heinemann et al., 2019). The Ross ice shelf has increased MP-freq along its southern and western sectors bordering the Transantarctic Mountains, which is probably associated with the southerly surface wind regime in this region referred to as the Ross ice shelf Air Stream (RAS). This is made up of interactions between barrier winds and katabatic winds and synoptic forcing from cyclonic systems in the Ross Sea (Parish et al., 2006), and has a marked warming effect on the surface of Ross (Coggins et al., 2014). Additionally, a narrow region of high MP-freq exists along the eastern section of Ross. This is probably associated with the frequent occurrence of foehn winds in this region, which are associated with localised warming that has been shown to cause surface melting (Zou et al., 2021).

Examination of HIRHAM5 MP-freq (Figure 4b) shows that they are broadly consistent with the MetUM results. Although it is noticeable that a) HIRHAM5 values are slightly lower than MetUM (as is also shown in Figure 3 and Table 3) and b) local details apparent in the MetUM results are often less apparent in the HIRHAM5 results (e.g., eastern sector of Ross and Amery).

The MetUM MP-int values vary from 0 to 5 K (Figure 4c). The higher values (around 5 K) are found over the northern and western sections of Larsen C (and parts of George VI), which is consistent with it being one of the warmest regions of Antarctica and the frequent occurrence of warm foehn winds (Orr et al., 2008; Elvidge et al., 2016; Gilbert et al., 2022). Furthermore, MP-int values are often largest over the region of the ice shelf nearest the slopes of the ice sheet for many Antarctic ice shelves, which again is likely explained by katabatic warm signatures. This is especially apparent over the katabatic wind confluence zones in East Antarctica (Parish and Bromwich, 1991), which show MP-int values of 3-5 K. Katabatic outflows and their accompanying warm signatures can extend more than 100 km over flat ice shelves, and even further if favourable synoptic conditions are present that cause katabatic surges (Bromwich et al., 1992; Heinemann et al., 2019). In West Antarctica, Pine Island is identified as a region of relatively high MP-int.

The lower values of MetUM MP-int occur over the southern sector of Ronne-Filcher and central sector of Ross, but these ice shelves are also characterised by noticeable spatial gradients. For example, values of MP-int are up to 2-3 K higher over the southern and eastern sections of the Ross, which are also likely associated with the warming effects associated with the RAS and foehn winds, as well as katabatic outflows (Bromwich et al., 1992; Coggins et al., 2014; Zou et al., 2021). For Ronne-Filcher, values of MP-int are 2-3 K higher over its western margins, which is likely related to synoptic conditions (Scott et al., 2019), i.e., many of the atmospheric circulation patterns that cause surface melting and anomalously warm near-surface temperatures over West Antarctica also affect Ronne-Filchner. For example, one of the patterns Scott et al. (2019) identify (labelled synoptic pattern #8) is related to a ridge over the Antarctic Peninsula, which promotes warm marine air intrusions from the Bellingshausen Sea onto eastern parts of West Antarctica (Ellsworth Land) that travel as far as Ronne-Filchner. This results in anomalous near-surface warming (up to 2 K) and surface melting (5-10% of the time) affecting the western margins of Ronne-Filchner during summer. High MP-int in this location could also be aided by foehn winds in the lee of the Ellsworth Mountains (>4500 m elevation) and southern section of the Antarctic Peninsula (Palmer Land).

Examination of HIRHAM5 MP-int (Figure 4d) shows that they are again broadly consistent with the MetUM results, albeit often slightly lower (Table 3) and less locally detailed. In particular, the high values near the slopes of the ice sheet are less apparent in the HIRHAM5 results (especially around East Antarctica), suggesting that a key difference in the models may be in their representation of katabatic winds and their flow over the ice shelves (Orr et al., 2014; Heinemann et al., 2019). Another key difference in the models could also be their representation of foehn winds, which are likely responsible for some of the detailed spatial variation in MP-int.

c. Interannual variability of "melt potential"

Figure 5 shows the timeseries of MetUM and HIRHAM5 summertime MP-freq for the 16 ice shelves, including the linear trend for the period and any change-points in the trend (Tables 4 and 5). The interannual variability and linear trends are broadly similar between models. Many of the ice shelves are characterised by a relatively high interannual variability. This is apparent in both West Antarctica (Sulzberger, Getz, Thwaites, Pine Island, Abbot, George VI) and East Antarctica (Fimbul, Baudouin, Amery, West, Shackleton, Totten). The former is consistent with the high variability of the Amundsen Sea Low that controls much of the climatic variability in West Antarctica (Hosking et al., 2013; Scott et al., 2019), while the latter is consistent with the large interannual variability in cyclone frequency (Simmonds and Keay, 2000b). By contrast, Ross and Ronne-Filchner have a relatively small range of interannual variability, which is perhaps because these are much larger ice shelves and so any averaged quantity is somewhat smoothed. The MetUM MP-freq results for many of the ice shelves in the eastern section of West Antarctica (Getz, Thwaites, Pine Island, Abbot, George VI) and East Antarctica (Amery, West, Shackleton, Totten) show a statistically significant negative trend, which is largest for

Getz (-4.0 % per decade; Table 4). These trends are largely corroborated by HIRHAM5 results. This is consistent with a general cooling trend of East Antarctica and the eastern section of West Antarctica in the late twentieth century and early twenty-first century, in response to decadal changes in the Madden-Julian Oscillation (Hsu et al., 2021).

Four of the ice shelves (Fimbul, Baudouin, Ross, Larsen C) show (sometimes multiple) change-points in their trends of MetUM MP-freq (Table 5). In Figure 5 the trend lines before and after a change-point are only given if the length of the timeseries on either side of the change-point is greater than 15 years. Ross (based on MetUM only) shows a decreasing trend of -11.7% dec^{-1} up to 1994, followed by a much weaker increasing trend of 2.1% dec^{-1}. This is consistent with a general cooling trend of East Antarctica in the late twentieth century (Hsu et al., 2021) followed by regional warming for Ross in the early twenty-first century (Clem et al. 2018, 2019). Fimbul (based on MetUM only) and Baudouin (based on MetUM and HIRHAM5) show broadly similar changes in trends in terms of both timing and sign to those for Ross, which as they are located in East Antarctica, could also be related to the aforementioned twentieth century cooling trend that has weakened in recent decades (Hsu et al., 2021). Larsen C (based on Met-UM only) shows an increasing trend of 1.1% dec^{-1} up to 1999, followed by a much stronger decreasing trend of -14.5% dec^{-1}. This is consistent with similar trends in temperature (Turner et al., 2016) in response to changes in the Interdecadal Pacific Oscillation. Based on satellite microwave-based estimates of melt, Scott et al. (2019; their Figure 13) found that melting from Ross to Pine Island/Thwaites decreased from 1979 to 1998, followed by a subsequent increase - with opposite melt trends for the Antarctic Peninsula and Ronne-Filchner.

Figure 6 is analogous to Figure 5, but showing the timeseries of MP-int. The trend lines are statistically insignificant for 10 of the 16 ice shelves (and there are also no change-points). The exception is Ronne-Filchner and Getz (MetUM only), Shackleton and Wilkins (HIRHAM5 only), and Pine Island and George VI (both MetUM and HIRHAM5), which all show a significant decreasing trend, which is largest for Ronne-Filchner (-0.4 K dec^{-1}; Table 4). These ice shelves also all show a decreasing trend in MP-int (Figure 5, Table 4). Interestingly, two ice shelves with the some of the highest MP values (George VI and Pine Island; Table 3) are characterised by significant negative trends in both MP-freq and MP-int

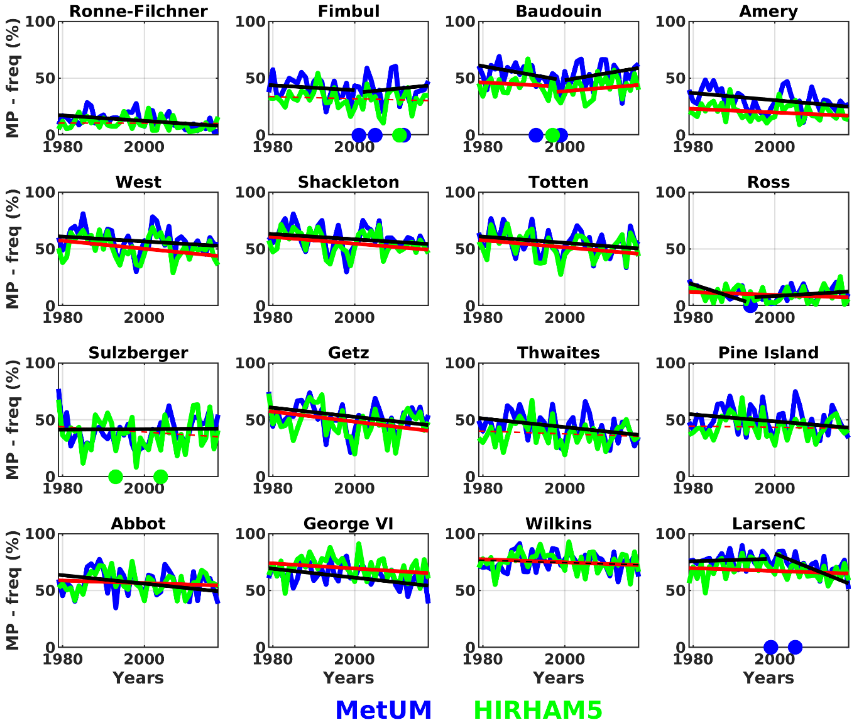

Figure 5: Timeseries of MP-freq for 39 summer melt seasons from 1979 to 2018 for 16 Antarctic ice shelves based on MetUM (blue) and HIRHAM5 (green) output. MP-freq is based on the percentage of the probability distribution of summer daily maximum near-surface temperatures exceeding a temperature/melt threshold value $T_0 = 271.15$ K. The solid (dashed) lines show the statistically significant (insignificant) linear trends based on MetUM (black) and HIRHAM5 (red) output. The solid circle shows when a change-point occurred based on MetUM (blue) and HIRHAM5 (green) simulations. The linear trend across change-points is only plotted when the length of the timeseries on either side of the change point is greater than 15 years (Fimbul, Baudouin, Ross, Larsen C). The ice shelves examined are (from top left to bottom right): Ronne-Filchner, Fimbul, Baudouin, Amery, West, Shackleton, Totten, Ross, Sulzberger, Getz, Thwaites, Pine Island, Abbot, George VI, Wilkins, and Larsen C.

Ice shelf	MetUM, HIRHAM5	
	MP-freq (%)	MP-int (K)
Ronne-Filchner	**-0.24**, -0.01	**-0.040**, -0.024
Fimbul	CP, -0.09	-0.013, -0.0091
Baudouin	CP, CP	-0.012, -0.0056
Amery	**-0.31**, **-0.16**	-0.012, -0.013
West	**-0.21**, **-0.35**	-0.0042, -0.0059
Shackleton	**-0.23**, **-0.30**	-0.013, **-0.011**
Totten	**-0.28**, **-0.31**	-0.0083, -0.0036
Ross	CP, **-0.12**	-0.0042, -0.022
Sulzberger	**0.02**, -0.23	0.0053, -0.000040
Getz	**-0.40**, **-0.44**	**-0.015**, **-0.014**
Thwaites	**-0.38**, -0.12	-0.012, -0.0067
Pine Island	**-0.30**, -0.05	**-0.022**, **-0.012**
Abbot	**-0.37**, **0.11**	-0.0088, -0.0011
George VI	**-0.39**, **-0.23**	**-0.025**, **-0.0098**
Wilkins	-0.11, **-0.13**	-0.012, **-0.014**
Larsen C	CP, **-0.12**	0.0012, 0.0023

Table 4: Linear trends in MP-freq (% yr^{-1}, second column) and MP-int (K yr^{-1}, third column) for the 16 ice shelves examined based on MetUM (shown first) and HIRHAM5 (shown second) output. Boldface trends are statistically significant at the 95% significance level. CP indicates the occurrence of a change-point, which only occurred for MP-freq for four ice shelves (Fimbul, Baudouin, Ross, Larsen C). Table 5 gives details of the linear trends in MP-freq before and after the change-point, as well as the date of the change-point, for these four ice shelves.

Ice Shelf	Model	CP year	Trend before CP	Trend after CP
Fimbul	MetUM	2001	**-0.21**	**0.36**
Baudouin	MetUM	1999	**-0.64**	**0.59**
Baudouin	HIRHAM5	1997	**-0.19**	**0.30**
Ross	MetUM	1994	**-1.17**	**0.21**
Larsen C	MetUM	1999	**0.11**	**-1.45**

Table 5: Linear trends in MP-freq (% yr^{-1}) before (fourth column) and after (fifth column) the occurrence of a change-point (CP) at a particular year (third column) for the four ice shelves in Figure 4 that show a change-point. Boldface trends are statistically significant at the 95% significance level.

d. Mechanisms responsible for interannual variability

Next, we investigate the large-scale atmospheric circulation associated with interannual variability in MP-freq. Only MP-freq is analysed as the MP-int and MP-freq timeseries are strongly positively correlated with values ranging from 0.49 (Wilkins) to 0.93 (Ross) (Table 6; based on MetUM). Figures 7 and 8 show detrended correlations of MetUM MP-freq for eight West Antarctic ice shelves (ordered west (Ross) to east (Larsen C)) with tropical SST and OLR and large-scale atmospheric circulation (Figure 7), and with regional atmospheric circulation (Figure 8). Analogous correlations for seven East Antarctic ice shelves (ordered west (Ronne-Filchner) to east (Totten)) are shown in Figures 9 and 10. The detrended correlations with SAM and ENSO (Niño 4 and SOI) indices are shown in Table 7. Similar results are found for HIRHAM MP-freq (not shown).

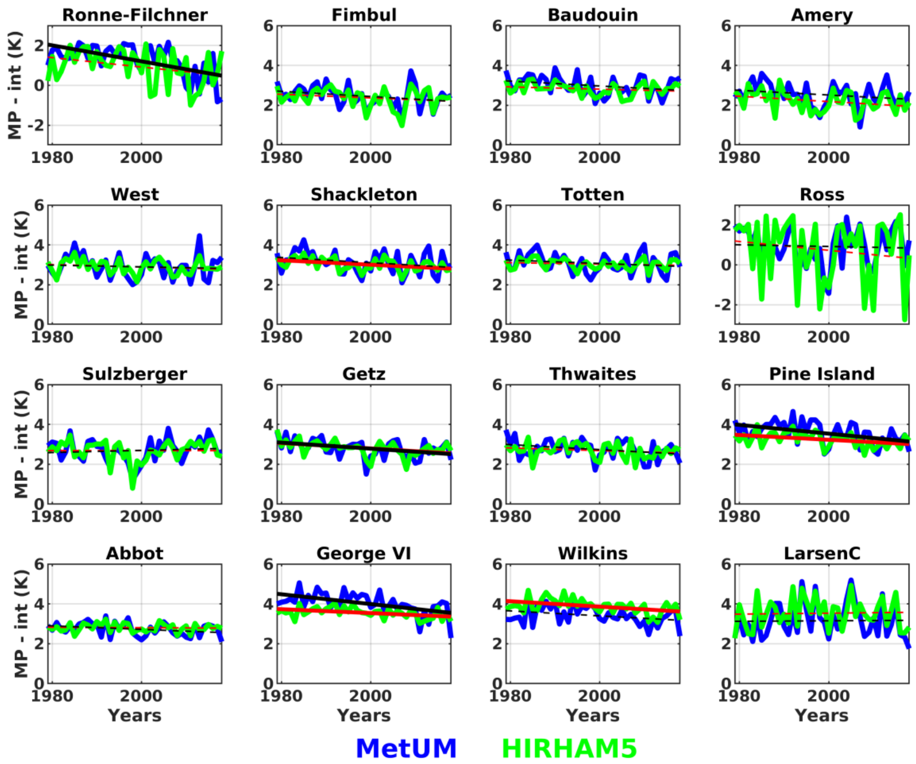

Figure 6: As Figure 5, but for MP-int (K). MP-int is based on the difference between the 95th percentile temperature of the probability distribution of summer daily maximum near-surface temperatures and a temperature/melt threshold value $T_0 = 271.15$ K.

In West Antarctica, most ice shelves show a positive correlation with SST in the tropical Indian and central tropical Pacific oceans (significant for Sulzberger to Pine Island), and a significant negative correlation with OLR (i.e., enhanced deep convection) in eastern equatorial Africa and in the central tropical Pacific, along with positive OLR correlations (i.e., suppressed deep convection) over the Maritime Continent (Figure 7). In general, the West Antarctic ice shelf correlations reflect an El Niño pattern, with the Amundsen Sea Embayment ice shelves (Getz, Thwaites, and Pine Island) showing the strongest correlations with this tropical pattern; additionally, Getz, Thwaites and Pine Island are significantly correlated with both the oceanic (Niño 4) and atmospheric (SOI) components of ENSO, suggesting a robust relationship between MP-freq and ENSO (Table 7). However, looking spatially the strongest positive SST correlations in the Pacific are located near the dateline rather than over the eastern tropical Pacific, possibly reflecting more of a Central Pacific El Niño rather than a canonical El Niño pattern (Ashok et al., 2007), and the strongest negative OLR correlations in the Pacific are oriented diagonally south of the Equator more characteristic of enhanced convective activity in the South Pacific

Ice shelf	MetUM	HIRHAM5
Ronne-Filchner	**0.85**	**0.87**
Fimbul	**0.78**	**0.84**
Baudouin	**0.67**	**0.73**
Amery	**0.80**	**0.88**
West	**0.57**	**0.69**
Shackleton	**0.71**	**0.70**
Totten	**0.62**	**0.60**
Ross	**0.93**	**0.88**
Sulzberger	**0.69**	**0.64**
Getz	**0.73**	**0.70**
Thwaites	**0.61**	**0.58**
Pine Island	**0.66**	**0.49**
Abbot	**0.79**	**0.47**
George VI	**0.68**	**0.64**
Wilkins	**0.49**	**0.49**
Larsen C	**0.53**	**0.59**

Table 6: Correlation between MP-freq and MP-int timeseries for the 16 ice shelves examined based on MetUM (second column) and HIRHAM5 (third column) output. Boldface correlations are statistically significant at the 95% significance level.

Convergence Zone (SPCZ). In fact, ice shelves east of the Amundsen Sea Embayment (Abbot, George VI, and Larsen C) show almost no correlation with equatorial Pacific SST or OLR and are significantly correlated with SPCZ convection only. Indeed, despite tropical teleconnections to southern high latitudes being generally weak in summer (Scott Yiu and Maycock, 2019), previous studies have shown both ENSO and SPCZ variability can have a significant influence on West Antarctic surface air temperature and surface melt in summer (Nicolas et al., 2017; Deb et al., 2018; Clem et al., 2019). The relationships found here are consistent with previous studies linking El Niño to strong summer surface melt on the Ross Ice Shelf (Nicolas et al. 2017), and the SPCZ to multi-decadal summer climate variability across West Antarctica (Clem et al., 2019).

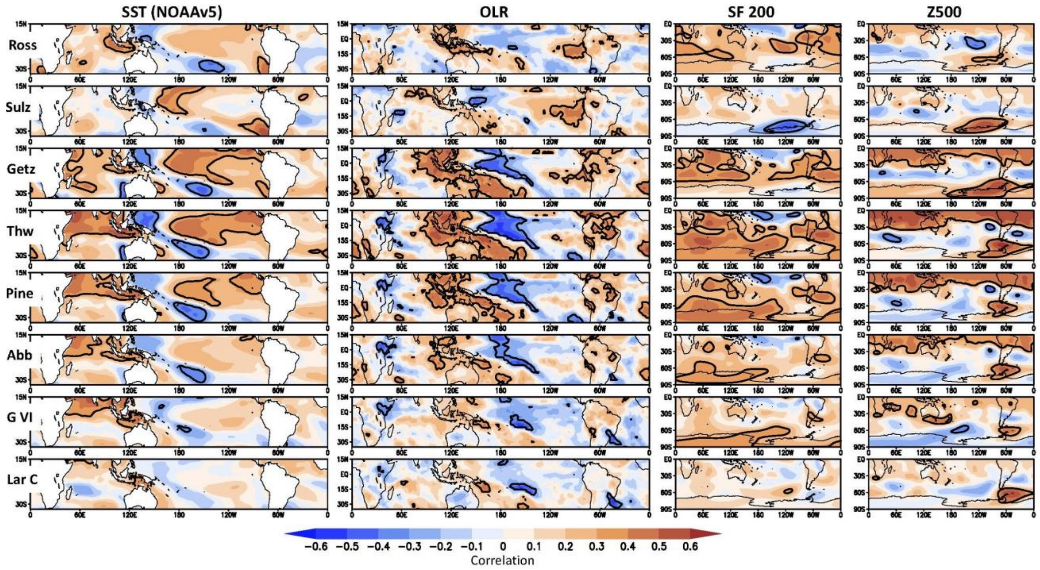

Figure 7: Detrended correlation (shaded) between MetUM MP-freq for West Antarctic ice shelves and sea surface temperature (first column), outgoing longwave radiation (second column), stream function at 200 hPa (third column), and geopotential height at 500 hPa (fourth column). The ice shelves examined are (from top to bottom) Ross, Sulzberger, Getz, Thwaites, Pine Island, Abbot, George VI, and Larsen C. The bold black contour denotes statistically significant correlations at the 95% significance level.

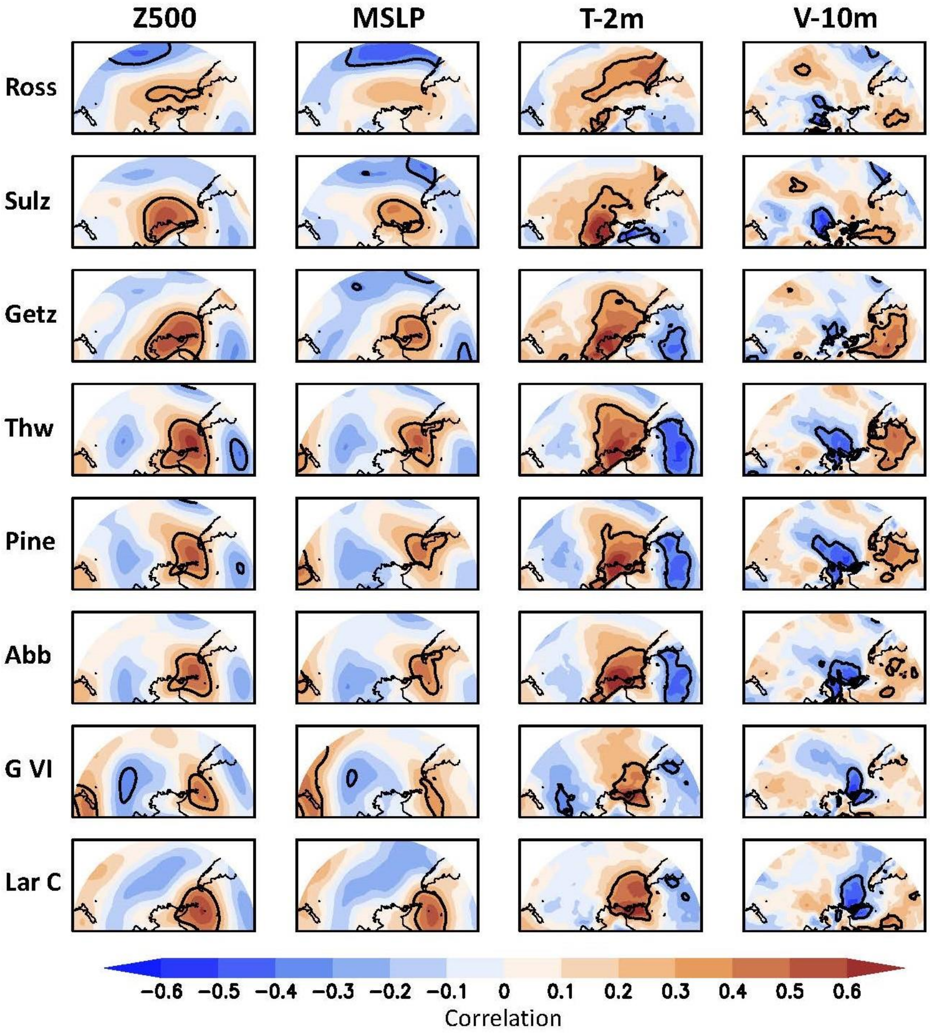

Figure 8: As Figure 7 but zoomed in over West Antarctica and showing results for geopotential height at 500 hPa (first column), mean sea level pressure (second column), 2 m temperature (third column) and 10 m meridional wind speed (fourth column).

The extra-tropical Southern Hemisphere atmospheric circulation is strongly zonally symmetric during summer reflecting the summertime SAM structure (Fogt et al., 2012), and the spatial pattern of the summertime ENSO teleconnection tends to also manifest as a zonally symmetric high-latitude response through a zonal-mean transfer of transient eddy momentum (Karoly, 1989; L'Heureux and Thompson, 2006). However, West Antarctic MP-freq correlations (Figure 8) show a zonally asymmetric pattern more characteristic of a Rossby wave, particularly over the South Pacific. The most prominent asymmetric feature is a strong regional high-pressure anomaly in the high-latitude South Pacific with which all West Antarctic ice shelves are significantly correlated (e.g., Scott et al., 2019); the only variation among ice shelves is the longitudinal location of the center of the anticyclone. Western ice shelves in this region (e.g., Ross and Sulzberger) are correlated with a broader high-pressure anomaly over the entire high-latitude South Pacific, while moving east toward the Amundsen Sea Embayment and Antarctic Peninsula, MP-freq becomes more strongly tied to a regional high-pressure anomaly over the Peninsula and Weddell Sea. The zonally asymmetric pattern is further reflected in West Antarctic ice shelves mostly showing no significant correlation between MP-freq and the SAM index (Table 7) (the only exception being a weak negative SAM correlation for Getz) as variability in the SAM would largely result in zonally symmetric circulation anomalies. By contrast, Scott et al. (2019, their Table 3) found that melting for Getz, Thwaites, Pine Island and Abbott based on satellite passive microwave observations were significantly negatively correlated with the SAM.

Figure 8 shows the 500 hPa anticyclonic anomaly over the South Pacific is equivalent barotropic and reflected at the surface as a strong high-pressure anomaly in MSLP. The correlations with 10 m meridional wind and 2 m temperature show that the surface high-pressure anomaly produces significant warm north-north-westerly flow to the coast along its western flank leading to enhanced MP-freq. The northerly wind and positive temperature correlations are maximized locally near each respective ice shelf, but the regional circulation pattern is similar for all the West Antarctic ice shelves and shows anomalous warm northerly flow along most of the coast, which would favour rather widespread enhanced MP-freq helping to explain the analogous circulation (and tropical) correlation patterns for all the West Antarctic ice shelves.

Ice shelf	Niño4	SOI	SAM
Ronne-Filchner	0.21, -0.13	-0.13, 0.18	0.14, 0.10
Fimbul	0.12, 0.17	-0.04, -0.14	**-0.44**, **-0.42**
Baudouin	0.17, 0.19	-0.25, -0.27	**-0.55**, -0.18
Amery	**0.32,** 0.20	-0.29, -0.22	**-0.62**, **-0.36**
West	**0.31, 0.41**	-0.27, **-0.48**	**-0.61**, **-0.54**
Shackleton	**0.38**, **0.40**	**-0.34**, **-0.45**	**-0.51**, **-0.54**
Totten	**0.37**, **0.36**	**-0.39**, **-0.46**	**-0.57**, **-0.57**
Ross	0.27, 0.18	-0.26, -0.28	-0.02, -0.27
Sulzberger	0.26, 0.15	-0.07, -0.23	-0.17, **-0.36**
Getz	**0.44**, **0.40**	**-0.35**, **-0.40**	**-0.31,** -0.13
Thwaites	**0.43**, **0.41**	**-0.43**, **-0.51**	-0.10, -0.01
Pine Island	**0.34**, **0.42**	**-0.39**, **-0.46**	0.06, 0.12
Abbot	0.23, **0.46**	-0.27, **-0.48**	0.05, 0.19
George VI	0.07, **0.37**	-0.19, **-0.37**	0.26, **0.45**
Wilkins	-0.12, 0.28	-0.02, -0.23	0.23, **0.61**
Larsen C	0.00, 0.17	-0.11, **-0.32**	-0.01, 0.21

Table 7: Detrended correlation between MP-freq and Niño 4 (second column), SOI (third column), and SAM (fourth column) for the 16 ice shelves examined based on MetUM (shown first) and HIRHAM5 (shown second) output. Boldface correlations are statistically significant at the 95% significance level.

Turning to East Antarctica, many ice shelves also show significant positive correlations with central tropical Pacific SSTs (Figure 9), with several being significantly correlated with Niño 4 SSTs (Amery, West, Shackleton, and Totten) and the SOI (Shackleton and Totten) (Table 7). Ronne-Filchner, technically located in West Antarctic but east of the Antarctic Peninsula, stands in stark contrast to the other East Antarctic ice shelves and generally shows a zonally asymmetric circulation pattern more consistent with the West Antarctic ice shelves, specifically a deepened Amundsen Sea Low and a regional high-pressure anomaly in the Weddell Sea (Figure 10), which together leads to anomalous warm northerly flow toward the ice shelf both from the Bellingshausen Sea across Ellsworth Land and from the Weddell Sea (Figure 10), and Ronne-Filchner shows no significant correlation with the SAM (Table 7). This is consistent with Scott et al. (2019) who found enhanced surface melt on Ronne-Filchner to be associated with warm advection from Ellsworth Land. In contrast, moving east toward the Indian Ocean sector, the atmospheric circulation associated with enhanced MP-freq becomes zonally symmetric, with strong positive geopotential height and MSLP correlations over continental Antarctica and a zonal band of negative geopotential height/MSLP correlations across middle latitudes, reflecting the negative phase of the SAM. Indeed, all East Antarctic ice shelves (Fimbul to Totten) are strongly and significantly negatively correlated with the SAM index (Table 7). The 10 m meridional wind and 2 m temperature correlations (Figure 10) show MP-freq variability is less related to northerly wind anomalies than in West Antarctica, but rather tied to a widespread temperature anomaly over all of East Antarctica, implying that variations in the zonally symmetric SAM pattern rather than meridional thermal advection may dominate interannual variability in East Antarctic ice shelf MP-freq.

We further investigate the circulation patterns and their mechanisms with a composite analysis of the top six highest minus the top six lowest MP-freq years (85th and 15th percentiles, respectively) (Figure 11). Given the similarity in the circulation patterns for East and West Antarctica, the years selected for compositing are based on averaged MP-freq anomalies on Pine Island and Thwaites ice shelves for "West Antarctica", and West and Amery ice shelves for "East Antarctica".

For West Antarctica (left column, Figure 11), high versus low MP-freq years are strongly associated with El Niño conditions including significant positive (negative) central and eastern (western) tropical Pacific SSTs. No significant SST differences are seen in the tropical Indian or Atlantic Ocean, suggesting the correlations seen there in Figure 7 may be spurious and more tied to the far-reaching impacts of El Niño on tropical SST (e.g., El Niño favours positive SST anomalies in the tropical Indian Ocean; Alexander et al., 2002) rather than being physically related to MP-freq. The 200 hPa stream function and wave flux more clearly illustrate a zonally asymmetric stationary Rossby wave arching from the central tropical Pacific into the high-latitude South Pacific and South Atlantic, with stationary wave propagation following a great circle path. This Pacific-South America-like pattern is reflected in the 500 hPa geopotential height field, and it results in a strong regional high-pressure anomaly centered over the Antarctic Peninsula region leading to significant warm northerly flow along the West Antarctic coast.

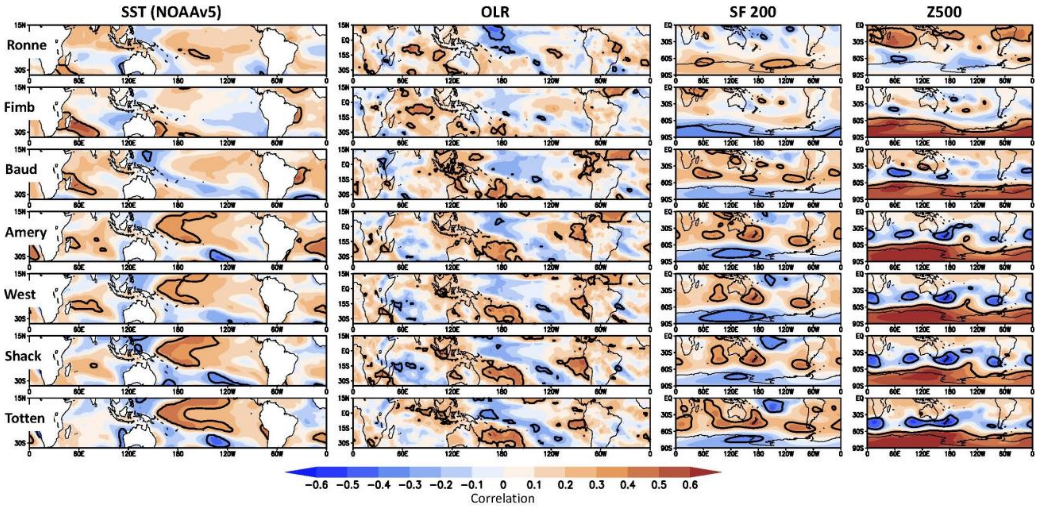

Figure 9: As Figure 7 but showing results for East Antarctic ice shelves. The ice shelves examined are (from top to bottom) Ronne-Filchner, Fimbul, Baudouin, Amery, West, Shackleton, and Totten.

For East Antarctica (right column, Figure 11), there is no significant difference in tropical SSTs between high and low MP-freq years, and the atmospheric circulation more strongly reflects the negative phase of the SAM with strong positive pressure anomalies over continental Antarctica and negative pressure anomalies along ~40°S. In contrast to West Antarctica, the horizontal wave activity broadly shows zonal propagation within the mid-latitude storm track, albeit the mid-latitude jet being highly amplified with four strong mid-latitude troughs that encircle the ridge over East Antarctica. There are two regions of strong poleward wave propagation into interior East Antarctica, each downstream of a trough, one near ~50°E and one near ~120°E. These regions of poleward wave propagation into East Antarctica may aid in dynamically building the locally amplified ridge of high pressure over East Antarctica that favours widespread warming. It is possible these may be related to tropical variability in the Atlantic or Indian Ocean, but given there are no significant tropical SST anomalies and the relatively short wavelengths suggests they may be more tied to internal short-wave propagation within the mid-latitude jet rather than a planetary Rossby wave forced from the tropics. Lastly, the strong high pressure over East Antarctica is associated with significantly weakened mid-latitude westerly winds and strengthened surface easterlies along coastal East Antarctica, which altogether appear to produce local conditions conducive for surface warming and enhanced MP-freq over the East Antarctic ice shelves.

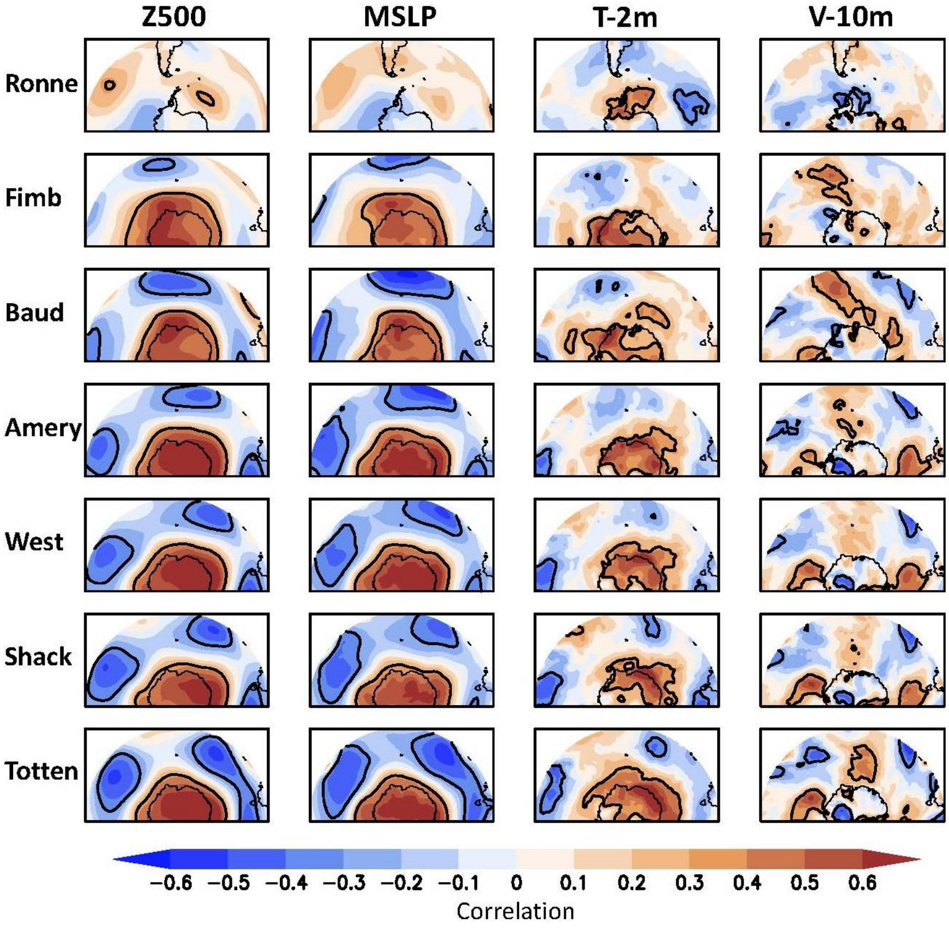

Figure 10: As Figure 8 but zoomed in over East Antarctica. The ice shelves examined are (from top to bottom) Ronne-Filchner, Fimbul, Baudouin, Amery, West, Shackleton, and Totten.

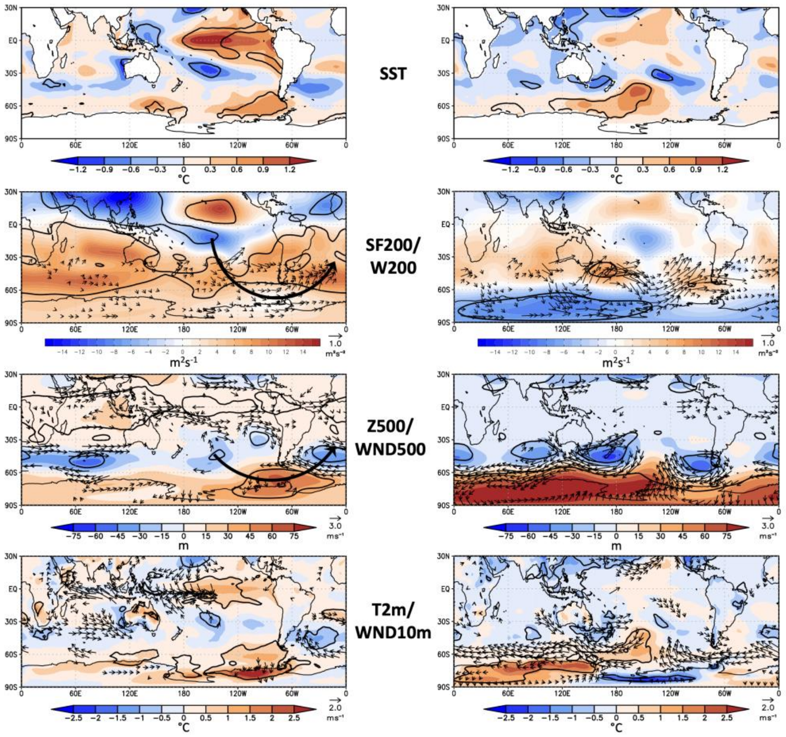

Figure 11: Composite differences between high minus low MP-freq years (top six minus bottom six, 85th/15th percentiles) of sea surface temperature (first row), stream function and horizontal wave flux at 200 hPa (second row), geopotential height and horizontal wind at 500 hPa (third row), and 2 m temperature and 10 m wind (fourth row) for Thwaites/Pine Island (left column; reflecting West Antarctic ice shelves) and West/Amery (right column; reflecting East Antarctic ice shelves). The bold black contour denotes differences that are significant at the 95% significance level; only vectors with at least one wind component significant at the 95% significance level are shown in the bottom two rows (wind at 500 hPa and at 10 m). The stationary Rossby wave propagation at 200 hPa and wave train at 500 hPa for West Antarctic ice shelves are schematically drawn with a black arrow.

4. Discussion and Conclusions

Clarification of the spatiotemporal characteristics of summertime temperature extremes over Antarctica's ice shelves, and the drivers of their variability, is important to identify regions that may be especially vulnerable to strong surface melting and potential hydrofracture. Our investigation identifies these regions using an air temperature-based index of possible melt, which we refer to as the “melt potential” (MP). This is characterised by two components measuring the frequency (MP-freq) and intensity (MP-int) of daily maximum temperatures exceeding a melt threshold of 271.15 K, which are derived from near-surface air temperature output from two high-resolution regional atmospheric model hindcasts. The advantage of using an index based on this model output is the comprehensive spatial coverage at high resolution and long timeseries (39 summer melt seasons), which enables extraction of meaningful statistics and characteristics for all Antarctic ice shelves. Additionally, investigation of results from two models enables model-dependence and consistency to be assessed. Both models, despite being generally cold biased, are able to adequately simulate actual daily maximum temperatures observed on or near to ice shelves (Figure 2, Table 2). This is especially the case for the MetUM, which we speculate is due to an improved ability to represent fine-scale local effects such as foehn winds (e.g., Orr et al., 2021; Gilbert et al., 2022).

We identify that MP-freq is highest for Antarctic Peninsula ice shelves (exceeding 70%), lowest (around 10%) for Ronne-Filchner and Ross, and typically between 40 and 60% for the other West and East Antarctic ice shelves (Figure 3, Table 3). Values of MP-int are also highest for Antarctic Peninsula ice shelves (4-5 K), lowest for Ronne-Filchner and Ross (1-2 K), and around 2-3 K for other West and East Antarctic ice shelves (Figure 3, Table 3). The timeseries of MP-freq and MP-int are also strongly positively correlated. The high values for Larsen C and Wilkins (Antarctic Peninsula) are particularly important as these regions are especially vulnerable to hydrofracture if inundated by surface melt water (Lai et al., 2020), in contrast to some others that despite high MP are located in regions that are more resilient to hydrofracture (e.g., George VI, Baudoin, and Amery). Our results further identify that Pine Island has an especially high MP-int value of 3.7 K (the highest outside of the Antarctic Peninsula), which suggests it is vulnerable to extreme surface melt events in addition to the well-known basal melting (Jenkins et al., 2010, 2016). Many ice shelves are characterized by pronounced spatial gradients in MP, which we suggest is explained by warm signatures associated by local effects such as foehn winds, katabatic winds, barrier winds, and the RAS (Figure 4). The ice shelves characterized by high MP largely agree with the those identified by Trusel et al. (2015), Feron et al. (2021), and Gilbert and Kittel (2021). Moreover, the cold bias in the model estimates of daily maximum temperatures suggests that the model-based estimates of MP could be underestimated than what they actually are in reality, i.e., regions characterized by high MP could experience even stronger surface melting than our results suggest.

Values of MP-freq for many ice shelves in East and West Antarctica show a significant negative trend (Figure 5, Table 4), which is consistent with a general cooling trend of East Antarctica and the eastern section of West Antarctica in the late twentieth century and early twenty-first century, in response to decadal changes in the Madden-Julian Oscillation (Hsu et al., 2021). Moreover, Pine Island shows a significant decreasing trend in both MP-freq and MP-int, suggesting that although it is clearly vulnerable to extreme surface melt events, widespread surface melting might be less common over recent decades while the ice shelf continues melting from below. Four of the ice shelves (Fimbul, Baudouin, Ross, Larsen C) show change-points in their trends of MP-freq (Figure 5, Table 5), with Fimbul, Baudouin, and Ross showing a decreasing trend up to the end of the twentieth century, followed by an increasing trend, consistent with the aforementioned twentieth century cooling trend that has weakened in recent decades. By contrast, Larsen C show s an increasing trend up to the end of the twentieth century, followed by a decreasing trend, which is consistent with changes in the Interdecadal Pacific Oscillation. Interestingly, two ice shelves with some of the highest MP values (George VI and Pine Island; Table 3) are characterised by negative trends in both MP-freq and MP-int.

The correlation (Figures 7-10, Table 7) and composite (Figure 11) analysis reveal distinctly different local and large-scale circulation patterns governing MP-freq in West and East Antarctica. In West Antarctica, warm thermal advection driven by a regional high-pressure anomaly over the high-latitude South Pacific appears to be the key mechanism leading to enhanced ice-shelf MP-freq, while high-pressure anomalies over continental Antarctica and associated weakened westerlies/local intensification of surface coastal easterlies appears to be the key feature enhancing MP-freq on East Antarctica’s ice shelves. The West Antarctic circulation shows a strong connection with El Niño activity, particularly central tropical Pacific SST anomalies and anomalous deep convection in the SPCZ, and the increase in La Niñas after 1999 (Purich et al., 2016) may explain the regional cooling and decreasing trend in MP-freq for West Antarctic ice shelves. Meanwhile the East Antarctic circulation is more strongly tied to negative SAM, which can be amplified (weakened) by El Niño (La Niña) conditions (Fogt et al., 2011). Therefore, the increase in La Niñas combined with predominantly positive SAM phases since 2000 (Clem et al., 2020) may explain the regional cooling and decreasing trend in MP-freq for East Antarctic ice shelves.

Climate model experiments suggest a higher frequency of positive SAM conditions by the end of the twenty-first century due to global warming (Zheng et al., 2013), as well as a trend towards stronger and more frequent El Niño activity (Power et al., 2013; Santoso et al., 2013; Cai et al., 2014). Our study therefore suggests that these conditions would decrease (increase) MP and atmospherically driven melt over East (West) Antarctic ice shelves in the future. However, Feron et al. (2021) suggests that even under a moderate-emission greenhouse gas scenario (RCP 4.5) the number of “very warm” summer days (i.e., days when the maximum temperature exceeds the 90th percentile threshold) will triple over East Antarctic ice shelves by the end of the twenty-first century. This suggests that although trends towards a more positive SAM might suppress average melt over East Antarctica ice shelves, this may be counter-balanced by more frequent extreme events like heatwaves and atmospheric rivers that are associated with a disproportionate amount of total melting (Wille et al., 2019, 2021). Meanwhile, the suggested increase in intensification of surface melting over West Antarctic ice shelves is consistent with other studies (Trusel et al., 2015; Feron et al., 2021; Gilbert and Kittel, 2021), and in turn could potentially trigger the destabilisation/retreat of the West Antarctic ice sheet (DeConto et al., 2021).

Further work should include using the models to downscale climate projections to investigate how the spatiotemporal characteristics of the MP index will evolve towards the end of the twenty-first century in response to low, medium, and high-emission greenhouse gas scenarios. Work should also focus on investigating the consequences of selected storylines of atmospheric circulation (Shepherd et al., 2018), with two potential storylines being increased positive SAM conditions and stronger and more frequent El Niño activity by the end of the twenty-first century. Additionally, it would be desirable to explore why there are some differences between melt results from satellite microwave observations (e.g., Scott et al., 2019) and the model-based results presented here. Deb et al. (2018) is a good example of this type of work.

Acknowledgments.

AO, FB, EG, RM, DP, and WJB are supported by the European Union funded Horizon 2020 project PolarRES. MN is supported by the Japan Society for the Promotion of Science through Grants-in-Aid for Scientific Research numbers JP18H05054 and JP20H04982. PD is supported by Indian Institute of Technology Kharagpur and the Ministry of Education, Govt. of India. KRC is supported by Royal Society of New Zealand Marsden Fund grant MFP-VUW2010. ML is supported by NSF grant number 1924730. DB and XZ are supported by NSF grant 1823135.

Data Availability Statement.

The maps of Antarctic ice shelves provided by the MEaSUREs program are available here: http://dx.doi.org/10.5067/AXE4121732AD. The weather station data is available here: https://legacy.bas.ac.uk/cgi-bin/metdb-form-1.pl?table_prefix=U_WMC,U_MET&acct=u_met&pass=weather and ftp://ftp.bas.ac.uk/src/ANTARCTIC_METEOROLOGICAL_DATA/ and https://amrc.ssec.wisc.edu/aws/index.html. The index describing the SAM (Marshall and NCAR staff, 2018) is available here: https://climatedataguide.ucar.edu/climate-data/marshall-southern-annular-mode-sam-index-station-based. The SOI index is available here: https://www.cpc.ncep.noaa.gov/data/indices. The ENSO index is available here: https://origin.cpc.ncep.noaa.gov/products/analysis_monitoring/ensostuff/ONI_v5.php. The OLR and SST data were provided by the NOAA/OAR/ESRL PSL, Boulder, Colorado, USA from their websites https://psl.noaa.gov/data/gridded/data.interp_OLR.html and https://psl.noaa.gov/data/gridded/data.noaa.ersst.v5.html, respectively. ERA5 data were accessed from the Climate Data Store (CDS) provided by the Copernicus program.

REFERENCES

Alexander, M. A., I. Bladé, M. Newman, J. R. Lanzante, N. Lau, and J. D. Scott, 2002: The Atmospheric Bridge: The Influence of ENSO Teleconnections on Air–Sea Interaction over the Global Oceans, *J. Clim.*, 15, 2205-2231, https://doi.org/10.1175/1520-0442(2002)015<2205:TABTIO>2.0.CO;2.

Arthur, J. F., C. Stokes, S. S. Jamieson, J. R. Carr, and A. A. Leeson, 2020: Recent understanding of Antarctic supraglacial lakes using satellite remote sensing. *Prog. Phys. Geogr.*, 44, 837–869, https://doi.org/10.1177/0309133320916114.

Ashok, K., S. K. Behera, S. A. Rao, H. Weng, and T. Yamagata, 2007: El Niño Modoki and its possible teleconnection. *J. Geophys. Res.*, 112, https://doi.org/10.1029/2006JC003798.

Banwell, A. F., D. R. MacAyeal, and O. V. Sergienko, 2013: Breakup of the Larsen B Ice Shelf triggered by chain reaction drainage of supraglacial lakes. *Geophys. Res. Lett.*, 40, 5872–5876, https://doi.org/10.1002/2013GL057694.

Banwell, A. F., and D. R. MacAyeal, 2015: Ice-shelf fracture due to viscoelastic flexure stress induced by fill/drain cycles of supraglacial lakes. *Antarctic Science*, 27, 587–597, https://doi.org/10.1017/S0954102015000292.

Banwell, A. F., I. C. Willis, G. J. Macdonald, B. Goodsell, and D. R. MacAyeal, 2019: Direct measurements of ice-shelf flexure caused by surface melt-water ponding and drainage. *Nat. Commun.*, 10, https://doi.org/10.1038/s41467-019-08522-5.

Banwell, A. F., R. T. Datta, R. L. Dell, M. Moussavi, L. Brucker, G. Picard, C. A. Shuman, and L. A. Stevens, 2021: The 32-year record-high surface melt in 2019/2020 on the northern George VI Ice Shelf, Antarctic Peninsula. *The Cryosphere*, 15, 909–925, https://doi.org/10.5194/tc-15-909-2021.

Bozkurt, D., R. Rondanelli, J. C. Marin, and R. Garreaud, 2018: Foehn event triggered by an atmospheric river underlies record-setting temperature along continental Antarctica. *J. Geophys. Res*., *123*, 3871– 3892, https://doi.org/10.1002/2017JD027796.

Bozkurt, D., D. H. Bromwich, J. Carrasco, and R. Rondanelli, 2021: Temperature and precipitation projections for the Antarctic Peninsula over the next two decades: contrasting global and regional climate model simulations. *Clim. Dyn.*, 56**,** 3853–3874, https://doi.org/10.1007/s00382-021-05667-2.

Bromwich, D. H., J. F. Carrasco, and C. R. Stearns, 1992: Satellite Observations of Katabatic-Wind Propagation for Great Distances across the Ross Ice Shelf. *Mon. Wea. Rev*., *120*, 1940-1949, https://doi.org/10.1175/1520-0493(1992)120<1940:SOOKWP>2.0.CO;2.

Cai, W., S. Borlace, M. Lengaigne, P. van Rensch, M. Collins, G. Vecchi, A. Timmermann, A., Santoso, M. J. McPhaden, L. Wu, M. H. England, G. Wang, E. Guilyardi, and F.-F. Jin, 2014: Increasing frequency of extreme El Niño events due to greenhouse warming. *Nature Clim. Change*, 4, 111–116, https://doi.org/10.1038/nclimate2100.

Chyhareva A., S. Krakovska, and D. Pishniak, 2019: Climate projections over the Antarctic Peninsula region to the end of the 21st century. Part I: cold temperature indices. *Ukrainian Antarctic Journal*, 1, 62-74, https://doi.org/10.33275/1727-7485.1(18).2019.131.

Clem, K. R., A. Orr, and J. O. Pope, 2018: The Springtime Influence of Natural Tropical Pacific Variability on the Surface Climate of the Ross Ice Shelf, West Antarctica: Implications for Ice Shelf Thinning. *Sci. Rep.,* 8, https://doi.org/10.1038/s41598-018-30496-5.

Clem, K. R., B. R. Lintner, A. J. Broccoli, and J. R. Miller, 2019: Role of the South Pacific Convergence Zone in West Antarctic decadal climate variability. Geophys. Res. Lett., 46, 6900– 6909, https://doi.org/10.1029/2019GL082108.

Clem, K. R., R. L. Fogt, J. Turner, B. R. Linter, G. J. Marshall, J. R. Miller, and J. A. Renwick, 2020: Record warming at the South Pole during the past three decades. *Nat. Clim. Chang.*, 10, 762–770, https://doi.org/10.1038/s41558-020-0815-z.

Coggins, J. H. J., A. J. McDonald, and B. Jolly, 2014: Synoptic climatology of the Ross Ice Shelf and Ross Sea region of Antarctica: k-mean clustering and validation. *Int. J. Climatol., 34*, 2330–2348, https://doi.org/10.1002/joc.3842.

Costanza, C. A., M. A. Lazzara, L. M. Keller, and J. J. Cassano, 2016: The surface climatology of the Ross Ice Shelf Antarctica. *Int. J. Climatol.*, 36, 4929–4941, https://doi.org/10.1002/joc.4681.

Deb, P., A. Orr, J. S. Hosking, T. Phillips, J. Turner, D. Bannister, J. O. Pope, and S. Colwell, 2016: An assessment of the Polar WRF representation of near-surface meteorological variables over West Antarctica. *J. Geophys. Res*., 121, 1532-1548, https://doi.org/10.1002/2015JD024037.

Deb, P., A. Orr, D. H. Bromwich, J. P. Nicolas, J. Turner, and J. S. Hosking, 2018: Summer drivers of atmospheric variability affecting ice shelf thinning in the Amundsen Sea Embayment, West Antarctica. *Geophys. Res. Lett.*, 45, 4124-4133, https://doi.org/10.1029/2018GL077092.

DeConto, R. M., D. Pollard, R. B. Alley, I. Velicogna, E. Gasson, N. Gomez, S. Sadai, A. Condron, D. M. Gilford, E. L. Ashe, R. E. Kopp, D. Li, and A. Dutton, 2021: The Paris Climate Agreement and future sea-level rise from Antarctica. *Nature*, 593, 83-89, https://doi.org/10.1038/s41586-021-03427-0.

Dee, D. P., S. M. Uppala, A. J. Simmons, P. Berrisford, P. Poli, S. Kobayashi, U. Andrae, M. A. Balmaseda, G. Balsamo, P. Bauer, P., Bechtold, A. C. M. Beljaars, L. van de Berg, J. Bidlot, N. Bormann, C. Delsol, R. Dragani, M. Fuentes, A. J. Geer, L. Haimberger, S. B. Healy, H. Hersbach, E. V. Hólm, L. Isaksen, P. Kållberg, M. Köhler, M. Matricardi, A. P. McNally, B.

M. Monge-Sanz, J. J. Morcrette, B. K. Park, C. Peubey, P. de Rosnay, C. Tavolato, J. N. Thépaut, and F. Vitart, 2011: The ERA-Interim reanalysis: configuration and performance of the data assimilation system. *Q. J. Roy. Met. Soc.*, 137, 553– 597, https://doi.org/10.1002/qj.828.

Dell, R., N. Arnold, I. Willis, A. Banwell, A. Williamson, H. Pritchard, and A. Orr, 2020: Lateral meltwater transfer across an Antarctic ice shelf. *The Cryosphere*, 14, 2313–2330, https://doi.org/10.5194/tc-14-2313-2020.

Djoumna, G., and D. M. Holland, 2021: Atmospheric rivers, warm air intrusions, and surface radiation balance in the Amundsen Sea Embayment. *J. Geophys. Res.*, 126, https://doi.org/10.1029/2020JD034119.

Doake, C. S. M., H. F. J. Corr, H. Rott, P. Skvarca, and N. W. Young, 1998: Breakup and conditions for stability of the northern Larsen Ice Shelf, Antarctica. *Nature*, 391, 778–780, https://doi.org/10.1038/35832.

Elvidge, A. D., I. A. Renfrew, J. C. King, A. Orr, and T. A. Lachlan-Cope, 2016: Foehn warming distributions in nonlinear and linear flow regimes: a focus on the Antarctic Peninsula. *Q. J. Roy. Met. Soc.*, 142, 618– 631, https://doi.org/10.1002/qj.2489.

Feron, S., R. R. Cordero, A. Damiani, A. Malhotra, G. Seckmeyer, and P. Llanillo, 2021: Warming events projected to become more frequent and last longer across Antarctica. *Sci. Rep.*, 11, https://doi.org/10.1038/s41598-021-98619-z.

Fogt, R. L., D. H. Bromwich, and K. M. Hines, 2011: Understanding the SAM influence on the South Pacific ENSO teleconnection. *Clim. Dyn.*, 36, 1555–1576, https://doi.org/10.1007/s00382-010-0905-0.

Fogt, R. L., J. M. Jones, and J. Renwick, 2012: Seasonal zonal asymmetries in the Southern Annular Mode and their impact on regional temperature anomalies. *J. Clim.*, 25, 6253-6270, https://doi.org/10.1175/JCLI-D-11-00474.1.

Genthon, C., D. Six, V. Favier, M. Lazzara, and L. Keller, 2011: Atmospheric temperature measurement biases on the Antarctic Plateau. *J. Atmos. Ocean. Technol, 28*, 1598–1605, https://doi.org/10.1175/JTECH-D-11-00095.1.

Gilbert, E., and C. Kittel, 2021: Surface melt and runoff on Antarctic ice shelves at 1.5°C, 2°C, and 4°C of future warming. *Geophys. Res. Lett.*, 48, https://doi.org/10.1029/2020GL091733.

Gilbert, E., A. Orr, I. Renfrew, J. C. King, and T. A. Lachlan-Cope, 2022: A 20-year study of melt processes over Larsen C Ice Shelf using a high-resolution regional atmospheric model: Part 2, Drivers of surface melt. *J. Geophys. Res.*, https://doi.org/10.1002/essoar.10508261.1.

Glasser, N. F., T. A. Scambos, J. Bohlander, M. Truffer, E. Pettit, and B. J. Davies, 2011: From ice-shelf tributary to tidewater glacier: Continued rapid recession, acceleration and thinning of Röhss Glacier following the 1995 collapse of the Prince Gustav Ice Shelf, Antarctic Peninsula. *J. Glaciol.*, 57, 397–406, https://doi.org/10.3189/002214311796905578.

Goyal, R., M. Jucker, A. Sen Gupta, H. H. Hendon, and M. H. England, 2021: Zonal wave 3 pattern in the Southern Hemisphere generated by tropical convection. *Nat. Geosci.*, 14, 732–738, https://doi.org/10.1038/s41561-021-00811-3.

Gutowski Jr., W. J., F. Giorgi, B. Timbal, A. Frigon, D. Jacob, H.-S. Kang, K. Raghavan, B. Lee, C. Lennard, G. Nikulin, E. O'Rourke, M. Rixen, S. Solman, T. Stephenson, and F. Tangang, 2016: WCRP COordinated Regional Downscaling EXperiment (CORDEX): a diagnostic MIP for CMIP6. *Geosci. Model Dev.*, 9, 4087–4095, https://doi.org/10.5194/gmd-9-4087-2016.

Heinemann, G., L. Glaw, S. A. Willmes, 2019: Satellite-Based Climatology of Wind-Induced Surface Temperature Anomalies for the Antarctic. *Remote Sensing*, 11, 1539, https://doi.org/10.3390/rs11131539.

Hersbach, H., and Coauthors, 2020: The ERA5 global reanalysis. *Q. J. R. Meteorol. Soc.*, 146, 1999–2049, https://doi.org/10.1002/qj.3803.

Hosking, J. S., A. Orr, G. J. Marshall, J. Turner, and T. Phillips, 2013: The influence of the Amundsen-Bellingshausen Sea Low on the climate of West Antarctica and its representation in coupled climate model simulations. *J. Clim.*, 26, 6633-6648, https://doi.org/10.1175/JCLI-D-12-00813.1.

Huang, B., C.-S. Shin, J. Shukla, L. Marx, M. A. Balmaseda, S. Halder, P. Dirmeyer, and J. L. Kinter III, 2017a: Reforecasting the ENSO Events in the Past 57 Years (1958–2014). *J. Clim.*, 30, 7669-7693, https://doi.org/10.1175/JCLI-D-16-0642.1.

Huang, B., P. W. Thorne, V. F. Banzon, T. Boyer, G. Chepurin, J. H. Lawrimore, M. J. Menne, T. M. Smith, R. S. Vose, and H.-M. Zhang, 2017b: NOAA Extended Reconstructed Sea Surface Temperature (ERSST), Version 5. NOAA National Centers for Environmental Information. https://doi.org/10.7289/V5T72FNM [accessed 27 August 2021].

Huang, B., C. Liu, V. Banzon, E. Freeman, G. Graham, B. Hankins, T. Smith, and H.-M. Zhang, 2021: Improvements of the Daily Optimum Interpolation Sea Surface Temperature (DOISST) Version 2.1. *J. Clim.*, 34, 2923-2939, https://doi.org/10.1175/JCLI-D-20-0166.1.

Hsu, P.-C., Z. Fu, H. Murakami, J.-Y. Lee, C. Yoo, N. C. Johnson, C.-H. Chang, and Y. Liu, 2021: East Antarctic cooling induced by decadal changes in Madden-Julian oscillation during austral summer. *Sci. Adv.*, 7, https://www.science.org/doi/10.1126/sciadv.abf9903.

Jenkins, A., P. Dutrieux, S. S. Jacobs, S. D. McPhail, J. R. Perrett, A. T. Webb, and D. White, 2010: Observations beneath Pine Island Glacier in West Antarctica and implications for its retreat. *Nat. Geosci.*, 3, 468–472, https://doi.org/10.1038/ngeo890.

Jenkins, A., P. Dutrieux, S. Jacobs, E. Steig, H. Gudmundsson, J. Smith, and K. Heywood, 2016: Decadal ocean forcing and Antarctic ice sheet response: Lessons from the Amundsen Sea. *Oceanography*, 29, 106–117, https://doi.org/10.5670/oceanog.2016.103.

Johnson, A., R. Hock, and M. Fahnestock, 2021: Spatial variability and regional trends of Antarctic ice shelf surface melt duration over 1979–2020 derived from passive microwave data. *Journal of Glaciology*, 1–14, https://doi.org/10.1017/jog.2021.112.

Karoly, D. J., 1989: Southern Hemisphere circulation features associated with El Nino-Southern Oscillation events. *J. Clim.*, 2, 1239-1252, https://doi.org/10.1175/1520-0442(1989)002<1239:SHCFAW>2.0.CO;2.

Kingslake, J., J. C. Ely, I. Das, and R. E. Bell, 2017: Widespread movement of meltwater onto and across Antarctic ice shelves. *Nature*, *5*44, 349-352, https://doi.org/10.1038/nature22049.

Kuipers Munneke, P., M. van den Broeke, J. C. King, T. Gray, and C. Reijmer, 2012: Near-surface climate and surface energy budget of Larsen C Ice Shelf, Antarctic Peninsula. *The Cryosphere*, 6, 353– 363, https://doi.org/10.5194/tc-6-353-2012.

Kuipers Munneke, P., A. J. Luckman, S. L. Bevan, C. J. P. P. Smeets, E. Gilbert, E., M. R. van den Broeke, W. Wang, C. Zender, B. Hubbard, D. Ashmore, A. Orr, J. C. King, and B. Kulessa, 2018: Intense winter surface melt on an Antarctic ice shelf. *Geo. Res. Lett.*, 45, 7615–7623, https://doi.org/10.1029/2018GL077899.

Krinner, G., and C. Genthon, 1999: Altitude dependence of the ice sheet surface climate. *Geophys. Res. Lett.*, 26, 2227-2230, https://doi.org/10.1029/1999GL900536.

Lai, C.-Y., J. Kingslake, M. G. Wearing, P.-H. Cameron Chen, P. Gentine, H. Li, J. J. Spergel, and J. M. van Wessem, 2020: Vulnerability of Antarctica's ice shelves to meltwater-driven fracture. *Nature*, 584, 574-578, https://doi.org/10.1038/s41586-020-2627-8.

Lazzara, M. A., G. A. Weidner, L. M Keller, J. E. Thom, and J. J Cassano, 2012: Antarctic Automatic Weather Station Program: 30 Years of Polar Observation. Bull. Amer. Meteor., 93, 1519-1537, https://doi.org/10.1175/BAMS-D-11-00015.1.

Lhermitte, S., S. Sun, C. Shuman, B. Wouters, F. Pattyn, J. Wuite, E. Berthier, and T. Nagler, 2020: Damage accelerates ice shelf instability and mass loss in Amundsen Sea Embayment. *P. Natl. Acad. Sci. USA*, 117, 24735–24741, https://doi.org/10.1073/pnas.1912890117.

L'Heureux, M. L., and D. W. J. Thompson, 2006: Observed relationships between the El Nino-Southern Oscillation and the extratropical zonal-mean circulation. *J. Clim.*, 19, 276-287, https://doi.org/10.1175/JCLI3617.1.

Liebmann, B., and C. A. Smith, 1996: Description of a Complete (Interpolated) Outgoing Longwave Radiation Dataset. *Bull. Am. Meteorol. Soc.*, 77, 1275-1277.

MacAyeal, D. R., T. A. Scambos, C. L. Hulbe, and M. A. Fahnestock, 2003: Catastrophic ice-shelf break-up by an ice-shelf-fragment-capsize mechanism. *Journal of Glaciology*, 49, 22–36, https://doi.org/10.3189/172756503781830863.

Mann, H. B., 1945: Non parametric test against trend. *Econometric*, 13, 245–259, https://doi.org/10.2307/1907187.

Marshall, G., 2003: Trends in the Southern Annular Mode from observations and reanalyses. *J. Clim.*, 16, 4134-4143, https://doi.org/10.1175/1520-0442(2003)016<4134:TITSAM>2.0.CO;2.

Marshall, G., and National Center for Atmospheric Research Staff (Eds). Last modified 19 Mar 2018. *The climate data guide: Marshall Southern Annular Mode (SAM) index (station-based)*. Retrieved from https://climatedataguide.ucar.edu/climate-data/marshall-southern-annular-mode-sam-index-station-based.

Mottram, R., N. Hansen, C. Kittel, J. M. van Wessem, C. Agosta, C. Amory, F. Boberg, W. J. van de Berg, X. Fettweis, A. Gossart, N. P. M. van Lipzig, E. van Meijgaard, A. Orr, T. Phillips, S. Webster, S. B. Simonsen, and N. Souverijns, 2021: What is the surface mass balance of Antarctica? An intercomparison of regional climate model estimates. *The Cryosphere*, 15, 3751–3784, https://doi.org/10.5194/tc-15-3751-2021.

Mouginot, J., E. Rignot, and B. Scheuchl, 2017: *MEaSURES Antarctic Boundaries for IPY 2007-2009 from Satellite Radar, Version 1*. Boulder, Colorado USA. NASA National Snow and Ice Data Center Distributed Active Archive Center.

Nicolas, J. P., and D. H. Bromwich, 2011: Climate of West Antarctica and Influence of Marine Air Intrusions. *J. Clim.*, 24, 49-67, https://doi.org/10.1175/2010JCLI3522.1.

Nicolas, J. P., A. M. Vogelmann, R. C. Scott, A. B. Wilson, M. P. Cadeddu, D. H. Bromwich, J. Verlinde, D. Lubin, L. M. Russell, C. Jenkinson, H. H. Powers, M. Ryczek, G. Stone, and J. D., 2017: January 2016 extensive summer melt in West Antarctica favoured by strong El Nino. *Nat. Commun.*, 8, https://doi.org/10.1038/ncomms15799.

Orr, A., D. Cresswell, G. J. Marshall, J. C. R. Hunt, J. Sommeria, C. G. Wang, and M. Light, 2004: A ‘low-level’ explanation for the recent large warming trend over the western Antarctic Peninsula involving blocked winds and changes in zonal circulation. *Geophys. Res. Lett.*, 31, https://doi.org/10.1029/2003GL019160.

Orr, A., G. J. Marshall, J. C. R. Hunt, J. Sommeria, C. G. Wang, N. P. M. van Lipzig, D. Cresswell, and J. C. King, 2008: Characteristics of airflow over the Antarctic Peninsula and its response to recent strengthening of westerly circumpolar winds. *J. Atmos. Sci*., *65*, 1396-1413, https://doi.org/10.1175/2007JAS2498.1.

Orr, A., T. Phillips, S. Webster, A. Elvidge, M. Weeks, S. J. Hosking, and J. Turner, 2014: Met Office Unified Model high resolution simulations of a strong wind event in Antarctica. *Q. J. Roy. Met. Soc*., 140, 2287-2297, https://doi.org/10.1002/qj.2296.

Orr, A., A. Kirchgaessner, J. King, T. Phillips, E. Gilbert, A. Elvidge, M. Weeks, A. Gadian, P. Kuipers Munneke, M. van den Broeke, S. Webster, and D. McGrath, 2021: Comparison of kilometre and sub-kilometre scale simulations of a foehn wind event over the Larsen C Ice Shelf, Antarctic Peninsula using the Met Office Unified Model (MetUM). *Q. J. Roy. Met. Soc.*, 147, 3472– 3492, https://doi.org/10.1002/qj.4138.

Paolo, F. S., H. A. Fricker, and L. Padman, 2015: Volume loss from Antarctic ice shelves is accelerating. *Science*, 348, 327-332, https://www.science.org/doi/abs/10.1126/science.aaa0940.

Parish, T. R., and D. H. Bromwich, 1989: Instrumented aircraft observations of the katabatic wind regime near Terra Nova Bay. *Mon. Wea. Rev.*, 117, 1570-1585, https://doi.org/10.1175/1520-0493(1989)117<1570:IAOOTK>2.0.CO;2.

Parish, T. R., and D. H. Bromwich, 1991: Continental-scale simulation of the Antarctic katabatic wind regime. *J. Clim.*, 4, 135-146, https://doi.org/10.1175/1520-0442(1991)004<0135:CSSOTA>2.0.CO;2.

Parish, T. R., J. J. Cassano, and M. W. Seefeldt, 2006: Characteristics of the Ross Ice Shelf air stream as depicted in Antarctic Mesoscale Prediction System simulations. *J. Geophys. Res.*, 111, https://doi.org/10.1029/2005JD006185.

Power, S., F. Delage, C. Chung, G. Kociuba, and K. Keay, 2013: Robust twenty-first-century projections of El Niño and related precipitation variability. *Nature*, 502**,** 541–545, https://doi.org/10.1038/nature12580.

Pritchard, H. D., S. R. M. Ligtenberg, H. A. Fricker, D. G. Vaughan, M. R. van den Broeke, and L. Padman, 2012: Antarctic ice-sheet loss driven by basal melting of ice shelves. *Nature*, 484, 502-505, https://doi.org/10.1038/nature10968.

Purich, A., M. H. England, W. Cai, Y. Chikamoto, A. Timmermann, J. C. Fyfe, L. Frankcombe, G. A. Meehl, and J. A. Arblaster, 2016: Tropical Pacific SST Drivers of Recent Antarctic Sea Ice Trends. *J. Clim.*, 29, 8931–8948, https://doi.org/10.1175/JCLI-D-16-0440.1.

Rignot, E., J. Mouginot, B. Scheuchl, M. van den Broeke, M. J. van Wessem, and M. Morlighem, 2019: Four decades of Antarctic Ice Sheet mass balance from 1979–2017. *P. Natl. Acad. Sci. USA*, 116, 1095–1103, https://doi.org/10.1073/pnas.1812883116.

Rott, H., P. Skvarca, and T. Nagler, 1996: Rapid collapse of northern Larsen ice shelf, Antarctica. *Science*, 271, 788-792, https://www.jstor.org/stable/2889887.

Santoso, A., S. McGregor, F.-F. Jin, W. Cai, M. H. England, S.-I. An, M. J. McPhaden, and E. Guilyardi, 2013: Late-twentieth-century emergence of the El Niño propagation asymmetry and future projections. *Nature*, 504, 126–130, https://doi.org/10.1038/nature12683.

Scambos, T. A., C. Hulbe, M. Fahnestock, and J. Bohlander, 2000: The link between climate warming and break-up of ice shelves in the Antarctic Peninsula. *Journal of Glaciology*, 46, 516-530, https://doi.org/10.3189/172756500781833043.

Scambos, T. A., H. A. Fricker, C.-C. Liu, J. Bohlander, J. Fastook, A. Sargent, R. Massom, and A.-M. Wu, 2009: Ice shelf disintegration by plate bending and hydro-fracture: Satellite observations and model results of the 2008 Wilkins ice shelf break-ups. *Earth & Planetary Sci. Lett.*, 280, 51-60, https://doi.org/10.1016/j.epsl.2008.12.027.

Scott Yiu, Y. Y., A. C. Maycock, 2019: On the Seasonality of the El Niño Teleconnection to the Amundsen Sea Region. *J. Clim.*, 32, 4829-4845, https://doi.org/10.1175/JCLI-D-18-0813.1.

Scott, R. C., J. P., Nicolas, D. H. Bromwich, J. R. Norris, and D. Lubin, 2019: Meteorological drivers and large-scale climate forcing on West Antarctic surface melt. *J. Clim.*, 32, 665-684, https://doi.org/10.1175/JCLI-D-18-0233.1.

Shepherd, T. G., E. Boyd, R. A. Calel, S. C. Chapman, S. Dessai, I. M. Dima-West, H. J. Fowler, R. James, D. Maraun, O. Martius, C. A. Senior, A. H. Sobel, D. A. Stainforth, S. F. B. Tett, K. E. Trenberth, B. J. J. M. van den Hurk, N. W. Watkins, R. L. Wilby, D. A. Zenghelis, 2018: Storylines: an alternative approach to representing uncertainty in physical aspects of climate change. *Clim. Change*, 151**,** 555–571, https://doi.org/10.1007/s10584-018-2317-9.

Simmonds, I., and K. Keay, 2000a: Mean Southern Hemisphere Extratropical Cyclone Behavior in the 40-Year NCEP–NCAR Reanalysis. *J. Clim*., 13, 873-885, https://doi.org/10.1175/1520-0442(2000)013<0873:MSHECB>2.0.CO;2.

Simmonds, I., and K. Keay, 2000b: Variability of Southern Hemisphere Extratropical Cyclone Behavior, 1958–97. *J. Clim.*, 13, 550-561, https://doi.org/10.1175/1520-0442(2000)013<0550:VOSHEC>2.0.CO;2.

Speirs, J. C., D. F. Steinhoff, H. A. McGowan, D. H. Bromwich, and A. J. Monaghan, 2010: Foehn Winds in the McMurdo Dry Valleys, Antarctica: The Origin of Extreme Warming Events. *J. Clim.*, 23, 3577-3598, https://doi.org/10.1175/2010JCLI3382.1.

Stokes, C. R., J. E. Sanderson, B. W. J. Miles, S. S. R. Jamieson, and A. A. Leeson, 2019: Widespread distribution of supraglacial lakes around the margin of the East Antarctic Ice Sheet. *Sci. Rep.*, 9, 13823, https://doi.org/10.1038/s41598-019-50343-5.

Takaya, K., and H. Nakamura, 2001: A Formulation of a Phase-Independent Wave-Activity Flux for Stationary and Migratory Quasigeostrophic Eddies on a Zonally Varying Basic Flow. *J. Atmos. Sci.*, 58, 608-627, https://doi.org/10.1175/1520-0469(2001)058<0608:AFOAPI>2.0.CO;2.

Trusel, L. D., K. E. Frey, S. B. Das, P. Kuipers Munneke, and M. R. van den Broeke, 2013: Satellite-based estimates of Antarctic surface meltwater fluxes. *Geophys. Res. Lett*., 40, 6148-6153, https://doi.org/10.1002/2013GL058138.

Trusel, L. D., K. E. Frey, S. B. Das, K. B. Karnauskas, P. Kuipers Munneke, E. van Meijgaard, M. R. van den Broeke, 2015: Divergent trajectories of Antarctic surface melt under two twenty-first-century climate scenarios. *Nat. Geosci.*, 8, 927–932, https://doi.org/10.1038/ngeo2563.

Turner, J., H. Lu, I. White, J. C. King, T. Phillips, J. C. Hosking, T. J. Bracegirdle, G. J. Marshall, R. Mulvaney, and P. Deb, 2016: Absence of 21st century warming on Antarctic Peninsula consistent with natural variability. *Nature*, 535, 411-415, https://doi.org/10.1038/nature18645.

Wei, T., Q. Yan, and M. Ding, 2019: Distribution and temporal trends of temperature extremes over Antarctica. *Environ. Res. Lett.*, 14, https://doi.org/10.1088/1748-9326/ab33c1.

Wille, J. D., V. Favier, A. Dufour, I. V. Gorodetskaya, J. Turner, C. Agosta, and F. Codron, 2019: West Antarctic surface melt triggered by atmospheric rivers. *Nat. Geosci.*, 12**,** 911–916, https://doi.org/10.1038/s41561-019-0460-1.

Wille, J. D., V. Favier, I. V. Gorodetskaya, C. Agosta, C. Kittel, J. C. Beeman, N. C. Jourdain, J. T. M. Lenaerts, and F. Codron, 2021: Antarctic atmospheric river climatology and precipitation impacts. *J. Geophys. Res.*, 126, https://doi.org/10.1029/2020JD033788.

Wille, J. D., V. Favier, N. C. Jourdain, C. Kittel, J. V. Turton, C. Agosta, I. V. Gorodetskaya, G. Picard, F. Codron, C. Leroy-Dos Santos, C. Amory, X. Fettweis, J. Blanchet, V. Jomelli, and A. Berchet, 2022: Intense atmospheric rivers can weaken ice shelf stability at the Antarctic Peninsula. *Commun Earth Environ.*, 3, https://doi.org/10.1038/s43247-022-00422-9.

Zheng, F., J. Li, R. T. Clark, and H. C. Nnamchi, 2013: Simulation and projection of the Southern Hemisphere annular mode in CMIP5 models. *J. Clim*., 26, 9860-9879, https://doi.org/10.1175/JCLI-D-13-00204.1.

Zou, X., D. H. Bromwich, A. Montenegro, S.-H. Wang, and L. Bai, 2021: Major surface melting over the Ross Ice Shelf part I: Foehn effect. *Q. J. Roy. Met. Soc.*, 147, 2874-2894, https://doi.org/10.1002/qj.4104.

A.7 Draft I

Benefits of using a sophisticated standalone snow scheme to simulate a surface melt event over the Ross Ice Shelf, West Antarctica in the HIRHAM5 and MetUM regional atmospheric models

Or

Added value of dedicated snow schemes for simulating a melt event over the Ross Ice Shelf

Nicolaj Hansen[1,2], Andrew Orr[3], Xun Zou[4,5], Ruth Mottram[2], Ella Gilbert[3], Fredrik Boberg[2], Tony Phillips[3], Stuart Webster[6], and Tom Bracegirdle

[1]Geodesy and Earth Observation, DTU-Space, Technical University of Denmark, Lyngby, Denmark
[2]Danish Meteorological Institute, Copenhagen, Denmark
[3]British Antarctic Survey, Cambridge, UK
[4]Byrd Polar and Climate Research Center, Columbus, USA
[5]Scripps Institute of Oceanography, La Jolla, USA
[6]Met Office, Exeter, UK

For submission to Atmospheric Science Letters?

Corresponding author: Nicolaj Hansen, nichsen@space.dtu.dk

Abstract

Melt events have become more frequent over the Antarctic ice shelves, it is therefore important to be able model the surface melt correctly in regional climate models (RCM). Here we investigate a case study for a melt event over the Ross ice shelf in January 2016. We compare satellite observations, with outputs from the RCMs HIRHAM5 and MetUM, and results from an offline firn model that are forced with the outputs from said models. We find that the RCM only underestimate the number of melt days, whereas the firn model overestimates the number of melt days. However, the firn model seems to represent the melt extent better. Furthermore, we study the wind regimes in the RCMs and argue the difference in melt extent arises from misrepresented wind patterns in the RCMs.

1. Introduction

Intense and/or prolonged atmospheric-induced melting can result in widespread surface meltwater ponds over Antarctic ice shelves (Kingslake et al., 2017; Stokes et al., 2019). This can lead to their potential collapse if the meltwater enters the ice and results in hydrofracturing (Scambos et al., 2000, 2009; Kuipers Munneke et al., 2014; Robert and Banwell 2019), resulting in an increase in discharge of grounded ice into the ocean and thus higher global sea levels (Dupont and Alley, 2005; Pritchard et al., 2012; The IMBIE team, 2018). Studies show that summertime surface melting of Antarctic ice shelves will likely increase in the future (Trusel et al., 2015; Kittel et al. 2021; Feron et al., 2021; Gilbert and Kittel, 2021; Boberg et al. 2022). Thus, improving information on surface melting (and surface mass balance) and using this as an indicator for possible ice shelf collapse (Kuipers Munneke et al., 2014) is vital for generating more accurate predictions of future Antarctic ice sheet stability and its contribution to sea level rise (Fox-Kemper et al., 2018).

Causes of the surface melting include local-scale atmospheric circulation patterns such as barrier winds and foehn winds (Orr et al., 2004, 2022; Coggins et al., 2014; Zou et al., 2021; Gilbert et al., 2022; Carter et al., 2022), as well as large-scale circulation patterns such as atmospheric rivers and warm air intrusions related to cyclonic activity (Nicolas and Bromwich, 2011; Nicolas et al., 2017; Scott et al., 2019; Wille et al., 2022). Realistically simulating local-scale melt patterns and climate variability necessitates running regional atmospheric models at high spatial resolution (~1-10 km) to simulate the local-scale atmospheric processes correctly, as well as resolve complex topography and the smaller ice shelves that exist on spatial scales of ~100 km (Deb et al., 2018; Lenaerts et al., 2018; Hansen et al. 2021; Orr et al., 2022). Other challenge faced by regional atmospheric models is to realistically represent the surface melting in response to the atmospheric-induced warming. The resulting changes to the properties of snow/firn in the upper part of the ice shelf. This includes aspects such as meltwater production and ponding on the surface, melt-albedo feedback, and subsurface melt water retention and refreezing (Best et al., 2011; van Wessem et al., 2018; Walters et al., 2019; Keenan et al., 2021). The ability/sophistication of land surface snow schemes in regional atmospheric models to capture these effects varies considerably (van Wessem et al., 2018; Mottram et al. 2021). For example, two regional atmospheric models that have been used to study surface melt (and surface mass balance) over Antarctica are HIRHAM5 and the UK Met Office Unified Model (MetUM) model (Mottram et al., 2021; Carter et al., 2022; Hansen et al., 2021). In these simulations HIRHAM5 uses a multilayer snow scheme that represents many of these processes (Langen et al., 2015), while the MetUM uses a simple composite snow/soil layer that is unable to hold liquid water that can subsequently re-freeze (Best et al., 2011).

The Ross Ice Shelf (RIS), the largest ice shelf in Antarctica, frequently experiences surface melt events due to a combined effects of synoptic and local scale processes (Nicolas et al., 2017; Zou et al., 2021). A prominent and semi-permanent feature of the RIS is the low-level southerly wind regime, also known as the Ross Ice Shelf Air Stream (RAS), bordering the Transantarctic mountains (Parish et al, 2006). The RAS is made up of interactions between cyclonic activity, barrier winds, and katabatic winds, and is associated with some of the warmest temperatures observed over the RIS (Parish et al., 2006; Coggins et al., 2014; Constanza et al., 2016; Orr et al., 2022). One such example is the prolonged and extensive surface melt occurred over the RIS during January 2016. This was due to strong and sustained warm-air advection of maritime air over the RIS, likely in response to a contemporaneous strong El Nino episode (Nicolas et al. 2017).

Dedicated standalone land surface snow schemes (Vionnet et al., 2012; Langen et al., 2017; Keenan et al., 2021) are a useful tool to overcome some of the deficiencies described above related to simple snowpack representation, however acknowledging they are far from complete in their description of this complex physical system. In this study we investigate the benefits of applying the Langen et al. (2017) standalone snow scheme to improve both MetUM and HIRHAM5 simulations of the January 2016 melt event over the RIS. Assessing the ability of models to estimate surface melt is important for identifying deficiencies and aspects of the models that will require improvements in the future.

2. Methods and materials

In this work we rely on output from two hindcasts using HIRHAM5 and MetUM (version 11.1) regional atmospheric model simulations of the Antarctic CORDEX (Antarctic COordinated Regional climate Downscaling EXperiment; Gutowski et al., 2016), which provides high-resolution regional climate information about Antarctica for intercomparison and impact studies, see Mottram et al. (2021) for description of model setup.

The HIRHAM5 model combines the hydrostatic dynamical core of the HIRLAM7 numerical weather prediction model and the physics of the ECHAM5 general circulation model (Christensen et al., 2007). It uses 31 vertical levels in the atmosphere. The model uses a five-layer snow scheme (extending to a depth of 10 m water equivalent) described by Langen et al. (2015), which calculates surface melt and the associated retention and refreezing of liquid water in the firn layer. The snow scheme also represents the dependence of snow albedo on temperature by linearly varying the albedo between 0.85 (for fresh dry snow / temperatures below -5°C) and 0.65 (for wet snow / temperatures at 0°C).

The MetUM model uses the Global Atmosphere 6.0 configuration (GA6; Walters et al., 2017), which is suitable for grid scales of 10 km or coarser. Its most significant upgrade from earlier versions is that it includes the ENDGame (Even Newer Dynamics for General atmospheric modelling of the environment) dynamical core that solves equations for a non-hydrostatic, fully compressible, deep atmosphere. It uses 70 vertical levels in the atmosphere (up to a height of 80 km). The model uses the so-called “zero-layer” snow scheme, which uses a composite snow/soil layer to simulate the thermal store of snow and does not include any information on firn processes (Best et al., 2011).

The HIRHAM5 and MetUM models were run over the standard Antarctic CORDEX domain (see Figure 1) at a grid spacing of 0.11° (~12 km) from 1979 to 2019, with lateral and lower-boundary conditions provided by ERA-Interim reanalysis data (Dee et al, 2011). Additionally, while the HIRHAM5 hindcast uses a long-term continuous integration approach, the MetUM hindcast uses a frequent re-initialisation approach (Lo et al., 2008). This consists of a series of twice-daily 24-hour forecasts (at 0000 and 1200 UTC), with output at T+12, T+15, T+18, and T+21 hr from each of the forecasts concatenated together to form a seamless series of 3-hourly model outputs, with the earlier output discarded as spin-up. The saved output used in this study are a) 3-hourly instantaneous values of near-surface (10 m) meridional and zonal wind speed components, and near-surface air temperature, b) 3-hourly averaged values of net surface fluxes of shortwave radiation, longwave radiation, sensible heat, and latent heat, and c) 6-hourly averaged values of surface sublimation, surface evaporation, total (liquid and solid) precipitation, solid precipitation, and surface snow melt. Note the near-surface air temperature is at 1.5 m (2 m) in the MetUM (HIRHAM5) models.

The physically based multilayer standalone snow model is based on the version implemented in HIRHAM5 (Langen et al., 2015), but heavily updated to include 32 vertical layers (extending to a depth of 60 m water equivalent) and a sophisticated firn model (Langen et al. 2017). The firn model includes processes such as densification, snow grain growth, irreducible water saturation, impermeable ice layers, and snow state dependent hydraulic conductivity. This enables a much more detailed representation of retention and refreezing of liquid water within the firn, and thus an improved representation of vertical firn water flow and refreezing. The version used here is identical to the version optimised for Greenland (Langen et al., 2017; Mottram et al., 2017), apart from the temperature dependent snow albedo range. For the Greenland setup this varied from 0.85 to 0.65, but in this work the lower range of snow albedo was set to 0.5, following Yang et al. (2016) who showed that a wet melting snow surface at a temperature of around 0°C typically doesn't have an albedo lower than this. Similar range was also used for their simulations of melting on the RIS by Zou et al. (2021).

The standalone snow model is subsequently driven by atmospheric forcing from the HIRHAM5 and MetUM hindcasts for the January 2016 case-study period. The atmospheric forcing required consists of 6-hourly averaged values of solid, precipitation, liquid precipitation, surface evaporation, surface sublimation, surface downwelling shortwave radiative flux, surface downwelling longwave radiative flux, sensible heat flux, and latent heat flux (which the snow model subsequently interpolates to hourly values before using them as forcing). The standalone snow model is spun-up for a period of 250 years (by repeating the same decade 25 times using HIRHAM5 forcing) before being driven by the hindcasts to ensure a realistic representation of the properties of the snow and firn. Additionally, before being driven by the MetUM hindcast it is additionally spun-up by repeating the January 2016 case study period 25 times using MetUM forcing.

The raw surface melt output from the HIRHAM5 and MetUM simulations, as well as output from the standalone HIRHAM5 and MetUM-forced standalone snow model simulations, are used to calculate patterns of daily melt extent (defined as days with at least 3 mm of melt occurring) during the January 2016 case study. For all snow models the heat flux used to melt the surface is calculated as the residual in the surface energy budget (SEB) whenever the surface temperature reaches above 0°C, after which it is reset to 0°C (Best et al., 2011; Langen et al., 2015). These are compared with daily melt extent estimates from satellite passive microwave measurements at a grid spacing of 25 km (Nicolas et al., 2017), using the same melt threshold of 3 mm.

3. Results

Figure 2 shows that extensive surface melting occurred over much of the central and eastern sectors of the RIS during January 2016, with the total number of satellite-observed melt days for this period approaching up to 15 in these locations. Examination of the observed melt pattern for individual days showed this period was roughly from 11 to 25 January (not shown). Much fewer melt days are observed over the western sector of the RIS during this period, with the transition between the high melt regime to the east and the low melt regime to the west abruptly occurring around 180°W. These results agree with Nicolas et al. (2017, Fig. 1).

Figure 2 further shows an underestimation in the total number of melt days calculated from the raw melt output from the HIRHAM5 and MetUM simulations. HIRHAM5 is being particular low with only a few melt days over the eastern sector and no melt days in the central sector. MetUM performance only slightly better in terms of both the number (up to 10) and pattern of the melt days, with the latter broadly agreeing with the observations. However, compared to the satellite observations there is an overestimate of the number of melt days calculated from the standalone snow model forced by HIRHAM5 and MetUM. The standalone snow model erroneously simulates a high number of melt days (up to 20) over the western sector of the RIS, which is most pronounced when forced by the MetUM.

To investigate further the discrepancies between the snow model and observations over the western sector of the RIS, Figure 3 shows maps of daily melt area for the period from 13 to 18 January 2016. These six days were selected as out of all of January 2016 they show the biggest differences between the observations and snow model (not shown). The observations show a distinct region of non-melting over the western sector of the RIS on each of these six days, and widespread melting occurring everywhere else. This observed region of non-melting is poorly captured by melt output from the standalone snow model forced by both HIRHAM5 and MetUM output. The snow model forced by HIRHAM5 partially captures the region of non-melting over the western sector of the RIS from 13 to 16 January, but the area it encompasses gets progressively smaller with each day, and by 17 and 18 January is non-existent, i.e., widespread melting over all the RIS is erroneously simulated. By contrast, the snow model forced by MetUM erroneously simulates melting over the western sector of the RIS for the entire six-day period.

We speculate that the erroneous representation of the local wind regime (i.e., competition between synoptic winds, katabatic winds from the high interior of East Antarctica, and the RAS) by the regional atmospheric models plays an important role in explaining the discrepancies in melt between the snow model and observations over the RIS. To explore this, Figure 4 shows maps of near-surface wind field, near-surface temperature, and SEB from HIRHAM5 for 11, 13, 15, and 17 January 2016, i.e., preceding and during the six-day period examined in Figure 3 (calculated by averaging the 3-hourly fields for each day). The near-surface temperature shows air temperatures around or above -2°C over much of the western sector of the RIS on all four days, and the SEB shows positive values, consistent with melt (the exception is a pool of cold air on the 13th, discussed later). The region of relatively warm temperatures / positive SEB broadly coincides with the distinct region of melting that is erroneously simulated by the snow model (Figure 3). We speculate that the cause of this (erroneous) relatively warm air / positive SEB/ melting over this region is likely the poor representation of the competition between the northerly wind regime over Marie Byrd Land moving heat towards the Transantarctic mountains and the formation of the RAS and its associated warm signature (Coggins et al., 2014) and the extremely cold katabatic winds (exceeding -10°C). If the katabatic winds were to drain into the western sector of the RIS they would bring much colder air onto the ice shelf. However, in the HIRHAM5 simulation the katabatic winds largely flow parallel to the southerly side of the Transantarctic mountains and are prevented from draining into the ice shelf. This is likely because the RAS dominates, resulting in enhanced near-surface temperatures parallel to the northerly side of Transantarctic mountains / western sector of RIS and associated melt. The RAS and associated warm signature are especially apparent on the 15th and 17th of January, i.e., dominating the flow regime. We speculate therefore that air temperatures around or below -2°C are occurring over the western sector of the RIS (i.e., consistent with the satellite observations showing no melt) and that this is associated with cold winds from the plateau draining onto the RIS - but this is not simulated by HIRHAM5. However, the exception is a pool of cold air (negative SEB) on the 13th over the north-west sector of the RIS where temperatures reach down to -10°C and associated with cold westerly winds from the plateau draining onto the ice shelf. This coincides with a distinct region of non-melt in the snow model, which is consistent with the observations (Figure 3). We speculate therefore that this wind regime is correctly simulated by HIRHAM5. Additionally, we note that the HIRHAM5 simulation shows air temperatures around or above -2°C and positive SEB over much of the eastern and central sectors of the RIS for all four days.

The MetUM results (Fig. 5) show temperatures above or around -2°C and positive SEB over almost the entire RIS on 15 and 17 January, which is consistent with the snow model showing melt over the entire RIS. This is clearly in response to the combination of northerly winds over Marie Byrd Land and the occurrence of a strong RAS, with the katabatic winds prevented from draining onto the RIS and largely flowing parallel to the northerly side of the Transantarctic mountains. The strengthening / domination of the RAS is especially apparent on 15 and 17 January. Similar to the argument with HIRHAM5 above, we argue that the distinct region of melting over the western sector of the RIS that is erroneously simulated by the snow model is therefore due to MetUM poorly simulating the local wind regime, and especially the possible occurrence of cold winds from the plateau draining onto the RIS and the affect of this on near-surface temperatures and the SEB.

4. Discussion and Conclusions

This study shows that the current snow schemes used by HIRHAM5 and MetUM are both unable to realistically represent the prolonged and extensive surface melt that occurred over the RIS during January 2016 (Figure 2). Although this study focused on a single case, it is likely that this poor performance is typical Antarctic ice shelves, a study beyond the scope of the current. This conclusion can be justified because firstly the snow schemes used by both models in this study are very limited, and secondly using a considerably more sophisticated standalone snow model resulted in more modelled melt (Figure 2). The standalone snow model includes a sophisticated representation of the firn layer, including processes such as meltwater percolation, retention, and refreezing. A recommendation is therefore that the MetUM and HIRHAM5 simulations use the standalone scheme in studies investigating melt and surface mass balance.

However, it’s important to bear in mind that although the standalone snow model is better able to simulate patterns of surface melt, crucial interactions/feedbacks between the cryosphere surface and the atmosphere are not simulated because the model is offline / uncoupled to the regional atmospheric model. These include the impact on the surface climate (surface mass balance) due to the a) evolution of surface albedo as snow melts and snow grains age, and b) influence of melt ponds on the evaporation rate. These processes become even more important to realistically simulate the future climate response of Antarctic ice shelves (and ice sheets), as it is projected to experience much more frequent and extensive summertime melting (e.g., Feron et al., 2021). Future development work for both these models should therefore be to include detailed coupled land surface snow schemes that are tuned for Antarctica. This is already the case for the RACMO2 regional atmospheric model, which realistically represent the evolution of the snow and firn layers, as well as changes in albedo (van Wessem et al., 2018).

The JULES (Joint UK Land Environment Simulator) multilayer snow scheme has been developed for coupled MetUM simulations as well as a standalone snow model (Best et al., 2011; Walters et al., 2019). This model has been used in a 3-layer configuration to model northern hemisphere seasonal snow, which only represents a thin surface snow layer (Walters et al., 2019). Further effort is needed to optimise the model for Antarctica, which will involve using more layers to capture snow compaction of the underlying snow layers to firn. Here, HIRHAM5 uses a long-term continuous integration approach, the MetUM simulations examined here use frequent re-initialisation (Lo et al., 2008). Frequent re-initialisation is an issue as it prevents any properties of the snow scheme (snow and/or firn layer) from evolving. Therefore, improvements in the MetUM would also likely necessitate using a long-term continuous integration approach so that the snow and firn layers of the JULES snow model can evolve. However, so-far a continuous integration approach using the MetUM has only been done by Elvidge et al. (2020) for the Antarctic Peninsula region (as attempts to use this mode to produce the Antarctic CORDEX hindcast simulations used in this study resulted in repeated model failures).

It is noticeable that despite its sophistication that the standalone snow scheme was unable to realistically represent the complete melt pattern over the RIS, and in particular the distinct region of non-melt that occurred over the western sector of the RIS (Figure 3). This we argue, however, is due to deficiencies in the representation of the local wind dynamics in the MetUM and HIRHAM5 models and the associated influence of this on near-surface temperatures and SEB (Figures 4 and 5). For example, Orr et al. (2021) also showed that simulating surface melting over the Larsen C ice shelf required the detailed representation of local circulation features, including foehn winds and low-level jets. They also highlighted that dynamically driven local turbulent processes are crucial for the erosion/displacement of ground-based cold-air pools, which offers another mechanism for explaining the patterns of melt and non-melt that are apparent over the RIS (Figures 3, 4 and 5) – this could also be a focus for future work.

Acknowledgements

AO, RM, and EG are supported by the European Union funded Horizon 2020 project PolarRES.

References

Best, M. J., Pryor, M., Clark, D. B., Rooney, G. G., Essery, R. L. H., Menard, C. B., Edwards, J. M., Hendry, M. A., Porson, A., Gedney, N., Mercado, L. M., Sitch, S., Blyth, E., Boucher, O., Cox, P. M., Grimmond, C. S. B. and Harding, R. J.: The joint UK Land Environment Simulator (JULES), model description – Part 1: Energy and water fluxes, Geoscientific Model Development, 4, 677– 699, https://doi.org/10.5194/gmd-4-677-2011, 2011.

Boberg, F., Mottram, R., Hansen, N., Yang, S., and Langen, P. L.: Uncertainties in projected surface mass balance over the polar ice sheets from dynamically downscaled EC-Earth models, The Cryosphere, 16, 17–33, https://doi.org/10.5194/tc-16-17-2022, 2022.

Carter, J., Leeson, A., Orr, A., Kittel, C., Melchior van Wessem, J.: Variability in Antarctic surface climatology across region climate models and reanalysis datasets. EGUsphere [preprint], https://doi.org/10.5194/egusphere-2022-86, 2022.

Christensen, O. B., Drews, M., Christensen, J. H., Dethloff, K., Ketelsen, K., Hebestadt, I., and Rinke, A.: The HIRHAM regional climate model, Version 5 (beta), Danish Climate Centre, Danish Meteorological Institute, Danish Meteorological Institute, Technical Report, 2007.

Coggins, J. H. J., McDonald, A. J., and Jolly, B.: Synoptic climatology of the Ross Ice Shelf and Ross Sea region of Antarctica: k-mean clustering and validation, International Journal of Climatology, 34, 2330–2348, https://doi.org/10.1002/joc.3842, 2014.

Costanza, C. A., Lazzara, M. A., Keller, L. M., and Cassano, J. J.: The surface climatology of the Ross Ice Shelf Antarctica, International Journal of Climatology, 36, 4929–4941, https://doi.org/10.1002/joc.4681, 2016.

Deb, P., Orr, A., Bromwich, D. H., Nicolas, J. P., Turner, J., and Hosking, J. S.: Summer drivers of atmospheric variability affecting ice shelf thinning in the Amundsen Sea Embayment, West Antarctica, Geophysical Research Letters, 45, 4124-4133, https://doi.org/10.1029/2018GL077092, 2018.

Dee, D. P., Uppala, S. M., Simmons, A. J., Berrisford, P., Poli, P., Kobayashi, S., Andrae, U., Balmaseda, M. A., Balsamo, G., Bauer, P., Bechtold, P., Beljaars, A. C. M., van de Berg, L., Bidlot, J., Bormann, N., Delsol, C., Dragani, R., Fuentes, M., Geer, A. J., Haimberger, L., Healy, S. B., Hersbach, H., Hólm, E. V., Isaksen, L., Kållberg, P., Köhler, M., Matricardi, M., McNally, A. P., Monge-Sanz, B. M., Morcrette, J.-J., Park, B.-K., Peubey, C., de Rosnay, P., Tavolato, C., Thépaut, J.-N., and Vitart, F.: The ERA-Interim reanalysis: Configuration and performance of the data assimilation system, Q. J. Roy. Meteorol. Soc., 137, 553–597, 2011.

Dupont, T., and Alley, R.: Assessment of the importance of ice-shelf buttressing to ice-sheet flow, Geophysical Research Letters, 32, https://doi.org/10.1029/2004GL022024, 2005.

Feron, S., Cordero, R. R., Damiani, A., Malhotra, A., Seckmeyer, G., and Llanillo, P.: Warming events projected to become more frequent and last longer across Antarctica. Scientific Reports., 11, https://doi.org/10.1038/s41598-021-98619-z, 2021.

Fox-Kemper, B., Hewitt, H., Xiao, C., Aðalgeirsdóttir, G., Drijfhout, S., Edwards, T., Golledge, N., Hemer, M., Kopp, R., Krinner, G., Mix, A., Notz, S. N., Nurhati, I., Ruiz, L., Sallée, J.-B., Slangen, A., and Yu, Y.: Ocean, Cryosphere and Sea Level Change Supplementary Material, in: Climate Change 2021: The Physical Science Basis. Contribution of Working Group I to the Sixth Assessment Report of the Intergovernmental Panel on Climate Change, edited by: Masson-Delmotte, V., Zhai, P., Pirani, A., Connors, S. L., Péan, C., Berger, S., Caud, N., Chen, Y., Goldfarb, L., Gomis, M. I., Huang, M., Leitzell, K., Lonnoy, E., Matthews,J. B. R., Maycock, T. K., Waterfield, T., Yelekçi, O., Yu, R., and Zhou, B., Cambridge University Press, available at: https://www.ipcc.ch/, 2021.

Gilbert, E., and Kittel, C.: Surface melt and runoff on Antarctic ice shelves at 1.5°C, 2°C, and 4°C of future warming. Geophysical Research Letters, 48, https://doi.org/10.1029/2020GL091733, 2021.

Gilbert, E., Orr, A., Renfrew, I., King, J. C., and Lachlan-Cope, T. A.: A 20-year study of melt processes over Larsen C Ice Shelf using a high-resolution regional atmospheric model: Part 2, Drivers of surface melt, Journal of Geophysical Research, https://doi.org/10.1002/essoar.10508261.1, 2022.

Gutowski Jr., W. J., Giorgi, F., Timbal, B., Frigon, A., Jacob, D., Kang, H.-S., Raghavan, K., Lee, B., Lennard, C., Nikulin, G., O’Rourke, E., Rixen, M., Solman, S., Stephenson, T., and Tangang, F.: WCRP COordinated Regional Downscaling EXperiment (CORDEX): a diagnostic MIP for CMIP6, Geoscientific Model Development, 9, 4087–4095, https://doi.org/10.5194/gmd-9-4087-2016, 2016.

Hansen, N., Langen, P. L., Boberg, F., Forsberg, R., Simonsen, S. B., Thejll, P., Vandecrux, B., and Mottram, R.: Downscaled surface mass balance in Antarctica: impacts of subsurface processes and large-scale atmospheric circulation, The Cryosphere, 15, 4315–4333, https://doi.org/10.5194/tc-15-4315-2021, 2021.

Keenan, E., Wever, N., Dattler, M., Lenaerts, J. T. M., Medley, B., Kuipers Munneke, P., and Reijmer, C.: Physics-based SNOWPACK model improves representation of near-surface Antarctic snow and firn density, The Cryosphere, 15, 1065–1085, https://doi.org/10.5194/tc-15-1065-2021, 2021.

Kingslake, J., Ely, J. C., Das, I., and Bell, R. E.: Widespread movement of meltwater onto and across Antarctic ice shelves, Nature, 544, 349-352, https://doi.org/10.1038/nature22049, 2017.

Kittel, C., Amory, C., Agosta, C., Jourdain, N. C., Hofer, S., Delhasse, A., Doutreloup, S., Huot, P.-V., Lang, C., Fichefet, T., and Fettweis, X.: Diverging future surface mass balance between the Antarctic ice shelves and grounded ice sheet, The Cryosphere, 15, 1215–1236, https://doi.org/10.5194/tc-15-1215-2021, 2021.

Kuipers Munneke, P., Ligtenberg, S. R., Van Den Broeke, M. R., and Vaughan, D. G.: Firn air depletion as a precursor of Antarctic ice-shelf collapse, Journal of Glaciology, 60, 205–214, https://doi.org/10.3189/2014JoG13J183, 2014.

Langen, P. L., Mottram, R. H., Christensen, J. H., Boberg, F., Rodehacke, C. B., Stendel, M., van As, D., Ahlstrøm, A. P., Mortensen, J., Rysgaard, S., Petersen, D., Svendsen, K. H., Aðalgeirsdóttir, G., and Cappelen, J.: Quantifying Energy and Mass Fluxes Controlling Godthåbsfjord Freshwater Input in a 5-km Simulation (1991–2012), Journal of Climate, 28, 3694-3713, https://doi.org/10.1175/JCLI-D-14-00271.1, 2015.

Langen, P. L., Fausto, R. S., Vandecrux, B., Mottram, R. H., Box, J. E.: Liquid Water Flow and Retention on the Greenland Ice Sheet in the Regional Climate Model HIRHAM5: Local and Large-Scale Impacts, Frontiers in Earth Science, 4, https://www.frontiersin.org/article/10.3389/feart.2016.00110, 2017.

Lenaerts, J., Ligtenberg, S., Medley, B., Van de Berg, W., Konrad, H., Nicolas, J. P., Van Wessem, J. M., Trusel, L. D., Mulvaney, R., Tuckwell, R. J., Hogg, A. E., and Thomas, E. R.: Climate and surface mass balance of coastal West Antarctica resolved by regional climate modelling, Annals of Glaciology, 59, 29-41, https://doi.org/doi:10.1017/aog.2017.42, 2018.

Lo, J. C.-F., Yang, Z.-L., and Pielke Sr., R. A.: Assessment of three dynamical climate downscaling methods using the Weather Research and Forecasting (WRF) model, Journal of Geophysical Research, 113, https://doi.org/10.1029/2007JD009216, 2008.

Mottram, R., Boberg, F., Langen, P. L., Yang, S., Rodehacke, C., Christensen, J. H., and Madsen, M. S.: Surface mass balance of the Greenland ice sheet in the regional climate model HIRHAM5: Present state and future prospects, Low Temperature Science, 75, 105-115, https://doi.org/10.14943/lowtemsci.75.105, 2017.

Mottram, R., Hansen, N., Kittel, C., van Wessem, M., Agosta, C., Amory, C., Boberg, F., van de Berg, W. J., Fettweis, X., Gossart, A., van Lipzig, N. P. M., van Meijgaard, E., Orr, A., Phillips., T., Webster, S., Simonsen, S. B., and

Souverijns, N.: What is the surface mass balance of Antarctica? An intercomparison of regional climate model estimates, The Cryosphere, 15, 3751–3784, https://doi.org/10.5194/tc-15-3751-2021, 2021.

Nicolas, J. P., and Bromwich, D. H.: Climate of West Antarctica and Influence of Marine Air Intrusions, Journal of Climate, 24, 49-67, https://doi.org/10.1175/2010JCLI3522.1, 2011.

Nicolas, J. P., Vogelmann, A. M., Scott, R. C., Wilson, A. B., Cadeddu, M. P., Bromwich, D. H., Verlinde, J., Lubin, D., Russell, L. M., Jenkinson, C., Powers, H. H., Ryczek, M., Stone, G., and Wille, J. D.: January 2016 extensive summer melt in West Antarctica favoured by strong El Nino, Nature Communications, 8, https://doi.org/10.1038/ncomms15799, 2017.

Nicolas, J. P. "Antarctic daily surface melt data estimated from SMMR, SSM/I, and SSMIS passive microwave observations, 1978-2016" (2018) Polar Data Centre, Natural Environment Research Council, UK, doi:10.5285/ffd24dd7-e201-4a02-923f-038680bf7bb5.

Orr, A., Cresswell, D., Marshall, G. J., Hunt, J. C. R., Sommeria, J., Wang, C. G., and Light, M.: 2004: A ‘low-level’ explanation for the recent large warming trend over the western Antarctic Peninsula involving blocked winds and changes in zonal circulation, Geophysical Research Letters, 31, https://doi.org/10.1029/2003GL019160, 2004.

Orr, A., Deb, P., Clem, K., Gilbert, E., Boberg, F., Bromwich, D., Colwell, S., Hansen, N., Lazzara, M., Mottram, R., Niwano, M., Phillips, T., Pishniak, D., Reijmer, C., van den Berg, W. J., Webster, S., and Zou, X: Summer air temperature extremes over Antarctic ice shelves and potential “hotspots” of surface melting, Journal of Climate, under review, 2022.

Parish, T. R., Cassano, J. J., and Seefeldt, M. W.: Characteristics of the Ross Ice Shelf air stream as depicted in Antarctic Mesoscale Prediction System simulations, Journal of Geophysical Research, 111, https://doi.org/10.1029/2005JD006185, 2006.

Pritchard, H. D., Ligtenberg, S. R. M., Fricker, H. A., Vaughan, D. G., van den Broeke, M. R., and Padman, L.: Antarctic ice-sheet loss driven by basal melting of ice shelves, Nature, 484, 502-505, https://doi.org/10.1038/nature10968, 2021.

Robel, Alexander A., and Alison F. Banwell. "A speed limit on ice shelf collapse through hydrofracture." *Geophysical Research Letters* 46.21 12092-12100, 2019.

Scambos, T. A., Hulbe, C., Fahnestock, M., and Bohlander, J.: The link between climate warming and break-up of ice shelves in the Antarctic Peninsula, Journal of Glaciology, 46, 516-530, https://doi.org/10.3189/172756500781833043, 2000.

Scambos, T. A., Fricker, H. A., Liu, C.-C., Bohlander, J., Fastook, J., Sargent, A., Massom, R., and Wu, A.-M.: Ice shelf disintegration by plate bending and hydro-fracture: Satellite observations and model results of the 2008 Wilkins ice shelf break-ups, Earth and Planetary Science Letters, 280, 51-60, https://doi.org/10.1016/j.epsl.2008.12.027, 2009.

Scott, R. C., Nicolas, J. P., Bromwich, D. H., Norris, J. R., and Lubin, D.: Meteorological drivers and large-scale climate forcing on West Antarctic surface melt, Journal of Climate, 32, 665-684, https://doi.org/10.1175/JCLI-D-18-0233.1, 2019.

Stokes, C. R., Sanderson, J. E., Miles, B. W. J., Jamieson, S. S. R., and Leeson, A. A.: Widespread distribution of supraglacial lakes around the margin of the East Antarctic Ice Sheet, Scientific Reports, 9, 13823, https://doi.org/10.1038/s41598-019-50343-5, 2019.

The IMBIE team: Mass balance of the Antarctic Ice Sheet from 1992 to 2017, Nature, 558, 219–222, https://doi.org/10.1038/s41586-018-0179-y, 2018.

Trusel, L. D., Frey, K. E., Das, S. B., Karnauskas, K. B., Kuipers Munneke, P., Van Meijgaard, E., and Van Den Broeke, M. R.: Divergent trajectories of Antarctic surface melt under two twenty-first-century climate scenarios, Nature Geoscience, 8, 927–932, https://doi.org/10.1038/ngeo2563, 2015.

van Wessem, J. M., van de Berg, W. J., Noël, B. P. Y., van Meijgaard, E., Amory, C., Birnbaum, G., Jakobs, C. L., Krüger, K., Lenaerts, J. T. M., Lhermitte, S., Ligtenberg, S. R. M., Medley, B., Reijmer, C. H., van Tricht, K., Trusel, L. D., van Ulft, L. H., Wouters, B., Wuite, J., and van den Broeke, M. R.: Modelling the climate and surface mass balance of polar ice sheets using RACMO2 – Part 2: Antarctica (1979–2016), The Cryosphere, 12, 1479–1498, https://doi.org/10.5194/tc-12-1479-2018, 2018.

Vionnet, V., Brun, E., Morin, S., Boone, A., Faroux, S., Le Moigne, P., ... & Willemet, J. M. . The detailed snowpack scheme Crocus and its implementation in SURFEX v7. 2. *Geoscientific Model Development*, *5*(3), 773-791, 2012.

Walters, D., Boutle, I., Brooks, M., Melvin, T., Stratton, R., Vosper, S., Wells, H., Williams, K., Wood, N., Allen, T., Bushell, A., Copsey, D., Earnshaw, P., Edwards, J., Gross, M., Hardiman, S., Harris, C., Heming, J., Klingaman, N., Levine, R., Manners, J., Martin, G., Milton, S., Mittermaier, M., Morcrette, C., Riddick, T., Roberts, M., Sanchez, C., Selwood, P., Stirling, A., Smith, C., Suri, D., Tennant, W., Vidale, P. L., Wilkinson, J., Willett, M., Woolnough, S., and Xavier, P.: The Met Office Unified Model Global Atmosphere 6.0/6.1 and JULES Global Land 6.0/6.1 configurations, Geoscience Model Development, 10, 1487–1520, https://doi.org/10.5194/gmd-10-1487-2017, 2017.

Walters, D., Baran, A. J., Boutle, I., Brooks, M., Earnshaw, P., Edwards, J., Furtado, K., Hill, P., Lock, A., Manners, J., Morcrette, C., Mulcahy, J., Sanchez, C., Smith, C., Stratton, R., Tennant, W., Tomassini, L., Van Weverberg, K., Vosper, S., Willett, M., Browse, J., Bushell, A., Carslaw, K., Dalvi, M., Essery, R., Gedney, N., Hardiman, S., Johnson, B., Johnson, C., Jones, A., Jones, C., Mann, G., Milton, S., Rumbold, H., Sellar, A., Ujiie, M., Whitall, M., Williams, K., and Zerroukat, M.: The Met Office Unified Model Global Atmosphere 7.0/7.1 and JULES Global Land 7.0 configurations, Geoscientific Model Development, 12, 1909–1963, https://doi.org/10.5194/gmd-12-1909-2019, 2019.

Wille, J. D., Favier, V., Jourdain, N. C., Kittel, C., Turton, J. V., Agosta, C., Gorodetskaya, I. V., Picard, G., Codron, F., Leroy-Dos Santos, C., Amory, C., Fettweis, X., Blanchet, J., Jomelli, V., and Berchet, A.: 2022: Intense atmospheric rivers can weaken ice shelf stability at the Antarctic Peninsula, Communications Earth and Environment, 3, https://doi.org/10.1038/s43247-022-00422-9, 2022.

Yang, Q., Liu, J., Leppäranta, M., Sun, Q., Li, R., Zhang, L., Jung, T., Lei, R., Zhang, Z., Li, M., Zhao, J., and Cheng, J.: Albedo of coastal landfast sea ice in Prydz Bay, Antarctica: Observations and parameterization, Advances in Atmospheric Sciences, 33, 535–543, https://doi.org/10.1007/s00376-015-5114-7, 2016.

Zou, X., Bromwich, D. H., Montenegro, A., Wang, S. H., and Bai, L.: Major surface melting over the Ross Ice Shelf part I: Foehn effect, Quarterly Journal of the Royal Meteorological Society, 147, 2874-2894, https://doi.org/10.1002/qj.4104, 2021.

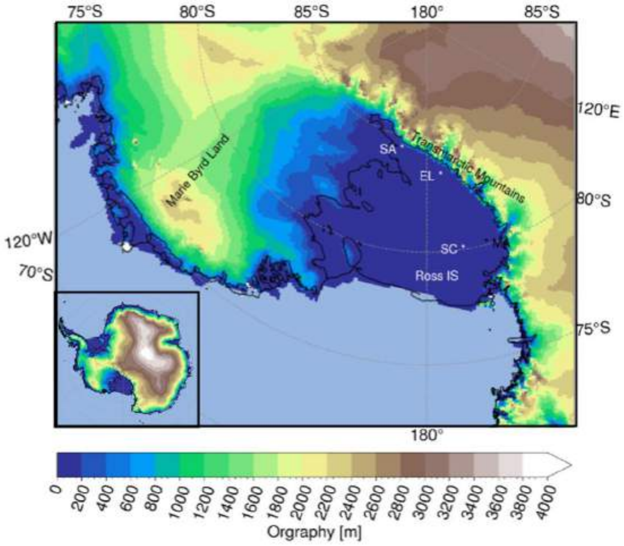

Figure 1: The model domain of the HIRHAM5 and MetUM simulations, with the orography (shading, m), coastline, and ice shelf extent (black lines) of the of the HIRHAM5 model, here zoomed into the region of West Antarctica and the Ross Ice Shelf. The location of the Ross Ice Shelf is labelled, as well as Marie Byrd Land and the Transantarctic Mountains. There are three weather stations marked over the ice shelf; SC is Schwerdtfeger, SA is Sabrina, and EL is Elaine.

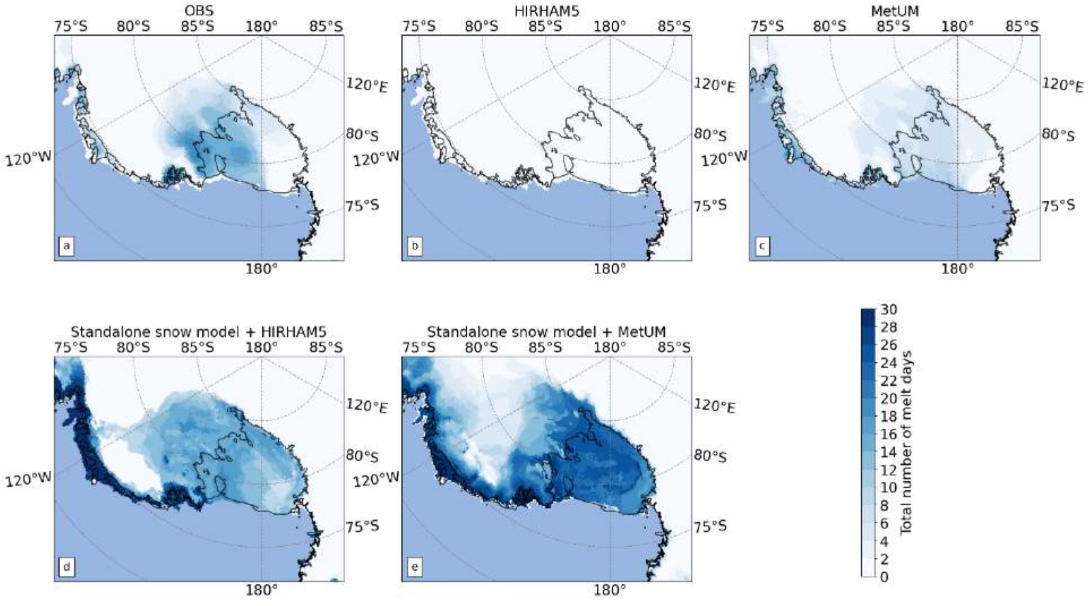

Figure 2: Total number of melt days (shading) in the ROI for January 2016. Here, a melt day is determined when the daily sum of melt exceeds 3 mm. (a) Observed satellite derived melt days. (b) HIRHAM5 simulated melt days (c) MetUM simulated melt days. (d) Melt days the standalone snow model forced by HIRHAM5. (e)Melt days from the standalone snow model forced by MetUM.

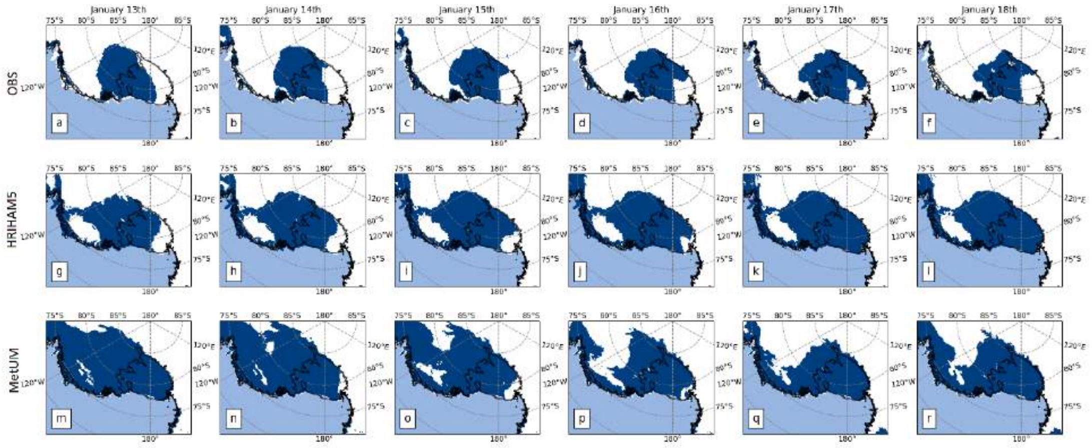

Figure 3: Maps of West Antarctica showing daily melt area for 13 to 18 (from left to right) January 2016 from (top row) satellite, (middle row) melt output from the standalone snow model forced by output from HIRHAM5, and (bottom row) melt output from the standalone snow model forced by output from MetUM. Areas of melt (no melt) are

indicated in blue (white) and defined as areas where the daily sum of melt exceeds 3 mm.

–

-

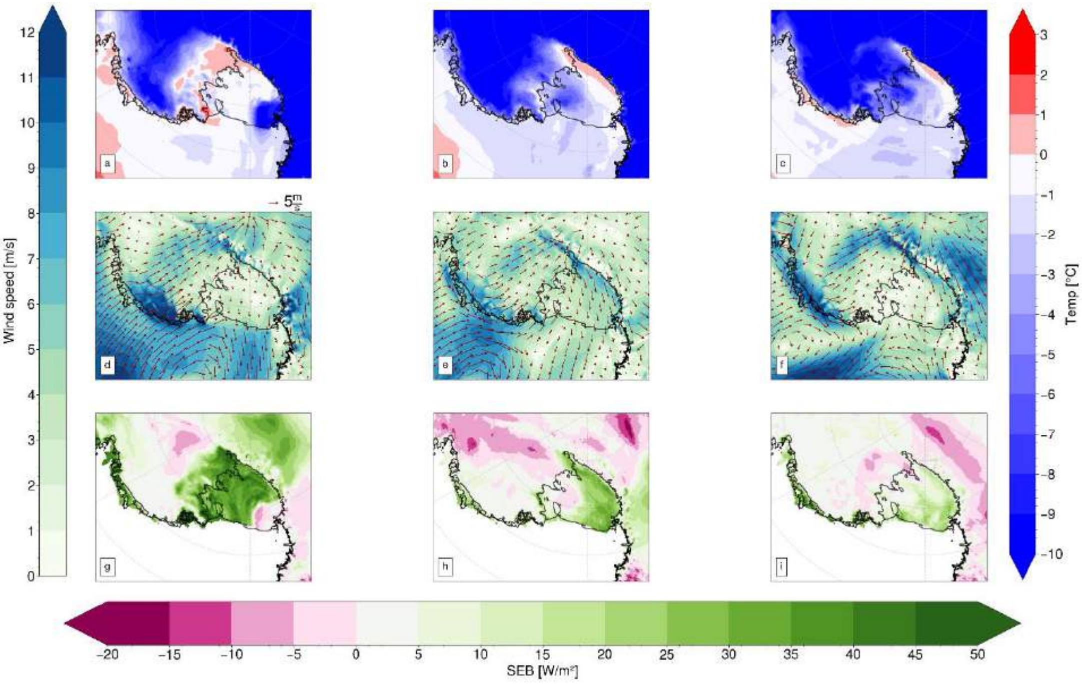

Figure 4: Maps of West Antarctica showing HIRHAM5 simulated near-surface air temperature (top row; K), near-surface wind speed and vectors (middle row; m s^{-1}, contours and arrows), and surface energy balance (bottom row; W m^{-2}) for 13, 15, and 17 (from left to right) January 2016. The length of the arrows relates to the wind speed. Results are daily averages based on averaging 3-hourly model output.

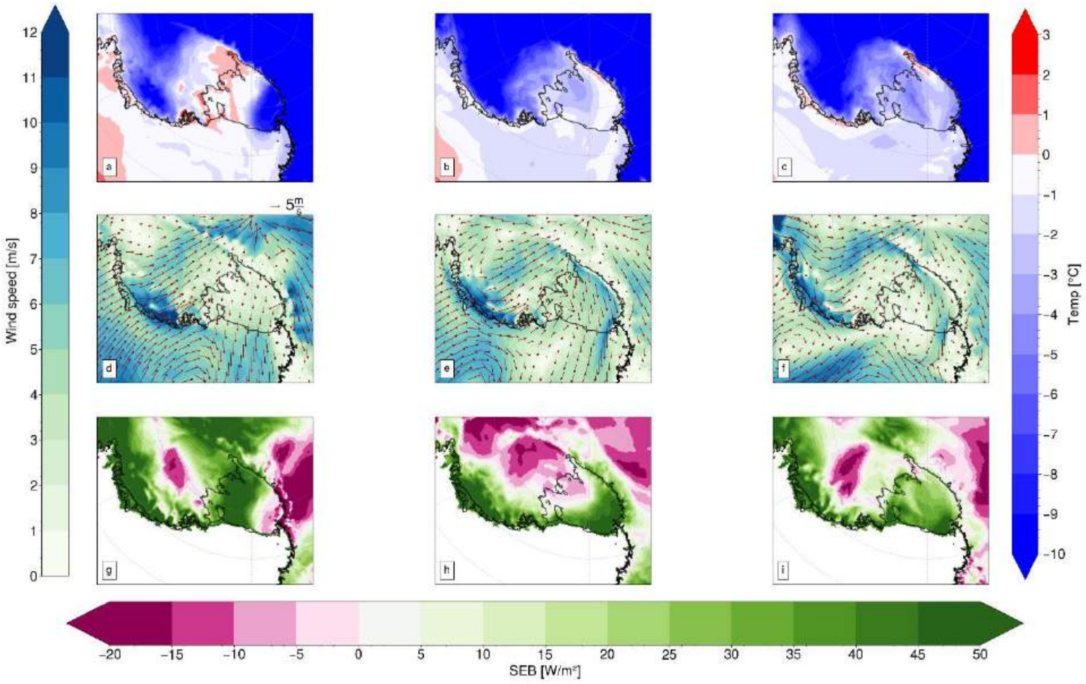

Figure 5: Maps of West Antarctica showing MetUM simulated near-surface air temperature (top row; K), near-surface wind speed and vectors (middle row; m s^{-1}, contours and arrows), and surface energy balance (bottom row; W m^{-2}) for 13, 15, and 17 (from left to right) January 2016. The length of the arrows relates to the wind speed. Results are daily averages based on averaging 3-hourly model output.

A.8 Draft II

Journal of Glaciology, Vol. 64, No. ?, 2022

High Resolution Simulations of Eemian Climate in Greenland

Carina H. BUNDE[1], Ruth MOTTRAM[2], Fredrik BOBERG[2], Nicolaj HANSEN[2,3], Christine S. HVIDBERG[1], Andrea M. U. GIERISCH[2], Chuncheng GUO[4]

[1] *Niels Bohr Institute, University of Copenhagen*

[2] *Danish Meteorological Institute, Copenhagen, Denmark*

[3] *Geodesy and Earth Observation, DTU-Space, Technical University of Denmark, Lyngby, Denmark*

[4] *NORCE Norwegian Research Centre, and Bjerknes Centre for Climate Research, Bergen, Norway*

Correspondence: Ruth Mottram <rum@dmi.dk>

ABSTRACT. The Eemian interglacial period, 130 ka to 115 ka ago, provides a much discussed analogue for the present-day and future warming in the polar regions. We present a new surface mass budget (SMB) dataset for the Greenland ice sheet for three different time-slices during the Eemian interglacial, for the periods 130 ka, 125 ka, and 115 ka. We investigate the implications of Eemian climate over Greenland by comparing SMB model output to ice core reconstructions of temperature and precipitation, with the ultimate goal to estimate surface mass budget of the Greenland ice sheet. The offline SMB model gives a lower SMB estimate than the SMB calculation in the regional climate model, pointing to the importance of specific process parameterizations in assessing SMB values for palaeo-timescales. We also note the pre-industrial SMB values are much lower than those computed using the ERA-Interim reanalysis, suggesting that model specific factors and boundary conditions may substantially skew estimates of SMB. Our analysis of ice core records also show that the difficulty in separating temperature and precipitation proxies makes it hard to reconstruct SMB based on ice core records alone.

INTRODUCTION

The Greenland ice sheet (GrIS) is the second largest land ice mass on the planet, containing around 2.85 million km^3 of ice and is a major contributor to observed sea level rise, adding on average 0.47 ± 0.23 mm $year^{-1}$ to global mean sea level between 1991 to 2015 (Mottram and others, 2019), with contributions set to accelerate due to climate change. There are still outstanding questions as to how fast and how much future sea level rise to expect from Greenland, with a wide spread in ice sheet model studies (Aschwanden and others, 2021). The Eemian interglacial has been considered a useful analogue of the present period of warming as palaeo proxy records indicate higher temperatures and smaller ice sheets in both Greenland and Antarctica (Yin and Berger, 2015) but the palaeo sea level record is difficult to reconcile with modelling studies (Jevrejeva and others, 2014). The Eemian interglacial period stretches from around 130 to around 115 thousand years (ka) before present (BP). Climate reconstructions suggest that the climate in the Arctic was about 2-4 degrees warmer during the Eemian, which makes it similar to projections for climate change pathways under RCP4.5 to RCP6.0 (Fischer and others, 2018)). During the Eemian, global mean sea level rose ∼ 6-9 m above the present level, with the Greenland ice sheet being one of the main contributors to the rise along with Antarctica (Rohling and others, 2019). Multiple and conflicting different reconstructions of the Eemian Greenland ice sheet exist (Helsen and others, 2013; Plach and others, 2021a), but the volume of the ice sheet during the Eemian is thought to have been about between 30 and 60% less than at present day (van de Berg and others, 2011; Rohling and others, 2019). As the nature and drivers of Greenland ice sheet change are critical to understanding future sea-level rise (Barlow and others, 2018), it is natural to look back at palaeo changes to understand the different processes.

In this study, we use a hierarchy of models to investigate Eemian climate in Greenland and the implications for ice sheet surface mass budget at the start, middle and end of the Eemian period. We use the high resolution regional climate model (RCM) HIRHAM5 to downscale palaeo-simulations for 20 year time slices. The RCM is forced on the boundaries by the NorESM global climate model with realistic orbital and greenhouse gas forcings for the three time slices (Guo and others, 2019). We then use RCM output to drive a full surface energy and mass budget model to estimate surface mass budget (SMB) of the GrIS and compare modelled SMB with proxy data from ice cores in Greenland to assess likely drivers of ice sheet change during the Eemian period.

Background

As the Eemian in Greenland is covered by ice core proxy records from the cold and dry interior of the ice sheet (e.g. Dahl-Jensen and others (2013)), we use these records to examine how well climate models represent Eemian climate at different periods. Yearly accumulation of ice on a glacier creates a record of the environmental conditions of the time of deposition. Measurements of stable water isotopes $\delta^{18}O_{ice}$, N_2O and CH_4 concentrations and the isotopes $\delta^{15}N$ of N_2 and $\delta^{18}O_{atm}$ of O_2 in the air content of ice cores are then used to calculate temperature and precipitation records (Cuffey and Paterson, 2010). Ice core studies from the Eemian show that the Eemian was warmer with reduced depletion of $\delta^{18}O$ suggesting a significant warming over the Greenland ice sheet as discussed in e.g. van de Berg and others (2013), Dahl-Jensen and others (2013) and Pedersen and others (2016). The highest temperatures at the NEEM drilling site occurred at the beginning of the Eemian, with a warming of 4-8 K warmer than the mean of the past millennium, and from this peak, average annual temperatures then gradually decreased, in step with decreasing summer insolation (Dahl-Jensen and others, 2013). The increase in temperature relative to today was associated with increased surface melt by Plach and others (2021b), and this may also potentially influence the ice core reconstructions of climate. As the warmer climate in the Eemian is driven by changes in summer insolation (Pedersen and others, 2016) rather than greenhouse gases, the relative sea level rise contribution from both hemispheres is different at different periods. For example, Rohling and others (2019) showed an initial high contribution to global sea level from Antarctica from ∼129 ka to ∼125 ka, but lower again around 125–124 ka while both Antarctica and Greenland contributed substantially to global mean sea level rise from ∼123.5 to ∼118 ka. Their proxy reconstruction combined with statistical modelling found that sea level rise from Greenland slowly increased from ∼127 ka onward, reaching a maximum sustained contribution from around ∼124 ka until the end of the last interglacial period. To investigate drivers of Greenland ice sheet mass loss, Helsen and others (2013) investigated the contribution of the Greenland ice sheet to the Eemian sea level highstand. They suggest that the Greenland mass loss contributed approx 0.5 m kyr^{-1} to sea level rise during the maximum of Eemian summertime insolation. The summertime insolation maximum is important as it suggests that loss of the ice sheet was driven by changes in surface mass budget, SMB, rather than ice dynamics. It is though, important to note that SMB forms the Greenland ice sheet and also indirectly drives the ice dynamics by the pattern in the difference between positive and negative mass changes over the ice sheet and its effect on the ice sheet geometry (Mottram, 2020). SMB and ice dynamics are therefore not independent processes. SMB is calculated from the sum of the accumulation, that is mostly snowfall, a positive term, and ablation, that is the melt and runoff a negative term. As climate change affects both snowfall and melt, surface processes are important in assessing how much melt runs off and how much refreezes, and it is therefore crucial to understand SMB in reconstructing the Eemian ice sheet. Ice core studies at the NEEM and Renland sites in Greenland have previously been incorporated into ice sheet and climate modelling studies using both SMB and ice dynamics models. For example, Pedersen and others (2016) used general circulation model experiments with the EC-Earth global model to disentangle the impacts of the insolation change and the changes in sea surface temperature and sea ice conditions to investigate the causes of warming in Greenland during the Eemian. The results show that the simulated Eemian precipitation-weighted warming at the NEEM site is low compared to the ice core reconstruction, partially due to missing feedbacks related to ice sheet changes and an extensive sea ice cover but possibly also related to model resolution. Insolation changes during the Eemian (the last interglacial period, 129 000–116 000 years before present) resulted in warmer than present conditions in the Arctic region. The NEEM ice core record suggests warming of 8±4K in northwestern Greenland based on stable water isotopes. Pedersen and others (2016) also showed the importance of climate feedbacks on the earth system and how these can have unexpected effects. For example, the oceanic conditions favoured increased accumulation, and potentially readvance in the southeast, while insolation was the dominant cause of ice sheet reduction elsewhere. Zolles and Born (2021) investigated ice sheet sensitivity to different parameters in a radiatively adjusted temperature index model and found significant uncertainty associated with atmospheric emissivity and down-welling longwave radiation as well as latent heat fluxes. Their findings emphasise the importance of the full surface energy balance model in assessing SMB. In this study we use an RCM to derive these inputs, but Merz and others (2014) also show that ice sheet topography is hard to reconstruct and is also a source of significant uncertainty in SMB estimates. This is a problem that is difficult to overcome without better constraints on ice sheet topography and we therefore follow two previous studies using high resolution RCMs to derive SMB by (Plach and others, 2018) and (van de Berg and others, 2011) in using present day topography in the absence of convincing reconstructions. Both Plach and others (2018) and van de Berg and others (2011) showed that correcting for different summertime insolation during the Eemian is key as is model resolution to resolve key processes.

METHODS

The hierarchy of models in this study is applied at three distinct time periods and compare with ice core proxies to examine the climate and ice sheet SMB on Greenland. Output from the high-resolution regional climate model, HIRHAM5, forced with the global climate model NorESM on the boundaries, is used to force the offline multi-layer SMB model developed at the Danish Meteorological Institute (DMI). We compare our model simulations with proxy data from ice core records. Simulations cover three Eemian time slices at 130 ka, 125 ka and 115 ka as well as a pre-industrial (PI) control run. We also compare the NorESM forced simulations with the same set-up forced with the ERA-Interim reanalysis.

Climate Modelling

NorESM

The Norwegian Earth System Model (NorESM) used in this study is a fast version, i.e., NorESM1-F, and is documented in detail by (Guo and others, 2019). The NorESM has a horizontal resolution of 2° for the atmosphere and land components and nominal 1° for the ocean and sea ice components which gives a resolution of around 200 km in the atmosphere. To simulate Eemian climate the orbital parameters and greenhouse gas forcing were modified as shown in Table 1 representing conditions 130, 125 and 115 ka BP and during the pre-industrial (PI, 1850) control simulation. Model spin-up and large-scale features are partly documented and the readers are referred to (Plach and others, 2018) for full details.

HIRHAM5

The global simulations were dynamically downscaled over Greenland with the regional climate model (RCM) HIRHAM5 (Mottram and others, 2017). HIRHAM5 is a hydrostatic model with 31 atmospheric layers and has been optimized to model ice sheet surface processes, including a simplified surface mass budget scheme. These processes are often neglected or simplified in GCMs. HIRHAM5 is forced at the lateral boundaries with 6-hourly intervals in the atmosphere, together with daily values for sea ice concentration and sea surface temperature and runs at a horizontal resolution of 0.05° x 0.05° on a rotated polar grid to reduce distortion near the poles. The high resolution of the RCM is particularly important in areas with high relief to resolve variables such as precipitation (Langen and others, 2015), (Hansen and others, 2021). To assess the performance of the downscaled NorESM simulations and compare pre-

	130 ka	125 ka	115 ka	Pre-industrial
CO_2 **[ppm]**	257.0	276.0	273.0	284.7
CH_4 **[ppb]**	512.0	640.0	472.0	791.6
N_2O **[ppb]**	239.0	263.0	251.0	275.7
Eccentricity	0.0382	0.0400	0.0414	0.0167
Obliquity [deg]	24.24	23.79	22.40	23.44
Long. of perih. [deg]	228.32	307.13	110.87	102.72

Table 1. *Greenhouse gas concentrations and orbital parameters for the palaeo climate simulations. These were implemented in both NorESM and HIRHAM5 to ensure a consistent climate forcing. (Plach and others, 2018).*

Simulation	Period	Forcing	Offline SMB model
ERAI	1980-2016	ERA-Interim reanalysis	Yes
130 ka	20 years	NorESM 130 ka	Yes
125 ka	20 years	NorESM 125 ka	Yes
115 ka	20 years	NorESM 115 ka	Yes
Pre-industrial	20 years	NorESM pre-industrial	Yes

Table 2. *HIRHAM5 simulation climate forcing. The Offline SMB column illustrates which periods the subsurface model has been run over.*

industrial with the present day, we also include a simulation forced on the lateral boundaries with the ERA-Interim reanalysis in our analysis (Dee and others, 2011).

Table 2 details the variation in climate forcing due to greenhouse gases and orbital forcing at different periods during the Eemian as specified in the different runs.

Surface Mass Budget Modelling

We use a full surface energy balance approach to calculate the SMB. Ice sheet SMB is calculated from accumulation, (the sum of snowfall and rain) and ablation which includes both sublimation and evaporation from the surface, E, as well as the runoff of liquid water, RO, from melt and where rain falls on exposed glacier ice. $SMB = A - E - RO$.

We use an offline SMB model, described in detail by (Hansen and others, 2021) to calculate melt based on the radiative and turbulent heat fluxes. It is a subsurface model, that also includes an advanced firn

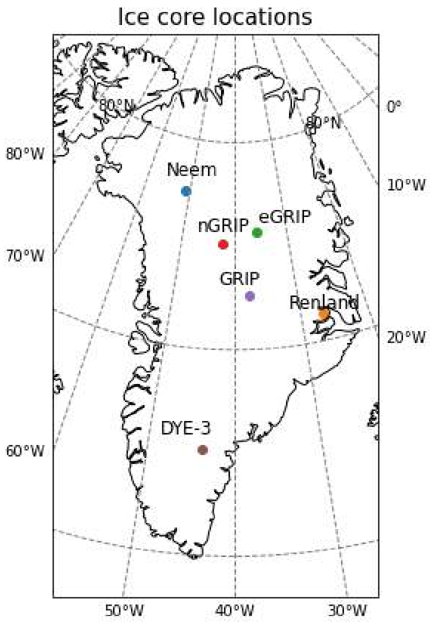

Fig. 1. *Overview of the six ice core locations considered in this study.*

scheme to account for the retention and refreezing of liquid water in underlying snow and firn layers. The model can use assimilated satellite albedo at the present day but for this study we use a simple broadband albedo scheme with values of 0.85 for dry snow, 0.65 for wet snow and the albedo for bare glacier ice is 0.4. The subsurface model is forced at 6-hourly intervals with the snow- and rainfall, evaporation, sublimation and surface energy fluxes from HIRHAM5, which include net latent and heat fluxes, downwelling short- and longwave radiation. More details are given in Hansen and others (2021). A simplified 5 layer version of this model is also included in the driving HIRHAM5 model to ensure that surface energy fluxes are realistic, especially over melting surfaces.

Ice core palaeoclimate data

Only few deep ice cores in Greenland exist that contain ice from the Eemian period and provide data suitable for evaluating the climate models. Here, we use data from six deep ice cores listed in tables 5 and 6, and the location of these ice cores are shown in the map in Figure 1 (Dansgaard and others, 1982, 1993; Andersen and others, 2004; Dahl-Jensen and others, 2013; Johnsen and others, 2001; Hvidberg and others, 2020).

From ice core isotope records we can estimate the ice sheet surface temperatures. These are calculated based on δ^{18}O values from ice core records using the following empirical relationship found for sites at the Greenland ice sheet under present conditions (Buchardt and others, 2012; Johnsen and others, 1989):

$$\delta^{18}O = 0.67T - 13.7 \tag{1}$$

Where T is the annual mean temperature at the location in $^{\circ}C$ (converted to K in table 10) and $\delta^{18}O$ is the annual mean isotopic value of the accumulation in $^{\circ}/_{\circ\circ}$. We use this relationship to infer an ice core based temperature estimate in the Eemian, assuming a similar relationship between $\delta^{18}O$ and T as at present. The accumulation rates are likewise calculated using $\delta^{18}O$ from ice records assuming the relationship between $\delta^{18}O$ and accumulation rate is exponential and depending on the location on the ice sheet according to the relation from Buchardt and others (2012):

$$A = 0.23e^{C_1(\delta^{18}O + C_2)} \tag{2}$$

Where A is the ice equivalent accumulation rate in myr^{-1} and then converted to the unit of millimeter water equivalent $mmyr^{-1}$. The factor 0.23 is the present day mean ice equivalent accumulation rate in myr^{-1}, here shown for the GRIP drilling site. The constants C_1 and C_2 are values depended on the location of the drill site due to geographical differences in precipitation, represented in table 6 by the group column, and tuned to fit data from the the last few hundreds to thousand years (Buchardt and others, 2012). We use the relationship to derive ice core based estimates for the Eemian, but acknowledging that the relation between $\delta^{18}O$ and accumulation rate in warmer climates is uncertain (Dahl-Jensen and others, 2013).

RESULTS

Our results show that modelled SMB during the Eemian was lower than modelled SMB at the present day (represented by SMB calculated using ERA-Interim forcing on the boundaries of HIRHAM5) as shown in Figure 2. Note also the variation in SMB at different time periods. The total SMB integrated over the ice sheet is shown in table 3 for the different time slices. However, the change in SMB is not uniformly distributed across the ice sheet as the maps of SMB shown in Figure 3.

We note a large difference between SMB calculated using the full offline subsurface model and the simplified SMB model inside the RCM (table 3. This is most likely related to the multi layer snow scheme

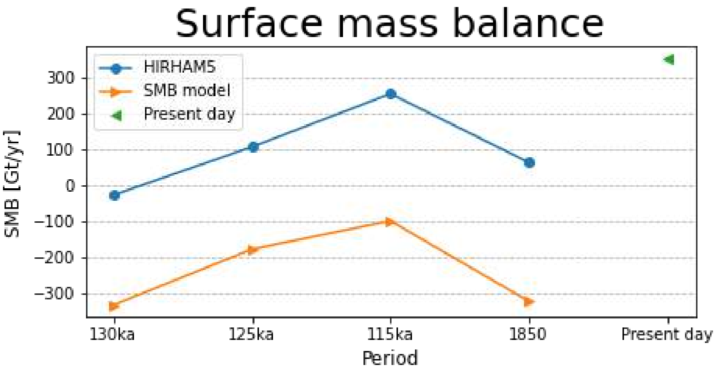

Fig. 2. *SMB estimations from the simple scheme in HIRHAM5 and the offline SMB model. The present day is forced by the ERA-Interim reanalysis (1980-2016) and the three palaeo periods, 130 ka, 125 ka, 115 ka as well as the pre-industrial period, 1850 are forced by downscaling NorESM1-F.*

and different, more sophisticated physics (see Hansen and others (2021)). In particular the offline model has many more and deeper layers which add up to a higher refreezing capacity, buffering runoff as well as a different albedo scheme. The precipitation that is fed into both models is however the same. The analysis of (Hansen and others, 2021) shows the offline model to be much closer to observed values of SMB than the simplified internal SMB scheme and therefore we use these values in the rest of the paper.

Climate Simulations

The lower SMB values in the early Eemian are driven partly by higher summer temperatures over most of the ice sheet (see Figure 4 leading to higher melt values. The mid-Eemian time slice has a very similar SMB to the pre-industrial in Table 4 but the map plot in Figure 3 shows that higher ice losses in southern Greenland were partly balanced by higher SMB in northern Greenland. The end of the Eemian by contrast is cooler than the pre-industrial reference period with lower melt and runoff compared to pre-industrial but roughly the same precipitation. In general, the smallest differences are in the interior part of Greenland, whereas the ablation zone has the highest differences between the periods. The plots in Figures 3 show the anomalies relative to the pre-industrial reference period calculated taking the individual runs minus the reference run.

We briefly compare the SMB from the simplified scheme in the HIRHAM5 model with the detailed

Anomalies relative to reference

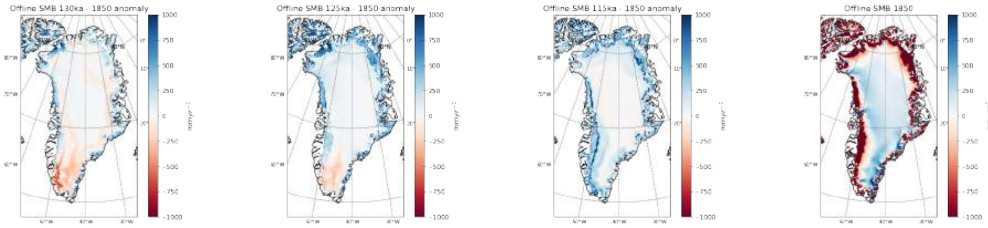

(a) 130ka **(b)** 125ka **(c)** 115ka **(d)** Reference

Fig. 3. *Development of SMB over Greenland during the Eemian interglacial period from the offline SMB model. Anomalies are calculated by taking the individual palaeo runs minus the pre-industrial run as reference. Red colours show where SMB is lower than the reference, and blue colours show where the SMB is higher than the reference period.*

Model	**Variable**	**Unit**	**Present day**	**Pre-industrial**	**115 ka**	**125 ka**	**130 ka**
			[ERAI]	[NorESM]	[NorESM]	[NorESM]	[NorESM]
HIRHAM5	SMB	[Gt/yr]		63.61	255.37	107.15	-27.09
Offline	SMB	[Gt/yr]	351.75	-323.77	-99.43	-178.22	-334.19

Table 3. *Mean values of SMB calculated using different model chains. The Offline SMB model is a stand alone offline model forced using output from HIRHAM5, which also contains a simplified SMB calculation. HIRHAM5 is forced by ERA-Interim for the present day and NorESM for the palaeo time slices and pre-industrial period.*

Anomalies relative to reference

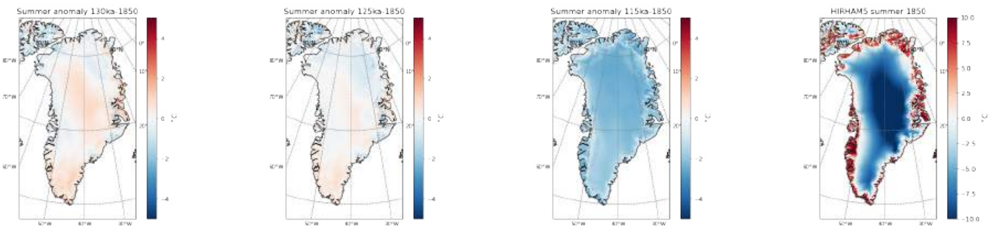

(a) 130ka **(b)** 125ka **(c)** 115ka **(d)** Reference

Fig. 4. *Development of summer (June, July, August) temperature over Greenland during the Eemian interglacial period from HIRHAM5. Anomalies calculated by taking the individual palaeo runs minus the pre-industrial run as reference.*

offline SMB model in Table 3. The lower SMB values in the Eemian are largely a result of the higher melt in the ablation zone in the offline model, related to the multi layer snow scheme. Similar results were shown between different types of SMB model forced by the MAR RCM by (Plach and others, 2018), who showed lower SMB related to higher melt and higher runoff in the ablation zone with increasing SMB model complexity. For brevity we omit this analysis in this paper and focus on the differences between the Eemian time slices relative to the pre-industrial reference.

To understand the differences between the Eemian time slices we examine the factors that control the SMB components in more detail. Figure 4 shows summer temperature anomalies. Periods of melt during the three summer months, particularly July are important for accumulated SMB over the ice sheet.

Figure 4 shows that the beginning of the Eemian at 130 ka is characterized with generally higher summer temperatures over the ice sheet compared with pre-industrial, indicating warmer climate during the beginning of the Eemian. This gradually changes and by the end of the Eemian at 115 ka the simulations show a colder summer climate than in the pre-industrial period.

The other component of the SMB calculation, accumulation, is approximated by precipitation. Table 4 shows relatively small changes in precipitation over the Eemian period integrated over the ice sheet, however, the plots in figure 5 show an interesting change in the distribution of precipitation over the ice sheet that likely has implications for both SMB and ice sheet dynamics.

The simulations show a wetter climate in the northwestern part of Greenland in the beginning and middle of the Eemian, illustrated in figure 5 with positive anomalies in precipitation in a) and b) compared

Anomalies relative to reference

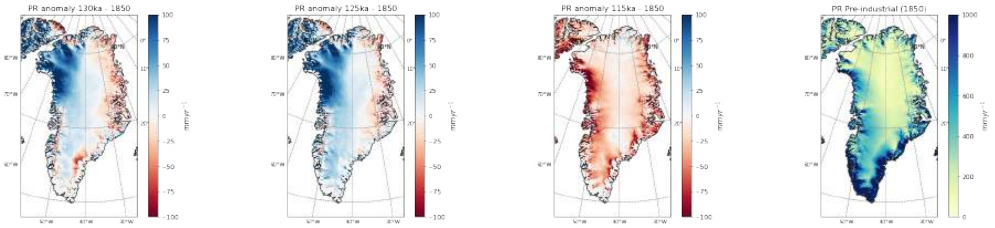

(a) 130ka **(b)** 125ka **(c)** 115ka **(d)** Reference

Fig. 5. *Development of precipitation over Greenland during the Eemian interglacial period from HIRHAM5. Anomalies calculated by taking the individual palaeo runs minus the pre-industrial run as reference.*

Anomalies relative to reference

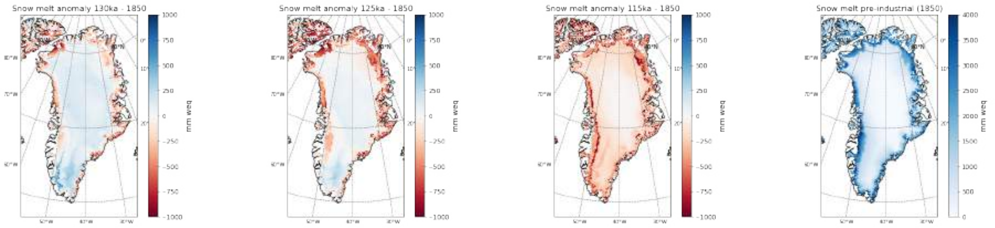

(a) 130ka **(b)** 125ka **(c)** 115ka **(d)** Reference

Fig. 6. *Development of snow melt over Greenland during the Eemian interglacial period from the offline model. Anomalies calculated by taking the individual palaeo runs minus the pre-industrial run as reference. Red colours indicate less melt compared to the reference period. Blue colours indicate more melt than the reference period.*

with the pre-industrial run. The end of the Eemian interglacial however shows a much drier climate in compared to the pre-industrial simulation. This drier climate as the earth system moves into a glacial period is represented in table 4 where lower melt rates also compensate leading to a similar SMB overall.

Figure 6 shows the differences in snow melt compared to pre-industrial. Over most of the ice sheet there are rather small differences, except for the ablation zone, which although accounting for a small part of the area has an outsize importance when accounting for ice melt. There is a higher snow melt in southern Greenland particularly during the early and middle Eemian compared to the pre-industrial. However the northern parts and especially the ablation zone show lower snow melt during the Eemian compared to the pre-industrial period. The increase in melt is also reflected in the refreezing on and runoff from the ice

Anomalies relative to reference

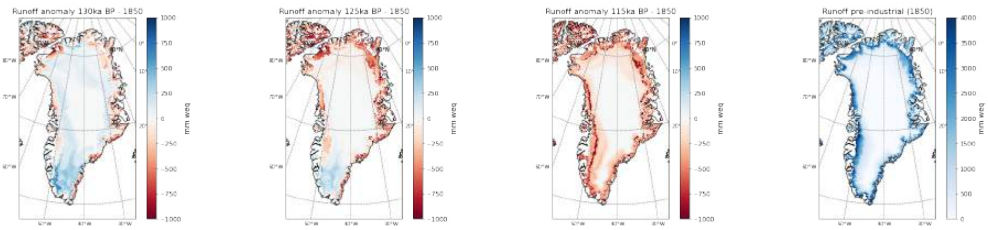

(a) 130ka **(b)** 125ka **(c)** 115ka **(d)** Reference

Fig. 7. *Development of runoff over Greenland during the Eemian interglacial period from the offline model. Anomalies calculated by taking the individual palaeo runs minus the pre-industrial run as reference.*

Anomalies relative to reference

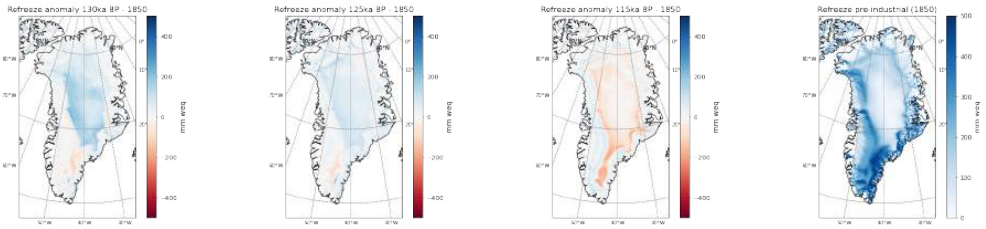

(a) 130ka **(b)** 125ka **(c)** 115ka **(d)** Reference

Fig. 8. *Development of refreeze over Greenland during the Eemian interglacial period from the offline model. Anomalies calculated by taking the individual palaeo runs minus the pre-industrial run as reference.*

sheet (shown in Figure 19 and 18 respectively).

In spite of the retention and refreezing capabilities of the deep snow pack model, the increase in production of melt water leads to an increase in both refreezing but also runoff (Table 4). Figure 7 shows more runoff in the beginning of the Eemian and a lot lower in the end compared to the pre-industrial, mirroring the melt figures.

The refreeze plots show only a small difference compared to the pre-industrial period, likely due to the rather small change in precipitation between the simulation periods. However, the difference is mostly pronounced in the interior part of the ice sheet. The beginning and middle of the Eemian simulations show slightly higher refreezing values than the pre-industrial, whereas the end of the Eemian generally throughout the ice sheet show lower values of refreezing due to the lack of snow melt as seen in figure 6.

Model	**Variable**	**Unit**	**Present day [ERAI]**	**Pre-industrial [NorESM]**	**115 ka BP [NorESM]**	**125 ka BP [NorESM]**	**130 ka BP [NorESM]**
HIRHAM5	Precipitation	[Gt/yr]	656.70	584.49	542.59	627.78	614.08
HIRHAM5	Temp. Annual	[°C]	-7.95	-19.98	-20.96	-21.76	-22.21
HIRHAM5	Temp. Summer	[°C]	1.99	-6.02	-8.02	-6.10	-5.83
Offline	Snow melt	[Gt/yr]	2425.01	1184.85	858.29	1122.66	1297.44
Offline	Runoff	[Gt/yr]	299.44	864.04	591.30	787.78	958.33
Offline	Refreeze	[Gt/yr]	141.12	285.05	254.96	347.21	371.55

Table 4. *As in Table 3 with mean values for precipitation and temperature (from the HIRHAM5 RCM), snow melt, runoff and refreezing.*

Ice core comparison

Values of $\delta^{18}O$ from ice core records are used to estimate surface temperature and accumulation in the Eemian. The tables refICRTASvalues and 6 show the calculated temperatures and accumulation for each drill site together with values of present day observations and simulated values of temperature and accumulation. The following plots show the monthly mean of ice properties such as SMB, temperature and precipitation for the different ice core drilling sites.

Figure 9 shows the monthly mean SMB at each drill site considered in this study, to specifically show the difference in SMB throughout the Greenland ice sheet. In the interior part of the Greenland ice sheet the SMB vary only a little from season to season due to the cold polar environment, whereas in the margins of the Greenland ice sheet due to warmer environment the SMB varies considerably over the seasons.

Figure 10 show the mean temperature of the different ice core locations over the time of a year with increase in temperatures on all drilling sites during the summer season, and decrease in temperatures during the winter as expected. The figure shows relatively low temperatures at EastGRIP, NorthGRIP and GRIP, which are all located in the interior of the Greenland ice sheet where the elevation is highest. Dye-3 is the location with the highest temperatures corresponding to the negative SMB values in the southeastern part of the Greenland ice sheet. The high temperatures of Dye-3 are close followed by the temperatures of NEEM and Renland. Renland is located close to the eastern shore of Greenland and NEEM is located on the north eastern site of Greenland. Values for both locations correspond to tendencies in SMB values. The sites where present day observations are available, represented by the grey lines, we see clear correlations

[H]

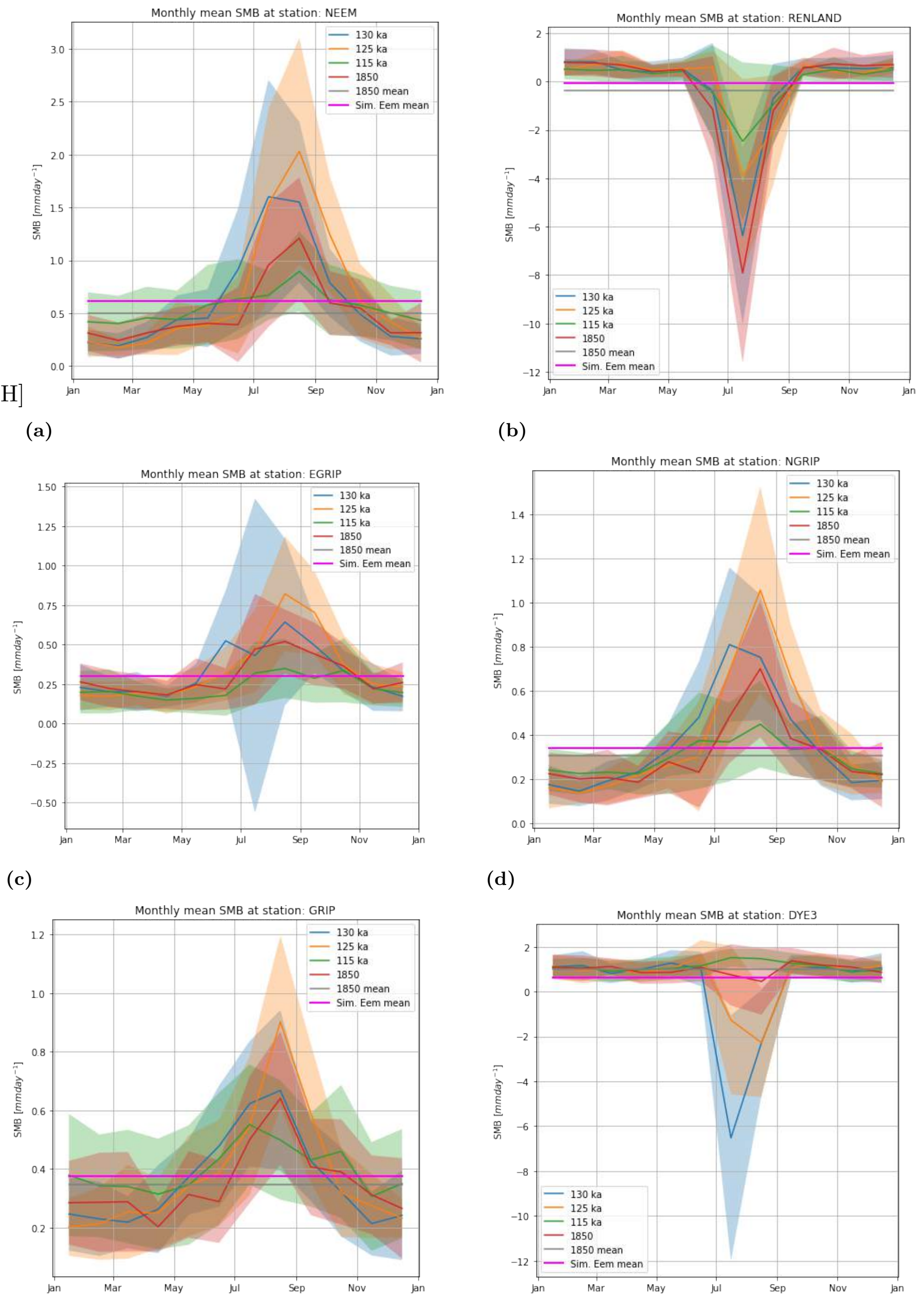

(a) (b)

(c) (d)

(e) (f)

Fig. 9. *Monthly mean SMB with standard deviation of the different ice core locations in Greenland, calculated from the SMB model developed at DMI. The pink line illustrates the mean SMB values for the whole of the Eemian interglacial.*

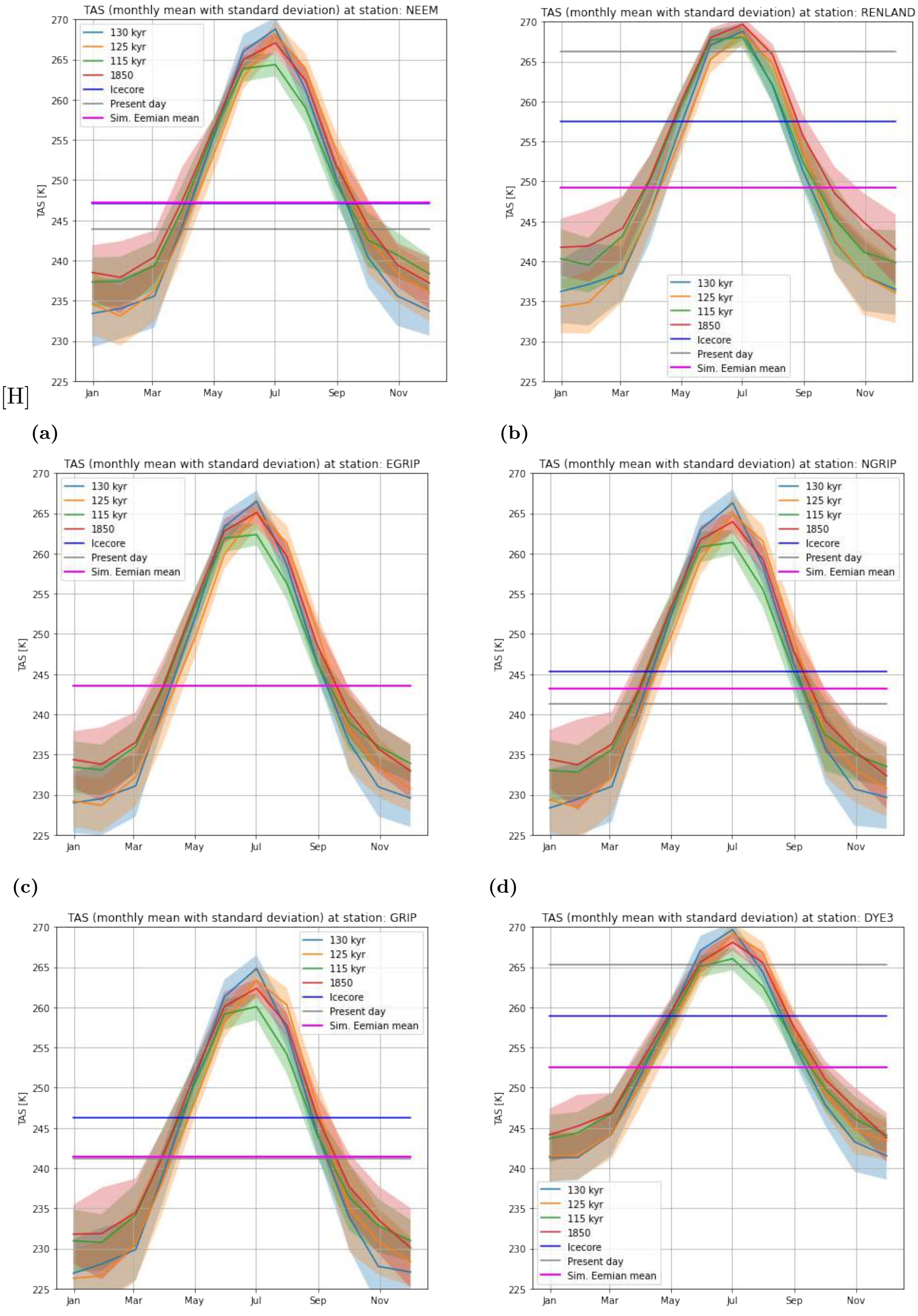

[H]

(a) **(b)**

(c) **(d)**

(e) **(f)**

Fig. 10. *Monthly mean temperatures of the different ice core locations in Greenland from HIRHAM5 with standard deviation. The grey line represents present day mean temperature. The dark blue line represents mean Eemian temperature calculated from* $\delta^{18}O$ *values from ice cores and covers the whole of the Eemian period. The pink line represents the simulated mean*

Location	**Lat** [°**N**]	**Lon** [°**W**]	**PD** δ^{18}**O** [‰]	**Eem** δ^{18}**O** [‰]	**Simulated PD temp.** [°**C**]	**Simulated Eem temp.** [°**C**]	**PD Ts** [°**C**]	**Eem Ts** [°**C**]
Neem	77.45	51.06	-33.0	-31.0	-24.95	-25.45	-29.15	-25.95
NGRIP	75.10	42.32	-35.5	-32.2	-27.65	-29.45	-31.65	-27.65
EGRIP	75.62	35.95			-27.85	-29.25		
GRIP	72.58	37.64	-34.9	-31.5	-26.55	-31.25	-31.85	-26.75
Renland	71.30	26.70	-27.0	-24.0	-20.05	-23.55	-6.75	-15.50
Dye-3	65.18	43.82	-28.0	-23.0	-18.35	-20.05	-7.75	-14.05

Table 5. *Calculation of temperature from ice core records and simulated estimations of mean temperatures. PD refers to the present day and Ts refers to surface temperature.*

with the simulated mean temperature, represented by the pink lines, during the Eemian. Temperatures from ice core records, represented by the dark blue lines, are generally a bit higher than the simulated, however only a few degrees.

We also calculate the precipitation from isotope values as described in the Methods section.

Figure 11 shows high precipitation for the NEEM and Dye-3 drill sites. The location of the NEEM drilling site and its high values of precipitation correlates with the relative high values of SMB. The drilling sites of EastGRIP, NorthGRIP and GRIP shows as expected low values of precipitation with only small peaks during the summer period. A tendency correlated with the low temperatures in the middle of the Greenland ice sheet. Precipitation generally increases from north to south, as temperatures increase and distance from the oceanic moisture source decreases. What is interesting to point out is the peak in precipitation at the NEEM drilling site at the beginning of the Eemian, for then gradually to decrease during the Eemian. Location where data of the present day accumulation is available, represented by the grey line, we see higher accumulation than simulated, represented by the pink line. The accumulation from ice core records, represented by the dark blue lines, are generally higher than the simulated values of precipitation and will be reviewed later in the discussion.

DISCUSSION

Our results show a marked evolution of SMB through the Eemian that is not resolved in ice core proxy records but that nevertheless has important implications for ice sheet and sea level rise reconstructions of

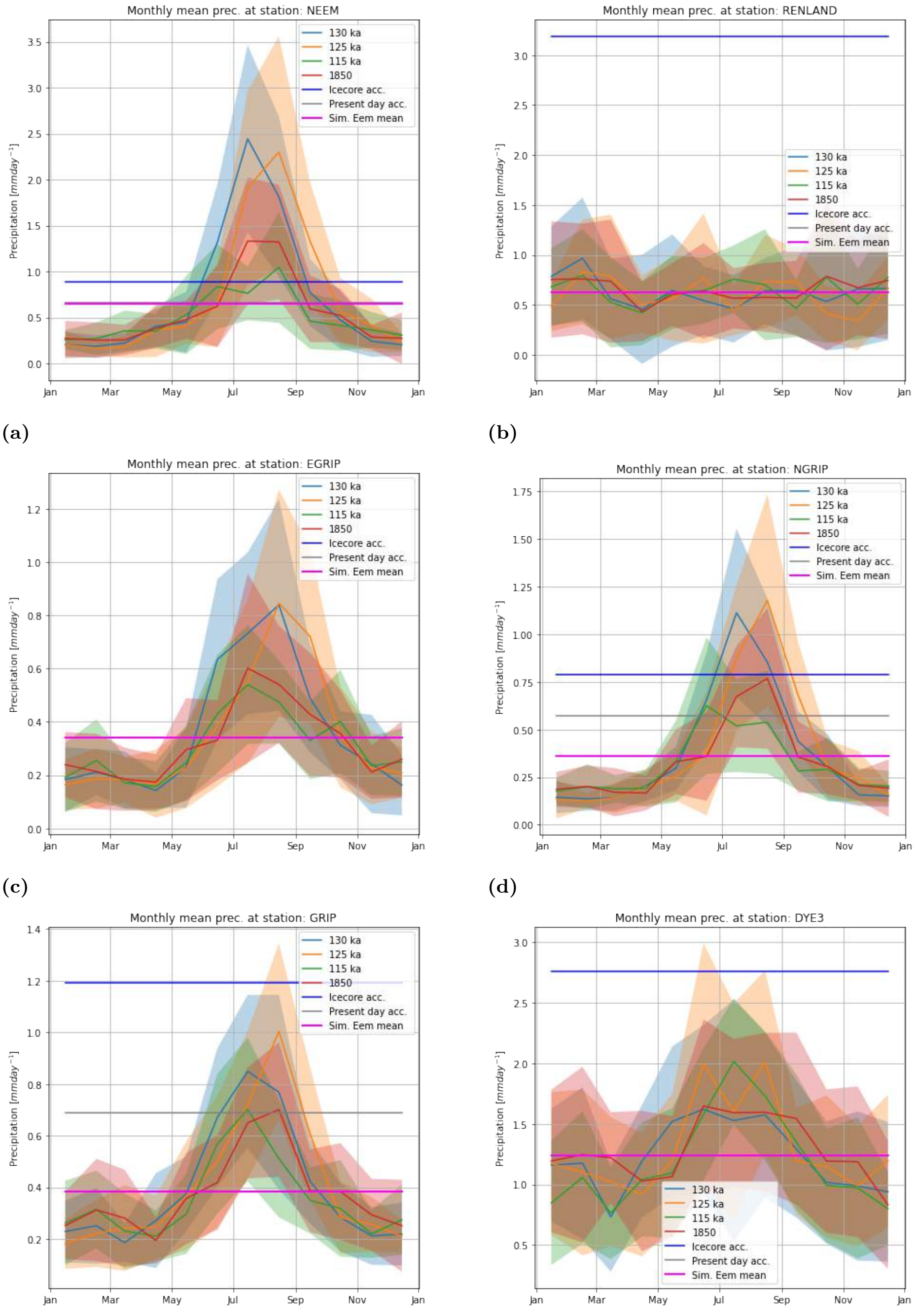

(a) **(b)**

(c) **(d)**

(e) **(f)**

Fig. 11. *Monthly mean precipitation of the different ice core locations in Greenland. The grey line illustrates the mean present day precipitation with standard deviation. The dark blue line represents the mean precipitation of the Eemian calculated from* $\delta^{18}O$ *values in ice cores. The pink line represents the simulated mean precipitation of the Eemian.*

Location	**Lat**	**Lon**	**PD**	**Eem**	**Simulated Eem prec.**	**PD acc.**	**Eem acc.**	**Group**
	[°**N**]	[°**W**]	δ^{18}**O** [$^{\circ}/_{\circ\circ}$]	δ^{18}**O** [$^{\circ}/_{\circ\circ}$]	$[mmday^{-1}]$	$[mmday^{-1}]$	$[mmday^{-1}]$	
Neem	77.45	51.06	-33.0	-31.0	0.57	0.66	0.89	NW
NGRIP	75.10	42.32	-35.5	-32.2	0.31	0.57	0.79	NW
EGRIP	75.62	35.95			0.29			NE
GRIP	72.58	37.64	-34.9	-31.5	0.33	0.69	1.19	CW
Renland	71.30	26.70	-27.0	-24.0	0.53		3.19	SE
Dye-3	65.18	43.82	-28.0	-23.0	1.13		2.76	CE

Table 6. *Calculation of precipitation from ice core records and simulated estimations of mean precipitation.Dye-3, GRIP, NGRIP, Neem, Renland, EGRIP: (Dansgaard and others, 1982, 1993; Andersen and others, 2004; Dahl-Jensen and others, 2013; Johnsen and others, 2001; Hvidberg and others, 2020)*

this period. At the start of the Eemian (130 ka), SMB is somewhat higher than the reference pre-industrial simulation. It gradually decreases through time, supporting the sea level rise reconstruction of e.g. Rohling and others (2019). Previous work (for example, Pedersen and others (2016)) that suggests solar insolation was key for ice sheet mass loss during the Eemian, rather than air temperatures is also confirmed by this analysis (see figure 4 and 5). A wider implication of this work therefore is that high sea levels reconstructed during this period may not be as relevant for comparisons of sea level rise under future climate change scenarios.

We also find lower SMB in the four offline model runs compared to the raw output from the RCM, which, as also found by Plach and others (2018), shows that full surface energy and mass balance models likely give different results than the simpler temperature index models often used to force ice sheet models on long timescales. We note that there is little difference between the RCM modelled SMB and offline modelled SMB in the interior part of the Greenland ice sheet but in the ablation zone, however, the Offline SMB model generally estimates higher melt than HIRHAM5. We attribute the higher SMB in the RCM than the offline model as likely due to the simple surface albedo scheme in the RCM as well as changes in runoff not captured in the simple five layer SMB scheme in HIRHAM5 (Hansen and others, 2021), in combination with a hundred year spin-up which likely gives a more realistic deep snow pack profile compared to the simpler scheme. This is explored in detail for simulations at the present day by Langen and others (2017).

It is important to remember that variables such as albedo are based on present day process understanding. Other factors, for example changes in dust load or circulation affecting clouds are not explicitly included in models and could potentially influence climate reconstructions based on physical models.

We also do not account for changes in ice sheet elevation or extent during the last interglacial as these are not well known and ice sheet model reconstructions disagree (e.g. Plach and others (2018)). The large spread in such simulations as well as proxy reconstructions are attributed to systematic underestimates in Arctic/north Atlantic warming in models as well as missing vegetation and ice sheet elevation feedbacks by Dahl-Jensen and others (2013). Assuming a constant ice sheet geometry and vegetation is an important limitation of our results, as it means we cannot account for the effect of the elevation-SMB feedback that can potentially enhance ice sheet retreat further, as for example changes in winds and turbulent heat fluxes from adjacent tundra, and changes in the ratio of precipitation that falls as snow or rain.

In comparison to the present-day simulation forced with the ERA-Interim reanalysis, the downscaled NorESM driven runs are rather dry. This also explains the rather low SMB in the pre-industrial reference and is the reason we here compare the NorESM runs to each other. Precipitation is very important for ice sheet mass budget and accurately simulating it is crucial for the SMB. Also crucial for absolute SMB estimates is the type of precipitation (rain or snow) and the seasonality. These are effects difficult to derive from ice core records and are therefore difficult to evaluate on palaeo-timescales.

Dynamical downscaling can give high temporal and spatial resolution information and in the case of Greenland, the high resolution of these simulations allows us to resolve the ice sheet ablation zone as well as high relief regions around the margin. However, the driving model still controls the amount of water vapour delivered to the boundary of the RCM. Resolution is a key difference between ERA-Interim ($\sim$ 79km) and NorESM ($\sim$ 222km) that may explain the somewhat drier forced simulations with the latter model. The RCM resolution likely also explains some of the differences we find in this study compared to Plach and others (2018), where the same NorESM runs were downscaled using the MAR model. Note also HIRHAM5 and MAR have different domains and ice masks, which can account for large differences in SMB estimates (Hansen and others, 2022). A full inter comparison is beyond the scope of this paper but Fettweis and others (2020) investigate the differences between the two RCMs plus other models at the present day. They show that while many of the models agree within error on the SMB of the ice sheet as a whole, there are important variations both spatially and in ice sheet SMB components. We note that both MAR and HIRHAM5 simulations show a similar pattern of precipitation (e.g. high precipitation in NW Greenland) and also a similar distribution to present day modelled precipitation, most likely because we use present day topography. HIRHAM5 however has higher precipitation in steeper regions that we attribute to the precipitation scheme (see also for example Hermann and others (2018). Precipitation anomalies in Greenland reflect dominance of difference in atmospheric circulation patterns - When comparing precipitation from the HIRHAM5 model forced with NorESM with present day data from the ERA-Interim reanalysis, we see higher values of precipitation at present, especially in southern Greenland this is particularly pronounced in the 115 ka anomaly run in figure 5. The results however also shows higher rates of precipitation in the southwestern part of Greenland during the Eemian, which is especially clear at the 125 ka run. The change in precipitation pattern, could affect the temperature reflected in the ice core records, suggesting oceanic and atmospheric circulation changes causing increased precipitation in the southeastern part of the ice sheet (Pedersen and others, 2016). As precipitation is the driver of the SMB of the ice sheet, a high accumulation rate will result in slower exposure of the glacier ice below. As the glacier below is darker it absorbs more energy resulting in an overall reduction in albedo. However, the form of precipitation is important, as precipitation in the form of snow will result in enhanced albedo effect, and precipitation in the form of rain may enhance mass loss. The importance of correct input of precipitation in the models is therefore high. The models usually give too much precipitation on the edge of the ice sheet, and too little precipitation in the middle of the ice sheet (Fettweis and others, 2020). This would give a slower melt rate at the edge of the ice sheet than actually occur, and a drier climate inland affecting the melt rate by accelerating the melt, because of the albedo feedback, as the ice layers are much darker than the snow at the surface. Substantial melting can have a significant effect on the reduction of the ice sheet near the margins that will reduce the volume of the ice sheet and thereby result in lower SMB.

Ice Core Reconstructions

The challenge of using ice core proxy data to evaluate climate models is clearly illustrated in figures 9 and 10 where a single value is given for the whole Eemian period to compare with much more detailed RCM output. We argue that the two are complementary, the RCM providing detailed spatial and temporal context in which to interpret the observational evidence, and the ice core data providing an approximate constraint of the Eemian maximum.

However, it is important to understand the context of ice core data when interpreting climate reconstructions. First, the isotopic value in the ice core is a proxy for the climate, not a direct observation, and the climatic interpretation of the proxy may be different for the Eemian compared to present day.

Second, the isotopic value of the precipitation depends on both climate and the surface elevation of the site. Third, the resolution of ice core records in the Eemian is low, and the full Eemian period has only been reliable covered by the NEEM ice core record so far (Dahl-Jensen and others, 2013). However, Eemian ice has been found in all the six ice cores, and we use the maximum isotopic value found in these records as an estimate for the Eemian maximum, assuming that ice from this part of the Eemian was retrieved in all cases. As mentioned above, we derive an estimate of the Eemian temperature, using the relationship between the temperature and the isotopic value of the precipitation at sites in Greenland calibrated with present observations (Buchardt and others, 2012). We neglected changes in surface elevation of the sites compared to present day. At NEEM the associated error was estimated to be appr. 1°C, and the total uncertainty of the estimate was ±4°C (Dahl-Jensen and others, 2013). We also estimate the Eemian accumulation rate using a relationship between accumulation rate the isotopic value of the precipitation calibrated by data from the Holocene (Buchardt and others, 2012). The relationship differs among regions at the Greenland ice sheet, depending on the wind regimes and ice sheet topography, making it sensitive to changes in surface elevation. Moreover, the relationship is mainly calibrated to data from climate as today or colder (Buchardt and others, 2012), and while a similar relation has been established for the GRIP ice cores reaching into the glacial (Dahl-Jensen and others, 1993), it remains uncertain whether the relationship holds in a warmer climate. These limitations must be noted when using the ice core based estimate of accumulation rate. The results of our simulations generally show lower temperatures for the Eemian than from ice record proxies as illustrated in table 5. The simulated accumulation rates are generally too low,

CONCLUSION

In this study, we examine the surface mass budget of the Greenland ice sheet during the last interglacial using a hierarchy of models. Based on the regional downscaling of NorESM with the HIRHAM5 RCM at key time steps of 130 ka, 125 ka, 115 ka, we show the evolution of the Greenland ice sheet SMB during the Eemian with an initially low SMB that gets progressively higher as summertime insolation decreases, reducing temperatures and melt rates. SMB values from the offline model in the early Eemian are -334.19 Gt/yr for 130 ka, -178.22 for 125 ka, increasing to -99.43 Gt/yr for 115 ka and -323.77 Gt/yr for the pre-industrial 1850. Compared to SMB of $\sim$ 351.75 Gt/yr for the present day, the lower SMB values are caused by lower precipitation in the NorESM driven runs with enhanced runoff driving the lowest SMB values in the early Eemian. We also identify a change in dominant precipitation patterns during the early to mid-

Eemian which has implications not only for ice sheet SMB but also for interpretation of ice core records. Our results confirm previous work showing the importance of using a full surface energy budget model in calculating SMB. We also note that given the insolation changes forcing changes to SMB, the Eemian cannot be treated as a single event and more attention should be paid to the climate and SMB evolution through the period. We furthermore confirm previous research that suggests that although temperature changes globally are similar to climate change projections, the insolation rather than greenhouse gas driven forcing does not make it a complete analogue for future climate change and caution needs to be used in interpreting ice sheet and sea level rise records from the Eemian and applying them to a warmer future.

ACKNOWLEDGEMENTS

REFERENCES

Andersen K, Azuma N, Barnola J, Bigler M, Biscaye P, Caillon N, Chappellaz J, Clausen H, DahlJensen D, Fischer H, Fluckiger J, Fritzsche D, Fujii Y, Goto-Azuma K, Gronvold K, Gundestrup N, Hansson M, Huber C, Hvidberg C, Johnsen S, Jonsell U, Jouzel J, Kipfstuhl S, Landais A, Leuenberger M, Lorrain R, Masson-Delmotte V, Miller H, Motoyama H, Narita H, Popp T, Rasmussen S, Raynaud D, Rothlisberger R, Ruth U, Samyn D, Schwander J, Shoji H, Siggard-Andersen M, Steffensen J, Stocker T, Sveinbjornsdottir A, Svensson A, Takata M, Tison J, Thorsteinsson T, Watanabe O, Wilhelms F, White J and Project NGIC (2004) High-resolution record of northern hemisphere climate extending into the last interglacial period. *NATURE*, **431**(7005), 147–151, ISSN 0028-0836 (doi: 10.1038/nature02805)

Aschwanden A, Bartholomaus TC, Brinkerhoff DJ and Truffer M (2021) Brief communication: A roadmap towards credible projections of ice sheet contribution to sea level. *The Cryosphere*, **15**(12), 5705–5715 (doi: 10.5194/tc-15-5705-2021)

Barlow NLM, McClymont EL, Whitehouse PL, Stokes CR, Jamieson SSR, Woodroffe SA, Bentley MJ, Callard SL, Cofaigh CO, Evans DJA, Horrocks JR, Lloyd JM, Long AJ, Margold M, Roberts DH and Sanchez-Montes ML (2018) Lack of evidence for a substantial sea-level fluctuation within the Last Interglacial. *Nature Geoscience*, **11**(9), 627–634, ISSN 1752-0908 (doi: 10.1038/s41561-018-0195-4), bandiera_abtest: a Cg_type: Nature Research Journals Number: 9 Primary_atype: Reviews Publisher: Nature Publishing Group Subject_term: Climate change;Cryospheric science;Palaeoclimate Subject_term_id: climate-change;cryospheric-science;palaeoclimate

Buchardt SL, Clausen HB, Vinther BM and Dahl-Jensen D (2012) Investigating the past and recent D18O-accumulation relationship seen in Greenland ice cores. *Climate of the Past*, **8**(6), 2053–2059, ISSN 1814-9332 (doi: 10.5194/cp-8-2053-2012)

Cuffey KM and Paterson WSB (2010) *The physics of glaciers.* Academic Press

Dahl-Jensen D, Johnsen SJ, Hammer CU and Jouzel J (1993) Past accumulation rates derived from observed annual layers in the grip ice core from summit, central greenland. *NATO ASI Series 1*, 517–532

Dahl-Jensen D, Albert MR, Aldahan A, Azuma N, Balslev-Clausen D, Baumgartner M, Berggren AM, Bigler M, Binder T, Blunier T, Bourgeois JC, Brook EJ, Buchardt SL, Buizert C, Capron E, Chappellaz J, Chung J, Clausen HB, Cvijanovic I, Davies SM, Ditlevsen P, Eicher O, Fischer H, Fisher DA, Fleet LG, Gfeller G, Gkinis V, Gogineni S, Goto-Azuma K, Grinsted A, Gudlaugsdottir H, Guillevic M, Hansen SB, Hansson M, Hirabayashi M, Hong S, Hur SD, Huybrechts P, Hvidberg CS, Iizuka Y, Jenk T, Johnsen SJ, Jones TR, Jouzel J, Karlsson NB, Kawamura K, Keegan K, Kettner E, Kipfstuhl S, Kjær HA, Koutnik M, Kuramoto T, Köhler P, Laepple T, Landais A, Langen PL, Larsen LB, Leuenberger D, Leuenberger M, Leuschen C, Li J, Lipenkov V, Martinerie P, Maselli OJ, Masson-Delmotte V, McConnell JR, Miller H, Mini O, Miyamoto A, Montagnat-Rentier M, Mulvaney R, Muscheler R, Orsi AJ, Paden J, Panton C, Pattyn F, Petit JR, Pol K, Popp T, Possnert G, Prié F, Prokopiou M, Quiquet A, Rasmussen SO, Raynaud D, Ren J, Reutenauer C, Ritz C, Röckmann T, Rosen JL, Rubino M, Rybak O, Samyn D, Sapart CJ, Schilt A, Schmidt AMZ, Schwander J, Schüpbach S, Seierstad I, Severinghaus JP, Sheldon S, Simonsen SB, Sjolte J, Solgaard AM, Sowers T, Sperlich P, Steen-Larsen HC, Steffen K, Steffensen JP, Steinhage D, Stocker TF, Stowasser C, Sturevik AS, Sturges WT, Sveinbjörnsdottir A, Svensson A, Tison JL, Uetake J, Vallelonga P, van de Wal RSW, van der Wel G, Vaughn BH, Vinther B, Waddington E, Wegner A, Weikusat I, White JWC, Wilhelms F, Winstrup M, Witrant E, Wolff EW, Xiao C, Zheng J and NEEM community members (2013) Eemian interglacial reconstructed from a Greenland folded ice core. *Nature*, **493**(7433), 489–494, ISSN 1476-4687 (doi: 10.1038/nature11789), bandiera_abtest: a Cg_type: Nature Research Journals Number: 7433 Primary_atype: Research Publisher: Nature Publishing Group

Dansgaard W, Clausen HB, Gundestrup N, Hammer CU, Johnsen SF, Kristinsdottir PM and Reeh N (1982) A New Greenland Deep Ice Core. *Science*, **218**(4579), 1273–1277 (doi: 10.1126/science.218.4579.1273), publisher: American Association for the Advancement of Science

Dansgaard W, Johnsen S, Clausen H, DahlJensen D, GUNDESTRUP N, HAMMER C, HVIDBERG C, STEFFENSEN J, SVEINBJORNSDOTTIR A, JOUZEL J and BOND G (1993) Evidence for general instability of past climate from a 250-kyr ice-core record. *NATURE*, **364**(6434), 218–220, ISSN 0028-0836 (doi: 10.1038/364218a0)

Dee DP, Uppala SM, Simmons AJ, Berrisford P, Poli P, Kobayashi S, Andrae U, Balmaseda MA, Balsamo G, Bauer P, Bechtold P, Beljaars ACM, van de Berg L, Bidlot J, Bormann N, Delsol C, Dragani R, Fuentes M, Geer AJ, Haimberger L, Healy SB, Hersbach H, Hólm EV, Isaksen L, Kållberg P, Köhler M, Matricardi M, McNally AP, Monge-Sanz BM, Morcrette JJ, Park BK, Peubey C, de Rosnay P, Tavolato C, Thépaut JN and Vitart F (2011) The ERA-Interim reanalysis: configuration and performance of the data assimilation system. *Quarterly*

Journal of the Royal Meteorological Society, **137**(656), 553–597, ISSN 1477-870X (doi: 10.1002/qj.828), _eprint: https://onlinelibrary.wiley.com/doi/pdf/10.1002/qj.828

Fettweis X, Hofer S, Krebs-Kanzow U, Amory C, Aoki T, Berends CJ, Born A, Box JE, Delhasse A, Fujita K, Gierz P, Goelzer H, Hanna E, Hashimoto A, Huybrechts P, Kapsch ML, King MD, Kittel C, Lang C, Langen PL, Lenaerts JTM, Liston GE, Lohmann G, Mernild SH, Mikolajewicz U, Modali K, Mottram RH, Niwano M, Noël B, Ryan JC, Smith A, Streffing J, Tedesco M, van de Berg WJ, van den Broeke M, van de Wal RSW, van Kampenhout L, Wilton D, Wouters B, Ziemen F and Zolles T (2020) GrSMBMIP: intercomparison of the modelled 1980–2012 surface mass balance over the Greenland Ice Sheet. *The Cryosphere*, **14**(11), 3935–3958, ISSN 1994-0416 (doi: 10.5194/tc-14-3935-2020), publisher: Copernicus GmbH

Fischer H, Meissner KJ, Mix AC, Abram NJ, Austermann J, Brovkin V, Capron E, Colombaroli D, Daniau AL, Dyez KA, Felis T, Finkelstein SA, Jaccard SL, McClymont EL, Rovere A, Sutter J, Wolff EW, Affolter S, Bakker P, Ballesteros-Cánovas JA, Barbante C, Caley T, Carlson AE, Churakova (Sidorova) O, Cortese G, Cumming BF, Davis BAS, de Vernal A, Emile-Geay J, Fritz SC, Gierz P, Gottschalk J, Holloway MD, Joos F, Kucera M, Loutre MF, Lunt DJ, Marcisz K, Marlon JR, Martinez P, Masson-Delmotte V, Nehrbass-Ahles C, Otto-Bliesner BL, Raible CC, Risebrobakken B, Sánchez Goñi MF, Arrigo JS, Sarnthein M, Sjolte J, Stocker TF, Velasquez Alvárez PA, Tinner W, Valdes PJ, Vogel H, Wanner H, Yan Q, Yu Z, Ziegler M and Zhou L (2018) Palaeoclimate constraints on the impact of 2 degree celsius anthropogenic warming and beyond. *Nature Geoscience*, **11**(7), 474–485, ISSN 1752-0908 (doi: 10.1038/s41561-018-0146-0), number: 7 Publisher: Nature Publishing Group

Guo C, Bentsen M, Bethke I, Ilicak M, Tjiputra J, Toniazzo T, Schwinger J and Otterå OH (2019) Description and evaluation of NorESM1-F: a fast version of the Norwegian Earth System Model (NorESM). *Geoscientific Model Development*, **12**(1), 343–362, ISSN 1991-959X (doi: 10.5194/gmd-12-343-2019)

Hansen N, Langen PL, Boberg F, Forsberg R, Simonsen SB, Thejll P, Vandecrux B and Mottram R (2021) Downscaled surface mass balance in Antarctica: impacts of subsurface processes and large-scale atmospheric circulation. *The Cryosphere*, **15**(9), 4315–4333, ISSN 1994-0416 (doi: 10.5194/tc-15-4315-2021), publisher: Copernicus GmbH

Hansen N, Simonsen SB, Boberg F, Kittel C, Orr A, Souverijns N, van Wessem JM and Mottram R (2022) Brief communication: Impact of common ice mask in surface mass balance estimates over the antarctic ice sheet. *The Cryosphere*, **16**(2), 711–718 (doi: https://doi.org/10.5194/tc-16-711-2022)

Helsen MM, van de Berg WJ, van de Wal RSW, van den Broeke MR and Oerlemans J (2013) Coupled regional climate–ice-sheet simulation shows limited Greenland ice loss during the Eemian. *Climate of the Past*, **9**(4), 1773–1788, ISSN 1814-9324 (doi: 10.5194/cp-9-1773-2013)

Hermann M, Box JE, Fausto RS, Colgan WT, Langen PL, Mottram R, Wuite J, Noël B, van den Broeke MR and van As D (2018) Application of PROMICE Q-Transect in Situ Accumulation and Ablation Measurements

(2000–2017) to Constrain Mass Balance at the Southern Tip of the Greenland Ice Sheet. *Journal of Geophysical Research: Earth Surface*, **123**(6), 1235–1256, ISSN 2169-9011 (doi: 10.1029/2017JF004408), _eprint: https://onlinelibrary.wiley.com/doi/pdf/10.1029/2017JF004408

Hvidberg CS, Grinsted A, Dahl-Jensen D, Khan SA, Kusk A, Andersen JK, Neckel N, Solgaard A, Karlsson NB, Kjaer HA and Vallelonga P (2020) Surface velocity of the northeast greenland ice stream (negis): assessment of interior velocities derived from satellite data by gps. *CRYOSPHERE*, **14**(10), 3487–3502, ISSN 1994-0416 (doi: 10.5194/tc-14-3487-2020)

Jevrejeva S, Grinsted A and Moore JC (2014) Upper limit for sea level projections by 2100. *Environmental Research Letters*, **9**(10), 104008, ISSN 1748-9326 (doi: 10.1088/1748-9326/9/10/104008)

Johnsen S, DahlJensen D, Gundestrup N, Steffensen J, Clausen H, Miller H, Masson-Delmotte V, Sveinbjornsdottir A and White J (2001) Oxygen isotope and palaeotemperature records from six greenland ice-core stations: Camp century, dye-3, grip, gisp2, renland and northgrip. *JOURNAL OF QUATERNARY SCIENCE*, **16**(4), 299–307, ISSN 0267-8179 (doi: 10.1002/jqs.622)

Johnsen SJ, Dansgaard W and White JWC (1989) The origin of arctic precipitation under present and glacial conditions. *TELLUS SERIES B-CHEMICAL AND PHYSICAL METEOROLOGY*, **41**(4), 452–468, ISSN 1600-0889 (doi: 10.1111/j.1600-0889.1989.tb00321.x)

Langen PL, Mottram RH, Christensen JH, Boberg F, Rodehacke CB, Stendel M, van As D, Ahlstrøm AP, Mortensen J, Rysgaard S, Petersen D, Svendsen KH, Adalgeirsdóttir G and Cappelen J (2015) Quantifying Energy and Mass Fluxes Controlling Godthåbsfjord Freshwater Input in a 5-km Simulation (1991–2012)*,+. *Journal of Climate*, **28**(9), 3694–3713, ISSN 0894-8755, 1520-0442 (doi: 10.1175/JCLI-D-14-00271.1)

Langen PL, Fausto RS, Vandecrux B, Mottram RH and Box JE (2017) Liquid Water Flow and Retention on the Greenland Ice Sheet in the Regional Climate Model HIRHAM5: Local and Large-Scale Impacts. *Frontiers in Earth Science*, **4**, 110, ISSN 2296-6463 (doi: 10.3389/feart.2016.00110)

Merz N, Born A, Raible CC, Fischer H and Stocker TF (2014) Dependence of Eemian Greenland temperature reconstructions on the ice sheet topography. *Climate of the Past*, **10**(3), 1221–1238, ISSN 1814-9324 (doi: 10.5194/cp-10-1221-2014)

Mottram R (2020) Surface Mass Balance of the Greenland Ice Sheet: Polar Portal

Mottram R, Boberg F, Langen PL, Yang S, Rodehacke C, Christensen JH and Madsen MS (2017) Surface mass balance of the Greenland ice sheet in the regional climate model HIRHAM5: Present state and future prospects. *Low Temperature Science*, **75**, 105–115 (doi: 10.14943/lowtemsci.75.105), publisher: The Institute of Low Temperature Science, Hokkaido University

Mottram R, B Simonsen S, Høyer Svendsen S, Barletta VR, Sandberg Sørensen L, Nagler T, Wuite J, Groh A, Horwath M, Rosier J, Solgaard A, Hvidberg CS and Forsberg R (2019) An Integrated View of Greenland Ice Sheet Mass Changes Based on Models and Satellite Observations. *Remote Sensing*, **11**(12), 1407 (doi: 10.3390/rs11121407), number: 12 Publisher: Multidisciplinary Digital Publishing Institute

Pedersen RA, Langen PL and Vinther BM (2016) Greenland during the last interglacial: the relative importance of insolation and oceanic changes. *Climate of the Past*, **12**(9), 1907–1918, ISSN 1814-9332 (doi: 10.5194/cp-12-1907-2016)

Plach A, Nisancioglu KH, Le clec'h S, Born A, Langebroek PM, Guo C, Imhof M and Stocker TF (2018) Eemian Greenland SMB strongly sensitive to model choice. *Climate of the Past*, **14**(10), 1463–1485, ISSN 1814-9324 (doi: 10.5194/cp-14-1463-2018)

Plach A, Vinther BM, Nisancioglu KH, Vudayagiri S and Blunier T (2021a) Greenland climate simulations show high Eemian surface melt which could explain reduced total air content in ice cores. *Climate of the Past*, **17**(1), 317–330, ISSN 1814-9324 (doi: 10.5194/cp-17-317-2021)

Plach A, Vinther BM, Nisancioglu KH, Vudayagiri S and Blunier T (2021b) Greenland climate simulations show high Eemian surface melt which could explain reduced total air content in ice cores. *Climate of the Past*, **17**(1), 317–330, ISSN 1814-9324 (doi: 10.5194/cp-17-317-2021)

Rohling EJ, Hibbert FD, Grant KM, Galaasen EV, Irvalı N, Kleiven HF, Marino G, Ninnemann U, Roberts AP, Rosenthal Y, Schulz H, Williams FH and Yu J (2019) Asynchronous Antarctic and Greenland ice-volume contributions to the last interglacial sea-level highstand. *Nature Communications*, **10**(1), 5040, ISSN 2041-1723 (doi: 10.1038/s41467-019-12874-3), bandiera_abtest: a Cc_license_type: cc_by Cg_type: Nature Research Journals Number: 1 Primary_atype: Research Publisher: Nature Publishing Group Subject_term: Palaeoceanography;Palaeoclimate Subject_term_id: palaeoceanography;palaeoclimate

van de Berg WJ, van den Broeke M, Ettema J, van Meijgaard E and Kaspar F (2011) Significant contribution of insolation to Eemian melting of the Greenland ice sheet. *Nature Geoscience*, **4**(10), 679–683, ISSN 1752-0908 (doi: 10.1038/ngeo1245), bandiera_abtest: a Cg_type: Nature Research Journals Number: 10 Primary_atype: Research Publisher: Nature Publishing Group Subject_term: Cryospheric science;Palaeoclimate Subject_term_id: cryospheric-science;palaeoclimate

van de Berg WJ, van den Broeke MR, van Meijgaard E and Kaspar F (2013) Importance of precipitation seasonality for the interpretation of Eemian ice core isotope records from Greenland. *Climate of the Past*, **9**(4), 1589–1600, ISSN 1814-9324 (doi: 10.5194/cp-9-1589-2013)

Anomalies relative to reference

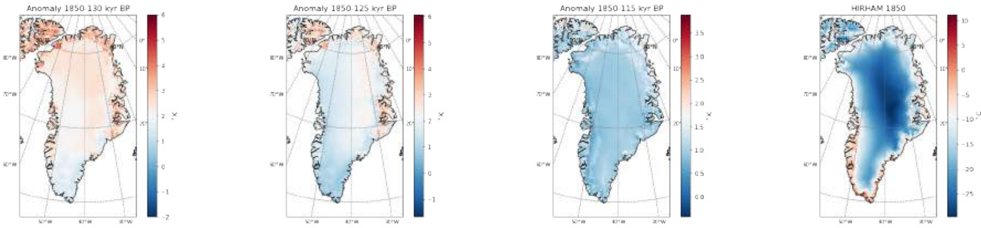

(a) 130ka **(b)** 125ka **(c)** 115ka **(d)** Reference

Fig. 12. *Development of temperature over Greenland during the Eemian interglacial period from HIRHAM5. Anomalies calculated by taking the individual palaeo runs minus the pre-industrial run as reference.*

Anomalies relative to reference

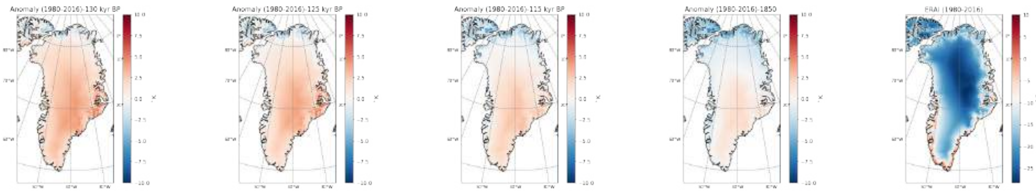

(a) 130ka **(b)** 125ka **(c)** 115ka **(d)** 1850 **(e)** Reference

Fig. 13. *Development of temperature over Greenland during the Eemian interglacial and pre-industrial period from HIRHAM5. Anomalies calculated by taking the individual model runs from HIRHAM5 minus present-day simulation from ERA-Interim as reference.*

Yin Q and Berger A (2015) Interglacial analogues of the Holocene and its natural near future. *Quaternary Science Reviews*, **120**, 28–46, ISSN 02773791 (doi: 10.1016/j.quascirev.2015.04.008)

Zolles T and Born A (2021) Sensitivity of the Greenland surface mass and energy balance to uncertainties in key model parameters. *The Cryosphere*, **15**(6), 2917–2938, ISSN 1994-0416 (doi: 10.5194/tc-15-2917-2021), publisher: Copernicus GmbH

Anomalies relative to reference

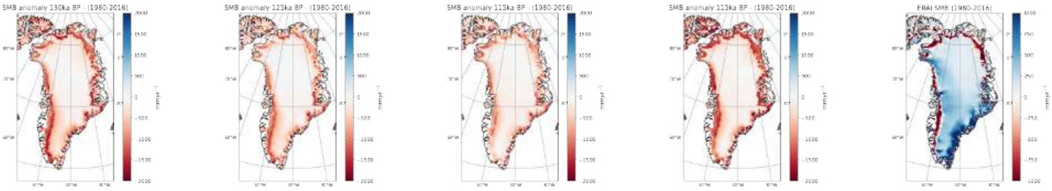

(a) 130ka **(b)** 125ka **(c)** 115ka **(d)** 1850 **(e)** Reference

Fig. 14. *Development of SMB over Greenland during the Eemian interglacial and pre-industrial period from the offline model. Anomalies calculated by taking the individual model runs from the offline model minus present-day simulation from ERA-Interim as reference.*

APPENDIX

TEMPERATURE

COMPARISON WITH ERA-INTERIM

In the plots above we generally see, that the SMB is lower in the Eemian compared to present day simulations of SMB.

The figure shows higher values of SMB in the present day, which we expected, as we know that the Greenland ice sheet was smaller during the Eemian than today. In comparing the SMB values from the offline model and the HIRHAM5 model that are forced with ERA-Interim in figure 14 we see, that that there is a lot more melt at the ablation zone during the Eemian than the present day.

Figure 15 generally show higher temperatures at the present day in the southern part of Greenland and the ablation zone. The simulations from the offline model thus disagrees with the consensus that the Eemian interglacial period were 1-2 degrees warmer in Greenland than the Holocene.

Figure 16 show that the ERA-Interim has a lot more precipitation in the southeastern part of Greenland corresponding to the higher temperatures in the same region at the temperature plot in figure 12. Generally we see that the southern part of Greenland gets the most precipitation in the present-day simulation form ERA-Interim.

When the climate simulations from the offline model are compared with present day simulation from ERA-Interim instead, we especially see lower melt in the ablation zone in the offline model than ERA-

Anomalies relative to reference

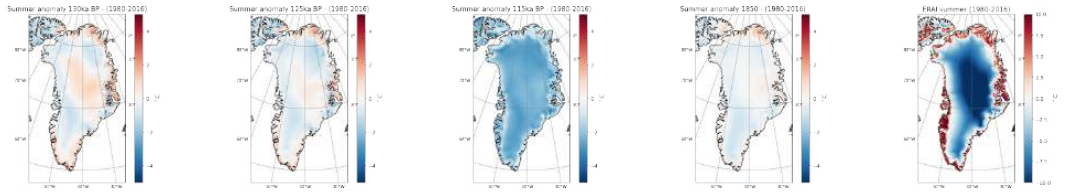

(a) 130ka **(b)** 125ka **(c)** 115ka **(d)** 1850 **(e)** Reference

Fig. 15. *Development of summer temperature over Greenland during the Eemian interglacial and pre-industrial period from HIRHAM5. Anomalies calculated by taking the individual model runs from HIRHAM5 minus present-day simulation from ERA-Interim as reference.*

Anomalies relative to reference

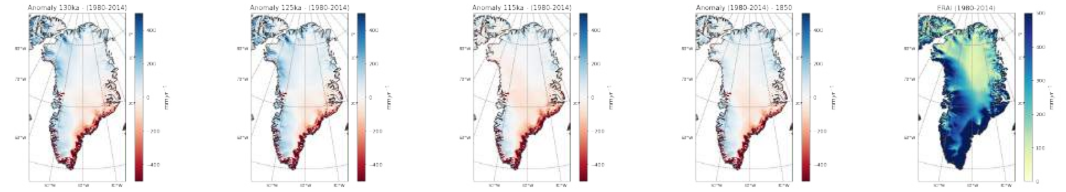

(a) 130ka **(b)** 125ka **(c)** 115ka **(d)** 1850 **(e)** Reference

Fig. 16. *Development of precipitation over Greenland during the Eemian interglacial and pre-industrial period from HIRHAM5. Anomalies calculated by taking the individual model runs from HIRHAM5 minus present-day simulation from ERA-Interim as reference.*

Anomalies relative to reference

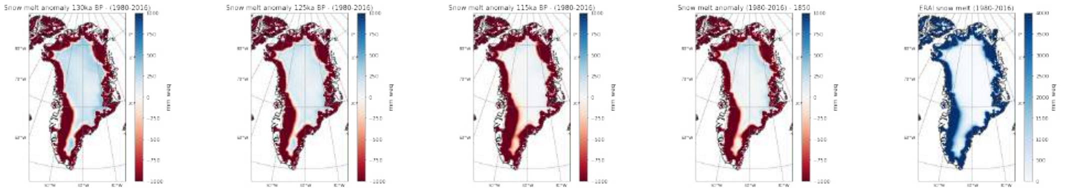

(a) 130ka **(b)** 125ka **(c)** 115ka **(d)** 1850 **(e)** Reference

Fig. 17. *Development of snow melt over Greenland during the Eemian interglacial and pre-industrial period from HIRHAM5. Anomalies calculated by taking the individual model runs from the offline model minus present-day simulation from ERA-Interim as reference.*

Anomalies relative to reference

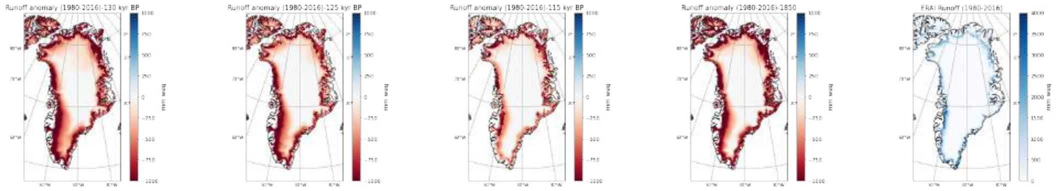

(a) 130ka **(b)** 125ka **(c)** 115ka **(d)** 1850 **(e)** Reference

Fig. 18. *Development of runoff over Greenland during the Eemian interglacial and pre-industrial period from HIRHAM5. Anomalies calculated by taking the individual model runs from the offline model minus present-day simulation from ERA-Interim as reference.*

Anomalies relative to reference

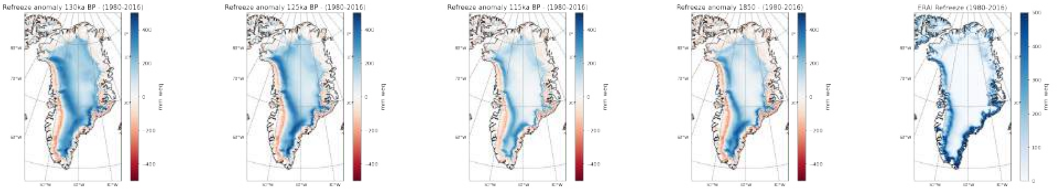

(a) 130ka **(b)** 125ka **(c)** 115ka **(d)** 1850 **(e)** Reference

Fig. 19. *Development of refreeze over Greenland during the Eemian interglacial and pre-industrial period from HIRHAM5. Anomalies calculated by taking the individual model runs from the offline model minus present-day simulation from ERA-Interim as reference.*

Interim. This is illustrated by the bright red of the Greenland ice sheet.

However compared to the present-day as shown in figure 18, we see lower values of runoff in both the Eemian and the pre-industrial from the offline model compared to present-day simulation from ERA-Interim.

The beginning and middle of the Eemian show higher refreezing values in the interior part of the Greenland ice sheet compared to present day simulation. However the ablation zone are lower than present-day.

The Antarctic ice sheet is the largest ice sheet on Earth, it has the potential to raise the global mean sea level by 58 metres if it melts completely. It is therefore important to know the mass balance of the ice sheet to see if it is losing or gaining mass. There are three ways to calculate the mass balance, altimetry, mass budget, and gravity. Two of these, altimetry and mass budget, require knowledge of the firn pack over the ice sheet. This Ph.D. thesis focuses on reconciling/determining those variables and estimating the mass balance. When using the mass budget method to estimate the mass balance you need the surface mass balance and the discharge values. In this project, a firn model has been further developed to model the Antarctic firn pack, this model also calculates the surface mass balance to use in the mass budget method. In the altimetry method, the satellite ICESat-2 has been used to measure the surface elevation change, this gives the volume change over the ice sheet, which can be converted into mass change. However, mass change is not the only variable that can contribute to surface elevation changes, firn compaction can also contribute to an elevation change without changing the mass. Therefore, a firn model is needed to calculate the contribution of this variable. This project has calculated the surface mass balance from 1979 to 2021 and used the altimetry method to derive the mass balance of Antarctica from 2018 to 2021.

Technical
University of
Denmark

Elektrovej, Building 327
2800 Kgs. Lyngby
Tlf. 4525 1700

www.space.dtu.dk